

# **Understanding Rate Effects in Cohesive Soils**

Kin Shing Oswald Li

*Thesis submitted to*

The University of Sheffield

Department of Civil and Structural Engineering

*for the degree of*

Doctor of Philosophy

April 2024



# Abstract

Military infrastructure composed of geomaterials and soils have been extremely commonplace in the construction of defensive structures to protect vital personnel and assets. The necessity for soils to withstand extreme loading from the effects of blast and fragmentation prompts the understanding of soil behaviour within these loading regimes to be of great significance, especially to enable the development of more rigorous soil models and proficient methods for design engineers to counteract new threats.

While the use of sand and gravel have been well researched in current literature, the behaviour of cohesive soils such as clays as a protective material against high-strain loading is an under explored area of research. Subsequently, a primary property of soils is the strength exhibited when the material is affected by a lateral confining pressure. The response of a material under particular confining mechanisms when subject to blast or fragmentation is a key area of investigation. While this is commonplace in standard geotechnical engineering testing at lower stresses and strains, it becomes considerably more challenging at higher stresses and strain rates

One-dimensional compression tests are conducted using the split-Hopkinson pressure bar (SHPB) to investigate strain rate dependence and strength of the soil. Conventional free field SHPB experiments typically used with solid materials is compared with rigid lateral confinement mechanisms traditionally used on soft materials, this provides a basis of extremity and prompts a foundation for the application of a modified SHPB setup that allows for the soil sample to be partial laterally confined within a water reservoir during SHPB tests. This modified SHPB apparatus allows for lateral stresses to be monitored by measuring the change in pressure in the water reservoir through the use of a pressure transducer, yet the test still proceeds in a similar manner to an unconfined case and hence allows for triaxial behaviour to be much better characterised.

Modern numerical modelling techniques to capture soil behaviour and high-strain-rate testing are evaluated using LS-DYNA. The performance of various material models and geometrical techniques was assessed to determine the effectiveness and limitations with current numerical modelling techniques. The development of numerical models are coupled with experimental data to provide a comprehensive characterisation of cohesive soils and the factors that affect their attenuation of high-strain-rate loading such as blast or fragmentation.



# Acknowledgements

Firstly, I extend my sincere gratitude to my PhD supervisors Prof. Sam Clarke and Dr. Andrew Barr, without whom this thesis would not have been possible. Sam, your generous guidance and friendship have genuinely made this PhD one of the most enjoyable and rewarding periods of my life. Even during the heights of COVID lockdown, our weekly catchups remained as one of the sessions I would always look forward to. I'm grateful to have had a supervisor as passionate and committed to their work and proud to be able to have been under your tutelage these last couple years. Andrew, thanks for always being open to help whenever needed, your technical insight has been invaluable and vital in guiding me throughout my PhD. Thanks especially for your assistance and expertise through all the SHPB work over these years.

I would like to thank everyone in the Blast and Impact Dynamics group with whom I have had numerous insightful discussions and interactions with over the years, all of which have greatly enriched my research and knowledge. I'm grateful to all the technicians on site at Buxton who provided invaluable assistance in setting up for experimental testing. I would also like to thank everyone who worked in D111 during my team here, and for creating such a welcoming and friendly environment for me to work in. Special thank you goes to Arthur, whose daily work discussions and friendly chats have provided immense support throughout this project, without which much of the final product of this research would not have come into fruition the way it has.

Lastly, I am deeply thankful to my family for their endearing support during my time in Sheffield, especially for giving me motivation to persist in the pursuit of my personal goals and aspirations.

*Oswald Li*

*April 2024*



# Contents

List of figures . . . . .	xiv
List of tables . . . . .	xxvi
<b>1 Introduction</b>	<b>1</b>
1.1 Background . . . . .	1
1.2 Scope and objective . . . . .	2
1.3 Thesis outline . . . . .	3
1.4 Published Work . . . . .	4
1.4.1 Published . . . . .	4
1.4.2 Under review . . . . .	5
<b>2 Literature review</b>	<b>7</b>
2.1 Introduction . . . . .	7
2.2 Testing strain effects on soils . . . . .	7
2.3 Material characterisation . . . . .	8
2.3.1 Kaolin clay . . . . .	11
2.4 Split-Hopkinson pressure bar . . . . .	11
2.4.1 Principles and theory . . . . .	12
2.4.2 Existing limitations to the SHPB method . . . . .	15

2.5	One-dimensional compression and strain rate testing . . . . .	17
2.5.1	Quasi-static . . . . .	17
2.5.2	High-strain-rate . . . . .	20
2.6	Numerical modelling of high-strain-rates . . . . .	26
2.6.1	Validation of LS-DYNA material models . . . . .	27
2.6.2	Existing approaches to model development with LS-DYNA . . . . .	35
2.6.3	Existing approaches to SHPB modelling . . . . .	36
2.7	Summary . . . . .	38
<b>3</b>	<b>Preliminary material testing and characterisation</b>	<b>39</b>
3.1	Introduction . . . . .	39
3.2	Material characterisation . . . . .	40
3.2.1	Particle density . . . . .	40
3.2.2	Particle shape . . . . .	41
3.2.3	Particle size distribution . . . . .	41
3.2.4	Particle mineralogy . . . . .	41
3.2.5	Atterberg limits . . . . .	43
3.3	Quasi-static testing . . . . .	45
3.3.1	Triaxial testing . . . . .	46
3.3.2	Oedometer testing . . . . .	50
3.3.3	Discussion and findings from quasi-static testing . . . . .	52
3.4	Sample preparation . . . . .	54
3.4.1	Initial material preparation . . . . .	54
3.4.2	Moisture content variation . . . . .	54
3.5	High-strain-rate test programme . . . . .	55



3.6	Summary . . . . .	57
<b>4</b>	<b>High-strain-rate testing of kaolin clay</b>	<b>59</b>
4.1	Introduction . . . . .	59
4.2	High-strain-rate methodology . . . . .	59
4.2.1	Split-Hopkinson pressure bar methodology . . . . .	59
4.2.2	Setup adjustments and invalid data . . . . .	61
4.2.3	Unconfined SHPB testing procedure . . . . .	64
4.2.4	Confined SHPB testing procedure . . . . .	65
4.2.5	Bar to bar calibration . . . . .	67
4.3	Signal processing and data analysis . . . . .	68
4.3.1	Overview and purpose of function . . . . .	68
4.3.2	Pulse detection via automatic trigger and optimisation of pulse boundaries . . . . .	70
4.3.3	Pulse alignment and stress equilibrium . . . . .	71
4.3.4	Adjustment of stresses for confinement mechanism . . . . .	73
4.3.5	Dispersion correction . . . . .	74
4.3.6	Function for dispersion correction . . . . .	75
4.3.7	Data processing capabilities with other materials . . . . .	79
4.3.8	Discussion and summary of algorithm functionality . . . . .	79
4.4	Unconfined testing of kaolin clay . . . . .	82
4.4.1	Material properties . . . . .	83
4.4.2	Experimental results . . . . .	83
4.4.3	Phase behaviour in unconfined testing . . . . .	85
4.4.4	Effect of strain rate . . . . .	88

4.5	Confined testing of kaolin clay . . . . .	95
4.5.1	Confined SHPB results . . . . .	96
4.5.2	Phase behaviour in confined SHPB testing . . . . .	97
4.5.3	Effect of strain rate . . . . .	100
4.6	Discussion of SHPB testing . . . . .	111
4.7	Summary . . . . .	113
<b>5</b>	<b>Partial lateral confinement for evaluation of confinement effects</b>	<b>115</b>
5.1	Introduction . . . . .	115
5.2	Partial lateral confined apparatus . . . . .	116
5.2.1	Experimental setup . . . . .	116
5.2.2	Reservoir support stand . . . . .	118
5.2.3	Partial lateral confined SHPB testing procedure . . . . .	118
5.2.4	Signal processing for partial lateral confined testing . . . . .	120
5.3	Partial lateral confined testing of kaolin clay . . . . .	120
5.3.1	Effects of moisture content . . . . .	121
5.3.2	Effects of strain rate . . . . .	127
5.4	High-strain-rate testing of water via partially lateral confined apparatus . . . . .	129
5.4.1	Methodology and setup for water tests . . . . .	129
5.4.2	Results of water testing . . . . .	131
5.4.3	Discussion of high-strain-rate water testing . . . . .	135
5.5	Discussion of partial lateral confined testing of kaolin clay . . . . .	135
5.5.1	Comparison with water . . . . .	135
5.5.2	Comparison with unconfined and confined SHPB testing . . . . .	137
5.5.3	Setup limitations and future development . . . . .	140

5.6	Discussion of confinement effects from partial lateral confined testing . . .	140
5.7	Summary . . . . .	141
<b>6</b>	<b>Development of numerical modelling techniques for high-strain testing</b>	<b>143</b>
6.1	Introduction . . . . .	143
6.2	Initial model setup and geometry . . . . .	144
6.3	Validation of material models . . . . .	148
6.3.1	Elastic Plastic Hydro . . . . .	148
6.3.2	Mohr-Coulomb . . . . .	151
6.4	Optimisation of model geometry . . . . .	154
6.4.1	Constrained nodes . . . . .	154
6.4.2	Transition to 3-D model . . . . .	155
6.4.3	ALE air domain . . . . .	159
6.4.4	Merging interfaces . . . . .	160
6.4.5	Boundary constraint over 3-D sample . . . . .	161
6.5	Smoothed Particle Hydrodynamics (SPH) . . . . .	164
6.5.1	Rigid confining ring . . . . .	170
6.5.2	Modifications to rigid confining ring . . . . .	171
6.6	Comparison to experimental results . . . . .	176
6.6.1	Unconfined model . . . . .	176
6.6.2	Confined model . . . . .	178
6.7	Numerical modelling for partial lateral confined testing . . . . .	182
6.7.1	Model material cards . . . . .	183
6.7.2	Model setup . . . . .	183
6.7.3	Results of numerical model . . . . .	184

6.7.4	Validation of pressure reading . . . . .	188
6.8	Internal sample stresses from numerical model . . . . .	190
6.8.1	Unconfined and confined conditions . . . . .	190
6.8.2	Partial lateral confined condition . . . . .	193
6.9	Discussion of numerical modelling . . . . .	198
6.9.1	Limitations and recommendations . . . . .	199
6.10	Effects of confinement in cohesive soils . . . . .	200
6.11	Summary . . . . .	203
<b>7</b>	<b>Summary and conclusions</b>	<b>205</b>
7.1	Summary . . . . .	205
7.2	Conclusions . . . . .	207
7.2.1	Quasi-static testing and material characterisation . . . . .	207
7.2.2	Confinement effects . . . . .	207
7.2.3	Phase behaviour and influence of moisture . . . . .	209
7.2.4	Strain rate effects . . . . .	209
7.2.5	Numerical modelling . . . . .	210
7.3	Future research . . . . .	210
7.3.1	Dependence on material properties . . . . .	211
7.3.2	Numerical modelling of cohesive soils . . . . .	211
7.3.3	Partial lateral confined apparatus . . . . .	212
7.3.4	Signal processing . . . . .	212
	<b>Bibliography</b>	<b>213</b>
	<b>A Published work</b>	<b>221</b>

A.1	Introduction . . . . .	221
A.2	Characterisation of cohesive soils under high-strain-rate via split-Hopkinson pressure bar . . . . .	222
A.3	An open-source algorithm for correcting stress wave dispersion in split-Hopkinson pressure bar experiments . . . . .	225
A.4	Split-Hopkinson pressure bar testing of water with partial lateral confinement	245
A.5	High-strain-rate behaviour of cohesive soils . . . . .	255
A.6	Impact of partial lateral confinement on high-strain-rate behaviour of cohesive soils . . . . .	298
<b>B</b>	<b>Sample measurement data</b>	<b>315</b>
B.1	Introduction . . . . .	315
B.2	Unconfined tests . . . . .	316
B.3	Confined tests . . . . .	321
B.4	Partial lateral confined tests . . . . .	324
<b>C</b>	<b>Striker bar velocity tests</b>	<b>327</b>
C.1	Introduction . . . . .	327
C.2	Speed test log . . . . .	327
<b>D</b>	<b>Signal processing and analysis of SHPB data with computational Python algorithm</b>	<b>331</b>
D.1	Introduction . . . . .	331
D.2	SHPB_processing.py . . . . .	332
D.3	dispersion.py . . . . .	354
<b>E</b>	<b>Relevant LS-DYNA keywords</b>	<b>357</b>
E.1	Introduction . . . . .	357

E.2	Material cards . . . . .	357
E.3	Contact algorithms . . . . .	359
E.4	Equations of state (EOS) . . . . .	360
<b>F</b>	<b>Additional SHPB designs</b>	<b>361</b>
F.1	Introduction . . . . .	361
F.2	Reservoir support stand . . . . .	362

# List of Figures

2.1	Strain rate classifications and examples of phenomena in soils . . . . .	8
2.2	Schematic of the main components of a SHPB test under unconfined conditions	12
2.3	Effects of specimen thickness (RTV 630 silicone rubber) on dynamic equilibrium under the same loading stress rate in SHPB tests ( $1.25 \times 10^5$ MPa $s^{-1}$ ): (a) 6.56 mm thick; (b) 4.59 mm thick; (c) 3.07 mm thick; (d) 1.52 mm thick, after Song and Chen (2004) . . . . .	16
2.4	Forces at the bar-sample interface for a) conventional SHPB experiment b) pulse shaped SHPB experiment, after Frew et al. (2005). . . . .	16
2.5	Void ratio versus applied vertical stress for Loose and dense specimens of Black Beauty Slag, after Hagerty et al. (1993) . . . . .	18
2.6	Variation of energy per unit volume at different loading speeds and soil moisture contents, after Niyamapa et al. (1992) . . . . .	19
2.7	a) e-log p curves of dry sand of several different densities under confinement of SHPB experiment and b) typical strain-rate and strain time history, after Luo et al. (2011) . . . . .	21
2.8	Modified SHPB apparatus with pressure confinement inducer: 1 – gas tank; 2 – pressure vessel; 3 – striker; 4 – thin baffle screen; 5 and 8 – elastic bars; 6 – strain gauge; 7 – specimen; 9 – steel frame; 10 – confining pressure setup; 11 – pressure loading unit, from Li et al. (2008). . . . .	21
2.9	Strain rate effect on triaxial behaviour of dry quartz sand at confining pressures of a) 50 MPa, b) 100MPa, after Martin et al. (2013). . . . .	22

2.10	Experimental results depicting variation of variables a) dynamic triaxial compressive strength with the confinement pressure at different strain rates, b) dynamic triaxial compressive strength with the strain rate at different confinement pressures, c) peak strain with the strain rate at different confinement pressures, d) peak strain with the confinement pressure at different strain rates, e) secant modulus with strain rate at different confinement pressures, and f) secant modulus with the confining confinement, from Gong et al. (2019).	24
2.11	Partial lateral confined SHPB tests on dry quartz sand a) axial and radial stresses, b) axial stress-strain response, after Barr et al. (2016).	25
2.12	Axial stress–dry density behaviour of Soil and Foam SHPB specimen compared to mean experimental data, from Barr (2016).	30
2.13	Pressure–volume behaviour of Soil and Foam SHPB specimen, and defined compressibility curve, from Barr (2016).	30
3.1	Electron microscope images of kaolin clay under magnification of a) 20000x, and b) 40000x.	42
3.2	Cumulative particle size distribution histogram of kaolin clay based on data sheet provided from supplier (Imerys, Performance Minerals).	43
3.3	Soil texture triangle describing soil texture based on mineral proportions of sand, silt and clay, adapted from Groenendyk et al. (2015).	44
3.4	X-ray diffraction data for kaolin clay.	44
3.5	Casagrande plasticity chart showing different soil classification zones. Sample is classified as a lean clay (CL) as shown by the marker.	45
3.6	Example of evidence of shear failure after triaxial test of kaolin sample consolidated at 400 kPa.	47
3.7	Triaxial tests (3 trials) on kaolin clay at moisture content of a) 44% b) 42% c) 41%. Points of shear failure are marked for each test with a red marker.	48
3.8	Mohr circles based on triaxial tests on kaolin clay at moisture contents of a) 44% b) 42% c) 41%.	49
3.9	Image after kaolin was dynamically consolidated using an oedometer to 3200kPa.	51



3.10	Variation of dry density with stress via oedometer test for kaolin consolidated dynamically and statically. . . . .	51
3.11	Variation of void ratio with stress via oedometer test for kaolin consolidated dynamically and statically. . . . .	52
4.1	Split-Hopkinson pressure bar a) strain gauge arrangement, b) Wheatstone bridge. . . . .	61
4.2	Schematic of old gas gun. . . . .	62
4.3	Incident and transmitted pulse stresses from preliminary SHPB tests. . . . .	63
4.4	Schematic of new gas gun with speed trap mechanism installed. . . . .	64
4.5	Schematic of the main components of a SHPB test under unconfined conditions	64
4.6	Confining ring a) strain gauge arrangement, b) Wheatstone bridge. . . . .	66
4.7	Typical incident, reflected, and transmitted stress pulses obtained from bar to bar calibration test. . . . .	67
4.8	Typical stress wave difference between stress at front and back interfaces, normalised by their mean for a) kaolin clay, b) aluminium, c) medium sand.	72
4.9	Processed results of front stress dispersion correction and simple timeshift for a) kaolin clay, b) aluminium, c) medium sand with confining ring. . . . .	78
4.10	Stress at sample interfaces for SHPB tests on a) aluminium, and b) medium sand with confining ring. . . . .	80
4.11	Average strain rate variation during unconfined SHPB tests on kaolin clay at 8, 12, and 16 m/s, corresponding to an average peak strain rate of 1200, 1900, and 2700 s <sup>-1</sup> . . . . .	82
4.12	Front and back stress for unconfined tests at 16 m/s on kaolin samples at 20% moisture content. . . . .	84
4.13	Typical front stress variation for unconfined SHPB tests at 8, 12, and 16 m/s.	85
4.14	Phase behaviour according to material properties for unconfined testing of kaolin clay at 16 m/s (2700 s <sup>-1</sup> ). Phase boundaries 2 and 3 are marked 'B2' and 'B3'. . . . .	86
4.15	Back stress from unconfined testing on kaolin clay at 16 m/s at moisture contents corresponding to a) phase 0, b) phase 1, c) phase 2, and d) phase 3	87

4.16	Typical stress vs time variation from unconfined SHPB tests on saturated kaolin clay at 8, 12, and 16 m/s . . . . .	89
4.17	Variation of stiffness with strain rate based on unconfined SHPB tests at three striker bar speeds of 8, 12, 16 m/s, with trend line to show strain rate dependence. . . . .	89
4.18	Typical strain-time history during unconfined SHPB tests on kaolin clay at 8, 12, and 16 m/s. . . . .	90
4.19	Phase behaviour according to material properties for unconfined testing of kaolin clay at a) 8 m/s ( $1900 \text{ s}^{-1}$ ) and b) 12 m/s ( $2700 \text{ s}^{-1}$ ). Phase boundaries 2 and 3 are marked 'B2' and 'B3'. . . . .	91
4.20	Back stress from unconfined testing on kaolin clay at 8 m/s at moisture contents corresponding to a) phase 0, b) phase 1, c) phase 2, and d) phase 3 . . .	92
4.21	Back stress from unconfined testing on kaolin clay at 12 m/s at moisture contents corresponding to a) phase 0, b) phase 1, c) phase 2, and d) phase 3 . . .	93
4.22	Strain rate variation during unconfined SHPB at 18, 20, and 22 m/s, corresponding to an average peak strain rate of 2800, 3000, and $3300 \text{ s}^{-1}$ . . . . .	94
4.23	Typical strain-time history during unconfined SHPB tests on kaolin clay at 18, 20, and 22 m/s. . . . .	95
4.24	Average strain rate variation during confined SHPB tests on kaolin clay at 18, 20, and 22 m/s, corresponding to an average of 2500, 2800, and $3100 \text{ s}^{-1}$ . . . . .	96
4.25	Front, back, and radial stresses for confined tests at 18 m/s on saturated kaolin samples at 41% moisture content. . . . .	97
4.26	Typical stress wave difference between front and back interfaces, normalised by their mean for saturated kaolin clay. . . . .	98
4.27	Typical front stress variation for confined SHPB tests at 18, 20, 22 m/s. . . . .	98
4.28	Phase behaviour according to material properties for confined testing of kaolin clay at 18 m/s ( $2500 \text{ s}^{-1}$ ). Phase boundaries 2 and 3 are marked 'B2' and 'B3'. . . . .	99
4.29	Back stress from confined testing on kaolin clay at 18 m/s at moisture contents corresponding to a) phase 0, b) phase 1, c) phase 2, and d) phase 3. . . . .	101
4.30	Radial stress from confined testing on kaolin clay at 18 m/s at moisture contents corresponding to a) phase 0, b) phase 1, c) phase 2, and d) phase 3. . . . .	102

4.31	Typical strain-time history during confined SHPB tests on kaolin clay at 12, 18, 20, and 22 m/s. . . . .	103
4.32	Phase behaviour according to material properties for confined testing of kaolin clay at a) 20 m/s ( $2800 \text{ s}^{-1}$ ) and b) 22 m/s ( $3100 \text{ s}^{-1}$ ). Phase boundaries 2 and 3 are marked 'B2' and 'B3'. . . . .	105
4.33	Back stress from confined testing on kaolin clay at 20 m/s at moisture contents corresponding to a) phase 0, b) phase 1, c) phase 3. . . . .	106
4.34	Radial stress from confined testing on kaolin clay at 20 m/s at moisture contents corresponding to a) phase 0, b) phase 1, c) phase 3. . . . .	107
4.35	Back stress from confined testing on kaolin clay at 22 m/s at moisture contents corresponding to a) phase 0, b) phase 1, c) phase 3. . . . .	108
4.36	Radial stress from confined testing on kaolin clay at 22 m/s at moisture contents corresponding to a) phase 0, b) phase 1, c) phase 3. . . . .	109
4.37	Typical stress vs time variation from confined SHPB tests on saturated kaolin clay at 8, 12, and 16 m/s . . . . .	110
4.38	Typical strain rate variation during confined SHPB tests on kaolin clay at 12 m/s, corresponding to an average of $1600 \text{ s}^{-1}$ . . . . .	110
4.39	Summary of average stress magnitude within each moisture content phase of kaolin clay, effect of moisture content within individual phases do not show clear relationship. . . . .	111
4.40	High-speed imagery of the instance after loading for confined SHPB test on kaolin clay, showing sample extrusion from the edges of the ring upon impact. . . . .	112
4.41	Typical circumferential strain history of confining ring, showing continual variation even after initial pulses. . . . .	112
5.1	Schematic of the partial lateral confined SHPB apparatus. . . . .	116
5.2	Schematic of the partial lateral confined SHPB apparatus: water reservoir section. . . . .	117
5.3	Image of the sample in between the reservoir support stands prior to the initiation of testing with the partial lateral confined SHPB apparatus; sample is secured between the pressure bars, enveloped by a latex membrane, and secured by small rubber o-rings. . . . .	117

5.4	Simplified schematic of the reservoir support stand used for partial lateral confined tests, water reservoir to be centred and secured between the ball bearings. . . . .	118
5.5	Schematic of sample measurement process a) before and b) after installation inside the reservoir. . . . .	120
5.6	Typical strain rate variation during partial lateral confined SHPB tests on kaolin clay at 12, 16, and 20 m/s, corresponding to an average peak strain rate of 1800, 2500, and 3000 s <sup>-1</sup> . . . . .	122
5.7	Typical strain time history during partial lateral confined SHPB tests on kaolin clay at 12, 16, and 20 m/s. . . . .	122
5.8	Typical front stress variation for partial lateral confined SHPB tests at 12, 16, and 20 m/s. . . . .	123
5.9	Partial lateral confined SHPB test on kaolin clay at 16 m/s: front, back and radial stresses. . . . .	123
5.10	Back stress from partial lateral confined testing on kaolin clay at 16 m/s at moisture contents corresponding to a) phase 0, b) phase 1, c) phase 3. . . .	125
5.11	Radial stress from partial lateral confined testing on kaolin clay at 16 m/s at a) phase 0, b) phase 1, and c) phase 3. . . . .	126
5.12	Typical back stress from partial lateral confined SHPB test on saturated kaolin clay at 12, 16, and 20 m/s . . . . .	128
5.13	Typical radial stress from partial lateral confined SHPB test on saturated kaolin clay at 12, 16, and 20 m/s . . . . .	128
5.14	Typical stress vs strain variation from partial lateral confined SHPB test on saturated kaolin clay at 12, 16, and 20 m/s . . . . .	129
5.15	Schematic of the partially lateral confined SHPB apparatus for water tests: water reservoir section. . . . .	130
5.16	Variation of strain rate during partially-confined SHPB experiments on water. 130	
5.17	Typical response of a partial lateral confined SHPB test on water showing axial and radial stress difference normalised by their mean. . . . .	132
5.18	Typical behaviour of a partial lateral confined SHPB experimental test on water at 16 m/s: incident and reflected pulses from the incident bar. . . . .	132

5.19	Partial lateral confined SHPB test on water at 16 m/s: front, back and radial stresses. . . . .	133
5.20	Partial lateral confined SHPB test on water at 20 m/s: front, back and radial stresses. . . . .	133
5.21	Typical stress vs strain variation from partial lateral confined SHPB test on water at 16 and 20 m/s. . . . .	134
5.22	Typical strain rate variation during SHPB tests for saturated kaolin clay under unconfined, confined, and partial lateral confined conditions with average peak strain rates of 1600, 1800, and 1900 s <sup>-1</sup> respectively. . . . .	136
5.23	Typical back and radial stresses from partial lateral confined SHPB tests on water and saturated kaolin clay at 16 m/s. . . . .	136
5.24	Typical back and radial stress from unconfined, confined, and partial lateral confined SHPB tests. . . . .	138
5.25	Difference between axial and radial stresses from confined SHPB tests on kaolin clay at varying moisture contents. . . . .	139
5.26	Difference between axial and radial stresses from partial lateral confined SHPB tests on kaolin clay at varying moisture contents. . . . .	139
5.27	Summary of average stress magnitude within each moisture content phase for partial lateral confined SHPB tests on kaolin clay, effect of moisture content within individual phases do not show clear relationship. . . . .	141
6.1	Initial LS-DYNA SHPB unconfined model set up containing the incident bar (blue), transmitted bar (green), striker bar (yellow), and sample (red). . . . .	144
6.2	Axial stress recorded with unconfined SHPB LS-DYNA model obtained at strain gauge locations. . . . .	146
6.3	Final time state for initial unconfined SHPB model. . . . .	146
6.4	Close up of initial confined SHPB model with confining ring (grey), with element mesh visualised. . . . .	147
6.5	Final time state for confined SHPB model before computation fails due to negative volume error. . . . .	147
6.6	Final time state for initial unconfined SHPB model with sample modelled using MAT_ELASTIC_PLASTIC_HYDRO. . . . .	150

6.7	Axial stress recorded with unconfined SHPB LS-DYNA model obtained at strain gauge locations, with sample modelled using MAT_ELASTIC_PLASTIC_HYDRO.	150
6.8	Final time state for initial unconfined SHPB model with sample modelled using MAT_MOHR_COULOMB. . . . .	152
6.9	Axial stress recorded with unconfined SHPB LS-DYNA model obtained at strain gauge locations, with sample modelled using MAT_MOHR_COULOMB. . .	152
6.10	Comparison between back stress from experimental and numerical model for unconfined SHPB test on saturated kaolin clay, with sample modelled using MAT_MOHR_COULOMB. . . . .	153
6.11	Axial stress recorded with confined SHPB LS-DYNA model obtained at strain gauge locations prior to failure due to negative volume error, with sample modelled using MAT_MOHR_COULOMB. . . . .	153
6.12	Close up of confined SHPB model with boundary constraint on nodes at edge of sample. . . . .	154
6.13	Top view of radial meshing of cylindrical elements in 3D SHPB model for: incident, transmitter, striker bars, and sample. . . . .	156
6.14	Final time state for 3-D unconfined SHPB model. . . . .	156
6.15	Axial stress recorded with 3-D unconfined SHPB LS-DYNA model obtained at strain gauge location. . . . .	157
6.16	Initial 3-D confined SHPB model with confining ring. . . . .	157
6.17	Final time state for 3-D confined SHPB model before computation fails due to negative volume error. . . . .	158
6.18	3-D confined SHPB model with surrounding ALE air domain. . . . .	159
6.19	Final time state for 3D model of confined SHPB test with ALE air domain before computation fails due to negative volume error. . . . .	160
6.20	Final time state for 3D model of confined SHPB test with all sample interfaces merged before computation fails due to negative volume error. . . . .	161
6.21	Axial stress recorded with confined SHPB LS-DYNA model with all sample interfaces merged, obtained at strain gauge locations prior to failure due to negative volume error. . . . .	162

6.22	Axial stress recorded with confined SHPB LS-DYNA model with all sample interfaces merged, obtained on the ring and on the bar directly adjacent to sample interface. . . . .	162
6.23	3-D confined SHPB model with confining ring, with boundary constraint on nodes at edge of sample. . . . .	163
6.24	Final time state for 3D model of confined SHPB test with all sample interfaces merged before computation fails due to negative volume error. . . . .	163
6.25	Top view of SPH node generation of sample. . . . .	164
6.26	Unconfined SHPB model with sample modelled using SPH nodes. . . . .	165
6.27	Final time state for unconfined SHPB model with sample modelled using SPH nodes. . . . .	165
6.28	Axial stress recorded with unconfined SHPB LS-DYNA model with sample modelled using SPH nodes. . . . .	166
6.29	Comparison between back stress from experimental and numerical model for unconfined SHPB test on saturated kaolin clay, with sample modelled as SPH nodes. . . . .	166
6.30	Confined SHPB model with sample modelled as SPH nodes. . . . .	167
6.31	Final time state for confined SHPB model with sample modelled as SPH nodes, illustrating extreme deformation of confining ring. . . . .	168
6.32	Axial stress recorded with confined SHPB LS-DYNA model with sample modelled as SPH nodes, large amounts of noise recorded. . . . .	168
6.33	High-speed imagery of the instance after loading for unconfined SHPB test on kaolin clay. . . . .	169
6.34	Radial stress recorded on confining ring with confined SHPB LS-DYNA model with sample modelled as SPH nodes. . . . .	170
6.35	Axial stress recorded with confined SHPB LS-DYNA model (SPH) with confining ring modelled as rigid material. . . . .	171
6.36	Comparison between back stress from experimental and numerical model for confined SHPB test on saturated kaolin clay, with confining ring modelled as a rigid ring in the numerical model. . . . .	172

6.37	Confined SHPB model with one “column” of elements on confining ring modelled as elastic material (pink) while rest of the ring is modelled as rigid (grey). . . . .	174
6.38	Top view of confining ring with outer radius made of rigid material (grey), and two radial elemental layers made of elastic material (pink). . . . .	174
6.39	Axial stress from pressure bars and radial stress from confining ring, recorded with confined SHPB LS-DYNA model (SPH) with half rigid and half elastic confining ring. . . . .	175
6.40	Confined SHPB model with half rigid and half elastic material. . . . .	175
6.41	Comparison between back stress from experimental and numerical model for unconfined SHPB tests on saturated kaolin clay. . . . .	177
6.42	Comparison between front stress from experimental and numerical model for unconfined SHPB test on saturated kaolin clay. . . . .	178
6.43	Incident and reflected stresses from unconfined SHPB numerical model. . .	179
6.44	Comparison between radial stress from experimental and numerical model for confined SHPB tests on saturated kaolin clay. . . . .	180
6.45	Comparison between back stress from experimental and numerical model for confined SHPB tests on saturated kaolin clay. . . . .	181
6.46	Comparison between front stress from experimental and numerical model for confined SHPB test on saturated kaolin clay. . . . .	181
6.47	Incident and reflected stresses from confined SHPB numerical model. . . .	182
6.48	LS-DYNA SHPB partial lateral confinement model set up containing the incident bar (blue), transmitted bar (green), striker bar(yellow), and water reservoir (grey). Sample and water annulus are modelled and inside the water reservoir. . . . .	182
6.49	LS-DYNA cross section zoom-in on the sample inside the partial lateral confinement SHPB set up containing the incident bar (blue), transmitted bar (green), water reservoir (grey), water annulus within reservoir, and the sample (red). . . . .	183
6.50	LS-DYNA cross section zoom-in on the sample inside the partial lateral confinement SHPB set up with water annulus (brown) modelled as SPH. . .	184



6.51	Final time state of partial lateral confined SHPB numerical model on saturated kaolin clay. . . . .	185
6.52	Image of kaolin clay sample forming a loop within latex membrane after partial lateral confined SHPB test. . . . .	185
6.53	Comparison between front stress from experimental and numerical model for partial lateral confined SHPB test on saturated kaolin clay. . . . .	186
6.54	Incident and reflected stresses from partial lateral confined SHPB numerical model. . . . .	186
6.55	Comparison between back stress from experimental and numerical model for partial lateral confined SHPB test on saturated kaolin clay. . . . .	187
6.56	Comparison between radial stress from experimental and numerical model for partial lateral confined SHPB test on saturated kaolin clay. . . . .	188
6.57	Comparison between recorded pressure at specific elements adjacent to reservoir wall and sample surface. . . . .	189
6.58	Locations of central, back, and front layers of sample used for measurement of internal radial stress. . . . .	191
6.59	Internal sample radial stress from central layer of unconfined SHPB numerical model. . . . .	192
6.60	Internal sample radial stress from central layer of confined SHPB numerical model. . . . .	192
6.61	Heatmap describing internal radial stress variation over time from unconfined SHPB numerical model for a) front layer, b) central layer, and c) back layer. . . . .	194
6.62	Heatmap describing internal radial stress variation over time from confined SHPB numerical model for a) front layer, b) central layer, and c) back layer. . . . .	195
6.63	Heatmap describing internal radial stress distribution from numerical model of PLC SHPB tests, with water modelled as $1000 \text{ kg/m}^3$ . . . . .	196
6.64	Heatmaps describing internal radial stress distribution from numerical models of a) unconfined SHPB and b) PLC SHPB with equivalent water annulus density ( $1 \text{ kg/m}^3$ ). . . . .	197

6.65	Heatmaps describing internal radial stress distribution from numerical models of a) confined SHPB and b) PLC SHPB with equivalent water annulus density ( $1.1 \times 10^9 \text{ kg/m}^3$ ). . . . .	197
6.66	Comparison between back stress from numerical model for unconfined, partial lateral confined SHPB test on saturated kaolin clay. . . . .	202
6.67	Comparison between radial stress from numerical model for confined, and partial lateral confined SHPB test on saturated kaolin clay. . . . .	202
7.1	General phase behaviour exhibited by kaolin clay under high-strain-rate, governed by material properties. . . . .	207
C.1	Relationship between gas gun pressure and striker bar velocity at each striker bar depth, with power regression trend line for each striker bar depth. . . .	329
F.1	Design for reservoir support stand for partial lateral confined SHPB apparatus.	362

## List of Tables

2.1	Particle size fractions from EN ISO 14688-1:2002 . . . . .	9
2.2	Typical coefficients of permeabilities for saturated soils, from Das and Sobhan (2014). . . . .	10
2.3	Kaolin clay properties characterised in existing literature. . . . .	11
2.4	Grouping of similar LS-DYNA models for comparison. Models indicated with an asterisk are the model selected to represent the group. . . . .	27
2.5	Comparison of LS-DYNA soil models, after Barr (2016) . . . . .	28
2.6	Variables for definition of LS-DYNA Soil and Foam. . . . .	29
2.7	Variables for definition of LS-DYNA Pseudo-Tensor in Mode 1. . . . .	31
2.8	Variables for definition of LS-DYNA Mohr–Coulomb . . . . .	32
2.9	LS-DYNA variables for Geologic Cap. . . . .	34
2.10	LS-DYNA variables for Hysteretic Soil. . . . .	34
2.11	Parameters for the EOS of water based on Shin et al. (1998) . . . . .	37
3.1	Summary of material characterisation tests and findings for kaolin clay. . .	40
3.2	Atterberg limits values compared to existing literature. . . . .	45
3.3	Test programme for three different confinement modes at various speeds and moisture content levels. . . . .	56
4.1	Definition of input arguments used in the function SHPB_processing.py. .	69

4.2	Confinement modes applicable in the function <code>SHPB_processing.py</code> . . .	73
4.3	Definition of input arguments used in the function <code>dispersion.py</code> . . . . .	76
4.4	Typical input arguments used in <code>SHPB_processing.py</code> for SHPB tests on different sample materials. . . . .	81
6.1	Material properties of steel pressure bars and sample used in SHPB model in LS-DYNA. . . . .	144
6.2	LS-DYNA material models considered to represent cohesive soil behaviour.	149
6.3	Variations of mass density and shear modulus that have been tested using the <code>MAT_ELASTIC_PLASTIC_HYDRO</code> material card . . . . .	149
6.4	Material parameters used for <code>MAT_MOHR_COULOMB</code> , units are based on unit conversion system for current model. . . . .	151
6.5	Input parameters to create cylindrical mesh . . . . .	156
6.6	Input parameters to create tubal ring mesh . . . . .	158
6.7	Cylindrical Block Mesher input variations used for mesh optimisation . . .	159
6.8	Combinations of node interfaces with duplicate nodes merged. . . . .	161
6.9	Summary of modifications to confining ring tested, and relevant findings .	173
6.10	Summary of variations of striker bar speed and bulk densities with the un- confined SHPB numerical model . . . . .	176
6.11	Summary of variations of striker bar speed and bulk densities with the con- fined SHPB numerical model . . . . .	180
6.12	Variations of water reservoir inner diameter tested with LS-DYNA model. .	189
6.13	Summary of numerical model iterations and required energy to displace con- fining elements. . . . .	196
B.1	Unconfined tests on kaolin clay at each striker bar velocity. . . . .	316
B.2	Log of unconfined SHPB tests at 8 m/s on kaolin clay sorted by moisture content. . . . .	317

B.3	Log of unconfined SHPB tests at 12 m/s on kaolin clay sorted by moisture content. . . . .	318
B.4	Log of unconfined SHPB tests at 16 m/s on kaolin clay sorted by moisture content. . . . .	319
B.5	Log of unconfined SHPB tests at 18 m/s on kaolin clay sorted by moisture content. . . . .	319
B.6	Log of unconfined SHPB tests at 20 m/s on kaolin clay sorted by moisture content. . . . .	320
B.7	Log of unconfined SHPB tests at 22 m/s on kaolin clay sorted by moisture content. . . . .	320
B.8	Unconfined tests on kaolin clay at each striker bar velocity. . . . .	321
B.9	Log of confined SHPB tests at 12 m/s on kaolin clay sorted by moisture content. . . . .	322
B.10	Log of confined SHPB tests at 18 m/s on kaolin clay sorted by moisture content. . . . .	322
B.11	Log of confined SHPB tests at 20 m/s on kaolin clay sorted by moisture content. . . . .	323
B.12	Log of confined SHPB tests at 22 m/s on kaolin clay sorted by moisture content. . . . .	323
B.13	Partial lateral confined tests on kaolin clay at each striker bar velocity. . . . .	324
B.14	Log of partial lateral confined SHPB tests at 12 m/s on kaolin clay sorted by moisture content. . . . .	325
B.15	Log of partial lateral confined SHPB tests at 16 m/s on kaolin clay sorted by moisture content. . . . .	325
B.16	Log of partial lateral confined SHPB tests at 20 m/s on kaolin clay sorted by moisture content. . . . .	325
C.1	Pressure and striker bar depth combinations tested with new gas gun, and measured striker bar velocities. . . . .	328
C.2	Trend line equations to derive striker bar velocities, $v_s$ , based on gas gun pressure, $p_g$ , at various striker bar depths. . . . .	329

---

E.1	Material card for MAT_ELASTIC, calibrated to represent steel pressure bars.	357
E.2	Material card for MAT_NULL, calibrated to represent water. . . . .	357
E.3	Material card for MAT_MOHR_COULOMB, calibrated to represent kaolin clay. .	358
E.4	Material card for MAT_NULL, calibrated to represent air at atmospheric pressure.	358
E.5	Material card for MAT_RIGID, calibrated to represent rigid steel reservoir. .	358
E.6	Contact card for CONTACT_AUTOMATIC_NODES_TO_SURFACE, calibrated to describe SPH node to Lagrangian solid surface interactions. . . . .	359
E.7	Contact card for CONTACT_AUTOMATIC_NODES_TO_SURFACE, calibrated to describe interactions between Lagrangian solid surfaces. . . . .	359
E.8	EOS card for EOS_LINEAR_POLYNOMIAL, calibrated to depict the behaviour of water. . . . .	360
E.9	EOS card for EOS_LINEAR_POLYNOMIAL, calibrated to depict the behaviour of air at atmospheric pressure. . . . .	360



## Chapter 1

# Introduction

## 1.1 Background

How structures behave when subject to explosions or high velocity projectiles will always be a matter of global importance. As terrorist incidents and tensions between countries become increasingly hostile, there is a pressing demand to develop adequate methods to minimise the effect of future threats. As such, it is vital to understand the feasibility of a broad range of geomaterials from a military defence perspective.

Modern military field fortifications must evolve to meet current military needs, hence it is crucial for defensive structures to be able to withstand extremely high impacts such as those from explosive or blast incidents. Soils and geomaterials are typically used in impromptu military defensive structures such as sandbag walls or Hesco bastions which are typically filled with sand or gravel.

The ability of soils to withstand extreme pressure makes it ideal for the safeguarding of personnel and assets from the effects of blast and fragmentation. However, the properties of soils greatly vary, and the behaviour under high-strain-rates such as during blast events have not been fully characterised. Furthermore, it is not well understood how intrinsic soil properties affect its ability to withstand high-strain-rate impact. Thus it is vital to improve understanding of the effects of material properties to enhance protection against future blast threats by developing constitutive models that act as a foundation for different soils and are adaptable to new military applications. While extensively studied for cohesionless soils like sands and gravels, research remains limited for cohesive soils.

While sands and gravels have been well characterised in previous research, the use of cohesive soils such as clays for military fortification is an area that has seen significantly lesser growth. Even though sand is just as readily available worldwide as clays, a key difference is the ability for cohesive soils to retain a much greater amount of water. The water retention capabilities in cohesive soils creates a necessary topic of discussion in terms of evaluating the feasibility of cohesive soils as an alternative in protective structure design.



One of the intrinsic properties of these geomaterials is that the strength exhibited by the material may increase depending on the confining pressure applied. When subject to extremely high and immediate loading such as that from blast or fragmentation, the material may respond differently due to the lateral inertia applying a confining pressure. Hence, it is important to identify the effect of confinement on the strength of the material as it will give fortification designers a better holistic picture of the response of protection structures.

## 1.2 Scope and objective

In the design of fortification structures especially against the effects of blast and fragmentation, it is vital to understand the behaviour of a material under the high-strain-rate load cases and the factors that affect material behaviour. The type of cohesive soil utilised in this study is kaolin clay, which is an indicative widely available clay, whose behaviour is representative of a wide range of cohesive soils. Kaolin clay is a simplified geotechnical material which has been subject to comprehensive research and thus a wealth of low-stress-strain-rate testing are available for comparison.

This study aims to determine the high-strain-rate effects of kaolin clay by investigating the factors that affect its material behaviour. The effect of factors such as moisture content on soil stress-strain behaviour and strength is investigated by considering the wider effect of confining pressure in order to obtain a holistic characterisation of high-strain-rate behaviour in real-life practical scenarios.

This research is primarily focused on assessing the effects of strain rate and the material properties that affects the compaction behaviour and the lateral response of cohesive soils. The main objectives of this research are therefore:

- To compare high-strain-rate and quasi-static compression behaviour of cohesive soils;
- To investigate the effect of different confinement modes under high-strain-rates on this behaviour;
- To evaluate current modelling approaches for computing the material response of cohesive soils under varying strain rates.
- To assess the lateral response of the soil under partial lateral confined high-strain-rate conditions;

## 1.3 Thesis outline

The following chapters of this thesis are organised as follows:

### **Chapter 2: Literature review**

This chapter highlights the existing research in published literature in relation to the study of rate effects in cohesive soils. Modern techniques used to investigate high-strain-rate behaviour are discussed, with an emphasis on the development of one-dimensional compression tests with the split-Hopkinson pressure bar. Existing high-strain-rate testing with attempts to consider lateral confining pressure are also discussed to highlight the gaps in existing research. Numerical modelling techniques and their viability in the context of high-strain-rate testing is also discussed.

### **Chapter 3: Preliminary material testing and characterisation**

This chapter details preliminary testing such as material characterisation and quasi-static tests conducted on kaolin clay samples. Findings from quasi-static testing are presented in terms of the effect of moisture content and the stress and strain behaviour exhibited when subject to loading. Methodology regarding sample preparation for subsequent high-strain-rate testing with split-Hopkinson pressure bar apparatus and the procedure to create varying moisture content samples are included.

### **Chapter 4: high-strain-rate testing of kaolin clay**

High-strain-rate tests of kaolin clay are designed and conducted to investigate the effect of moisture content and strain rate. Findings are analysed and contextualised to determine the effect of moisture content and strain rate. The effect of confinement and opportunities for development are discussed based on results from unconfined and confined split-Hopkinson pressure bar tests. Methods to process and analyse split-Hopkinson pressure bar signal data are discussed with the focus on cohesive soil testing.

### **Chapter 5: Partial lateral confinement for evaluation of confinement effects**

The application of a modified split-Hopkinson pressure bar fitted with a partial lateral confinement apparatus is discussed, with the objective to evaluate the viability of the apparatus in high-strain-rate testing. The ability to investigate triaxial stress behaviour bridges the gap between existing confinement mechanisms used in current high-strain-rate testing techniques. Effects of confinement are investigated by comparing experimental results to unconfined and confined conditions.

### **Chapter 6: Development of numerical modelling techniques for high-strain testing**

Techniques to numerically model split-Hopkinson pressure bar testing using LS-DYNA are

investigated with the objective to create a functional model to assist in the characterisation of high-strain-rate behaviour. The material models typically used for soils and fluid-like materials are evaluated based on their feasibility. Limitations of modern numerical modelling techniques are highlighted and recommendations are made for the use of LS-DYNA for simulating high-strain-rate behaviour of cohesive soils. Combination of experimental and numerical results are used to characterise high-strain-rate behaviour of cohesive soils under various confinement modes.

## **Chapter 7: Summary and conclusions**

This chapter provides a summary of the current work and highlights the main conclusions, as well as an overview on potential avenues for future work.

## **1.4 Published Work**

While portions of the experimental and numerical modelling work was carried out in collaboration with Arthur Van Lerberghe, all data analysis, processing, and conclusions within this thesis were independently conducted and based on individual research. Consequently, several papers have been published with both names listed as authors, including selected papers where I served as the main author.

This thesis contains work that has been published or are awaiting publication in peer-reviewed academic journals or presented at international conferences. These works are listed below and are available in Appendix A.

### **1.4.1 Published**

- Li K. S. O., Clarke S. D., Barr A. D. Characterisation of cohesive soils under high-strain rate via split Hopkinson pressure bar. *17th International Conference on Advances in Experimental Mechanics - University of Glasgow*, August 2023.
- Van Lerberghe A., Li K. S. O., Barr A. D., Clarke S. D. An open-source algorithm for correcting stress wave dispersion in split-Hopkinson pressure bar experiments. *Experimental Mechanics* (2025)
- Li K. S. O., Van Lerberghe A., Barr A. D., Clarke S. D. Split-Hopkinson pressure bar testing of water with partial lateral confinement. *Experimental Mechanics* (2025)

### 1.4.2 Under review

- Van Lerberghe, A., Li, K. S. O., Barr, A. D., & Clarke, S. D. (2024). High-strain-rate behaviour of cohesive soils. *Submitted for publication in International Journal of Impact Engineering*.
- Li, K. S. O., Van Lerberghe, A., Barr, A. D., & Clarke, S. D. (2024). Impact of partial lateral confinement on high-strain-rate behaviour of cohesive soils. *Submitted for publication in Experimental Mechanics*.



## Chapter 2

# Literature review

## 2.1 Introduction

This chapter presents an overview of published literature relevant to the study of rate effects on geomaterials. This includes the description of current methods to test strain rate effects, with a focus on the split-Hopkinsin pressure bar (SHPB) to test the behaviour of soils in high-strain-rate scenarios, and highlighting the theory and experimental limitations of the set-up. A discussion of existing studies pertaining to the operation of the SHPB test and modifications to allow for lateral confinement of a SHPB specimen to provide a tri-axial stress state is presented. Numerical modelling from existing studies are introduced, particularly in regards to the use of the finite element program LS-DYNA, to emphasise the limitations of numerical modelling, as well as emphasising the capabilities of material models for soils to simulate the effect in high-strain-rate conditions.

## 2.2 Testing strain effects on soils

Modelling the effect of soils under blast and impact scenarios requires an understanding of their behaviour under different rates of deformation, especially as the material response can vary for different strain rates. This enables for an accurate and effective analysis of the response of these materials when subject to various real-life conditions. In general, strain rate corresponds to one of five different regimes, as shown in Figure 2.1. The strain rate ranges depicted is used as the definition for strain rate regimes throughout this work.

Material behaviour when subject to undrained or drained loading is vital to this research. While slow tests are effective in determining drained behaviour, higher loading rates introduce complexities especially in saturated soil samples where water plays a significant part in generating resistance until undrained behaviour is reached. This is especially the case during conditions with rapid loading, where cohesive soils that are capable of retaining greater

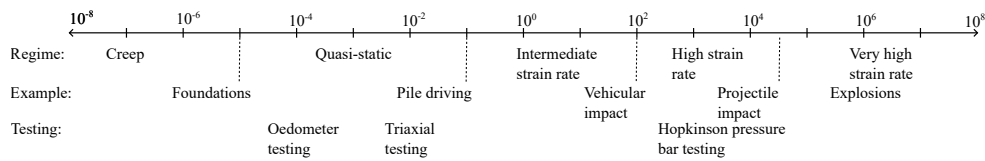


Figure 2.1: Strain rate classifications and examples of phenomena in soils

volumes of water typically cannot dissipate pore water pressure quickly enough, leading to the occurrence of undrained behaviour and the sensitivity to changes in strain and strength.

Typical civil engineering applications assume that the system is in a state of stress equilibrium, this corresponds to the creep or quasi-static strain rate regimes ( $< 10^{-1} \text{ s}^{-1}$ ). Compressive stresses could be applied accurately to measure the stress and strain of materials in this range using hydraulic frames to provide an axial load (Pajak, 2011). Even though the behaviour of soils at this strain rate are relatively simple to determine experimentally, as the soil is accelerated from an initial static to dynamic state, additional resistance is generated from inertial forces. Hence, measurements must be analysed under consideration of the effect of inertia (Yamamuro et al., 2011).

The characterisation of soil behaviour at high-strain-rates is especially vital in understanding the effect of extreme loading from blast or impact events. However, the difficulty to conduct testing at high-strain-rate conditions ( $10^2 \text{ s}^{-1}$  to  $10^4 \text{ s}^{-1}$ ) arises from the rapid nature of the loading, where the stress wave propagates within the material and affects its dynamic response (Mishra et al., 2015). A common method to experimentally emulate high-strain-rate loading is using the SHPB, the SHPB is useful for measuring the stress strain response of materials when subject to a transient load. The SHPB is one of the focuses of this work and will be further discussed in the following section.

Other methods exist to measure high-strain-rate response such as the use of cyclic testing (Dogyun & Brandes, 2020), drop hammers (Shibusawa & Oida, 1992), or triaxial testing (Veyera, 1994), however even though strain rates within the regime of  $10^{-1} \text{ s}^{-1}$  could be obtained, the inability to guarantee high stress condition means that they are not directly practical to the application towards the context of blast or ballistics.

## 2.3 Material characterisation

The focus of this research is based on the evaluation of strain rate effects of cohesive soils, this category of soils is characterised by their fine-grained particle size and typically exhibit a tendency for soil particles to adhere. Cohesive soils are defined if the proportion of fine-grained material exceeds 50% of the weight of the soil (Gautam, 2018). Cohesive soils are typically characterized by their high compressibility and low strength, whose behaviour is primarily dictated by the soil's permeability (Clarke et al., 2016).

Table 2.1: Particle size fractions from EN ISO 14688-1:2002

<i>Soil type</i>	<i>Fraction</i>	<i>Subfraction</i>	<i>Particle size, mm</i>
Very coarse soil	Boulders	Large boulder	> 630
		Boulder	200-630
	Cobbles		63-200
Coarse soil	Gravel	Coarse gravel	20-63
		Medium gravel	6.3-20
		Fine gravel	2.0-6.3
	Sand	Coarse sand	0.63-2.0
		Medium sand	0.2-0.63
	Fine sand	0.63-0.2	
Fine soil	Silt	Coarse silt	0.02-0.0063
		Medium silt	0.0063-0.02
		Fine silt	0.002-0.0063
	Clay	< 0.002	

The particles in different soils vary immensely, as shown in Table 2.1, cohesive soils are defined by their fine-grained nature and encompasses both silts and clays. As this work investigates kaolin clay, the particles are smaller than 0.002 mm. However, even within the corresponding particle size range, the particle shape, size distribution, surface roughness, and angularity of particles can be distinctly different. This could be attributed to the fact that most soils are formed by a process of fracturing of larger rocks by weathering or chemical processes, hence these properties depend greatly on the origin and history of the mineral particle. Kaolin clay is mainly comprised of kaolinite, however it frequently contains minerals of quartz, mica, feldspar, illite, and montmorillonite (Adamis & Williams, 2005).

Apart from the mineral particles in a soil, void spaces exist that consist of air, water, or a mix of both. As such, soil properties such as the void ratio, moisture content, and saturation ratio are used to express the proportions in the void spaces (Atkinson & Bransby, 1978).

$$\text{Void ratio, } e = \frac{\text{Volume of voids}}{\text{Volume of solids}} = \frac{V_v}{V_s} \quad (2.1)$$

$$\text{Moisture content, } w = \frac{\text{Mass of water}}{\text{Mass of solids}} = \frac{M_w}{M_s} \quad (2.2)$$

$$\text{Saturation ratio, } S_r = \frac{\text{Volume of water}}{\text{Volume of voids}} = \frac{V_w}{V_v} \quad (2.3)$$

Void ratio is especially useful as it is used as a scale for how compacted the material is, a soil with a void ratio close to zero indicates that there are very little void spaces and the soil is close to being composed purely of its constituent minerals.



Table 2.2: Typical coefficients of permeabilities for saturated soils, from Das and Sobhan (2014).

<i>Soil type</i>	<i>k, cm/s</i>
Clean gravel	1.0 – 100.0
Coarse sand	1.0 – 0.01
Fine sand	0.01 – 0.001
Silt	0.001 – 0.00001
Clays	< 0.000001

Since cohesive soils are characterised by their low permeability, they also contain the ability to retain larger volumes of water compared to cohesionless soils. This makes moisture content a key variable in governing shear strength for cohesive soils. Typical values for the coefficient of permeability are shown in Table 2.2, indicating the significantly lower permeability of clays in comparison to other soil types such as sand or gravel.

The significance of moisture content necessitates the determination of Atterberg limits to measure the critical moisture content levels in which fine-grained soils such as clays and silts transition between each of the four states: solid, semi-solid, plastic, and liquid. The liquid limit (LL), plastic limit (PL) and plasticity index (PI) were initially derived by Atterberg (1911) to evaluate the plasticity of clays. The fall cone test is now typically used as an accurate method to determine these limits, as demonstrated by theoretical plasticity analysis performed by Houlsby (1982). The Atterberg limits are defined by:

$$PI = LL - PL \quad (2.4)$$

$$LL = \frac{w - PL}{PI} \quad (2.5)$$

The LL signifies the moisture content as a percentage by weight of the dry soil at which the soil starts to slightly flow. Conversely, PL is characterised by the minimum moisture content expressed as a percentage by weight of the dry soil at which the soil can be rolled into thin threads measuring 3.2 mm without breaking (White, 1949).

Table 2.3: Kaolin clay properties characterised in existing literature.

	<i>Specific gravity, <math>Mgm^{-3}</math></i>	<i>LL, %</i>	<i>PL, %</i>	<i>PI, %</i>
White (1949)	-	71.6	39.3	32.3
Yoshinaka and Kazama (1973)	2.69	70.5	33.6	32.3
Horpibulsuk et al. (2011)	2.65	46.0	24.0	22.0
Abbey et al. (2019)	2.60	58.0	30.0	29.0
Oluwatuyi et al. (2020)	2.65	45.2	24.2	21.0

### 2.3.1 Kaolin clay

While other types of commonly researched cohesive soils include adobe clay, London clay, and silts, this study is focused on investigating the behaviour of kaolin clay as it is a versatile geomaterial that exhibits properties that are indicative of common cohesive soil behaviour. The abundance and low cost of kaolin also makes it one of the most widespread used industrial clay materials. Comprised mostly of kaolinite, the material is typically less reactive when integrated into industrial formulations compared to other clays and so see versatile uses such as in paper, paints, ceramics, cosmetics, cement, and ink production (Murray, 2006).

The prevalence of kaolin clay makes it an extensively characterised soil. White (1949) examines the Atterberg limits of clay minerals including kaolin clay. Yoshinaka and Kazama (1973) conducts characterisation tests to investigate the intrinsic microstructural properties of kaolin clay. Horpibulsuk et al. (2011) compares the relevant physical and engineering properties of Bangkok clay with kaolin clay. Oluwatuyi et al. (2020) characterises kaolin clay as part of an investigation on the effects of crude oil contaminated kaolin clay. Abbey et al. (2019) presents research on factors that affect the swelling and structural characteristics of kaolin clay blended with concrete. Results of characterisation of kaolin clay from the studies mentioned are summarised in Table 2.3.

## 2.4 Split-Hopkinson pressure bar

The original split-Hopkinson pressure bar was developed by Hopkinson (1914) as a method of measuring the pressure produced in the detonation of explosives or the impact of bullets. Hopkinson's original pressure bar system consisted of using a steel bar to measure the impulse produced from a collision or impact.

Davies (1948) improved the setup further by developing a technique to make use of condenser units connected to a cathode-ray oscilloscope to measure the movement of the pressure bar. Using the setup with condensers, Davies (1948) worked out a proportional relation-

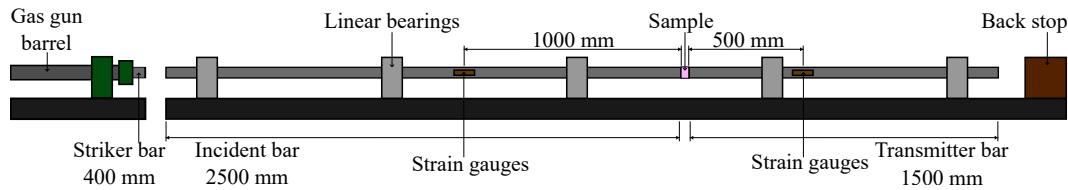


Figure 2.2: Schematic of the main components of a SHPB test under unconfined conditions

ship between the output of the condensers and the displacement-time relations, in which are proportional to the pressure-time relations under the assumption that the bar is under elastic conditions. Kolsky (1964) added a second pressure bar to the system, the system was developed to have the material specimen placed between the two pressure bars. This enabled the dynamic stress-strain response of the material specimen to be recorded by condenser units on the pressure bars, when a transient pulse was applied at one end.

The following sections describe the techniques involved in stress-strain response testing of materials under high-strain-rate compression through the utilisation of a SHPB test. Emphasis was placed on the methodology of conducting SHPB compression tests on material specimens, the process of analysis and interpretation of experimental data, and a discussion of the experimental variables and limitations associated with high-strain-rate stress-strain data obtained from SHPB testing.

### 2.4.1 Principles and theory

#### Main components and methodology of SHPB

The SHPB works based on the theory of one-dimensional wave propagation. The SHPB test consists of placing a specimen between two long, cylindrical steel pressure bars. Then a stress pulse is fired by propelling a striker bar into the end of the first pressure bar, known as the incident bar, using a pressurised gas gun. The impact produces an elastic compression wave that travels along the incident bar to the specimen. Part of the wave is then reflected (reflected pulse) and part of the wave goes through to the second pressure bar (transmitted pulse), known as the transmitter bar. Hence it is vital to ensure that the stress pulse remains within the proportional limit of the pressure bars so that the wave produced within the striker, incident, and transmitter bar remains elastic. Strain gauges are fitted on each bar and connected to a half Wheatstone bridge circuit to minimise the effects of bending and to more precisely measure the axial stress waves produced. The output is then connected to an oscilloscope to be recorded. Figure 2.2 depicts a schematic of a SHPB test under unconfined conditions.

The following stages describe the order of events that occur in reference to Figure 2.2.

1. Gas gun propels striker bar to impact the end of the incident bar, creating a compressive stress wave that propagates right along the incident bar and left along the striker bar. As the wave along the striker bar reaches the free surface on the left end of the striker bar, a tension wave is produced by reflection that negates the stress in the striker bar. Resulting in a compressive stress wave twice the length of the striker bar that travels right along the incident bar.
2. Strain gauge on the incident bar detects resultant compressive wave, known as the incident wave,  $\sigma_i$ .
3. Incident wave reaches the right end of the incident bar. Part of the wave goes into specimen while part of the wave is reflected at the right face in tension. These are known as the transmitted wave,  $\sigma_t$ , and the reflected wave,  $\sigma_r$ , respectively. The proportion of the transmitted and reflected waves depend on the relative impedance of the bars and specimen.
4. Strain gauge on the transmitter bar detects the compressive transmitted wave.
5. While the reflected wave travels back left along the incident bar and is detected by the strain gauge on the incident bar.
6. The stress waves continue to oscillate along the pressure bars, but sufficient data has been collected.

### Application of one-dimensional wave theory to SHPB

To facilitate the understanding of the theory and principle of the SHPB, the following section briefly discusses the application of one-dimensional wave theory to infer the stress-strain response at the two ends of the specimen, which is applied under the assumption that stress waves propagate longitudinally according to:

$$c_0 = \sqrt{E/\rho} \quad (2.6)$$

where  $c_0$  is the wave velocity,  $E$  is the Young's modulus of the bar and  $\rho$  is the density of bar, and that transverse deflections are small or negligible.

By considering a small length of the bar of the bar,  $\delta x$ , if stress on one face is  $\sigma_x$ , the stress on the other face is  $\sigma_x + (\delta\sigma_x/\delta x)\delta x$ . Hence, if the resulting displacement is  $u$ , then Newton's second law of motion gives

$$A \frac{\delta\sigma_x}{\delta x} \delta x = \rho A \delta x \frac{\delta^2 u}{\delta t^2} \quad (2.7)$$

This is rearranged to give the one-dimensional wave equation

$$\rho \frac{\delta^2 u}{\delta t^2} = E \frac{\delta^2 u}{\delta x^2} \quad (2.8)$$

Which is rearranged due to the assumption from Equation 2.7 as

$$\frac{\delta^2 u}{\delta t^2} = c_0^2 \frac{\delta^2 u}{\delta x^2} \quad (2.9)$$

By applying the general solution to a partial differential equation, a solution is expressed as

$$u = f(x + c_0 t) + g(x - c_0 t) \quad (2.10)$$

where  $f$  and  $g$  are functions that correspond to waves travelling with negative and positive velocity. By using the function corresponding to negative velocity as an example, and differentiating with respect to  $x$  and  $t$  gives

$$\frac{\delta u}{\delta x} = f'(x + c_0 t) \quad (2.11)$$

$$\frac{\delta u}{\delta t} = c_0 f'(x + c_0 t) \quad (2.12)$$

and hence, combining Equations 2.11 and 2.12,

$$\frac{\delta u}{\delta t} = c_0 \frac{\delta u}{\delta x} \quad (2.13)$$

Since  $\delta u / \delta x = \sigma_x / E$ , Equation 2.13 can be expressed in terms of stress as

$$\frac{\delta u}{\delta t} = c_0 \left( \frac{\sigma_x}{E} \right) = \frac{\sigma_x}{\rho c_0} \quad (2.14)$$

where it can be seen that the particle velocity and stress have a proportional relationship. By taking the time integral of Equation 2.14, the displacement of the bar can be expressed as

$$u = \frac{1}{\rho c_0} \int_0^t \sigma_x dt \quad (2.15)$$

The signals recorded by the stress gauges are translated along the time axis by:

$$t_{\text{shift}} = \frac{l_{\text{offset}}}{c_0} \quad (2.16)$$

where  $l_{\text{offset}}$  is the distance from the strain gauge to the specimen end of the bar. By superposition of the incident and reflected waves, the stress in the bar at the interface between the incident bar and the specimen (front stress) is

$$\sigma_1 = \sigma_i + \sigma_r \quad (2.17)$$

while the stress on the interface between the specimen and transmitter bar (back stress) only consists of the transmitted wave

$$\sigma_2 = \sigma_t \quad (2.18)$$

Hence the mean axial stress along the specimen can be expressed as

$$\sigma_s = \frac{\sigma_1 + \sigma_2}{2} \quad (2.19)$$

Moreover, using Equation 2.15, we can obtain the displacements of the incident and transmitter bars at their respective specimen interface by

$$u_1 = \frac{1}{\rho c_0} \int_0^t \sigma_i + \sigma_r dt \quad (2.20)$$

$$u_2 = \frac{1}{\rho c_0} \int_0^t \sigma_t dt \quad (2.21)$$

Hence the mean axial strain along the length of the specimen can be expressed as

$$\epsilon_s = \frac{u_1 - u_2}{l_{s,0}} \quad (2.22)$$

where  $l_{s,0}$  is the original length of the specimen. By applying the one-dimensional wave theory, the axial stress-strain response of the specimen can be derived through the conduction of SHPB tests.

#### 2.4.2 Existing limitations to the SHPB method

An assumption made when obtaining results from a SHPB test is that there is uniform axial stress and strain throughout the whole specimen, however, the reality is that axial and radial inertia has a significant effect as both the bar and the specimen may be susceptible to radial expansion or contraction due to compressive and tensile strains according to the material's Poisson's ratio (Kolsky, 1964).

This is especially significant in the investigation of soil specimens due to the fact that the wave speed for soils is typically very low (approximately 300 m/s) compared to traditional materials used for SHPB experiments such as steel (approximately 5000 m/s) in the cylindrical pressure bars (Felice, 1986). Furthermore, the stress wave begins to attenuate once it passes through the specimen because of the non-linear hysteretic behaviour of soils (Hendron & Auld, 1969).

A method applied by Felice (1986) to prevent the effects of axial and radial inertia was to use compacted soil specimens that were constrained to a state of near uniaxial strain within a confining cylinder, effectively negating the ability for the specimen to deform radially. However, this method does not create a fully accurate model for the dynamic strain behaviour of soils as the inability for the soil to laterally deform is an idealised depiction of real life events.

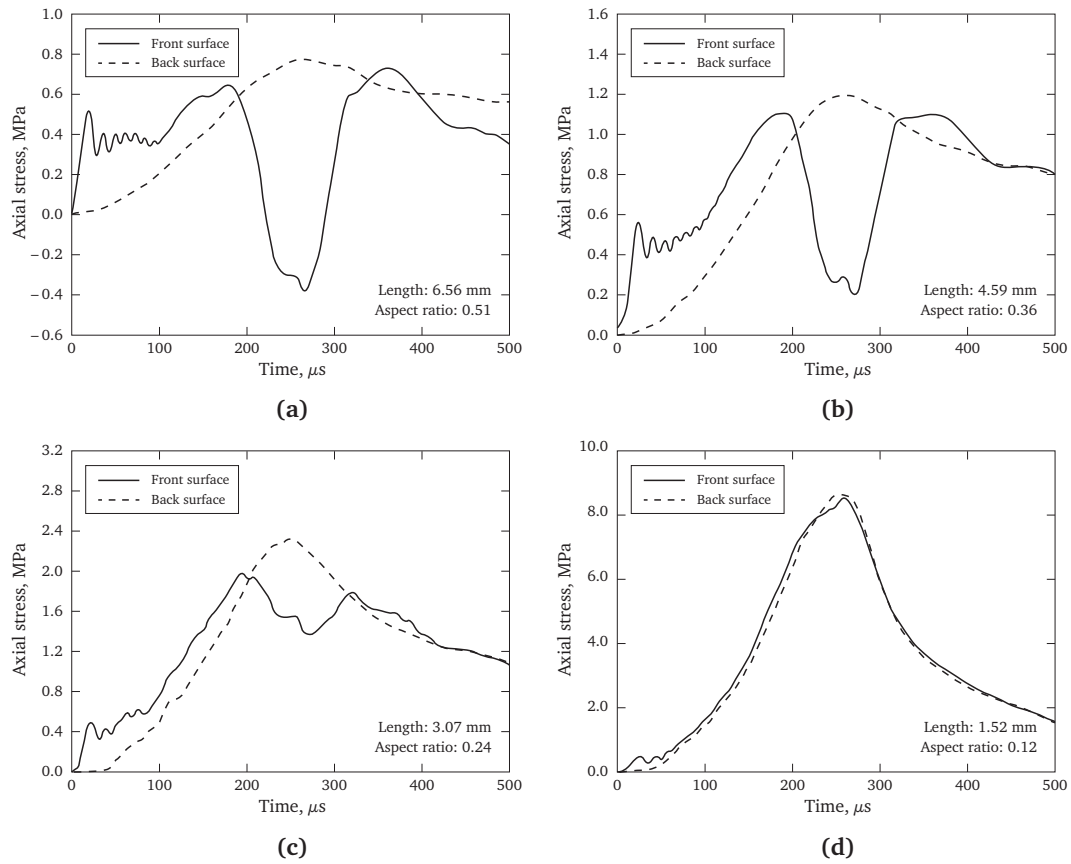


Figure 2.3: Effects of specimen thickness (RTV 630 silicone rubber) on dynamic equilibrium under the same loading stress rate in SHPB tests ( $1.25 \times 10^5 \text{ MPa s}^{-1}$ ): (a) 6.56 mm thick; (b) 4.59 mm thick; (c) 3.07 mm thick; (d) 1.52 mm thick, after Song and Chen (2004)

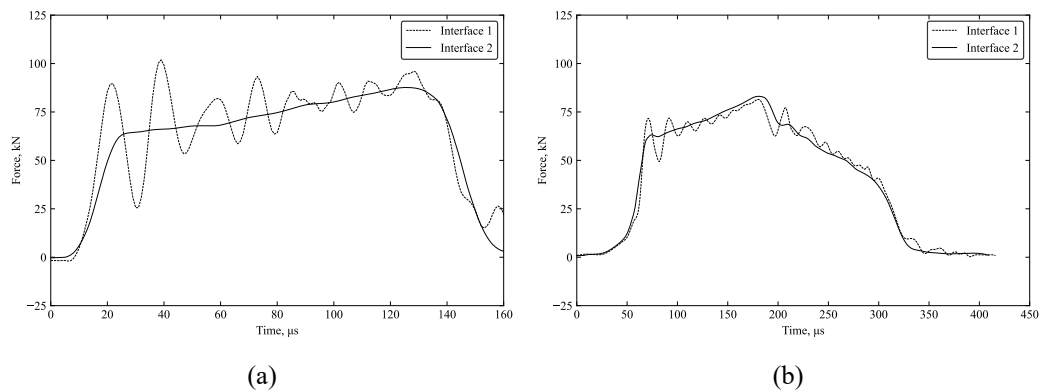


Figure 2.4: Forces at the bar-sample interface for a) conventional SHPB experiment b) pulse shaped SHPB experiment, after Frew et al. (2005).

Another method to reduce radial and axial forces is to attempt to reduce the transit time within the specimen to reduce to number of reflections that occur within the specimen. This causes the stress gradient between the two faces of the specimen to flatten out, resulting in uniform distribution of stress over the specimen. If transit time is too long, the stress wave will continue to propagate within the specimen rather than reach stress equilibrium (Felice, 1986). In order to combat this limitation, Song and Chen (2004) tested the effects of specimen thickness on state equilibrium, and deduced that reducing the thickness of the specimen would improve the stress equilibrium obtained, as seen in Figure 2.3.

An alternative procedure to ensure stress equilibrium is by altering the incident pulse shape so the stress is applied more gradually. Frew et al. (2005) placed metal discs between the striker and incident bars, this increased the rising of the incident pulse as the plastic deformation of the discs would create a gradual increase in stress upon impact. This effect is observed as the interface forces in Figure 2.4a reaches equilibrium considerably later compared to with copper-steel pulse shapers, as seen in Figure 2.4b. (Frew et al., 2005)

## **2.5 One-dimensional compression and strain rate testing**

This section highlights methods in existing literature that apply one-dimensional compression to evaluate soil behaviour at a variety of strain rates. While this study is primarily concerned with cohesive soils, it also evaluates methods of strain rate testing on various soil types to identify similarities to cohesive soils. Additionally, the investigation of existing one-dimensional strain rate testing contributes to a greater understanding of the methodologies applied in literature to investigate dynamic stress-strain behaviour.

### **2.5.1 Quasi-static**

When a soil is subject to one-dimensional compression, a uniaxial stress is applied to the soil but strain only occurs in the same direction of applied stress. Under uniaxial compression, the void ratio of the soil decreases due to deformation and reformation. As the void ratio decreases, the specimen becomes more stiff, the relationship between the logarithmic stress and the void ratio at higher stresses can then be expressed as a linear line known as the normal compression line (NCL).

Due to the high stresses that soils may be subject to under blast or impact events, the behaviour under quasi-static loading is initially due to particle rearrangement, but becomes primarily a result of particle crushing, as seen in Figure 2.5 (Hagerty et al., 1993).

However, McDowell et al. (1996) demonstrated that crushing strength is affected by the particle size, meaning that less particle crushing occur in finer soils, to this effect, it can also be said that less particle crushing can occur in well-graded versus poorly graded soils.



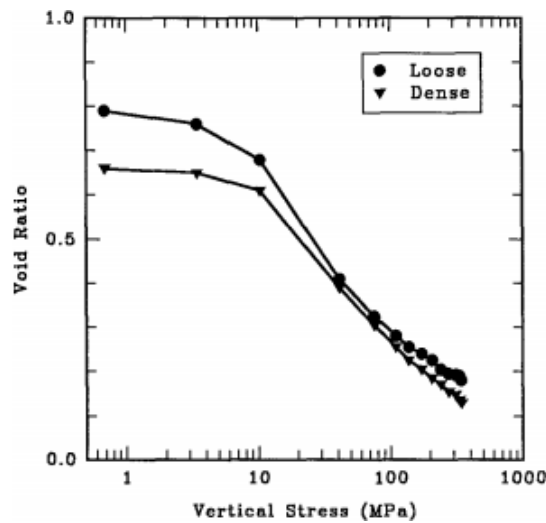


Figure 2.5: Void ratio versus applied vertical stress for Loose and dense specimens of Black Beauty Slag, after Hagerty et al. (1993)

### Triaxial compression tests

A common method to investigate the mechanical properties of soils is through triaxial compression tests. Triaxial tests are typically used to uncover soil properties that include permeability, consolidation coefficient, and compressibility.

The process of a triaxial test consists of applying an initial lateral cell pressure,  $\sigma_3$ , before an axial load,  $\sigma_1$  is gradually applied at the top of the cell until the specimen reaches failure. These two phases dictate the type of triaxial test conditions and the corresponding soil properties. The draining valve within the triaxial cell controls whether excess pore water pressure is generated in each phase. Consequently, there are theoretically four types of triaxial compression tests: unconsolidated undrained (UU), consolidated drained (CD), consolidated undrained (CU), and unconfined compression (not performed with triaxial cell). Since the purpose of quasi-static testing is to provide a basis of comparison with high-strain-rate testing, UU tests are most applicable due to the inability for pore water pressure to dissipate during the entire tests. UU tests allow for the undrained shear strength to be calculated, which is pertinent for evaluating soil stability (Rees, 2013).

Anantanasakul et al. (2012) investigated the drained behaviour of normally consolidated, anisotropic stresses in kaolin clay by conducting CD triaxial tests. The tests were conducted on cross-anisotropic kaolin clay samples under a constant mean effective stress of 250 kPa to reveal that both of the relative magnitude of intermediate principal stress and initial cross-anisotropy have a significant impact on stress-strain behaviour and soil strength during shearing. CD tests are conducted slowly, especially for cohesive soils, to prevent the accumulation of excess pore water pressure. While they are capable of sustaining high-stress

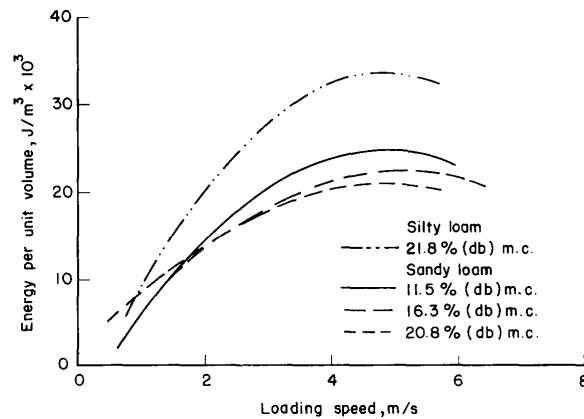


Figure 2.6: Variation of energy per unit volume at different loading speeds and soil moisture contents, after Niyamapa et al. (1992)

loads, they are not the best indication of immediate loading, which is crucial for comparison with high-strain-rate tests.

Niyamapa et al. (1992) conducted triaxial compression testing on unsaturated silty loam and sandy loam soils to evaluate the conditions of soil failure. It was found that the energy used in breaking soil was found to be an effect of the moisture content of the soil. Furthermore, the energy used for breaking the soil is seen to increase as the loading rate is increased until a critical speed of  $4.5\text{--}5\text{ ms}^{-1}$ , after which it started to decrease as seen in Figure 2.6. At lower loading speeds, the soil specimen is observed to shear along a slip plane. However, at higher speeds, the cylindrical specimen is observed to undergo barrelling.

### Oedometer testing

Another common method for testing dynamic response of material is through the use of an oedometer setup. This method consolidates a sample to a specific load over 24 hours in an oedometer cell, the deformation response as the load is incremented is monitored to determine soil behaviour when subject to critical loading.

Onitsuka et al. (1995) presented findings on oedometer tests on natural clays, incrementally loading samples of Ariake and Shimabura clays from 10 to 1280 kPa. This study demonstrated the capabilities to determine the yield stress and compressibility based on experimental data. Mesri and Feng (2019) conducted oedometer tests to characterise the behaviour of soft clays under incremental loading, the relationship between specific parameters such as void ratio, permeability, and effective stress was investigated. Oedometer tests are crucial in garnering greater understanding of intrinsic material properties when subject to uniaxial quasi-static compression and would provide a useful method of comparison to high-strain-rate results.

### 2.5.2 High-strain-rate

While high-strain-rate tests on soils and geomaterials such as sands and clays are fairly common, most of the work has been centred around investigating particle size distribution, moisture content, and high strain confinement of cohesionless soils, with limited work focused on the behaviour of cohesive soils.

Felice et al. (1985) performed SHPB tests on dense clayey sands at saturation ratios of 45%, 86%, and 97%. The sand specimens of length 12.7 mm and 6.35 mm were confined in a long, thick cylindrical cell with length of 44.5 mm, inside diameter of 60.33 mm, and outside diameter of 102 mm. Loading was provided by applying incident pulses of approximately 250 MPa and 400 MPa respectively. The 12.7 mm 86% and 97% specimens stiffened once they became fully saturated, and were also comparatively stiffer than the unsaturated 45% specimen. The 6.35 mm 86% and 97% specimens also stiffened once they became fully saturated, but the strain and stiffness at lock up were distinctly different but the presaturation responses of the specimens appear to be identical. However, strain rate variation has not been documented even though it is mentioned that various strain rates were used. Hence the difference in behaviour between these two specimen lengths cannot be definitively concluded due to differences in strain rate loading and specimen length.

Martin et al. (2009) performed SHPB testing on fine silica sand of various saturation ratios between 0% and 67% by laterally confining the sand samples using a hardened steel tube with a length of 50.8 mm, outer diameter of 25.4 mm, and inner diameter of 19.1 mm. The steel tube was utilised to create an environment that emulates uniaxial strain conditions through high confinement levels. It was found that wet specimens were less stiff compared to dry specimens, albeit with a considerably large variation between tests. However, there seemed to be no major difference in behaviour at these various moisture contents.

Luo et al. (2011) used a confined SHPB experiment to evaluate the dynamic compressive behaviour of sand under high-strain-rates using different mass densities of dry quartz sand. Tests on sand with initial densities of 1.57, 1.63, 1.69, and 1.75 g/cm<sup>3</sup> at high-strain-rates of near 600s<sup>-1</sup> (Figure 2.7b) was conducted. Stress-strain followed a power law relationship with the initial bulk density, however, results are expressed in terms of void ratio (Figure 2.7a) to investigate the compressibility as an effect of pressure. Notably, initially loosely packed specimens converged at higher axial stresses towards a normal compression line.

Li et al. (2008) developed a modified SHPB apparatus such that the specimen was subjected to axial static pre-stress, axial impact loading, and optional lateral confinement in order to carry out tests under coupled static and dynamic loads. This modified apparatus includes a confining pressure inducer, comprising a steel frame and an oil cylinder, allowing manual increase of oil pressure to replicate high confining stress levels. However, lateral deformation of the specimen persisted despite recording lateral stress, indicating a degree of uncertainty and error in the resulting data. Figure 2.8 shows the modified SHPB apparatus used, including the pressure induction setup used to replicate confining stress.

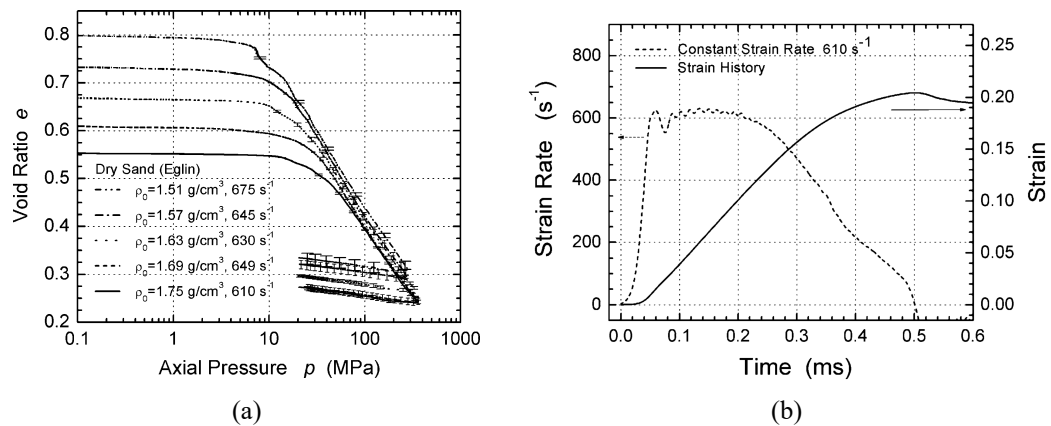


Figure 2.7: a)  $e$ -log  $p$  curves of dry sand of several different densities under confinement of SHPB experiment and b) typical strain-rate and strain time history, after Luo et al. (2011)

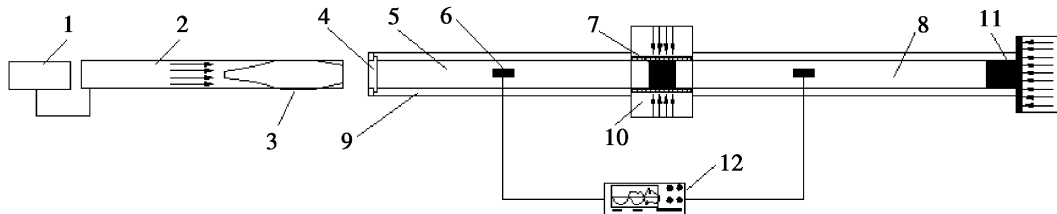


Figure 2.8: Modified SHPB apparatus with pressure confinement inducer: 1 – gas tank; 2 – pressure vessel; 3 – striker; 4 – thin baffle screen; 5 and 8 – elastic bars; 6 – strain gauge; 7 – specimen; 9 – steel frame; 10 – confining pressure setup; 11 – pressure loading unit, from Li et al. (2008).

Other authors have adapted the conventional triaxial cell (CTC) for high-strain-rate testing. Christensen et al. (1972) performed triaxial tests on sandstone to confining stresses of 207 MPa within a long pressure vessel that contained the specimen and SHPB apparatus. This modified apparatus allowed for both axial and radial stresses and strains to be known or recorded from loading up until the specimen reaches failure.

Frew et al. (2010) developed a triaxial SHPB with pressure vessels around both the specimen and transmitter bar ends in order to allow hydrostatic loading to be followed by a high-strain-rate deviatoric phase. This modified apparatus was utilised by Martin et al. (2013) to test the shear response of sand at varying confining stresses between 25 MPa and 150 MPa, as well as strain rates of 500 s<sup>-1</sup> and 1000 s<sup>-1</sup>. The results were compared with quasi-static data to determine the effect of strain rate, as shown in Figure 2.9. It could be observed from experimental results that little change in shear strength occurred at confining stresses of 50 MPa and 100 MPa.

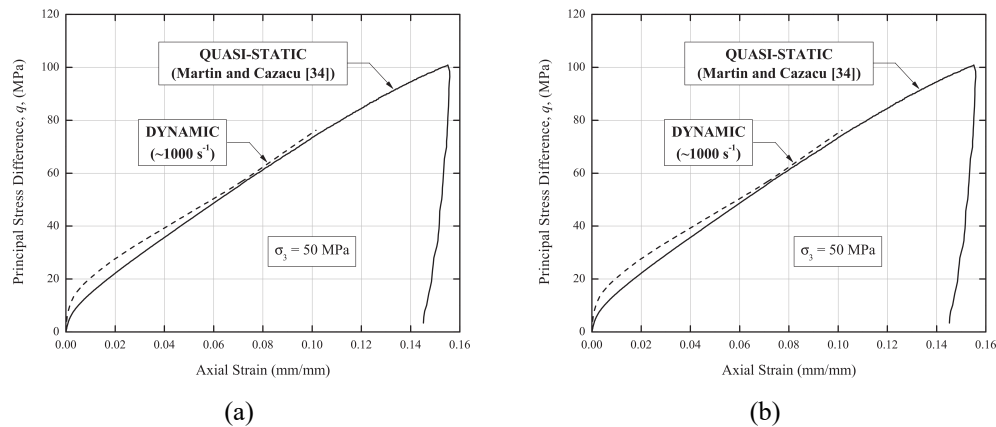


Figure 2.9: Strain rate effect on triaxial behaviour of dry quartz sand at confining pressures of a) 50 MPa, b) 100 MPa, after Martin et al. (2013).

Even though this suggests that shear strength is not dependent of strain rate, the use of dynamic CTC tests may not be accurate in depicting the loading of a real life blast or impact event, where a soil may deform uniaxially before developing significant lateral confinement. This confinement may be influenced by various factors such as the inertia of the surrounding soil, accounting for the inertial effect in the soil would require an alternative approach to allow confining stresses to develop passively (Barr et al., 2016). More importantly, the focus was focused on cohesionless materials, the behaviour of cohesive materials are intrinsically different due to the ability for particles to adhere to each other without friction.

Several authors have developed methods to allow for lateral confinement to change during a SHPB test in order to provide a triaxial stress state. Pierce and Charlie (1990) used a steel tube lined with a membrane to investigate the wave speed of partially saturated sands at varying confining stresses of 0 kPa and 310 kPa. Even though, lateral strains were unable to develop due to the steel tubes, water pressure was applied between the tube and membrane in order to apply an additional confining stress to the specimen, in addition, a piston assembly apparatus was setup to similarly apply the confining stress along the pressure bars.

Bragov et al. (2008) investigated dry, fine quartz sand under high-strain-rate tests with a SHPB setup with a steel confinement jacket to measure radial stresses. However, even though uniaxial stress states were obtained, the lateral and axial stresses were used to deduce the lateral stresses for plate impact experiments. Furthermore, investigation of the strength of dry clay was investigated using a similar setup, where a rigid confinement mechanism was used to secure a specimen of clay, even though the exact properties of the clay samples were not specified, it described the ability to test the effect of a confined rigid setup on cohesive soils. Furthermore, the inherent resistance to dynamic axial loading was found to be non-linear, this emphasises the complexity associated with characterising high-strain-rate behaviour of cohesive soils such as clays (Konstantinov et al., 2022).

Bailly et al. (2011) employed brass confining rings which simulated approximately elastic behaviour (near perfectly plastic) at high-strain-rates. The material specimen would initially be laterally confined within the rings and deform in uniaxial strain until the radial stress reaches the yield point in the ring, after which the specimen would begin to laterally deform.

Gong et al. (2019) also applied a modified triaxial SHPB setup that consists of an active axial static pre-compression stress device and an active confining pressure device. This modified SHPB setup was used to determine the relationships between compressive strength, secant modulus, peak strain, strain rate, and confining pressures by performing experimental testing on sandstone. The results are visualised in Figure 2.10.

While various methods of confinement have been explored, the specific effect of confining pressure on changes in cohesive soil stress-strain behaviour and strength has not been fully characterised, such that there was a lack of comparison between the modes of confinement and unconfined tests. A modified SHPB experiment involving a partial lateral confinement was initially developed by Barr et al. (2016) that allows confining stress to passively develop during high-strain-rate axial loading. The apparatus consists of surrounding the sample of a SHPB setup with a water annulus, enclosed within a steel reservoir. As the stress wave travels through the sample, lateral pressure within the water annulus was allowed to develop and was monitored with a pressure transducer installed on the inner walls of the steel reservoir. This method combines aspects of unconfined experiments (typically with a thin membrane) and fully confined experiments (with a steel ring) to provide a more comprehensive picture of the behaviour of soils under high-strain events. This is especially relevant to blast and impact events as the investigation of strain rate dependent behaviour of soils exhibited during high-strain-rates prompts its application in buried explosive scenarios.

The design initially pioneered by Barr et al. (2016) was employed and subjected to development through this research to investigate the confinement effects of cohesive soils by providing a medium between unconfined and rigid confined experimental setups. Initial tests with the setup on dry quartz sand reveal the capability of the modified apparatus to emulate a condition where both uniaxial compression and lateral deformation was promoted as seen in Figure 2.11, this allowed for inertial effects dictating shear behaviour to be better quantified.

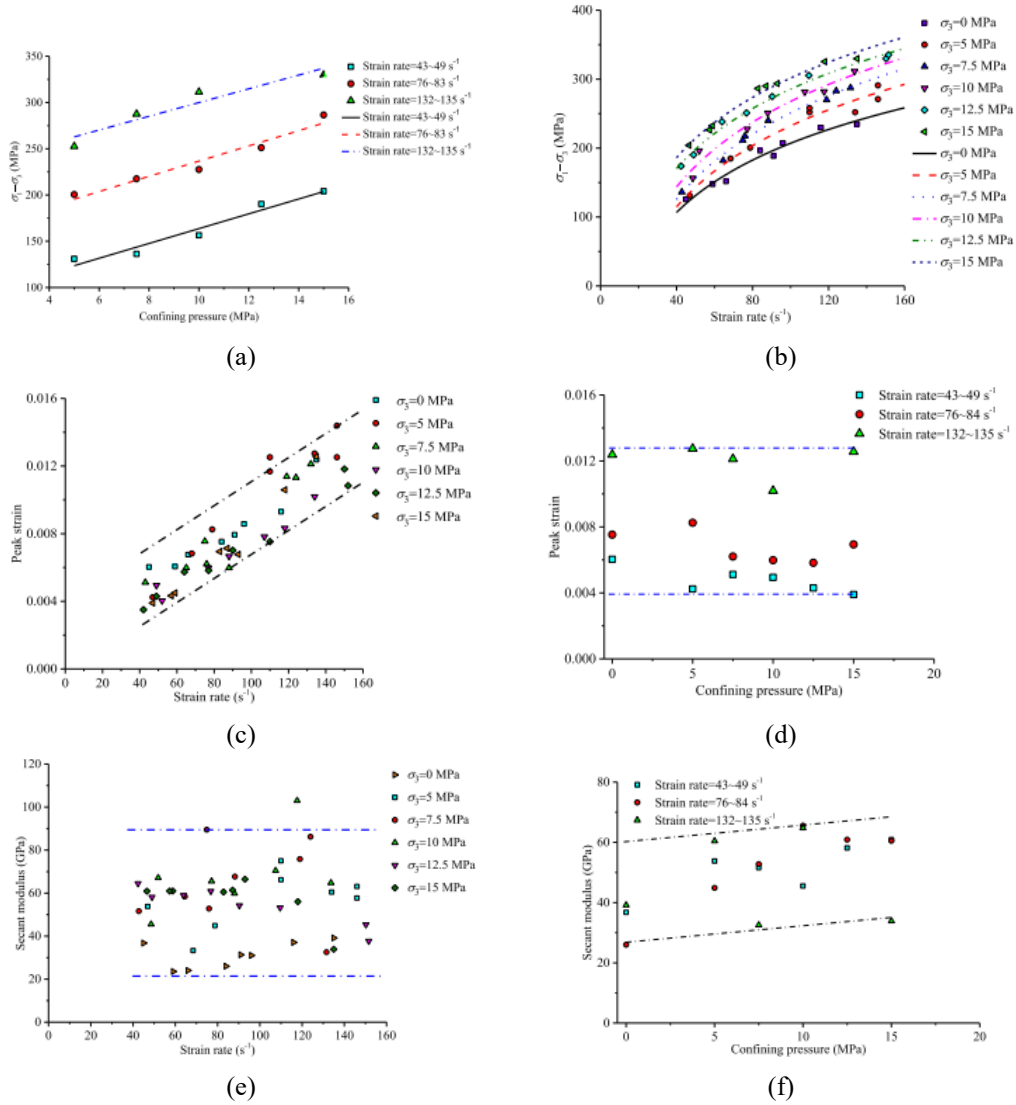
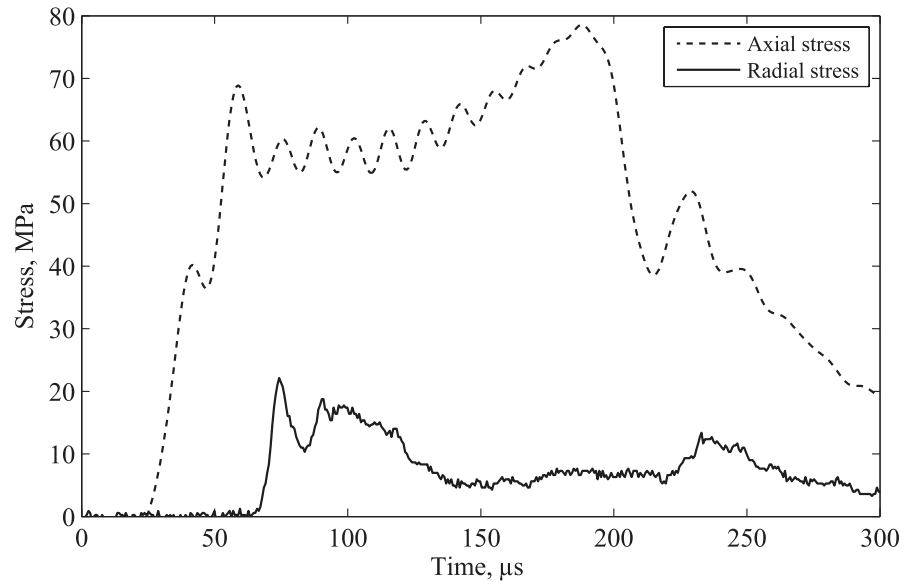
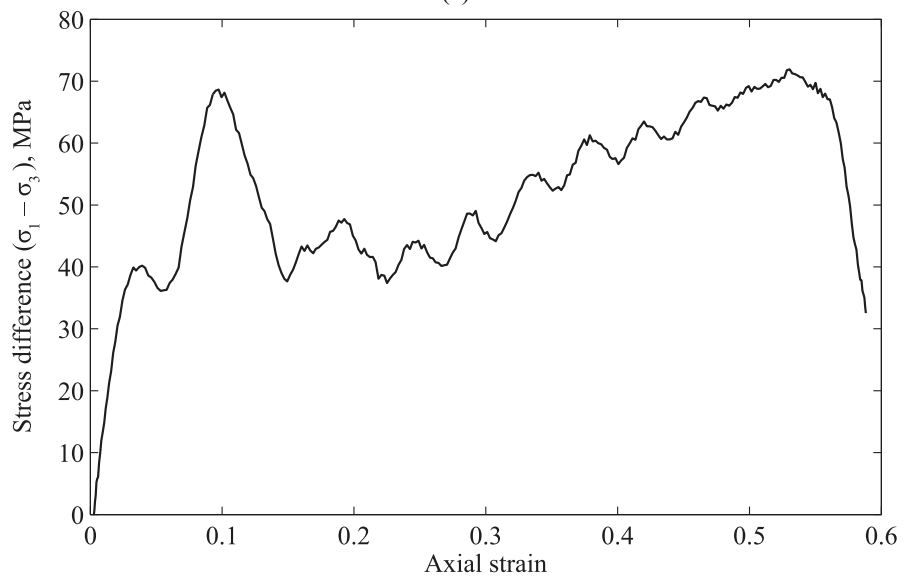


Figure 2.10: Experimental results depicting variation of variables a) dynamic triaxial compressive strength with the confinement pressure at different strain rates, b) dynamic triaxial compressive strength with the strain rate at different confinement pressures, c) peak strain with the strain rate at different confinement pressures, d) peak strain with the confinement pressure at different strain rates, e) secant modulus with strain rate at different confinement pressures, and f) secant modulus with the confinement, from Gong et al. (2019).



(a)



(b)

Figure 2.11: Partial lateral confined SHPB tests on dry quartz sand a) axial and radial stresses, b) axial stress-strain response, after Barr et al. (2016).



## 2.6 Numerical modelling of high-strain-rates

It is unpractical and inefficient to perform elaborate tests and physical models of explosive or ballistic events, as such modern techniques allow for numerical models to be utilised to carry out investigation of specific parameters and the behaviour of distinct parts of a model. Software that apply the Finite Element Method (FEM) such as LS-DYNA are ideal in modelling problems that are transient and non-linear. The FEM is a method that solves a complex problem by discretising the spatial domain into individual elements. By time integrating each individual element based on the mechanical properties assigned to the material, a solution for each element could be used to solve for the holistic problem (Shahrin et al., 2019).

The precision of the model parameters are reflective of the effectiveness of the numerical modelling at being an accurate representation of reality. The geometry and resolution of the mesh dictates the contact interactions between elements, however the behaviour of an element is still defined by how the constitutive model is created. More importantly is that the mechanical properties assigned to a material model are an accurate representation of the physical behaviour, this is done by using material characterisation experiments to validate the material model used to represent it in the numerical model. This ensures that the model is an accurate representation of how a material behaves (Church et al., 2014).

Modern development of numerical techniques have led to increasing use of the Discrete Element Method (DEM), initially proposed by Cundall and Strack (1979), which indicates that the behaviour of the material is dictated by the contact of the individual particles in the material. DEM considers the motion of each spherical particle and evaluates the particle-particle or particle-wall interactions of dry and wet particles to determine the expected collision state and resultant behaviour (Karajan et al., 2014). However, the use of DEM requires intricate understanding of the contact effects between particles such as friction and particle fracture, that coupled with the fact that large scale DEM models are extremely difficult to model even computationally, even more so when considering fine soils.

As such, the continuum model are generally more effective at modelling high-strain soil events such as blast and impact events. However, since the behaviour of particles are not being solved individually in a continuum model, it is necessary to assign an appropriate constitutive model that dictates the material behaviour based on the predefined bulk properties typically obtained via experimental tests. LS-DYNA has an assortment of built-in material models that could be applied to simulate the behaviour of soils.

Table 2.4: Grouping of similar LS-DYNA models for comparison. Models indicated with an asterisk are the model selected to represent the group.

<i>Group</i>	<i>Models</i>
Soil and Foam	Soil and Foam* Soil and Foam with Failure Pseudo Tensor* Soil and concrete
Mohr-Coulomb	Mohr-Coulomb* Druger-Prager FHWA Soil
Cap Models	Geological Cap* Schwer-Murray Cap
Nested Surface	Hysteric Soil*

### 2.6.1 Validation of LS-DYNA material models

LS-DYNA documentation identifies several constitutive material models suitable for the modelling of soils (LSTC, 2021). These models vary from simple compressibility curves or perfectly plastic yield surfaces, to the more sophisticated models that consider the effects of pore water pressure, dilatancy, hardening, and strain rate effects. A summary of some of the models typically used to simulate soils have been outlined in Table 2.5, along with a comparison of their primary features.

To validate the use of each of the LS-DYNA soil material models for modelling high-strain-rate compression, the material models have been grouped according to Table 2.4. The following sections include a brief overview on the required parameters and theory of each representative model, as well as their suitability for modelling cohesive soils in LS-DYNA.

#### Soil and Foam

Soil and Foam (MAT\_SOIL\_AND\_FOAM) is a simple pressure-dependent model optimised for modelling foams and soils confined within a structure (LSTC, 2021). Pressure-dependency refers to the yield surface of a material model being dependent on pressure. The material model requires the input parameters shown in Table 2.6, and notably includes the definition of a compressibility curve, shear strength function, bulk moduli, and tensile cut-off.

Table 2.5: Comparison of LS-DYNA soil models, after Barr (2016)

<i>Model no.</i>	<i>Model name</i>	<i>Failure surface space</i>	<i>Failure surface definition</i>	<i>Pressure dependent</i>	<i>Strain rate dependent</i>	<i>Hardening criteria</i>	<i>Dilatancy</i>	<i>Compressibility control</i>
005	Soil and Foam	$J_2-P$	Quadratic	Yes	No	None	No	$P-\epsilon_p$ , tabulated
014	Soil and Foam with Failure	$J_2-P$	Quadratic	Yes	No	None	No	$P-\epsilon_p$ , tabulated
016	Pseudo Tensor	$q-P$	Tabulated	Yes	Shear strength scale factor	None	Dilatancy	Defined EOS
025	Geological Cap	$\sqrt{J_2}-I_3$	Coefficients	Yes	No	Associated, kinematic	Yes	Cap surface
078	Soil and Concrete	$J_2-P$	Tabulated	Yes	No	No	No	$P-\epsilon_p$ , tabulated
079	Hysteretic Soil	$\tau-\gamma$	Tabulated, coefficients	Yes	No	(Nested PP surfaces)	Yes	Elastic moduli
145	Schwer-Murray Cap	$\sqrt{J_2}-I_3$	Coefficients	Yes	Viscoplasticity	Nonassociated, kinematic	Yes	Cap surface
147	FHWA Soil Model	$P, J_2, J_3$	$\phi, c, c$ coefficients	Yes	Viscoplasticity	Associated	Yes	No
173	Mohr-Coulomb	$\tau, \sigma$	$\phi, c$	Yes	No	Nonassociated	Yes	No
193	Drucker-Prager	$\tau, \sigma$	$\phi, c$	Yes	No	Nonassociated	Yes	No

Table 2.6: Variables for definition of LS-DYNA Soil and Foam.

<i>Variable</i>	<i>Description</i>
ro	Initial density, $\text{kg m}^{-3}$ .
g	Elastic shear modulus, Pa.
bulk	Bulk modulus (to define unloading response), Pa.
pc	Tensile pressure cut off, Pa.
eps1-eps10	Volumetric strain values corresponding to pressures p1-p10 and is given by natural log of relative volume. Values are negative in compression.
p1-p10	Pressure values corresponding to volumetric strains eps1-eps10, Pa. Values are positive in compression.
a0, a1, a2	Constants to create quadratic yield function within $J_2$ - $P$ space.
vcr	Volumetric crushing option (boolean): 0 for on, 1 for loading and unloading defined by pressure strain curve.
ref	Use reference geometry to initialise pressure (boolean): 0 for off, 1 for on.

Figure 2.12 compares the experimental and numerical behaviour of sand modelled with the Soil and Foam numerical model in terms of axial stress and dry density. Barr (2016) found that the numerical specimen demonstrates a lower stiffness than experimental results from both quasi-static and high-strain-rate tests, indicating that this material model is not particularly suited to represent sands. Figure 2.13 depicts the compressibility curve, defined based on data from a quasi-static test apparatus known as  $\text{mac}^{2T}$  that applies three-dimensional loading to sand samples.  $\text{mac}^{2T}$  is a multi-axial loading device, typically used for concrete, that has been adapted for use on sands and was used to provide high pressure-volume data. The initial sharp increase refers to the instance the load is applied. However, it was noted that the numerical model experiences pressures that far exceed 400 MPa, suggesting that the material has insufficient resistance to shear forces.

While this model is simple to populate with experimental data, due to a fixed shear modulus, any large changes in bulk modulus causes Soil and Foam to deviate significantly from the expected soil behaviour. As a result it is not suitable for modelling soil behaviour at high pressures. Furthermore, since pressure-volume behaviour was defined based on quasi-static tests using  $\text{mac}^{2T}$ , the dynamic behaviour exhibited by cohesive soils make it difficult to determine a compressibility curve that can be accurately extrapolated for high-stresses due to the strain-rate dependent property and tendencies for deformation.

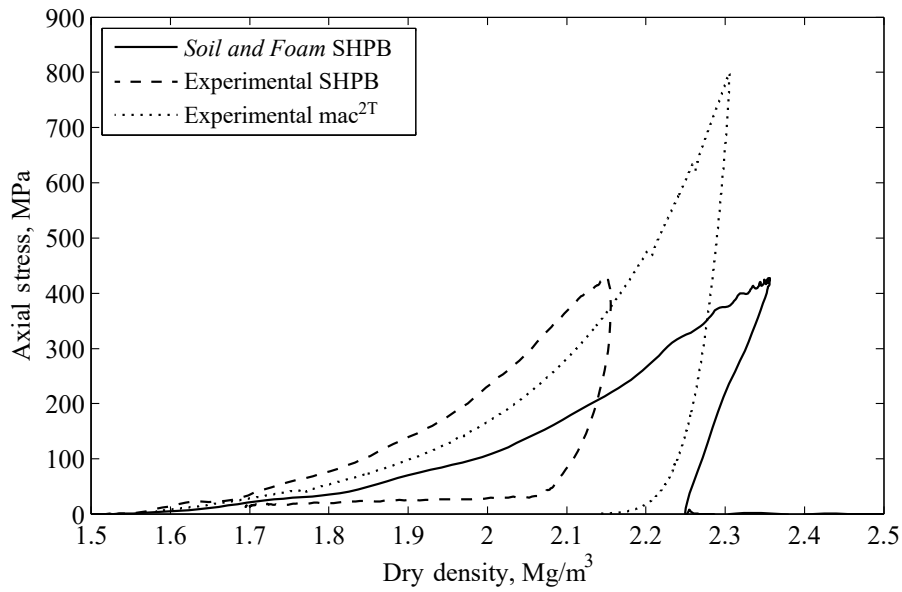


Figure 2.12: Axial stress–dry density behaviour of Soil and Foam SHPB specimen compared to mean experimental data, from Barr (2016).

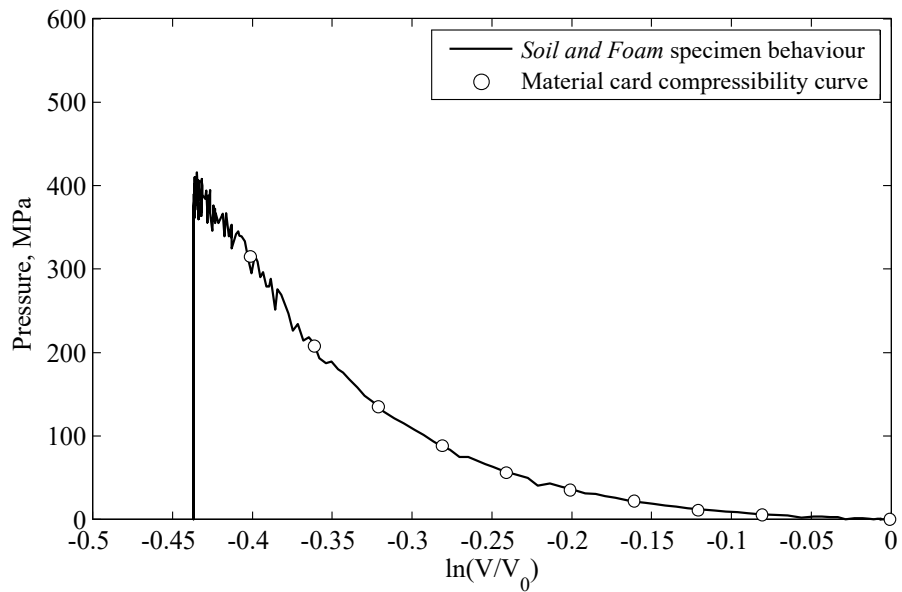


Figure 2.13: Pressure–volume behaviour of Soil and Foam SHPB specimen, and defined compressibility curve, from Barr (2016).

Table 2.7: Variables for definition of LS-DYNA Pseudo-Tensor in Mode 1.

<i>Variable</i>	<i>Description</i>
ro	Initial density, kg m <sup>-3</sup> .
g	Shear modulus, Pa.
pr	Poisson's ratio.
sigf	Tensile cut off, Pa.
x1-x10	Yield surface: pressures, Pa.
ys1-ys10	Yield surface: yield stresses, Pa.

### Pseudo-Tensor

Pseudo-Tensor (MAT\_PSEUDO\_TENSOR) is a simple model optimised for modelling concrete (LSTC, 2021). However, the model can be adapted for soils by omitting the inputs for steel reinforcement, this model then follows a similar format to Soil and Foam except with the addition of an explicitly defined Poisson's ratio. The input variables required for this material model are listed in Table 2.7.

Pseudo-Tensor draws many similarities with Soil and Foam, with the added ability to explicitly define Poisson's ratio and for the shear modulus to vary through the simulation. However, the Poisson's ratio is found to vary (from the explicitly defined value) through the model computation, meaning the axial stiffness is not a reliable representation of experimental data. Similarly, Barr (2016) obtained compressibility data by extrapolating results from quasi-static tests with the mac<sup>2T</sup> apparatus, which allows for multi-axial compression of a material with independent control of loads or displacements in the x, y, and z directions, however, the apparatus is not suitable for application on cohesive soils due to the strain-rate dependence and tendency for cohesive soils to experience drastic deformation.

### Mohr-Coulomb

The Mohr-Coulomb (MAT\_MOHR\_COULOMB) model applies the Mohr-Coulomb constitutive model for soils, of which the yield criterion can be expressed as:

$$\tau = \sigma' \tan \phi' + c' \quad (2.23)$$

where  $\tau$  is the shear strength,  $\sigma'$  is the effective normal stress,  $\phi'$  is the angle of shearing resistance and  $c'$  is the intercept of the yield surface with the  $\tau$  axis. This parameters required by this model to define the yield function and plastic potential function are shown in Table 2.8, with only the variables relevant to soils listed (LSTC, 2021).

Mohr-Coulomb failed with negative volume errors at low stresses in the SHPB model, as the lack of a compaction response leads it to behave linear-elastically throughout the loading (Barr, 2016).

Table 2.8: Variables for definition of LS-DYNA Mohr–Coulomb

<i>Variable</i>	<i>Description</i>
ro	Initial density, $\text{kg m}^{-3}$ .
gmod	Elastic shear modulus, Pa.
rnu	Poisson’s ratio.
phi	Angle of shearing resistance, rad.
cval	Cohesion, Pa.
psi	Dilation angle, rad.

The variables required to populate the Mohr-Coulomb material material consists primarily of commonly determined geotechnical parameters, coupled with the ability to explicitly define Poisson’s ratio, this material model is an appealing choice to model soil behaviour. However, the drawback is its inability to model compaction response, especially at high pressures. The lesser required material parameters yet reasonable accuracy in modelling soils make this material model suitable to depicting simplified material behaviour. Conversely, the fact this material model does not require an input EOS means that the process to implement is easier and more readily adaptable to represent a wider range of soil types.

Konstantinov et al. (2022) also found from high-strain-rate tests on dry clay that shear resistance of dry clays are capable of being described to a reasonable degree of accuracy by the Mohr-Coulomb law, indicating the while the material model contains limitations, it can be adapted to represent cohesive soil behaviour.

The required parameters for this material model can be obtained from preliminary quasi-static testing on the designated soil. Construction of Mohr’s circles of stress based on triaxial compaction testing allow for values for the angle of shearing resistance and cohesion to be obtained.

### Cap models

Geologic Cap (MAT\_GEOLOGIC\_CAP) is a two-invariant cap model, composed of yield, cap and tension cut-off surfaces, and require the variables shown in Table 2.9. Interactions with cap surfaces, as modelled with this material model, experience plastic compaction according to a hardening law (LSTC, 2021). The requirement of a hardening function makes the adoption of this model incapable for cohesive soils due to the inability to acquire the re-

quired curve values. The Schwer–Murray Cap model (MAT\_SCHWER\_MURRAY\_CAP\_MODEL) requires the same exponential hardening function, and so has been excluded due to its unsuitability to replicate high levels of compaction behaviour.

### **Nested Surface**

The Hysteretic Soil model (MAT\_HYSTERETIC\_SOIL) is a complex nested-surface model that accommodates up to ten elastic–perfectly-plastic surfaces, facilitating the representation of hysteretic soil behavior. These nested yield surfaces are sequentially activated as shear stress increases resulting in material behaviour reflecting the combined effects of these active surfaces. Both bulk and shear moduli exhibit pressure sensitivity and govern the material response to compaction. Model definition is provided by the input variables in Table 2.10.

Barr (2016) employed the least squares method to align experimental data to the required parameters, but found that the Hysteretic soil model fails to depict compressibility of sands at stresses over 100MPa, making it unsuitable for modelling high-stress SHPB tests.

### **Summary**

All of the material models considered above have intrinsic limitations that prevent fully accurate depiction of high-strain-rate soil behaviour, most notably the inability to simulate soil compaction behaviour due to:

- lack of compaction mechanism;
- exponential mechanism opposed to logarithmic one; or
- incapability to model consider effects of shear modulus or Poisson’s ratio.

While limitations prevent a fully reliable model from being developed, the simplification of material behaviour still allows for the optimisation of numerical models that can assist with simulating SHPB tests on cohesive soils. While Barr (2016) found Pseudo-Tensor most reliable for sands, the inability to conduct multi-axial compression tests on cohesive soils renders this model incapable. However, the simplicity of the Mohr-Coulomb model still allows for a reasonably accurate depiction of soil behaviour, such that the numerical model should be coupled with experimental testing to fully characterise soil behaviour. Further development regarding the optimisation of material models for use with numerical modelling will be discussed in Chapter 6.



Table 2.9: LS-DYNA variables for Geologic Cap.

<i>Variable</i>	<i>Description</i>
ro	Initial density, kg m <sup>-3</sup> .
k	Initial bulk modulus, Pa.
g	Initial shear modulus, Pa.
alpha	Failure envelope parameter ( $\alpha$ ).
theta	Failure envelope linear coefficient ( $\theta$ ).
gamma	Failure envelope exponential coefficient ( $\gamma$ ).
beta	Failure envelope exponent ( $\beta$ ).
r	Cap surface axis ratio (r).
d	Hardening law exponent (d).
w	Hardening law coefficient (w).
x0	Hardening law exponent ( $x_0$ ).
toff	Tension cut off ( $t < 0$ ).

Table 2.10: LS-DYNA variables for Hysteretic Soil.

<i>Variable</i>	<i>Description</i>
ro	Initial density, kg m <sup>-3</sup> .
k0	Initial bulk modulus, Pa.
p0	Cut-off/datum pressure, Pa.
b	Exponent for pressure-sensitive moduli.
a0, a1, a2	Yield function constants.
df	Damping factor.
rp	Reference pressure, Pa.
lcid	Load curve id defining shear stress against shear strain.
sflld	Scale factor to apply to shear stress in lcid.
dil_a-dil_d	Dilation parameters A, B, C, D.
gam1-gam5	Shear strains $\gamma_1$ - $\gamma_5$ (alternative to lcid).
tau1-tau5	Shear stresses $\tau_1$ - $\tau_5$ (alternative to lcid).

## 2.6.2 Existing approaches to model development with LS-DYNA

### Comparison between 2-D and 3-D models

In finite element analysis, shell elements are modelled as extremely thin sections, which greatly reduces computational time due to the decreased number of mesh elements. On the other hand, the structure and material of solid elements are fully modelled. Shell elements are a simplification of solid elements by only accounting for the outer “shell” of the material to save computational time. However, the drawback of shell elements is their hollow definition prevents stresses through the thickness of the shell to be considered during computation, which means shear deformation may not be accurately simulated. The main advantage of creating the model in 2D with shell elements is the ability to create an axisymmetric model, where only half of the model is considered by assuming the model is symmetrical along an axis. This greatly decreases computational time without compromising the result of the simulation (L'Eplattenier & Caldichoury, 2016). When comprehensive models are developed, both 3-D and 2-D models are generated to provide a basis of comparison with regards to accuracy and reliability of model results.

### ALE

The Arbitrary Lagrangian-Eulerian (ALE) technique is a method that combines the common Lagrangian and Eulerian formulation methods. The Lagrangian method follows the motion of individual particles in space over time, while the Eulerian method describes the behaviour of a material at specific space and time. The ALE method follows individual particles like the Lagrangian method, but also allows the mesh to move like the Eulerian method. This allows for more complex motion or deformation to be more appropriately modelled (Krayterman & Laboratory, 2022).

This method has been used by Busch and Tarefder (2017) to model blast scenarios in LS-DYNA, where significant deformation is expected. The model was compared to experimental results and while the modelled crater was not an exact representation of the physical crater, it provided a result that still followed a similar deformation and scatter pattern.

Rigby et al. (2018) also utilised this method to model near-field blast loading with LS-DYNA, an ALE air domain and explosive charge was modelled. The propagation of blast wave through the domain of air was able to be monitored through the numerical model, qualitative comparisons show a good agreement between numerical and experimental results.

### SPH Nodes

The smoothed particle hydrodynamics (SPH) method is a meshless Lagrangian method that is commonly employed when elements are expected to experience large deformations or

fragmentation (Colagrossi & Landrini, 2003). The technique represents elements as a collection of particles that interact with each other rather than the traditional Lagrangian mesh approach where elements move as a fixed structure as it deforms, this allows it to be used to model complex geometries and boundary conditions.

This method has been used to model blast phenomena due to the immense deformation typically associated with fragmentation. Chen and Lien (2018) describes the use of SPH method at modelling sand behaviour in TNT explosions, the results and comparison with experimental results show that the SPH method is capable of simulating large deformation and problems with high density ratio.

Standard SPH to SPH interactions are handled through the SPH interpolation functions rather than contact interactions between solid interfaces being explicitly defined like for typical solid elements. The material properties defined to a part consisting of SPH particles is smoothed over a certain spatial distance (smoothing length) of each particle. When smoothed quantities of SPH with different densities interact with each other, inaccurate values of density and mass can develop due to the smoothing lengths colliding with each other. Since macroscopic flow in SPH modelling is generally dictated by density, the over and underestimation of densities result in inaccurate characterisation of fluid behaviour due to unnatural acceleration of particles near SPH to SPH boundaries, as highlighted by Ihmsen et al. (2011) who performed SPH modelling of interactions between air and water particles.

### **2.6.3 Existing approaches to SHPB modelling**

There are existing attempts to numerically model SHPB experiments via LS-DYNA, however the lack of research into high-strain-rate testing on cohesive soils instinctively creates a gap in development in modelling SHPB experiments on materials susceptible to extreme deformation such as cohesive soils.

Existing soil work with the SHPB have typically been on materials such as sands or concrete, as such the numerical models that have been developed are geared towards these materials. Tang et al. (2020) developed a numerical model based on experimental work performed on SHPB tests on frozen soil. The FEM model developed using LS-DYNA involves a confinement system where the soil sample is enveloped by an aluminium sleeve. This indicates the viability of using LS-DYNA to develop a model that describes a confined SHPB experiment, however the behaviour of frozen soil is starkly different from cohesive soils or clays, especially when the material has been saturated.

Another use of numerical modelling involves SHPB tests on dry clay samples (Eremeyev et al., 2023). Due to the expectation of large deformation during impact, the sample was modelled using multi-material ALE and using the MAT\_SOIL\_AND\_FOAM material model based on compressibility data obtained by varying striker bar speed in SHPB tests.

Table 2.11: Parameters for the EOS of water based on Shin et al. (1998)

<i>Parameters</i>	<i>Value</i>
$c_1$	$2.190 \times 10^9$
$c_2$	$9.224 \times 10^9$
$c_3$	$8.767 \times 10^9$
$c_4$	0.4934
$c_5$	1.3937
$c_6$	0
$E$	205 J/kg
$\rho$	1000 kg/m <sup>3</sup>

The main finding is that most models employ either ALE or Lagrangian element formulation to model the sample, however the viability of the model when the sample is subject to more extreme cases of deformation is yet to be fully evaluated.

When considering numerical modelling simulations for the partial lateral confined SHPB apparatus, the existence of water within the setup means that the relevant material behaviour must be properly defined in the model. Varas et al. (2017) presented the use of LS-DYNA to model the effect of an hydrodynamic ram. The viability in usage to model high velocity loads draws similarity to the high-strain-rate testing to be performed with the SHPB. Since the model consists of a tank of water, with a projectile that travels through the medium. The model considers the use of both ALE and SPH as a method to model the fluid and concludes that although SPH results in higher accuracy compared to experimental results, however at the drawback of greater computation time and processing.

To facilitate the study of shockwaves as it travels through a medium of water like the partial lateral confined reservoir, a numerical model characterising the behaviour of water is required. Shin et al. (1998) determined the equations of state of water by investigating effects of experimental shock Hugoniot and analytical predictions for air shock. The polynomial equation of state obtained can then be applied in finite element method programs to model the behaviour of water. The constants for the equation of state found is shown in Table 2.11.

In the development of the partial lateral confined SHPB apparatus, Barr et al. (2016) modelled all parts of the setup as axisymmetric Lagrangian elements. The numerical model was optimised to indicate the feasibility of the physical setup and validate that stress readings from the reservoir were accurate representations of sample behaviour. However, while the preliminary model was crucial in the development of the physical apparatus, the model was not fully adapted to depict cohesive soil behaviour.

## 2.7 Summary

This chapter introduced existing literature regarding testing of cohesive soils. Material characterisation properties were investigated, highlighting the significance of research into cohesive soils such as kaolin clay and the intrinsic differences in behaviour to cohesionless soils due to internal soil structure. Conducting tests on cohesive soils poses challenges due to their low permeability, which becomes particularly significant during high-strain-rate testing where saturated samples display undrained behaviour due to the inability for pore water pressure to dissipate effectively.

Types of one-dimensional compression testing were introduced as potential methods to characterise cohesive soil behaviour. Quasi-static methods such as triaxial compression and oedometer tests were discussed to determine the viability of using these methods to obtain bases of comparison to high-strain-rate testing of cohesive soils. By conducting UU triaxial compressions tests, the undrained behaviour of cohesive soils at low strain rates can be characterised. In addition, oedometer testing has been discussed as a method to induce sustained loads, resulting in the determination of vital geotechnical variables. This highlights the necessity to conduct quasi-static tests to facilitate a basis for high-strain-rate testing, but also to acquire necessary parameters for future numerical modelling.

In addition to quasi-static testing, the use of the SHPB as a method of investigating high-strain-rate behaviour is introduced, including its application of one-dimensional wave theory. Existing methods that employ the SHPB to examine soil behaviour are considered, and key experimental considerations are highlighted. While coarser grained soils such as sands and gravel have been extensively tested under high-strain-rates, there is comparatively less work done on cohesive soils due to their innate ability to extrude laterally. Methods of applying a confining pressure to obtain a triaxial stress state has been discussed, with most common methods to applying a form of static confining pressure to limit lateral deformation. However, the exact effect of confining pressure have not been comprehensively investigated. This facilitates the development of the partial lateral confined SHPB apparatus, initially introduced by Barr et al. (2016) to allow for lateral stresses to passively develop during axial loading of the specimen.

Numerical modelling as a complementation to experimental data is crucial in characterising soil behaviour. LS-DYNA has been introduced as a software that explicitly applies the FEM method to numerically model a wide range of physical scenarios including blast or ballistic events. Material behaviour is defined in LS-DYNA through the implementation of specific material models, the validity of a selection of common soil models was considered. While each material models contain intrinsic limitations that hinder a full depiction of cohesive soil behaviour under high-strain-rates, the use of simplistic models such as the Mohr-Coulomb model would still prove beneficial. The development of these numerical models, when used in conjunction with experimental testing offers a valuable approach in reaching useful conclusions.

## Chapter 3

# Preliminary material testing and characterisation

## 3.1 Introduction

This chapter presents preliminary experimental work done in preparation for high-strain-rate testing of kaolin clay. This includes in-depth material characterisation to ensure reliability and replicability of results. The method of which samples are prepared are discussed in this chapter, in regards to the process of preparing kaolin clay from kaolin powder for testing. Since the moisture content of kaolin clay is a key variable of investigation, the controlled sample preparation process to obtain samples at appropriate moisture content levels is discussed. While saturation level is intuitively correlated with moisture content, ease to measure moisture content makes it the preferred variable to investigate.

Moreover, it is necessary to personally characterise quasi-static behaviour of kaolin clay by conducting triaxial and oedometer tests in order to provide a comparison between the effects of the drastically different strain rate regimes on material behaviour. Finally, the collation of results from preliminary testing allows for the development of a testing programme for high-strain SHPB testing of kaolin clay under the various confinement modes.

The primary objective of preliminary testing within this section is to investigate the intrinsic geotechnical properties of the material, and to evaluate material behaviour when subject to traditional quasi-static loading. This ultimately provides a foundation for reproducibility and allows preliminary results for strain rate dependence to be investigated by comparing with subsequent tests under high-strain-rates.

Table 3.1: Summary of material characterisation tests and findings for kaolin clay.

<i>Properties</i>	<i>Findings</i>	<i>Tests</i>
Primary mineral	Kaolinite	XRD diffraction
$D_{50}$	$0.748 \mu m$	Data sheet
Particle density	$2.65 Mg m^{-3}$	Pycnometer test
Particle sphericity	Low-Medium	SEM
Angularity	SR-SA	SEM
Surface texture	Smooth	SEM
Liquid limit	39.5%	Fall cone test
Plastic limit	24.6%	Fall cone test
Plastic index	14.9%	Fall cone test

## 3.2 Material characterisation

The material selected is kaolin clay and is defined using EN ISO 14688-1:2002 soil descriptions as ‘white fine kaolin clay’. The focus of this work is to investigate the strain rate effects by assessing the sensitivity of soil properties to changes in strain rate. As such it is vital to properly characterise the properties of kaolin clay to guarantee data is accurate and results are repeatable. A summary of the tests conducted and material characterisation properties found for kaolin clay is shown in Table 3.1.

### 3.2.1 Particle density

The particle density,  $\rho_s$ , is the density of the solid mineral particles, and is used with the bulk dry density,  $\rho_d$ , to calculate the void ratio of a soil with the relation

$$e = \frac{\rho_s}{\rho_d} - 1 \quad (3.1)$$

The particle density of kaolin clay is established by comparing the masses of a volume of water and the same volume of a soil-water suspension, as described in BS 1377-2:1990 §8.2. The particle density of kaolin clay samples was validated using a Pycnometer test and found to be  $2.65 Mg/m^3$ . This value corresponded with the values for kaolinite.

### 3.2.2 Particle shape

Due to the fineness of kaolin clay, the use of traditional optical microscope to was incapable of providing a definitive image for characterisation of the particle shape, prompting the use of an electron microscope to obtain a clear image of kaolin clay particles. The scanning electron microscope (SEM) was used according to EN ISO 1468801:2002. Kaolin clay was coated with gold and placed into the SEM for imaging and are shown in Figure 3.1. Based on SEM imaging of different kaolin samples at various magnifications, kaolin clay particles were characterised to vary from low to medium sphericity, sub-rounded to subangular, and have a smooth surface texture based on qualitative observation.

### 3.2.3 Particle size distribution

The particle size distribution (PSD) of kaolin clay was obtained from the data sheet provided by the supplier (Imerys Performance Minerals). While initial characterisation of particle distribution was conducted using a Malvern Masterizer 3000 particle size analyser fitted with a dry dispersion unit, the results show the clumping of clay particles due to the presence of moisture prior to the drying process. The inability to fully disperse the clumped particles without fully grinding the material back down hinders the accuracy of these tests.

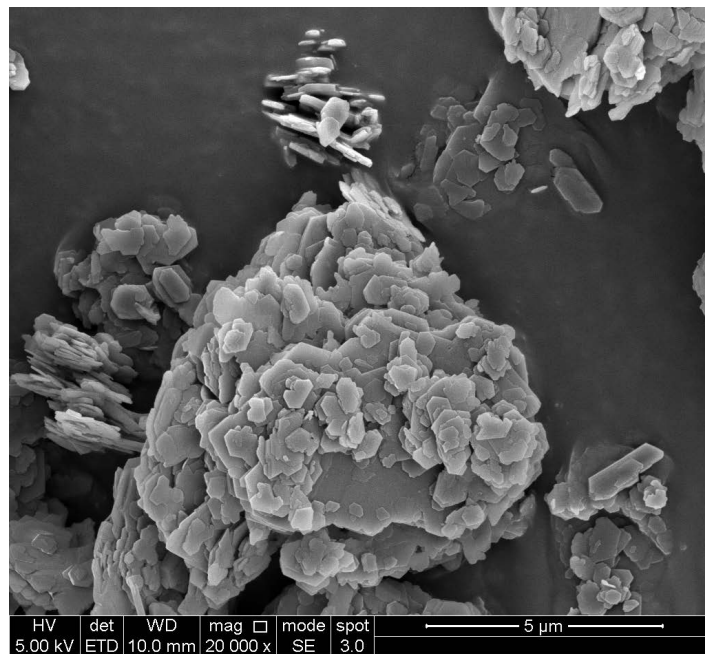
Therefore, the data sheet provided by the kaolin clay supplier was used as a basis to characterise particle size distribution. The data sheet specified that the particle size of up to 83% of the material was less than  $2\ \mu\text{m}$  (particle size range for clay). Based on additional particle size distribution data provided, a cumulative particle size distribution graph is produced as shown in Figure 3.2. The boundaries of particle size fraction is shown, and indicates that the sample material is defined as primarily being a clay.

The particle proportions of clay and silt were found to be 81% and 19% respectively, with none of the proportion corresponding to sand according to the data sheet provided. This mineral fraction corresponds to the “clay” soil texture based on the soil texture triangle shown in Figure 3.3.

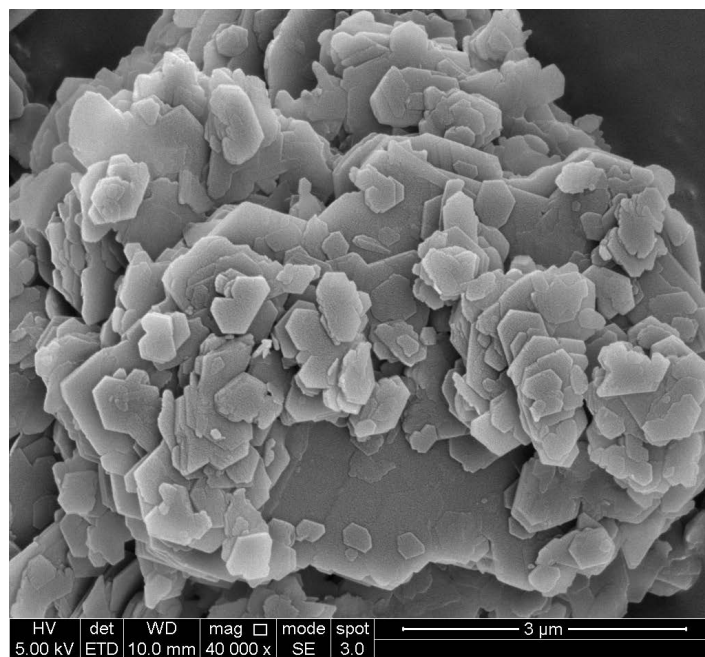
### 3.2.4 Particle mineralogy

The mineralogy of kaolin clay was determined via x-ray diffraction (XRD). The XRD process consists of measuring the intensity of diffraction at various angles of incidence,  $\theta$ , as an incident x-ray beam is diffracted by the regular atomic structure of a crystalline specimen. This is compared to a database of known diffraction patterns to identify the mineralogy of the specimen. XRD analysis was performed using a siemens D5000 diffractometer with a  $\text{Cu}_\alpha 1$  radiation source, and the ICDD’s Powder Diffraction file (PDF-4+).





(a)



(b)

Figure 3.1: Electron microscope images of kaolin clay under magnification of a) 20000x, and b) 40000x.

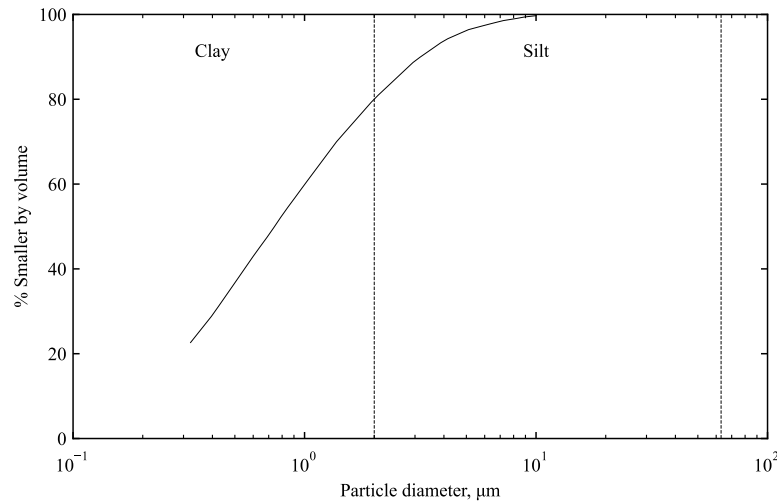


Figure 3.2: Cumulative particle size distribution histogram of kaolin clay based on data sheet provided from supplier (Imerys, Performance Minerals).

Figure 3.4 shows the results of XRD diffraction patterns corresponding with associated minerals. It could be observed that kaolinite is the most abundant mineral found in kaolin clay, which is to be expected as kaolin clay is known to be rich in kaolinite. Kaolin clay was also found to contain minor quantities of quartz, though because the quantities are only present in small quantities, it is not expected to have an influence on the mechanical properties of the clay and kaolin clay could be presumed to consist of primarily kaolinite.

### 3.2.5 Atterberg limits

To ensure consistency and reliability, the liquid limit (LL), plastic limit (PL) and plasticity index (PI) of kaolin clay was determined via the Atterberg limits tests. These values are used as a reference point during sample preparation to guarantee validity and reproducibility. The LL, PL, and PI are constant across quasi-static and high-strain-rate testing and are characteristic properties of the material.

To determine the corresponding Atterberg limits, the fall cone test, based on BS 1377-2:1990, has been conducted on kaolin clay samples. The LL is found to be 39.5%, PL is 24.6%, and PI is 14.9%.

Based on the obtained Atterberg Limits, the soil could be characterised according to the Casagrande plasticity chart as seen in Figure 3.5. The sample fits is classified as a lean clay (CL) based on the chart.

Material characterisation tests on kaolin clay have been conducted in existing literature as

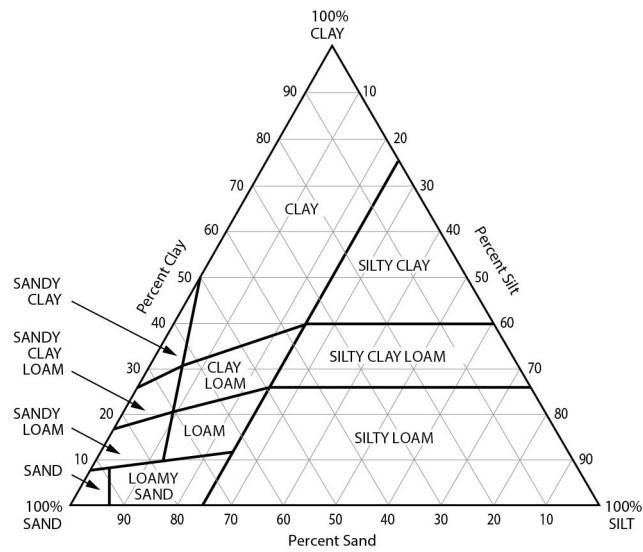


Figure 3.3: Soil texture triangle describing soil texture based on mineral proportions of sand, silt and clay, adapted from Groenendyk et al. (2015).

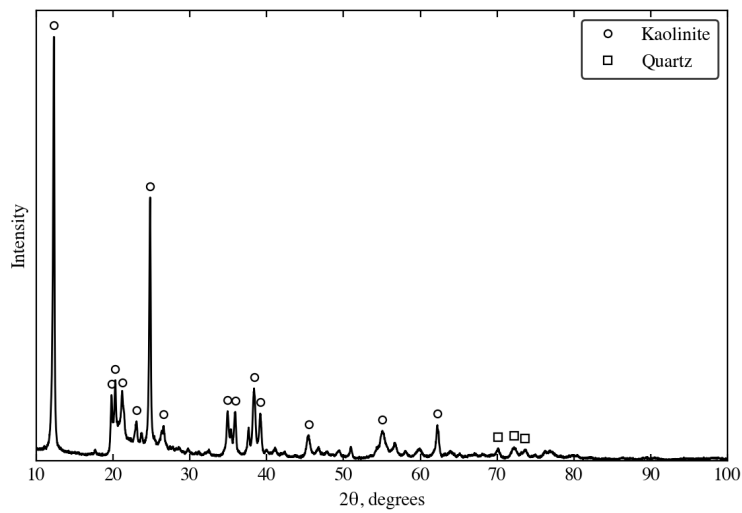


Figure 3.4: X-ray diffraction data for kaolin clay.

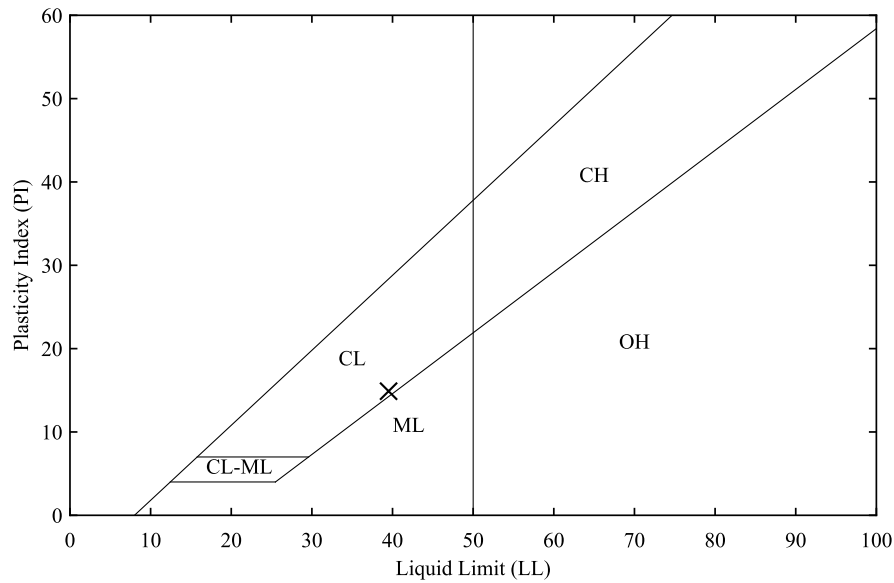


Figure 3.5: Casagrande plasticity chart showing different soil classification zones. Sample is classified as a lean clay (CL) as shown by the marker.

discussed in Chapter 2, obtained values are compared with existing literature in Table 3.2, indicating the obtained values are within a reasonable consistency with existing tests on kaolin clay.

### 3.3 Quasi-static testing

Prior to high-strain-rate testing on kaolin clay, it is crucial to conduct quasi-static testing in order to provide a basis to compare to high-strain-rate behaviour. In addition, quasi-static tests allow for intrinsic material properties to be better characterised and a baseline for un-

Table 3.2: Atterberg limits values compared to existing literature.

	<i>Specific gravity, <math>Mgm^{-3}</math></i>	<i>LL, %</i>	<i>PL, %</i>	<i>PI, %</i>
White (1949)	-	71.6	39.3	32.3
Yoshinaka and Kazama (1973)	2.69	70.5	33.6	32.3
Horpibulsuk et al. (2011)	2.65	46.0	24.0	22.0
Abbey et al. (2019)	2.60	58.0	30.0	29.0
Oluwatuyi et al. (2020)	2.65	45.2	24.2	21.0
Obtained values	2.65	39.5	24.6	14.9

derstanding the effects of strain rate. Unconsolidated undrained triaxial tests are conducted to best serve as a comparison to the conditions that occur during high-strain-rate events. The methodologies and relevant results are described with the context of compressibility and strain rate sensitivity.

### 3.3.1 Triaxial testing

Quasi-static one-dimensional compression tests was performed using conventional triaxial compression (CTC) tests on the kaolin clay specimen, the samples were shaped accordingly for the tests and undertook undrained consolidation. The triaxial testing system used is the: Pro Automatic Triaxial Testing System from VJ Tech. The triaxial cell employed is the 75mm triaxial cell also provided by VJ Tech (VJT0475), which is capable of sustaining cell pressure of up to 3500 kPa.

The samples are placed in a conventional triaxial cell and sheared accordingly. An unconsolidated undrained (UU) test is conducted, so the test only involves the shearing stage and pore pressures are not measured. The procedure is performed in accordance with BS EN ISO 17892-7:2018 for UU triaxial testing. As the sample is sheared to failure, the major principal stress or axial stress,  $\sigma_1$ , was measured. Furthermore, the cell pressure of the cell after consolidation prior to shearing is indicative of the minor principal stress or radial stress,  $\sigma_3$ . When subjected to high-strain-rate loading, pore pressure is unable to dissipate quickly enough. Therefore, UU triaxial tests serve as the best indication of quasi-static behavior for comparison.

Using these results, axial ( $\sigma_1$ ) and radial stresses ( $\sigma_3$ ) for the kaolin clay specimen under quasi-static compression was obtained. Kaolin clay samples under quasi-static loading was tested three times, for each moisture content level previously specified.

Prior to testing using the triaxial cell, samples were created by preparing cylinders with radius of 38 mm and length of 76 mm. At least three cylindrical samples were prepared for each kaolin consolidated at pressures of 400 kPa, 500 kPa, and 600 kPa, which corresponds to 41%, 42%, and 45% respectively.

#### Triaxial results

Figure 3.6 shows an example of shear failure from a triaxial test trial on kaolin clay. Distinct shearing was observed through the diagonal of the specimen. The result of the triaxial tests is shown in Figure 3.7. From the results, it was easily observed the point at which the sample reaches shear failure as the stress curve plateaus when the specimen reaches failure. In some cases, the stress measured in the test continues to rise even after shear failure, this is due to the fact that the compression of the specimen caused the cross sectional area of the specimen to increase even after reaching failure, hence the stress that the sample can withstand appears to

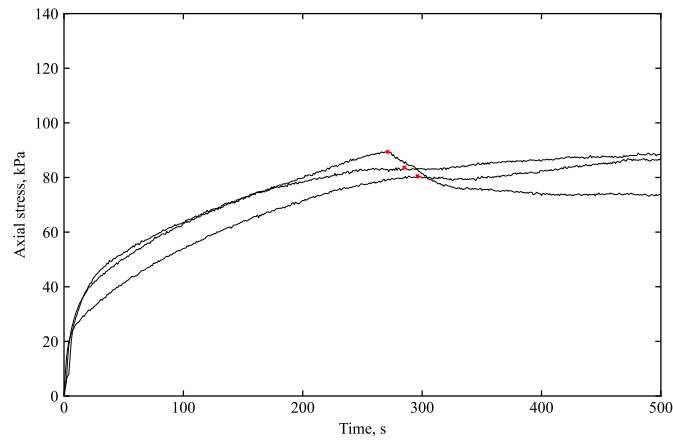


Figure 3.6: Example of evidence of shear failure after triaxial test of kaolin sample consolidated at 400 kPa.

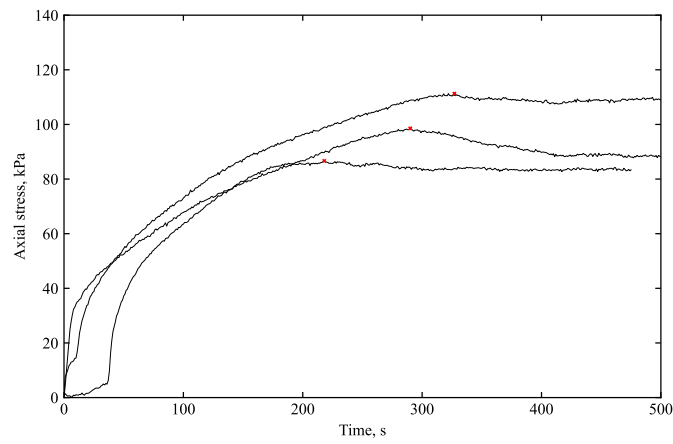
continue to increase even though the sample has effectively reached shear failure. However, the stresses endured after the sample reaches failure are not significant to the results, so those portions may be omitted.

Mohr circles from triaxial tests on kaolin clay at the three different moisture contents are shown in Figure 3.8. Since an unconsolidated undrained triaxial test was performed, maximum shear strength is expected to be the same for tests with different confining pressure. This is reflected as the radius of the Mohr circles are within a reasonable range of 5 kPa.

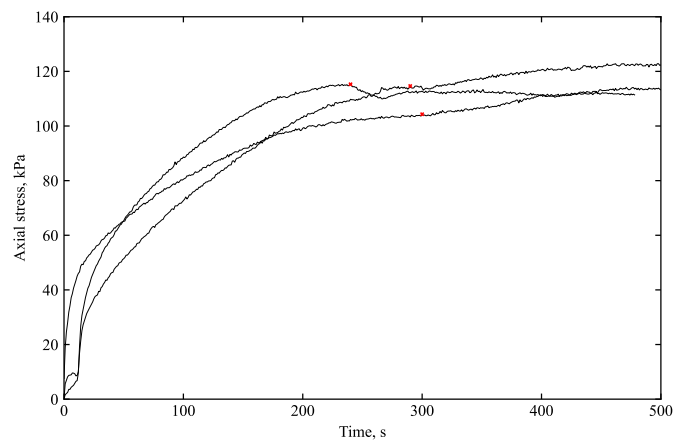
The point at which shear failure occurs is typically indicated by a distinct peak followed by a curve plateau on the stress-time plot. While this point is clear in most tests, this was not always the case and the point of failure was not obvious in certain tests. Hence each test was analysed individually to obtain the initial instance where the gradient turns negative (even if the curve eventually becomes positive again), the point of maximum stress between the initiation of the test and the first instance of negative gradient is then designated as the point of shear failure for the construction of Mohr circles, the points of failure for each test are indicated by a red point on Figure 3.7.



(a) Kaolin consolidated at 400kPa.

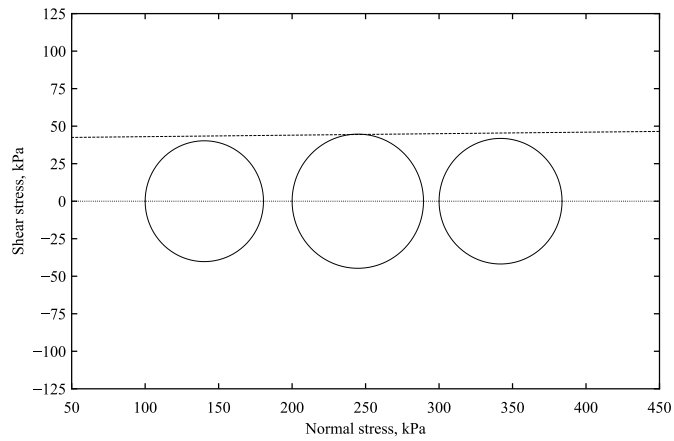


(b) Kaolin consolidated at 500kPa.

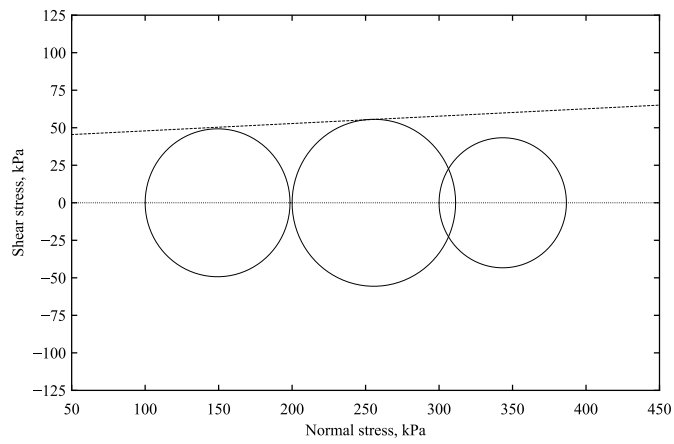


(c) Kaolin consolidated at 600kPa.

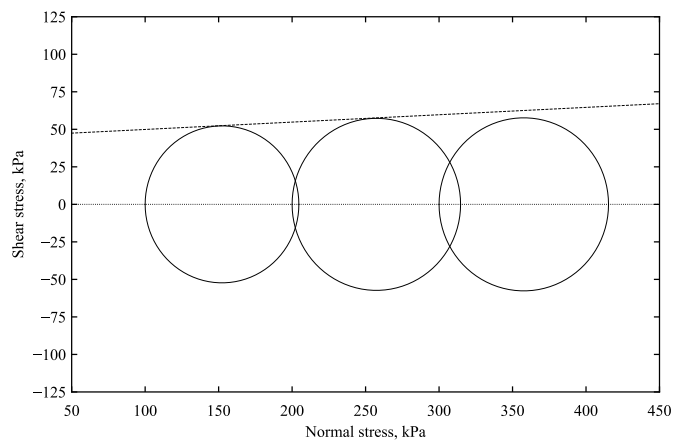
Figure 3.7: Triaxial tests (3 trials) on kaolin clay at moisture content of a) 44% b) 42% c) 41%. Points of shear failure are marked for each test with a red marker.



(a) Kaolin consolidated at 400kPa.



(b) Kaolin consolidated at 500kPa.



(c) Kaolin consolidated at 600kPa.

Figure 3.8: Mohr circles based on triaxial tests on kaolin clay at moisture contents of a) 44% b) 42% c) 41%.



### 3.3.2 Oedometer testing

Oedometer tests on the kaolin clay samples with the three existing moisture content levels are conducted to measure the effect of quasi-static compression. Oedometer testing is used to help bridge the results between the triaxial testing and SHPB testing, the strain rates between the quasi-static loading from the triaxial tests and the high-strain-rate testing from SHPB tests are ideally connected via the results from oedometer tests. This allows for the relationship of strain rate to be better investigated.

Oedometer tests were performed on the kaolin clay up to 3200 kPa. Loading was provided in 8 stages, the applied load started at 25 kPa and doubled every stage. Each load increment is applied over 24 hours to ensure the sample is properly consolidated to each load stage. This gradual loading process ensured that internal moisture was permitted to escape from the soil voids, and void compaction is observed through the test.

The consolidation system used for oedometer testing is the: ACONS pro motorised automatic consolidation system from VJ Tech. The consolidation cell employed is of diameter of 75 mm and is also provided by VJ Tech (VJT0665). The software used is the VJT-csODO: Clisp studio Oedometer Software, used specifically with the consolidation system from VJ Tech. The consolidation system is used in accordance with BS EN ISO 17892-5 : 2017 for incremental loading oedometer tests.

Oedometer tests were performed on three different kaolin samples (400 kPa, 500 kPa, and 600 kPa consolidated kaolin). During a traditional oedometer test, the load is applied 7 times to apply an axial load corresponding to the 8 loadings stages (25 kPa, 50 kPa, 100 kPa, 200 kPa, 400 kPa, 800 kPa, 1600 kPa, 3200 kPa). Once all the loading stages have been completed, data is collected from the apparatus to evaluate the behaviour of kaolin clay under quasi-static conditions. To achieve a stress condition that emulates high-strain rate testing, dynamic tests are also conducted where consolidation pressure was immediately set to 3200 kPa.

#### Oedometer results

Comparison of static tests where the consolidation pressure was gradually increased over time with dynamic tests where the consolidation pressure was immediately set to 3200 kPa revealed significant disparities in the behaviour of the kaolin. As seen from Figure 3.10, dynamic tests show no increase in density over the course of the consolidation phase, this is reflected by visible extrusions of kaolin from the consolidation cell as seen in Figure 3.9.

This behaviour is similar to SHPB tests in which the sample extrudes laterally rather than becomes consolidated (with limited axial stress transmission through the sample). Similarly, water experiences the same zero change in dry density when a stress is applied, as shown by the dashed line in Figure 3.10. This behaviour is comparable to the behaviour observed



Figure 3.9: Image after kaolin was dynamically consolidated using an oedometer to 3200kPa.

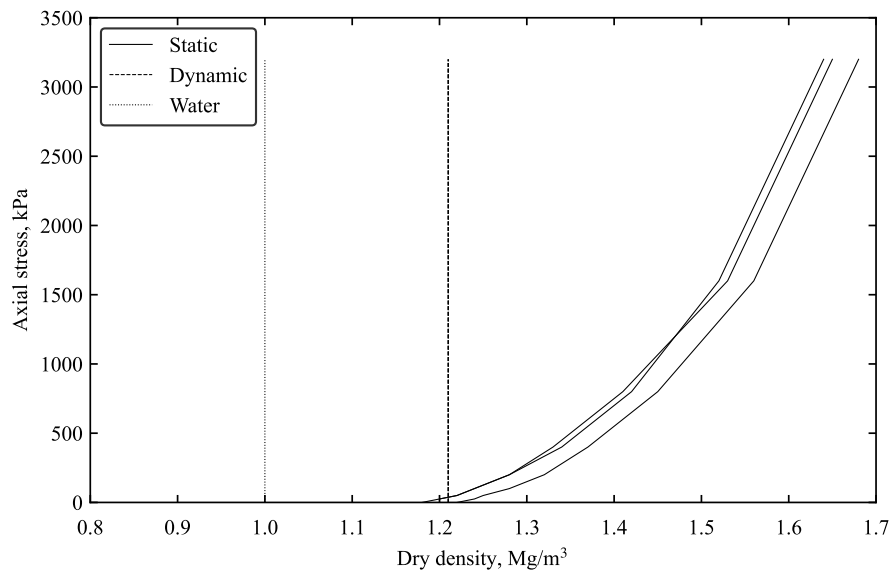


Figure 3.10: Variation of dry density with stress via oedometer test for kaolin consolidated dynamically and statically.

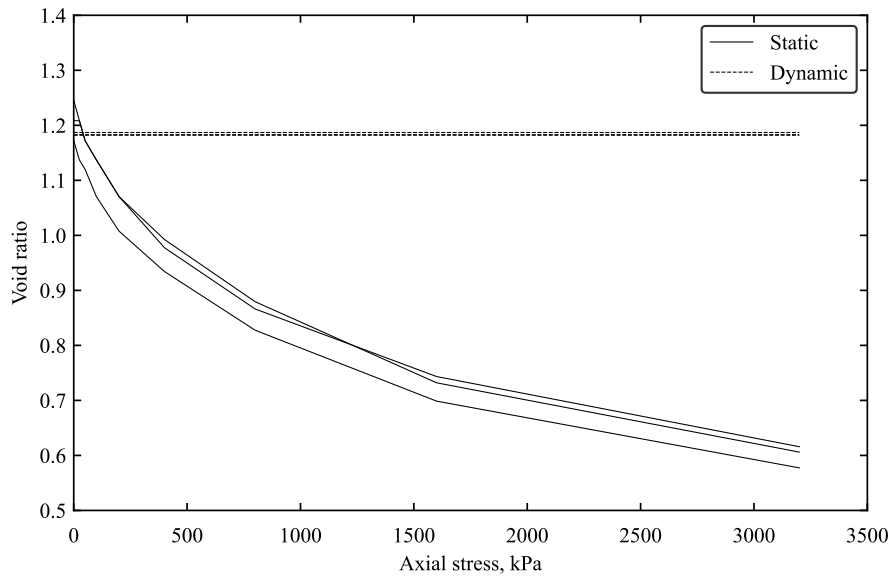


Figure 3.11: Variation of void ratio with stress via oedometer test for kaolin consolidated dynamically and statically.

in kaolin clay, implying that the behaviour of kaolin clay when subject to consolidation is influenced by the internal moisture

The permeability of cohesive soils such as clays play a crucial role in this behaviour, notably inability for pore water to dissipate quickly enough. This results in the moisture in the clay sample, rather than the soil structure, being the primary component being dynamically loaded. PSD for samples of kaolin clay revealed that the material consists of 81% clays, and particle mineralogy tests classified the material as a lean clay (CL).

This resistance to axial loading prompts the development of lateral pressure when kaolin clay is subject to the application of axial stress, resembling the behaviour of fluids. The fluid-like behaviour demonstrated from oedometer testing is revisited in Chapter 4, where preliminary SHPB tests on kaolin clay reveal a similar effect of lateral extrusion.

### 3.3.3 Discussion and findings from quasi-static testing

Quasi-static testing provided a vital basis of understanding of the material behaviour, as well as providing a point of comparison between quasi-static and high-strain-rate behaviour in order to gauge strain rate effects of the material. A notable result from dynamic oedometer loading is that kaolin clay exhibits fluid like behaviour even at much lower strain rates. This is attributed to the low permeability of clays which hinders the dissipation of pore water pressure and essentially takes over material behaviour.

Conducting UU triaxial tests on kaolin clay provided crucial material characterisation, but also provides a brief insight into the potential effects of moisture content. Kaolin clay consolidated with the Rowe cell at 400kPa, 500kPa, and 600kPa resulted in variations of moisture content, even though all samples are considered to be fully saturated.

A comparable aspect of triaxial tests is the existence of a confining pressure provided by the water pressure within the triaxial cell. However, since the test performed was a UU test, the extent of confining pressure is not fully conclusive due to the absence of a proper consolidation phase. The use of oedometer testing allowed for further characterisation of quasi-static behaviour. While consolidated drained triaxial tests could have been conducted, undrained strength is the most indicative representation of blast and impact events since it prevents the dissipation of pore pressure during loading.

Performing oedometer testing on kaolin clay provided insight of the behaviour when subject to gradual load increments increasing up to 3200kPa. When the sample was statically loaded by load increments, the behaviour observed was consistent with existing knowledge pertaining to quasi-static consolidation of cohesive soils. However, when the loading was set to the maximum of 3200kPa immediately at the start of the test, the material exhibited behaviour similar to the behaviour of fluid-like materials. Although not within the same strain rate range, this behaviour was indicative of the effects of high-strain-rate testing in that the behaviour of cohesive soils may be comparable to fluids.

Both methods of quasi-static testing provided evidence of key characteristics of cohesive soil properties and behaviour. Triaxial testing allowed for the material to be better characterised and for fundamental parameters to be obtained that can be used for reliability of future numerical analysis. Oedometer testing also provided insight on behaviour when the material was subject to sustained quasi-static loading. By increasing the strain rate of the oedometer loading stages, an effect similar to fluids begin to appear in the results.

### 3.4 Sample preparation

The importance of moisture has been highlighted through quasi-static testing, hence it is crucial to develop a method that allows for moisture content levels to be varied throughout high-strain-rate testing with the SHPB apparatus.

#### 3.4.1 Initial material preparation

Initial kaolin clay specimens were prepared using powdered Speswhite kaolin clay, which was mixed with water and sieved then finally compacted to create a solid homogenous kaolin clay sample. Three different compaction pressures were used to consolidate samples with a Rowe cell to varying moisture contents; the varying pressures were 400kPa, 500kPa, and 600kPa. Each sample's volume and weight was recorded and one of each sample was oven dried at 110°C overnight and reweighed to determine the respective moisture contents of each sample.

The average moisture content of the samples compacted under 400 kPa, 500 kPa, and 600 kPa was 44.08%, 42.35%, and 41.63% respectively. The dry bulk density of the samples was determined using a measured volume of a specimen and the mass of the dried soil. The dry density for samples compacted under 400 kPa, 500 kPa, and 600 kPa were 1.20 Mgm<sup>3</sup>, 1.25 Mgm<sup>3</sup>, and 1.27 Mgm<sup>3</sup> respectively.

#### 3.4.2 Moisture content variation

To investigate the effects of moisture content and by extension saturation ratio, an air drying procedure was undertaken in order to obtain moisture contents of the levels: 0%, 5%, 10%, 15%, 20%, 25%, 30%, 35%, as well as 41%, 42% and 45% which are assumed to be fully saturated. This provided a range of saturation levels to investigate whether there is a distinct difference in behaviour between unsaturated, partially saturated, and fully saturated specimens.

Samples at varying moisture contents are prepared with the intent for use in all SHPB testing using the following procedure:

1. Initially prepared fully saturated kaolin clay samples are cut using a stainless-steel, cylinder shaped cutting tool. Specimens are cut to a diameter of 25 mm and a nominal length of 5 mm. Initial weight and dimensions of the specimens are noted immediately after cutting.
2. Specimens are air-dried in a 20°C temperature controlled room, and are weighed at regular intervals until they reach the desirable moisture content. An approximation of

the moisture content at certain time intervals was obtained based on the initial moisture content and volume of the specimen.

3. After air-drying, specimens were wrapped in polyvinyl chloride to prevent changes in moisture content prior to testing. As sample preparation and SHPB testing is conducted in separate laboratories, wrapped specimens are placed in sealed plastic bags for transport and to minimise the risk of contamination.

While the air-drying process inevitably results in a degree of volume loss, the change in volume between fully saturated and oven dried samples remain less than 5% of the original sample volume. In addition, the samples are reweighed and measured immediately prior to testing to ensure that the most accurate sample measurements are obtained for each experimental trial.

### **3.5 High-strain-rate test programme**

Based on quasi-static testing and material characterisation of kaolin clay, a test programme has been developed with the aim of evaluating the effects of moisture content and strain rate. Of which ultimately leads to the evaluation of the effects of confinement by comparing the effects under different confinement mechanisms. Samples with moisture content greater than 40% are samples prepared immediately after Rowe cell consolidation and are assumed to all be at a saturation ratio of 100%, hence all samples above 41% are grouped together.

All trials in the test programme are conducted within the spectrum of high-strain-rate at magnitudes of  $10^3 \text{ s}^{-1}$  on kaolin clay. For the current SHPB setup, increasing the speed of the striker bar similarly increases the strain rate of the test setup. Hence the test programme was designed based on the striker speed, however the striker speed for each confinement mechanism corresponds to a particular strain rate (all within the  $10^3 \text{ s}^{-1}$  range), of which the exact strain rate values for each test was revealed through post-test data processing.

Table 3.3: Test programme for three different confinement modes at various speeds and moisture content levels.

<b>Unconfined tests</b>		
Striker speed, m/s	Total trials	Moisture contents tested, %
8	37	0, 5, 10, 15, 20, 25, 30, 35, 40
12	27	0, 10, 15, 20, 25, 30, 35, 40
16	27	0, 10, 15, 20, 25, 30, 35, 40
18	3	0, 20, 40
20	2	0, 20
22	2	20, 25
98		
<b>Confined tests</b>		
Striker speed, m/s	Total trials	Moisture contents tested, %
12	9	0, 20, 40
18	20	0, 10, 20, 25, 30, 35, 40
20	7	0, 20, 41
22	10	0, 10, 20, 30, 40
46		
<b>Partial lateral confined tests</b>		
Striker speed, m/s	Total trials	Moisture contents tested, %
12	3	40
16	9	0, 20, 40
20	3	40
15		

### 3.6 Summary

This chapter introduced kaolin clay as the material of focus, and discussed the in-depth characterisation of the material through a wide range of tests. This allowed for kaolin clay used in this study to be compared with existing literature, and to ensure reproducibility of results. Material characterisation tests regarding the particle density, particle shape, particle size distribution, particle mineralogy, and the Atterberg limits were uncovered from testing.

UU triaxial compression tests were conducted to characterise the behaviour of kaolin clay under quasi-static conditions. This has been coupled with oedometer tests to reveal the dynamic effects on cohesive soils. Quasi-static tests shows that the inability of cohesive soils to dissipate pore water pressure causes the moisture to be the key factor in governing the behaviour of cohesive soils when loaded dynamically. This is crucial as this indicates that even at lower strain rates, cohesive soils such as kaolin clay mostly exhibit fluid-like behaviour.

Since moisture has been determined to be a crucial variable in dictating the behaviour of cohesive soils, a method to control moisture content was developed that would facilitate SHPB tests at various moisture levels. This consisted of the initial consolidation of to obtain fully saturated kaolin samples, and the subsequent air-drying process to ensure the sample reached the desired moisture content level. A testing programme for high-strain-rate testing with the SHPB was devised with an intention to not only uncover the effects of moisture, but also compare the results with different confinement mechanisms.





## Chapter 4

# High-strain-rate testing of kaolin clay

## 4.1 Introduction

The investigation of kaolin clay under high-strain-rate was conducted using one-dimensional compression tests at strain rates to the order of  $10^3 \text{ s}^{-1}$  using a split-Hopkinson pressure bar. Kaolin samples with a diameter of 25 mm and a nominal length of 5 mm were prepared as previously specified. Tests were conducted at different moisture contents and strain rates to evaluate the effects they have on stress propagation and material behaviour. The comparison between free field unconfined and rigid steel ring confined SHPB tests were used as a foundation for the investigation of confinement effects. Experimental results are processed with an computational algorithm, `SHPB_processing.py`, which has been developed to process a wide range of SHPB testing, correct for experimental limitations, and facilitate deeper analysis. Relevant results from high-strain-rate testing of cohesive soils have been documented and submitted for publication (Van Lerberghe et al., 2024b), the corresponding journal paper is included in Appendix A.5.

## 4.2 High-strain-rate methodology

Methodology and detailed setup procedures within this section primarily pertain to unconfined and confined SHPB testing. However, aspects of methodology and apparatus developments are similarly applicable to the partial lateral confined SHPB apparatus discussed in Chapter 5.

### 4.2.1 Split-Hopkinson pressure bar methodology

As discussed in Section 2.4, SHPB apparatus is utilised to perform high-strain-rate testing on the kaolin clay specimen. The SHPB is struck from one end by a steel striker bar fired from

a gas gun, so that a compressive stress pulse propagates through the system consisting of two EN24T steel pressure bars. The pressure bars are calibrated by comparing the incident signal from the impact of the striker of known velocity and the theoretical strain in the bar given by the relationship

$$\varepsilon_b = \frac{v_s}{2c_0} \quad (4.1)$$

where  $\varepsilon_b$  is the longitudinal strain in the bar,  $v_s$  is the velocity of the striker bar on impact, and  $c_0$  is the longitudinal wave speed of the bar. The wave speed is found by the following relationship

$$c_0 = \frac{2l}{t} \quad (4.2)$$

where  $l$  is the distance between the strain gauge and specimen end of the bar and  $t$  is the time between incident and reflected pulses. The gauge factor,  $F$ , is defined as the ratio between voltage across the gauge's Wheatstone bridge and the strain,  $\varepsilon_b$ :

$$F = \frac{2V_o}{\varepsilon_b V_i} \quad (4.3)$$

where  $V_i$  and  $V_o$  are the input and output voltages across the Wheatstone bridge.

The experimental setup consists of 25 mm diameter steel incident, transmitter and striker pressure bars with lengths of 2500, 1500, and 350 mm respectively, and arranged in a typical SHPB arrangement. The wave speed and gauge factors for the specific pressure bar arrangement are determined prior to testing by conducting preliminary dummy tests and processing raw data with the equations discussed above. SHPB tests are initiated by firing the striker bar onto the free end of the incident bar with a gas gun apparatus.

Tests were initially conducted with a traditional unconfined SHPB setup to understand free field stress behaviour of kaolin clay, SHPB apparatus equipped with a steel confining ring was subsequently used to gain initial understanding of high-strain-rate behaviour when subject to rigid lateral confinement. This was crucial in understanding the effect of various confinement modes and consequently the effects of lateral confinement and triaxial stress state on mechanical properties of kaolin clay.

### **Instrumentation and Wheatstone bridge processing**

When loading is provided by firing the steel striker with a gas gun at the incident bar, the signals from the pressure bar strain gauges (Kyowa KSP-2-120-E4 semiconductor strain gauges) and pressure transducer was recorded using a TiePie Handyscope four channel digital oscilloscope, using 14-bit resolution and a sampling rate of 1.562 MHz.

Two strain gauges were installed onto each pressure bar in an arrangement so that strain caused by bending is eliminated, ensuring only longitudinal strain is obtained as shown in Figure 4.1a. The strain gauges on each pressure bar is configured as a half Wheatstone

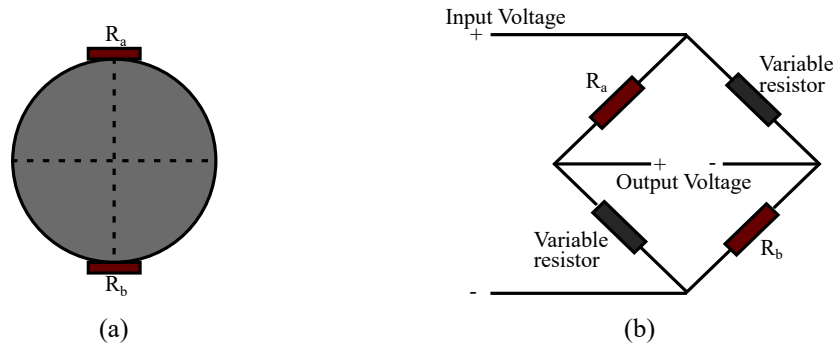


Figure 4.1: Split-Hopkinson pressure bar a) strain gauge arrangement, b) Wheatstone bridge.

bridge, in order to obtain an analogue voltage signal when the pressure bar is subject to even the slightest change in strain. Variable resistors are adjustable to balance out temperature-induced strains. The Wheatstone bridge circuit is shown in Figure 4.1b, where  $R_a$  and  $R_b$  are variable resistors used to balance the Wheatstone bridge.

The recorded voltages from the incident and transmitter pressure bars are then processed to calculate the strain using the equation:

$$\varepsilon_b = 2 \frac{V_o}{FV_i} \quad (4.4)$$

#### 4.2.2 Setup adjustments and invalid data

The initial series of SHPB testing on the three different confinement modes was conducted in 2021 on saturated kaolin clay samples in order to obtain a preliminary understanding of kaolin clay under high-strain-rates, as well as evaluating the previous experimental setup and propose modifications. The previous SHPB apparatus was equipped with a gas gun that consisted of a barrel and reservoir component as seen in Figure 4.2. A thin 0.2 mm brass diaphragm was used to seal the boundary between the barrel and reservoir components. As the gas reservoir is pressurised during a test, the brass diaphragm ruptures and fires a nylon piston inserted a set distance in the barrel onto the striker bar.

Although the result were indicative of high-strain-rate behaviour, there are primary limitations that make the previous setup not feasible and prompts the development of a newer SHPB apparatus and setup. These issues include:

- Uncertainty of striker bar speed and gas gun pressure
- Corrosion of strain gauge wiring and electronics

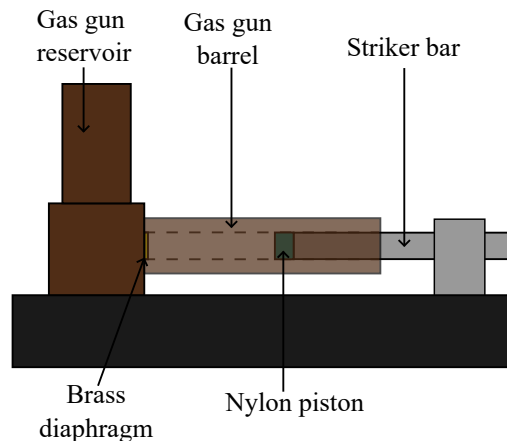


Figure 4.2: Schematic of old gas gun.

- Expansion of old confining ring due to repeated testing leading to ineffective confinement and increased volume loss to extrusion.

However, key findings could still be obtained from the tests and are briefly described in the following section.

### Findings from initial SHPB testing

A set of nine initial SHPB tests were conducted on saturated kaolin clay with a confining ring. The strain rate of these tests are processed to be approximately  $2300 \text{ s}^{-1}$ , however the inability to control the pressure of the gas gun prevents the exact striker bar velocity from being controlled. Qualitative observation of the experiments also revealed that the previous gas gun experiences pressure loss prior to the experiment, leading to even greater unreliability regarding striker bar velocities and subsequent experimental strain rates.

In addition, saturated kaolin tests were conducted with the partial lateral confined SHPB reservoir as initially discussed in Chapter 2. As seen from Figure 4.3, while the pulse from the transmitted bar could be briefly seen, a significant portion of noise interferes with the pulse signal. However, this gives an indication that the material prevents a significant portion of wave propagation, reducing the transmitted stresses to an extremely low magnitude compared to the incident stress. Hence it is evident stress signals need to be implemented with amplification capabilities to enhance the signal such that behaviour at much lower stresses could be more accurately monitored.

The use of aluminium or polymer bars have been considered to resolve the issue of low acoustic impedance characteristic of the kaolin sample. The use of pressure bars with a lower stiffness than steel reduces the impedance mismatch for soft materials such as clays

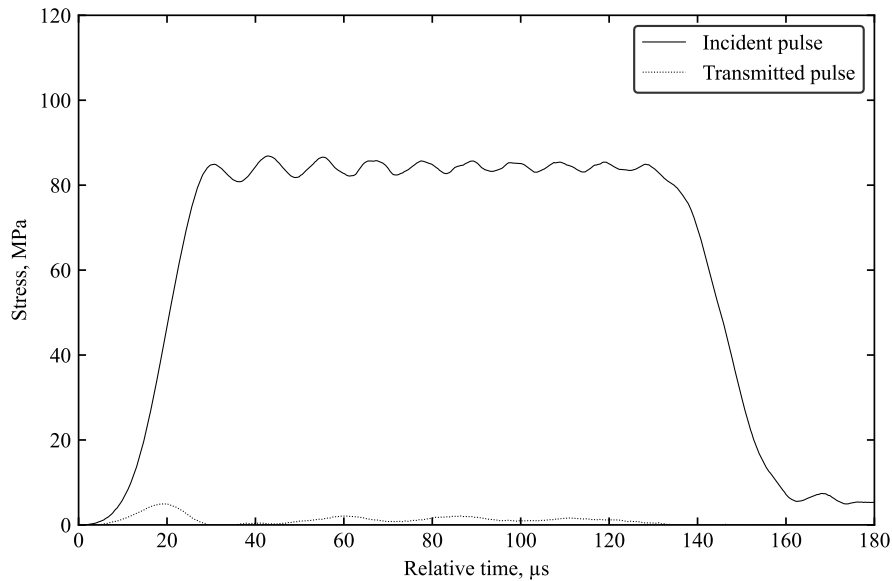


Figure 4.3: Incident and transmitted pulse stresses from preliminary SHPB tests.

Jakkula et al. (2021). If the acoustic mismatch between the pressure bars and the sample material is significant, then the stress wave experiences full reflection. However, the difference between incident and reflected pulses indicate that the opposite occurs, such that a large portion of the initial stress wave still propagates into the sample from the steel pressure bars. While the use of pressure bars composed of less stiff materials would be valuable, this indicates that tests performed with steel pressure bars are sufficiently accurate in illustrating the effect on kaolin clay.

### Modifications from old SHPB apparatus

A new gas gun setup was developed that allows for a controlled amount of nitrogen gas to be pressurised in a closed gas gun reservoir. The striker bar is inserted a certain distance into the gas gun chamber. Finally, when test is ready to be initiated, a poppet valve in the gas gun reservoir releases the pressurised gas into the chamber and fires the striker bar, as seen in Figure 4.4. Pressure gauges are installed to monitor the exact pressure (with an accuracy of  $\pm 1$  psi) within the reservoir immediately prior to loading, and this pressure could be adjusted by letting in or releasing air to the desired pressure setting. This controlled environment allowed for the velocity of the striker bar to be specifically defined and consistent throughout all tests.

A speed trap mechanism was installed on the free end of the gas gun chamber to record the striker bar distance as it leaves the chamber and prior to impacting the incident bar. The speed trap consists of a 50 mm wide light gate connected to the TiePie Handyscope

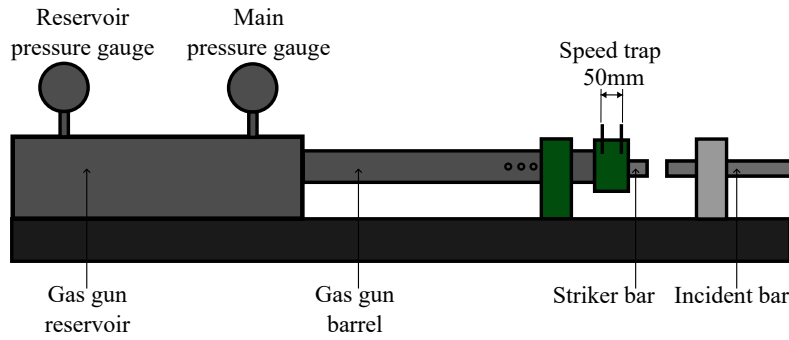


Figure 4.4: Schematic of new gas gun with speed trap mechanism installed.

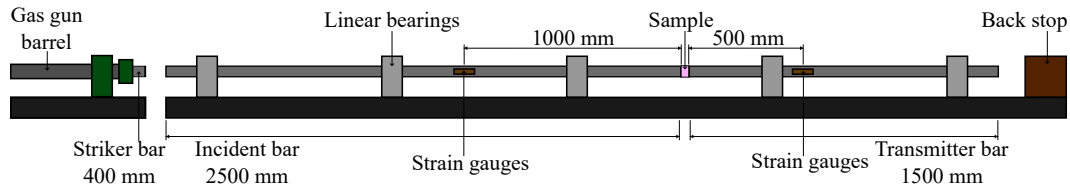


Figure 4.5: Schematic of the main components of a SHPB test under unconfined conditions

oscilloscope, the time difference between the activation of both ends of the light gate is used to determine the precise velocity of the striker bar as it exits the barrel of the gas gun,  $v_s$ , according to:

$$v_s = \frac{l_s}{t_b - t_f} \quad (4.5)$$

where  $l_s$  is the speed trap distance (50 mm),  $t_b$  and  $t_f$  are the time at which the back and front end of the speed trap are activated. A simplified schematic of the current setup after modifications and redevelopment is shown in Figure 4.5, including the new gas gun and speed trap mechanism.

### 4.2.3 Unconfined SHPB testing procedure

While the following test procedure contains elements characteristic of conventional SHPB experimental methodology, key aspects are specifically applicable for current experimental testing on kaolin clay and thus detailed procedural sequences are described.

Directly prior to testing, kaolin clay samples are weighed using an RS Pro scale, that measures the mass of kaolin samples to an accuracy of  $\pm 0.001$  g. Three different measurements are made for both the diameter and thickness of the kaolin clay sample using digital calipers with an accuracy of  $\pm 0.01$  mm. An average of the diameter and thickness based on the three measurements are used to account for sample shape variability. All diameter and thickness data recorded from unconfined tests are included in Appendix B.

Testing of kaolin clay with the unconfined SHPB then proceeds as follows:

1. Measured kaolin clay sample was carefully placed in between the incident and transmitter bars situated inside a polymer containment box, then the lid of the containment box was closed to limit contamination of the setup from eventual sample extrusion.
2. Striker bar was inserted at a specific distance inside of the chamber of the gas gun.
3. Isolator valve on gas gun was opened to allow nitrogen gas into the gas gun, the pressure from the gas supply must be greater than the eventual desired reservoir pressure (pressure from gas supply was indicated on main pressure gauge).
4. Main valve on gas gun was gradually opened to release the specific gas pressure into the reservoir of the gas gun (current pressure can be seen on reservoir pressure gauge)
5. Isolator valve was closed to stop nitrogen gas flow from nitrogen gas tank.
6. Test was initiated by opening the activation valve, this simultaneously opens the poppet valve and releases the pressurised nitrogen gas from the reservoir into the chamber and propels the striker bar.

The specific gas pressure and distance that the striker bar is inserted in the gas chamber factor into the final velocity of the striker bar leaving the chamber. Thorough speed tests to determine the ideal gas pressure and striker bar distances have been conducted to establish the ideal combinations to obtain the desired striker bar velocities. Details of speed tests and results are included in Appendix C.

#### 4.2.4 Confined SHPB testing procedure

Soil specimens in confined SHPB tests are restricted using a steel confining ring with internal diameter of 25 mm, external diameter of 35 mm, and length of 5 mm. A singular strain gauge is attached on the external edge of the confining ring, which allows for the measurement of the circumferential strain during loading, as seen in Figure 4.6a. As only one strain gauge is used to measure radial stresses from the confining ring, a quarter Wheatstone bridge is constructed (Figure 4.6b) to obtain analogue voltage readings correlating to the slight changes in strains.

The internal radial pressure from the specimen onto the confining ring,  $P_i$ , can be determined by applying thick walled pipe theory and is obtained by applying the expression

$$P_i = \frac{r_o^2 - r_i^2}{2r_i^2} E \epsilon_\theta \quad (4.6)$$

where  $E$  is the Young's modulus of the ring,  $\epsilon_\theta$  is the circumferential strain measurement on the outside of the ring (with strain gauge), and  $r_o$  and  $r_i$  are the outer and inter radii of



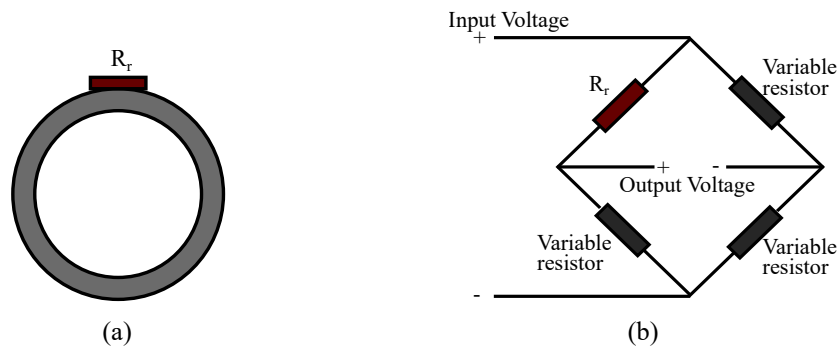


Figure 4.6: Confining ring a) strain gauge arrangement, b) Wheatstone bridge.

the confining ring respectively (Stephens, 1970). Based on the current confining ring and arrangement, the value of  $P_i = 0.48E\epsilon_\theta$ . To account for change in the length of the sample during loading, the internal pressure acting on the shortened sample length given by  $P_s$  can be expressed by

$$P_s = P_i \frac{l_r}{l_s} \quad (4.7)$$

where  $l_r$  is the length of the confining ring (5 mm), and  $l_s$  is the length of the sample obtained from processing pressure bar axial strain data.

The procedure to conduct a confined SHPB test is similar to the unconfined SHPB procedure, after measuring the sample for testing, the following steps are followed:

1. Slide confining ring slight onto the incident bar and place the sample in between the incident and transmitter bars.
2. Confining ring is carefully slid over to overlap the sample, ensuring that the sample is centred within the confining ring and contact between the confining ring and pressure is limited.
3. Containment box lid is closed and gas gun is setup for initiation and test proceeds in the same manner as unconfined SHPB testing.

Prior to all confined tests, measurements of the sample diameter and mass are recorded in the same manner as unconfined tests. All diameter and thickness data recorded from confined tests are included in Appendix B.

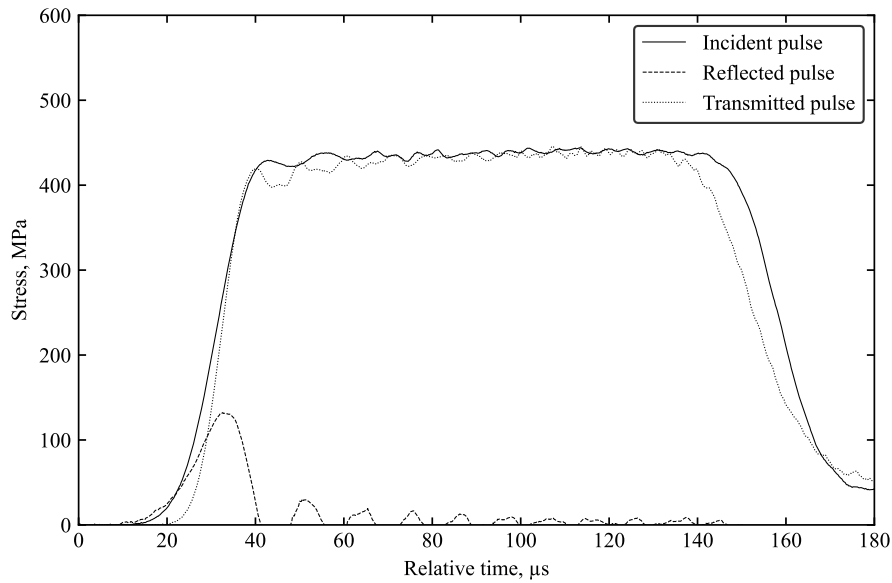


Figure 4.7: Typical incident, reflected, and transmitted stress pulses obtained from bar to bar calibration test.

#### 4.2.5 Bar to bar calibration

Prior to each testing day, bar to bar calibration tests are performed in which the incident and transmitter pressure bars are directly in contact prior to loading of the gas gun. This ensures that the apparatus is functional and signals obtained from gauge input are accurate. This verifies that the standard condition of stress equilibrium characteristic for conventional SHPB tests is true and ensures signal inputs are accurate and reliable.

Typical signal inputs from bar to bar tests is illustrated in Figure 4.7, where a near full transmission of stress pulse is seen between the incident and transmitted pulses. Since there is direct contact between the two steel pressure bars, the amplitude of the incident pulse should be directly transferred to the transmitted pulse. The reflected pulse should remain at a minimal level, while any small discrepancies should be due to imperfections at the end of the pressure bars (likely an inevitable consequence of repeated testing) or issues associated with the gauge or amplification box. The results fulfil the condition for stress equilibrium, where the superposition of incident and reflected should equate the transmitted pulse. This calibration test checks that the apparatus is working as expected, hence validating the accuracy of subsequent test results.

### 4.3 Signal processing and data analysis

In order to facilitate the signal processing and data analysis of raw signal data from SHPB tests, an innovative computational algorithm was developed for the intention of processing a variety of SHPB tests. While the primary aim of the function is to process and analyse data from SHPB testing, specific elements of the function are key to complement the viability for high-strain-rate analysis of strain gauge signals from SHPB testing. The function has been tested against SHPB test data on samples of kaolin, aluminium, and medium sand. Medium sand data is acquired from processing existing raw test data from Barr (2016). The full source for `SHPB_processing.py` can be found in Appendix D.

The key elements of the function can be subdivided into the following functionalities:

- Pulse detection via automatic trigger and optimisation of pulse boundaries
- Pulse alignment and stress equilibrium
- Adjustment of stresses for various confinement mechanisms
- Dispersion correction (with the inclusion of the subroutine `dispersion.py`)

#### 4.3.1 Overview and purpose of function

Although the algorithm `SHPB_processing.py` was tested on SHPB samples of aluminium, sand, and kaolin clay, the algorithm was designed with the capability to process SHPB test results regardless of sample type, confinement mechanism, or sample dimensions. The method of data analysis and data processing are based on one dimensional wave theory and SHPB apparatus setup principles (Section 4.2).

The command line prompt to execute the function is in the form:

```
SHPB_processing(csv_path, sample_data, confinement, signal_channels,  
               signal_amp, disp_correction, alignment, speedtrap)
```

where the specified input arguments correspond to the variables defined in Table 4.1. By providing the input arguments specified, the function is capable of determining the axial and radial (if confinement specified) stresses at the sample, sample strain and strain rate histories, and other derivative variables.

Table 4.1: Definition of input arguments used in the function `SHPB_processing.py`.

<i>Input arguments</i>	
<code>csv_path</code>	File directory to CSV file containing raw voltage data in the form of: Time, Channel 1, Channel 2, Channel 3, Channel 4...
<code>sample_data</code>	A list containing 3 elements that correspond to length (mm), mass (g), and dry mass (g) for the initial sample. i.e. <code>[initial_length, mass, dry_mass]</code> .
<code>confinement</code>	Specify confinement mechanism of SHPB test. i.e. 'None', 'Ring', or 'Reservoir'.
<code>signal_channels</code>	Specify oscilloscope channels for input, output bars and any confinement mechanism used to record raw voltage data. i.e. <code>[in_bar_gauge_channel, out_bar_gauge_channel, ring_gauge_channel or reservoir_gauge_channel]</code> .
<code>signal_amp</code>	Specify oscilloscope signal amplification factors for input, output bars and any confinement mechanism. i.e. <code>[in_bar_gauge_amp, out_bar_gauge_amp, ring_gauge_amp]</code> .
<code>disp_correction</code>	Specify if dispersion correction or simple timeshift is used to process pulse ( <code>dispersion.py</code> must be attached if dispersion correction is specified). i.e. True for dispersion correction, False for simple timeshift.
<code>alignment</code>	Specify the alignment mode for aligning stress waves at front and back of sample interface. i.e. 'start' aligns the start of the transmitted pulse to the start of the incident pulse, 'end' aligns the end of the transmitted pulse to the end of the incident pulse, 'mid' aligns the median time of the transmitted pulse to the median time of the incident pulse, integer/float values greater than 1 aligns the peaks of the incident and transmitted pulses to the specified value, and float values between 0 and 1 align the transmitted to the incident pulse based on a fraction of the maximum strain.
<code>speedtrap</code>	Specify if speed trap is employed and whether velocity of striker bar is determined. i.e. True to include velocity calculation using speed trap.

The brief operational procedure of the function can be described as follows:

1. Analysing striker velocity based on raw speed trap data
2. Preparing raw data for dispersion correction via initial pulse detection and signal re-formatting
3. Dispersion correction of strain pulses (omit if dispersion correction is not specified)
4. Processing sample stress data
  - Incident, reflected, transmitted pulse detection based on trigger
  - Sample strain determined from displacement of the pressure bars based on strain gauge data
  - Determining sample axial stress and strain by using one-dimensional wave theory to obtain stresses at both bar-specimen interfaces
5. Processing radial stress and strain data if confinement mechanism is applied
  - Radial pulse detection based on trigger
6. Compile final output stress and strain data at sample into CSV files in 'Processed data' folder, along with test log.

### **4.3.2 Pulse detection via automatic trigger and optimisation of pulse boundaries**

The incident, transmitted, and reflected pulses were detected using a trigger value that was determined by automatically evaluating the range of noise prior to initiation of loading over the first 1000  $\mu\text{s}$ . The initial noise is due to minor electromagnetic interference or innate equipment imperfections. This trigger value was then applied to detect the starting locations of the pulses based on the time step where strain exceeds the trigger value. This is applicable when considering cases in which the magnitude of the pulses are unknown or significantly different.

This is noticeable when observing SHPB data on kaolin clay under unconfined conditions, where preliminary tests revealed that extremely low transmitted signals make analysis of stresses on the back of the specimen interface difficult. In addition to amplification of the balance box when processing the raw voltage signals from the strain gauge, data processing must also account for the near zero values of transmitted stress. Hence the automatic trigger allows for the order of magnitude of the pulse to be automatically detected based on initial noise, and for the pulse limits to be accurately determined.

While the start of the incident and transmitted pulses are determined this way, the start of the reflected pulse is obtained based on the location of the incident pulse and determined by applying Equation 4.2. The length of the pulse is determined based on when the sample strain has reached its maximum and when strain-time history curve starts to flatten, this ensures that all aspects of the three pulses are accounted for even when the lengths of the three pulses may differ due to material behaviour.

### 4.3.3 Pulse alignment and stress equilibrium

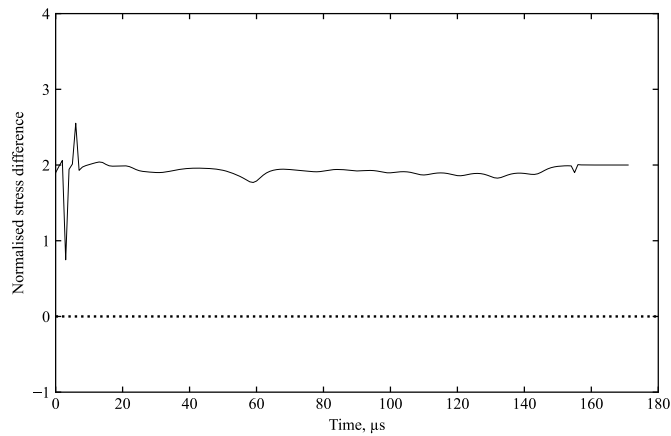
When SHPB tests are conducted on materials where there is an impedance mismatch, the rising edges of the incident, reflected, and transmitted pulses are usually not all the same, leading to an issue of alignment between the pulses. This is important for alignment of the incident and reflected stress to obtain accurate front stress, and also the alignment of the front and back stress to obtain accurate mid stress.

In accordance with one-dimensional wave theory, the following condition should be met if stress equilibrium is obtained in a SHPB test

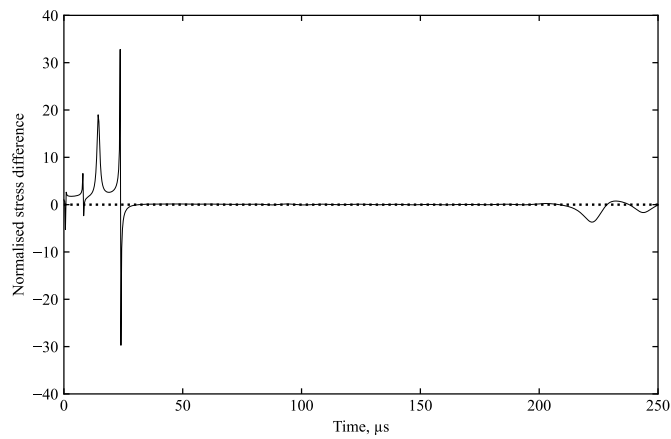
$$\epsilon_t(t) = \epsilon_i(t) + \epsilon_r(t) \quad (4.8)$$

where  $\epsilon_t(t)$ ,  $\epsilon_i(t)$ , and  $\epsilon_r(t)$  are the instantaneous values of the transmitted, incident, and reflected pulse strain-time histories (Wu & Gorham, 1997). In idealistic scenarios, stress equilibrium occurs such that momentum is conserved axially. While, this scenario is applicable to the majority of SHPB tests on solid materials, this case does not apply to all cases especially when a material tends to propagate stress laterally rather than axially when subject to high-strain-rate loading. Since the stress within the specimen is calculated by obtaining an average of the stresses at both the front and back ends of the interfaces by extrapolating strain gauge data, a mismatch in pulse length leads to the inability to determine an accurate average sample stress. By specifying an appropriate alignment mechanism, this effect was minimised and front and back stresses can still be compared.

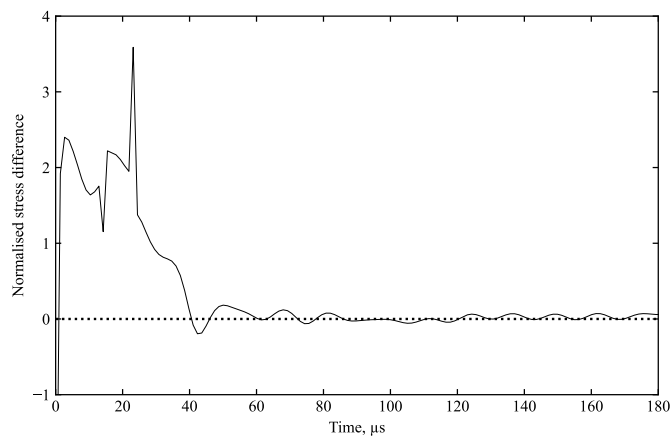
An example of this is the current case with kaolin clay, as seen in Figure 4.8a, where the difference between front stress (proportional to the superposition of  $\epsilon_i(t)$  and  $\epsilon_r(t)$ ) and back stress (proportional to  $\epsilon_t$ ) reveals a stress difference greater than zero, indicating that stress equilibrium is never truly obtained through the experiment. The difference between the front and back specimen stresses have been normalised over the mean, this enables for the release of inertial effects to be observed as the normalised stress difference tends to zero aligns with when front and back stress equalise. Comparatively, SHPB tests on aluminium and medium sand (Figures 4.8b and 4.8c) reveal that even though stress equilibrium is not initially obtained due to inertial effects, the front and back stresses eventually equalise as inertial effects start to release for materials without this impedance mismatch.



(a)



(b)



(c)

Figure 4.8: Typical stress wave difference between stress at front and back interfaces, normalised by their mean for a) kaolin clay, b) aluminium, c) medium sand.

Table 4.2: Confinement modes applicable in the function `SHPB_processing.py`.

<i>Confinement</i>	
None	Unconfined SHPB tests contain no calculation of radial stresses or strains.
Ring	SHPB tests conducted with a confining ring are processed based on thick-walled pipe theory described in Section 4.2.4. Radial pulse detection follows a similar method as incident and transmitted pulses. Lateral stresses and strains are calculated based on circumferential strain in confining ring.
Reservoir	SHPB tests conducted with the partial lateral confined reservoir fitted with pressure gauge are processed. Wave propagation through reservoir fluid is taken into account to derive lateral stress at sample surface. Refer to Chapter 5 for further details of theory and setup. Radial pulse detection follows a similar method as incident and transmitted pulses. Lateral stresses and strains are calculated based on changes in pressure measured with pressure transducer.

However, even though stress equilibrium is not obtained, it is still possible to draw findings and results from test data. It is vital to still be able to compare front and back stress data even when the pulses are of starkly different magnitudes and lengths. In order to align the front and back stresses, the addition of an alignment criteria allows for the pulses to be aligned based on the shape of the curves regardless of difference in pulse lengths. The opportunity to still visualise front and back stress data for stress-strain analysis enables the ability for SHPB data to be used for characterisation of high-strain-rate behaviour.

#### 4.3.4 Adjustment of stresses for confinement mechanism

The effects of confinement are especially pertinent to this research, as such it is crucial to obtain valuable radial stress data if the confinement mechanism allows for it. There are currently three input options for confinement: None, Ring, and Reservoir. The methods to process each mode of confinement can be summarised in Table 4.2.

For tests with confining ring and reservoir, radial stresses and strains are calculated based on gauge readings. By assuming the confining ring limits volumetric loss, the variation of density and dry density can be estimated by considering the change in volume based on the instantaneous sample strain-time history. However, changes in density during loading cannot be calculated for tests on materials that result in significant sample extrusion such as cohesive soils.



### 4.3.5 Dispersion correction

According to one-dimensional wave theory, the longitudinal stress waves in the pressure bars of an SHPB are traditionally presumed to only travel one-dimensionally along the pressure bars at an elastic wave velocity,  $c_0$ , thus readings at strain gauges are simply time shifted based on the travel time of the stress wave to obtain stresses at the sample interfaces (Gray III, 2000). However, the Poisson's ratio of the pressure bars actually has a significant impact on the wave, inducing phases of expansion and contraction radially in accordance to the compressive and tensile strains of the pressure bar as the wave travels through. The result of this radial expansion and contraction is the distortion of the stress distribution across the cross sectional area of the pressure bar (Kolsky, 1963).

Bancroft (1941) discovered that the stress wave actually travels at a certain phase velocity,  $c_\omega$ , which can be expressed by the function below:

$$(x - 1)^2 \varphi(ha) - (\beta x - 1)[x - \varphi(\kappa)] = 0 \quad (4.9)$$

where

$$\beta = (1 - 2\nu) \quad (4.10)$$

$$x = \left( \frac{c_\omega}{c_0} \right)^2 (1 + \nu) \quad (4.11)$$

$$h = \gamma(\beta x - 1)^{1/2} \quad (4.12)$$

$$\kappa = \gamma(2x - 1)^{1/2} \quad (4.13)$$

$$\varphi(y) = y \frac{J_0(y)}{J_1(y)} \quad (4.14)$$

and where  $c_\omega$  is the phase velocity,  $a$  is the bar radius,  $\nu$  is the wave number given by  $2\pi/\lambda$ ,  $\lambda$  is the wavelength, and  $J_n(y)$  is the Bessel function of the first kind of order  $n$ .

While standard practice as detailed from the ASM handbook states that using simple timeshift on the gauge signals is sufficient, it may still hinder the accuracy of the results and result in severe inaccuracies in data processing. These errors are especially prominent at higher frequencies ( $a/\lambda > 0.5$ ), Tyas and Watson (2001) developed a method to correct both the amplitudes and phase angles of each frequency from the raw signal.

### Phase angle correction

Adjustment was made to the phase angle to correct for dispersion by determining the phase velocity of each frequency component from Equation 4.2, and shifting each phase angle by a factor,  $\theta'_w$ , as described by:

$$\theta'_w = \left( \frac{c_0}{c_\omega} - 1 \right) \frac{\omega z}{c_0} \quad (4.15)$$

where  $\omega$  is the angular frequency of the frequency component, and  $z$  is the correction distance as initially pioneered by Gorham (1983). The adjustment of phase angles was applied to account for the dispersion of each frequency component over the distance between the strain gauge and the end of the pressure bar.

### Amplitude correction

Specific factors were applied to the amplitude of each frequency component. Tyas and Watson (2001) proposed the factors  $M_1$  and  $M_2$  to correct for the radial strain variation and Young's modulus respectively, and are defined in the following equations:

$$M_1 = \frac{2\left(1 + \frac{1-\beta x}{x-1}\right)}{\varphi(ha) + \frac{1-\beta x}{x-1}\varphi(\kappa a)} \quad (4.16)$$

$$M_2 = E \left( \frac{c_\omega}{c_0} \right)^2 \quad (4.17)$$

where  $E$  is the Young's modulus. The application of the factors  $M_1$  and  $M_2$  to the amplitude of the frequency components are detailed in the operation of the dispersion correction function designed for data processing.

#### 4.3.6 Function for dispersion correction

The algorithm `dispersion.py` was developed as a method of applying the phase angle and amplitude corrections as discussed, and is an optional subroutine of `SHPB_processing.py`. While the use of simple timeshift is possible within `SHPB_processing.py`, the option to apply the preferable dispersion correction method is included. The operation of `dispersion.py` involves the mandatory subroutine of `dispersion_factors.py`, which is employed to determine the suitable dispersion factors required for dispersion correction. The core capabilities of the dispersion function consist of the following two aspects, and is primarily focused on employing the `fft` function in python to adjust signal input.

**Frequency domain conversion via fast Fourier Transform (FFT):** By applying the FFT algorithm from the Python `numpy` library and `fft` function, the input strain signal is converted into a sum of sinusoidal waves with individual frequencies and amplitudes, known as a frequency domain.

Table 4.3: Definition of input arguments used in the function `dispersion.py`.

<i>Input arguments</i>	
<code>x</code>	Zero-padded strain signal in time domain.
<code>fs</code>	Sampling frequency, Hz.
<code>a</code>	Bar radius, m.
<code>c0</code>	One-dimensional wave velocity of pressure bar, m/s.
<code>E</code>	Young's modulus of the bar, GPa.
<code>z</code>	Distance to correct over, positive in direction of wave propagation, m.

**Correction bandwidth:** FFT operates based on discrete frequency values based on the sampling rate and length of the strain signal. The lowest readable frequency is determined by the sampling rate, with higher frequencies being multiples of this fundamental frequency up to the Nyquist frequency which is equal to half of the sampling rate, this prevents aliasing by ensuring a minimum of two samples per period. Undersampling can lead to inaccurate representation of signals, but frequency resolution can be enhanced by increasing sampling duration or zero-padding the input signal.

The `fft` function generates an N-length frequency domain vector  $X(\omega)$  from an N-length time-domain vector  $x(t)$ . Due to aliasing, the second half of  $X(\omega)$  mirrors the complex conjugate of the first half around the Nyquist frequency. Thus, modifications are only needed for the first  $N/2 + 1$  bins in  $X(\omega)$ , which can then be reflected to complete the vector.

Low strain signals on the bar surface limit frequency modifications from 39  $\mu$ Hz to 94 kHz for a 25 mm diameter stainless steel bar arrangement. After 94 kHz, a periodogram demonstrates a sharp decrease in signal strength, indicating the need for a low-pass filter to eliminate higher frequencies in order to correct for dispersion.

### Operation of `dispersion.py`

After the locations of the incident, transmitted, and reflected pulses are determined from the raw input signals, `dispersion.py` can be applied to determine the stress and strains at the front and back interfaces of the sample and bar by calling the function in the form:

```
dispersion(x, fs, a, c0, E, z)
```

where the specified input arguments correspond to the variables defined in Table 4.3.

By applying this subroutine, the dispersion correction method detailed by Tyas and Watson (2001) is applied to the current data set to obtain accurate axial stress and strains at sample interfaces. The resultant output is in the form of `x_strain` and `x_stress`, which are the

dispersion stress and strain signals, which can be fed back into `SHPB_processing.py` for further processing.

The brief operational procedure of the function can be described as follows:

1. FFT is used to translate strain input into frequency domain signal.
2. Ideal low-pass filter is employed to remove frequency components greater than the correction cut-off,  $M_1$ .
3. For each of remaining components below the Nyquist frequency:
  - (a) `dispersion_factors.py` is called to determine required phase shift, and the factors  $M_1$  and  $M_2$ .
  - (b) Dispersion corrected strain component is calculated by applying:

$$z_e = M_1 A e^{i(\theta - \theta'_w)} \quad (4.18)$$

where  $A$  is the original amplitude,  $\theta$  is the original phase angle, and  $\theta'_w$  is the derived phase angle correction.

- (c) Dispersion corrected stress component is calculated by applying:

$$z_\sigma = M_1 M_2 A e^{i(\theta - \theta'_w)} \quad (4.19)$$

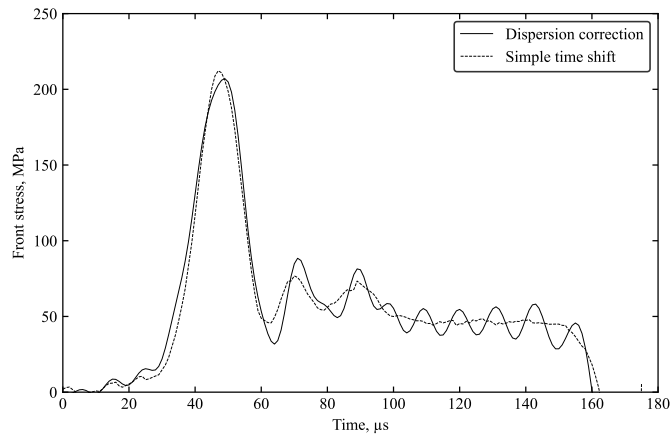
4. Complex conjugate of the adjusted stress and strains are used to define the frequency components above the Nyquist frequency.
5. Frequency-domain signals are translated back to time domain signals using inverse FFT to obtain output stress and strains, `x_stress` and `x_strain`.

### Application of dispersion correction method in SHPB testing

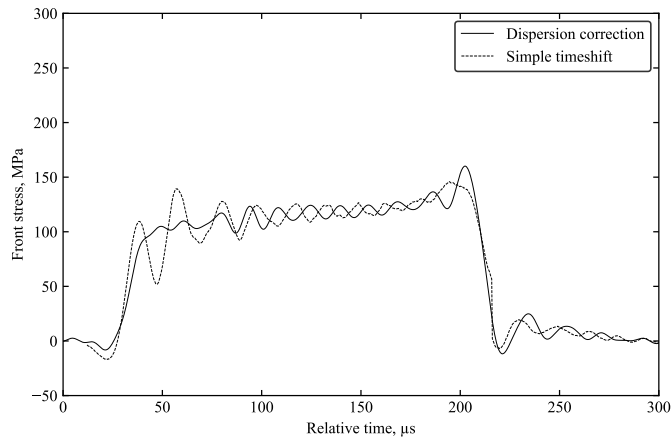
To evaluate the functional application of the dispersion correction algorithm, three different materials were processed by applying dispersion correction via `dispersion.py`. A comparison between the axial stress signals processed by applying simple timeshift and dispersion correction can be illustrated in Figures 4.9a, 4.9b, and 4.9c, which correspond to SHPB tests on kaolin clay, aluminium, and sand respectively.

The effect of applying the dispersion correction algorithm are immediately apparent. When dispersion corrected are applied to the incident and reflected pulses, the reductions of specious oscillations result in substantially more accurate processing of axial stress data.

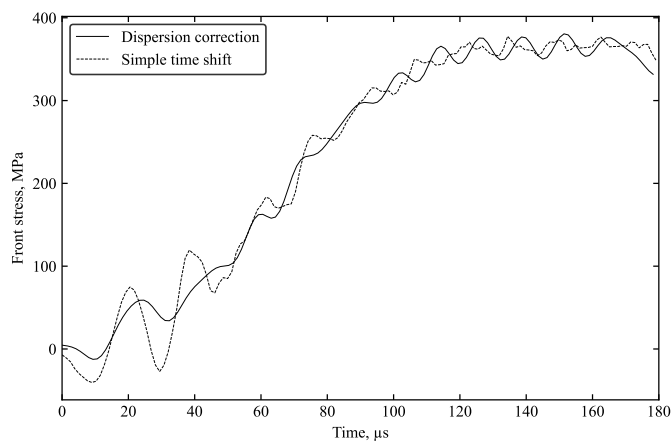
Full description of the dispersion correction functionality within `SHPB_processing.py`, the development of `dispersion.py` and associated subroutines, and the full application overview of the dispersion correction code has been published as a journal paper (Van Lerberghe et al., 2024a). The paper has been included in Appendix A.3 for reference.



(a)



(b)



(c)

Figure 4.9: Processed results of front stress dispersion correction and simple timeshift for a) kaolin clay, b) aluminium, c) medium sand with confining ring.

### 4.3.7 Data processing capabilities with other materials

While results on kaolin clay will be further discussed in detail in the following sections, processed data for SHPB tests on aluminium and sand have been included to validate the functionality and capabilities of the algorithm.

Tests on 12 mm samples of aluminium and 25 mm samples of medium sand were tested using the SHPB apparatus detailed in Section 4.2. Input arguments used to process test data using `SHPB_processing.py` for samples of aluminium, medium sand, and kaolin clay are described in Table 4.4.

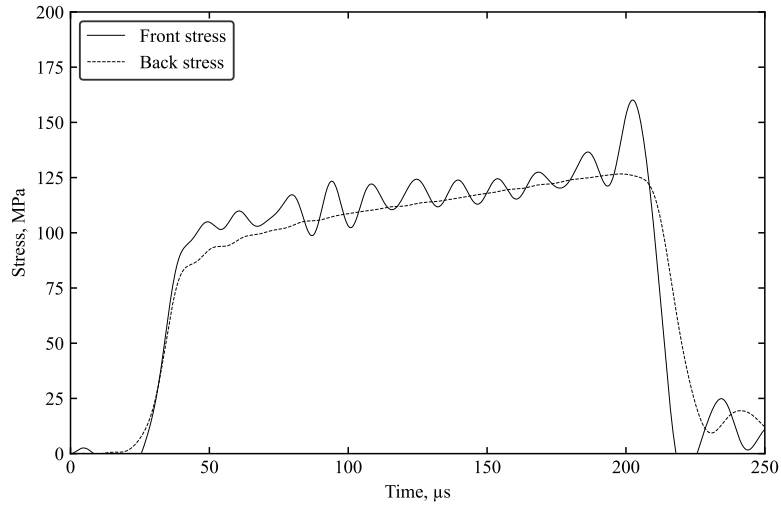
Figure 4.10 illustrates the ability to process raw SHPB strain gauge data to obtain stress data at sample interfaces, this is useful in characterising the ability of the material to enable the propagation of stress when subject to high-strain-rate loading. When confined tests are conducted, radial stress calculations could be obtained as seen for tests on medium sand in Figure 4.10b.

### 4.3.8 Discussion and summary of algorithm functionality

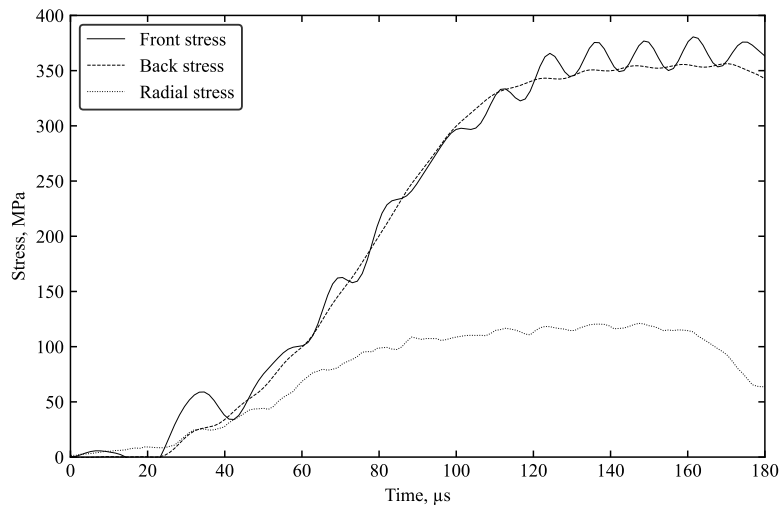
This script is capable of processing a variety of conditions relevant to SHPB testing including different confinement, and material properties. The optimisation of the pulse detection and the alignment process allow for SHPB data to be useful to characterise stress propagation behaviour under high-strain-rates, even when stress equilibrium is not obtained such in conventional SHPB tests due to the mapping of the three pulses individually. Furthermore, the addition of `dispersion.py` as a subroutine allows for strain signals to be corrected for effects of dispersion as a result of the Poisson's ratio of the pressure bar.

By evaluating tests with kaolin clay, aluminium, and medium sand, the capabilities of this method to process SHPB test data is demonstrated. While the capability to apply the algorithm on unconfined and confined tests have been discussed, the application of the function on partial lateral confined testing will be further described in Chapter 5.

Even though the current iteration of the function has been comprehensively tested with stainless steel pressure bars, further testing on different SHPB setups should be investigated. SHPB tests conducted with aluminium or polymer pressure bars was valuable in ensuring the function is accurate in processing test data of bar materials with different Poisson's ratio. While the alignment of front and back stresses are crucial in circumventing the impedance mismatch, there may still exist intrinsic limitations due to the lack of sufficient testing with an even larger sample size of materials.



(a)



(b)

Figure 4.10: Stress at sample interfaces for SHPB tests on a) aluminium, and b) medium sand with confining ring.

Table 4.4: Typical input arguments used in SHPB\_processing.py for SHPB tests on different sample materials.

<i>Aluminium input arguments</i>	
sample_data	[5.000, 1.530, 1.530]
confinement	'None'
signal_channels	[1, 2]
signal_amp	[1, 1]
disp_correction	True
alignment	'start'
speedtrap	True
<i>Medium sand input arguments</i>	
sample_data	[4.726, 3.50, 3.50]
confinement	'Ring'
signal_channels	[1, 2, 3]
signal_amp	[10, 10, 1]
disp_correction	True
alignment	'start'
speedtrap	True
<i>Kaolin clay input arguments (unconfined)</i>	
sample_data	[5.377, 4.215, 3.031]
confinement	'None'
signal_channels	[3, 4]
signal_amp	[10, 100]
disp_correction	True
alignment	50
speedtrap	True
<i>Kaolin clay input arguments (confined)</i>	
sample_data	[5.897, 4.109, 2.946]
confinement	'Ring'
signal_channels	[7, 8, 5]
signal_amp	[10, 10, 5]
disp_correction	True
alignment	50
speedtrap	True



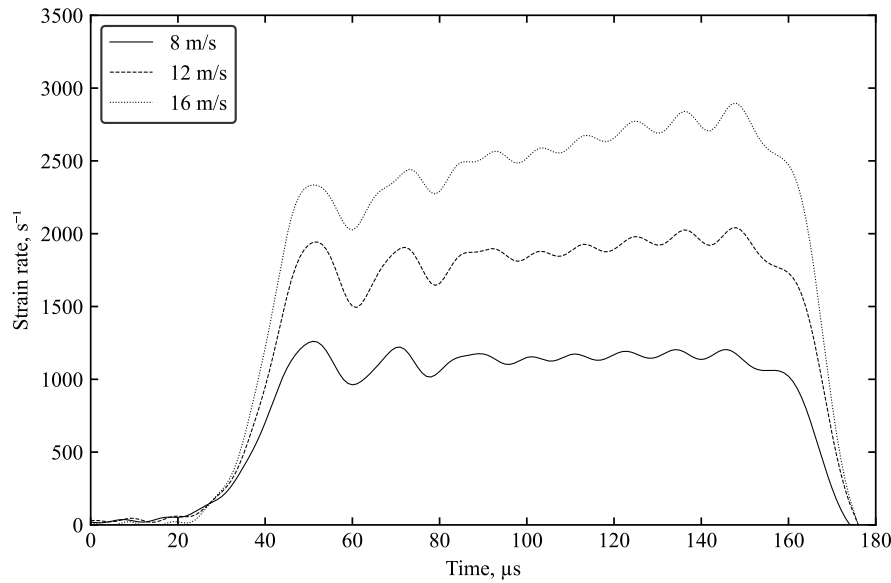


Figure 4.11: Average strain rate variation during unconfined SHPB tests on kaolin clay at 8, 12, and 16 m/s, corresponding to an average peak strain rate of 1200, 1900, and 2700  $\text{s}^{-1}$ .

#### 4.4 Unconfined testing of kaolin clay

Unconfined SHPB tests were conducted on kaolin clay to determine the factors that affect high-strain-rate behaviour. The effect of moisture content and strain rate are the primary components of unconfined testing. SHPB tests under free field conditions demonstrate high-strain-rate behaviour when there are minimal lateral pressure acting on the material and is crucial in gauging the holistic effect that confinement has on high-strain-rate behaviour.

As discussed in the initial test programme (Section 3.5), unconfined SHPB tests on kaolin clay were conducted at a wide range of moisture contents and at various striker bar speeds. Variations of striker bar speed correspond to various strain rate levels, prompting the characterisation of strain rate dependent behaviour. The test programme was centred around tests at 8, 12, and 16 m/s, which correspond to an average peak strain rate of 1200, 1900, and 2700  $\text{s}^{-1}$  for unconfined conditions. The typical strain rate variation corresponding to the three striker bar speeds is shown in Figure 4.11. While striker speed is used as a basis of comparison in this study, the strain rate at each striker speed is dependent on individual setups, and different SHPB apparatus may yield varying strain rates at similar striker bar speeds.

#### 4.4.1 Material properties

While the focus of the tests is to uncover the underlying effects of saturation ratio, the relationship between moisture content and degree of saturation are intrinsically linked. Based on the equations discussed in Chapter 2, the saturation ratio and moisture content is proportional at constant volume such that:

$$S_r = w \times k \quad (4.20)$$

where  $S_r$  and  $w$  are the saturation ratio and moisture contents, and  $k$  is a constant that depends on the specific gravity and void ratio of the material. Assuming specific gravity maintains constant due to the same soil being used, the range of moisture content levels correspond to a spectrum of saturation ratio ranging from fully saturated, partially saturated, and fully dry. For each SHPB test, the intrinsic material properties were investigated based on measurements of weight, thickness, diameter, and mass. While a range of properties was investigated, the key material properties that have been found to have a direct effect on high-strain-rate behaviour are highlighted as the air-volume ratio and water-volume ratio.

As the moisture content levels are varied, the respective material composition changes are pertinent to dictating material behaviour. As such, the air-volume ratio can be expressed as:

$$\text{Air-volume ratio} = \frac{V_{air}}{V} \quad (4.21)$$

where  $V_{air}$  is the volumetric amount of air within the volume of voids, and the  $V$  is the total volume of the sample. The water-volume ratio is described as the:

$$\text{Water-volume ratio} = \frac{V_{water}}{V} \quad (4.22)$$

where  $V_{water}$  is the volume of moisture in the sample and is directly related to the saturation ratio previously discussed. The analysis of material composition enhance the understanding behind unique material behaviours at specific moisture content levels.

#### 4.4.2 Experimental results

The initial conclusion upon conducting unconfined testing on kaolin clay is the absence of a significant transmitted pulse reading. This indicates that while the stress wave propagates through the sample specimen, rather than transmitting the stress wave fully axially, it can be assumed that the vast majority of the stress wave propagated laterally. Hence the magnitude of front and back stresses of the unconfined tests are shown to of notably different magnitudes. This also leads to a case where stress equilibrium was not conventionally obtained, thus the method discussed in Section 4.3.3 was applied to evaluate stresses at the front, back

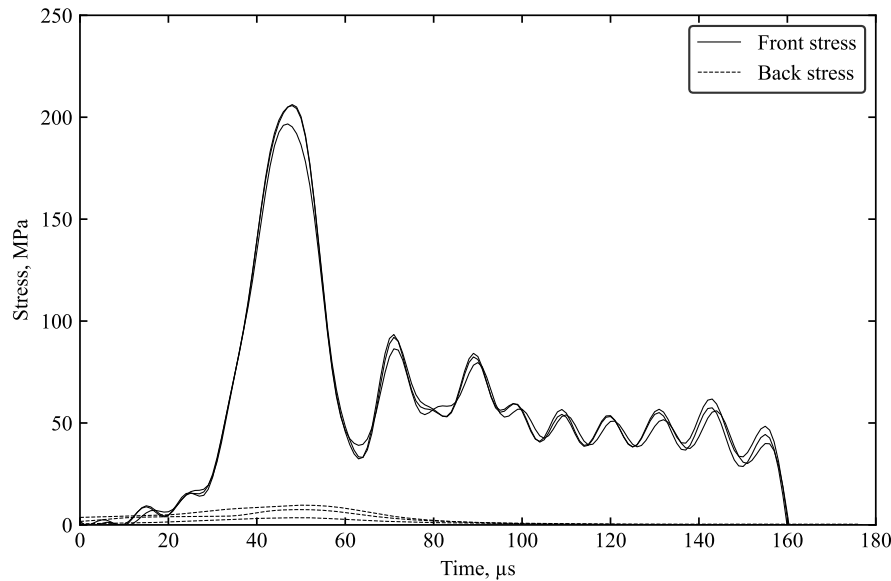


Figure 4.12: Front and back stress for unconfined tests at 16 m/s on kaolin samples at 20% moisture content.

and middle of the specimen. The front and back stresses for trials on kaolin clay at 16 m/s at 20% moisture content can be shown in Figure 4.12 to show the disparity between the front and back stresses on the same axis.

From dynamic oedometer tests from quasi-static compression, it was found that saturated kaolin clay experiences compaction behaviour similar to fluids. Based on those results, similarities can be drawn to high-strain SHPB tests, where the material also tends to expand laterally rather than axially. Thus the moisture within kaolin clay samples can be said to be the primary governing factor behind stress propagation under dynamic loads.

Upon conducting tests at the same strain rate at different moisture content, front stress and strain variation all followed similar patterns, typical front stress behaviour at the three different striker bar speeds is shown in Figure 4.13. While both front stress and back stress are equally important in determining the stress experienced in the middle of the sample (sample stress), front stresses at the same strain rate all yield near exact results, so the back stress was the main governing factor in the stress experienced by the sample. Since the front stress is derived from the the superposition of the incident and reflected pulses, the significantly greater front stress indicates that the stress wave is propagating through into the sample, rather than experiencing full reflection due to acoustic mismatch.

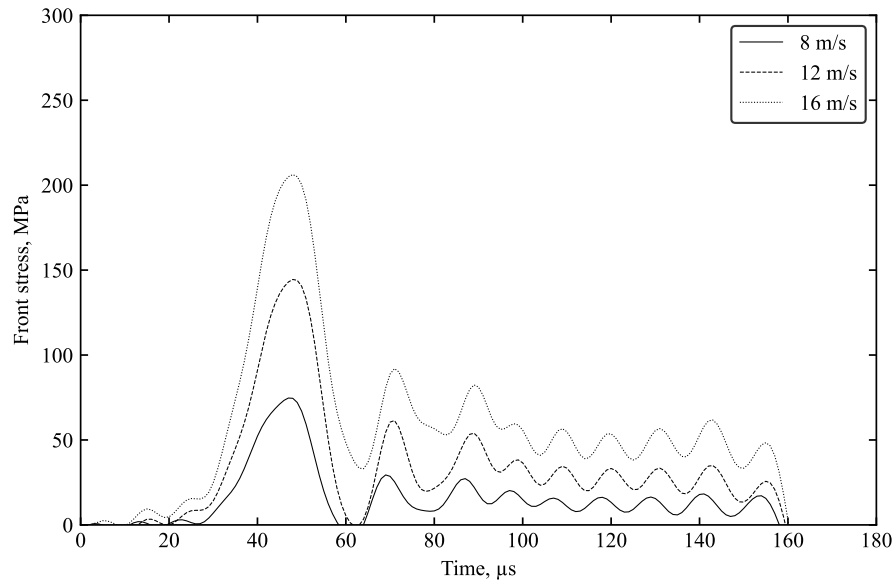


Figure 4.13: Typical front stress variation for unconfined SHPB tests at 8, 12, and 16 m/s.

#### 4.4.3 Phase behaviour in unconfined testing

The existence of four unique types of back stress behaviour began to emerge depending on the moisture content level of the sample, indicating that certain intrinsic moisture content boundaries exist that dictate stress propagation through a kaolin clay sample. While tests are not fully conclusive of a specific relationship between moisture content and back stress within each of the specific phases, the existence of these specific phases and the boundaries that dictates patterns of stress propagation is pertinent in characterising high-strain-rate behaviour and has immediate implications in the stress dampening capabilities that kaolin clay possesses. Each of the four back stress behaviour types within this study has been defined as a “phase”, each of which are associated with the samples with specific moisture content levels which consequently have direct effect on material composition.

Since moisture content is the direct factor leading to the existence of the unique phases, the material composition is crucial in governing the value of each of the phase boundaries. While the initial phase (phase 0) only applies to fully dried kaolin clay samples, the other phases can be expressed in terms of its material and experimental properties corresponding to the various levels of moisture content as seen in Figure 4.14. Consequently, it could be observed that specific boundaries are correlated to specific material properties.

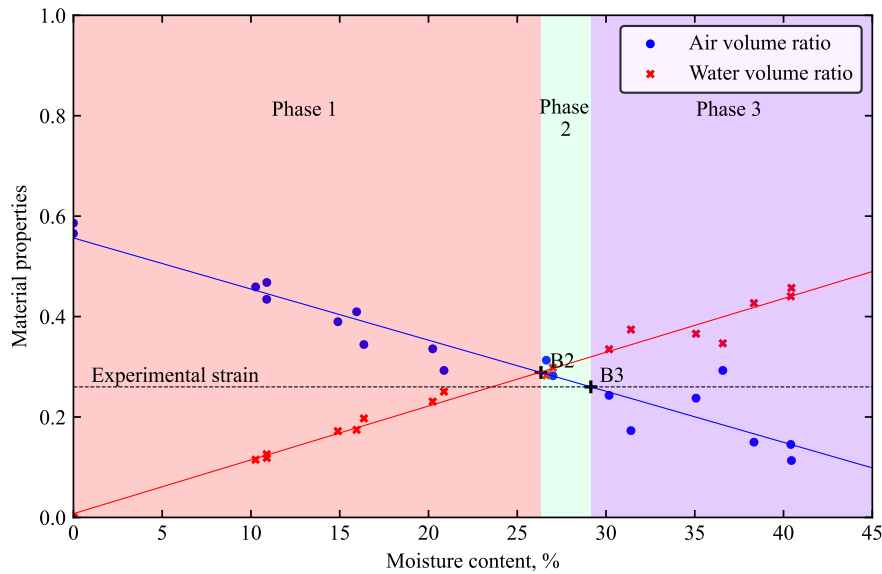


Figure 4.14: Phase behaviour according to material properties for unconfined testing of kaolin clay at 16 m/s ( $2700 \text{ s}^{-1}$ ). Phase boundaries 2 and 3 are marked 'B2' and 'B3'.

The boundary points between the unique phases have been determined based empirical evidence and material analysis of each test sample as an interpretation of behaviour within certain moisture content regimes. Consequently, relationships have been found that led to the emergence of three phase boundaries, which are listed as follows:

- **Boundary 1 (Phase 0-1):** Since phase 0 applies to dried samples, the first phase boundary is simply when the sample is partially saturated due to the initial presence of water.
- **Boundary 2 (Phase 1-2):** This boundary exists at the value of moisture content in which the trend lines between air and water-volume ratio intersect.
- **Boundary 3 (Phase 2-3):** This boundary exists at the value at which the air-volume ratio intersects the value of maximum experimental strain obtained from SHPB tests.

Figure 4.15 shows the unique back stresses that correspond to each of the four phases tested at 16 m/s. While the tests are described based on the estimated moisture content for ease of illustration, there is an inevitable deviation between the exact and estimated moisture contents, however the existence of specific phase behaviour is still evident. The characteristics of each of the four phases can be described as follows:

**Phase 0:** This phase corresponds to fully dried samples. For unconfined tests, this phase experiences the highest amount of axial stress propagation, the peak back stresses experienced

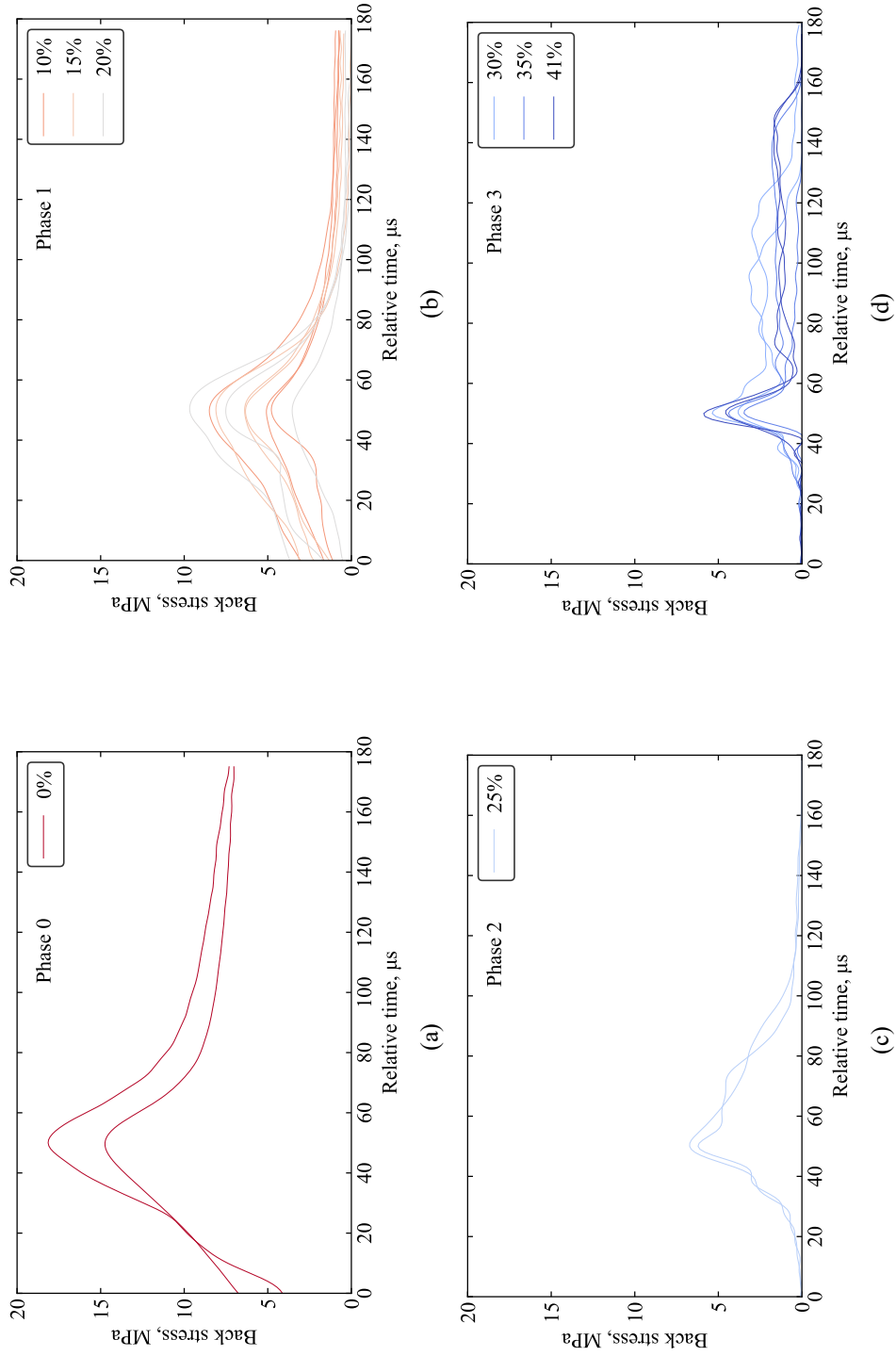


Figure 4.15: Back stress from unconfined testing on kaolin clay at 16 m/s at moisture contents corresponding to a) phase 0, b) phase 1, c) phase 2, and d) phase 3

in this phase are the highest compared to the other phases. This corresponds with moisture content being the key factor in encouraging lateral stress propagation as most stress is being transmitted through the sample due to the lack of moisture. A characteristic of behaviour within this phase is that back stress does not fully return to zero, this is due to the forced consolidation of the sample after loading and is also the phase of which there is visually the least extrusion. The greatest presence of air voids and resultant forced consolidation causes the length of the stress wave to become elongated, leading to the value of back stress not returning to zero until after the duration of the initial pulse length.

**Phase 1:** This phase corresponds to samples with a moisture content greater than 0% until boundary 1, and are considered partially saturated. This phase is characterised by an initial peak followed by a slow and gradual return to zero. The presence of moisture within samples in this phase causes a considerable amount of sample extrusion, leading to the gradual return to zero back stress. Since the volume of water is still less than the volume of the soil and air, the gradual return to zero is attributed to the presence of air voids within the sample, hence leading to a similar but lesser elongation effect as observed in phase 0 as the sample experiences axial compression. While different moisture contents within this phase do not exhibit a direct relationship between moisture content and back stress, the peak back stresses in this phase are still generally greater than the latter two phases but still less than phase 0.

**Phase 2:** This phase corresponds to samples with moisture content between boundaries 1 and 2, and are considered partially saturated. While qualitatively, this phase resembles phase 1 due to the amount of extrusion, there is a distinct difference in shape after the back stress reaches its peak, such that there is a more immediate return to zero compared to phase 1. The peak back stress is generally lower than phase 0 and 1, but greater phase 3.

**Phase 3:** This phase corresponds to all samples with moisture contents greater than boundary 3, and contains samples from partial to full saturation. Since this phase is associated with the greatest proportion of moisture, the characteristics of this phase are heavily influenced by the effects of moisture and hence the greatest amount of extrusion is observed, this is consistent with the least stress being propagated onto the back interface of the specimen due to the tendency for stress to propagate laterally instead.

#### 4.4.4 Effect of strain rate

While the presence of moisture on kaolin clay is crucial in governing high-strain-rate behaviour, it is also crucial to investigate the effect that strain rate has on the respective phase boundaries. Tests performed at the three striker bar speeds (8, 12, and 16 m/s) all show the existence of the four distinct phases, albeit at increasing magnitudes due to greater striker bar induced stresses.

The variation of sample stress was obtained by taking an average of the stresses at the front and back of the sample. This was compared with the variation of strain as illustrated in

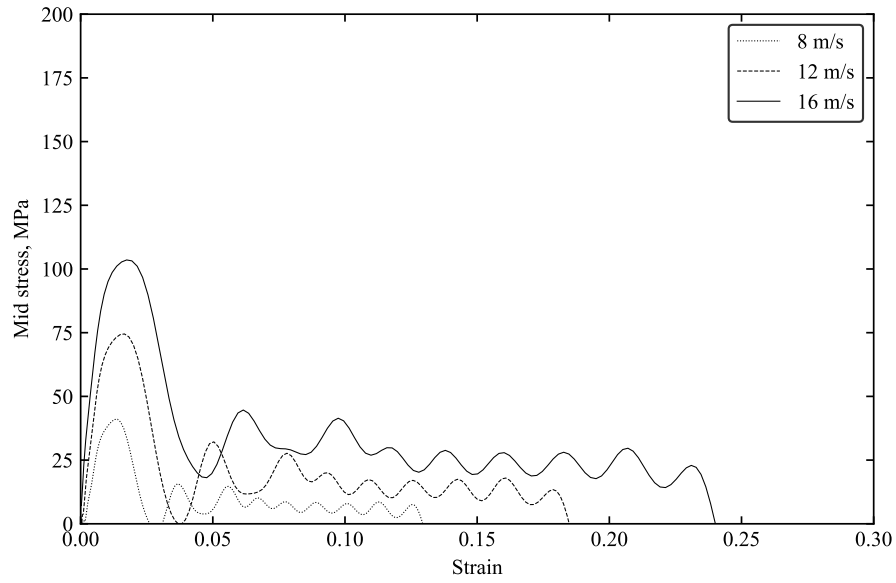


Figure 4.16: Typical stress vs time variation from unconfined SHPB tests on saturated kaolin clay at 8, 12, and 16 m/s

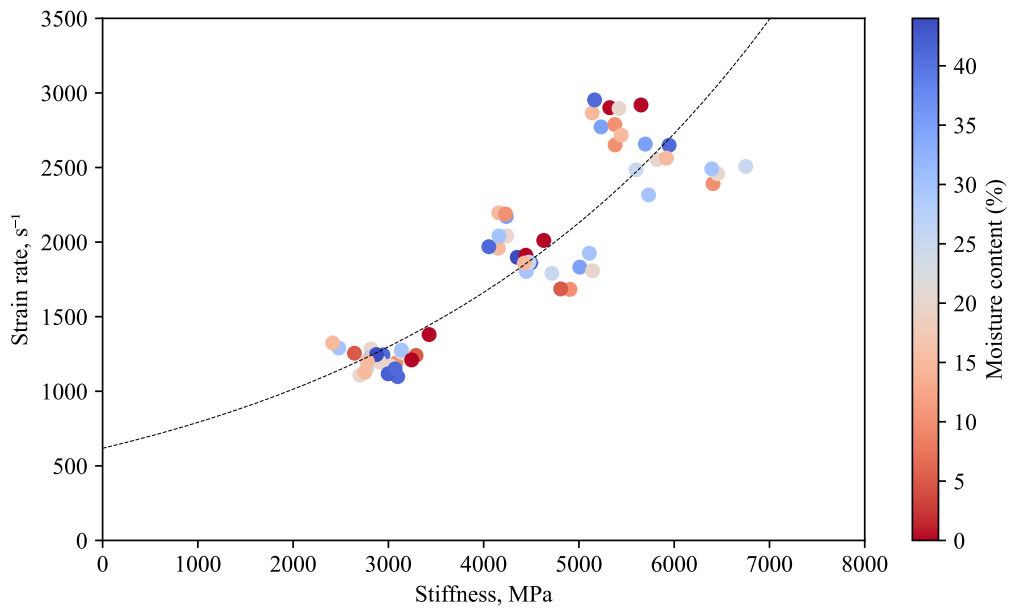


Figure 4.17: Variation of stiffness with strain rate based on unconfined SHPB tests at three striker bar speeds of 8, 12, 16 m/s, with trend line to show strain rate dependence.



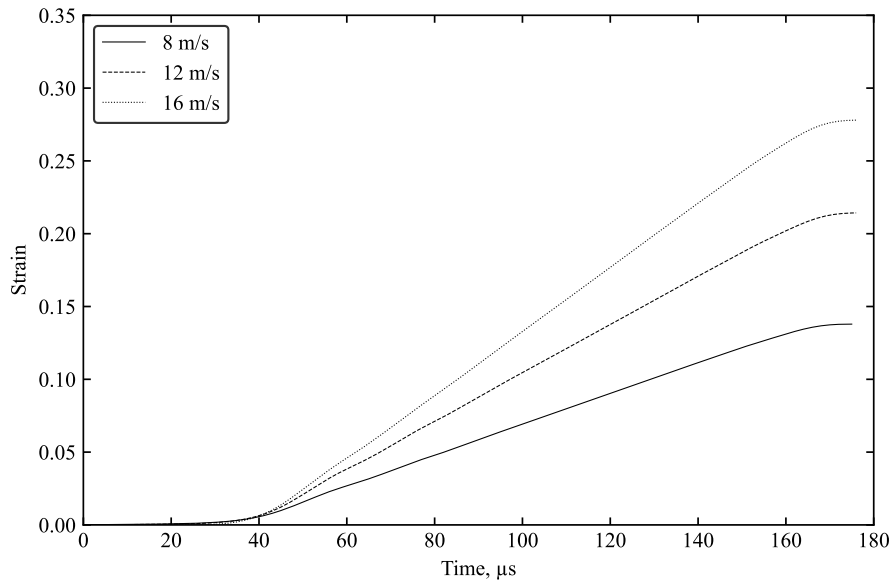


Figure 4.18: Typical strain-time history during unconfined SHPB tests on kaolin clay at 8, 12, and 16 m/s.

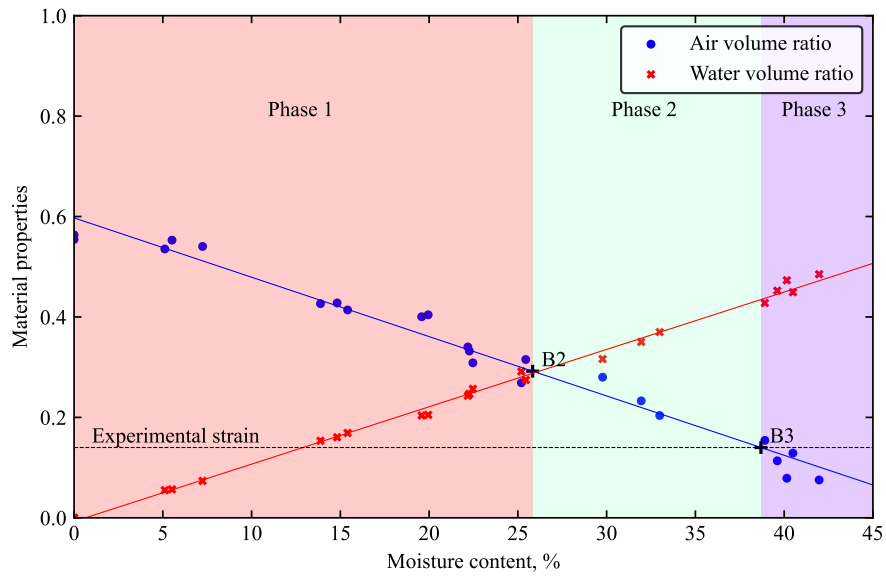
Figure 4.16. This emphasises the strain rate dependency of the material as increases in strain rate as increases in strain rate correspond to non-linear increases in the ratio between stress and strain, this is visualised in Figure 4.17 where stiffness is calculated based on the ratio between the maximum axial stress and the respective sample strain at that value. While moisture content has not been shown to have a distinct relationship with stiffness, the exponential relationship that develops between strain rate and stiffness has been obtained by performing exponential regression on the data points. Based on the exponential trend line, the relationship between stiffness (MPa) and strain rate ( $s^{-1}$ ) can be defined by the equation:

$$\text{Stiffness} = \frac{\ln(\text{Strain rate})}{0.0025} - 2570.41 \quad (4.23)$$

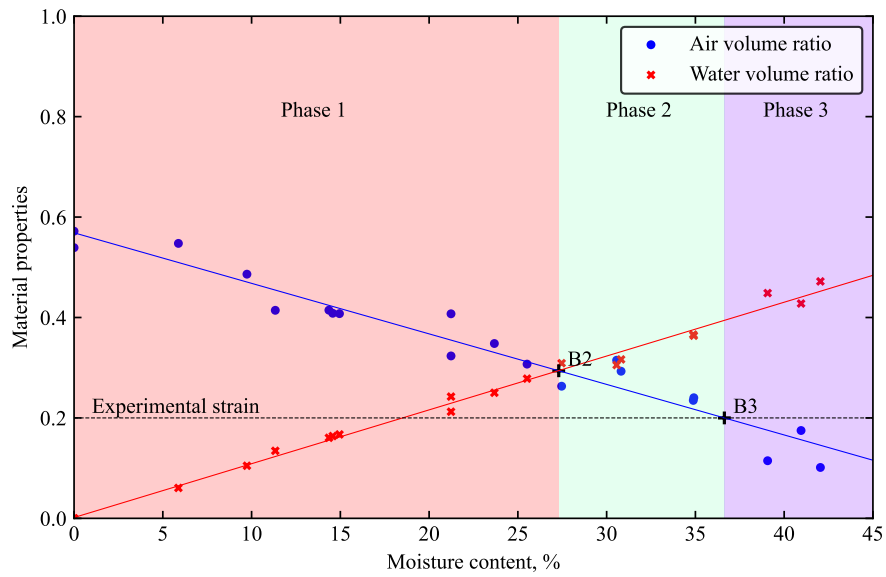
The coefficient of determination ( $r^2$  value) for the trend line is amounted to 0.75, this indicates that the relationship between strain rate and stiffness as represented by the trend line is considered to be highly correlated.

Consequently, the boundaries of the four phases can be similarly determined based on material properties. The key difference is the increase in maximum experimental material strain as striker speed is increased as seen in Figure 4.18, this has a direct effect on the value of boundary 3. Since boundary 3 is the intersection between the final experimental strain and the trend line for air-volume ratio, increases in experimental strain naturally corresponds to boundary 3 reducing. Ultimately, this results in the moisture content range of phase 2 decreasing as strain rate is increased.

As observed in Figure 4.19, the phase boundaries at 8 and 12 m/s are still based directly on



(a)



(b)

Figure 4.19: Phase behaviour according to material properties for unconfined testing of kaolin clay at a) 8 m/s ( $1900 \text{ s}^{-1}$ ) and b) 12 m/s ( $2700 \text{ s}^{-1}$ ). Phase boundaries 2 and 3 are marked 'B2' and 'B3'.

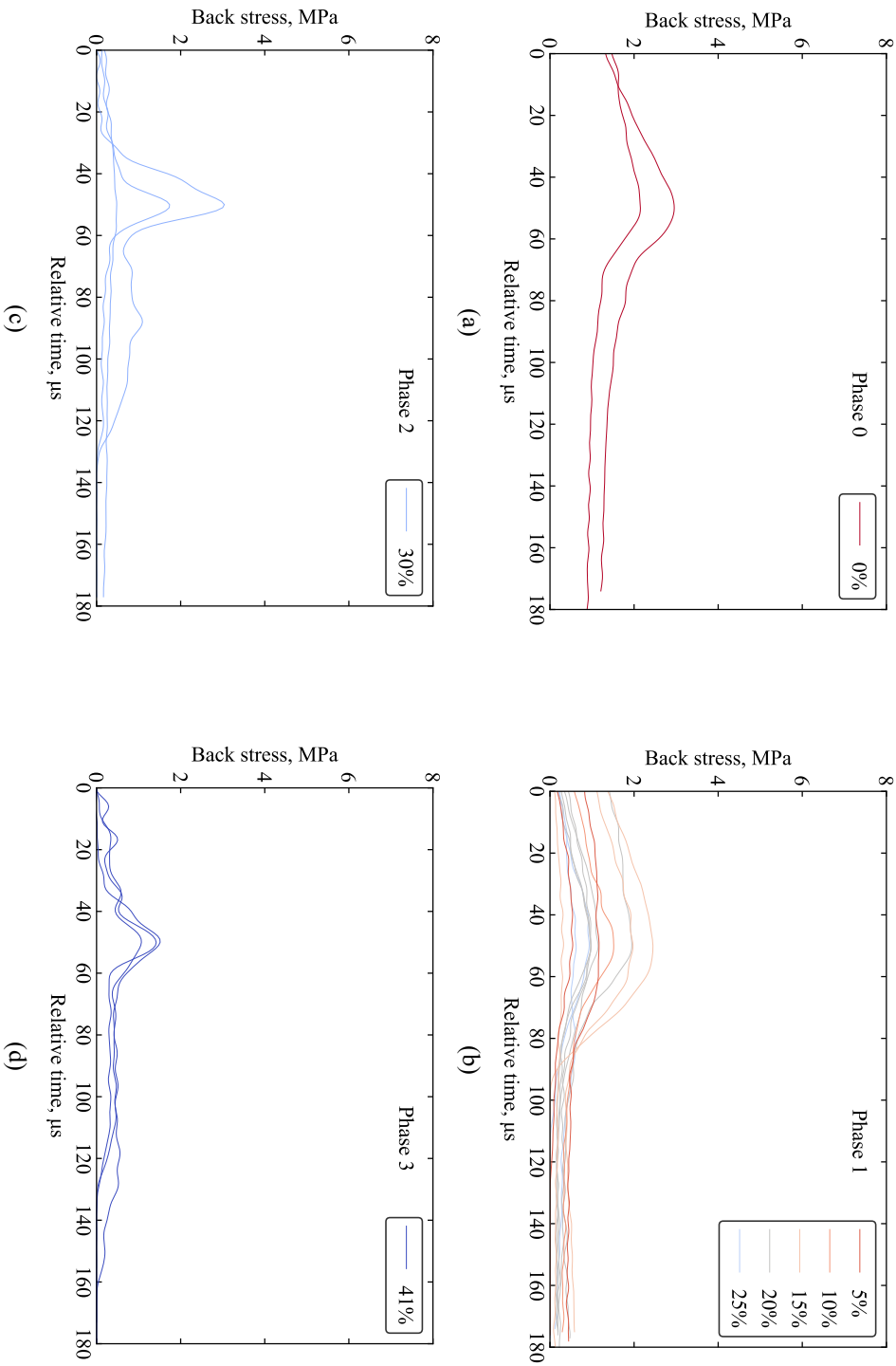


Figure 4.20: Back stress from unconfined testing on kaolin clay at 8 m/s at moisture contents corresponding to a) phase 0, b) phase 1, c) phase 2, and d) phase 3

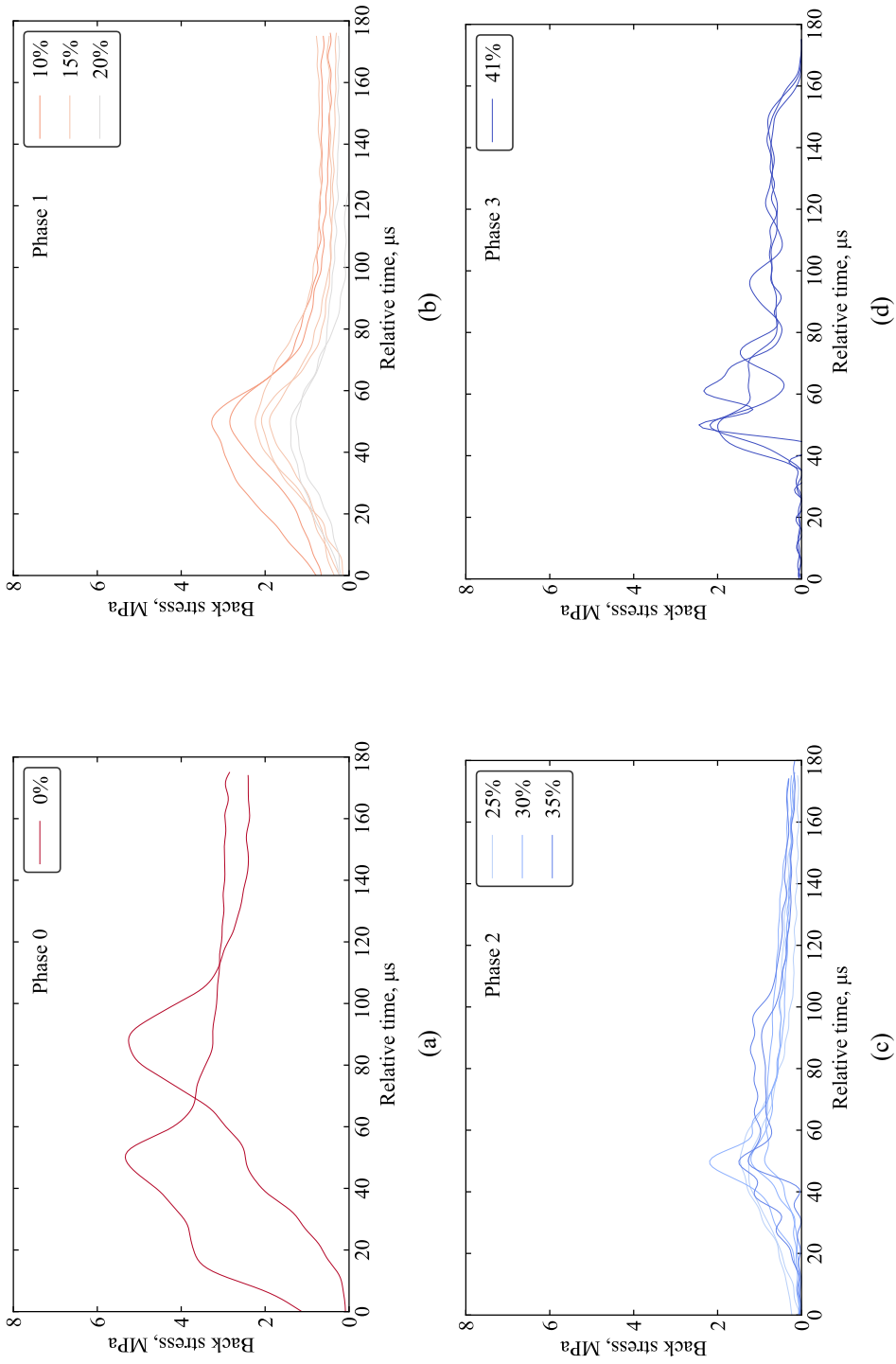


Figure 4.21: Back stress from unconfined testing on kaolin clay at 12 m/s at moisture contents corresponding to a) phase 0, b) phase 1, c) phase 2, and d) phase 3

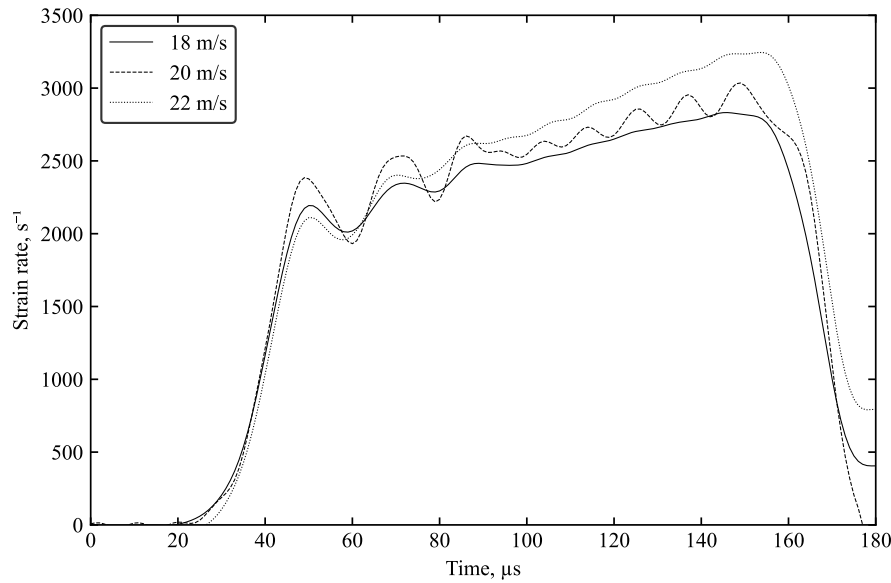


Figure 4.22: Strain rate variation during unconfined SHPB at 18, 20, and 22 m/s, corresponding to an average peak strain rate of 2800, 3000, and 3300  $\text{s}^{-1}$ .

the material properties. While boundary 1 and 2 remain the same due no change in intrinsic material composition, boundary 3 has reduced as a result of testing at higher strain rates and hence higher maximum material strain. While the moisture content ranges of the phases have seen change and the magnitude of back stress is proportionally higher at greater loads, the pulse shape remains fairly consistent with phase behaviour previously described regardless of strain rate variation. This can be observed in Figure 4.20 for the four phases tested at 8 m/s, and in Figure 4.21 for the four phases tested at 12 m/s. Evidently, the number of trials obtained at 16 m/s in phase 2 are limited, thus prompting additional testing at even greater strain rates to validate the reduction of boundary 3 due to strain rate.

Unconfined SHPB tests were conducted at 18, 20, and 22 m/s to verify the range for phase 2 behaviour gradually reducing at higher strain rates (Figure 4.22). These three striker bar speeds correspond to an average peak strain rate of 2800, 3000, and 3300  $\text{s}^{-1}$ . As seen in Figure 4.23, strain-time history at higher strain rates produced a maximum strain of values closer to 0.29. When considering the phase boundary is dependent on the maximum experimental strain during loading, maximum experimental strains approaching 0.29 corresponds with the value of boundary 3 decreasing. Essentially indicating that the moisture content range for phase 2 is gradually decreasing. However, a crucial physical limitation is the inability to produce precise samples with exact moisture content levels within the increasingly small phase 2 limits in order to determine if boundary 3 approaches but never reaches boundary 2, or if phase 2 disappears at a certain strain rate.

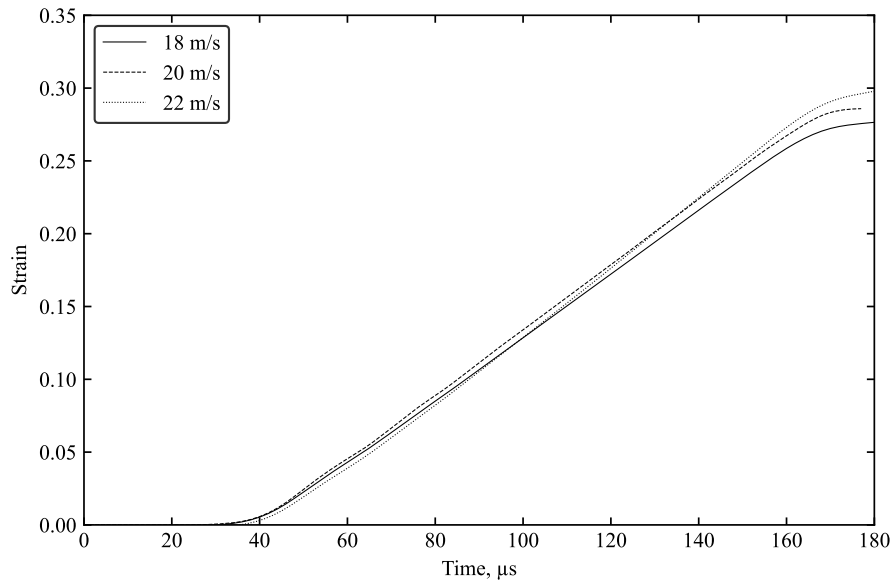


Figure 4.23: Typical strain-time history during unconfined SHPB tests on kaolin clay at 18, 20, and 22 m/s.

## 4.5 Confined testing of kaolin clay

Confined SHPB tests are conducted on kaolin clay to determine the factors that affect high-strain-rate behaviour. The discovery of unique phase behaviour corresponding to changing moisture content boundaries during unconfined testing is explored when kaolin clay is under a rigid confinement mechanism instead. The addition of a confining ring was crucial in mapping the effect of confinement by providing the basis of comparison between free field and rigid confinement in the context of high-strain-rate behaviour.

Confined tests on kaolin clay were conducted based on the initial test programme set in Section 3.5 at various moisture contents and striker bar speeds. Similar to unconfined tests, the initial test programme is focused on three striker bar speeds of 18, 20, and 22 m/s, which correspond to an average peak strain rate of 2600, 2800, and 3100  $\text{s}^{-1}$ , the strain rate variation for these three striker bar speeds under confined conditions are illustrated in Figure 4.24. Strain rates are expectedly different even at same striker bar speeds between confined and unconfined tests due to the confining ring being a major factor in the rate the sample is strained during loading.

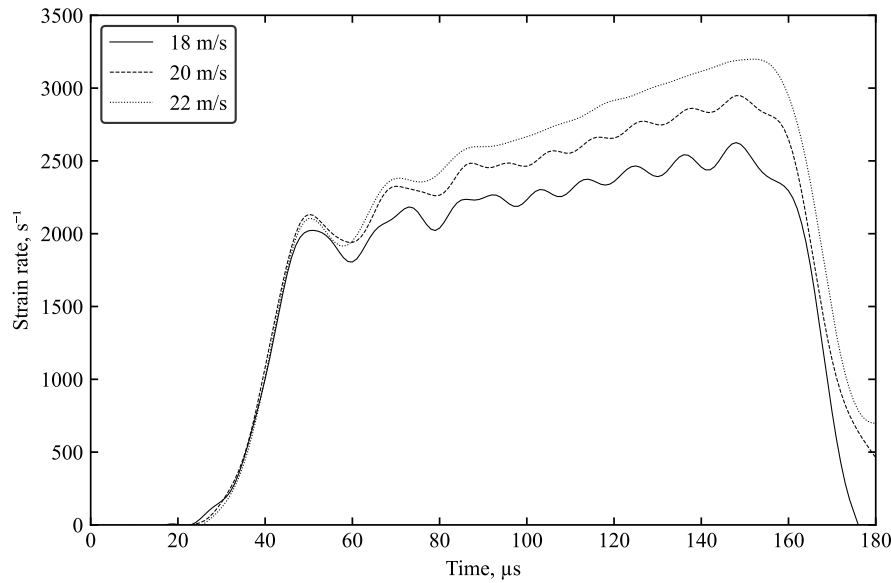


Figure 4.24: Average strain rate variation during confined SHPB tests on kaolin clay at 18, 20, and 22 m/s, corresponding to an average of 2500, 2800, and 3100  $\text{s}^{-1}$ .

#### 4.5.1 Confined SHPB results

The existence of unique phases revealed from unconfined testing on kaolin clay remains the primary focus of investigation, specifically on the influence of the rigid lateral confinement on the moisture content effects in kaolin clay. Contrary to unconfined SHPB tests on kaolin clay, a larger variation in the magnitude of back stress is observed in confined SHPB tests as a result of moisture content. Notably, saturated kaolin clay samples exhibit much greater stress propagation capabilities when under rigid confinement. In unconfined SHPB tests, saturated kaolin clay encourages lateral extrusion and stress propagation, however the presence of the confining ring acts as a barrier that prohibits lateral stress flow. When lateral movement is being restricted, lateral stress is redirected in the axial direction towards the back end of the sample, and in the form of sample extrusion on the edges of the confining ring.

The redirection of lateral stress when under rigid confinement means that SHPB tests on saturated kaolin clay under confined conditions show a much greater disparity between front and back stresses when compared to unconfined tests (Figure 4.25). As discussed in Section 4.3.3, the difference in pulse lengths between front and back stresses make it difficult to designate an accurate alignment. Figure 4.25 has been aligned based on setting the peak of the pulse peaks to be the same value. Although the normalised stress difference still show the overall lack of stress equilibrium being obtained, there are now instances where the the normalised stress difference actually reaches zero, as seen in Figure 4.26.

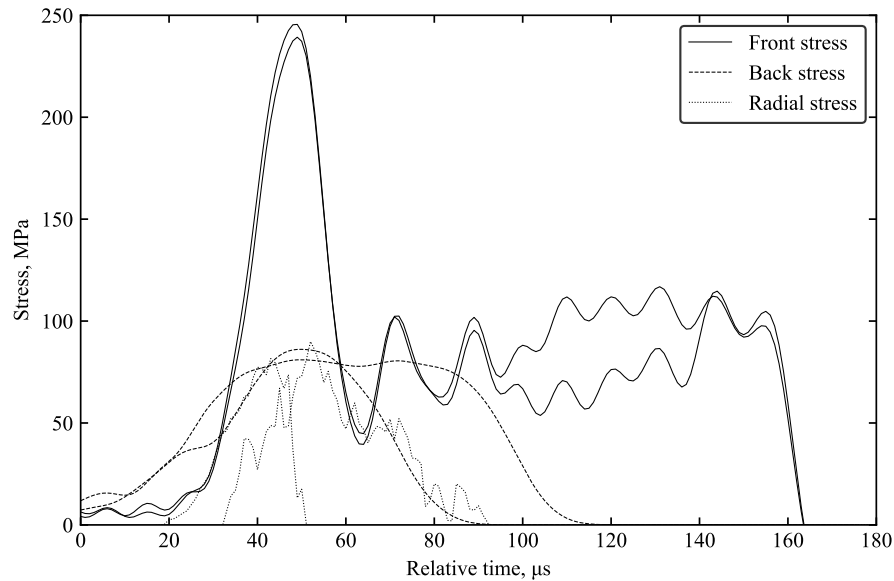


Figure 4.25: Front, back, and radial stresses for confined tests at 18 m/s on saturated kaolin samples at 41% moisture content.

Conducting confined SHPB tests with a confining ring also allow for radial stresses to be calculated, this is crucial in understanding not only the effect that rigid confinement has on axial stress propagation, but also the subsequent induced lateral stresses. The tendency for axial stress to be redirected in the lateral direction is emphasised when radial stresses are measured, evident from Figure 4.25 and the significant radial stresses being recorded.

As seen in Figure 4.25, the magnitudes of the radial and back stress pulses are relatively similar. This aligns with the notion that the lateral stress is being redirected axially, hence the lateral stress measured by the confining ring results in axial stress being transferred towards the back of the specimen and onto the transmitted bar.

Similar to unconfined tests, sample stress was determined by taking the average at the front and back interfaces of the specimen, but back stress was the main component that undergoes drastic change. The typical front stresses for confined SHPB tests is shown in Figure 4.27.

#### 4.5.2 Phase behaviour in confined SHPB testing

After conducting tests at a range of moisture content under confined SHPB conditions, the unique phases discovered via unconfined testing still correlated to specific behaviour. However, the effects of rigid confinement are revealed with the addition of the confining ring, where a comparatively much greater back stress is recorded in each phase due to the redi-



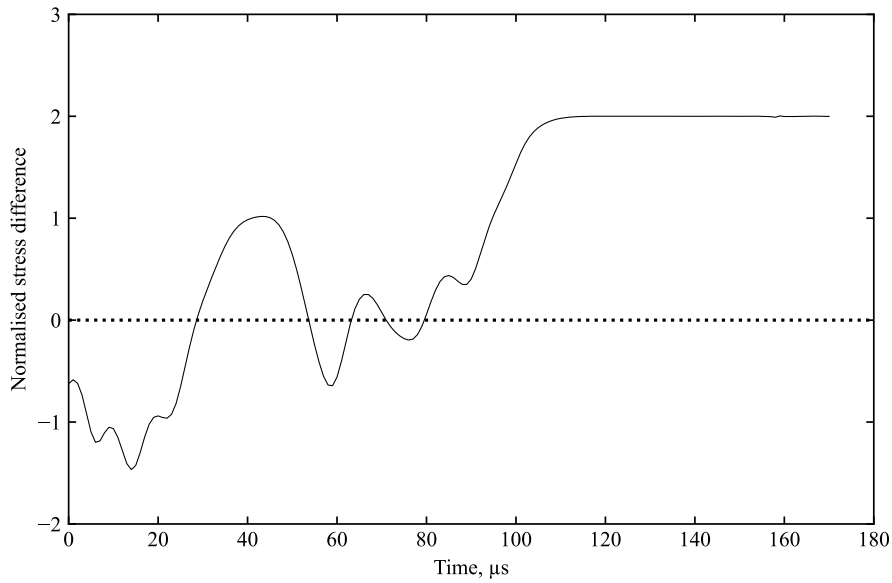


Figure 4.26: Typical stress wave difference between front and back interfaces, normalised by their mean for saturated kaolin clay.

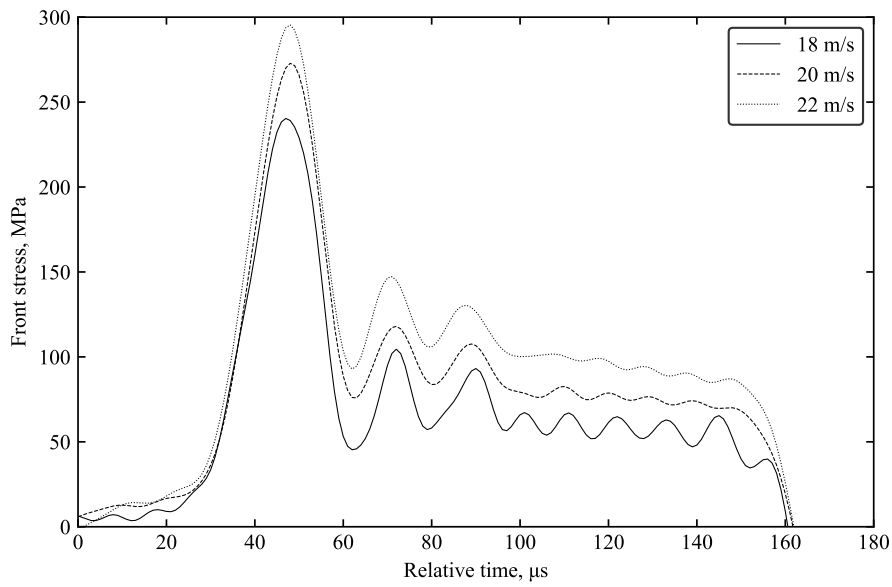


Figure 4.27: Typical front stress variation for confined SHPB tests at 18, 20, 22 m/s.

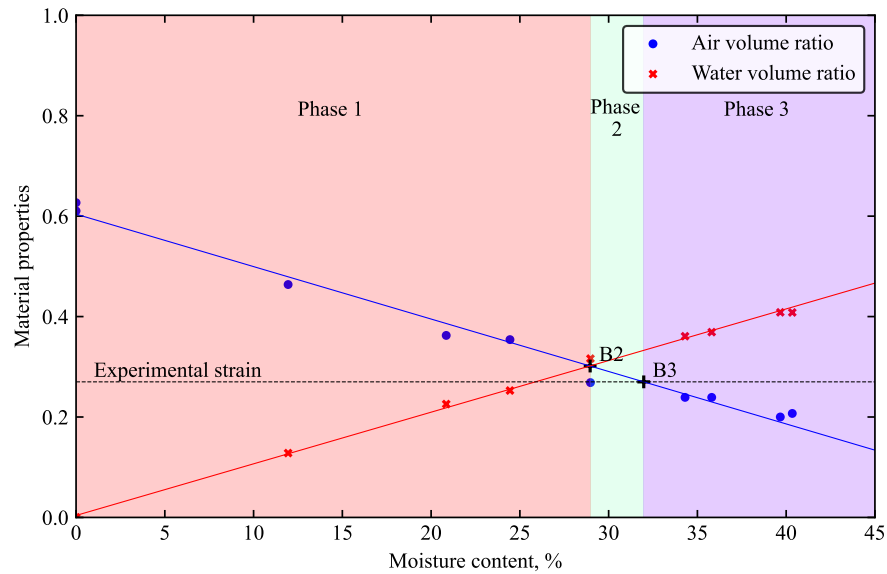


Figure 4.28: Phase behaviour according to material properties for confined testing of kaolin clay at 18 m/s ( $2500 \text{ s}^{-1}$ ). Phase boundaries 2 and 3 are marked 'B2' and 'B3'.

rection of lateral stresses. The phase boundaries described for unconfined SHPB tests are similarly applicable for confined tests since the limits are based on intrinsic material composition and experimental properties. Boundaries 1 and 2 remain as constants, while boundary 3 continues to be variable as it is dependent on the maximum experimental strain at each strain rate. The individual phases in confined testing dependent on material and experimental properties can be observed in Figure 4.28.

The key characteristic differences between phase behaviour in unconfined and confined tests are described below. Soil saturation and boundary limit details are the same as phases in unconfined testing so have been omitted (refer to Section 4.4.3 for details of individual phase behaviour from unconfined testing). Figures 4.29 and 4.30 shows the back and radial stresses at each of the four phases for confined tests at 18 m/s.

**Phase 0:** The magnitudes of back stresses recorded within this phase are significantly lower compared to phases 2 and 3, which contrasts prior phenomena observed during unconfined testing. This is attributed to the absence of moisture in the sample to redirect stress laterally and the highest proportion of air voids in samples in this phase, forcing the sample to undergo axial compaction during loading. The confining ring prevents lateral extrusion of the soil, exacerbating the effect of compaction by essentially creating a cell that dynamically compacts the dry soil. Subsequently, radial stresses are also the lowest in this phase because the lack of moisture results in the least amount of stress being forced to propagate laterally during the initial radial pulse.

**Phase 1:** In this phase, the volume of water is less than the volume of soil and air, thus the same effects of compaction was observed as in phase 0. The presence of moisture, even in limited amounts, forces parts of the stress wave to redirect laterally, emphasising the increased radial stresses observed in this phase. However, the low volume of moisture means that samples within this phase still mostly exhibit compaction behaviour similar to phase 0 due to the large amount of air voids, evident from the considerably lower magnitudes of back stress compared to the latter phases as the stress wave is being dampened by the effect of compaction.

**Phase 2:** This phase was only prevalent during testing at 18 m/s, this is because the maximum experimental strains experienced during tests at 20 and 22 m/s exceeds 0.29, which coincides with the upper limit for phase 1. Since the volume of water is much greater than previous phases, the sample properties show aspects of saturated kaolin clay. However, the magnitude of back stress is still a comparable amount less than the final phase which is akin to performing dynamic tests on fluids. Radial stresses incurred in this phase are greater than previous phases but still less than the final phase.

**Phase 3:** The final phase exists when there is an abundance of moisture and the sample is fully saturated, hence the effects of moisture govern the majority of soil behaviour within this phase. This is the phase that exhibits the greatest radial stresses as the tendency for moisture to propagate laterally dictates the behaviour of the sample. Subsequently, the back stresses are also the greatest in this phase as the rigid confining ring redirects lateral stresses into the axial direction and onto the transmitted bar.

The effect of the confining ring in translating radial stress towards the transmitted bar is similarly observed by comparing Figures 4.29 and 4.30. Where the magnitude of the radial stress is always greater than the axial stress. This was still the case when there was minimal axial stress transmission through the sample such as in phase 0 and 1, where majority of stress was lost due to extrusion induced volume loss or consolidation of internal air voids.

### 4.5.3 Effect of strain rate

While the addition of the confining ring has a clear effect on the moisture content associated boundaries, tests at other strain rates allow for the holistic effect of rigid confinement on the factors that affect high-strain-rate behaviour to be investigated. When confined SHPB tests at higher strain rates were conducted (striker velocities of 20 and 22 m/s), phase 2 behaviour was not observed in any SHPB tests. This is because boundary 3 is dependent on the maximum experimental strains, while the maximum strains experienced in tests at 20 and 22 m/s that are extremely close or greater than 0.29 as seen in Figure 4.31. As the moisture content range for phase 2 decreases, it becomes increasingly difficult to obtain precise moisture contents that theoretically fit within phase 2 limits.

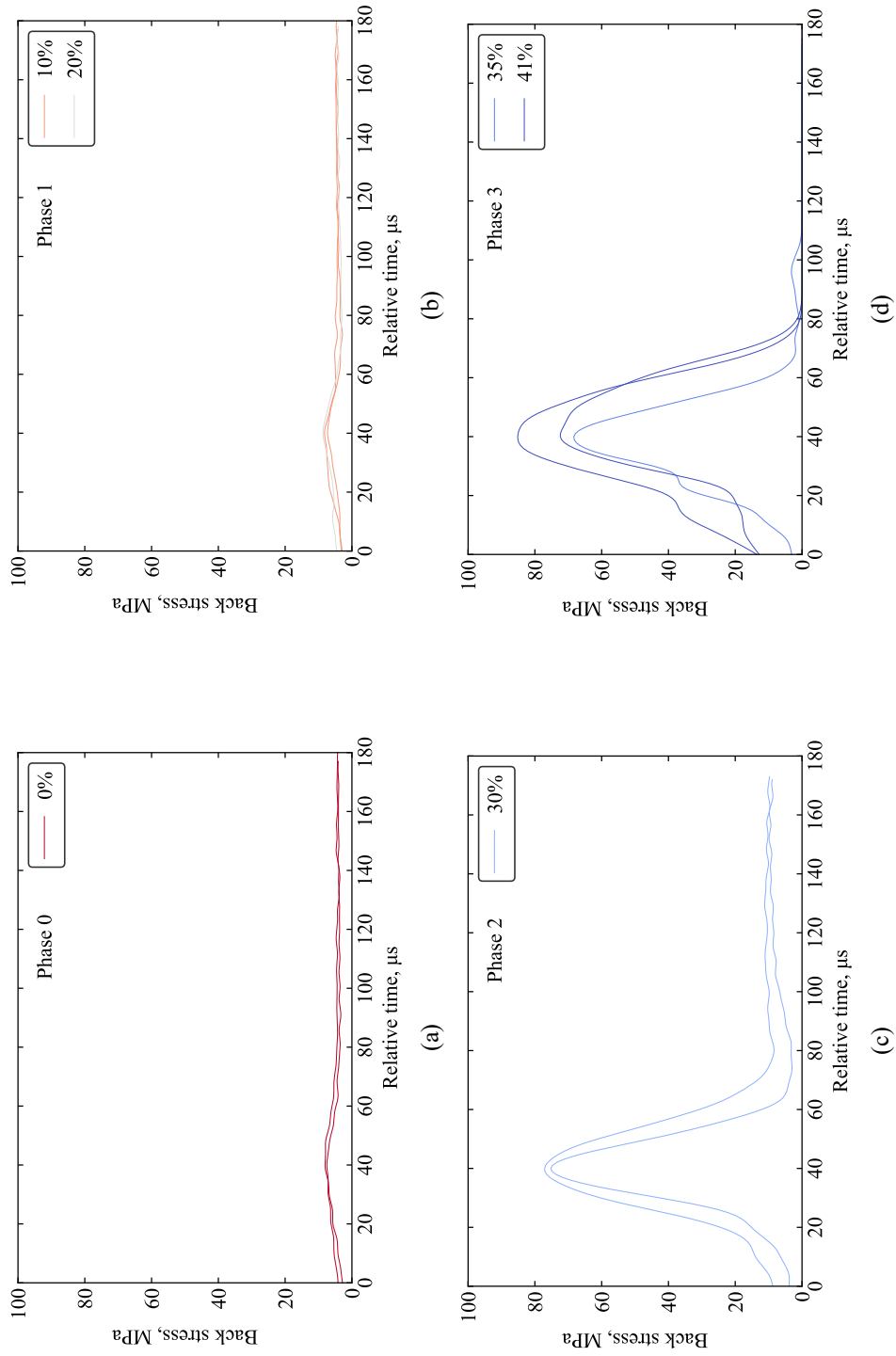


Figure 4.29: Back stress from confined testing on kaolin clay at 18 m/s at moisture contents corresponding to a) phase 0, b) phase 1, c) phase 2, and d) phase 3.

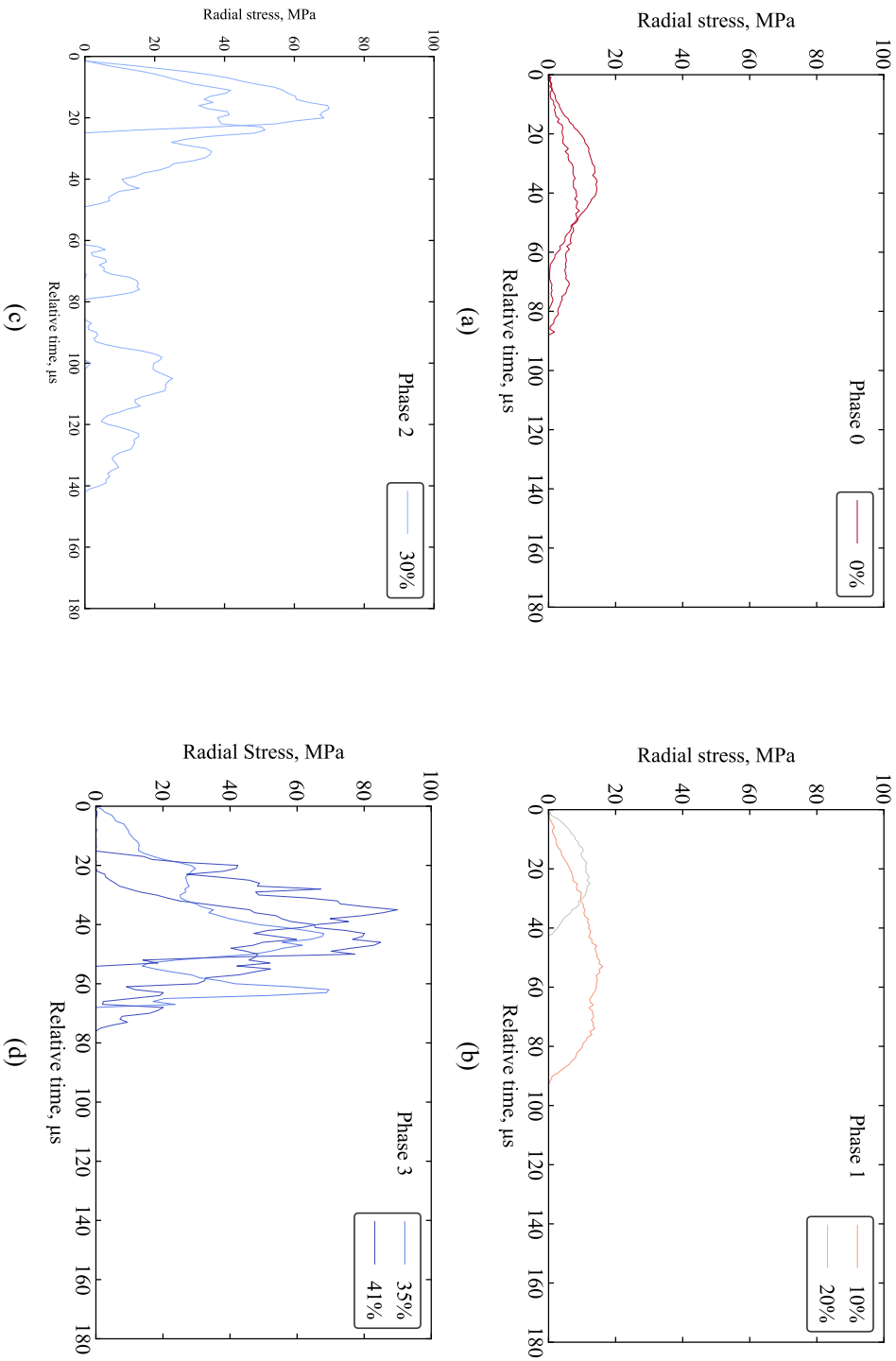


Figure 4.30: Radial stress from confined testing on kaolin clay at 18 m/s at moisture contents corresponding to a) phase 0, b) phase 1, c) phase 2, and d) phase 3.

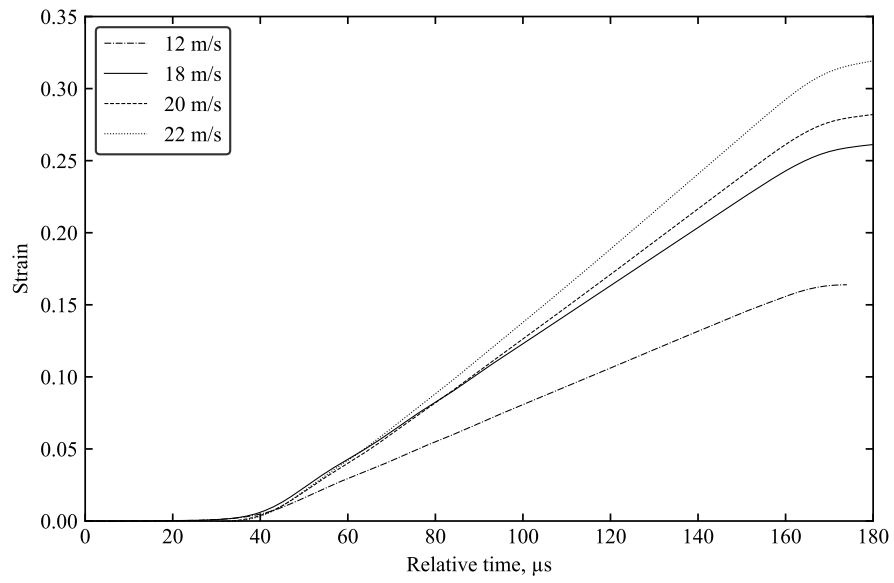


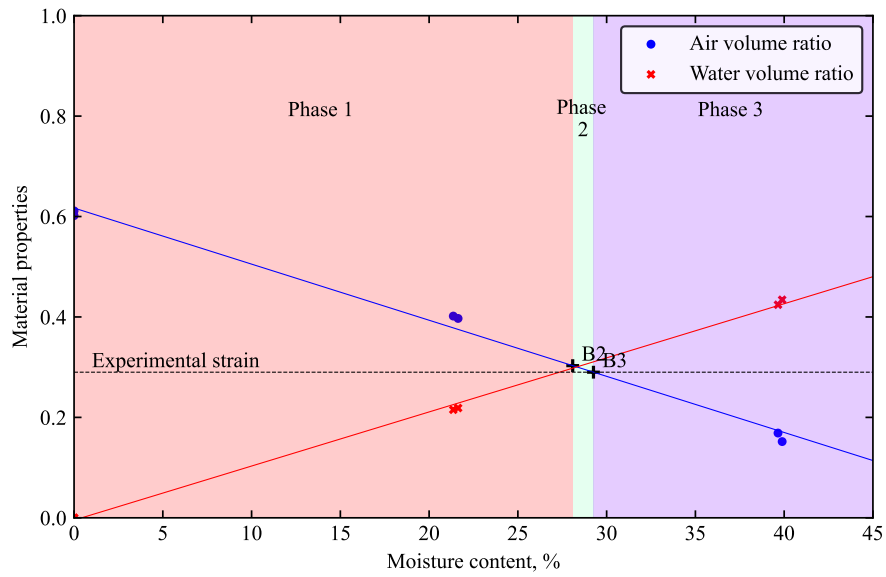
Figure 4.31: Typical strain-time history during confined SHPB tests on kaolin clay at 12, 18, 20, and 22 m/s.

By considering the material and experimental properties of the samples at 20 and 22 m/s, the increase in experimental strain results in boundary 2 seemingly disappearing as seen in Figure 4.32. While Figure 4.33 suggested that phase 2 behaviour was theoretically possible, the practical attainment was extremely challenging due to the narrow moisture content range, which was determined to be less than 1% based on the average maximum experimental strain values of 0.29. In the case of 22 m/s, the maximum experimental strain was 0.31, this value theoretically exceeds the moisture content for boundary 2. Hence it can be said that once strain rate reaches the point at which the intercept between the air-volume ratio and air-volume ratio is equal to the maximum average strain rate, phase 2 disappears as the theoretical boundary 3 becomes less than boundary 2.

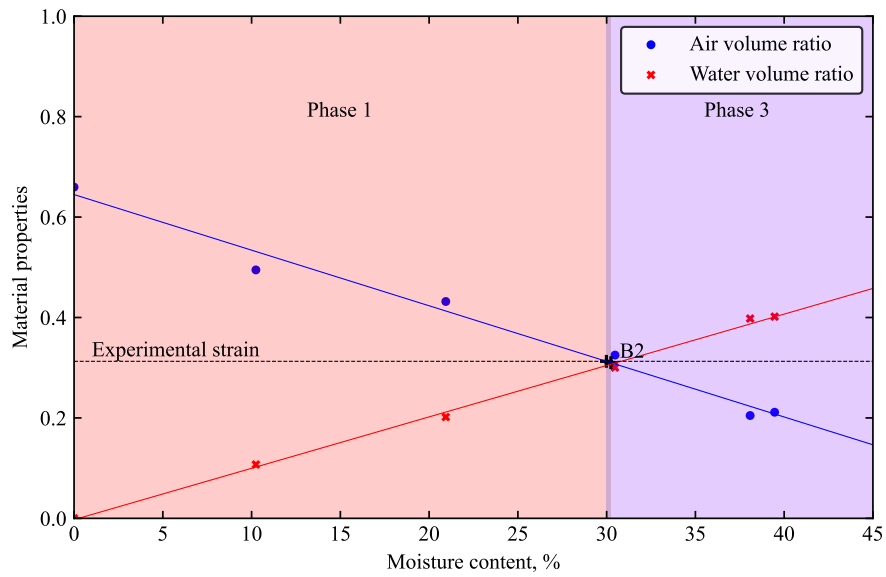
Since phase 2 behaviour was not attainable at higher strain rates, the back and radial stresses for each of the individual phases can be seen in Figures 4.33 and 4.34 for 20 m/s, and Figures 4.35 and 4.36 for 22 m/s. Similar to unconfined tests, sample stress-strain at the three different strain rates is shown in Figure 4.37 to consider the effect of strain rate.

The effect of strain rate on the magnitude of radial stress pulses are comparatively minimal, this is potentially attributed to the volume loss during confined tests. Unconfined tests have proved that regardless of confinement, increases in strain rate leads to a greater back stress. However, radial stress measurements have signified a much less distinguishable effect, this may be due to a limit of confining ring used in the current setup that prompts volume loss from extrusion when deformation of the ring becomes too great. In order to better understand the effect of a rigid confinement in an idealistic environment without volume loss, numerical modelling will be discussed in subsequent sections.

To supplement the effect of strain rate, further tests were completed at a lower strain rate in order to validate the same behaviour still persists. Tests conducted at 12 m/s correspond to an average strain rate of  $1600 \text{ s}^{-1}$  as seen in Figure 4.38.



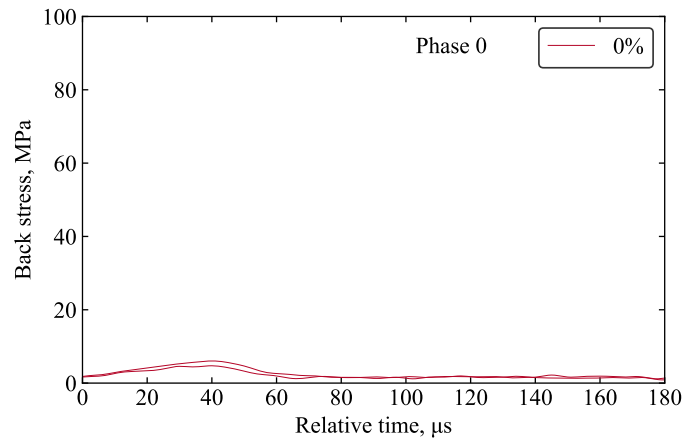
(a)



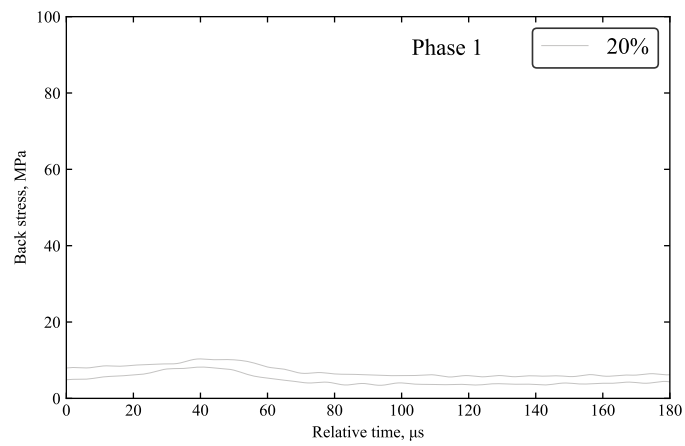
(b)

Figure 4.32: Phase behaviour according to material properties for confined testing of kaolin clay at a) 20 m/s ( $2800 \text{ s}^{-1}$ ) and b) 22 m/s ( $3100 \text{ s}^{-1}$ ). Phase boundaries 2 and 3 are marked 'B2' and 'B3'.

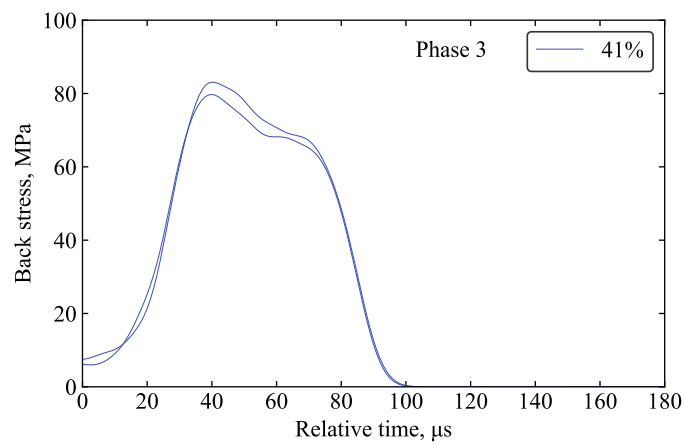




(a)

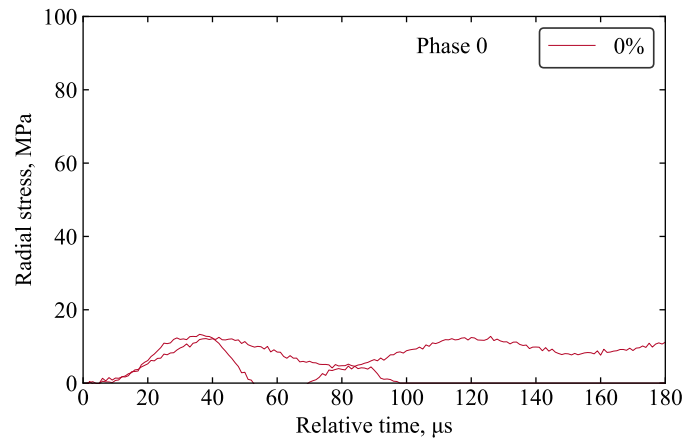


(b)

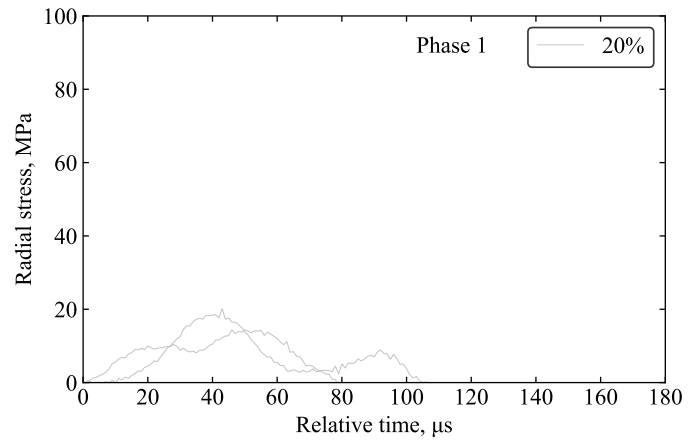


(c)

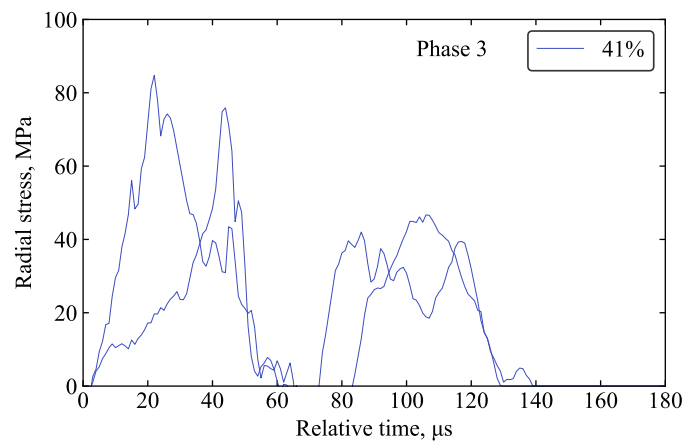
Figure 4.33: Back stress from confined testing on kaolin clay at 20 m/s at moisture contents corresponding to a) phase 0, b) phase 1, c) phase 3.



(a)

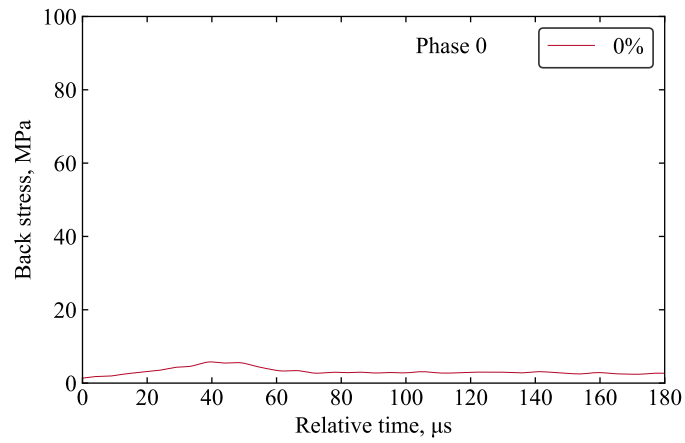


(b)

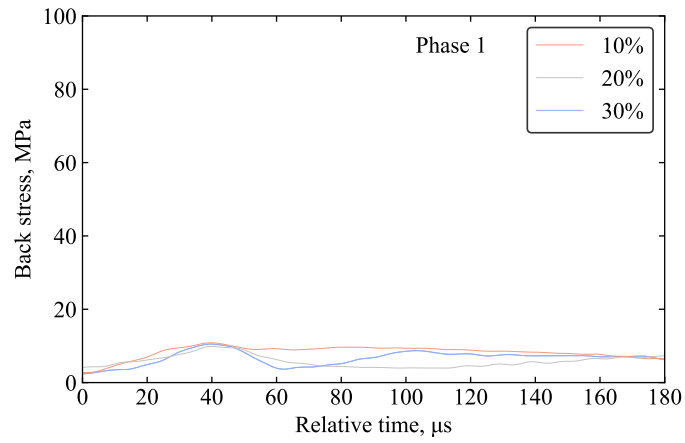


(c)

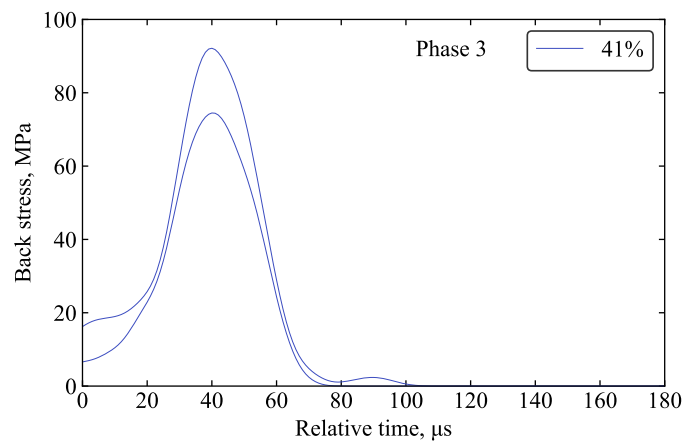
Figure 4.34: Radial stress from confined testing on kaolin clay at 20 m/s at moisture contents corresponding to a) phase 0, b) phase 1, c) phase 3.



(a)

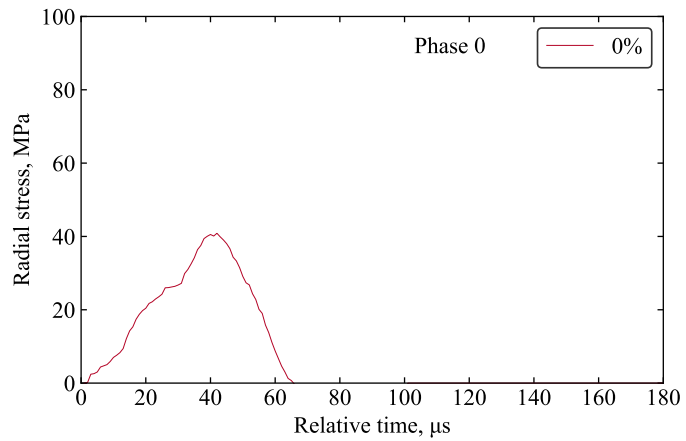


(b)

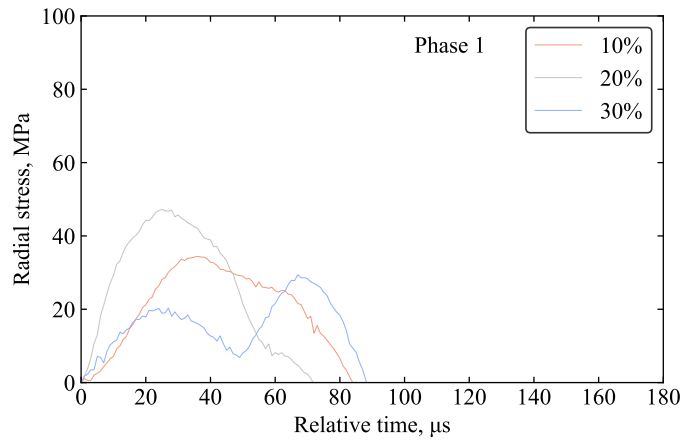


(c)

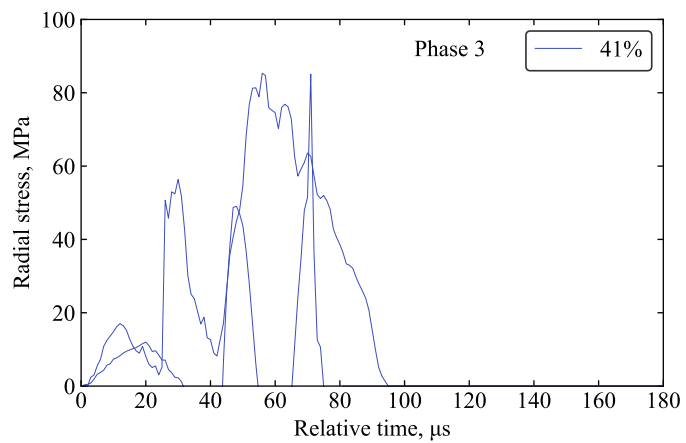
Figure 4.35: Back stress from confined testing on kaolin clay at 22 m/s at moisture contents corresponding to a) phase 0, b) phase 1, c) phase 3.



(a)



(b)



(c)

Figure 4.36: Radial stress from confined testing on kaolin clay at 22 m/s at moisture contents corresponding to a) phase 0, b) phase 1, c) phase 3.

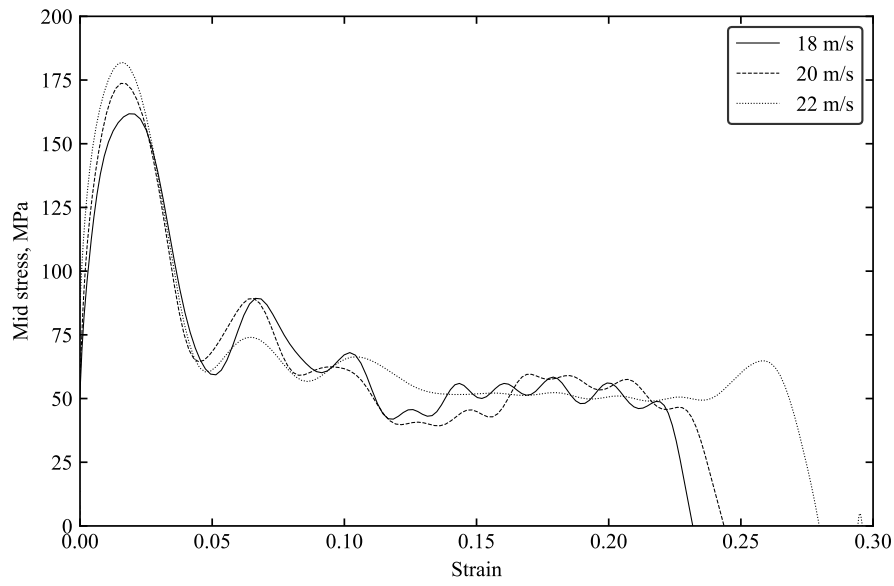


Figure 4.37: Typical stress vs time variation from confined SHPB tests on saturated kaolin clay at 8, 12, and 16 m/s

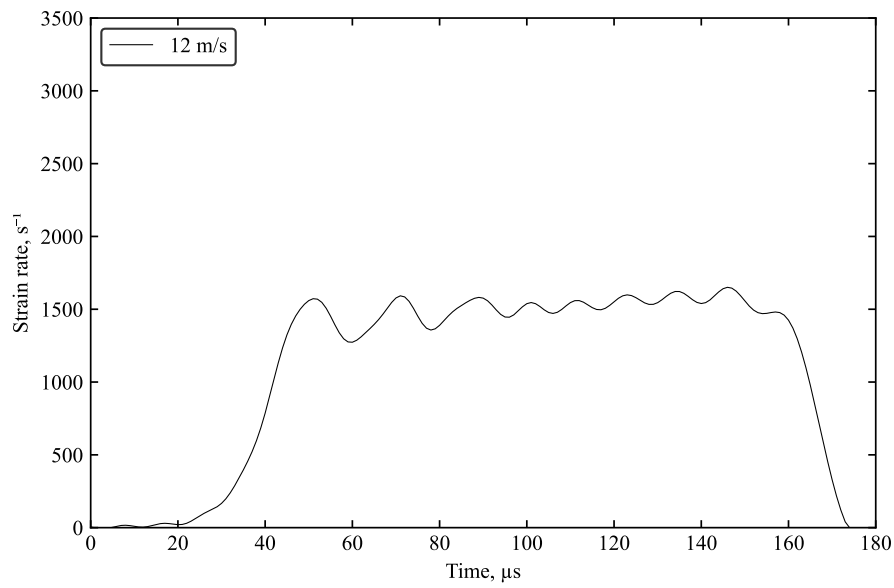


Figure 4.38: Typical strain rate variation during confined SHPB tests on kaolin clay at 12 m/s, corresponding to an average of  $1600 \text{ s}^{-1}$ .

## 4.6 Discussion of SHPB testing

The presence of unique phase behaviours being dependent on saturation is crucial in the practical application of cohesive soils with high water retention capabilities such as kaolin clay. This behaviour is primarily dictated by the tendency for stress to propagate laterally when subject to high-strain-rate axial loading. This leads to a unique scenario when rigid lateral pressure is applied and lateral movement of the sample is restricted. The result leads to the redirection of lateral stresses towards the axial direction, ultimately still leading to the greatest amount of stress wave propagation through the sample. A brief summary of the effects of each phase on the respective stress behaviour in unconfined and confined SHPB conditions is expressed in Figure 4.39.

While the effect of moisture content is clearly significant in influencing high-strain-rate behaviour in cohesive soils such as kaolin clay. It is also equally important to consider the effect of confining pressure especially as it is evident that restriction of lateral movement results in an increase of stress transmission as the lateral stress gets redirected axially.

The blast attenuation properties of kaolin clay is emphasised even when under confined conditions, such that the back stress is still significantly less than the front stress. While it is presumed that it is an intrinsic property for kaolin clay to translate axial stress laterally, the recorded radial stresses are still considerably low. However, this can be attributed to experimental limitations caused by volumetric loss due to extrusion. Similar to the behaviour of fluids, the internal lateral pressure within the ring forces the sample to extrude from the edges of ring when subject to extreme loading. Qualitative assessment from high-speed imaging of confined SHPB experiments on kaolin clay show this behaviour as seen in Figure 4.40. This is further backed up by numerical modelling in which a rigid confining ring that restricted any sample extrusion created a scenario in which volumetric loss was restricted and full lateral stress translation occurs, where there were comparable magnitudes of front and back stresses. Refer to Chapter 6 for a comprehensive description of the development of the numerical model and findings.

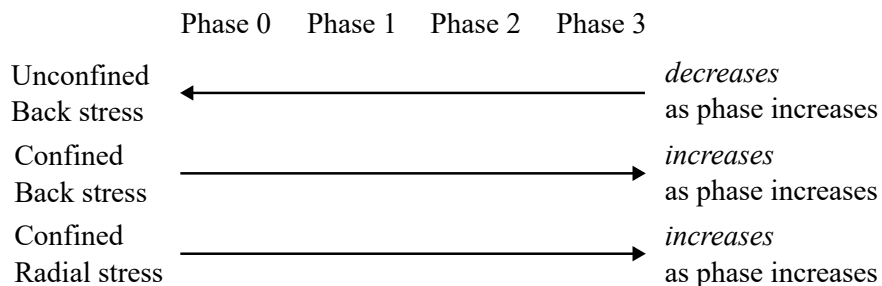


Figure 4.39: Summary of average stress magnitude within each moisture content phase of kaolin clay, effect of moisture content within individual phases do not show clear relationship.

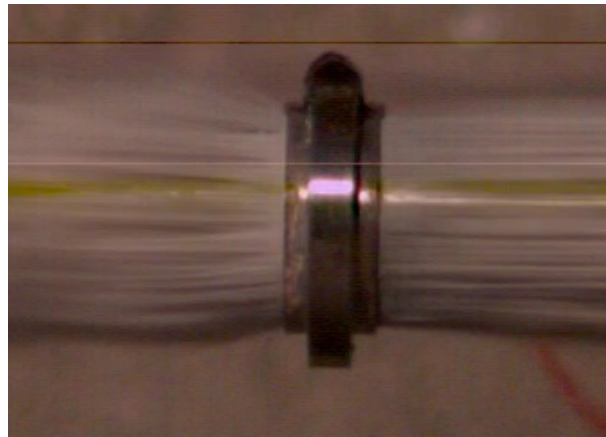


Figure 4.40: High-speed imagery of the instance after loading for confined SHPB test on kaolin clay, showing sample extrusion from the edges of the ring upon impact.

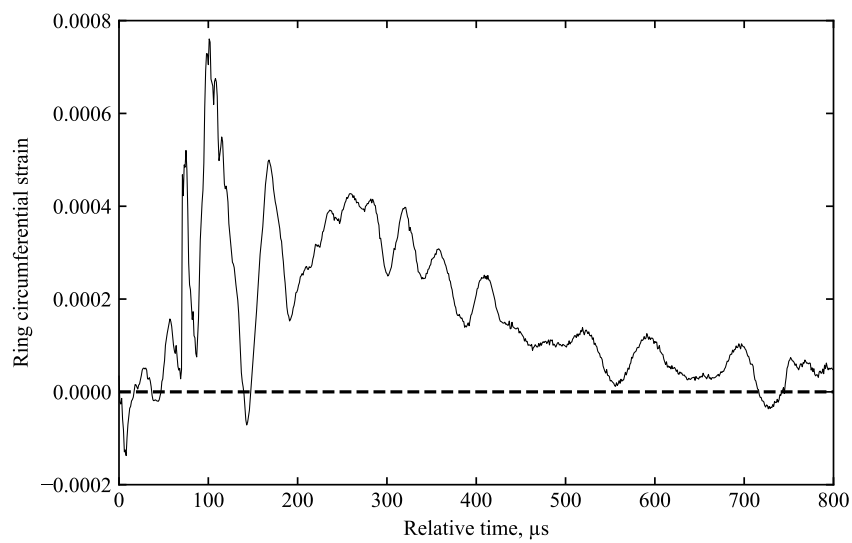


Figure 4.41: Typical circumferential strain history of confining ring, showing continual variation even after initial pulses.

In addition to the presence of volumetric loss due to extrusion, physical limitations associated with the material of the confining ring mean that the resultant radial stress pulse experiences multiple oscillations due to vibration upon impact. While the effect of vibration was not as significant since the magnitude of the initial peak in the incident and reflected pulses were the primary points of concern, the vibration of the steel confining ring meant that circumferential strain measured by the strain gauges on the confining ring were inevitably affected by internal reflections of the initial stress pulse. Figure 4.41 shows an expanded view of the radial stress history starting from the instance of impact, to illustrate the magnitude of oscillations that develop over time even after the stress wave has passed through the sample. Moreover, unavoidable contact between the confining ring and pressure bars also lead to minor additions to circumferential strain measurements from the strain gauge, these factors are key objectives that prompt the need for numerical modelling to aid in the interpretation of confinement effects.

The initial conditions prior to the propagation of the stress wave was such that the confining ring provided a tight seal over the specimen and the pressure bars, preventing any gaps for extrusion. The continual oscillations of expansion and contraction after the initial pulse means that gaps exist that prompt the continuous extrusion of sample volume. An inherent trade-off exists between tightness of the ring around the sample to provide full confinement, and the ring's hindrance of bar movement that affects the loading phase through the sample. While high-speed imagery conducted was insufficient to provide the exact instance of extrusion, initial circumferential strains of less than 0.0004 implies that while portions of the sample are extruded on the initial loading, the stress wave still propagates into the sample. However, this is subsequently addressed via numerical modelling, where the ability to create a fully sealed confinement mechanism without hindering bar and loading phases allows for the effect of confined high-strain-rate conditions to be better understood.

By considering the effects of a rigid confining ring, it becomes imperative to also determine if radial pressure during unconfined conditions are consistent with the findings regarding the translation of axial stresses. The ability for the partial laterally confined setup allows for the sample to be contained in a state that replicates a free field environment but allow for radial pressure to be recorded through changes in water pressure.

## 4.7 Summary

This chapter investigates high-strain rate behaviour of kaolin clay by conducting SHPB tests. Detailed methodology of the apparatus and setup was discussed, along with the introduction of the algorithm `SHPB_processing.py` to facilitate the signal processing of SHPB tests. This was vital as preliminary tests reveal that the conventional condition of stress equilibrium could not be obtained from SHPB tests due to impedance mismatch. This leads to the use of SHPB tests as a method of characterisation of stress wave propagation, and uncovered the effects of high-strain-rate testing on cohesive soils.



The effect of moisture is especially significant for cohesive soils, traditional free field unconfined SHPB tests demonstrate the four unique boundaries within cohesive soil behaviour corresponding to varying levels of moisture content. While results within each phase are not conclusive, there is a clear trend that shows phases with lower saturation typically experience lower axial stress propagation as a significant portion is translated into lateral stress and lost through sample extrusion. The boundaries of which these phases are shown to be directly correlated with intrinsic material properties and experimental conditions, notably air-volume ratio, water-volume ratio, and maximum experimental strain. The first two properties dictate the behaviour within each of the phases, with the volume of air affecting the degree of consolidation, and volume of water dictating the tendency for lateral stress propagation. The maximum experimental strain is directly related to the strain rate, this is supported by tests at greater strain rates which show phase boundary 3 decrease accordingly.

By juxtaposing unconfined tests with SHPB tests with a rigid steel confining ring, the effects of both confinement conditions are compared. Similarly, four unique types of behaviour was observed corresponding to each of the four phases. However, the trend differed from unconfined tests due to the restriction of lateral stress propagation. The addition of the confining ring served to concentrate lateral stresses at the edge of the sample and ultimately redirect the stress back towards the axial direction and onto the transmitter bar. This leads to an increase in both back stress and radial stress as saturation within each phase increases.

However, experimental limitations prevent full characterisation of these confinement modes, hence numerical modelling is required to facilitate characterisation of cohesive soil behaviour.

## Chapter 5

# Partial lateral confinement for evaluation of confinement effects

## 5.1 Introduction

While the presence of a rigid confining ring has been shown to have an effect on the resultant stress transmitted through a kaolin clay specimen, it is necessary to investigate whether this effect is consistent when the confining pressure is reduced. It becomes critical for triaxial behaviour under high-strain-rates to be evaluated when confining pressure is not limited. Unconfined SHPB tests allow for free field high-strain-rate tests to be conducted, but does not enable for radial stresses and lateral deformation to be precisely examined. This novel avenue bridges the gap between conventional free field unconfined SHPB testing for solid materials, and rigid confined SHPB testing typically used in soil testing.

Hence work is done to develop the setup initially pioneered by Barr et al. (2016) for testing on cohesive soils. The development of the setup not only provides the ability to record changes in lateral stress during standard free-field SHPB tests on soils, but also opens up the possibility for other types of testing such as with fluids and bridges the gap between triaxial behaviour from rigid confined and conventional unconfined conditions. The modified apparatus, as initially developed by Barr et al. (2016), consists of the addition of a steel reservoir that envelopes the pressure bars and soil sample. Prior to testing, the reservoir was filled with water and changes in water pressure resulting from lateral deformation of the sample during axial loading was used to monitor triaxial behaviour.

While the setup was conceptualised and preliminarily developed for sands and rubber samples, the setup has not been adapted for a wider range of material samples. Further development of the apparatus and signal processing procedure for this study was crucial in enabling the investigation of high-strain-rate triaxial behaviour. While the focus of equipment development was focused on facilitating the application of the apparatus on cohesive soils and fluids, the goal is to serve as a proof of the viability of this apparatus in wider range of materials with unique behavioural tendencies, in addition to enhancing the holistic

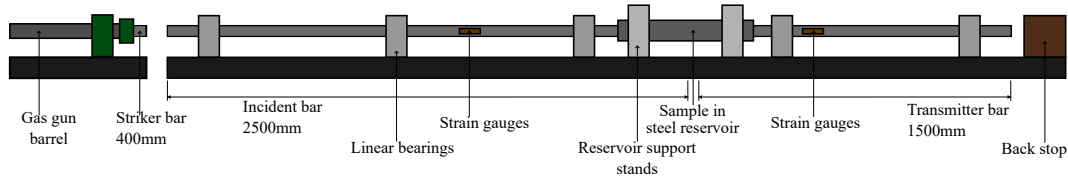


Figure 5.1: Schematic of the partial lateral confined SHPB apparatus.

understanding of cohesive soil behaviour under high-strain-rate conditions especially with regards to confinement effects and triaxial behaviour.

In contrast to experiments where the hydrostatic pressure is applied before the axial loading, the method discussed in this chapter allows the lateral confinement of the specimen to develop during the deviatoric phase. As the sample is loaded axially, the inertia of the water annulus resists radial deformation that occurs in response to the behaviour of the sample. A pressure transducer in the wall of the reservoir allows radial stresses to be quantified. The pressure transducer to be used is the Kulite HKM—375–2500, calibrated by the manufacturer to perform linearly to a pressure of 25MPa.

Kaolin clay samples are prepared accordingly at a range of moisture contents for testing with the modified SHPB setup. The aims of partial lateral confined testing on kaolin clay was to:

- Demonstrate the capability of the modified SHPB apparatus for high-strain-rate testing on cohesive soils.
- Compare radial behaviour of cohesive soils under modified SHPB apparatus with existing SHPB conditions to evaluate effects of confinement.

## 5.2 Partial lateral confined apparatus

### 5.2.1 Experimental setup

The modified SHPB is made up of a standard pressure bar arrangement which consists of a striker, an incident and a transmitter bar, 25 mm in diameter, with a 350 mm, 2500 mm and 1500 mm length, respectively, as shown in Figure 5.1. In addition, as illustrated in Figure 5.2, a 600 mm long steel water reservoir is set on linear bearings and centred around the specimen. A 0.05mm thick friable latex membrane enveloped over the sample and both the incident and transmitter bars, and secured by small rubber o-rings (Figure 5.3), this is to preserve to saturation level of the sample and to prevent water from the water annulus from contaminating the sample prior to loading.

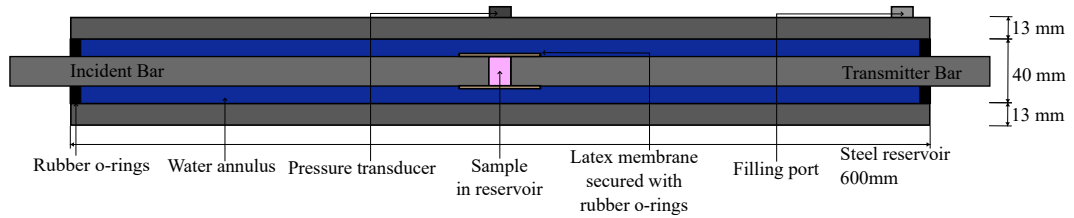


Figure 5.2: Schematic of the partial lateral confined SHPB apparatus: water reservoir section.

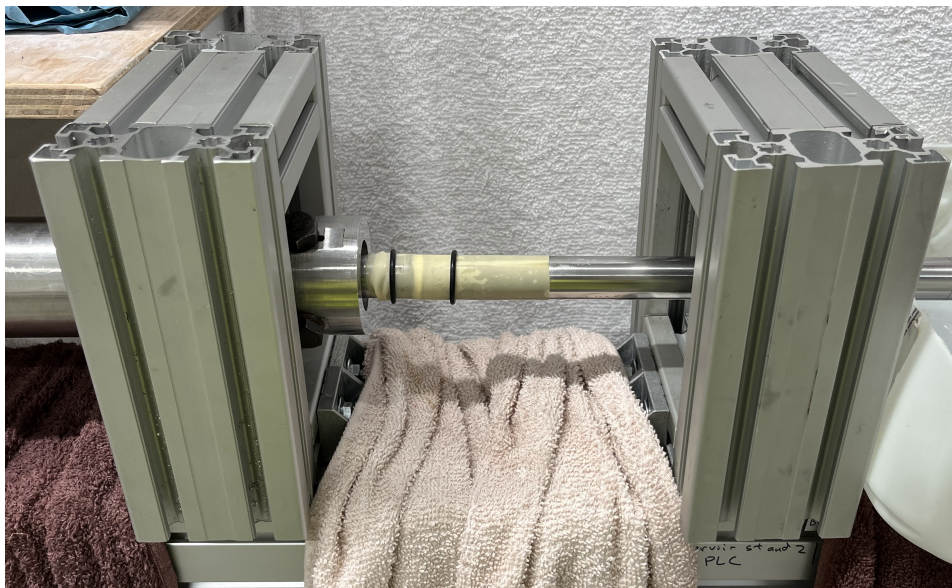


Figure 5.3: Image of the sample in between the reservoir support stands prior to the initiation of testing with the partial lateral confined SHPB apparatus; sample is secured between the pressure bars, enveloped by a latex membrane, and secured by small rubber o-rings.

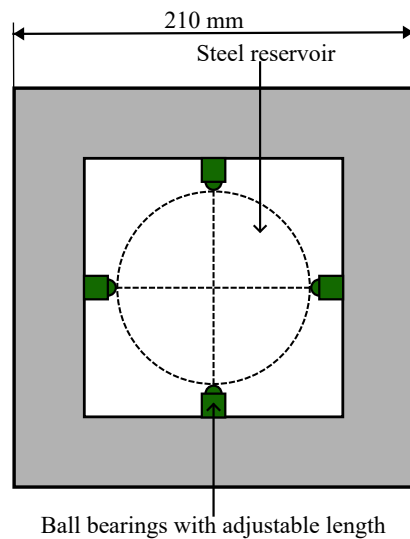


Figure 5.4: Simplified schematic of the reservoir support stand used for partial lateral confined tests, water reservoir to be centred and secured between the ball bearings.

The reservoir length was designed so that the time required for a stress wave initiated at the specimen surface to travel to and from the reservoir's end exceeds the loading duration in the specimen, guaranteeing that inward-travelling waves from the boundary do not interfere with pressure measurements. This simplifies the seal between the reservoir and the pressure bars, which are only needed to keep the water at atmospheric pressure.

### 5.2.2 Reservoir support stand

To facilitate the use of the water reservoir for partial lateral confined testing, new reservoir support stands were designed that allowed for precise manual adjustment of the the reservoir alignment, as well as accessible removal of the water reservoir before and after testing. The ball bearings are loosely screwed onto the aluminium frame and capable of being manually adjusted to ensure the reservoir is centred between the pressure bars and secure prior to testing. Figure 5.4 shows a simplified design of the reservoir support stand, however detailed design drawings can be found in Appendix F.2.

### 5.2.3 Partial lateral confined SHPB testing procedure

While the initiation process of partial lateral confined tests follow a similar procedure previously described for unconfined and confined SHPB tests, the fitting of the sample in preparation for testing was crucial to ensure sample measurements are accurately obtained and the sample is properly secured prior to axial loading.

The procedure to load the sample into the apparatus was as follows:

1. Reservoir support stand was secured onto the channel prior to installation of the water reservoir and fitting of the sample. Incident bar was pushed all the way to the left and movement of the bar was restricted prior to testing.
2. Linear bearing support closest to specimen interface on incident bar was moved to the left.
3. Water reservoir was slotted in between the reservoir support stands and in between the incident and transmitted pressure bars.
4. Water reservoir was slid to the left in the space of the vacated linear bearing support.
5. Small plastic o-rings were slid onto the incident and transmitted bars.
6. Half of latex membrane was slid onto the incident bar.
7. Sample was carefully placed in between the incident and transmitted pressure bars.
8. Latex membrane was carefully slid over to fully encompass the specimen and sealed onto the pressure bars with the small o-rings.
9. Water reservoir was slid back and pressure port was aligned directly on top of the specimen.
10. Linear bearing support was slid back towards its original position.
11. Ball bearings on reservoir support stand were manually adjusted to ensure the water reservoir was centred on both the incident and transmitted pressure bars and secured in place.
12. Large o-rings were used to seal the two open ends of the water reservoir.
13. The reservoir was slowly filled with water through the filling port and the pressure transducer is secured onto the pressure port.
14. Measurement of the sample length is performed based on the distance between the end of the transmitted bar and the final linear bearing support (Figure 5.5)

The test then proceeded like previous SHPB tests, loading was provided by initiating the gas gun and firing the striker bar onto the incident bar at the desired striker bar velocity.

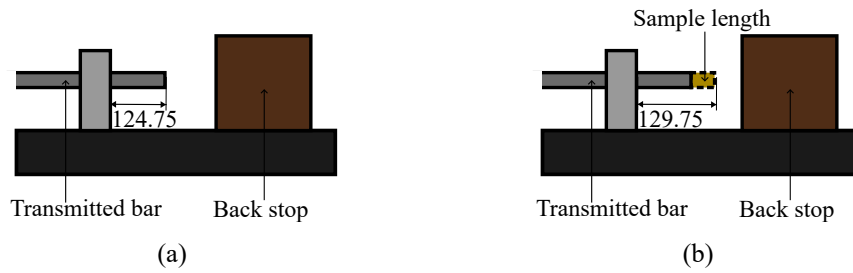


Figure 5.5: Schematic of sample measurement process a) before and b) after installation inside the reservoir.

### 5.2.4 Signal processing for partial lateral confined testing

Signal processing for partial lateral confined SHPB tests were similarly handled with the `SHPB_processing.py` function, with the confinement mode set to ‘Reservoir’. While signal processing for axial stress and strains follow the same method, the signals obtained from the pressure transducer does not require a Wheatstone bridge circuit as the transducer directly outputs a voltage that can be translated into the pressure experienced at the location of the pressure port.

The transit time between the radial stresses through the water annulus has been taken account by considering the time required to travel through the medium of fluid within the annulus. Thus the time for the the stress pulse,  $t_{\text{transit}}$ , to travel through the reservoir annulus can be given by:

$$t_{\text{transit}} = \frac{l_{\text{reservoir}}}{v_{\text{fluid}}} \quad (5.1)$$

where  $l_{\text{reservoir}}$  is the thickness of the reservoir annulus, and  $v_{\text{fluid}}$  is the wave speed of the fluid in the annulus. The radial stress directly obtained from processing pressure transducer signal is then timeshifted by the transit time in order to acquire the radial stress experienced at the surface of the specimen, with the assumption that the fluid wave speed for water is 1482 m/s.

### 5.3 Partial lateral confined testing of kaolin clay

Unconfined and confined SHPB tests have been fundamental in the understanding of high-strain-rate behaviour of kaolin clay. While radial stresses under rigid confinement have been investigated, the partial lateral confined SHPB apparatus allows radial stresses to be measured yet the sample is still allowed to deform laterally during loading. Results from high-strain-rate testing of kaolin clay with the partial lateral confined SHPB apparatus have been documented and submitted for publication (Li et al., 2024a), the journal paper has been included in Appendix A.6 for reference.

As highlighted, the main objectives are to demonstrate the capabilities of the partial lateral confined SHPB apparatus in assessing triaxial behaviour of cohesive soils under high-strain-rate conditions, and to connect the findings between unconfined and confined SHPB testing regarding the effects of confinement. As such, the test programme using the partial lateral confined apparatus, is focused on testing at various saturation levels and striker speeds, as discussed in Section 3.5. Although radial deformation is allowed to develop under this modified setup, the radial inertia caused by the development of hydrostatic pressure means the lateral confining pressure is still greater than free field unconfined tests, hence a difference in strain rate is expected.

Different moisture contents are tested to investigate the unique phase behaviour under high-strain-rate loading. The majority of the test programme with the partial lateral confined SHPB on kaolin clay is focused around tests at 16 m/s, which corresponds to an average peak strain rate of  $2500 \text{ s}^{-1}$ . Previous SHPB testing on kaolin clay revealed that the boundaries of the phases are reflective of the intrinsic properties of the material and maximum experimental strains (Figure 5.7). Hence the moisture contents selected for testing are based on verifying the existence of the same phases and validating prior knowledge about the material properties of kaolin clay. Additional tests on saturated kaolin clays are conducted at striker bar speeds of 12 and 20 m/s, which correspond to peak average strain rates of 1900 and  $3000 \text{ s}^{-1}$  (Figure 5.6). This is used to check the effect of strain rate and compare to existing results. Ultimately, by comparing the results from unconfined, confined, and partial lateral confined tests, the holistic effect of confinement was evaluated.

Similar to existing SHPB testing, sample stress is determined by taking the average at the front and back interfaces of the specimen, back stress is the main component that undergoes drastic change. The typical front stresses for confined SHPB tests is shown in Figure 5.8.

### 5.3.1 Effects of moisture content

Axial data from experimental results on kaolin clay exhibit similarities to behaviour from unconfined SHPB tests where a lesser magnitude of axial stress is recorded on the back of the specimen, as seen in Figure 5.9. This is because when the sample is allowed to deform laterally, cohesive soils such as kaolin clay tend to propagate stress laterally and result in the lack of direct translation of axial stress on the initial transmitted pulse.

#### Axial effects

As such, the intrinsic phase behaviour previously investigated in both confined and unconfined testing is assumed to exist. This has been validated as tests on saturated, partially saturated, and dried samples are shown in Figure 5.10, where unique variations of back stress are recorded within each individual moisture content phase. While there is no conclu-



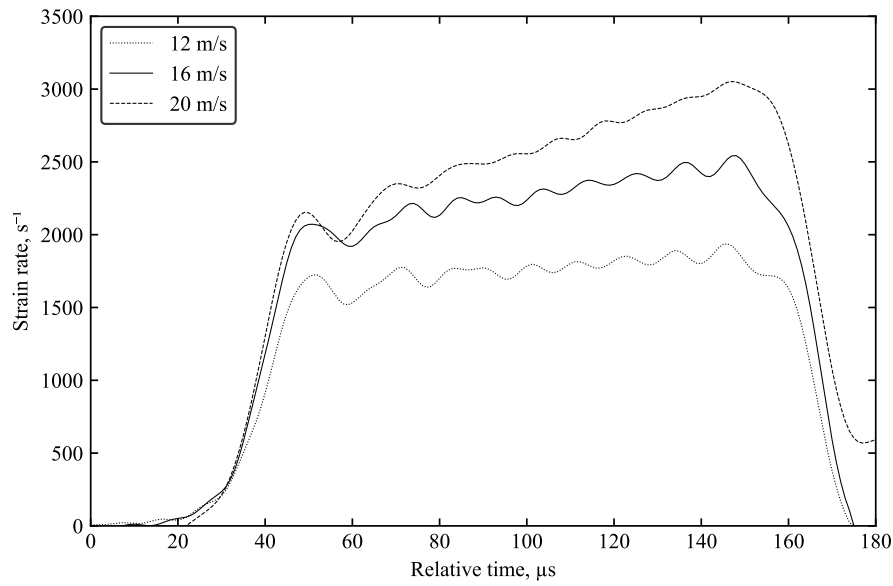


Figure 5.6: Typical strain rate variation during partial lateral confined SHPB tests on kaolin clay at 12, 16, and 20 m/s, corresponding to an average peak strain rate of 1800, 2500, and 3000  $s^{-1}$ .

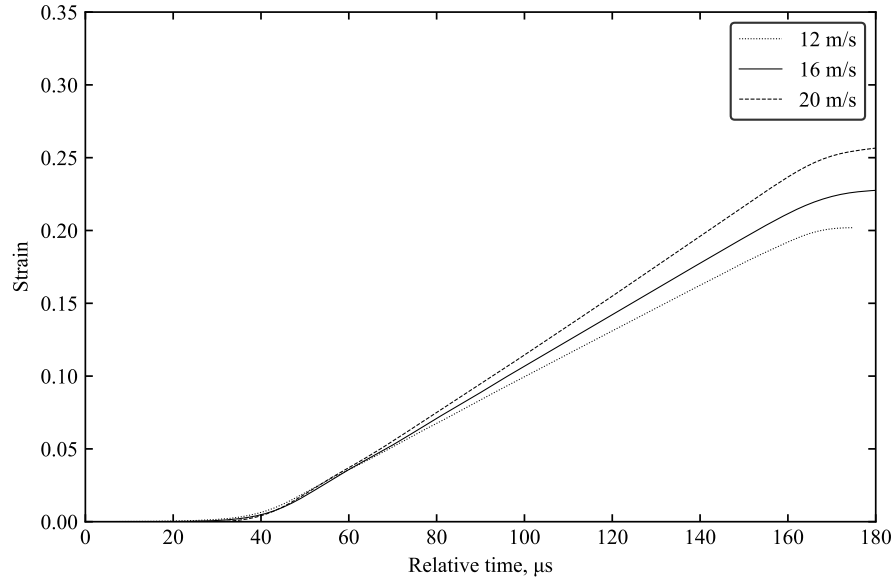


Figure 5.7: Typical strain time history during partial lateral confined SHPB tests on kaolin clay at 12, 16, and 20 m/s.

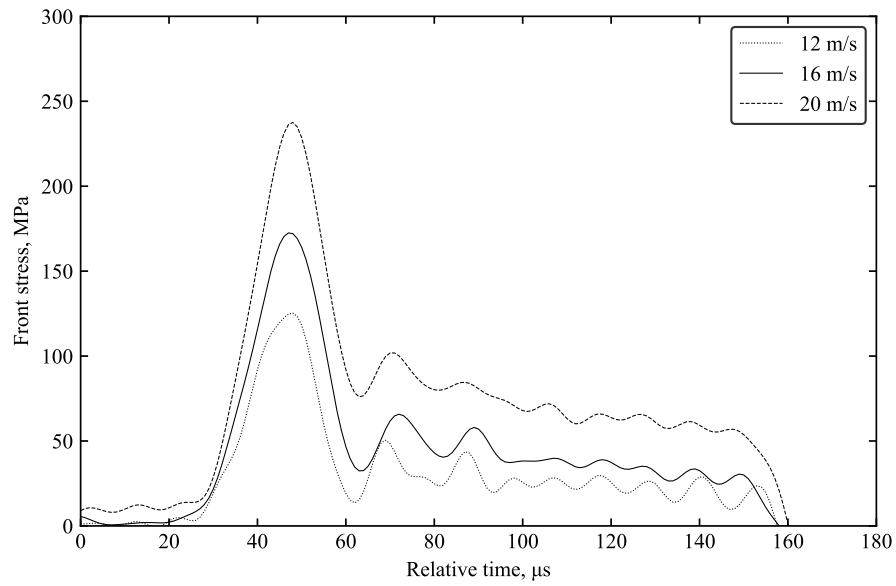


Figure 5.8: Typical front stress variation for partial lateral confined SHPB tests at 12, 16, and 20 m/s.

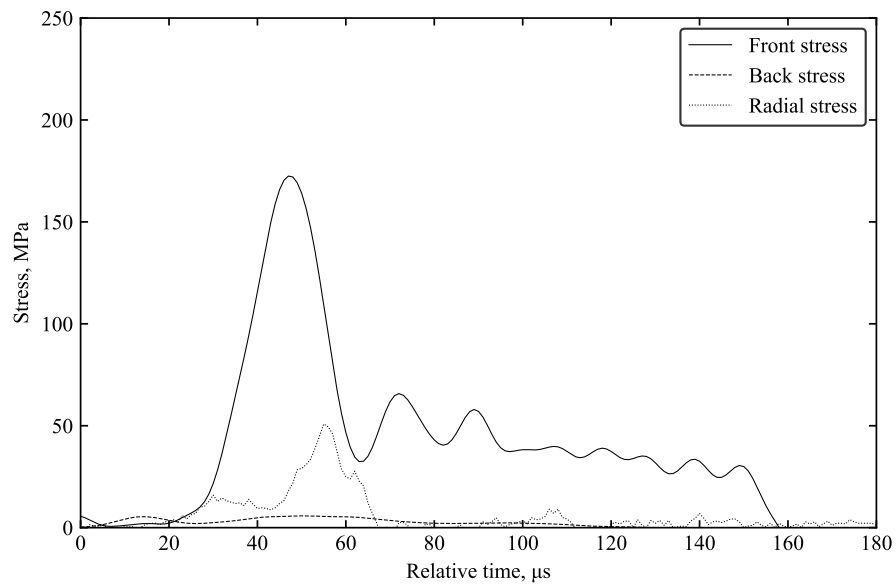


Figure 5.9: Partial lateral confined SHPB test on kaolin clay at 16 m/s: front, back and radial stresses.

sive relationship between saturation and back stress within individual phases, the stress on the back interface of the specimen generally increases as phase increases.

**Phase 0:** Axial stress during phase 0 still retains the same characteristic from unconfined tests that back stress does not return to zero, this is attributed to energy being used to consolidate the dry sample by filling in the existing air gaps. Stress propagation through the sample is the greatest in this phase due to lack of moisture to force lateral propagation.

**Phase 1:** Behaviour within this phase is similar to phase 0, except the presence of moisture means that there is a lesser degree of consolidation due to a portion of the stress being propagated laterally, hence the curve gradually returns to zero over the course of the pulse.

**Phase 3:** This phase exhibits the lowest amount of axial stress propagation, the high volume of water in saturated samples induce lateral stress propagation, resulting in the least amount of back stress being recorded.

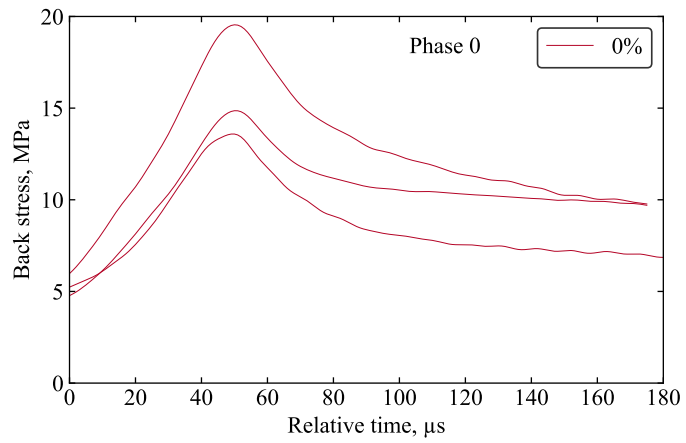
While tests have not been conducted to explicitly determine the behaviour within phase 2, the consistency between characteristics of the other phases indicate the same behaviour exist in phase 2, however further tests should be performed in the future to validate the existence of phase 2 boundaries.

### Radial effects

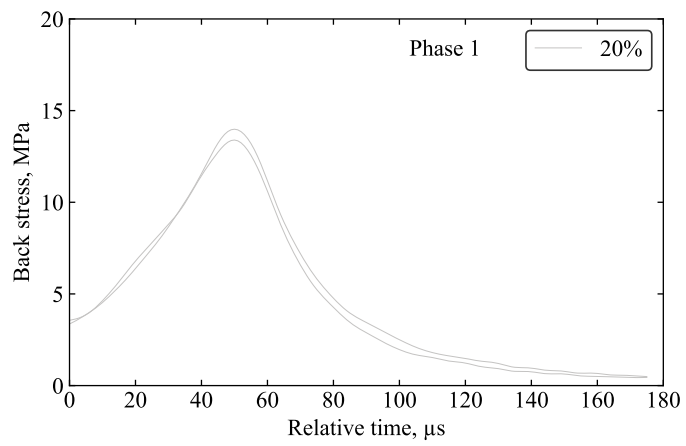
A primary advantage of the modified SHPB setup is the ability to simultaneously characterise lateral behaviour without a confining ring that restricts lateral deformation. This can be evident from Figure 5.9, where even though axial behaviour resembles closely to unconfined SHPB tests on kaolin clay, significant radial stress can be recorded. This allows for the development of lateral stress to be monitored even while the sample is allowed to laterally deform under the different saturation phases.

While the algorithm `SHPB_processing.py` was developed with capabilities to automatically detect the radial pulses, the magnitudes of the radial stresses in certain tests were too low. This meant that often noise would interfere with detection of the radial pulse. For these instances, manual selection of the radial pulses was performed by approximation of the starts of the pulse. While the noise recorded at lower radial stress levels deems radial stress behaviour as inconclusive, the magnitude of the radial pulse can still be estimated and used as a basis of comparison to tests that yielded higher radial stress.

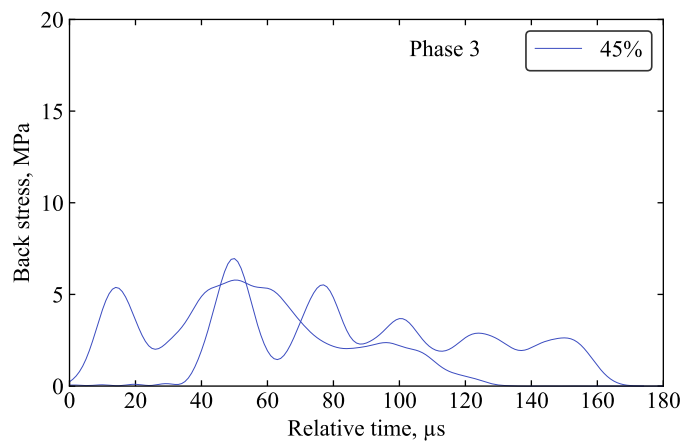
**Phase 0:** As seen in Figure 5.11a, while a radial pulse is still marginally visible, the noise recorded by the pressure transducer overlaps the majority of the stress pulse. The prime characteristic of this phase is that the sample undergoes consolidation and significantly more axial stress is able to translate through the sample, naturally this indicates that the magnitude of the radial pulse is much lower due to a lesser degree of lateral propagation. Since the noise recorded can reach up to 3 MPa, this means that up to 50% of the recorded radial



(a)

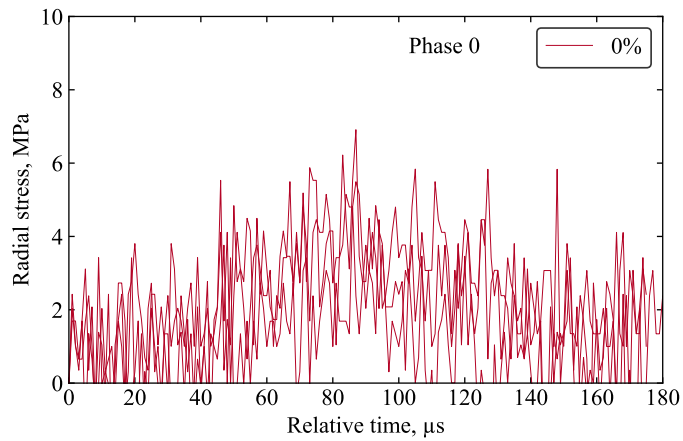


(b)

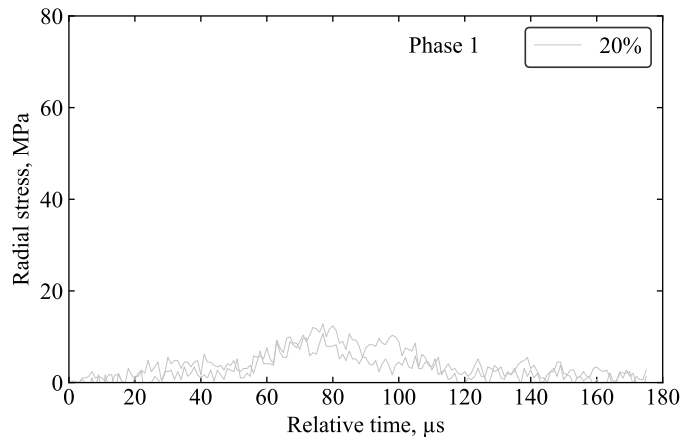


(c)

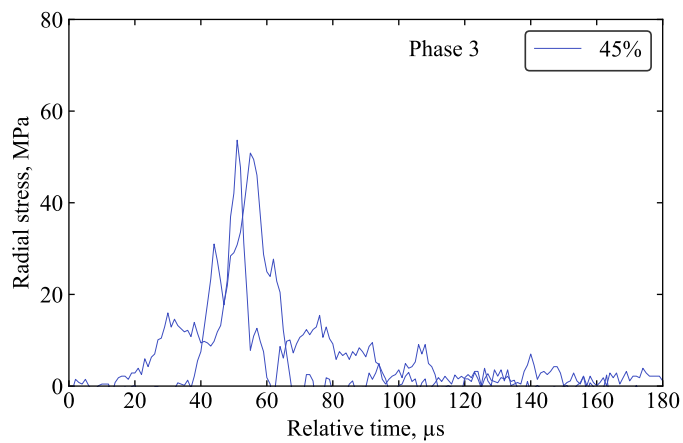
Figure 5.10: Back stress from partial lateral confined testing on kaolin clay at 16 m/s at moisture contents corresponding to a) phase 0, b) phase 1, c) phase 3.



(a)



(b)



(c)

Figure 5.11: Radial stress from partial lateral confined testing on kaolin clay at 16 m/s at a) phase 0, b) phase 1, and c) phase 3.

pulse overlaps with equipment noise. Hence, other than the interpolation that radial stress is at a minimum, it is not feasible to reach accurate conclusions from tests at low moisture contents at this time.

**Phase 1:** The greater degree of saturation within the sample causes a portion of the stress to propagate laterally. Hence the magnitude of the recorded radial stresses show a considerable increase from phase 0 as seen in Figure 5.11b.

**Phase 3:** For saturated samples of kaolin clay, the capability of the apparatus to measure radial stress is demonstrated. The high proportional volume of moisture in samples within this phase mean that high-strain-rate loading tends to cause the sample to expand laterally. This invokes the greatest magnitude of radial stress, evident from Figure 5.11c, where there is a distinct radial stress pulse.

### 5.3.2 Effects of strain rate

In addition to tests at 16 m/s, tests on saturated kaolin clays are conducted at 12 and 20 m/s which correlate to average peak strain rates of 1800 and 3000 s<sup>-1</sup> (Figure 5.6). Tests at 16 m/s demonstrated that the inability of the current setup to detect lower radial stresses indicate that results obtained at lower degrees of saturation may not be reliable due to the significant amount of noise. However, as discussed in Chapter 4, while strain rate has an effect on the magnitudes of the stresses obtained at each moisture content phase, the typical behaviour and pulse shapes exhibited at each phase remained consistent. Thus, even though samples with lower degrees of saturation are not explicitly tested at different strain rates with the partial lateral confined apparatus, the behaviour can be extrapolated based on proven material behaviour from existing testing.

The back stresses from tests conducted on saturated kaolin clay can be visualised in Figure 5.12. The back stresses are still characterised by much lower magnitudes, and a minor negative correlation can be observed as strain rate is increased. Similarly, radial stress exhibited the same effect as expected, the shape of the radial pulse remained the same but the magnitude increases with strain rate as seen in Figure 5.13. Based on this, the stress-strain relationship can be visualised in Figure 5.14.

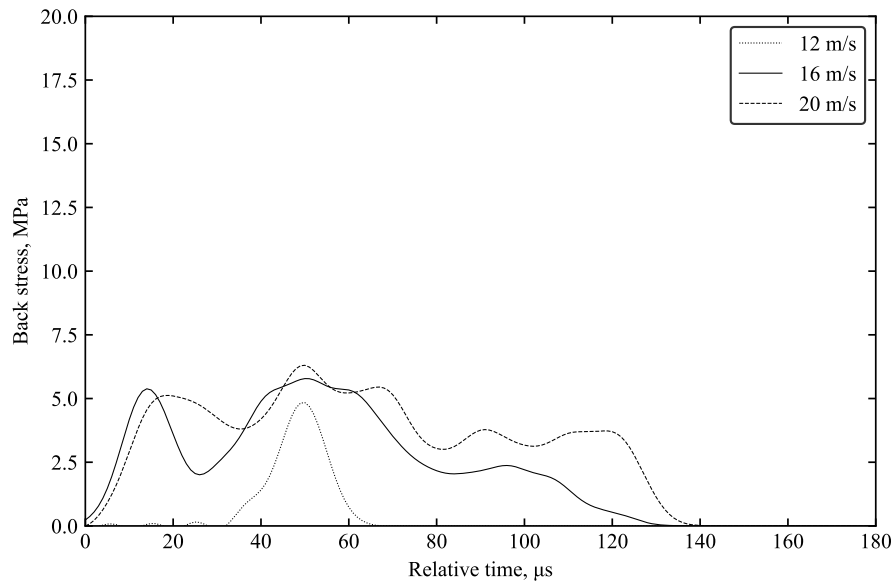


Figure 5.12: Typical back stress from partial lateral confined SHPB test on saturated kaolin clay at 12, 16, and 20 m/s

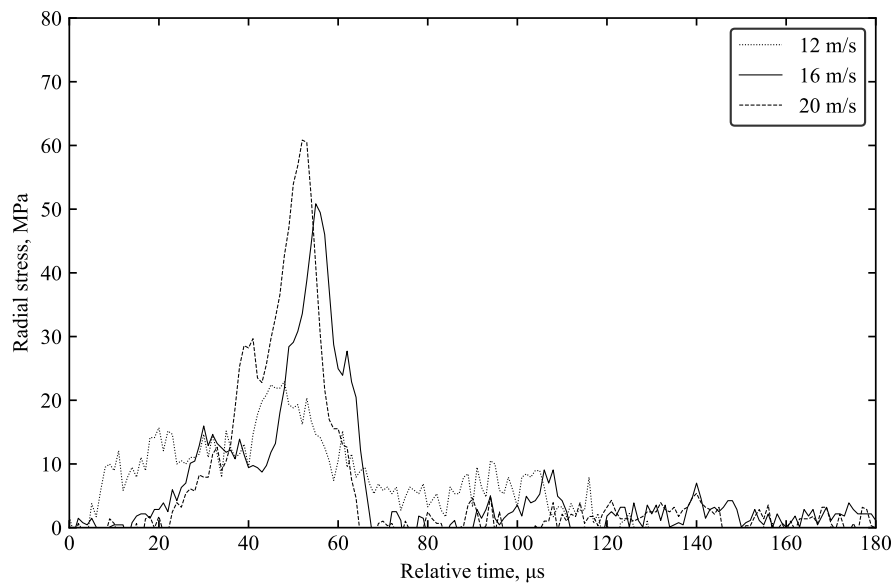


Figure 5.13: Typical radial stress from partial lateral confined SHPB test on saturated kaolin clay at 12, 16, and 20 m/s

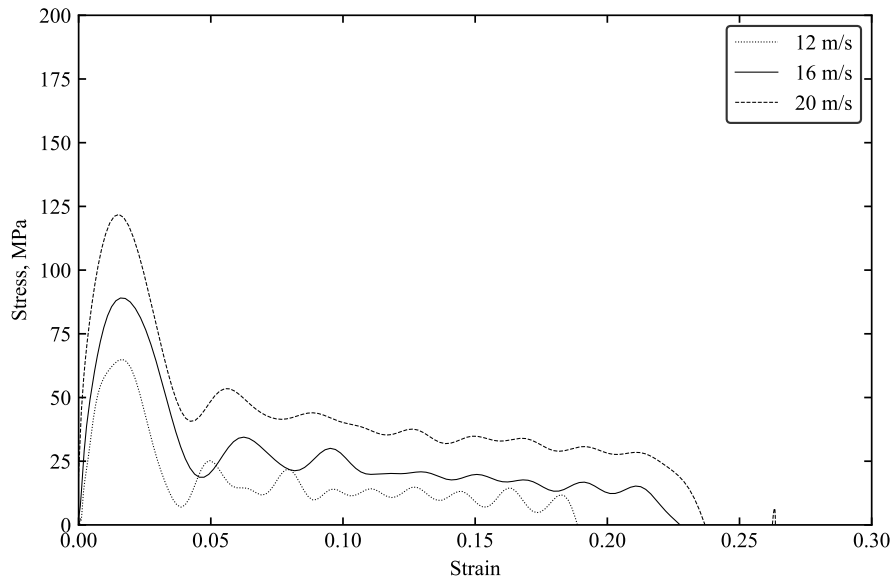


Figure 5.14: Typical stress vs strain variation from partial lateral confined SHPB test on saturated kaolin clay at 12, 16, and 20 m/s

## 5.4 High-strain-rate testing of water via partially lateral confined apparatus

This section aims to cover the investigation of high-strain-rate effects of liquids, specifically water, through the employment of the modified SHPB with partial lateral confinement. While this provides a novel element such that it opens the possibility to conduct high-strain-rate testing on fluids, it also acts as a source of comparison between the high-strain-rate behaviour between kaolin clay and water. Work covering the application of the partial lateral confined SHPB on water has been submitted for publication (Li et al., 2024b), the corresponding journal paper can be found in Appendix A.4.

### 5.4.1 Methodology and setup for water tests

The methodology to setup the modified SHPB apparatus for water is a simplified version of the standard methodology for soil samples. Without the latex membrane and o-rings to envelope the sample, a 5 mm gap is left between the incident and transmitted bars in the space where the sample was originally secured as seen in Figure 5.15. As water at atmospheric pressure fills the water reservoir, the space in between the pressure bars was subsequently filled with water and subjected to high-strain-rate compression during loading.



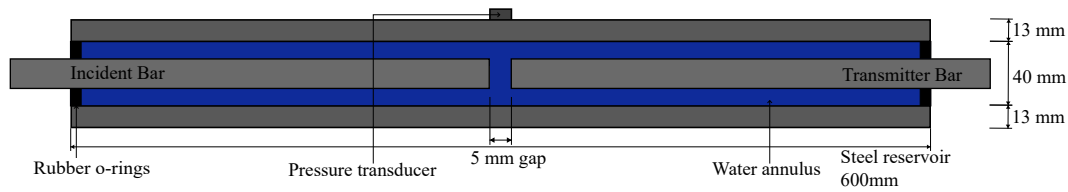


Figure 5.15: Schematic of the partially lateral confined SHPB apparatus for water tests: water reservoir section.

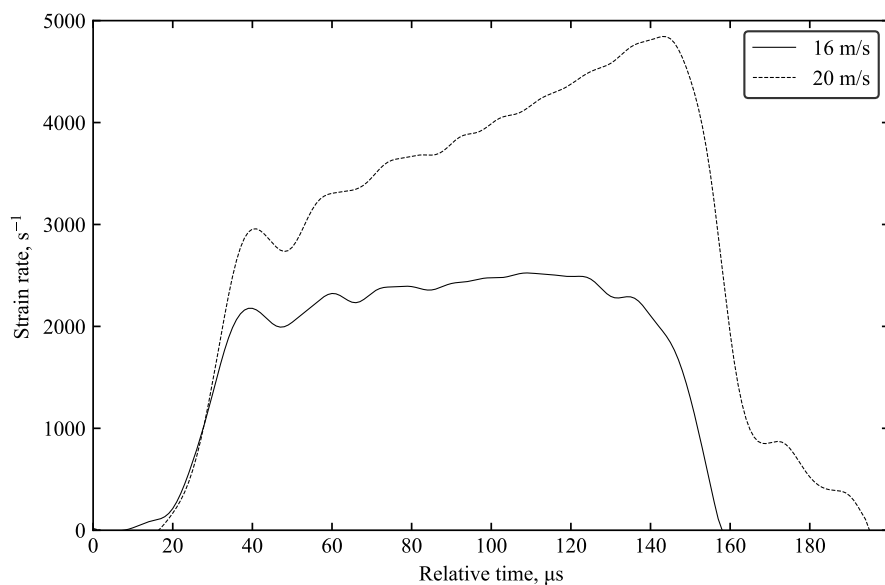


Figure 5.16: Variation of strain rate during partially-confined SHPB experiments on water.

Partial lateral confined SHPB tests were then conducted in the same manner as previously described. Tests were conducted at designated striker bar speeds of 16 and 20 m/s, and were measured with the speed trap at the end of the gas gun barrel. From the tests conducted at the two different speeds, a broad range of strain rate was captured, as shown in Figure 5.16, where the strain rate increases to an average peak of  $2095 \text{ s}^{-1}$  and  $4844 \text{ s}^{-1}$ , over approximately  $150 \mu\text{s}$ . Under these high-strain-rate conditions, both the axial and radial stresses of the specimen were measured.

## 5.4.2 Results of water testing

Figure 5.17 display the typical stress difference between axial and radial stress, illustrating the viability of the current configuration in assisting with the triaxial response of a liquid. The time delay between the radial and axial stresses can be attributed to the effects of water's radial inertia, which is an avenue that can be investigated in the future.

Figure 5.18 shows the incident and reflected pulses, indicating that while a major portion of the wave is reflected, a significant portion is shown to travel through the incident bar and onto the water medium.

Tests were performed using the modified SHPB fitted with the partial lateral confinement reservoir on water, at 16 m/s and 20 m/s. Figures 5.19 and 5.20 show similarities in terms of response behaviour, with a logical increase in amplitude associated with higher test speeds.

Figures 5.19 and 5.20 depict the experimentally measured front, back and radial stresses. The radial stress directly adjacent to the water in between the pressure bars was calculated by taking into account the transit time of the radial stress wave through the water annulus (5.1  $\mu$ s, assuming a wave speed in water of 1482 m/s). The recorded radial stress shows a radial stress wave with peaks that align relatively well with front and back stresses, indicating that the lateral response recorded with the pressure transducer is a direct result of the axial loading from the SHPB test.

Looking at the Poisson's ratio, experimentally at 16 m/s, the maximum front, back and radial stress recorded are 180, 5 and 46 MPa, respectively, resulting in a Poisson's ratio of 0.5 (Figure 5.19), when the axial stress ( $[180 + 5]/2 = 92.5$  MPa) is divided by the radial stress (46 MPa). Since the theoretical Poisson's ratio for water is 0.5, this indicates that the axial and radial stress data obtained by employing this modified SHPB setup exhibit a degree of accuracy reflected in theory.

At higher striker speeds, the incident bar's inertia and the partial lateral confinement water reservoir has an impact on the front, back and radial stresses, as seen in Figure 5.20. This also affects the Poisson's ratio of the water specimen, progressively lowering its value. The stress-strain variation from tests at both speeds on water is visualised in Figure 5.21.

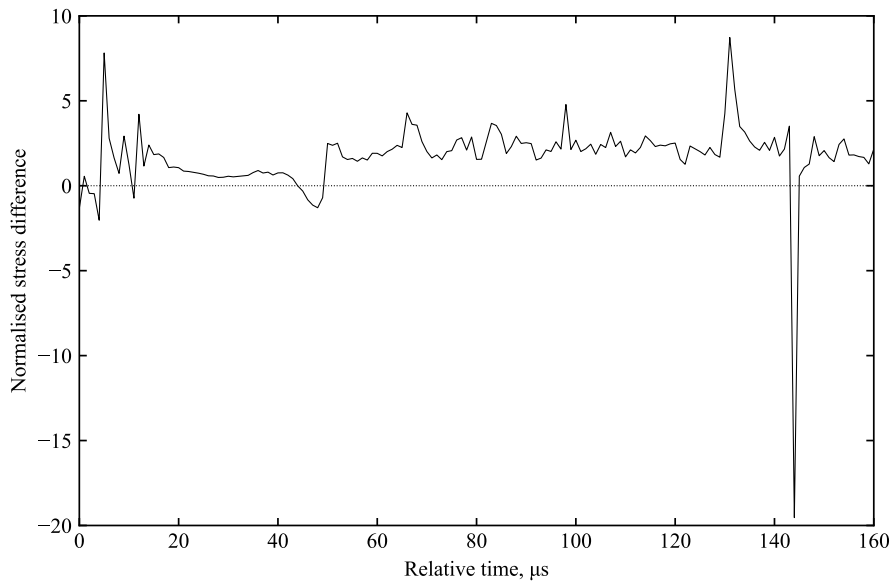


Figure 5.17: Typical response of a partial lateral confined SHPB test on water showing axial and radial stress difference normalised by their mean.

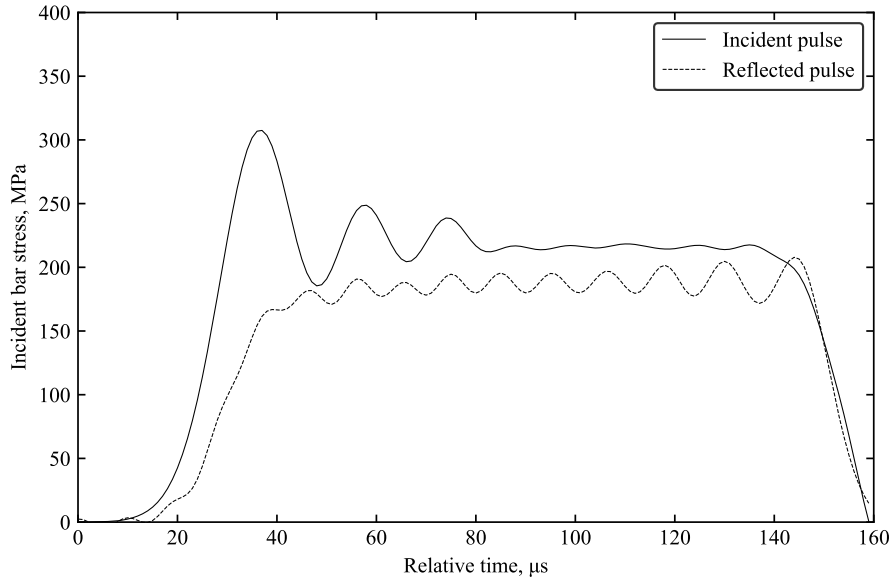


Figure 5.18: Typical behaviour of a partial lateral confined SHPB experimental test on water at 16 m/s: incident and reflected pulses from the incident bar.

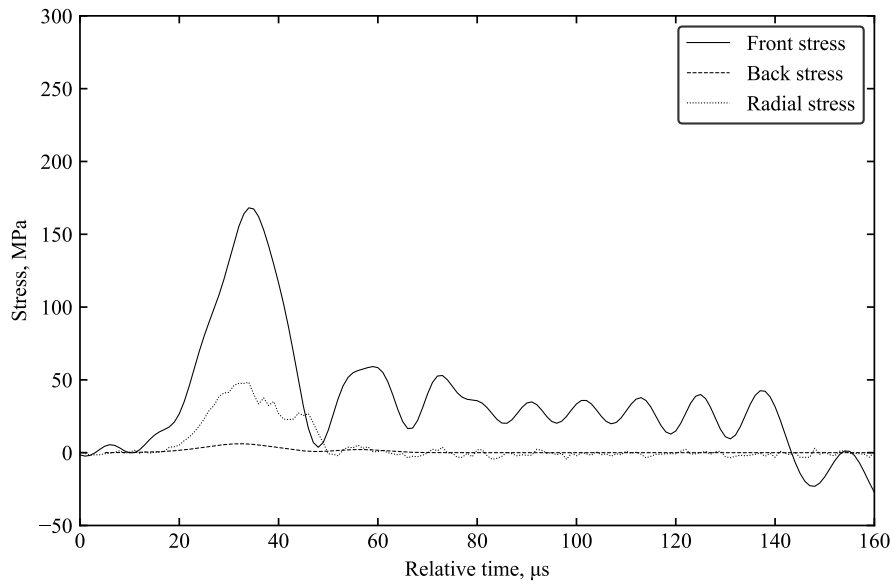


Figure 5.19: Partial lateral confined SHPB test on water at 16 m/s: front, back and radial stresses.

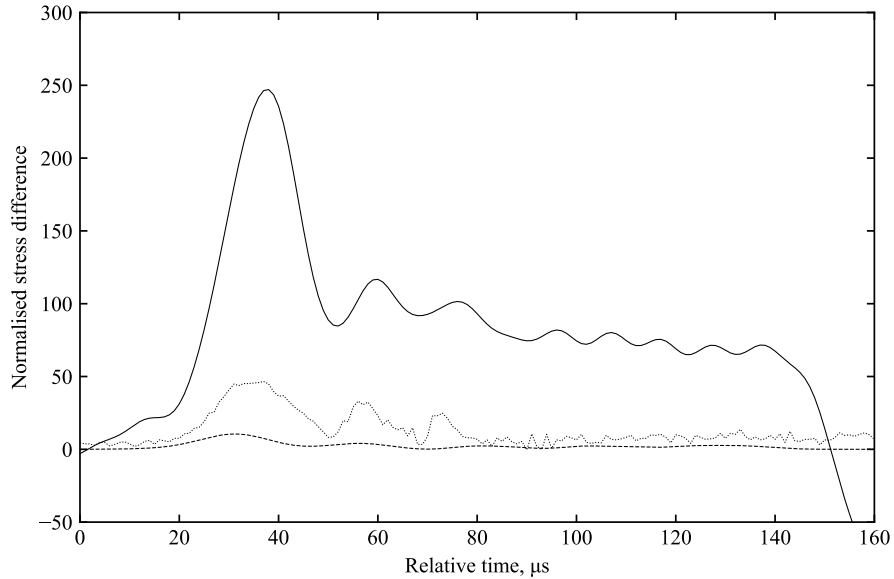


Figure 5.20: Partial lateral confined SHPB test on water at 20 m/s: front, back and radial stresses.

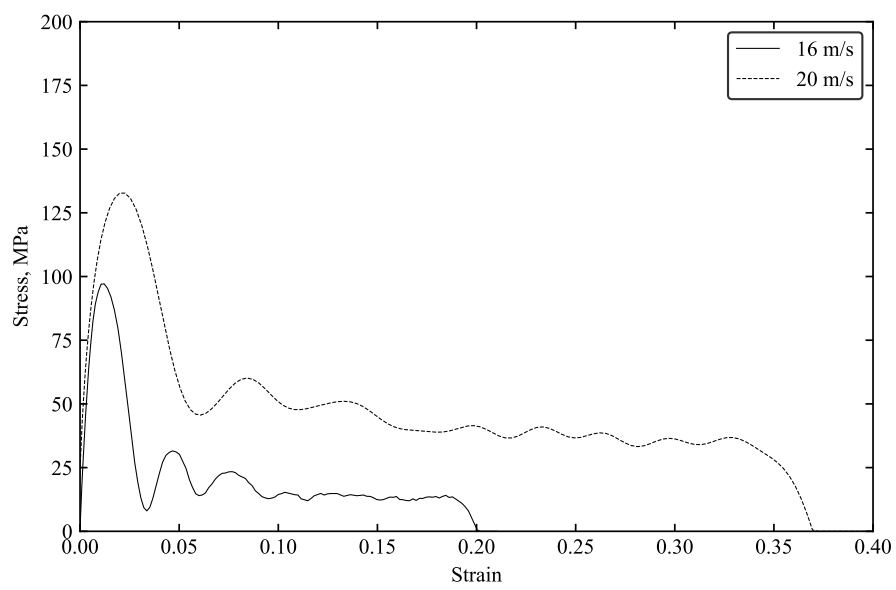


Figure 5.21: Typical stress vs strain variation from partial lateral confined SHPB test on water at 16 and 20 m/s.

### 5.4.3 Discussion of high-strain-rate water testing

The capabilities of the modified SHPB with lateral confinement apparatus enables high-strain-rate testing of water and the ability to investigate its axial and lateral response. This fills a crucial gap in present research that previously restricted SHPB testing to non-fluid materials.

Furthermore, the ability to conduct high-strain-rate testing on water opens up the possibility to use this apparatus to compare the effect of saturation in other materials to the behaviour of water itself. Hence this apparatus can be directly applied in the testing of soils in order to better understand the effect of moisture content under high-strain-rate conditions. The specific effect of soil factors such as particle size or density can be investigated further by comparing high-strain and quasi-static triaxial tests on fully saturated soils.

In addition to being used as a comparison tool for material characterisation, the capability to evaluate high-strain-rate behaviour of fluids opens up the possibility of using the apparatus to investigate high-strain-rate effects of other fluid mediums and characterise their practicality to withstand real life conditions that resemble high-strain-rate effects. The computational function `SHPB_processing.py` includes adjustable parameters for certain input variables specific to the type of fluid in the reservoir, so further work can be established regarding testing other fluids with additional calibration of the function or apparatus.

## 5.5 Discussion of partial lateral confined testing of kaolin clay

Even though striker bar to strain rate ratios are setup-specific, the initial incident stress should be similar at the same striker speeds, with identical striker bar configurations and pressure bar setups. As previously highlighted during confined testing, the confining ring affects the rate at which the sample is strained, even when the magnitude of stress from the initial striker bar is the same. By comparing the strain rate variations with the exact same initial incident stress (all at 12 m/s), the effects of confinement on sample strain rate can be observed in Figure 5.22. It is evident that while there is a clear decrease in strain rate between unconfined and confined test setups, there is only a minimal decrease between unconfined and partial lateral confined conditions. This supports the capability for the modified apparatus to emulate unconfined conditions, whilst still measuring radial stress transmission.

### 5.5.1 Comparison with water

Since saturated kaolin clay has demonstrated high-strain-rate behaviour similar to fluids, the capability of the setup to test water was crucial in establishing the influence of moisture in cohesive soil samples.

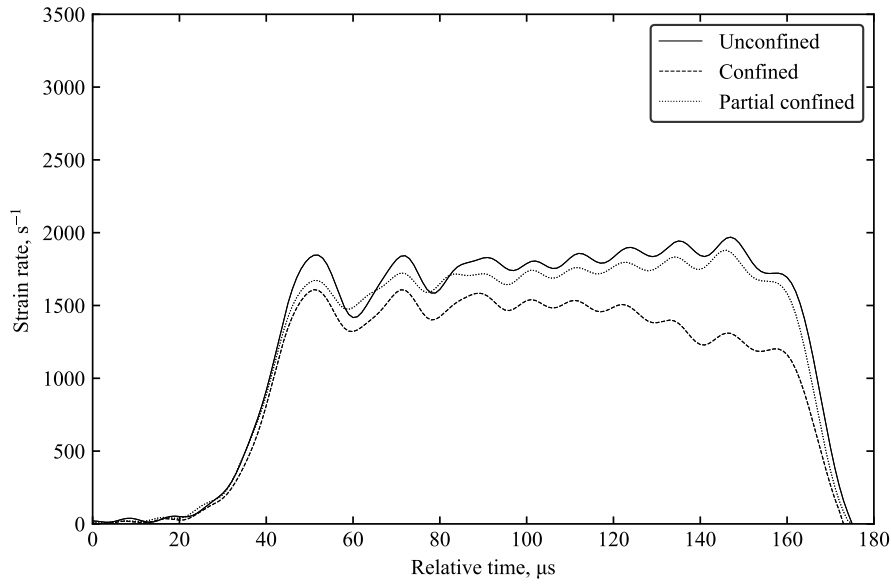


Figure 5.22: Typical strain rate variation during SHPB tests for saturated kaolin clay under unconfined, confined, and partial lateral confined conditions with average peak strain rates of 1600, 1800, and 1900  $s^{-1}$  respectively.

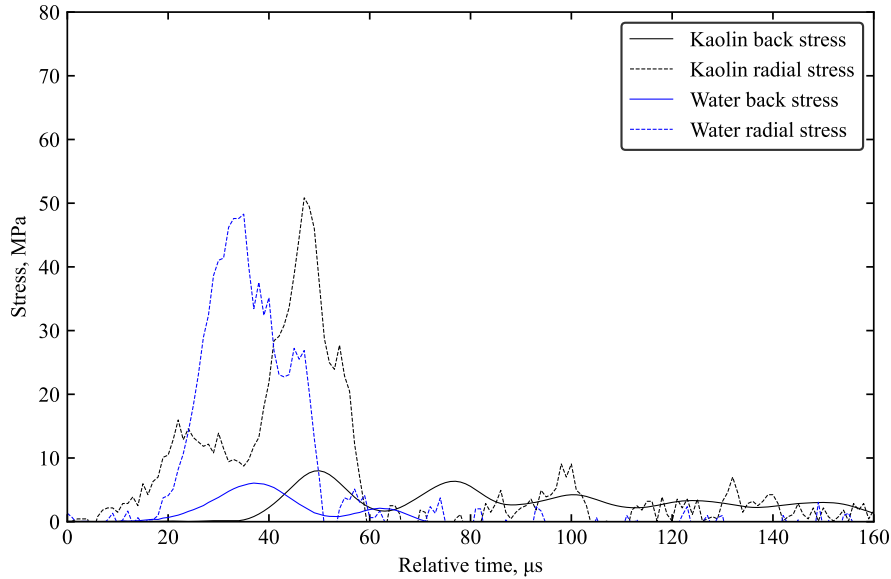


Figure 5.23: Typical back and radial stresses from partial lateral confined SHPB tests on water and saturated kaolin clay at 16 m/s.

There is a notable similarity between experimental results of water and saturated kaolin clay (Figure 5.23). The same effect is observed where axial stress from the incident bar fails to propagate through the sample (or water medium) onto the interface of the transmitted bar. Radial stress results also show a similar effect, where the magnitude of tests with kaolin clay and water show stark similarities. This supports the claim that high-strain-rate tests on kaolin clay is not dissimilar to testing on fluids.

When a rigidly contained volume of water endures axial compression, the water pressure increases and a force is exerted on its surroundings. This is similar to kaolin clay under high-strain-rate loading, where lateral pressure develops on the surface of a confinement mechanism as a result of axial compression. Without lateral restriction, the kaolin clay sample naturally tends to extrude. However, a fully rigid confinement system creates an environment similar to water where the build-up of internal pressure results in stress translating back in the axial direction.

### **5.5.2 Comparison with unconfined and confined SHPB testing**

To compare the effect of the partial lateral confined SHPB results with existing results, the pulses from the three confinement modes are visualised in Figure 5.24. This highlights that partial lateral confined testing serves as a medium between the two opposite confinement modes and the effect that confinement has on high-strain-rate behaviour.

The magnitude of the back stress pulse greatly resemble unconfined tests, albeit to a slightly greater magnitude. This is due to the fact that while the sample is largely allowed to deform laterally, the water annulus and latex membrane still exerts minimal confining pressures. These pressures contribute to the redirection effect observed in confined testing but to a much lesser extent. However, magnitudes of unconfined and partial lateral confined tests are still considerably less compared to confined testing. This demonstrates that the partial lateral confinement mechanism still emulates an environment relatively similar to unconfined test conditions, but allows for radial pressures to be measured.

Similarly, the radial stresses between confined and partial lateral confined conditions are compared. The disparity in radial stress compared to confined tests can be attributed to the concentration of stresses on a rigid ring. The replication of a free field environment within the reservoir prompts lateral stresses to dissipate without being concentrated directly on the surface of the specimen. However, the lack of a rigid restriction means that the stress does not get redirected towards the transmitter bar like confined results, hence the lower recorded back stress. This shows that the tendency for stress to propagate laterally is an intrinsic property of cohesive soils such as kaolin clay, and that this effect is attributed to its similarity in behaviour to water especially in a rigidly confined environment.



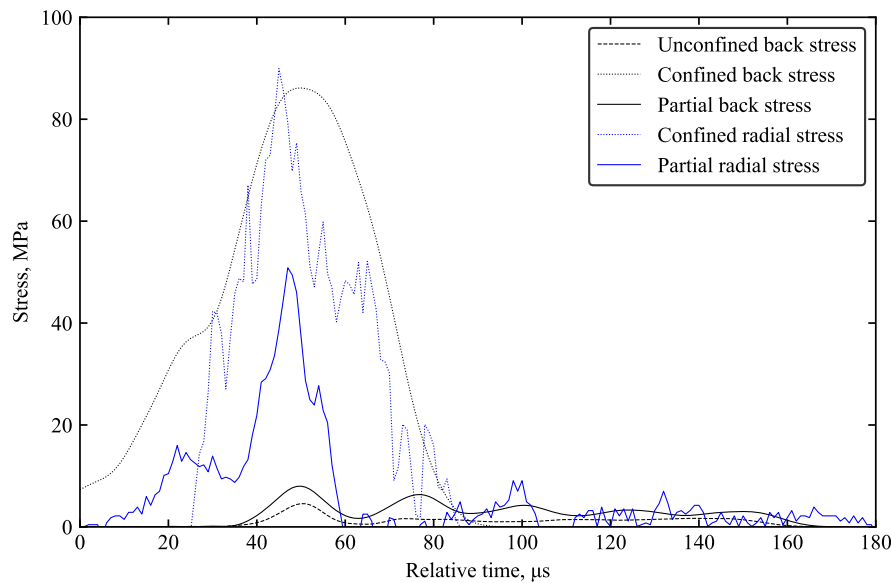


Figure 5.24: Typical back and radial stress from unconfined, confined, and partial lateral confined SHPB tests.

### Triaxial stress state

Radial stress data obtained from partial lateral confined SHPB tests on kaolin allows for the triaxial stress state to be evaluated. The difference between sample axial and radial stresses for confined and partial lateral confined SHPB tests on kaolin clay is shown in Figures 5.25 and 5.26.

Moisture content evidently has the same effect regardless of confinement, such that each phase typically experiences lower difference in axial and radial stresses. The concentration of radial stresses experienced under confined conditions emphasises the triaxial stress state, where in addition to the initial axial stress wave, the confinement mechanism serves to provide a confining pressure to restrict lateral deformation. This ultimately enables stress to propagate through to the back of the sample, unlike what occurs in unconfined SHPB tests.

This is juxtaposed with partial lateral confined test conditions, where the confining pressure is allowed to passively develop instead. The measured radial stresses correspond to the confining pressure that develops as the sample is strained axially. The magnitude of the stress difference is much lower compared to when a rigid confining ring is present. Consequently, this corresponds to a significantly reduced amount of stress that is able to propagate to the back of the sample.

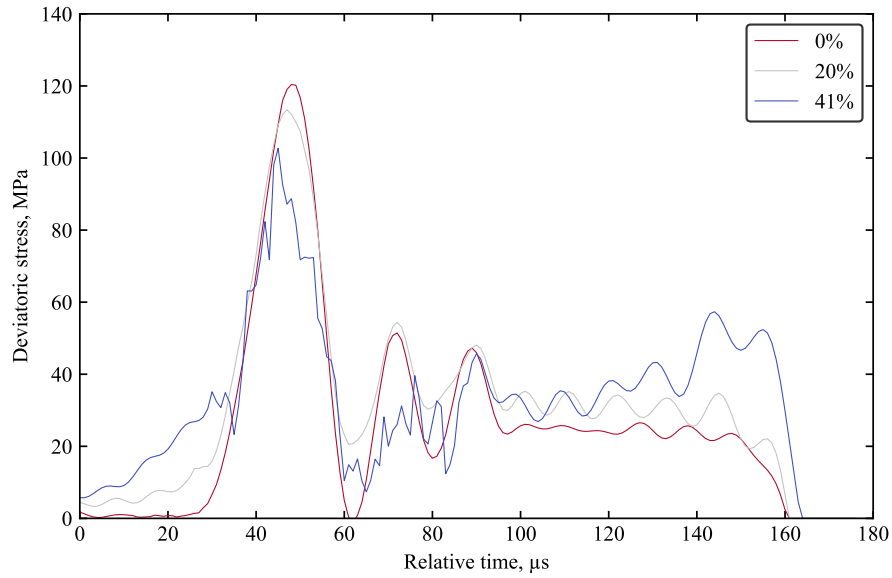


Figure 5.25: Difference between axial and radial stresses from confined SHPB tests on kaolin clay at varying moisture contents.

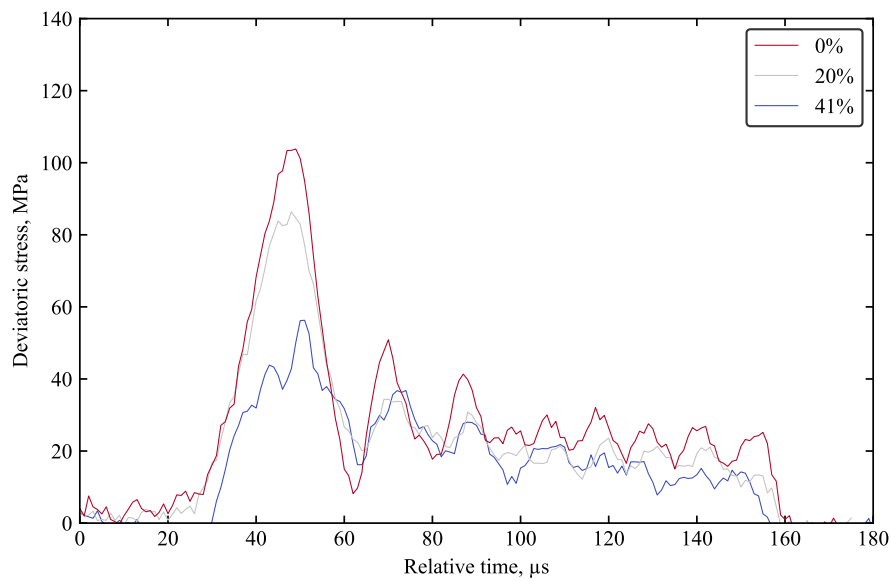


Figure 5.26: Difference between axial and radial stresses from partial lateral confined SHPB tests on kaolin clay at varying moisture contents.

### 5.5.3 Setup limitations and future development

As highlighted previously, there still exists an inherent inability to accurately measure radial stresses if the magnitude is less than 10 MPa. While this problem was mitigated in the pressure gauge strain gauges by adding an amplifier unit to the balance box containing the Wheatstone bridge, a similar amplification method cannot be utilised with the current pressure transducer setup. However, further developments to the setup may include the addition of pressure transducer that have built-in amplification functionalities, allowing for the precise pressure measurement of lower radial pressures and reducing the influence of noise. Ultimately, this should increase the reliability of results at lower radial stresses, such as that of lower moisture content samples. While material behaviour can be extrapolated based on existing testing, improved pressure transducer amplification will allow for the full saturation range to be evaluated like in unconfined and confined testing with a higher degree of precision.

Data processing limitations associated with noise from the pressure transducer can also be mitigated by the use of more sophisticated pressure transducers. While the processing algorithm has the capability to detect radial pulses, the sensitivity of the pressure transducer means that slight changes in pressure affect the accuracy of the algorithm to always determine the precise starting points of the radial pulse, prompting the manual estimation of pulse starts.

## 5.6 Discussion of confinement effects from partial lateral confined testing

The effect of lateral confinement caused by the addition of the confining ring has been discussed in Section 4.6, where it is evident that rigid confinement from the confining ring causes radial stress to redirect axially. Due to the ability of cohesive soils such as kaolin clay to retain a larger proportion of moisture, the effect of moisture content is vital in dictating material behaviour. When subject to high-strain-rate axial loading, moisture forces the stress to propagate laterally, this typically creates volume loss as an after effect of the loading. This is supported by partial lateral confined testing, where it is evident that when under limited confinement conditions, lateral stress is at its greatest, and the opposite is true for the recorded back stress. This can be summarised in Figure 5.27.

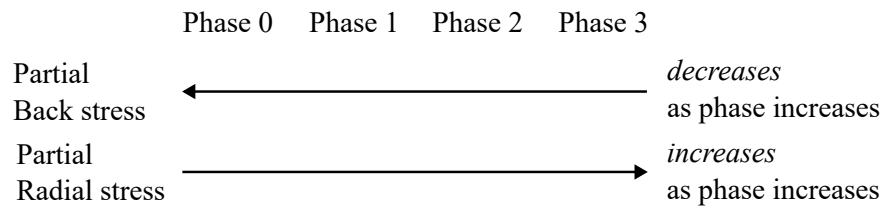


Figure 5.27: Summary of average stress magnitude within each moisture content phase for partial lateral confined SHPB tests on kaolin clay, effect of moisture content within individual phases do not show clear relationship.

When the results from the three confinement modes was compared, the effects of confinement become more apparent. While a particular behaviour is observed within each mode of confinement, the general behaviour can all be attributed to the presence of moisture and the unique tendency for cohesive soil behaviour at high-strain-rates to be wholly dictated by water. The similarity in behaviour with fluids mean that when cohesive soils are subject to high-strain-rate axial loading under free field conditions, the material tends to propagate stress laterally. However, when confining pressures are applied, the confining pressure has a direct effect on resisting the propagation of lateral stress, thus causing the stress to be redirected in the axial direction and towards the back interface of the sample.

## 5.7 Summary

This chapter demonstrates the capabilities of the partial lateral confined apparatus to measure the development of lateral pressure during the deviatoric phase. The modified apparatus was developed for use with the current SHPB setup.

Tests on kaolin clay illustrated that the partial lateral confined apparatus bridged the gap between unconfined and confined testing, where the sample was allowed to deform laterally but radial stress was still allowed to develop. Results show that radial stresses still began to concentrate on the edge of the sample, resulting in a subsequent change in pressure in the water annulus. While the intrinsic tendency for kaolin clay to propagate stress laterally occurs regardless of confining pressure, partial lateral confined tests corroborates that confinement creates an effect of radial stress concentration that subsequently leads to the redirection of stresses. When under limited confined conditions, the radial stresses exhibited on the edge of the sample are evidently lower than those recorded from fully confined SHPB tests, even while axial stress propagation remains at a minimal magnitude. The inherent limitations with physical testing was subsequently addressed with numerical modelling of the modified setup in 6, with the aim to validate conclusions drawn.

The fluid-like behaviour exhibited by kaolin clay from experimental tests prompted the adaptation of the partial lateral confined SHPB procedure to conduct impact tests on water. Comparison between stress propagation behaviour through water act as a basis of comparison to kaolin clay. The results show a clear similarity, such that limited axial stress is propagated onto the transmitted bar through the medium of water. An increase in radial pressure is recorded corresponding with axial wave propagation into the water annulus. This similarity demonstrates that moisture is the primary governing factor behind cohesive soil behaviour.

Comparisons between the three different confinement modes also allowed for the holistic effect of confinement to be analysed, with increased confining pressure having a distinct effect on the concentration of radial stress. However, in order to understand the internal mechanisms and explain the effects of confinement, comprehensive numerical models are required alongside experimental data.

## Chapter 6

# Development of numerical modelling techniques for high-strain testing

## 6.1 Introduction

As highlighted in Chapter 4 and 5, it is not possible to obtain a comprehensive view from experimental testing alone due to the limitations associated with apparatus and the inability to create a fully controlled physical environment. This prompts the development of numerical models that aim to assist with the characterisation of high-strain-rate behaviour and validate conclusions from experimental testing.

Numerical modelling has been conducted by use of LS-DYNA, an explicit simulation software that utilises the finite element method (FEM) to conduct numerical analysis. The development of numerical models was focused on simulating kaolin clay under SHPB testing for unconfined and confined scenarios. In addition to emulating experimental results, evaluation of modern numerical modelling techniques highlight the current limitations associated with modelling high-strain-rate scenarios and cohesive soils. Validation of numerical modelling techniques was conducted based on the ability of the numerical model in replicating experimental conditions and behaviour.

While intrinsic limitations may limit the capability to develop fully accurate numerical models, the primary objective is to evaluate the extent of current numerical modelling techniques and to assist in drawing conclusions regarding material behaviour. As such, numerical models were developed based on emulating the conditions from physical testing, this allows for the combination of results from numerical and experimental conditions to provide more comprehensive conclusions of constitutive behaviour.

Table 6.1: Material properties of steel pressure bars and sample used in SHPB model in LS-DYNA.

<i>Steel pressure bars</i>	MAT_ELASTIC
Mass density, $\text{kgm}^{-3}$	7666
Young's modulus, Pa	1.680e+11
Poisson's ratio	0.29

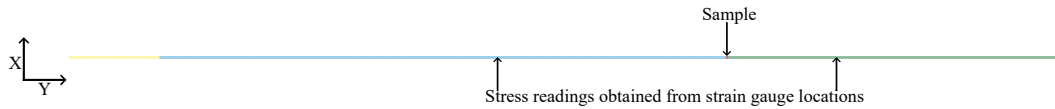


Figure 6.1: Initial LS-DYNA SHPB unconfined model set up containing the incident bar (blue), transmitted bar (green), striker bar (yellow), and sample (red).

## 6.2 Initial model setup and geometry

The initial approach for numerical modelling was centred around emulating traditional unconfined and confined SHPB experimental conditions, numerical models generated prompts for the internal mechanisms that occur during high-strain-rate loading of cohesive soils to be better understood.

The initial model for unconfined SHPB tests was a 2-D axisymmetric model with all parts modelled as Lagrangian shell solids is shown in Figure 6.1 based on the component dimensions of the experimental setup. Striker, transmitter, and incident bar sections were modelled as an elastic material model with the properties of steel as shown in Table 6.1. The mesh files used to generate this initial model was generated using a MATLAB script developed by Dr. Sam Rigby (personal communication, 2021). Dr. Rigby previously conducted sensitivity studies to determine the suitable mesh adopted in the material model for the two steel pressure bars and the sample as 2.5 mm and 0.625 mm respectively.

Due to the limited contact interfaces and for simplicity, an automatic contact model was utilised to define element interaction (CONTACT\_2D\_AUTOMATIC\_SINGLE\_SURFACE). This contact algorithm automatically detects interfaces between 2-D Lagrangian elements and defines contact interactions based on material parameters and geometrical arrangement.

The striker bar was given an initial velocity of 16 m/s, aligning with the striker bar speed used in tests. Since experimental results are obtained at a specified location from the specimen-bar interface, data collected from the constitutive model reflect the same locations on the bar surface to mirror strain gauge locations (1000mm away from incident bar-sample interface, and 500m away from transmitted bar-sample interface).

Due to the material's tendency to exhibit dynamic behaviour similar to water, the sample was

initially modelled using the null material model (MAT\_NULL) with the material properties of water. This algorithm is a simplistic model used to define a void material without stiffness and is typically used to simulate fluids such as water or air. Since this material model requires an equation of state (EOS), the associated EOS for water based on existing literature was applied. An EOS characterises the hydrostatic or bulk behaviour of a material by relating its pressure,  $P$ , to density. The value of mass density was set to  $1000 \text{ kgm}^{-3}$ . The EOS implemented is based on the linear polynomial model type, which is characterised in LS-DYNA by the equation:

$$P = C_0 + C_1\mu + C_2\mu^2 + C_3\mu^3 + (C_4 + C_5\mu + C_6\mu^2)E \quad (6.1)$$

where  $C_0, C_1, C_2, C_3, C_4, C_5$  and  $C_6$  are constants,  $\mu = \rho/\rho_0 - 1$ ,  $\rho$  and  $\rho_0$  are the current and initial densities of the fluid, and  $E$  is the specific internal energy of the fluid (Shin et al., 1998). The parameters used to generate the EOS are designed based on existing research used for modelling water in blast or high impact testing. However, this is used to verify the geometrical setup based on its ability to qualitatively emulate experimental conditions, the suitability of other material models for modelling kaolin clay has also been investigated. The full LS-DYNA null material card and associated EOS is included in Appendix E.

Evidence of stress behaviour from experimental testing is reflected in the data obtained from points on each pressure bar indicative of strain gauge locations (Figure 6.2). As seen from Figure 6.3, a similar effect is observed in the numerical model as in experimental testing, where a significant amount of sample is extruded. While a minor transmitted pulse is notable, the majority of the stress wave does not propagate through to the transmitted bar.

This model is adapted for the confined case, where a steel ring is placed on the edge of the sample as shown in Figure 6.4 and the same contact algorithm is applied between the ring and other model parts. This replicates an experimental SHPB test under confined conditions. However, the model fails to reach its assigned termination state due to a “negative volume error”. The time frame immediately prior to failure is shown in Figure 6.5, which depicts the state prior to sample extrusion from the edge of the steel ring. Since the pressure bars and confining rings are modelled as elastic materials, they experience deformation when under stress. The instance that ring is subject to the change in lateral stress from the sample, it deforms and allows gaps for sample extrusion. The immense distortion of the mesh shape as a result of extrusion prevents the model from accounting for all elements and results in computational failure. Overcoming this computational error is a major topic of discussion in subsequent sections.



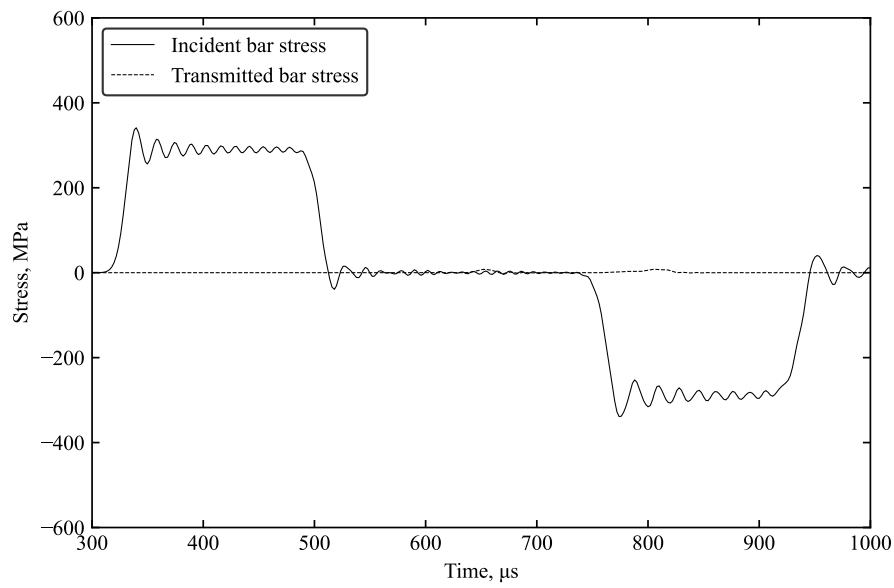


Figure 6.2: Axial stress recorded with unconfined SHPB LS-DYNA model obtained at strain gauge locations.

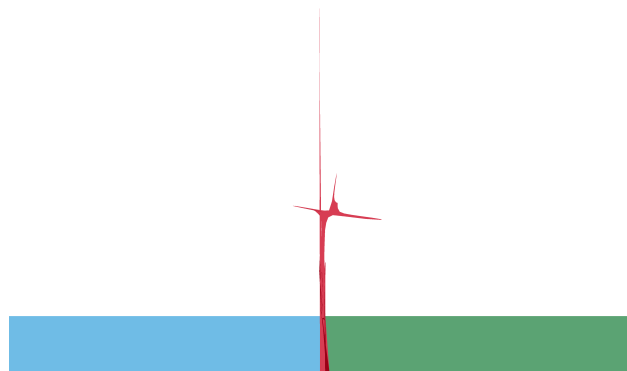


Figure 6.3: Final time state for initial unconfined SHPB model.

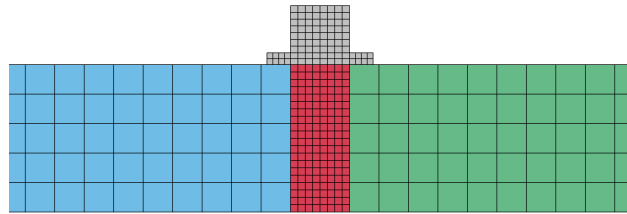


Figure 6.4: Close up of initial confined SHPB model with confining ring (grey), with element mesh visualised.

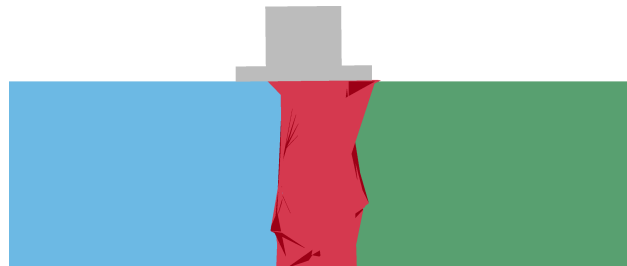


Figure 6.5: Final time state for confined SHPB model before computation fails due to negative volume error.

### 6.3 Validation of material models

While the null material model was viable in testing the functionality of the model geometry, it is not indicative of the material properties attributed to kaolin clay. Hence in order to develop a model that best represents cohesive soil behaviour, investigation into the possible material models in LS-DYNA has been conducted and applied based on known parameters of kaolin clay. This was then evaluated against physical test data to evaluate the feasibility of each material model.

The primary concern with kaolin clay is the inability to obtain a fully accurate equation of state due to the strain rate dependence of the material. This limitation hinders the capability to apply the majority of soil-based material cards. While the material models typically used to simulate soil behaviour have also been investigated and their viability is discussed, numerical modelling of kaolin clay was focused on the application and evaluation of material models that do not require an EOS.

Various other material models typically used in literature to model fluid-like materials or soils have also been investigated to determine their viability in simulating the behaviour of kaolin clay. However, many have been neglected due to the inability to acquire certain model parameters. Table 6.2 shows some of the other material models typically used to model soils or cohesive behaviour, but have been deemed unfit to model kaolin clay under high-strain-rates.

#### 6.3.1 Elastic Plastic Hydro

The Elastic Plastic Hydro material model was implemented into the numerical model, it combines the fluid-specific behaviour from the null material model but allows for certain soil properties to be designated. Based on confined SHPB testing, the Poisson's ratio is found to approach 0.5 by comparing axial and lateral strain, indicating a stark similarity in behaviour to water. Thus the model was initially set up with the same linear polynomial EOS used for water (previously assigned to sample modelled as water) assuming it behaves in a similar manner as water. The main configurable parameters of the Elastic Plastic Hydro model were values of mass density and shear modulus. Table 6.3 shows the different variations of mass density that have been tested.

The results from all combinations of unconfined tests yielded a similar result when modelled with MAT\_ELASTIC\_PLASTIC\_HYDRO, with full sample extrusion as seen in Figure 6.6. Figure 6.7 shows the axial stress response, notably the minimal transmitter bar signal recorded. This shows that both mass density and shear modulus have a minimal significant effect on the results with this material model. Figure 6.6 shows the final state in which the sample has fully extruded. This material model appears to best represent the sample such

Table 6.2: LS-DYNA material models considered to represent cohesive soil behaviour.

<i>Material model</i>	<i>Viability</i>
Soil and Foam	Requires an EOS.
Pseudo Tensor	Requires an EOS.
Geological Cap	Requires hardening function, parameters cannot be obtained for cohesive soils.
Hysteretic Soil	Requires definition of a yield function, unsuitable for cohesive soils.
FHWA	Designed for road-based soils and requires viscoplastic parameters.
Drucker-Prager	Similar parameters to Mohr Coulomb but does not account for tensile behaviour within cohesive soils.
Cohesive Mixed Mode	Cohesive model but not optimised for cohesive soils, especially under high-strain-rates.
Cohesive Elastic/TH/General	Not optimised for cohesive soil behaviour.
Arup Adhesive	Models cohesion but designed for adhesive bonding between aluminium structures.
Null	Designed for simple modelling of fluids, no intrinsic cohesion properties but suitable as point of reference.

Table 6.3: Variations of mass density and shear modulus that have been tested using the MAT\_ELASTIC\_PLASTIC\_HYDRO material card

<i>Confinement</i>	<i>Mass density, kg/m<sup>3</sup></i>	<i>Shear modulus, Pa</i>	<i>Pass/fail</i>
Unconfined	1000	0	Pass
Unconfined	1000	4.00E+09	Pass
Unconfined	2500	4.00E+09	Pass
Confined	1000	0	Fail
Confined	1000	4.00E+09	Fail
Unconfined	1000	1.00E+10	Pass
Unconfined	1000	5.00E+10	Pass
Unconfined	1000	7.50E+10	Pass
Unconfined	3000	7.50E+10	Pass
Unconfined	5000	7.50E+10	Pass

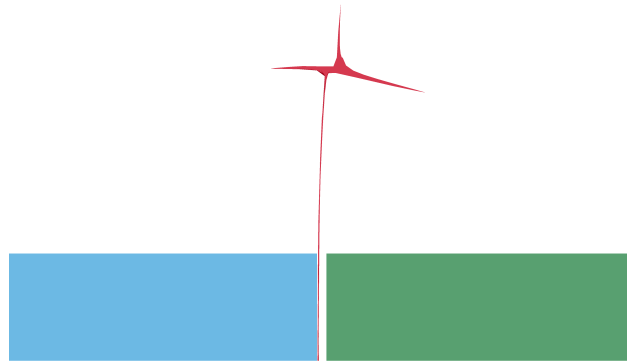


Figure 6.6: Final time state for initial unconfined SHPB model with sample modelled using MAT\_ELASTIC\_PLASTIC\_HYDRO.

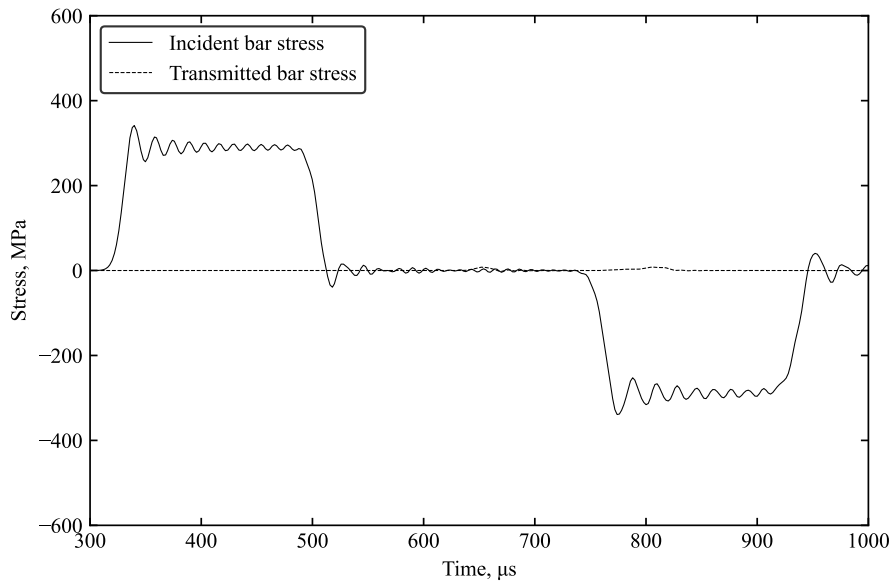


Figure 6.7: Axial stress recorded with unconfined SHPB LS-DYNA model obtained at strain gauge locations, with sample modelled using MAT\_ELASTIC\_PLASTIC\_HYDRO.

that when subject to SHPB loading, it behaves similar to a fluid. This is expected as this material model is typically used to model fluid-like materials, so even when soil parameters were altered, the water-based equation of state dictates the behaviour of elements with this material model.

Table 6.4: Material parameters used for MAT\_MOHR\_COULOMB, units are based on unit conversion system for current model.

<i>Model parameters</i>	
Mass density, kg/m <sup>3</sup>	1730
Elastic shear modulus, Pa	1.264e+7
Poisson's ratio	0.44
Angle of friction, rad	0.08075
Cohesion value, Pa	55759

### 6.3.2 Mohr-Coulomb

The Mohr-Coulomb material model was applied to the sample. This material model is traditionally used to model simple soil behaviour, and does not require an EOS. The parameters that were used in this model is shown in Table 6.4, the rest were set to 0. These parameters are the properties obtained during material characterisation of 600kPa consolidated kaolin clay samples. The mass density of the sample is dependent on the moisture content of the sample and is a variable that was subject to investigation. Since it is impossible to assign a Poisson's ratio value greater than 0.49 without compromising the computation, the Poisson's ratio was initially set to a relatively close value of 0.44 to maintain functionality and accuracy. The remaining parameters were determined from quasi-static testing, based on experimental data obtained from conducting triaxial compression tests on samples of kaolin clay (as discussed in Chapter 3).

The results from this material model for unconfined test was the best representation of physical testing since the numerical behaviour resembled SHPB tests on kaolin. The model eventually reached a point of failure, but not before sufficient data could be recorded to reflect the behaviour of an unconfined SHPB experiment on kaolin as shown in Figures 6.8 and 6.9 showing the graphs and final time states respectively.

However, the key indicator is the resultant back stress from the application of this material model. Figure 6.10 shows the transmitted pulse recorded with the MAT\_MOHR\_COULOMB material model. The magnitude of the back stress pulse shows a similar magnitude to the back stresses obtained from experimental testing. While the maintenance of back stress after the initial stress peak was not visualised, a secondary pulse was observed that may be an indication of similar behaviour occurring.

Even though the above model was acceptable for unconfined tests, the same "negative volume" error occurs when the model was applied to confined tests where the model crashes before any data is able to be collected as shown in Figure 6.11. Evidently, there was potentially axial stress data observed on the transmitter signal as there were signs of a rising pulse at approximately 700  $\mu$ s, but the model computation fails before sufficient data was observed.

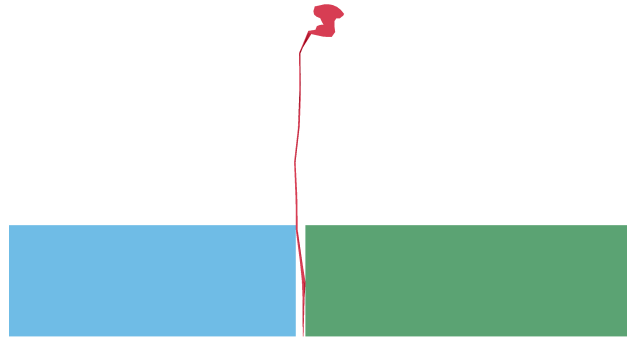


Figure 6.8: Final time state for initial unconfined SHPB model with sample modelled using MAT\_MOHR\_COULOMB.

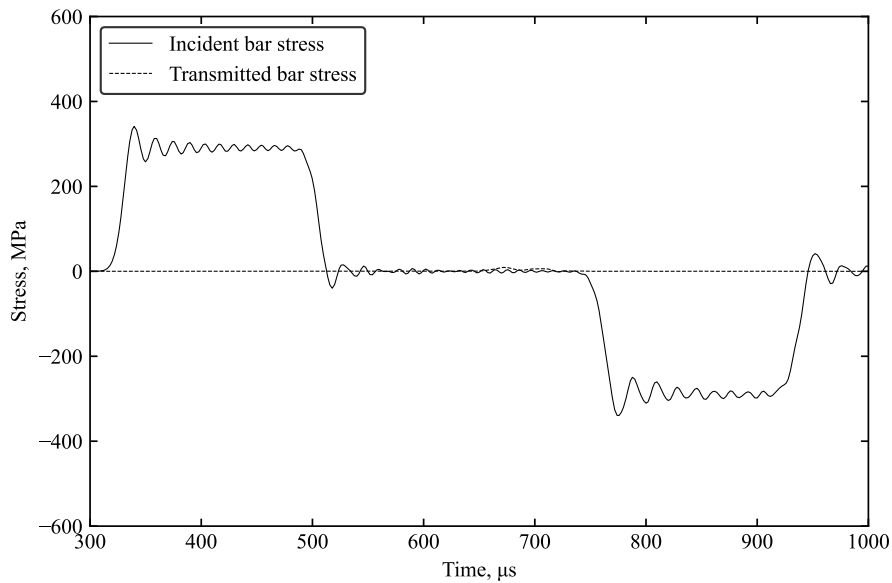


Figure 6.9: Axial stress recorded with unconfined SHPB LS-DYNA model obtained at strain gauge locations, with sample modelled using MAT\_MOHR\_COULOMB.

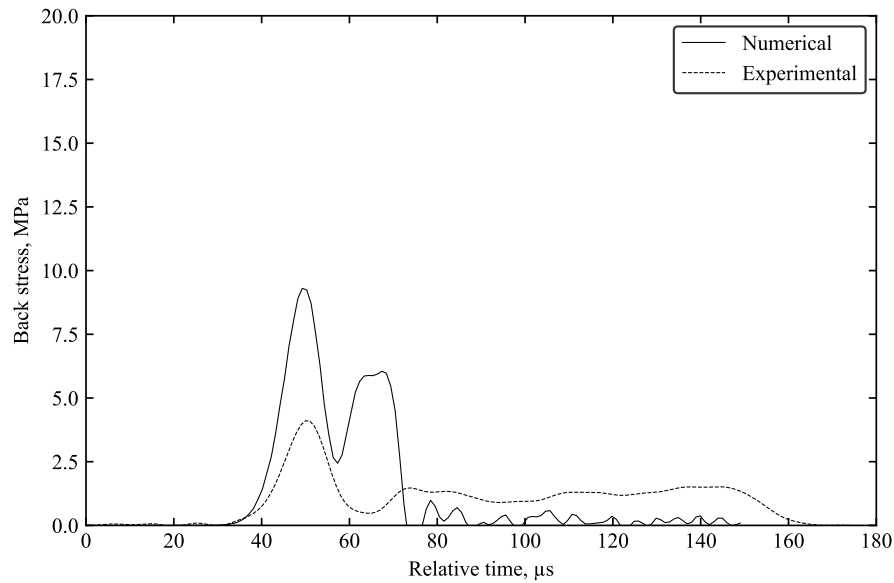


Figure 6.10: Comparison between back stress from experimental and numerical model for unconfined SHPB test on saturated kaolin clay, with sample modelled using MAT\_MOHR\_COULOMB.

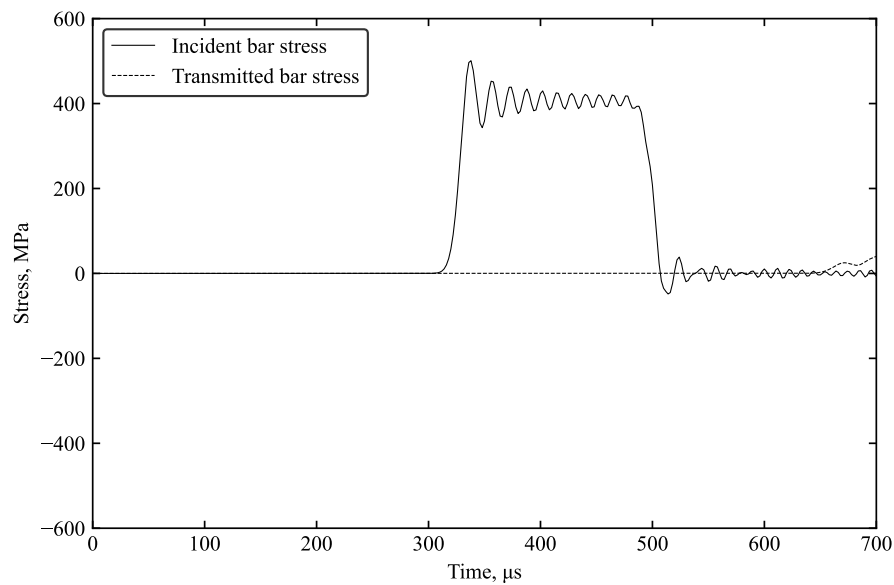


Figure 6.11: Axial stress recorded with confined SHPB LS-DYNA model obtained at strain gauge locations prior to failure due to negative volume error, with sample modelled using MAT\_MOHR\_COULOMB.





Figure 6.12: Close up of confined SHPB model with boundary constraint on nodes at edge of sample.

## 6.4 Optimisation of model geometry

While the initial unconfined numerical model has been shown to be functional, data could not be obtained from the confined model due to the immense mesh distortion associated with the fluid-like behaviour of kaolin clay. This created a negative volume error and the model computation automatically terminates before any data could be obtained. Hence the development of model geometry was primarily focused on bypassing this error and subsequently obtaining a valid numerical model for confined SHPB tests on kaolin clay. Since the Mohr-Coulomb material model has been chosen to be most appropriate to model kaolin clay given the available material properties, it was the material model applied to subsequent numerical models.

### 6.4.1 Constrained nodes

The first attempt to replicate a steel confining ring was the development of a boundary constraint along the nodes on the edge of the sample to prevent lateral displacement as seen in Figure 6.12. All of the nodes on the edge of the sample were set as a boundary node set, the implementation of a boundary constraint requires the designation of the degrees of freedom to restrict. The aim is to prevent lateral displacement yet still allow translational movement of the sample along the y-axis. Thus the degrees of freedom associated with translational movement along the x-axis, and all three rotational axes were restricted.

However, the negative volume error still persisted even with the boundary constraint assigned. While the boundary on the edge of the sample may prevent immediate lateral extrusion, the pressure bars still naturally experience deformation when stress passes through.

Hence the sample is still unable to be fully constricted and the negative volume error occurs at the instance that the sample extrudes through any gaps caused by deformation of the pressure bars.

### 6.4.2 Transition to 3-D model

While an asymmetric 2-D model has the benefit of significantly reduced computation time, the model is designed for simplicity, hence certain numerical techniques cannot be applied to 2-D models. Thus the development of a 3-D model was necessary to proceed with the evaluation of suitable numerical techniques, especially in overcoming the persisting negative volume error.

The dimensions of the 3-D model were similarly based on the experimental SHPB apparatus. All of the striker, incident, transmitted bars and the sample were modelled as 3-D Lagrangian solids, rather than the initial 2-D shell elements. To create a cylindrical mesh, the LS-DYNA Block Mesher was used to generate butterfly blocks with the appropriate dimensions and mesh size. The input parameters expressed in Table 6.5 was applied to create the mesh used in the 3-D numerical model, with the length of the cylinder and elements in axial direction based on the individual lengths of each of the respective model parts. By ensuring the same element mesh size radially on all cylindrical elements like in Figure 6.13, the risk of improper transfer of axial stress along each of the elements is minimised.

Finally contact interactions were specifically set for each interfaces. A node set is assigned to each of the following surface interfaces: striker-incident bar, incident bar-sample, and sample-transmitted bar. The CONTACT\_SURFACE\_TO\_SURFACE algorithm was applied to assign contact interaction between each of the node sets at the corresponding surface interfaces. While CONTACT\_AUTOMATIC\_SURFACE\_TO\_SURFACE would theoretically achieve the same result, manual surface interface definition significantly reduces computational time. The full contact card used to define contact interaction between Lagrangian surfaces is included in Appendix E.

The unconfined 3-D numerical model was developed in order to enhance model functionality. The state after normal termination is shown in Figure 6.14 along with the stress history in Figure 6.15, both are reflective of physical behaviour from experimental testing. Evidently, Figures 6.9 and 6.15 appear considerably similar, indicating little change between the two models, this is unsurprising as the 2-D numerical model has been evaluated to be a sufficient model under conditions where immense mesh distortion occur. However, the 3-D model prompts the application of 3-D numerical techniques with LS-DYNA that facilitate the modelling of confined SHPB conditions.

To generate the confining ring, the same Block Mesher was employed to generate a tubal butterfly block mesh with the parameters in Table 6.6, the 3-D model with the confining ring is visualised in Figure 6.16. Since no restriction was included to prevent deformation of the

Table 6.5: Input parameters to create cylindrical mesh

<i>Block Mesher input parameters</i>	
Density of cylinder perimeter	10
Radius of cylinder	0.0125
Number of elements in radial direction	8

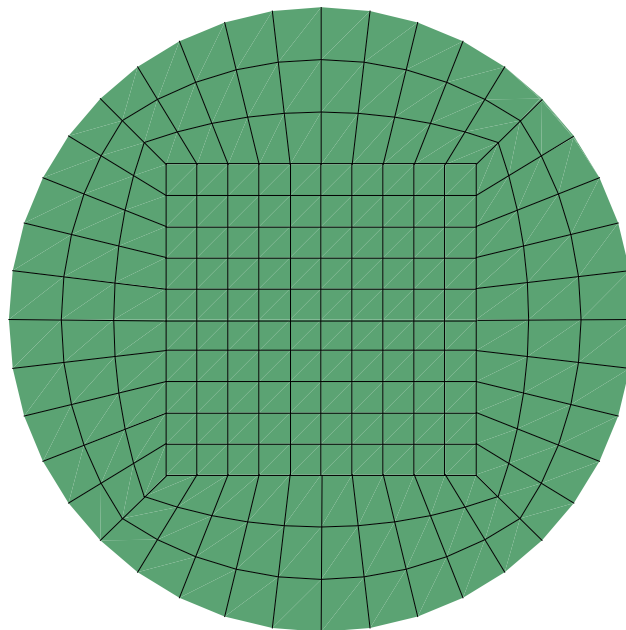


Figure 6.13: Top view of radial meshing of cylindrical elements in 3D SHPB model for: incident, transmitter, striker bars, and sample.

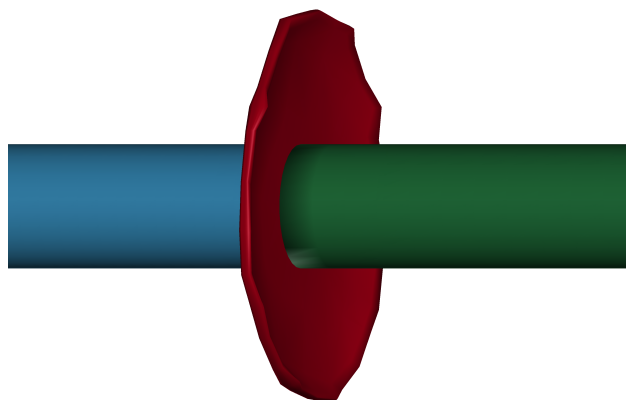


Figure 6.14: Final time state for 3-D unconfined SHPB model.

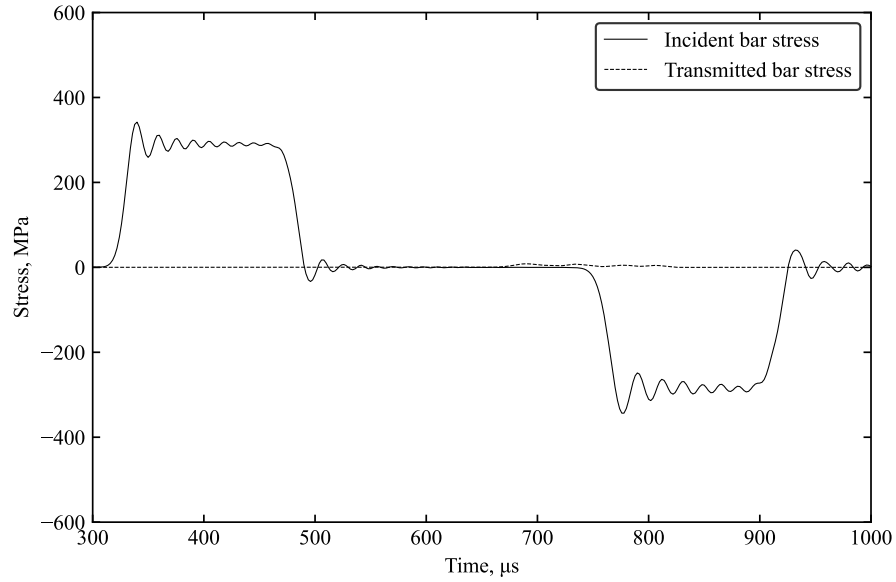


Figure 6.15: Axial stress recorded with 3-D unconfined SHPB LS-DYNA model obtained at strain gauge location.

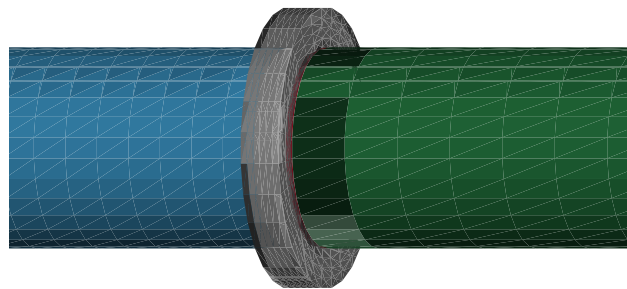


Figure 6.16: Initial 3-D confined SHPB model with confining ring.

Table 6.6: Input parameters to create tubal ring mesh

<i>Block Mesher input parameters</i>	
Density of cylinder perimeter	10
Outer radius of cylinder	0.0175
Inner radius of cylinder	0.0125
Number of elements in radial direction	3

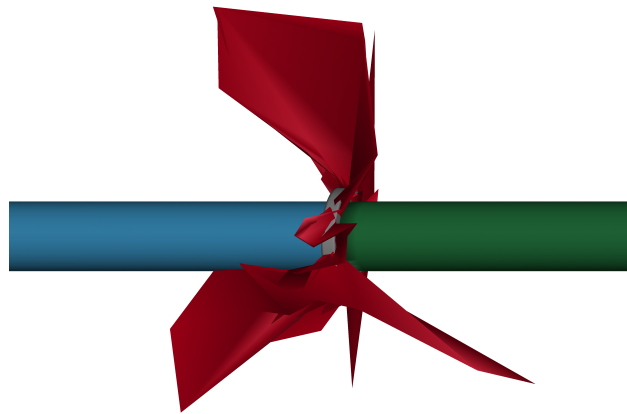


Figure 6.17: Final time state for 3-D confined SHPB model before computation fails due to negative volume error.

sample upon extrusion, the negative volume error still persisted. The drastic mesh distortion is illustrated in Figure 6.17, where tiny gaps that develop causes the pressure built up within the sample to immediately expand.

### Sensitivity analysis for mesh size

Optimisation for numerical model mesh size was performed in the process of generating the 3-D numerical model. The primary factors being monitored were the maximum stress at a designated stress location, and the computation time. Table 6.7 shows variations of density and radial elements inputs for the Block Mesher to generate cylindrical sections with various mesh sizes, where density refers to the quantity of central cubic elements within the cylindrical section and radial element refers to the quantity of elements from the radial edge to the centre of the section.

It became evident that increasing the mesh size increased appeared to cause convergence of stresses to an approximate value of 373.4 MPa. Hence the mesh size used in further numerical models was set to the values from Table 6.5, to balance accuracy without compromising

Table 6.7: Cylindrical Block Mesher input variations used for mesh optimisation

<i>Density</i>	<i>Elements</i>	Recorded stress, MPa	<i>Computation time, min</i>
10	6	374.0	4
10	8	374.4	6
10	10	374.4	12
10	12	374.5	22
6	8	374.3	9
8	8	374.4	8
12	8	374.4	9
14	8	374.4	10

significant computation time. Computation time are based on user-specific computer specifications so may vary for different users.

### 6.4.3 ALE air domain

The initial reasoning behind the transition towards a 3-D model was not only to improve accuracy from the simplistic 2-D asymmetric model, but also to allow for numerical modelling techniques to be applied in attempt to override the negative volume error. By generating an ALE air domain surrounding the sample and bars, the aim was to create a containment system that limited extrusion of the sample, restricting sample extrusion towards the confines of the air domain. The issue was that ALE modelling is not fully compatible with 2-D asymmetric shell elements, hence the transition to 3-D allows for ALE mesh to be properly developed.

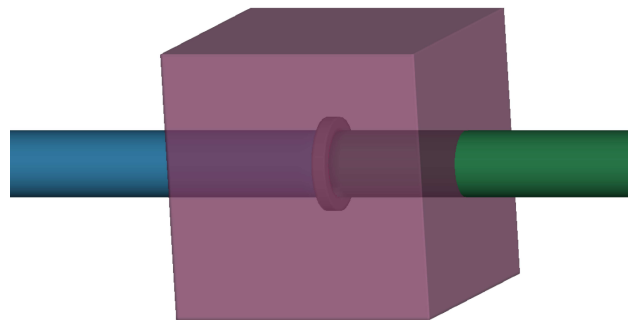


Figure 6.18: 3-D confined SHPB model with surrounding ALE air domain.

A 100 mm cubic box was generated with a mesh size of 2mm and modelled as an ALE

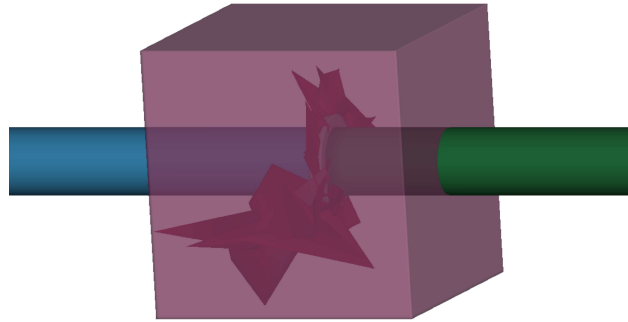


Figure 6.19: Final time state for 3D model of confined SHPB test with ALE air domain before computation fails due to negative volume error.

solid with the MAT\_NULL material model. As discussed, this material model is a simplistic algorithm to simulate fluids, the mass density in the material model was set to  $1.225 \text{ kgm}^{-3}$  to reflect atmospheric air. The full material card and EOS is found in Appendix E. The generated ALE air domain can be visualised in Figure 6.18.

This method contained the extrusion of the sample within the confines of the ALE domain, however the error is still triggered by the rapid change in mesh shape as shown in Figure 6.19. Hence even whilst the extruded mesh remains within the ALE domain, the sudden shape change still causes the model to terminate before useful data could be obtained.

#### 6.4.4 Merging interfaces

Since the “negative volume” was caused by the sudden mesh distortion during extrusion, certain combinations of the duplicate nodes at particular interfaces were merged to restrict volume loss. This would theoretically prevent any extrusion as it would create a scenario where the ring and pressure bars are permanently connected by their interface.

As shown in Table 6.8, most combinations still led to “negative volume” being generated as a result of the sudden extrusion of the sample. The final two combinations (combination no. 4 and 5) resulted in some transmitter signal being recorded. When all interfaces were fully merged, the model was able to run and there was no visible extrusion as seen in Figure 6.20. Furthermore, the transmitter signal was able to be obtained as shown in Figure 6.21.

To evaluate this model approach, the stress was compared at two points – at the ring and on the transmitter bar. It can be seen in Figure 6.22 that the stress on the ring follows the same trends as the stresses directly adjacent to the sample interface on the transmitter bar. This indicates that the stiffness of the ring was being recorded rather than the sample itself, as

Table 6.8: Combinations of node interfaces with duplicate nodes merged.

<i>No.</i>	<i>Duplicate nodes at merged at interface</i>	<i>Effect</i>	<i>Pass/fail</i>
1	Sample-Transmitter	Extrusion	Fail
2	Sample-Incident	Extrusion	Fail
3	Sample-Ring	Extrusion	Fail
4	Sample-Incident and Sample-Transmitter	Extrusion	Fail
5	Sample-Incident, Sample-Transmitter, Sample-Ring	No Extrusion	Pass

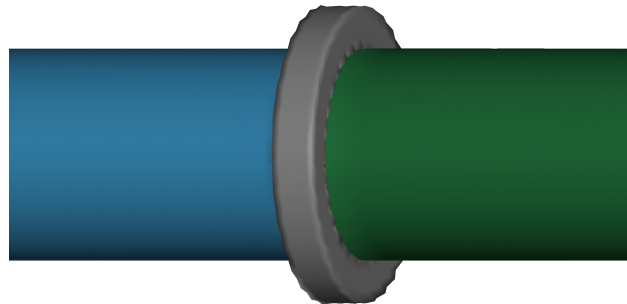


Figure 6.20: Final time state for 3D model of confined SHPB test with all sample interfaces merged before computation fails due to negative volume error.

the stress wave is propagating through the ring material instead, thus rendering this method invalid.

#### 6.4.5 Boundary constraint over 3-D sample

The use of a boundary constraint to prevent lateral displacement is revisited to reevaluate this approach with regards to the updated 3-D model. The nodes surrounding the sample were constrained on five of the six degrees of freedom, only the translational y-axis was left unrestricted to allow axial movement of the sample. The model with boundary constraints is shown in Figure 6.23. While the negative volume error persisted, it can be seen in Figure 6.24 that cause of the negative volume is from deformation of the pressure bars. As the pressure bar deforms under stress, it creates gaps that allow the sample to extrude outside of the boundary surface. As such, the fluid-like nature of kaolin clay may not be solvable by traditional Lagrangian solid meshes.



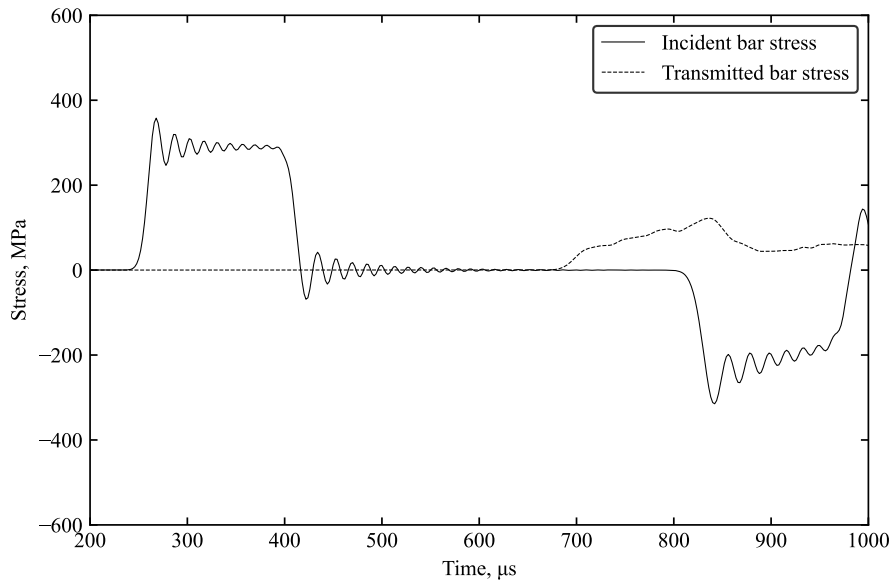


Figure 6.21: Axial stress recorded with confined SHPB LS-DYNA model with all sample interfaces merged, obtained at strain gauge locations prior to failure due to negative volume error.

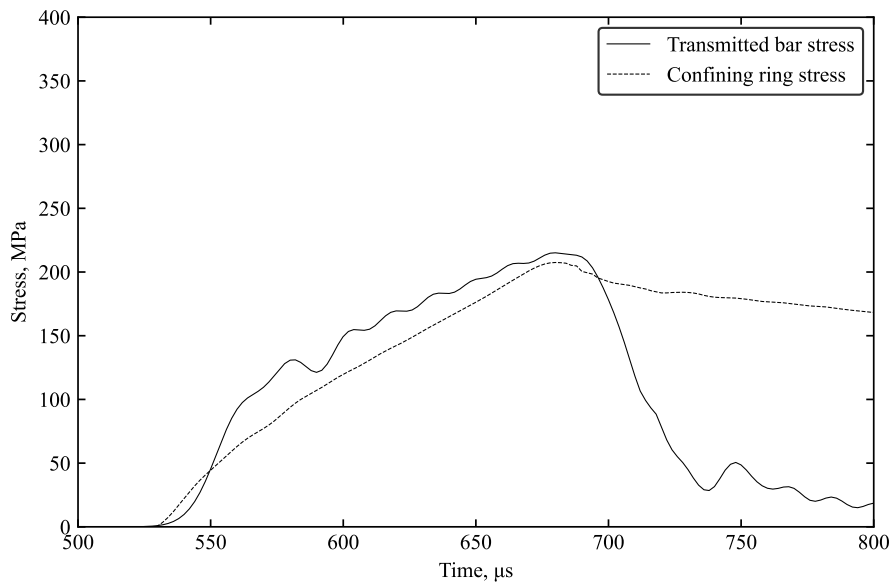


Figure 6.22: Axial stress recorded with confined SHPB LS-DYNA model with all sample interfaces merged, obtained on the ring and on the bar directly adjacent to sample interface.

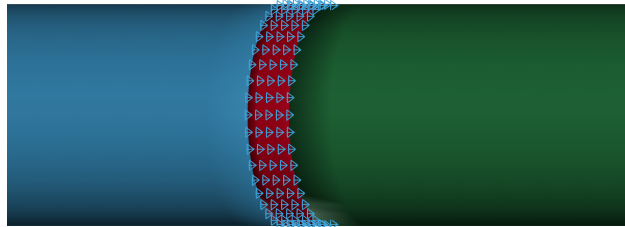


Figure 6.23: 3-D confined SHPB model with confining ring, with boundary constraint on nodes at edge of sample.

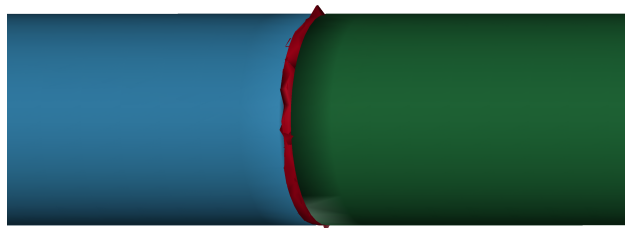


Figure 6.24: Final time state for 3D model of confined SHPB test with all sample interfaces merged before computation fails due to negative volume error.

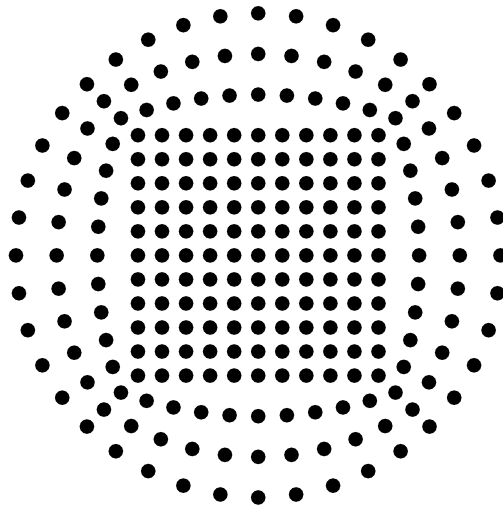


Figure 6.25: Top view of SPH node generation of sample.

## 6.5 Smoothed Particle Hydrodynamics (SPH)

SPH modelling is an innovative meshless Lagrangian numerical technique typically used to model materials that behave similar to fluid flows and continuum media, and is based on interpolating individual particles rather than the usual mesh-based approach employed in traditional Lagrangian solids. While the use of SPH modelling in SHPB testing is extremely limited, the dynamic loading associated with SHPB testing and the dynamic behaviour of cohesive soils such as kaolin clay make the use of SPH modelling a valuable tool.

By nature, SPH does not consist of a solid mesh, making it ideal for problems that involve extreme levels of deformation since connectivity between particles is generated during computation and varies based on development of the model. Considering the tendencies for kaolin clay to induce lateral deformation resulting in major volumetric loss, the application of the SPH method would be the most logical solution to the present negative volume error.

An SPH model was generated by transforming the existing solid mesh for the sample, maintaining the same sample volume and material properties. The result was the sample being represented by 1205 SPH nodes as shown in Figures 6.25 and 6.26. Since contacts are no longer between the surfaces of solid meshes, contact interactions need to be redefined for SPH nodes interaction. For this model, the `CONTACT_AUTOMATIC_NODE_TO_SURFACE` contact algorithm was selected to represent the contacts between SPH nodes and each of the incident and transmitter bar surfaces. The contact card implemented to define SPH and Lagrangian solid surface interactions has been included in Appendix E.

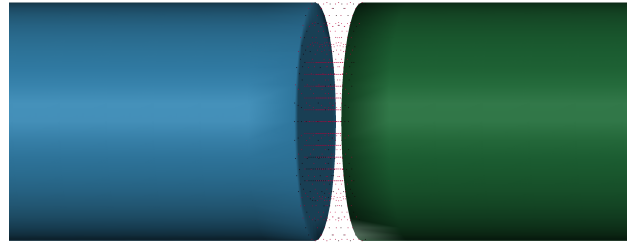


Figure 6.26: Unconfined SHPB model with sample modelled using SPH nodes.

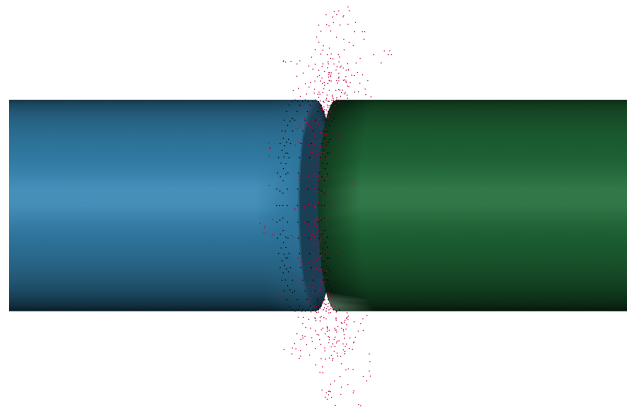


Figure 6.27: Final time state for unconfined SHPB model with sample modelled using SPH nodes.

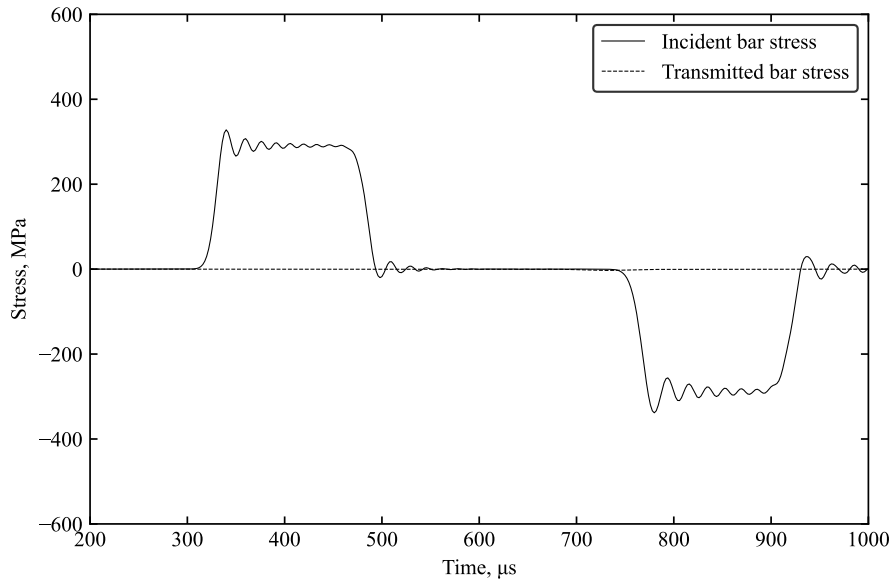


Figure 6.28: Axial stress recorded with unconfined SHPB LS-DYNA model with sample modelled using SPH nodes.

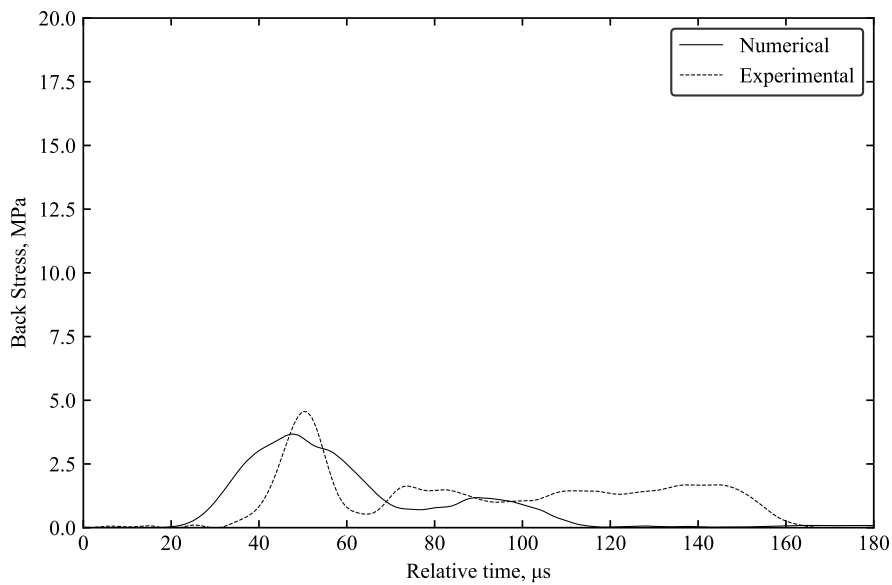


Figure 6.29: Comparison between back stress from experimental and numerical model for unconfined SHPB test on saturated kaolin clay, with sample modelled as SPH nodes.

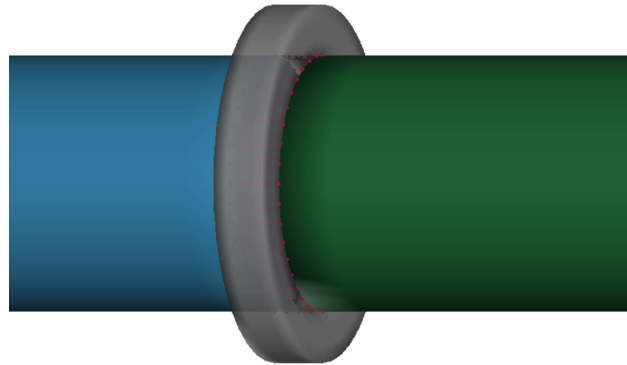


Figure 6.30: Confined SHPB model with sample modelled as SPH nodes.

While the existing numerical model already provides a reasonably accurate representation of unconfined SHPB tests, evaluation of the unconfined model to experimental results prior to optimisation of the confined model guarantees that the base model is functional for all confinement scenarios. Thus stress from the unconfined model with SPH nodes is shown in Figures 6.28. The final time state of this model (Figure 6.27) is comparable with the high-speed imagery of unconfined SHPB tests (Figure 6.33). When the back stresses between experimental and numerical tests on saturated kaolin clay was considered, the magnitudes of the pulses are extremely similar as shown in Figure 6.29, this indicates that the accuracy of the model has increased with the implementation of SPH nodes. Moreover, this also supports the notion that cohesive soils like kaolin clay that exhibit large deformations under high-strain-rate are more suited to being modelled as SPH nodes to facilitate sudden volumetric changes without compromising mesh consistency.

The addition of the confining ring involved the redefining of contacts between the confining ring and SPH nodes, once again the `CONTACT_AUTOMATIC_NODE_TO_SURFACE` contact algorithm was selected to simplify designation of contact interfaces, at the cost of computation time. The confined SHPB model with the sample modelled as SPH is shown in Figure 6.30.

The use of SPH node modelling was successful in preventing the occurrence of the negative volume error, but the restriction of lateral sample deformation created immense vibrational movement and resulted in extreme deformation of the steel confining ring as seen in Figure 6.31. This vibrational effect was also observed in experimental testing as highlighted in Chapter 4. However, since the numerical model creates a perfect seal that fully limits sample volume loss, the reflections arising from vibrations are amplified, creating higher magnitudes of noise compared to experimental results and effectively voiding reliable results. Large amounts of noise were found in the stresses on the incident and transmitted bar (Figure 6.32), but the deformation of the confining ring resulted in unrealistic proportions of radial stress developments (Figure 6.34).

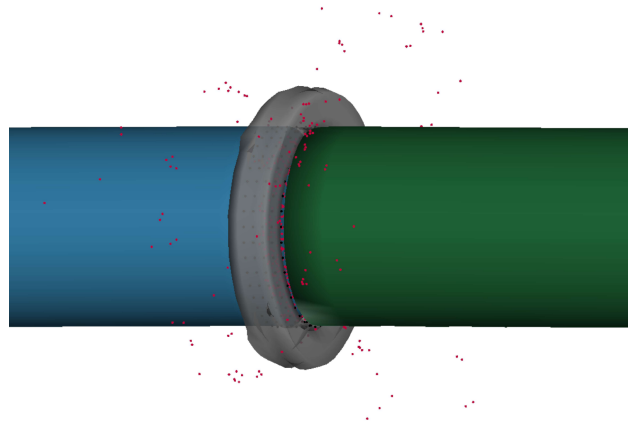


Figure 6.31: Final time state for confined SHPB model with sample modelled as SPH nodes, illustrating extreme deformation of confining ring.

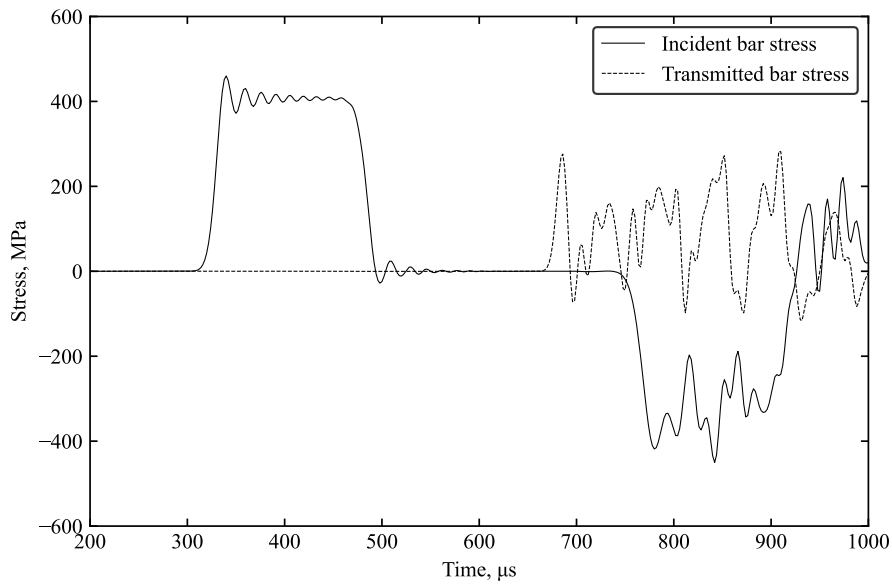


Figure 6.32: Axial stress recorded with confined SHPB LS-DYNA model with sample modelled as SPH nodes, large amounts of noise recorded.

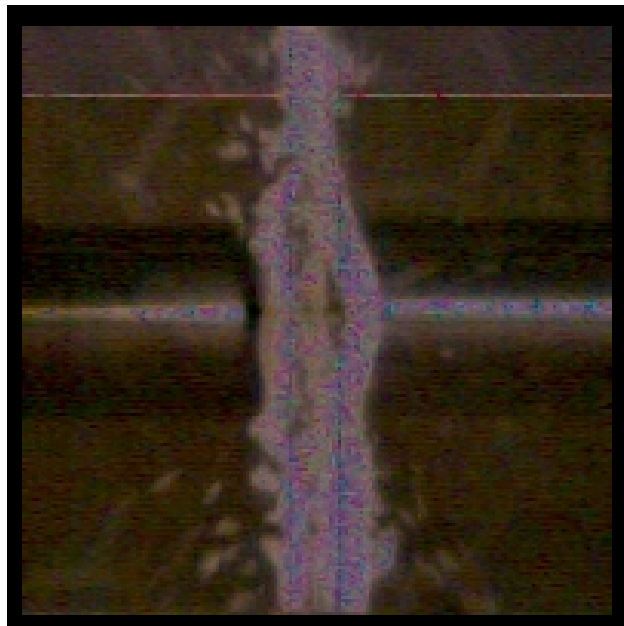


Figure 6.33: High-speed imagery of the instance after loading for unconfined SHPB test on kaolin clay.



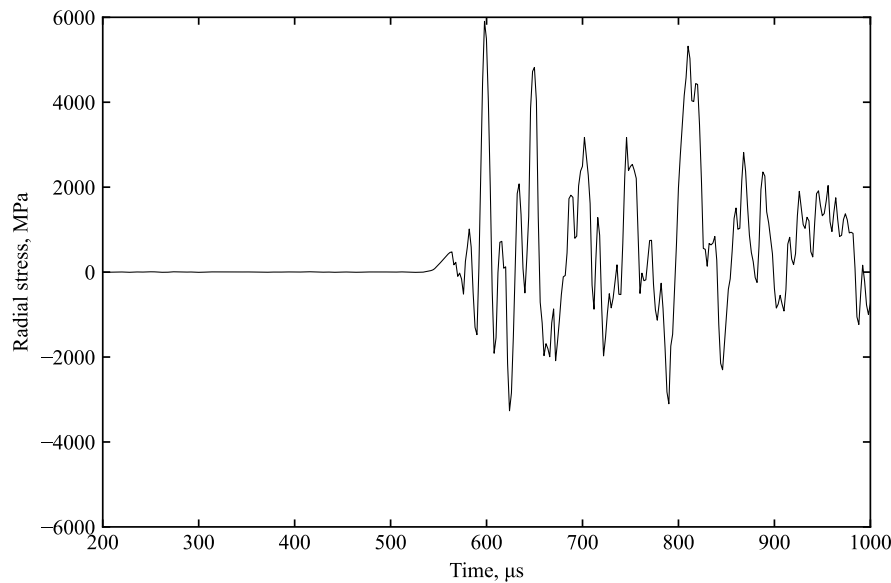


Figure 6.34: Radial stress recorded on confining ring with confined SHPB LS-DYNA model with sample modelled as SPH nodes.

### 6.5.1 Rigid confining ring

The solution to the negative volume error was the use of SPH nodes to model sample behaviour, however the extreme deformation of the confining ring still renders the results unreliable. Thus adjustments to the confining ring need to be made in order to limit deformation of the confining ring. The material model `MAT_RIGID` allows for the degrees of freedom of the material to be constrained. The material of the ring in the updated SPH model was then changed to this material model with the following constraints:  $x$  and  $z$  translational, and  $x$ ,  $y$ , and  $z$  rotational. This prevented the ring from deforming, but still allowed for the ring to translate vertically along the axis of the pressure bars.

This model successfully recorded the propagation of stress through the sample onto the transmitter with limited noise interference (Figure 6.35). The stress directly adjacent to the sample on the ring differs from the stress on the sample indicating that the ring's stiffness is not being measured. However, since the sample is restricted from experiencing lateral deformation, stress propagation through the ring material is impeded. As a result, radial stress cannot be recorded, and thus the validity of radial stress readings cannot be confirmed by this model.

This emphasises that the current confined numerical model is still a reasonable depiction of physical phenomena. Since the ring acts as a rigid boundary that fully prevents lateral displacement and extrusion of the sample, there is now significant axial stress propagation

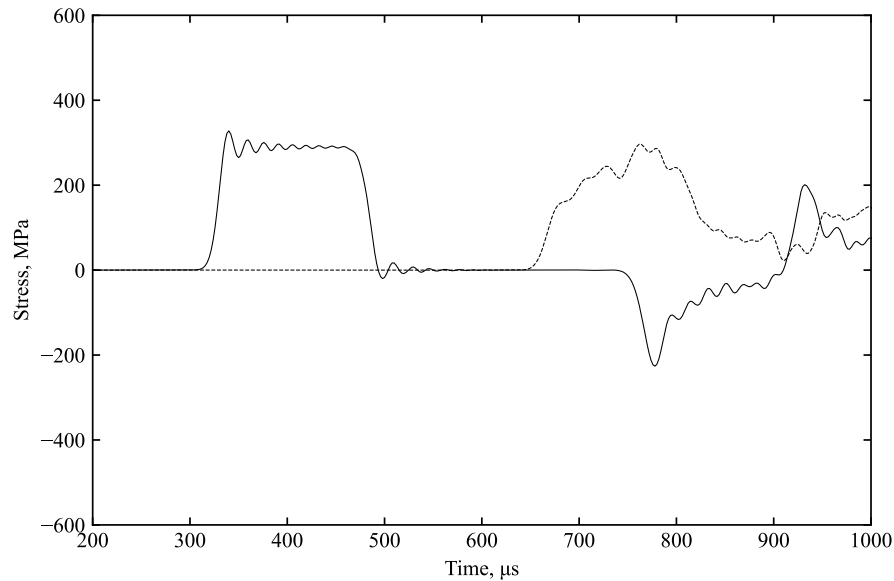


Figure 6.35: Axial stress recorded with confined SHPB LS-DYNA model (SPH) with confining ring modelled as rigid material.

through the sample even when the sample model material has been calibrated to accurately depict the tendency to primarily propagate stress in the lateral direction when subject to high-strain-rate loading. This is reflected in confined tests on kaolin clay and is the reason that experimental back stresses experience much greater magnitudes compared to unconfined conditions. As seen in Figure 6.36, there is still a disparity between the back stresses on the numerical and experimental models. However, this aligns with the limitations of the confining ring, where deformation of the ring and surrounding apparatus prompts significant lateral extrusion and volumetric loss.

### 6.5.2 Modifications to rigid confining ring

While the rigid confining ring was able to confirm existing knowledge about cohesive soil behaviour under high-strain-rate, it is still beneficial to develop a numerical model that allows for radial stress to develop on the confining ring. This ensures that a numerical model can be accurately used as a basis of comparison with experimental results in order to garner conclusive insight on high-strain-rate behaviour.

Since `MAT_RIGID` prevents any stress from forming on the material, the addition of an elastic element would, in theory, allow for the confining ring to maintain its ability to resist extreme deformation but still allow radial stresses to propagate through a singular elastic element.

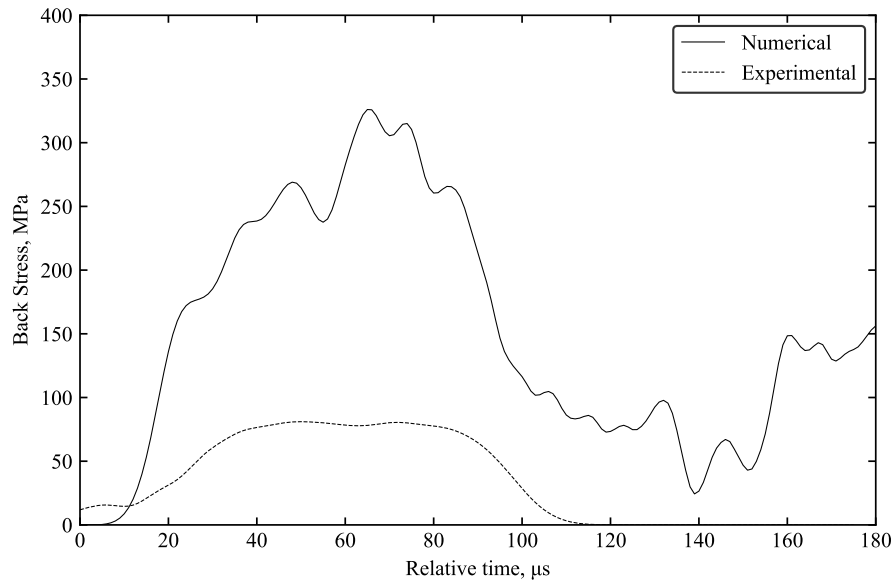


Figure 6.36: Comparison between back stress from experimental and numerical model for confined SHPB test on saturated kaolin clay, with confining ring modelled as a rigid ring in the numerical model.

By merging the elastic and rigid parts of the confining ring, the vibrational movement of the elastic elements should be reduced while still retaining the restrictive properties of the rigid ring.

The initial approach consisted of minimising the amount of elastic elements as much as possible, thus elements along the same radial axis on the confining ring (Figure 6.37) were separated and assigned the same elastic steel material properties as the original confined model. This created a potential scenario where stress could travel through the three elements on the “column” to the edge of the confining ring (the location of the strain gauge on the physical confining ring). However, the radial stresses recorded at elastic element on the edge of the confining ring remained at zero, indicating the elements are still resisting the propagation of radial stress. This is likely due to the close proximity it is with other rigid elements. Since the nodes of the elastic elements are merged in nearly all directions with the nodes of rigid elements, it is incapable for any deformation to occur since each elastic element is essentially being fixed in place on all 8 edges.

Other modifications to the confining ring have been tested to limited success in simulating an accurate radial stress pulse, a summary of the methods tested is shown in Table 6.9.

Table 6.9: Summary of modifications to confining ring tested, and relevant findings

<i>Modification</i>	<i>Radial stress</i>	<i>Findings</i>
Fully elastic ring with four rigid “columns”	Yes	Radial stresses were obtained, but the limited rigid elements failed to contain the extreme vibration and subsequent deformation, leading to unrealistic radial stresses.
Fully rigid ring with four elastic “columns”	No	Same result as with only one “column”, where rigid material restricted the elastic elements.
Fully rigid ring with 8 elastic “columns”	No	Freedom of the elastic elements still remained mostly restricted, but small levels of noise is observed radially.
All inner radius elements as elastic material	Yes	This was successful in prompting the development of some radial stress, all of the elements in the inner radius only have four of their eight nodes restricted but rigid elements
Only outer radius elements as rigid material	Yes	This yielded the highest radial stress as stress was still able to propagate radially but the outer layer minimised noise from vibrational movement.

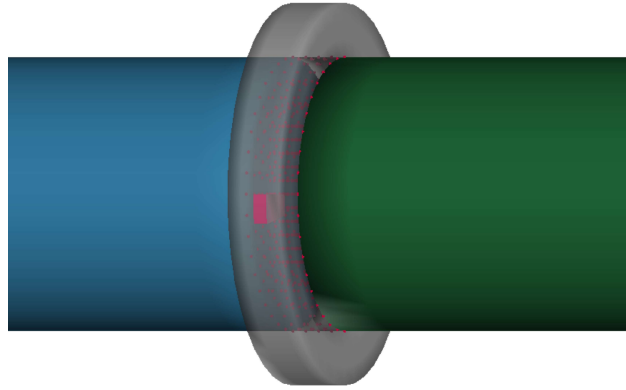


Figure 6.37: Confined SHPB model with one “column” of elements on confining ring modelled as elastic material (pink) while rest of the ring is modelled as rigid (grey).

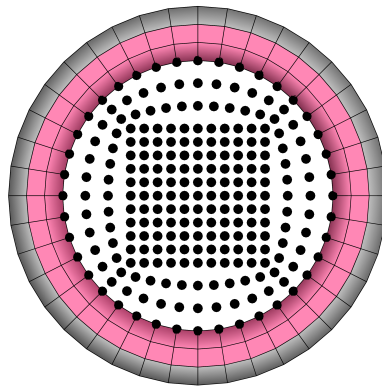


Figure 6.38: Top view of confining ring with outer radius made of rigid material (grey), and two radial elemental layers made of elastic material (pink).

This indicated that a larger volume of elastic elements is required, such that the element of which radial stresses are expected to propagate through are not directly adjacent to fully rigid elements. The final combination was most successful in providing a balance of radial stress propagation but limited vibrational noise. The mesh used in the final iteration of confining ring modification is shown in Figure 6.38, with nodes at the rigid-elastic material boundaries merged to ensure the entire ring acts like a single model part.

As seen in Figure 6.39, incident and transmitted stresses are present like when the ring was fully rigid, yet when taking radial stress readings from the elastic element directly adjacent to the sample (Figure 6.40), a considerable magnitude of radial stress was found.

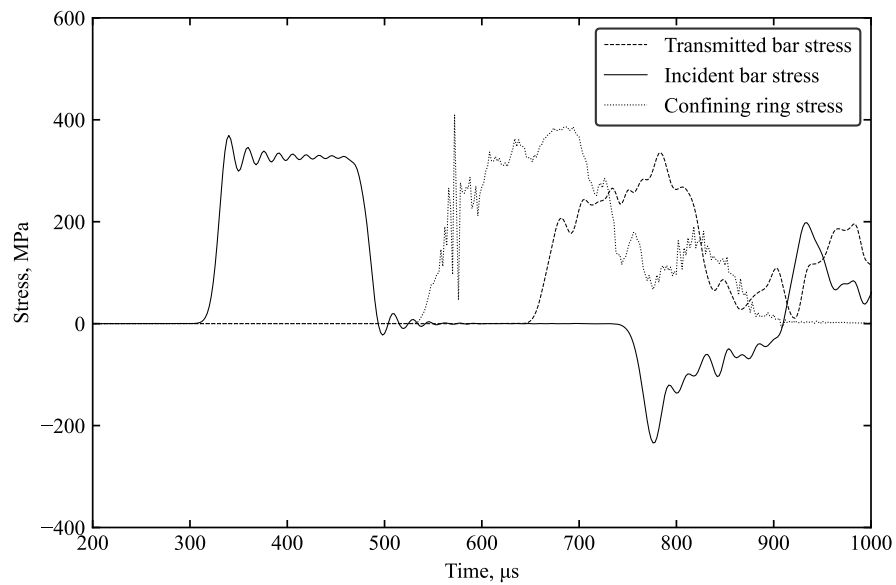


Figure 6.39: Axial stress from pressure bars and radial stress from confining ring, recorded with confined SHPB LS-DYNA model (SPH) with half rigid and half elastic confining ring.

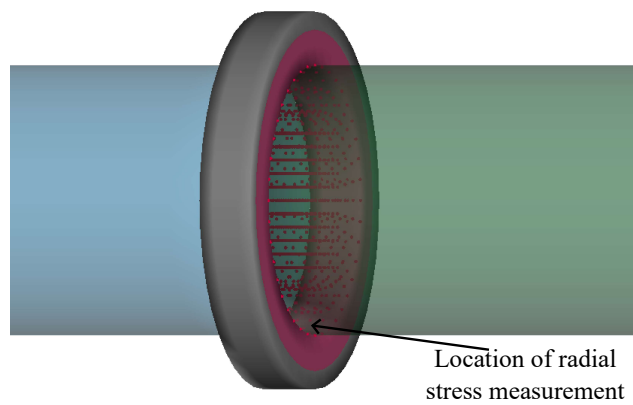


Figure 6.40: Confined SHPB model with half rigid and half elastic material.

Table 6.10: Summary of variations of striker bar speed and bulk densities with the unconfined SHPB numerical model

<i>Striker speed, m/s</i>	<i>Moisture content, %</i>	<i>Bulk density, kgm<sup>-3</sup></i>	<i>Peak front stress, MPa</i>	<i>Peak back stress, MPa</i>	<i>Poisson's ratio</i>
8	0	934	27.0	2.4	0.40-0.49
8	20	1087	27.0	2.4	0.40-0.49
8	41	1296	27.0	2.4	0.40-0.49
12	0	934	41.2	3.4	0.40-0.49
12	20	1087	41.2	3.4	0.40-0.49
12	41	1296	41.2	3.4	0.40-0.49
16	0	934	54.1	3.9	0.40-0.49
16	20	1087	54.1	3.9	0.40-0.49
16	41	1296	54.1	3.9	0.40-0.49

## 6.6 Comparison to experimental results

Comparison between experimental and numerical results have been discussed throughout the process of model development. However, the focus has been on ensuring that the numerical model was capable of reflecting physical behaviour. Both the final unconfined and numerical model are contrasted against experimental results, depicting similarities and differences to evaluate the limitations of numerical modelling in depicting physical behaviour of cohesive soils under high-strain-rate conditions.

### 6.6.1 Unconfined model

In order to optimise the material to fit moisture content conditions, attempts were made to alter the bulk density and Poisson's ratio in the Mohr-Coulomb material card. Based on the physical properties of kaolin clay at specific moisture contents, varying levels of bulk density should correspond to respective moisture contents. Thus the bulk density input is varied at 934, 1087, and 1296 which corresponds to moisture contents of 0, 20, and 41% respectively. A summary of the tests at various bulk densities at all three of the experimental striker bar speeds are shown in Table 6.10. In accordance with prior testing, the Poisson's ratio of kaolin clay is known to approach 0.5 when subject to high-strain-rate. However, as expected the model computation fails when the Poisson's ratio was defined as 0.5. Despite testing variations of Poisson's ratio from 0.40 to 0.49, attempts to change its values and assess their impact on model behaviour yielded no discernible change.

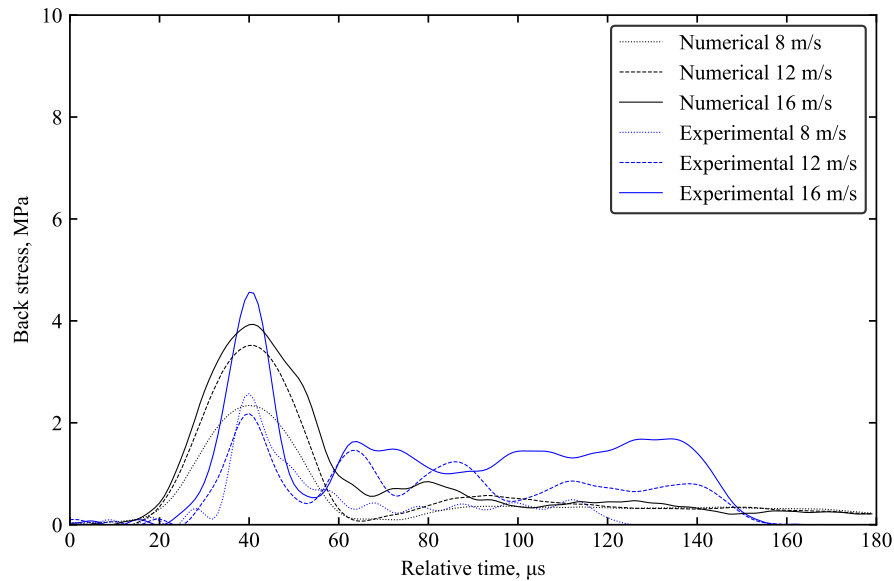


Figure 6.41: Comparison between back stress from experimental and numerical model for unconfined SHPB tests on saturated kaolin clay.

As shown in Table 6.10, changing bulk density did not invoke any change in the front or back stresses. This is a major limitation of the numerical model as this means varying levels of moisture content do not result in any change, which does not align experimental results. This can primarily be attributed to the incapability of the current material model in modelling high-strain-rate flows, the Mohr-Coulomb material model is typically a simplified approach and thus may not be ideal when modelling complex events. Moreover, further comprehensive sensitivity analysis regarding the effect of these parameters are necessary in order to facilitate changes in moisture content in the numerical model.

To accurately model a change in moisture content in the soil material, changes in stiffness and strength are also required in addition to bulk density. However, it becomes an intrinsic limitation of quasi-static testing such that the exact values for these properties cannot be experimentally determined to facilitate depiction in numerical modelling.

Increasing the striker bar speed induces greater strain rates and effectively increased both front and back stresses in the numerical model as expected. Figure 6.41 shows the direct comparison between numerical and experimental back stresses from unconfined SHPB tests on saturated kaolin clay. It was observed that the magnitude and shape of the back stress pulse are extremely similar. The deviations in period or rise time can be attributed to differences between experimental and numerical conditions such as the limitations of the material model, inability to accurately model cohesive behaviour, and the effect of inevitable errors associated with the experimental process.



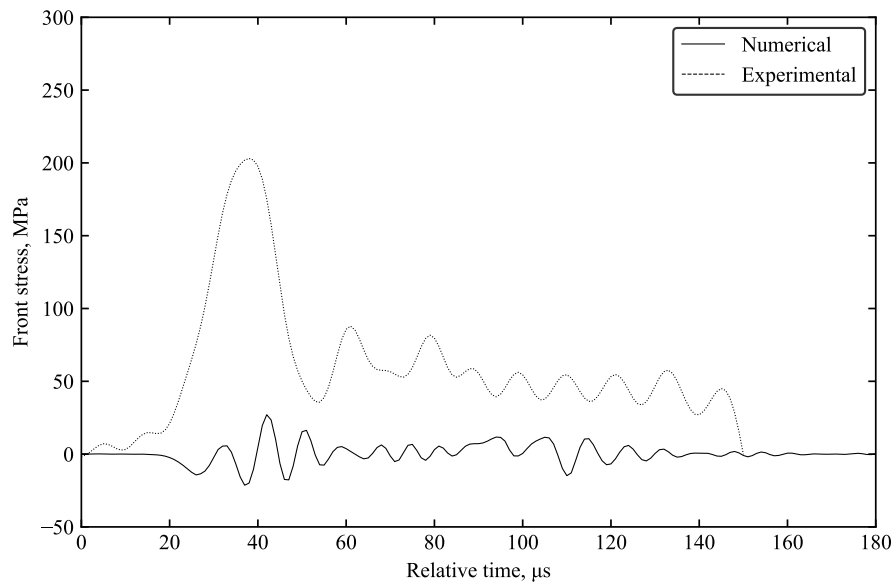


Figure 6.42: Comparison between front stress from experimental and numerical model for unconfined SHPB test on saturated kaolin clay.

At the same designated striker bar speed, the front stress (superposition of incident and reflected pulses) is shown in Figure 6.42, where it is observed that the numerical front stress remains close to zero for the entire duration of the pulse. This indicates that a significant portion of the stress is reflected back from the sample interface on the incident bar (Figure 6.43). This is the opposite in experimental tests, even though the initial peak is similar, the experimental front stress wave properly propagates through, evident from the non-zero front stress before returning to zero.

This is attributed to the lack of a cohesion mechanism within the material model used to describe the numerical sample, hence when the stress wave reaches the sample interface it prompts the immediate displacement of the SPH particles. In reality, internal cohesive properties act to adhere sample material and resist lateral deformation to some extent. This also explains the lack of any change when moisture content was altered as limited stress is actually able to transmit through. Thus while the numerical model can accurately depict qualitative behaviour, the lack of cohesive properties to bind individual particles together during high-strain-rate loading cause exact stress values to not be reliable.

## 6.6.2 Confined model

A similar analysis to unconfined tests was performed with the confined model, where similar attempts to vary moisture content via changes of bulk density were conducted (Table 6.11).

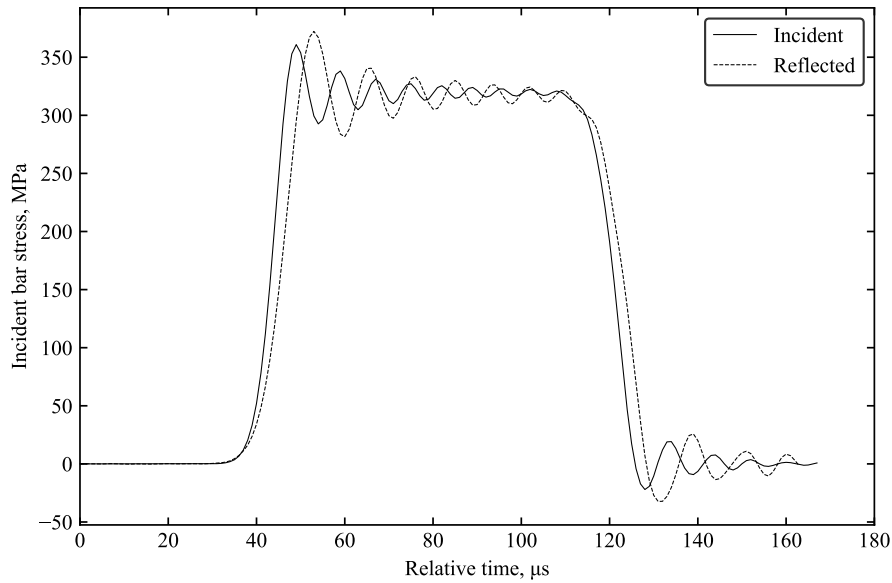


Figure 6.43: Incident and reflected stresses from unconfined SHPB numerical model.

Expectedly, the results were the same as unconfined tests, where no evident changes in results was observed when the bulk density and Poisson's ratio were altered, underscoring the inherent problem with the current material card and its ability to fully characterise high-strain-rate behaviour of cohesive soils.

While changes in moisture content were not feasible, the base model was still able to capture changes in strain rate. Since the confined model created an idealistic scenario of perfect confinement, the lateral displacement of sample volume was significantly minimised. With this the translation of stresses from lateral to axial (onto the transmitted bar) is evident, where a significant magnitude of lateral stresses are recorded on the confining ring as a product of lateral displacement and impact from the SPH nodes (Figure 6.44). But simultaneously a significant amount of back stress is recorded (Figure 6.45). The characteristic of the numerical model to prevent extrusion and volumetric loss meant that all stress from the sample is guaranteed to be propagated either laterally towards the confining ring or axially towards the transmitter bar, naturally, this results in a much larger back and radial stress reading from the numerical model compared to experimental data.

Finally, the effect of the confinement mechanism also promoted the transfer of stress into the sample in the numerical model, this is evident from a higher magnitude of front stress exhibited by the model (Figure 6.46). While the incident stress remains consistent due to the same initial striker bar speed, the value of reflected stress is significantly lower (Figure 6.47). This scenario resembles cases of stress equilibrium, where there is a clear axial stress propagation, hence traditional one-dimensional wave theory was applied to equate the superposition of incident and reflected pulses with the back stress.

Table 6.11: Summary of variations of striker bar speed and bulk densities with the confined SHPB numerical model

Striker speed, m/s	Moisture content, %	Bulk density, $\text{kgm}^{-3}$	Peak front stress, MPa	Peak back stress, MPa	Peak radial stress, MPa	Poisson's ratio
18	0	934	329.0	289.2	509.0	0.40-0.49
18	20	1087	329.0	289.2	509.0	0.40-0.49
18	41	1296	329.0	289.2	509.0	0.40-0.49
20	0	934	365.2	322.2	624.0	0.40-0.49
20	20	1087	365.2	322.2	624.0	0.40-0.49
20	41	1296	365.2	322.2	624.0	0.40-0.49
22	0	934	407.6	369.2	674.0	0.40-0.49
22	20	1087	407.6	369.2	674.0	0.40-0.49
22	41	1296	407.6	369.2	674.0	0.40-0.49

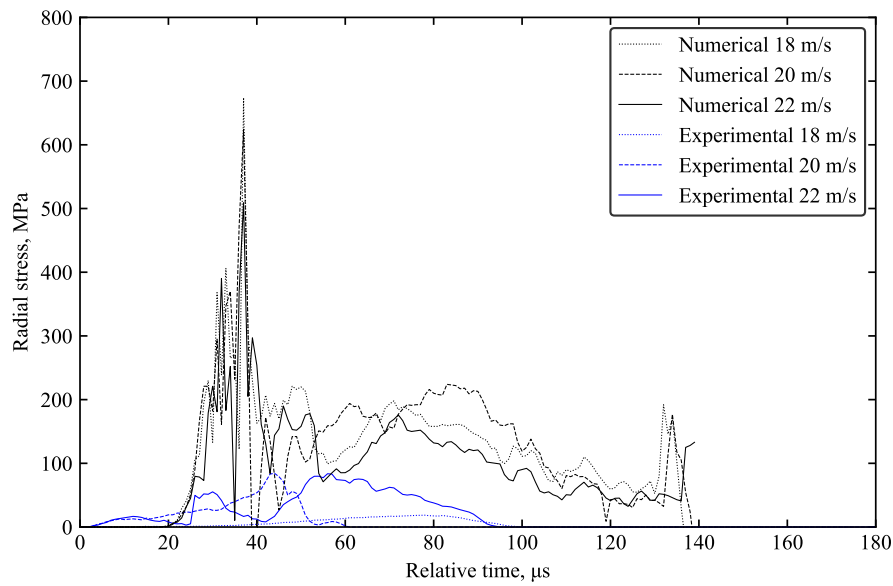


Figure 6.44: Comparison between radial stress from experimental and numerical model for confined SHPB tests on saturated kaolin clay.

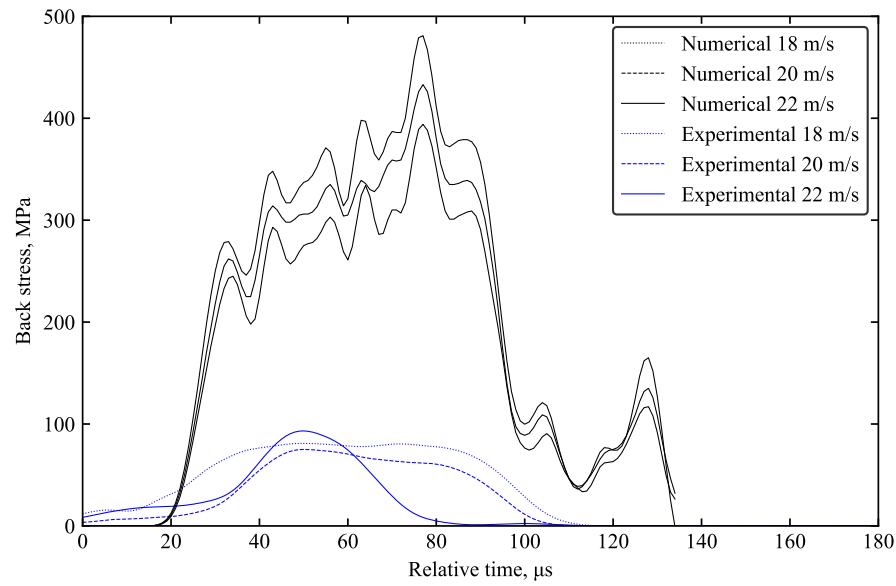


Figure 6.45: Comparison between back stress from experimental and numerical model for confined SHPB tests on saturated kaolin clay.

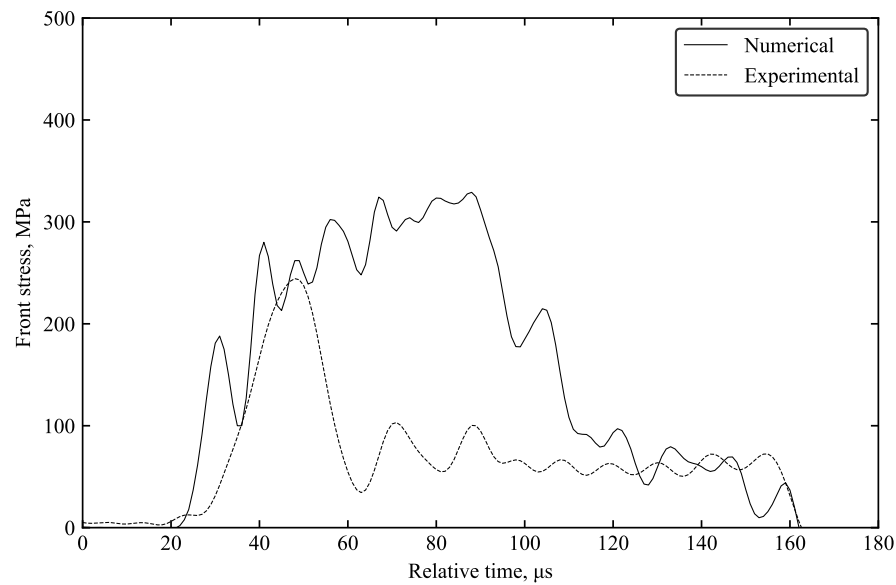


Figure 6.46: Comparison between front stress from experimental and numerical model for confined SHPB test on saturated kaolin clay.

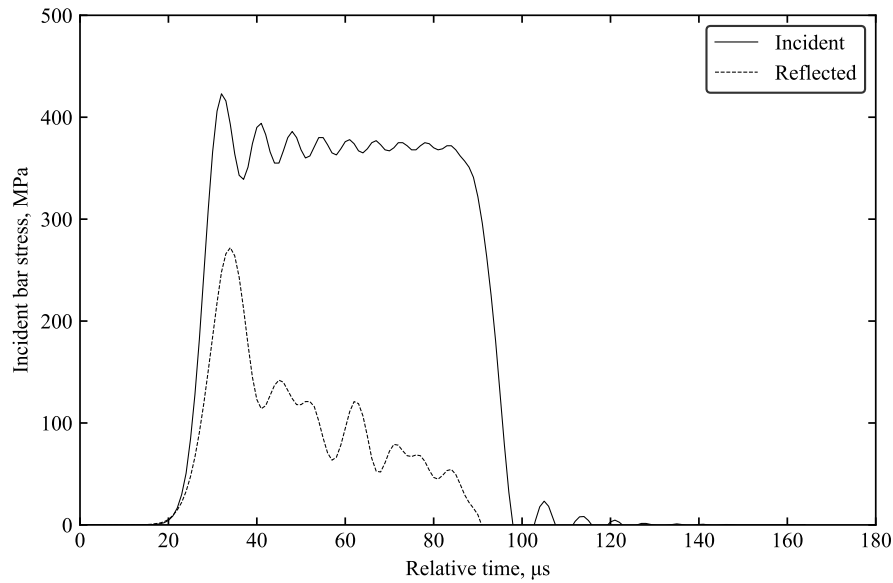


Figure 6.47: Incident and reflected stresses from confined SHPB numerical model.



Figure 6.48: LS-DYNA SHPB partial lateral confinement model set up containing the incident bar (blue), transmitted bar (green), striker bar (yellow), and water reservoir (grey). Sample and water annulus are modelled and inside the water reservoir.

## 6.7 Numerical modelling for partial lateral confined testing

The numerical modelling of the PLC arrangement was carried out using the explicit finite element code in LS-DYNA, in order to compare numerical and experimental results as seen in Figure 6.48, while radial signals can be obtained from experimental testing, they cannot be fully interpreted without the use of numerical modelling. A more detailed representation of the final sample and confinement reservoir are shown in Figure 6.49. The model is a further development of the 3-D numerical model initially developed for the unconfined SHPB setup but with the addition of the steel reservoir and water annulus sections. Refer to Appendix E for input variables used in LS-DYNA keywords discussed in this section.

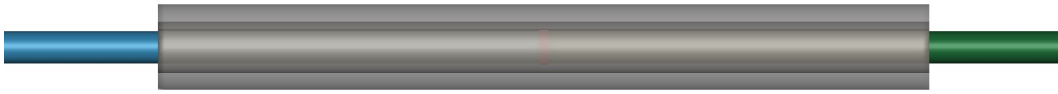


Figure 6.49: LS-DYNA cross section zoom-in on the sample inside the partial lateral confinement SHPB set up containing the incident bar (blue), transmitted bar (green), water reservoir (grey), water annulus within reservoir, and the sample (red).

### 6.7.1 Model material cards

The three pressure bars were modelled with a linear elastic material model (MAT\_ELASTIC) with a density, Young's modulus, and Poisson's ratio of  $\rho = 7850 \text{ kg m}^{-3}$ ,  $E = 168 \text{ GPa}$ ,  $\nu = 0.29$  respectively, these values are obtained based on existing knowledge about steel and properties of the pressure bars used in the experimental apparatus.

The rigid material card (MAT\_RIGID) was employed for the water reservoir, this restricts deformation of the water reservoir at any phase of the simulation. The water reservoir is made of steel, hence the density, Young's modulus, and Poisson's ratio used as input parameters remain the same as the steel pressure bars.

The null material model typically used for modelling of fluids as employed for the water annulus. Since this material model required an EOS, the linear polynomial EOS discussed in Section 6.2 is implemented, with the parameters for the EOS based on work previously done by Shin et al. (1998).

Finally, the sample is modelled based on previous validation of suitable material models as discussed in Section 6.3. Due to the inability to characterise certain parameters required for other material models, the Mohr-Coloumb material model has been designated to represent kaolin clay within the sample.

### 6.7.2 Model setup

Similar to the 3-D model previously developed for unconfined SHPB tests, the numerical model consists of striker, incident, and transmitted bars modelled as solid Lagrangian meshes. The interfaces between the three pressure bars were manually picked and surface-to-surface contact algorithm was selected. The sample was modelled using SPH node modelling, with contact interactions between other Lagrangian model parts and the sample assigned automatically via the CONTACT\_AUTOMATIC\_NODE\_TO\_SURFACE contact algorithm.

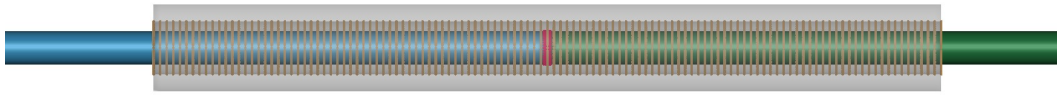


Figure 6.50: LS-DYNA cross section zoom-in on the sample inside the partial lateral confinement SHPB set up with water annulus (brown) modelled as SPH.

The water reservoir was modelled as a solid Lagrangian mesh, but a rigid material was used to represent the reservoir. This assumes that the fluid pressures generated within the reservoir were not significant enough to induce deformation of the water reservoir. This simplifies the computational process, and prevents movement of the steel reservoir during loading. The large rubber o-rings used to seal the water reservoir have also been replaced with a boundary constraint, preventing any elements within the water annulus from exiting, thus creating an idealistic seal. The same kaolin clay sample was situated in between the incident and transmitted bars, and has been modelled as SPH nodes.

While it is possible to model both the water and kaolin clay sample as SPH nodes, there are inherent limitations regarding the method SPH particles are computed that prevent accurate modelling between two different SPH “fluids”. This is demonstrated by model iterations that depict the water annulus and sample as separate SPH node parts (Figure 6.50). However, the methods used to define contact interactions between two different SPH “fluids” with varying densities often result in computational errors in delineating boundaries between the two SPH components. This is attributed to the method of which densities are modelled over quantities of SPH particles (Ihmsen et al., 2011). While methods discussed in Xu and Wang (2014) to improve contact SPH to SPH have been tested to variable degrees of accuracy, results show greater reliability when the water annulus is modelled as a solid Lagrangian mesh as deformation of the annulus during simulation remains minimal.

The final water annulus, modelled as a solid Lagrangian mesh, is shown in Figure 6.49 to facilitate efficiency during computation and the ability to change sample model in future developments of the numerical model. Automatic surface-to-surface contact interaction is specified between the water annulus part and all of the adjacent parts, including the incident bar, transmitted bar, water reservoir, and the sample.

### 6.7.3 Results of numerical model

The final state after the model reached completion is shown in Figure 6.51, the qualitative behaviour exhibited by the SPH nodes are similar to experimental results. The sample extrudes laterally and the large concentration of sample form a loop over the pressure bars, the

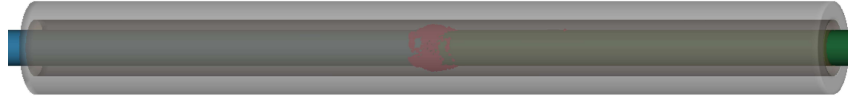


Figure 6.51: Final time state of partial lateral confined SHPB numerical model on saturated kaolin clay.



Figure 6.52: Image of kaolin clay sample forming a loop within latex membrane after partial lateral confined SHPB test.

same behaviour occurs during physical experiments, where a loop of kaolin clay is formed within the latex membrane after testing (Figure 6.52).

The inability to account for cohesion is still present in this numerical model. Figure 6.53 shows that the superposition of the incident and reflected pulses yielded a near zero front stress, indicating that both incident and reflected pulses are near equal (Figure 6.54). Similar to unconfined and confined SHPB models, while the consideration of cohesive properties can be implemented by defining cohesion values in the material model or contact interactions between SPH particles, the methods currently incorporated into LS-DYNA have not been designed for cases with extreme deformation and so still results in considerable inaccuracy.

Figure 6.55 shows the difference in back stress between experimental results and the numerical model. While qualitative behaviour shows the same results, the back stress from



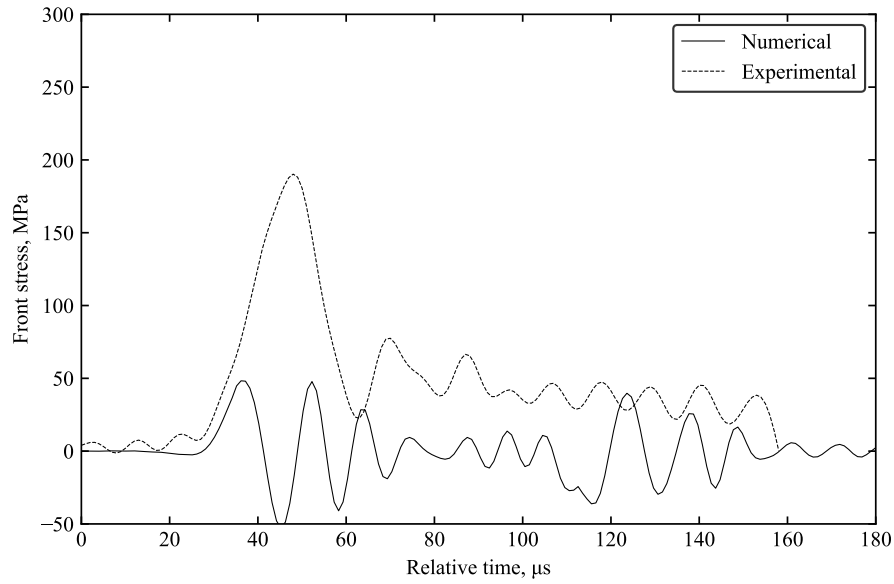


Figure 6.53: Comparison between front stress from experimental and numerical model for partial lateral confined SHPB test on saturated kaolin clay.

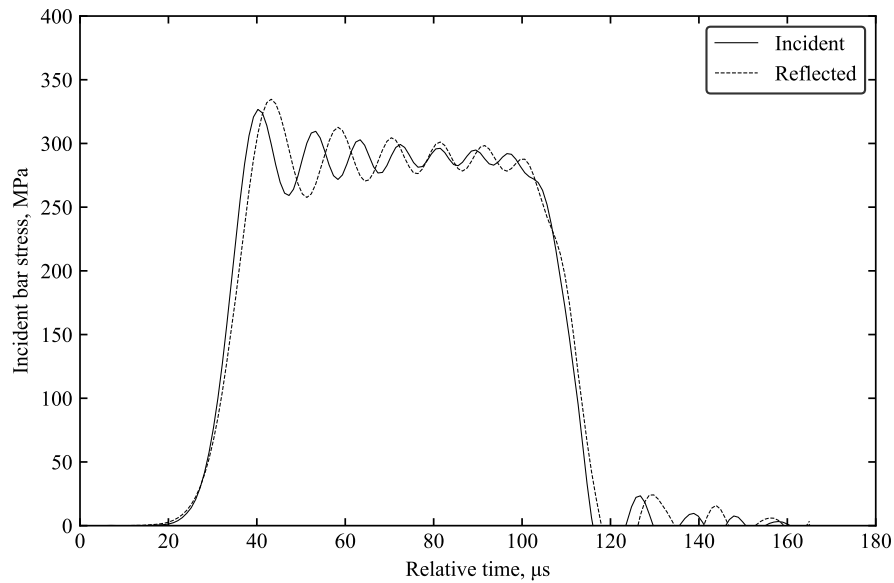


Figure 6.54: Incident and reflected stresses from partial lateral confined SHPB numerical model.

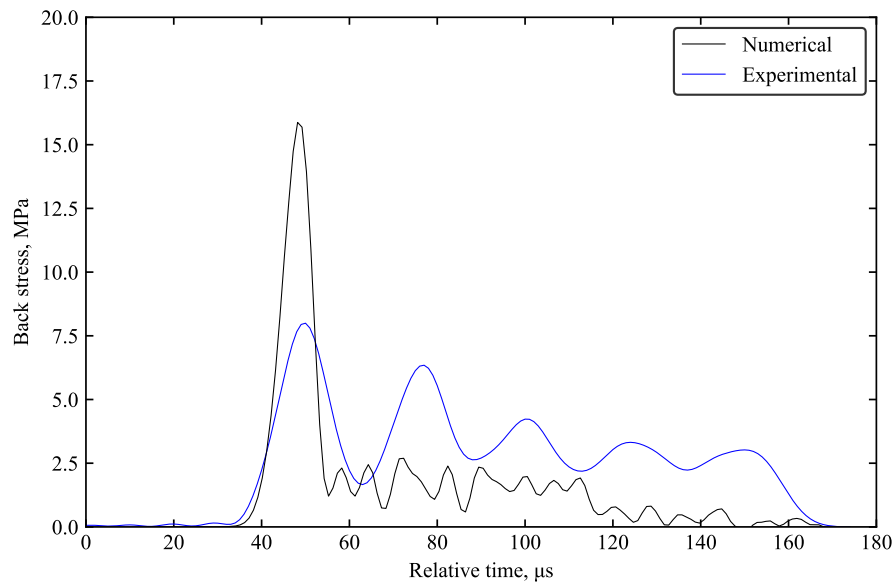


Figure 6.55: Comparison between back stress from experimental and numerical model for partial lateral confined SHPB test on saturated kaolin clay.

the numerical model is nearly twice as high as experimental results. While this can be attributed to the lack of cohesion modelling capabilities, the numerical model is not limited by the rubber o-rings to create a sealed environment within the water annulus. The ability of the boundary constraints in the numerical model to prevent the leakage of water without interfering with the movement of the pressure bars creates a perfect condition where both axial and radial stresses can develop within the reservoir. This is the idealistic environment when the apparatus was conceptualised, where the sample is initially confined by water under atmospheric pressure but axial loading causes lateral confining pressure. In actuality, multiple factors affect the development of lateral confining pressure, notably the movement of the o-rings when stress wave passes through the pressure bars created leakage and caused disruption of the internal water pressure.

Figure 6.56 shows the difference in radial stress between the numerical model and typical experimental results. Evidently, while a similar peak and pulse pattern can be inferred, the numerical model experienced significantly lower lateral stresses. This is primarily a result of the lack of the capability to model cohesion properties, resulting a much higher reflected pulse in the model. In turn, this culminates in a much lower portion of stress that actually gets transmitted through the sample both radially and axially.

The inability to depict cohesive properties is again highlighted as the primary limitation of the numerical model, leading to the difference between experimental and numerical results. Furthermore, the effect of moisture content is unable to be replicated within the numerical model due to the ineffectiveness of altering values of Poisson's ratio and bulk density to

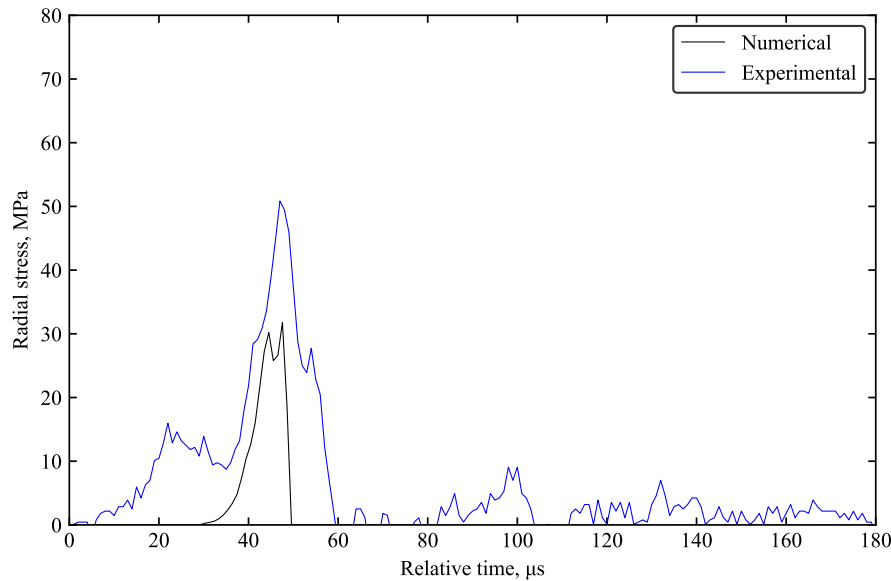


Figure 6.56: Comparison between radial stress from experimental and numerical model for partial lateral confined SHPB test on saturated kaolin clay.

match material properties at varying moisture contents. Indicating that while the model is able to visualise changes in strain rate and general behaviour, further development is necessary to prompt reliable modelling of cohesive soils under high-strain-rate. Overall, while the limitations associated with numerically modelling cohesive soils still exist, development of the numerical model still promotes a greater understanding of high-strain-rate behaviour.

#### 6.7.4 Validation of pressure reading

In addition to timeshifting the pressure readings to account for the width of the water annulus, the numerical model is used to validate that the pressure transducer readings on the wall of the water reservoir is an effective indication to the radial pressure at the edge of the sample. To accomplish this, the pressure of the water element next to the steel wall is compared with the element directly adjacent to the sample. Tests have been conducted with the numerical model via altering the width of the water annulus to determine the ideal width of the reservoir according to Table 6.12. It was observed that a thicker fluid annulus increases the disparity in pressure between specimen surface and reservoir wall as the delay in development of radial pressure causes recorded pressures to be an inaccurate representation of sample stresses. A reservoir with a 40 mm inner diameter was found to be optimal based on variation of water pressure from the numerical model (Figure 6.57), where the shape of the pulses depicting water pressure at the specimen surface and reservoir walls show a near perfect match ( $r^2 = 0.94$ ), this validates the inner diameter of the reservoir used in the experimental setup.

Table 6.12: Variations of water reservoir inner diameter tested with LS-DYNA model.

<i>Inner diameter, mm</i>	<i>r<sup>2</sup> value</i>
35	0.93
40	0.94
45	0.85
75	0.38

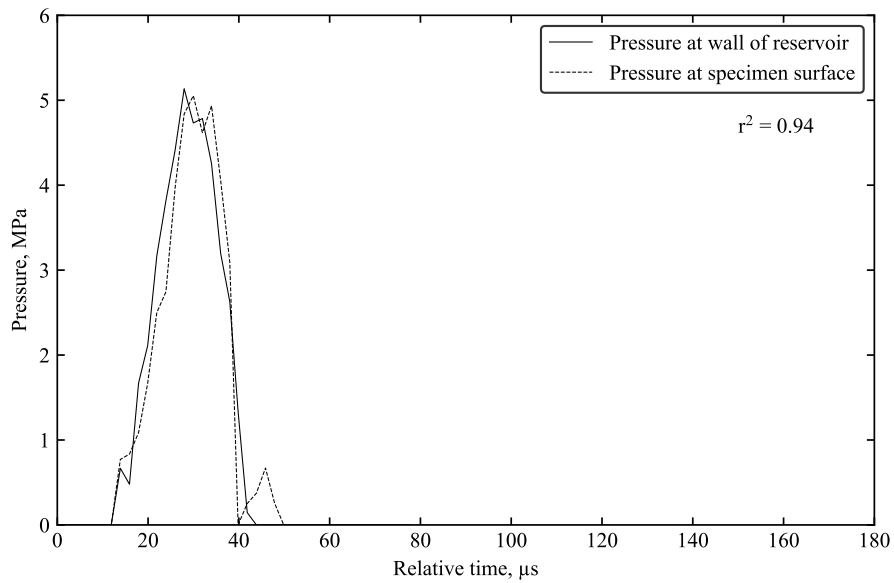


Figure 6.57: Comparison between recorded pressure at specific elements adjacent to reservoir wall and sample surface.

## 6.8 Internal sample stresses from numerical model

The development of numerical models that reflect results from SHPB testing facilitates the investigation of internal material behaviour and the mechanisms that lead to the specific material behaviour observed from existing experimental data. Ultimately, the combination of experimental and numerical results prompts the evaluation of confinement effects in cohesive soils when subject to high-strain-rate loading.

### 6.8.1 Unconfined and confined conditions

In addition to strain gauge locations corresponding to the experimental setup, the benefit of the numerical model is the ability to record stresses at other locations. From comparisons with experimental testing, the current numerical models is capable of reflecting the physical effects of high-strain-rate loading on kaolin clay with reasonable accuracy, albeit with specific limitations. This means that in addition to the measurements of radial stresses from the location of the confining ring, the internal lateral stresses and propagation of stress from the centre of the sample can be monitored by recording the variation of stress at each individual SPH node. The internal stress distribution on three of the five sample node layers have been identified and used for analysis, the layers correspond to the central, front (incident-sample interface), and back (sample-transmitted interface) layers as shown in Figure 6.58.

Figure 6.59 shows the maximum stresses from all of the SPH nodes in the  $z$ -axis within the central layer of the sample in an unconfined SHPB test, with  $z$ -displacement of zero indicating the centre of the sample. While LS-DYNA is incapable of obtaining circumferential stresses along a polar coordinate system, the stresses along the  $z$ -axis reflect the propagation of lateral stresses from the centre to the edge of the sample. Furthermore, the stresses of the sample nodes along the  $x$ -axis yielded a near exact same when the same distribution was determined, indicating rotational symmetry along the axis of axial loading ( $y$ -axis).

As expected, the centre of the sample experiences the least maximum lateral stress given that it is theoretically the point of greatest axial stress. The distribution illustrates a gradual increase of lateral stress from the centre towards near the outermost radius of SPH nodes. The outermost radius is noteworthy as it demonstrates that the initial propagation of stress from the centre triggers an effect that begins to displace the outermost nodes, hence when the maximum stress wave reaches the edge of the sample, most of the nodes are already displaced resulting in a drastic juxtaposition of stresses.

Similarly, similar internal stress distribution is obtained for the SPH nodes in the confined SHPB model as illustrated in Figure 6.60. The same gradual increase in maximum lateral stress can be observed from the centre to the edge of the sample. However, due to the presence of a rigid confinement to prevent extrusion of the outer nodes, the stress wave fully propagates through to the edge of the sample. The magnitude of this initial internal

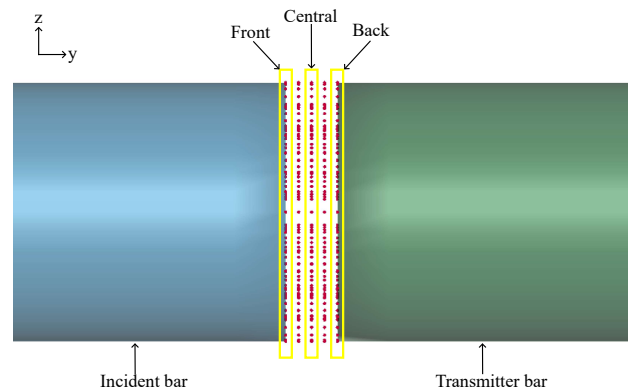


Figure 6.58: Locations of central, back, and front layers of sample used for measurement of internal radial stress.

wave is observed to be of a similar magnitude to its unconfined counterpart, even without the presence of any confinement mechanism.

By considering only the nodes at  $x=0$ , the variation of  $z$ -stress over time can be visualised in the heatmap to show variation over time. Figure 6.61b shows the distribution over time for the central layer under unconfined conditions. When the axial stress wave reaches the front interface of the sample at approximately  $550 \mu\text{s}$ , lateral stress is observed to gradually increase outwards from the centre of the sample. As discussed, the maximum lateral stress does not reach the outermost nodes because the nodes have been fully extruded by the time the maximum pulse reaches the edge.

In addition to the central layer, the same distribution of stresses along the  $z$ -axis are obtained for the front and back layers to illustrate the variation of lateral stresses over time (Figures 6.61a and 6.61c). The magnitude of stresses within the back layer are the greatest, this is due to the direct adjacency to the transmitter pulse, which effectively creates a barrier that promotes lateral stress propagation. Contrastingly, the front layer experiences the least lateral stress as the proximity to the incident bar promotes the greatest axial stress..

The heatmap for confined tests reveal internal reflection and subsequent superposition of the stress wave as shown in Figure 6.62. The initial wave starting from the centre to the edge of the sample is followed by an inward travelling wave (approximately  $600 - 650 \mu\text{s}$ ), before the wave travels outward again and reaches a peak lateral stress ( $700 \mu\text{s}$ ). This demonstrates that the rigid boundary prevents the dissipation of stress and prompts the reflection of the stress wave, when the stress wave begins to overlap, the pulse superimposes and hence a much greater magnitude of lateral stress is observed. Ultimately, the superposition of internal radial waves creates the concentration of radial stress, this concentrated stress is eventually redirected axially as a result of pressure build-up within the idealistically sealed confining ring.

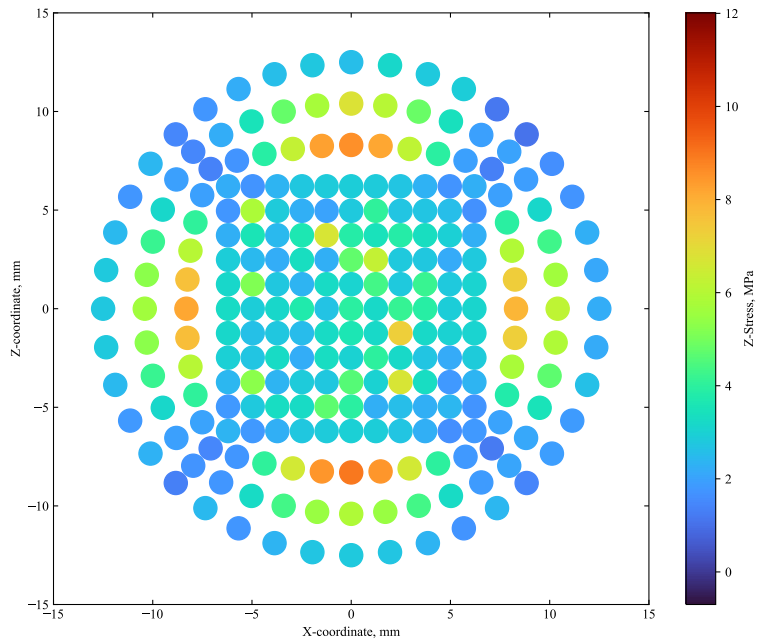


Figure 6.59: Internal sample radial stress from central layer of unconfined SHPB numerical model.

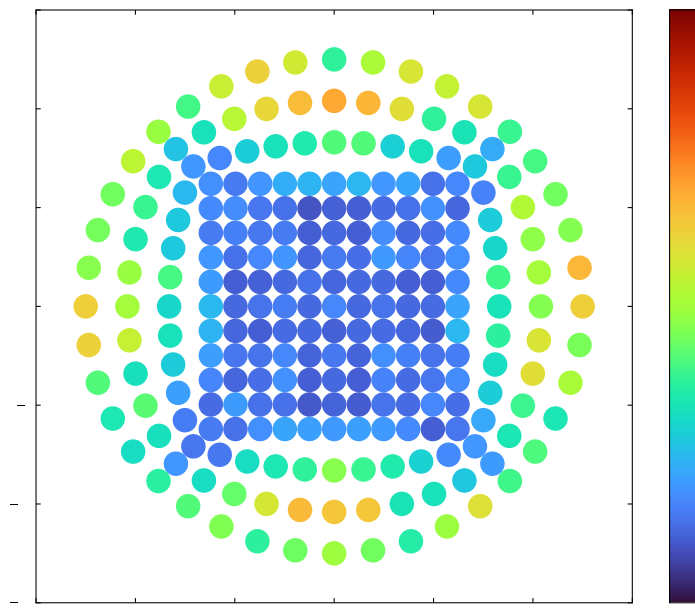


Figure 6.60: Internal sample radial stress from central layer of confined SHPB numerical model.

When comparing Figures 6.62a and 6.62c, the presence of the confining ring affected behaviour at the front and back layers of the sample. The magnitude of maximum stress at the back layer is lower than front layer, which contrasts with conditions when sample extrusion was unrestricted. However, since the maximum lateral stress is observed in the second wave and is a direct effect of internal reflection, the maximum stress from the initial wave remains similar to unconfined tests, indicating that the tendency for stress waves to redirect laterally is unaffected by confinement, but confinement serves to urge wave superposition. The eventual build-up of lateral pressure results in the stress wave being redirected onto the back interface axially.

Overall, this corroborates the notion that confinement does not directly influence the initial internal radial stress propagation within the sample. Instead, it acts as a redirection mechanism, where the addition of confining pressure to resist lateral deformation once the radial pulse reaches the edge of sample causes stress to reflect and superimpose, ultimately leading to the concentration of lateral pressure near the edge of the sample. This pressure is eventually redirected towards the axial direction, giving the effect of increased axial stress propagation as a consequence of confinement. Furthermore, the evidence of internal stress wave behaviour within the numerical model demonstrate the capability of the numerical model to reproduce experimental conditions. With the numerical model providing insight in explaining the internal effects of confinement as observed from physical results.

### 6.8.2 Partial lateral confined condition

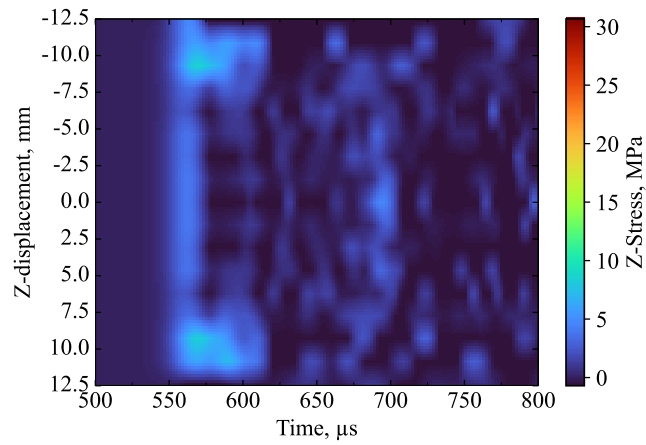
The same method was applied to investigate radial stresses distribution within the sample during loading in a PLC SHPB test. The heatmap for internal radial stresses within the sample is shown in Figure 6.63 with the water annulus modelled as water at  $1000 \text{ kg/m}^3$ . It was observed that while the maximum stresses are similar to unconfined tests, a second pulse develops as a result of confining pressure developing as the sample deforms laterally.

In order to examine the effects of confinement in promoting the amplification of radial stress via wave reflection, the density of the “water” was modified in the PLC numerical model to alter the effective inertia of the reservoir annulus. Figure 6.64b shows the heatmap when the fluid density was set to  $1 \text{ kg/m}^3$ , which theoretically resembles a fluid medium with limited resistance like free-field SHPB tests. Evidently, the subsequent reflected wave disappears, coinciding with preconceived behaviour from unconfined SHPB tests.

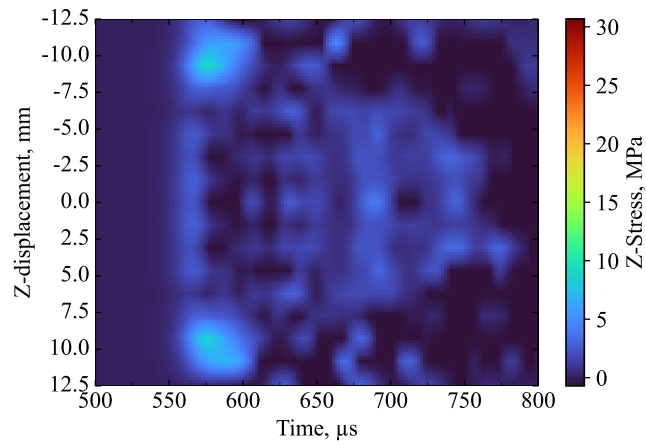
Contrarily, the density of water was increased to create an effect of greater confinement as the energy required to displace elements of the water annulus were now comparatively greater. Multiple model iterations were developed at various densities to assess the maximum velocity of adjacent fluid elements during lateral deformation of the sample, as summarised in Table 6.13.

While the initial pulse remained the same regardless of density, the magnitude of the sub-

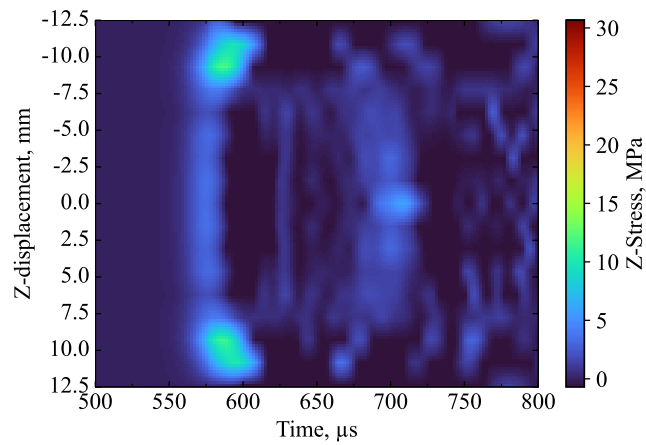




(a)

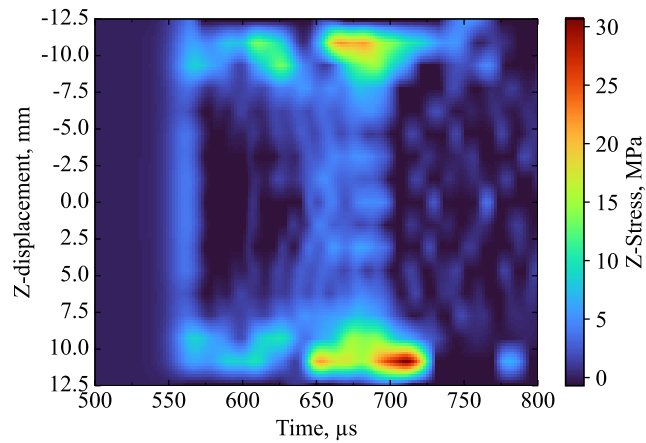


(b)

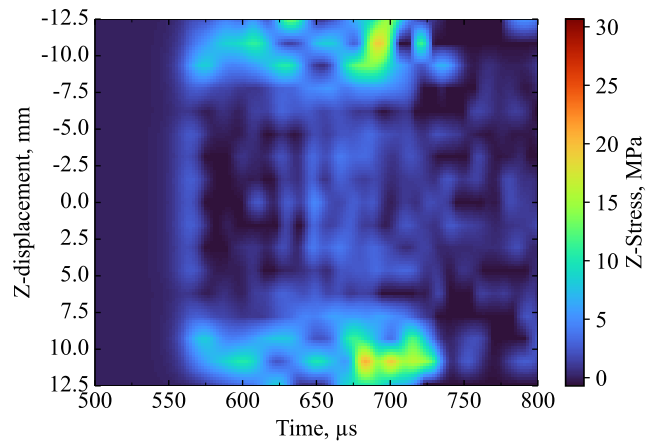


(c)

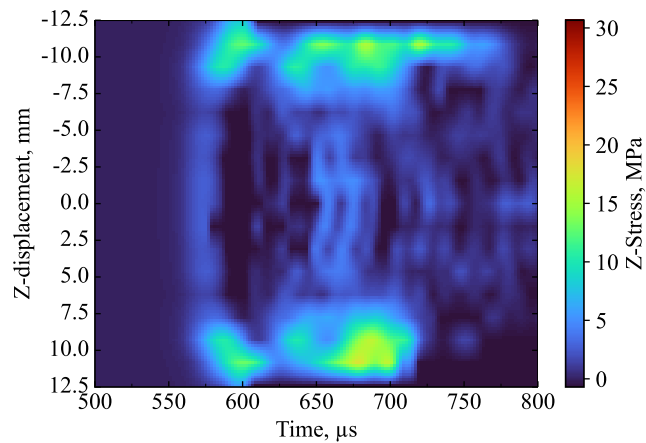
Figure 6.61: Heatmap describing internal radial stress variation over time from unconfined SHPB numerical model for a) front layer, b) central layer, and c) back layer.



(a)



(b)



(c)

Figure 6.62: Heatmap describing internal radial stress variation over time from confined SHPB numerical model for a) front layer, b) central layer, and c) back layer.

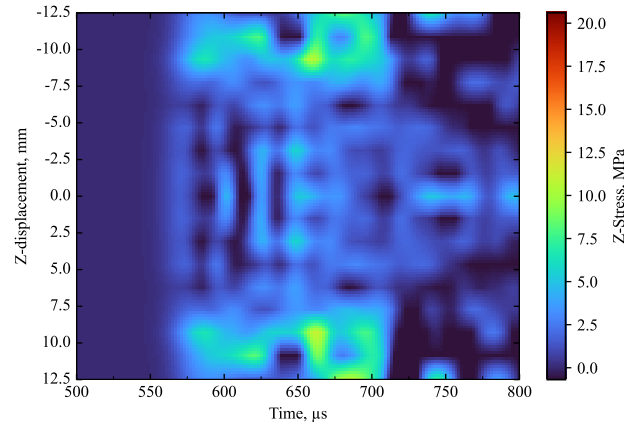


Figure 6.63: Heatmap describing internal radial stress distribution from numerical model of PLC SHPB tests, with water modelled as  $1000 \text{ kg/m}^3$ .

Table 6.13: Summary of numerical model iterations and required energy to displace confining elements.

<i>Material</i>	<i>Density, kg/m<sup>3</sup></i>	<i>Mass, kg</i>	<i>Peak radial velocity, m/s</i>	<i>Kinetic energy, J</i>
Steel	7850	$3.42 \times 10^{-5}$	0.0822	$1.16 \times 10^{-7}$
Water	1	$1.98 \times 10^{-8}$	28.90	$8.26 \times 10^{-6}$
Water	1000	$1.98 \times 10^{-5}$	8.08	$6.45 \times 10^{-4}$
Water	5000	$9.88 \times 10^{-5}$	2.81	$3.90 \times 10^{-4}$
Water	$1 \times 10^7$	0.20	$8.37 \times 10^{-3}$	$6.92 \times 10^{-6}$
Water	$2 \times 10^7$	0.40	$4.73 \times 10^{-3}$	$4.42 \times 10^{-6}$
Water	$6 \times 10^7$	1.19	$1.70 \times 10^{-3}$	$1.71 \times 10^{-6}$
Water	$1 \times 10^8$	1.98	$1.01 \times 10^{-3}$	$1.01 \times 10^{-6}$
Water	$9 \times 10^8$	17.79	$1.23 \times 10^{-4}$	$1.35 \times 10^{-7}$
Water	$1 \times 10^9$	19.77	$1.15 \times 10^{-4}$	$1.31 \times 10^{-7}$
Water	$1.1 \times 10^9$	21.71	$1.06 \times 10^{-4}$	$1.22 \times 10^{-7}$
Water	$2.5 \times 10^9$	49.4	$6.57 \times 10^{-5}$	$1.07 \times 10^{-7}$

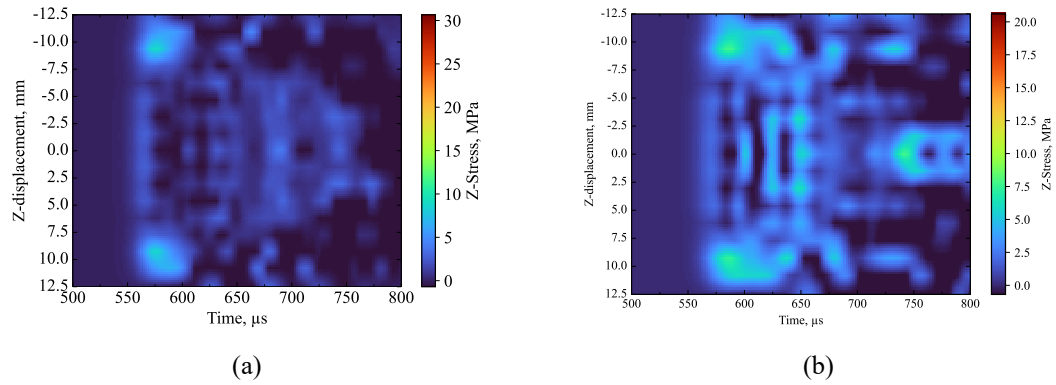


Figure 6.64: Heatmaps describing internal radial stress distribution from numerical models of a) unconfined SHPB and b) PLC SHPB with equivalent water annulus density ( $1 \text{ kg/m}^3$ ).

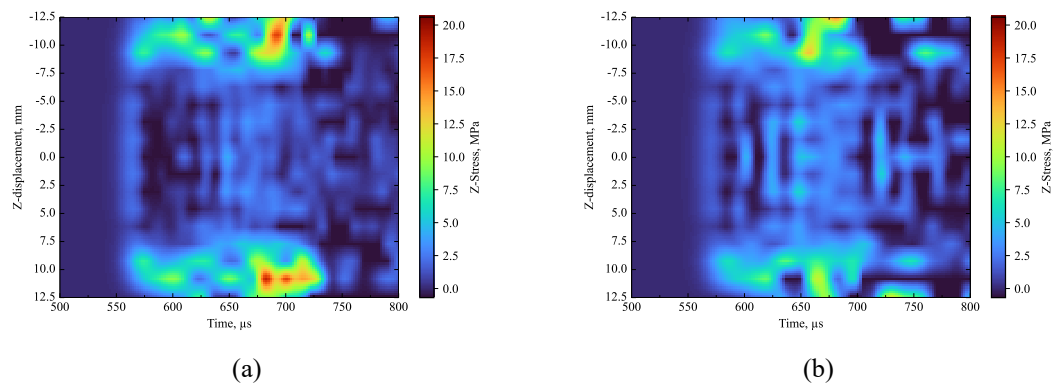


Figure 6.65: Heatmaps describing internal radial stress distribution from numerical models of a) confined SHPB and b) PLC SHPB with equivalent water annulus density ( $1.1 \times 10^9 \text{ kg/m}^3$ ).

sequent pulse increases as the density of the fluid annulus increases. This corroborates the notion that increasing confinement encourages pulse reflection and the build-up of internal lateral stress.

To compare the confinement conditions with the numerical model with a steel confining ring, the corresponding energy required to displace a fluid element with a defined volume from rest,  $E$ , is derived for each density,  $\rho$ , to reveal a power-law relationship expressed by:

$$E = 0.3542\rho^{-0.727} \quad (6.2)$$

The  $r^2$  value for Equation 6.2 was determined to be 0.951, indicating an excellent relationship.

As such, the density of the modelled fluid with an equivalent energy to the elastic steel confining ring is determined to be  $1.1 \times 10^9 \text{ kg/m}^3$ . The heatmaps illustrating the PLC numerical model with a fluid annulus modelled with this density can be compared to the results from the confined model in Figure 6.65.

Evidently, the lateral stresses found in the second pulse exhibit similarities in peak stress. Intrinsic differences between material behaviour explain the difference between the two models, notably the difference in compressibility between the water modelled as a null material and steel modelled as an elastic material, resulting in the pulse with a steel confining ring maintaining its peak magnitude for a longer duration as the stress wave travels within elastic steel ring elements.

This emphasises the effects of confinement in cohesive soils when subject to high-strain-rate loading, where the confining pressure prompts the internal reflection of radial stress and culminates in the concentration of radial stress in eventual internal radial waves. This intensification of radial stress ultimately results in the axial redirection of amplified radial stress.

## 6.9 Discussion of numerical modelling

The development of numerical models to depict cohesive soil behaviour under high-strain-rate conditions is crucial in the understanding of intrinsic dynamic properties. The ability of SPH node modelling to override scenarios in which materials exhibit sudden volume change or extreme deformation makes it the ideal numerical method to model behaviour of cohesive soils that exhibit fluid-like properties. However, there are still inevitable disparities between the idealised numerical model and physical testing, emphasising the necessity to couple the use of numerical modelling with experimental testing to provide a comprehensive analysis of physical phenomena.

### 6.9.1 Limitations and recommendations

The use of the numerical model has been pivotal in facilitating the understanding of internal mechanisms that occur during experimental testing, but there are still intrinsic limitations associated with modern numerical modelling techniques that prevent it from fully emulating the behaviour of cohesive soils under high-strain-rate.

The obvious limitation is the lack of fully suitable material to represent kaolin clay. The Mohr-Coulomb model was chosen as it was a simplified soil model that did not require a compression curve, hence the material input parameters could be estimated based on quasi-static testing. The strain rate dependence of kaolin clay, and its intrinsic inability to withstand multi-axial compression without instant extrusion results in the difficulty to define a fully functional EOS that represents cohesive soil behaviour. While LS-DYNA has a wide range of material models available to model soil or cohesion behaviour, most require an EOS.

Another key limitation is the incapability to alter the moisture content with the material model currently selected. As discussed, attempts have been made to develop kaolin clay samples with varying levels of moisture content by altering density parameters within the material model. However, the efforts proved futile as it resulted in little to no change in the resultant axial and radial stresses. This meant that even though certain intrinsic properties were able to be characterised with numerical modelling, the phase behaviour highlighted through experimental testing could not be properly evaluated with the numerical model. This is directly correlated to the lack of fully suitable material model, but also highlights in lack of current techniques to model cohesive soils under high-strain-rates.

While the conception of SPH node modelling has long existed, there have been significantly less development in the use of SPH particles to depict soils. This meant that current modelling techniques lack the capabilities to model unique soil properties. The cohesive properties of kaolin clay is a primary deficiency, where numerical models are unable to fully characterise the tendency for soil particles to stick together. Whilst some material models in LS-DYNA account for cohesion, they are still unable to fully characterise the behaviour cohesive soil particles under high-strain-rate loading, or they require a compression curve to be fully utilised.

While MAT\_MOHR\_COULOMB or other geological cap material models contain a cohesion value or other methods to define internal particle adhesion, they are not designed for high-velocity impacts. This is especially the case for LS-DYNA and SPH model calculation, the internal adhesive forces are typically defined over a specific surface. However, the value for cohesion defined to this surface becomes considerably difficult to estimate if the interface experiences extreme distortion (Profizi et al., 2016). This emphasises that while future work should be done to further evaluate the available techniques to apply internal adhesion to SPH particles, the built-in methods to apply cohesive properties values may not be practical for high-strain-rate applications. This implies that future development is required regarding the definition of cohesive properties between individual SPH particles in order to

obtain a numerical model that more accurately reflects real-life phenomena.

Lastly, physical limitations lead to the existing disparity between numerical models and experimental testing. As highlighted in the previous sections, the capability for numerical models to create an idealistic scenario inevitably led to deviations with physical testing. Namely, the ability to create fully rigid elements that withstand any form of displacement is unrealistic. However, this was fundamental to the development of the confining ring in the numerical model since it prevented mass vibrations. The lack of lateral translation meant that the confining ring was able to provide a near perfect seal during the first instance of stress wave propagation. Contrarily the confining ring in physical testing experiences significant amounts of lateral extrusion and volumetric loss upon stress wave propagation, of which is not observed in the numerical model, ultimately leading to the experimental results producing a much lower output stress than the numerical model.

With exception to unavoidable experimental differences, numerical modelling was able to provide a clear basis of comparison and facilitate the understanding of cohesive soil behaviour. Most other limitations are characteristics of cohesive soils that current numerical modelling techniques fail to consider. The development of an advanced material model catered to the behaviour of cohesive soils would be paramount in future advancements within this subject area. Nevertheless, the fluid-like behaviour exhibited by cohesive soils under high-strain-rates make numerical modelling via the employment of SPH particles a prime subject for future development.

## **6.10 Effects of confinement in cohesive soils**

The development of a numerical model alongside experimental data allows for the internal mechanisms during high-strain-rate loading to be characterised, especially due to the influence of confinement. This is evident by utilising internal stress distribution patterns from numerical modelling as a tool to explain experimental results.

Even though experimental results have provided an idea of the effect of confinement, apparatus limitations prevent the full characterisation of confinement effects without numerical modelling. In the case of confined setups, the limitations of the confining ring not being fully rigid and movements due to vibration or loading result in inaccuracies between idealistic and realistic setups. From numerical models on confined SHPB tests, a fully rigid ring demonstrates the ability to fully translate lateral stress into axial stress at the back of the specimen interface by creating a condition that prevents volume loss, which was compared to the behaviour of water under axial compression. This similarity also prompted the testing of water using the partial lateral confined apparatus, revealing results that indicate notable similarities in behaviour between saturated cohesive soils and water.

The development of the numerical model for partial lateral confined SHPB tests demonstrate

a similar phenomena that compensates for specific limitations from experimental testing. A prime instance of this is the ability to create perfect boundary conditions. Large rubber o-rings are utilised to seal the water reservoir and ideally create a condition of controlled pressure within the water annulus, yet still allow for the pressure bars to move and propagate stress during loading. The subsequent effect of loading typically involves the water seal being broken immediately, invoked by lateral movement of the rubber o-rings by the sudden pressure change and movement of the pressure bars. While the effect may not be as noticeable given only the initial radial pulse is of primary concern, numerical modelling allows for an idealistic scenario where the pressure in the water annulus was fully controlled without hindering the stress propagation through the pressure bars.

While the same material limitations exist between the unconfined, confined, and partial lateral confined SHPB numerical models, the juxtaposition between the three confinement modes allows for the effects of confining pressure to be magnified by developing idealistic situations for each of the three different cases.

Figure 6.66 shows the difference in back stress experienced by the numerical model under unconfined and partial lateral confined conditions. The back stress under confined conditions is significantly greater than both confined and unconfined cases due to the immense pressure that develops within a condition where no volume loss is permitted by forcibly preventing any sample extrusion. The ability for the partial lateral confined sample to deform laterally is evident due to its similarity to unconfined cases, the lack of rigid confinement to redirect stress back towards the axial direction like results in a significantly lesser back stress unlike confined cases.

The radial effects of confinement can be visualised in Figure 6.67 depicting the radial stresses obtained from the confining ring and the water pressure directly adjacent to the sample. Evidently, a significant disparity is observed as the model for the confining ring acts as a perfect seal, and forces all lateral stress to be concentrated on the ring through the build-up of internal pressure. This indicates that the confinement mechanism directly affects the axial transmission as internal radial stresses of the specimen are wrapped and redirected towards the back interface according to the degree of confinement. Hence why a system with limited confinement such as the partial lateral confined depicts low measured radial stresses and equally low axial back stresses.

While there are obvious physical differences between the three confinement modes, the partial lateral confined approach was considered a combination of the unconfined and confined cases. Hence the similarities to each of the extreme confinement conditions are a reliable basis of comparison to gauge the effects of confinement.

Numerical modelling has demonstrated that under the same material and test conditions, cohesive soils have proven to have an equal tendency to propagate stress in the lateral direction regardless of initial confining pressure. However, the addition of confining pressure restricts lateral deformation of the sample and causes the concentration of lateral stress to develop



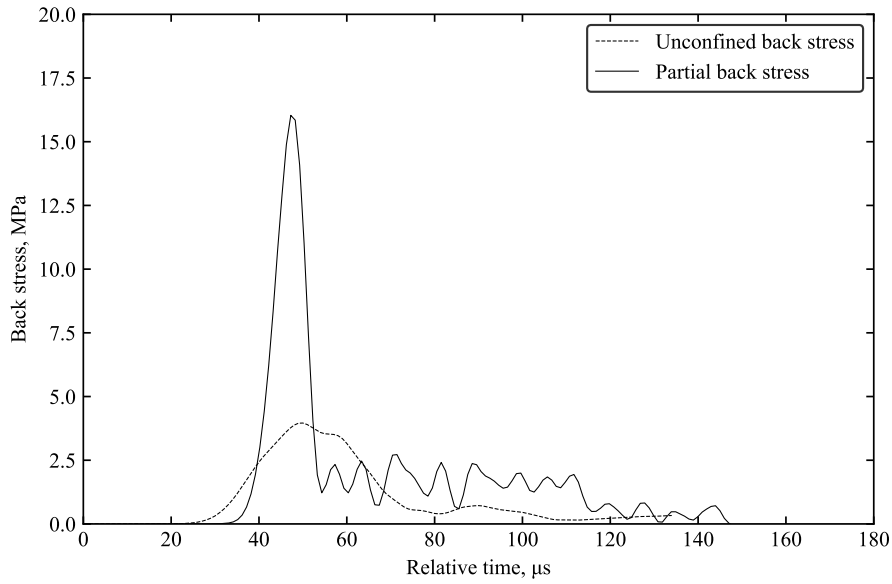


Figure 6.66: Comparison between back stress from numerical model for unconfined, partial lateral confined SHPB test on saturated kaolin clay.

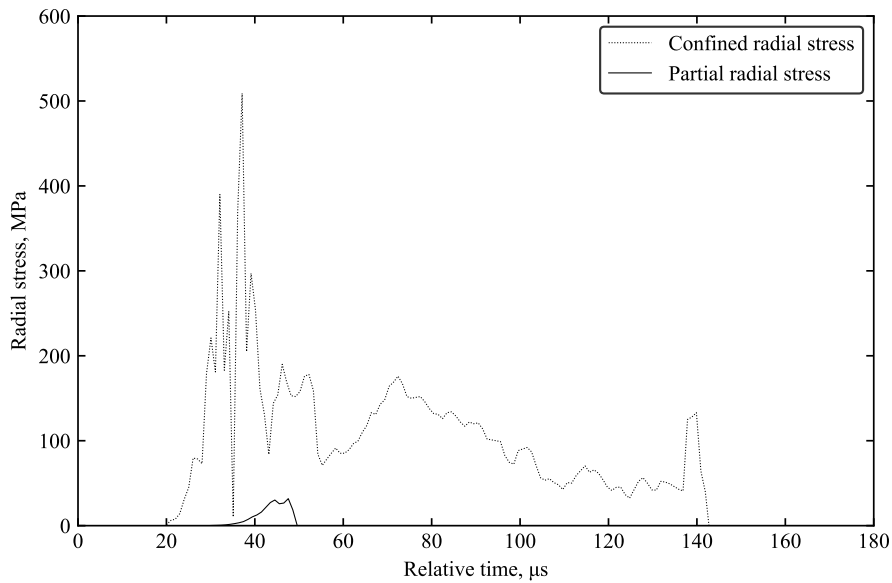


Figure 6.67: Comparison between radial stress from numerical model for confined, and partial lateral confined SHPB test on saturated kaolin clay.

at the edge of the sample. The eventual build-up of lateral pressure causes the subsequent redirection of stress back towards the axial direction and prompting a perceived increase in axial stress propagation.

The use of the partial lateral confined apparatus for experimental testing, and the subsequent development of the numerical model was crucial in the understanding of confinement behaviour. Since the partial lateral confined reservoir creates an intermediate condition between the confined and unconfined cases, the lateral pressure from the water annulus creates an environment of partial pressure that differs from the atmospheric air pressure under unconfined conditions. By comparing the three confinement modes, the effect confinement in prompting the redirection of lateral stress is much better visualised.

Hence the overall blast attenuation ability of kaolin clay can be characterised by its ability to behave akin to a fluids when under high-strain-rate conditions, with a tendency to propagate stresses in the lateral direction and minimise wave propagation through the material axially if placed under conditions where stress is permitted to dissipate radially. This also underscores the importance of volume loss in minimising axial stress propagation, as volume loss is inherently linked to the degree to which lateral deformation is restricted. Numerical models of confined systems with an theoretical perfect seal restricts sample extrusion and thus forces the build-up of lateral pressure and enhances propagation of axial stress through the material.

## 6.11 Summary

This chapter discusses the development of numerical models to simulate high-strain-rate SHPB results for kaolin clay. Material models were selected to best represent the fluid-like behaviour exhibited by cohesive soils, in addition to the implementation of relevant geotechnical variables. An initial axisymmetric model was developed with the capability to depict unconfined SHPB behaviour with kaolin clay to a reasonable degree of accuracy when modelled with the Mohr-Coulomb material model. However, the immense mesh distortion induced by the instantaneous sample extrusion during confined SHPB tests caused the model computation to terminate prior to recording any useful stress data.

Various numerical modelling techniques were considered to overcome the apparent “negative volume error”, with the adoption of SPH node modelling proving most effective. Modelling of SPH nodes was designed to simulate fluids that experience large amounts of deformation and volume change, making it an ideal approach to simulate high-strain-rate cohesive soil behaviour. Physically confined testing typically resulted in lateral extrusion from the edges of the confining ring. However, in the modelled scenario, the presence of a confining ring restricts lateral extrusion, amplifying the vibrational effect of the steel elements caused by the sample’s lateral deformation. Ultimately, this led to a combination of rigid and elas-

tic elements to develop a confining ring that restricts translational movement but was still capable of recording stress data.

Comparison between numerical and experimental results show that the numerical model was capable of depicting high-strain-rate behaviour to some extent. While behaviour for saturated kaolin clay samples show a reasonable degree of accuracy, the key limitation is the inability to model cohesive properties within the current material model. This prevents individual SPH particles from adhering, and is a crucial component of cohesive soil behaviour. Nonetheless, the numerical model was able to verify the tendencies for kaolin clay to propagate stress laterally when subject to high-strain-rate loading, and for the confining ring to act a boundary and redirect lateral stress towards the back end of the specimen.

Furthermore, the development of numerical models also prompted the investigation of internal stress propagation within the sample. Distribution of stresses within the sample show that the initial radial wave from the centre of the sample outwards are unaffected by confinement. But that the addition of confinement prevents sample volume loss and facilitates the superposition of internal radial stress waves, culminating in the concentration of lateral stresses at the edge of the specimen. Ultimately, this proves that even with limitations in designing models for cohesive soil behaviour, the combination of experimental and numerical results assist in drawing valuable conclusions to indicate high-strain-rate behaviour of cohesive soils.

Finally, the combination of numerical modelling and experimental data allows for conclusions regarding high-strain-rate behaviour of cohesive soils under various confinement conditions to be validated. While experimental results revealed the tendency for lateral stress propagation during loading and the significance of moisture in dictating stress propagation behaviour, numerical modelling provided insight in how this behaviour is affected by confinement mechanisms by demonstrating the existence of internal reflection within the sample volume. The degree of confinement applied to the sample can then be said to be directly related to the proportion of internal stress reflection. The internal reflection ultimately accumulates as lateral pressure and is eventually redirected back towards the axial direction, leading to conditions of rigid confinement recording highest levels of axial stress propagation through the sample.

## Chapter 7

# Summary and conclusions

## 7.1 Summary

This thesis aimed to evaluate the strain rate dependence of cohesive soils through investigation of kaolin clay with SHPB experimentation. The variation of confinement prompted the characterisation of cohesive soil behaviour under the effects of varying confining pressure

Full material characterisation and preliminary testing under quasi-static conditions formed the basis of experimental testing, initiating the evaluation of kaolin clay under varying strain rates. Oedometer tests on saturated kaolin clay revealed the resemblance of stress behaviour to fluids when subject to dynamic loading, prompting the further investigation of the effect of moisture and its overall influence on stress propagation through the cohesive soils.

High-strain-rate tests were conducted on kaolin clay under both unconfined and confined conditions. The inherent impedance mismatch between incident and transmitted signals meant the development of a unique data processing algorithm, `SHPB_processing.py`, was necessary to properly evaluate experimental results. The existence of unique phase boundaries correlated to material-specific parameters and experimental conditions was discovered when cohesive soils were subjected to high-strain-rate loading and can be summarised in Figure 7.1. Moisture is found to be the primary dictating factor in the determination of each phase. While confined testing revealed the same unique phase boundaries, the addition of the confining ring created a redirection effect to translate lateral stress back towards the axial direction and to the back sample interface.

While confined and unconfined experimental testing provided a view on high-strain-rate behaviour of cohesive soils under the two confinement conditions, the adoption of the partial lateral confined SHPB allowed for the behaviour in between traditional free field unconfined and rigid confined testing to be characterised in order to better understand the effects of confinement. The partial lateral confinement mechanism enabled the understanding of radial stress development when the sample was allowed to deform laterally. Experimental results revealed the conclusion that moisture within cohesive soils encourages radial deformation

and lateral stress propagation irregardless of confinement, but the degree of confinement affects the concentration of radial stress on the edge of the sample. In addition to tests on kaolin clay, the partial lateral confined apparatus was employed to conduct impact tests of water, revealing results that greatly resemble saturated kaolin clay data and supporting the significance of moisture in governing high-strain-rate behaviour of cohesive soils.

However, inherent limitations with the physical setup led to the inability to develop a comprehensive characterisation of confinement effects and the holistic characterisation of cohesive soils under high-strain-rate loading. Hence modern numerical modelling techniques was evaluated using the FEM software LS-DYNA. Various material models were considered to replicate kaolin clay, but the inability to obtain an accurate EOS and take into account cohesive properties meant no material model was fully equipped to accurately reflect the behaviour of cohesive soils. The extreme deformation and sudden volume changes induced by high-strain-rate loading meant that the “negative volume error” was a critical problem during numerical modelling. Different methods were considered but the use of SPH node modelling to simulate cohesive soils was optimal due to its capability to tackle conditions with extreme deformation and its inherent ability to simulate fluid-like behaviour. The model demonstrated the capability to reproduce experimental conditions to a reasonable degree of accuracy, while still considering the inevitable numerical limitations. The development of the numerical model allowed for the internal sample stresses to be investigated, which revealed the presence of internal stress wave reflection as a result of confinement. While numerical accuracy is inevitably hindered by inherent limitations, the combination of numerical and experimental results were crucial in understanding the mechanisms that lead to the empirical behaviour exhibited by cohesive soils under high-strain-rates. Notably, the effect of confinement can be characterised by the build-up of internal lateral pressure which leads to the eventual redirection of stress towards the back end of the sample

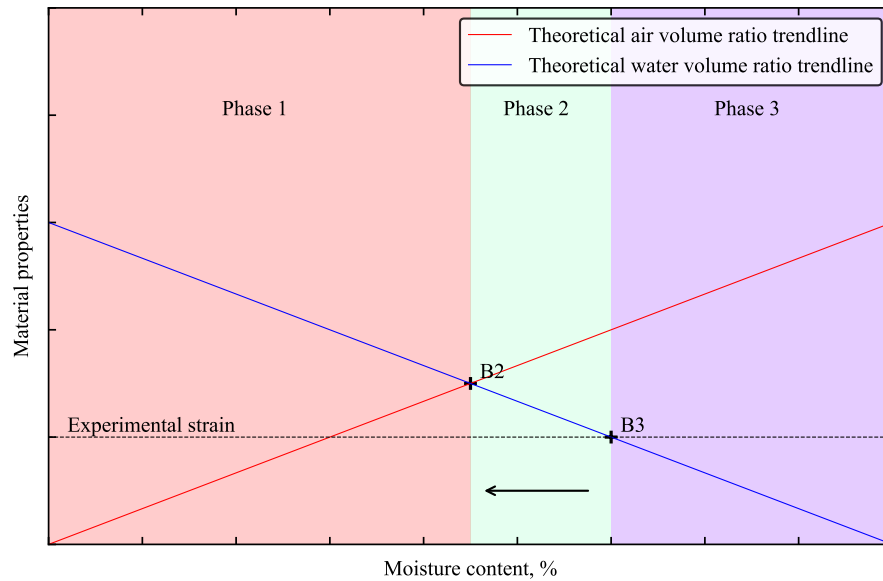


Figure 7.1: General phase behaviour exhibited by kaolin clay under high-strain-rate, governed by material properties.

## 7.2 Conclusions

### 7.2.1 Quasi-static testing and material characterisation

- Dynamic oedometer testing demonstrated that cohesive soils, and particularly kaolin clay, exhibited results that resemble the behaviour of fluids.
- The thorough material characterisation of kaolin clay not only ensured the reproducibility of the work presented in this thesis, but also enhanced the understanding of intrinsic material properties and contributed to the development of numerical models.

### 7.2.2 Confinement effects

For unconfined SHPB tests on kaolin clay:

- Minimal axial stress propagation through kaolin clay when subject to high-strain-rate loading, as evident from low magnitudes of back stresses recorded, even though superposition of incident and reflected pulses show that axial stress wave is propagating through into the sample from the incident pressure bar.

- Large proportion of material volume is lost in the form of lateral extrusion, prompting the indication that stress is propagating in the radial direction when subject to high-strain-rate axial loading.

For confined SHPB tests on kaolin clay:

- Rigid confinement results in a significantly greater recorded back stress when compared to unconfined results.
- Significant radial stresses were observed by measuring the circumferential strain of the steel confining ring during lateral deformation of the sample.
- Increased back stress from confining tests is attributed to the redirection of radial stresses as a result of the confining ring, the rigid boundary enhanced the concentration of radial stresses on the edge of the sample boundary and translated radial stresses towards the direction of the transmitted bar (back stress).

For partial lateral confined SHPB tests on kaolin clay:

- Modified apparatus has been developed to demonstrate its capability to characterise cohesive soils.
- Low back stress occurs due to the sample's ability to deform laterally with minimal restriction from confinement, indicating similarities with unconfined tests. However, the water pressure still minimally redirects lateral stresses, resulting in slightly higher back stress.
- Radial stresses at the sample surface obtained from processing pressure transducer results reveal lateral stress propagation during deviatoric phase.
- The capability for the sample to deform laterally reduces the concentration of radial stresses at the edge of the sample, leading an overall lesser radial stress recorded than compared to confined tests.
- Experimental results demonstrate the partial lateral confined SHPB apparatus as a medium between unconfined and confined tests such that minimal initial confining pressure is provided by the apparatus yet radial stresses can be measured through changes in water pressure.

### 7.2.3 Phase behaviour and influence of moisture

Based on evidence of axial stress propagation from SHPB testing:

- Cohesive soils under high-strain-rate conditions tended to propagate stress laterally rather than transmit stress axially through the sample, this effect has been demonstrated to be heavily influenced by the content of water within the material.
- Unique phase behaviours were discovered within specific moisture content ranges, with boundaries dependent on the air-volume, water-volume ratio, and maximum experimental strain.
- Behaviour within each phase was closely related to the content of water within the material, highlighting the importance of moisture in dictating high-strain-rate behaviour of cohesive soils.

Impact of confinement on moisture content effects:

- Distinct radial stresses were observed within the same moisture content phases in both confined and partial lateral confined testing, showcasing the influence of moisture in promoting lateral stress propagation and the subsequent effect on the recorded radial stresses.
- The magnitude of radial stresses are significantly less compared to rigidly confined tests, this is attributed to the concentration of radial stresses directly on the surface of the sample due to the prevention of lateral deformation and limited opportunity for volume loss due to extrusion.

From partial lateral confined SHPB tests on water:

- The similarity between cohesive soils and water is demonstrated by adapting the partial lateral confined SHPB apparatus for water, revealing similarities in behaviour between saturated kaolin clay and water
- The significance of moisture in dictating the general behaviour of saturated cohesive soils is highlighted, and explains the apparent fluid-like behaviour.

### 7.2.4 Strain rate effects

- Experimental testing at higher strain rates yielded greater magnitudes of axial and radial stresses.



- Unique phases at various moisture contents still exists at higher strain rates, however the boundary between the second and third phases decreases as strain rate increases due to a greater maximum experimental strain.
- The effects of moisture content and confinement were consistent for strain rates tested within magnitudes of  $10^3 \text{ s}^{-1}$ , although the back and radial stress pulses naturally exhibited higher magnitudes when strain rate was increased, the general behaviour remained unchanged.

### 7.2.5 Numerical modelling

- Inability to obtain an accurate equation of state to model cohesive soil behaviour make the selection of material models difficult, MAT\_MOHR\_COULOMB was selected as it best represents the available parameters deduced from experimental testing.
- The fluid-like behaviour exhibited by cohesive soils is best represented by the use of SPH modelling due to the tendency of the material to experience extreme deformation and sudden volume changes.
- Current material model fails to account for cohesion properties leading to a greater portion of stress being reflected at the sample-incident bar interface, this hinders the reliability of model results.
- Numerical models with LS-DYNA were able to replicate high-strain-rate behaviour of saturated kaolin clay to a reasonable accuracy, however phase behaviour associated to kaolin clay at varying degrees of saturation failed to be fully captured.
- Internal sample radial stress behaviour was found to be similar regardless of confinement, indicating the intrinsic tendency for the material to propagate stress laterally.
- Addition of confinement mechanisms such as the partial lateral confinement and confining rings created a concentration of radial stresses at the edge of the sample, that ultimately leads to the redirection of radial stress axially based on the varying degree of confining pressure.

## 7.3 Future research

The findings outlined above have identified various areas that could be further explored through additional research. Such research would greatly enhance the understanding of the underlying mechanisms involved in cohesive soil behaviour, but would also improve the practical application of modern high-strain-rate material characterisation techniques.

### 7.3.1 Dependence on material properties

Although a large spectrum of moisture contents have been conducted under unconfined, confined, and partial lateral confined conditions to reveal the significance of moisture in dictating high-strain-rate behaviour of cohesive soils. Even though saturated kaolin clay (phase 3) has demonstrated stark similarities to water, the existence of air voids in partially saturated or fully dry samples reveal that internal air voids also has an effect on soil behaviour. Phase 0 and phase 1 behaviour demonstrate the elimination of air voids within fully dried and partially saturated samples. While these intrinsic material properties resulted in the development of specific phases, the exact relationship between the material properties and soil behaviours within the phases are inconclusive, hence further work is required to derive stress-strain behaviour within specific phases.

Phase 2 behaviour is characterised by its variable upper boundary being dependent on the maximum experimental strain, tests with increasing strain rates are conducted, the upper limit tends to approach the lower limit resulting in an increasingly small phase 2 range. While phase 2 has been expected to disappear at these higher strain rates, its possible that physical limitations associated with producing kaolin clay samples with uniformly exact moisture content hinder the capability to obtain experimental data at the smaller phase 2 windows. Further work may be done to develop methods to characterise phase 2 behaviour at even higher strain rates when the moisture content range for phase 2 is expected to be small.

### 7.3.2 Numerical modelling of cohesive soils

As discussed in Chapter 6, one of the key limitations in the current numerical modelling techniques is the inability for soil material models to properly account for the effect of suction. This is especially important when considering cohesive soils, where the existence of water is a major dictating factor in soil behaviour especially in high-strain-rate scenarios. The intrinsic cohesion between particles create an internal suction force that prevents the immediate detachment of individual particles. While some LS-DYNA material models contain the ability to input a parameter for cohesion, those material models are not optimised for cohesive soils due to the difficulty in populating an equation of state at high-strain-rates. Hence, the development of an updated material model that can be optimised for soil behaviour yet also accounts for the effect of water and cohesion would be of paramount importance in the development of an effective model to depict high-strain-rate cohesive soil behaviour.

In addition, the current numerical model fails to depict the unique phase behaviours observed at different moisture contents. Despite modifications made to the current material model by varying values of bulk density and Poisson's ratio, attempts to change the moisture content were to no avail, with all numerical models yielding near exact same behaviour. Future work regarding the optimisation of soil material model properties especially with regards to SPH

modelling of high-strain-rate cohesive soils would be highly beneficial in developing more accurate numerical modelling simulations.

Finally, more work regarding internal wave reflection should be investigated with the numerical model, especially to optimise the partial lateral confined model. Developments that enable the variation of confining pressure would allow for the effects of confinement on the degree of internal reflection to be quantified.

### **7.3.3 Partial lateral confined apparatus**

The application of the partial lateral confined apparatus on cohesive soils in Chapter 5 demonstrated the capability of the setup in obtaining valuable results for saturated kaolin clay, the inability to amplify the pressure transducer signal hinders the apparatus' capability to monitor low radial pressures. Further work is required to either design a signal amplification system or replace the pressure transducer with a more advanced and precise model.

The inaccuracies regarding pressure transducer readings at low radial pressures mean that conducting tests at lower moisture contents have yielded varying outcomes. While improvements to instrumentation is required, the full characterisation of the moisture content spectrum would enhance the current understanding of radial stress development when cohesive soils are placed in a condition where lateral pressure is allowed to freely develop during axial loading.

The ability to investigate the high-strain-rate effects of fluids, specifically water, prompts an opportunity to investigate the behaviours of other fluids under similar conditions. This could include fluids with shear thickening capabilities, of which their strain rate dependence could be a crucial aspect of exploration.

### **7.3.4 Signal processing**

The development of `SHPB_processing.py` has been highly effective in processing SHPB test data especially when cases of stress equilibrium are not obtained. While the pulse alignment function for incident and back stress has undergone multiple optimisations, the alignment of front and back stress pulses still occasionally require manual adjustment especially when both pulses are drastically different in shape. Further development of the algorithm is required to optimise the pulse alignment system.

Since the algorithm has been designed with the capability to process high-strain-rate test data under conditions without stress equilibrium, the algorithm is theoretically capable of being adapted to tackle a greater range of high-strain-rate or impact test setups, but would require further calibration and optimisation based on test parameters and conditions.

## Bibliography

- Abbey, S., Eyo, E. U., & Ngambi, S. (2019). Swell and micro-structural characteristics of high-plasticity clay blended with cement. *Bulletin of Engineering Geology and the Environment*, 79(4), 2119–2130.
- Adamis, Z., & Williams, R. B. (2005). *Bentonite, kaolin, and selected clay minerals*.
- Anantanasakul, P., Yamamuro, J. A., & Lade, P. V. (2012). Three-dimensional drained behavior of normally consolidated anisotropic kaolin clay. *Soils and Foundations*, 52(1), 146–159.
- Atkinson, J. H., & Bransby, P. L. (1978). *The mechanics of soils: An introduction to critical state soil mechanics*.
- Atterberg, A. (1911). Die plastizität der tone. *Intern mitt. boden.*, 4–37.
- Bailly, P., Delvare, F., Vial, J., Hanus, J. L., Biessy, M., & Picart, D. (2011). Dynamic behavior of an aggregate material at simultaneous high pressure and strain rate: Shpb triaxial tests. *International journal of impact engineering*, 38(2-3), 73–84.
- Bancroft, D. (1941). The velocity of longitudinal waves in cylindrical bars. *Physical Review*, 59(7), 588.
- Barr, A. D. (2016). *Strain-rate effects in quartz sand* [Doctoral Dissertation]. University of Sheffield.
- Barr, A. D., Clarke, S. D., Rigby, S. E., Tyas, A., & Warren, J. A. (2016). Design of a split hopkinson pressure bar with partial lateral confinement. *Measurement Science and Technology*, 27(12), 125903.
- Bragov, A. M., Lomunov, A. K., Sergeichev, I. V., Tsembelis, K., & Proud, W. G. (2008). Determination of physicommechanical properties of soft soils from medium to high strain rates. *International Journal of Impact Engineering*, 35(9), 967–976.

- Busch, C. L., & Tarefder, R. A. (2017). Evaluation of appropriate material models in ls-dyna for mm-scale finite element simulations of small-scale explosive airblast tests on clay soils. *Indian Geotechnical Journal*, 47, 173–186.
- Chen, J.-Y., & Lien, F.-S. (2018). Simulations for soil explosion and its effects on structures using sph method. *International Journal of Impact Engineering*, 112, 41–51.
- Christensen, R. J., Swanson, S. R., & Brown, W. S. (1972). Split-hopkinson-bar tests on rock under confining pressure. *Experimental Mechanics*, 12(11), 508–513.
- Church, P., Cornish, R., Cullis, I., Gould, P., & Lewtas, I. (2014). Using the split hopkinson pressure bar to validate material models. *Philosophical Transactions of the Royal Society A: Mathematical, Physical and Engineering Sciences*, 372(2023), 20130294.
- Clarke, S., Rigby, S., Tyas, A., Fay, S., Reay, J., Warren, J., Gant, M., & Elgy, I. (2016). Reflected pressures from explosives buried in idealised cohesive soils.
- Colagrossi, A., & Landrini, M. (2003). Numerical simulation of interfacial flows by smoothed particle hydrodynamics. *Journal of computational physics*, 191(2), 448–475.
- Cundall, P. A., & Strack, O. D. L. (1979). A discrete numerical model for granular assemblies. *geotechnique*, 29(1), 47–65.
- Das, B. M., & Sobhan, K. (2014). *Principles of geotechnical engineering, si edition*. Cengage Learning.
- Davies, R. M. (1948). A critical study of the hopkinson pressure bar. *Philosophical Transactions of the Royal Society of London. Series A, Mathematical and Physical Sciences*, 240(821), 375–457.
- Dogyun, O., & Brandes, H. G. (2020). High strain damping for sands from load-controlled cyclic tests: Correlation between stored strain energy and pore water pressure. *Soil Dynamics and Earthquake Engineering*, 134, 106134.
- Eremeyev, V. A., Balandin, V. V., Balandin, V. V., Bragov, A. M., Konstantinov, A. Y., & Igumnov, L. A. (2023). Experimental study and numerical simulation of the dynamic penetration into dry clay. *Continuum Mechanics and Thermodynamics*, 35(2), 457–469.
- Felice, C. W. (1986). *The response of soil to impulse loads using the split-hopkinson pressure bar technique*. AIR FORCE WEAPONS LAB KIRTLAND AFB NM.

- Felice, C. W., Brown, J. A., Gaffney, E. S., & Olsen, J. (1985). *Investigation into the high strain-rate behavior of compacted sand using the split-hopkinson pressure bar technique*. Air Force Inst. of Tech., Wright-Patterson AFB, OH (USA).
- Frew, D. J., Forrestal, M. J., & Chen, W. (2005). Pulse shaping techniques for testing elastic-plastic materials with a split hopkinson pressure bar. *Experimental mechanics*, 45(2), 186.
- Frew, D. J., Akers, S. A., Chen, W., & Green, M. L. (2010). Development of a dynamic triaxial kolsky bar. *Measurement Science and Technology*, 21(10), 105704.
- Gautam, T. P. (2018). Cohesive soils. In P. T. Bobrowsky & B. Marker (Eds.), *Encyclopedia of engineering geology* (pp. 161–162). Springer International Publishing.
- Gong, F.-Q., Si, X.-F., Li, X.-B., & Wang, S.-Y. (2019). Dynamic triaxial compression tests on sandstone at high strain rates and low confining pressures with split hopkinson pressure bar. *International Journal of Rock Mechanics and Mining Sciences*, 113, 211–219.
- Gorham, D. A. (1983). A numerical method for the correction of dispersion in pressure bar signals. *Journal of Physics E: Scientific Instruments*, 16(6), 477.
- Gray III, G. T. (2000). Classic split-hopkinson pressure bar testing. *ASM handbook, mechanical testing and evaluation*, 8, 462–476.
- Groenendyk, D., Ferré, T., Thorp, K., & Rice, A. (2015). Hydrologic-process-based soil texture classifications for improved visualization of landscape function. *PloS one*, 10, e0131299.
- Hagerty, M. M., Hite, D. R., Ullrich, C. R., & Hagerty, D. J. (1993). One-dimensional high-pressure compression of granular media. *Journal of Geotechnical Engineering*, 119(1), 1–18.
- Hendron, A. J. J., & Auld, H. E. (1969). Effect of soil properties on the attenuation of airblast-induced ground motions. pp 29-47 of *Proceedings of International Symposium on Wave Propagation and Dynamic Properties of Earth Materials held on August 23–25, 1967 at Albuquerque, New Mexico*. Triandafilidis, George E.(ed).
- Hopkinson, B. (1914). X. a method of measuring the pressure produced in the detonation of high, explosives or by the impact of bullets. *Philosophical Transactions of the Royal Society of London. Series A, Containing Papers of a Mathematical or Physical Character*, 213(497-508), 437–456.

- Horpibulsuk, S., Yangsukkaseam, N., Chinkulkijniwat, A., & Du, Y. J. (2011). Compressibility and permeability of bangkok clay compared with kaolinite and bentonite. *Applied Clay Science*, 52(1), 150–159.
- Houlsby, G. T. (1982). Theoretical analysis of the fall cone test. *Géotechnique*, 32(2), 111–118.
- Ihmsen, M., Bader, J., Akinci, G., & Teschner, M. (2011). Animation of air bubbles with sph. *International Conference on Computer Graphics Theory and Applications*, 2, 225–234.
- Jakkula, P., Ganzenmueller, G., Beisel, S., Rüttnick, P., & Hiermaier, S. (2021). The symmpact: A direct-impact hopkinson bar setup suitable for investigating dynamic equilibrium in low-impedance materials. *Experimental Mechanics*, 62.
- Karajan, N., Han, Z., Teng, H., & Wang, J. (2014). On the parameter estimation for the discrete-element method in ls-dyna®. *Proceedings of the 13th International LS\_DYNA Users Conference, Dearborn, MI, USA*, 8–10.
- Kolsky, H. (1963). *Stress waves in solids* (Vol. 21). Dover Publications.
- Kolsky, H. (1964). Stress waves in solids. *Journal of Sound and Vibration*, 1(1), 88–110.
- Krayterman, D., & Laboratory, D. A. R. (2022). Investigation of arbitrary lagrangian-eulerian (ale) modeling and alternative material formulations of roma plastilina ballistic clay using ls-dyna numerical model, 42.
- L'Eplattenier, P., & Caldichoury, I. (2016). A coupled 3d/2d axisymmetric method for simulating magnetic metal forming processes in ls-dyna. *7th International Conference on High Speed Forming, April 27th-28th 2016, Dortmund, Germany*.
- Li, K. S. O., Van Lerberghe, A., Barr, A. D., & Clarke, S. D. (2024a). Impact of partial lateral confinement on high-strain-rate behaviour of cohesive soils. *Submitted for publication in Experimental Mechanics*.
- Li, K. S. O., Van Lerberghe, A., Barr, A. D., & Clarke, S. D. (2024b). Split-Hopkinson pressure bar testing of water with partial lateral confinement. *Submitted for publication in Experimental Mechanics*.
- Li, X., Zhou, Z., Lok, T.-S., Hong, L., & Yin, T. (2008). Innovative testing technique of rock subjected to coupled static and dynamic loads. *International Journal of Rock Mechanics and Mining Sciences*, 45(5), 739–748.

- LSTC. (2021). *Ls-dyna keyword users manual*.
- Luo, H., Lu, H., Cooper, W. L., & Komanduri, R. (2011). Effect of mass density on the compressive behavior of dry sand under confinement at high strain rates. *Experimental mechanics*, 51(9), 1499–1510.
- Martin, B. E., Chen, W., Song, B., & Akers, S. A. (2009). Moisture effects on the high strain-rate behavior of sand. *Mechanics of Materials*, 41(6), 786–798.
- Martin, B. E., Kabir, M. E., & Chen, W. (2013). Undrained high-pressure and high strain-rate response of dry sand under triaxial loading. *International journal of impact engineering*, 54, 51–63.
- McDowell, G. R., Bolton, M. D., & Robertson, D. (1996). The fractal crushing of granular materials. *Journal of the Mechanics and Physics of Solids*, 44(12), 2079–2101.
- Mesri, G., & Feng, T. W. (2019). Constant rate of strain consolidation testing of soft clays and fibrous peats. *Canadian Geotechnical Journal*, 56(10), 1526–1533.
- Mishra, S., Chakraborty, T., & Basu, D. (2015). High strain rate stress-strain response of soils-a review. *Japanese Geotechnical Society Special Publication*, 3(2), 80–85.
- Murray, H. H. (2006). Chapter 5 kaolin applications. In H. H. Murray (Ed.), *Applied clay mineralogy* (pp. 85–109, Vol. 2). Elsevier.
- Niyamapa, T., Namikawa, K., & Salokhe, V. M. (1992). Soil failure under undrained quasi-static and high speed triaxial compression test. *Journal of terramechanics*, 29(2), 195–205.
- Oluwatuyi, O. E., Ojuri, O. O., & Khoshghalb, A. (2020). Cement-lime stabilization of crude oil contaminated kaolin clay. *Journal of Rock Mechanics and Geotechnical Engineering*, 12(1), 160–167.
- Onitsuka, K., Hong, Z., Hara, Y., & Yoshitake, S. (1995). Interpretation of oedometer test data for natural clays. *Soils and Foundations*, 35(3), 61–70.
- Pajak, M. (2011). Dynamic response of sfrc under different strain rates - an overview of test results.
- Pierce, S. J., & Charlie, W. A. (1990). *High-intensity compressive stress wave propagation through unsaturated sands* (tech. rep.). COLORADO STATE UNIV FORT COLLINS.



- Profizi, P., Combescure, A., & Ogawa, K. (2016). Sph modeling of adhesion in fast dynamics: Application to the cold spray process [Computational simulation of manufacturing processes]. *Comptes Rendus Mécanique*, 344(4), 211–224.
- Rees, S. (2013). Part one: Introduction to triaxial testing. *Published on the GDS website www.gdsinstruments.com*, 1, 1–4.
- Rigby, S., Fuller, B., & Tyas, A. (2018). Validation of near-field blast loading in ls-dyna.
- Shahrin, M. I., Abdullah, R. A., Jeon, S., & Sa'ari, R. (2019). Calibration of a uniaxial compression test for rock using the discrete element method in ls-dyna. *Technology*, 10(3), 2133–2142.
- Shibusawa, S., & Oida, A. (1992). Transient load test system for evaluating dynamic soil behavior hierarchies by differences in the period of motion. *Journal of Terramechanics*, 29(2), 161–171.
- Shin, Y. S., Lee, M., Lam, K. Y., & Yeo, K. S. (1998). Modeling mitigation effects of watershed on shock waves. *Shock and Vibration*, 5(4), 225–234.
- Song, B., & Chen, W. (2004). Dynamic stress equilibration in split hopkinson pressure bar tests on soft materials. *Experimental mechanics*, 44(3), 300–312.
- Stephens, R. C. (1970). *Strength of materials: Theory and examples*. Hodder Arnold.
- Tang, W. R., Zhu, Z. W., Fu, T. T., Zhou, Z. W., & Shangguan, Z. H. (2020). Dynamic experiment and numerical simulation of frozen soil under confining pressure. *Acta Mechanica Sinica*, 36, 1302–1318.
- Tyas, A., & Watson, A. J. (2001). An investigation of frequency domain dispersion correction of pressure bar signals. *International Journal of Impact Engineering*, 25(1), 87–101.
- Van Lerberghe, A., Li, K. S. O., Barr, A. D., & Clarke, S. D. (2024a). An open-source algorithm for correcting stress wave dispersion in split-Hopkinson pressure bar experiments. *Submitted for publication in Experimental Mechanics*.
- Van Lerberghe, A., Li, K. S. O., Barr, A. D., & Clarke, S. D. (2024b). High-strain-rate behaviour of cohesive soils. *Submitted for publication in Experimental Mechanics*.
- Varas, D., Lopez-Puente, J., Artero-Guerrero, J. A., & Pernas-Sanchez, J. (2017). Numerical modelling of fluid structure interaction using ale and sph: The hydrodynamic ram phenomenon. *11th European LS-DYNA Conference*.

- Veyera, G. E. (1994). Uniaxial stress-strain behavior of unsaturated soils at high strain rates. *Wright Laboratory Flight Dynamics Directorate, OH*.
- White, W. A. (1949). Atterberg plastic limits of clay minerals\*. *American Mineralogist*, 34(7-8), 508–512.
- Wu, X. J., & Gorham, D. A. (1997). Stress equilibrium in the split hopkinson pressure bar test. *Le Journal de Physique IV*, 7(C3), C3–91.
- Xu, J., & Wang, J. (2014). Interaction methods for the sph parts (multiphase flows, solid bodies) in ls-dyna. *Proceedings of the 13th International LS-DYNA Users Conference, Detroit, MI, USA*, 8–10.
- Yamamuro, J. A., Abrantes, A. E., & Lade, P. V. (2011). Effect of strain rate on the stress-strain behavior of sand. *Journal of Geotechnical and Geoenvironmental Engineering*, 137(12), 1169–1178.
- Yoshinaka, R., & Kazama, H. (1973). Micro-structure of compacted kaolin clay. *Soils and foundations*, 13(2), 19–34.
- Konstantinov, A. Y., Bragov, A. M., Igumnov, L. A., Eremeyev, V. A., Balandin, V. V., & Balandin, V. V. (2022). Experimental study and identification of a dynamic deformation model of dry clay at strain rates up to 2500 s<sup>-1</sup>. *Journal of Applied and Computational Mechanics*, 8(3), 981–995.



## **Chapter A**

# **Published work**

## **A.1 Introduction**

This appendix includes copies of published work, including papers submitted to academic journals and presented at international conferences.

## **A.2 Characterisation of cohesive soils under high-strain-rate via split-Hopkinson pressure bar**

*Li, K. S. O., Clarke, S. D. & Barr, A. D. (2024). Characterisation of cohesive soils under high-strain-rate via split-Hopkinson pressure bar. BSSM 17th International Conference on Advances in Experimental Mechanics (2023).*

Work was presented at BSSM 17th International Conference on Advances in Experimental Mechanics. Extended abstract for conference presentation is included for reference.

# Characterisation of cohesive soils under high-strain rate via split Hopkinson pressure bar

O. K. S. Li, S. D. Clarke and A. D. Barr

Department of Civil and Structural Engineering, The University of Sheffield, Sheffield, S1 3JD, UK

ksoli1@sheffield.ac.uk

## Abstract:

This paper presents the difficulties associated with high-strain rate testing on cohesive soils using the split Hopkinson pressure bar apparatus. Experimental testing reveals the intrinsic properties of cohesive soils like kaolin clay when subject to high-strain rate. Numerical approaches to modelling this behaviour is adopted using modern FEM techniques such as LS-DYNA. Various geometric techniques and material models have been investigated to determine the most suitable methods to simulate the high-strain effect on kaolin clay via split-Hopkinson pressure bar.

## Introduction:

The response of soils when subject to extreme loading is vital in developing constitutive models that can be employed to evaluate the effect of blast and fragmentation. While characterisation of soils such as sands and gravel have been extensively investigated, there exists a gap in research in high-strain rate effects in cohesive soils [1]. Cohesive soils such as kaolin clay are found all over the world and are typically classified as being fine-grained, and easily subject to deformation. This paper focuses on the investigation of the behaviour of kaolin clay when subject to split Hopkinson pressure bar (SHPB) tests, the effect will be analysed and the properties of kaolin clay under high-strain rate loading will be properly characterised. This will be coupled with numerical modelling to investigate the existing approaches to modelling SHPB testing and kaolin clay under high-strain rates.

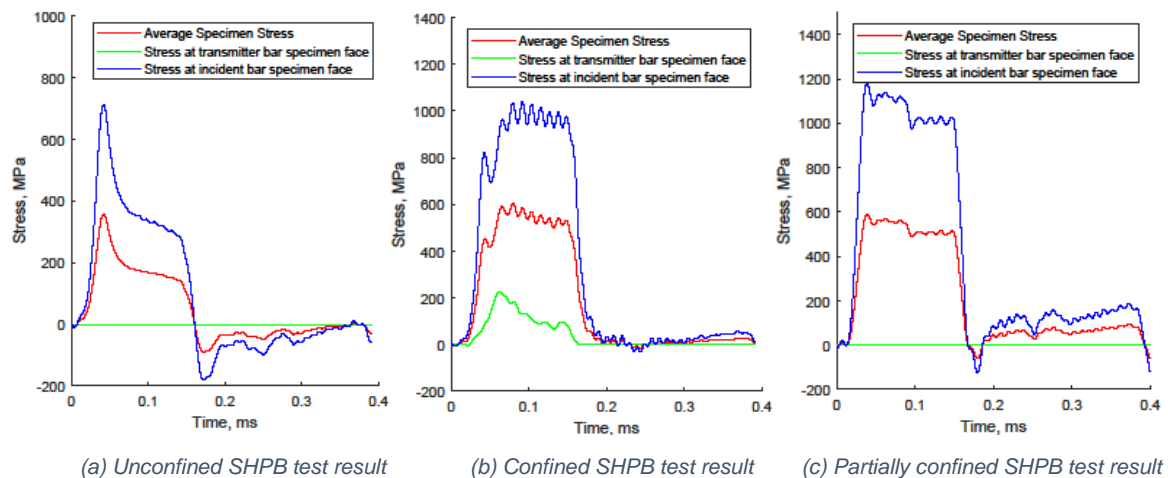


Figure 1: Stress over time of unconfined, confined, partially confined SHPB test on kaolin clay.

## Experimentation:

The split Hopkinson pressure bar (SHPB) is typically used to investigate material response at high-strain rates of up to  $10^4\text{s}^{-1}$  [2]. Experimental tests from unconfined SHPB tests reveal that upon impact, stress is transferred laterally rather than being propagated onto the transmitter bar as seen in Figure 1. The results show that it is an intrinsic property of kaolin to expand laterally rather than axially when subject to high-strain rate, this can be seen in Figure 2 which shows the moment the kaolin sample is ejected laterally from a SHPB test. This is due to the loading being taken via the pore water rather than the soil skeleton and hence behaving like a fluid when subject to compression.

Various forms of confinement methods were employed in SHPB tests to determine the effect under different scenarios. A ring confinement to prevent any lateral deformation, and a partially confined confinement method was utilised where a water reservoir was used to envelop the sample.

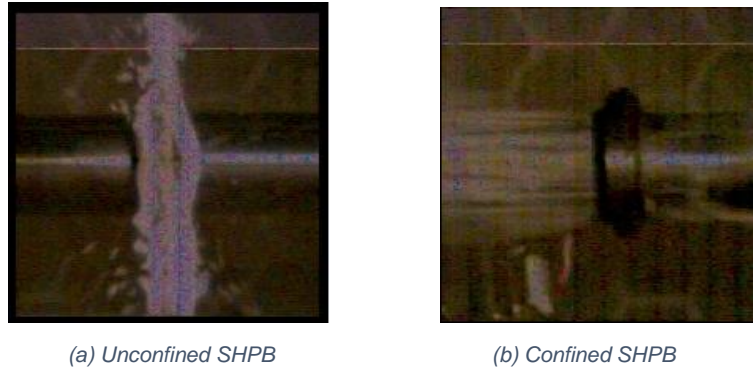


Figure 2: Images from high-speed camera of SHPB tests on kaolin clay samples.

### Numerical modelling:

The difficulties with accurately modelling the SHPB tests on kaolin clay are intrinsically linked to the fluid-like properties exhibited by kaolin clay when subject to high-strain rates as revealed from experimental testing. Numerous material models have been employed in existing research to model soil behaviour using LS-DYNA such as Soil and Foam, Pseudo-tensor etc. [3]. Subsequently, the Mohr-Coulomb material model was found to be the most appropriate due to the accessibility of the relevant parameters via triaxial testing and the material model not requiring an associated equation of state.

Various geometric techniques were tested and adapted to validate the Mohr-Coulomb model in modelling high-strain behaviour of kaolin clay in SHPB testing. Modelling the ring confinement setup proved difficult as the kaolin clay behaves like fluids upon impact, causing the sample to deform laterally and extrude from the ring confinement. Techniques such as use of arbitrary Lagrangian-Eulerian (ALE) elements, and smoothed particle hydrodynamics (SPH) methods to model the sample were tested (seen in Figure 3).

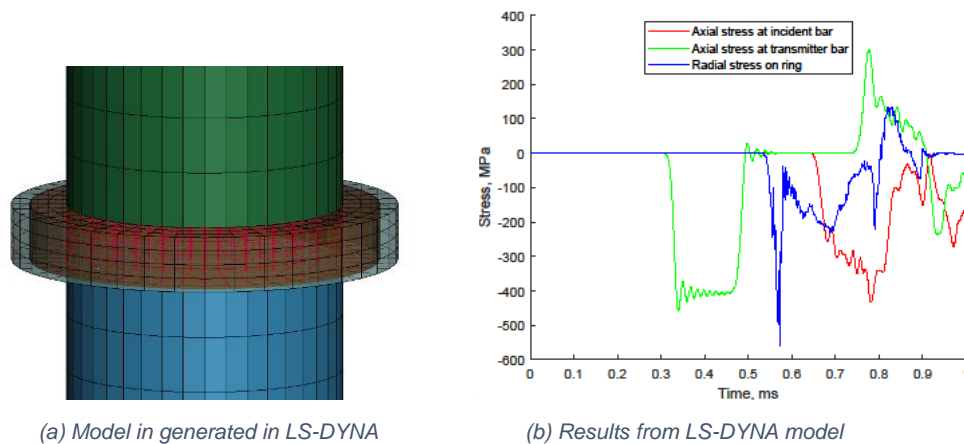


Figure 3: LS-DYNA model displaying sample confined SHPB model and stress results recorded from the model.

### Conclusion:

The characterisation of kaolin clay when subject to high-strain rates have been presented through SHPB experiments and further investigated by developing numerical models capable of simulating the behaviour under those conditions. The experimental tests reveal that kaolin clay tends to deform laterally when subject to immense loading, with behaviour comparable to fluids when placed under similar conditions. Subsequent numerical modelling using LS-DYNA was performed to validate the experimental results and to further investigate the effect on kaolin clay.

### References:

- [1] Sobczyk, K., Chmielewski, R., Kruszka, L. and Reucki, R. (2021). Strength Characterization of Soils' Properties at High Strain Rates Using the Hopkinson Technique—A Review of Experimental Testing. *Materials*, 15(1), p.274.
- [2] Kolsky, H. (1964), 'Stress waves in solids', *Journal of Sound and Vibration* 1(1), 88–110.
- [3] Busch, C.L. and Tarefder, R.A. (2016). Evaluation of Appropriate Material Models in LS-DYNA for MM-ALE Finite Element Simulations of Small-Scale Explosive Airblast Tests on Clay Soils. *Indian Geotechnical Journal*, 47(2), pp.173–186. doi:<https://doi.org/10.1007/s40098-016-0196-4>.

### **A.3 An open-source algorithm for correcting stress wave dispersion in split-Hopkinson pressure bar experiments**




*Van Lerberghe, A., Li, K. S. O., Barr, A. D., & Clarke, S. D. (2024). An open-source algorithm for correcting stress wave dispersion in split-Hopkinson pressure bar experiments. Submitted for publication in Experimental Mechanics*

Work detailing the dispersion correction capabilities and the implementation of the signal processing algorithm was submitted for publication to Experimental Mechanics. Journal paper is included as reference.



Article

# An Open-Source Algorithm for Correcting Stress Wave Dispersion in Split-Hopkinson Pressure Bar Experiments

Arthur Van Lerberghe , Kin Shing O. Li, Andrew D. Barr  and Sam D. Clarke \* 

School of Mechanical, Aerospace &amp; Civil Engineering, University of Sheffield, Sheffield S1 3JD, UK

\* Correspondence: sam.clarke@sheffield.ac.uk

**Abstract:** Stress wave dispersion can result in the loss or distortion of critical high-frequency data during high-strain-rate material tests or blast loading experiments. The purpose of this work is to demonstrate the benefits of correcting stress wave dispersion in split-Hopkinson pressure bar experiments under various testing situations. To do this, an innovative computational algorithm, `SHPB_Processing.py`, is created. Following the operational run through of `SHPB_Processing.py`'s capabilities, it is used to process test data acquired from split-Hopkinson pressure bar tests on aluminium, sand and kaolin clay samples, under various testing conditions. When comparing dispersion corrected and simple time shifting data obtained from SHPB experiments, accounting for dispersion removes spurious oscillations and improves the inferred measurement at the front of the specimen. The precision of the stress and strain results gathered from its application emphasises its importance through the striking contrast between its application and omission. This has a significant impact on the validity, accuracy and quality of the results. As a result, in the future, this tool can be utilised for any strain rate testing situation with cylindrical bars that necessitates dispersion correction, confinement, or stress equilibrium analysis.

**Keywords:** signal processing; dispersion correction; high-strain-rate testing; stress waves; split-Hopkinson pressure bar; material applications; open-source algorithm



Academic Editors: Tadeusz Stepinski, Meho-Saša Kovačević, Mario Bačić, Kenneth Gavin and Vassilis Marinou

Received: 12 November 2024

Revised: 21 December 2024

Accepted: 26 December 2024

Published: 6 January 2025

**Citation:** Van Lerberghe, A.; Li, K.S.O.; Barr, A.D.; Clarke, S.D. An Open-Source Algorithm for Correcting Stress Wave Dispersion in Split-Hopkinson Pressure Bar Experiments. *Sensors* **2025**, *25*, 281. <https://doi.org/10.3390/s25010281>

**Copyright:** © 2025 by the authors. Licensee MDPI, Basel, Switzerland. This article is an open access article distributed under the terms and conditions of the Creative Commons Attribution (CC BY) license (<https://creativecommons.org/licenses/by/4.0/>).

## 1. Introduction

Traditionally, a Hopkinson pressure bar (HPB) is used to quantify a transitory pulse generated by the impact of near-field blast events or bullets. The split-Hopkinson pressure bar (SHPB), also known as the Kolsky bar, has been widely utilised to measure dynamic material properties such as stress–strain and strain rate–strain curves of versatile materials at a strain rate ranging from  $10^2$  to  $10^4$  s<sup>-1</sup>. The shape of the elastic wave in SHPB and HPB distorts as it travels; this phenomenon is referred to as dispersion [1].

From the standpoint of medium particle motion, the physical origin of dispersion is inertia in the lateral motion associated with the axial disturbance. From the standpoint of wave propagation, a high-frequency wave component that constitutes the total elastic wave is slower than a lower-frequency wave component [2].

The wave profile is typically assessed at the interim axial position of the bar, using strain gauges. In the case of the HPB, the front surface of the bar is the location of interest where an impact pulse enters the bar, whereas in the case of the SHPB, the specimen location is of interest. Consequently, the measured wave profiles in HPB and SHPB must be corrected to obtain the wave profiles at the locations of interest, a procedure known as dispersion correction [1,3].

The one-dimensional wave theory assumes that all longitudinal waves in the bar travel at a constant velocity,  $c_0$ . It also assumes that transverse cross sections of the bar remain flat and that stresses are uniformly distributed across these sections. However, as the wave moves along the bar, it causes radial expansion and contraction due to axial strains, influenced by the bar's Poisson's ratio. This radial motion disturbs the stress distribution across the bar's cross section, resulting in the distortion of plane sections [2].

The effect of this deviation from the idealised conditions is evident in the three-dimensional wave equations developed by Pochhammer [4] and Chree [5], which were later applied by Bancroft [6] to longitudinal waves in a cylindrical bar. Instead of propagating uniformly at a velocity  $c_0$ , longitudinal waves were shown to propagate at a specific velocity  $c_\omega$ , which depends on the wavelength, the bar's diameter, the one-dimensional wave speed, and Poisson's ratio as described in Equation (1):

$$(x - 1)^2 \varphi(ha) - (\beta x - 1)[x - \varphi(\kappa a)] = 0 \quad (1)$$

where

$$\begin{aligned} \beta &= (1 - 2\nu)/(1 - \nu) \\ x &= (c_\omega/c_0)^2(1 + \nu) \\ h &= \gamma(\beta x - 1)^{\frac{1}{2}} \\ \kappa &= \gamma(2x - 1)^{\frac{1}{2}} \\ \varphi(y) &= yJ_0(y)/J_1(y) \end{aligned}$$

and where  $c_\omega$  is the phase velocity,  $c_0$  is the one-dimensional elastic wave velocity,  $a$  is the bar radius,  $\nu$  is the Poisson's ratio,  $\gamma$  is the wave number,  $2\pi/\lambda$ ,  $\lambda$  is the wave length, and  $J_n(\ )$  is the Bessel function of the first kind, of the order  $n$ .

This equation has an infinite number of solutions, each corresponding to a specific propagation mode in the bar, with the first modes illustrated in Figure 1. This implies that low-frequency waves propagate at a velocity approximately equal to  $c_0$ , but the phase velocity decreases as the frequency increases, particularly when the wavelength approaches the bar's diameter.

The complex waveforms generated during an SHPB experiment encompass a broad range of frequency components. Due to this frequency dependence, stress disperses as it travels along the bar. This phenomenon is illustrated in Figure 2, which shows the dispersion of a trapezoidal wave in a stainless-steel pressure bar. The dispersion of the stress pulse is accompanied by frequency-dependent variations in stress and strain across the bar's cross section [7]. As shown in Figure 3, when the frequency of the forcing function increases, the strains recorded on the bar surface become smaller compared to those measured at the bar's axis. These effects on phase velocity and amplitude mean that a strain signal recorded at the surface of the bar may not accurately represent the mean strain and stress at the bar face in contact with the specimen, some distance away.

Standard practice, as discussed by Gray III [8] in the ASM handbook, assumes that simply time shifting all the signals collected from SHPB testing is a suitable strategy; however, this method can result in severe errors and inaccuracies.

Previous work by Shin [1,3,9] developed dispersion-related MATLAB and Excel scripts to process SHPB test data. These algorithms focused on phase velocity corrections but not amplitude correction. While useful for many applications, experiments with high-frequency components, or a large diameter, will experience significant stress and strain variation over the bar cross section, making amplitude correction desirable for accurately evaluating specimen behaviour [10].

The current work seeks to develop an algorithm capable of solving the issues associated with dispersion in SHPB experiments. To accomplish this, the key theory of dispersion correction, stress wave equilibrium and confinement analysis in SHPB experiments is addressed first. Then, the aforementioned tool, `SHPB_Processing.py`, is presented with all its functionalities and subroutines. Finally, it is applied to SHPB test data collected, demonstrating its practical importance.

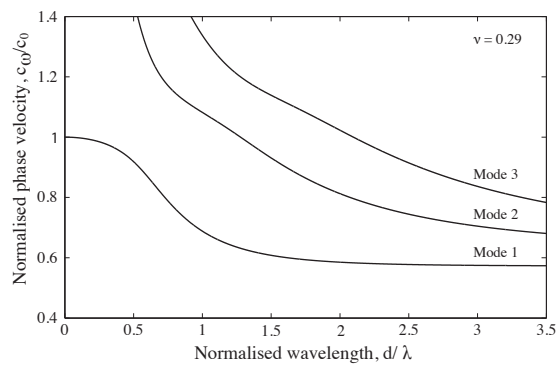


**Figure 1.** Relationship of phase velocity to wavelength for the first 3 modes of propagation of a longitudinal wave in a stainless-steel cylindrical bar for  $\nu = 0.29$  [7].

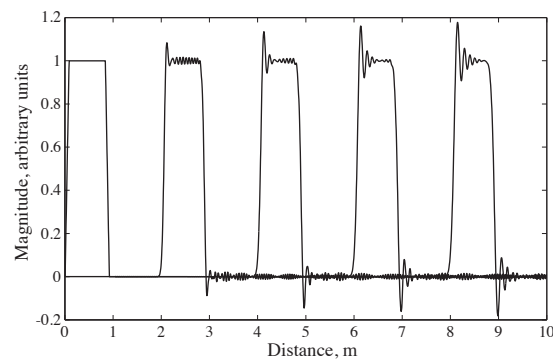


**Figure 2.** Dispersion of a trapezoidal wave in a cylindrical stainless-steel pressure bar, with recordings at 2 m increments [7].

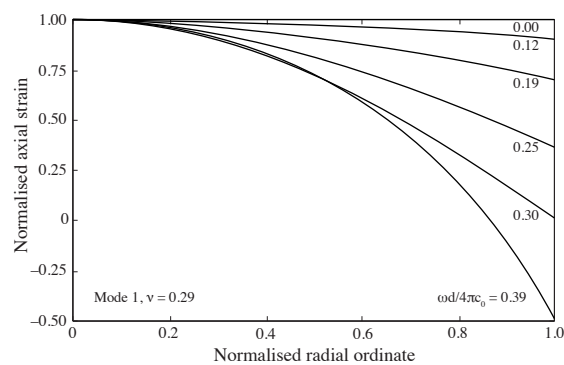


**Figure 3.** Distribution of axial strain over a stainless-steel ( $\nu = 0.29$ ) bar cross section for an infinite duration single frequency forcing function [7], after [11].

## 2. Dispersion Correction in SHPB Experiments

At higher frequencies ( $a/\lambda > 0.05$ ), the errors mentioned above become considerable, but they can be addressed using the method outlined by Tyas and Pope [10], where corrections are applied to the amplitudes and phase angles of each frequency component of the signal.

### 2.1. Phase Angle Correction

The first correction made to the SHPB signals is the adjustment of the phase angle to account for the dispersion of each frequency component over the distance between the strain gauge and the bar end. This is accomplished, according to Gorham [12] and Follansbee and Frantz [13], by computing the phase velocity  $c_\omega$ , of each component using Bancroft's [6] equation (Equation (1)) and then applying a phase shift,  $\theta'_\omega$  as portrayed in Equation (2):

$$\theta'_\omega = \left( \frac{c_0}{c_\omega} - 1 \right) \frac{\omega z}{c_0} \quad (2)$$

where  $\omega$  is the component's angular frequency, and  $z$  is the distance over which the correction is performed, positive in the direction of wave propagation.

Barr et al. [14] conducted tests to understand how energy is distributed between higher modes of propagation, concluding that the frequency content in common SHPB experiments only requires consideration of the first mode of propagation.

### 2.2. Amplitude Correction

The second correction to the SHPB signals involves applying factors to the amplitude of the frequency components. Tyas and Watson [11] established the factors  $M_1$  and  $M_2$  to account for the radial variation of strain and Young's modulus, respectively, derived from Davies' [15] investigation of these radial effects. Using these factors, the strain measurement obtained on the bar's surface can be utilised to calculate the mean axial stress and strain acting over the entire cross section. In a SHPB experiment, phase angle (dispersion) correction transforms a bar surface measurement at the strain gauge to a bar surface measurement at the specimen interface; the amplitude correction transforms this bar surface measurement into the mean strain and stress experienced across the face of the specimen.

The factors are defined in Equations (3) and (4) as follows:

$$M_1 = \frac{2 \left( 1 + \frac{1-\beta x}{x-1} \right)}{\varphi(ha) + \frac{1-\beta x}{x-1} \varphi(\kappa a)} \quad (3)$$

$$M_2 = E \left( \frac{c_\omega}{c_0} \right)^2 \quad (4)$$

where details of the variables in Equations (3) and (4) are the same as in Equation (1), with  $E$  being the Young's modulus.

Figure 4 shows the fluctuation in  $M_1$  and  $M_2$  with normalised wavelength for a stainless-steel bar with a Poisson's ratio of 0.29. Due to the discontinuity in  $M_1$  at  $a/\lambda = 0.375$ , which corresponds to the point where the strain recorded on the surface of the bar falls to zero, the reciprocal of  $M_1$  is displayed; at even higher frequencies, the recorded strain has the opposite sign to the mean cross-sectional response. As the adjustments applied at  $a/\lambda = 0.375$  require multiplying a low-magnitude signal by a very large

correction factor, noise in the signal is likely to affect the accuracy of the result significantly. This effectively establishes an upper limit on the frequency range that can be corrected: according to Tyas and Watson [11], the approach can be used at normalised wavelengths below  $a/\lambda \approx 0.3$ .

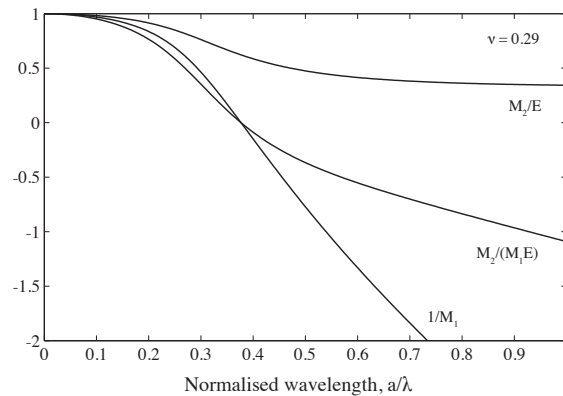


**Figure 4.** Variation in factors  $M_1$  and  $M_2$  in a cylindrical stainless-steel bar for  $\nu = 0.29$  [7].

### 3. SHPB\_Processing.py

SHPB\_Processing.py is an open-source Python algorithm for high-strain-rate SHPB signal processing. This function includes a subroutine titled dispersion.py that is optimised to process raw signal strain data using dispersion correction (Section 4).

This function, SHPB\_Processing.py, is designed to take strain gauge input data from high-strain-rate SHPB tests and, by specifying the additional input variables defined in Table 1, determine the axial and radial (if confinement specified) stress developments of the sample, its strain and strain rate history variations through impact, and other related parameters derived from these output variables.

The following command line is necessary to run this algorithm:

```
SHPB_Processing (csv_path, sample_data, confinement, signal_channels,
                 signal_amp, disp_correction, alignment, speedtrap)
```

The optimal approach to running this function is detailed below, with Figure 5 depicting this as a concise flowchart:

1. Calculate stress wave speed and gauge factors of the cylindrical bars used for SHPB testing using the gauge\_factor.py script, available on [GitHub](#) and [ORDA](#) [16].
2. Use phase\_velocity.py to calculate the dispersion factors required to perform the dispersion correction of the collected SHPB signals using dispersion.py based on the material properties of the cylindrical bar used for SHPB testing. The algorithm phase\_velocity.py is available on [GitHub](#) and [ORDA](#).
3. The algorithm SHPB\_Processing.py is ready to be run, with dispersion.py, to effectively process the SHPB test data with dispersion correction, based on the input parameters chosen. The results are returned in a designated processed data folder. Dispersion.py is available on [GitHub](#) and [ORDA](#).

The full source code for SHPB\_Processing.py is available on [GitHub](#) and [ORDA](#) [17].

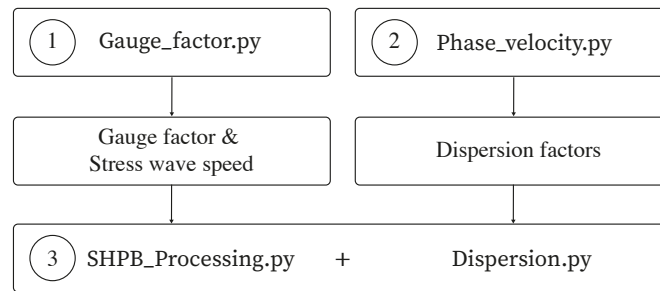


**Figure 5.** Flowchart illustrating the steps to run SHPB\_Processing.py efficiently.

**Table 1.** Input and output variables used in SHPB\_Processing.py.

Inputs	Description
csv_path	File directory containing CSV file with raw test data.
sample_data	Array containing the initial length, mass, and dry mass of the sample, i.e., [initial length, mass, dry mass].
confinement	Confinement mechanism applied, i.e., 'None', 'Ring', or 'Reservoir'.
signal_channels	Oscilloscope channel numbers used to record raw data, i.e., [in_bar_gauge_channel, out_bar_gauge_channel, ring_gauge_channel or reservoir_gauge_channel].
signal_amp	Strain gauge amplification applied to strain gauge measurement, i.e., [in_bar_gauge_amp, out_bar_gauge_amp, ring_gauge_amp].
disp_correction	Apply dispersion correction or simple time shift processing for signal data, i.e., "True" for dispersion correction using dispersion.py.
alignment	Specify alignment mode for aligning stress waves at sample interfaces, i.e., 'start' aligns the start of incident and transmitted pulse, 'end' aligns the end, and 'mid' aligns the median time of the pulse. Integer/float values greater than 1 align the peaks of the incident and transmitted pulse to specific times. Float values between 0 and 1 align the incident and transmitted pulse on a specific fraction of the max value.
speedtrap	Specify speed trap data to determine striker bar velocity, i.e 'True' for speed trap velocity calculation.
Outputs	Description
Processed data folder	Folder with all the CSV processed data files, and test log for history monitoring.

The function's operation can be summarised as follows:

1. The oscilloscope data from SHPB strain gauges are read.
2. The striker bar velocity is determined based on the raw speed trap data.
3. The raw data file is prepared for correction and confinement analysis via pulse detection and signal reformatting.
4. The correction ('True' for dispersion correction, or 'False' for simple time shift) and confinement ('None', 'Ring' or 'Reservoir') requirements are applied on the strain data collected based on the input specifications.
5. The incident, reflected, and transmitted pulses are detected using the trigger and wave speed propagation in the bars used during SHPB testing.
6. The pulse end is marked when the sample strain reaches its maximum.
7. The dispersion-corrected stresses and strains for each wave are calculated using dispersion.py, the details of which are present below. For simple time shifting, simple signal restructuring is conducted.
8. The axial stresses and strains in the specimen are calculated using the incident, reflected, and transmitted wave signals.
9. Based on the strain gauge strain, the sample strain is determined from the displacement of the pressure bars.

10. Based on the confinement type selected, 'None', 'Ring', or 'Reservoir', the following will happen:
  - (a) For a SHPB test with 'None' as the confinement type, no radial stresses or strains are calculated for the specimen.
  - (b) For a SHPB test with 'Ring' as the confinement type, using thick-walled pipe theory, the radial stress and strain in the specimen are calculated from the circumferential strain in the ring.
  - (c) For a SHPB test with 'Reservoir' as the confinement type, pressure data collected from the gauge in the reservoir are used to calculate the specimen's radial stress and strain.
11. The specimen density and dry density are calculated for the 'Ring' and 'Reservoir' confinement types.
12. All results are saved as csv files into the Processed data folder, along with the test log.

## 4. Dispersion.py

### 4.1. A Python Function for Dispersion Correction

`Dispersion.py` is an open-source Python algorithm that has been developed to automate the application of phase-angle and amplitude corrections to SHPB signals as part of the main processing of `SHPB_Processing.py`. This substitutes basic time shifting of signals with manipulation of individual frequency components. The capabilities of this function are described in this section, with the complete source code for `dispersion.py` and its accompanying subroutine available on [GitHub](#) and [ORDA](#) [18].

### 4.2. Frequency Domain in Python

The fast Fourier transform (FFT) is an algorithm used to convert a signal into the frequency domain. This technique portrays a signal as the sum of a sequence of sinusoidal waves of varying frequencies and amplitudes. FFT is implemented in Python using the `numpy` library and `fft` function, which takes any regularly sampled signal and returns amplitude and phase information with frequency as a matrix of complex vectors of the form  $z = z_r + iz_i$ . At a given frequency, amplitude  $A$  (Equation (5)) and phase angle  $\theta$  (Equation (6)) of the Fourier component are calculated as

$$A = \sqrt{z_r^2 + z_i^2} \quad (5)$$

$$\theta = \tan^{-1}\left(\frac{z_i}{z_r}\right) \quad (6)$$

These relationships are illustrated in Figure 6a, where  $z$  and its complex conjugate  $\bar{z}$  are represented in the complex plane, and in Figure 6b, where these values are utilised to represent the amplitude and phase angle of a specific sinusoid.

The Fourier component can be reconstituted using the relationship in Equation (7) once suitable corrections have been applied to the amplitude and phase angle as seen below:

$$z = A \cos(\theta) + iA \sin(\theta) = Ae^{i\theta} \quad (7)$$

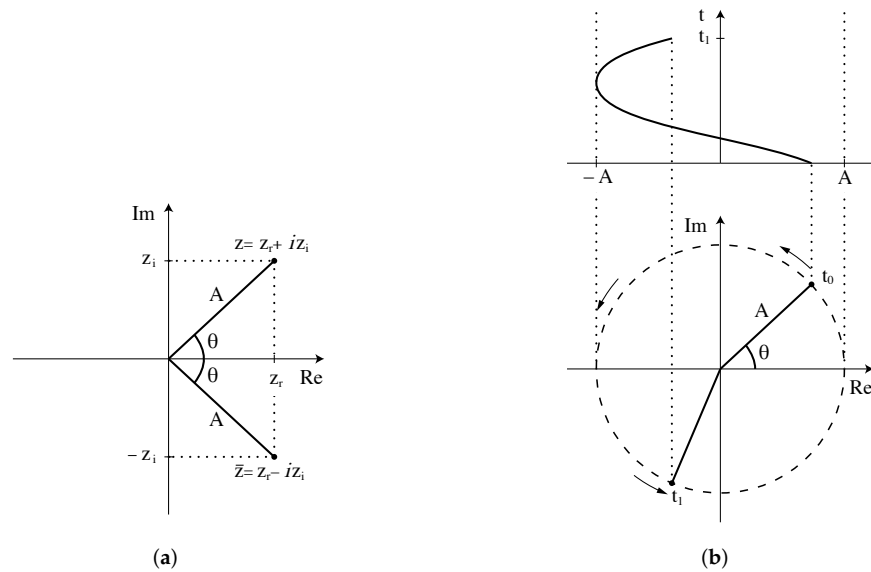


**Figure 6.** A Fourier component  $z$  in the complex plane with (a) relationship to amplitude and phase angle and (b) description of a sinusoid [7].

#### 4.3. Correction Bandwidth

The FFT is an algorithm to efficiently compute the discrete Fourier transform (DFT) of a signal. The DFT calculates frequency components at a finite number of values, which depend on the original signal's sampling rate and length. If a signal is sampled  $N$  times at a frequency  $f$ , the lowest readable frequency is equal to  $f/N$ , describing a single wave occupying the sampling window (Figure 7a). Higher frequencies are multiples of the fundamental frequency, all the way up to the highest readable frequency, or Nyquist frequency, which equates to  $f/2$  (Figure 7b). This limit is set because at least two samples are necessary for each period to prevent aliasing as shown in Figure 7c. Due to undersampling, two different sinusoids can be fitted to the sample data. The oscilloscope's sample rate ( $f/2 = 500$  kHz in the current tests) limits the highest readable frequency, although the frequency resolution can be improved by raising  $N$ , either by increasing the recording duration, or by zero-padding the input signal.

The `fft` function will generate an  $N$ -length frequency domain vector  $X(\omega)$ , given an  $N$ -length time-domain vector  $x(t)$ . As a result of the aliasing explained above, the second half of  $X(\omega)$  is the complex conjugate of the first half, reflected about the Nyquist frequency as seen in Figure 8. This means that modifications only need to be individually applied to the first  $N/2 + 1$  bins in  $X(\omega)$ , which may then be reflected to complete the vector.

As stated in Section 2.2, the very low strain signals measured on the surface of the bar at wavelengths below  $a/\lambda \approx 0.3$  impose an additional frequency limit. For example, for a 25 mm diameter stainless-steel bar, adjustments can only be successfully made between 39  $\mu$ Hz and 94 kHz in the current SHPB setup. Figure 9 depicts a frequency domain portrayal of a typical experimental incident pulse in the form of a modified periodogram. Power is measured in logarithmic units, with a change of 10 dB denoting an order of magnitude shift in the power of the signal. The periodogram, as explained above, indicates that the power of the signal recorded on the surface of the bar rapidly decreases to zero between 94 kHz and 110 kHz. Since dispersion correction can only be implemented at frequencies below 94 kHz, for this setup, the signal is sent through a low-pass filter to remove the higher frequencies.



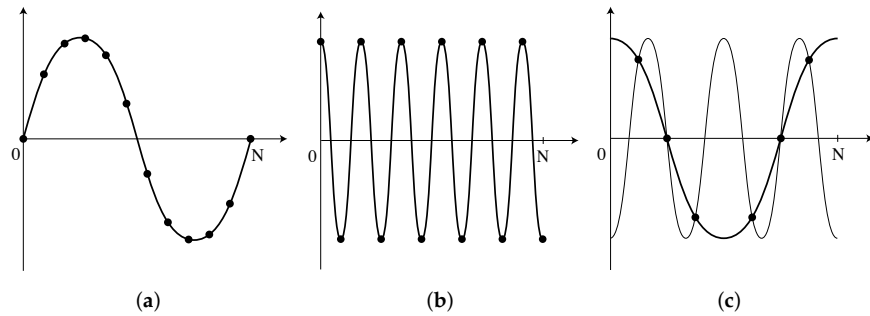


**Figure 7.** Frequency limitations in the FFT: (a) minimum readable frequency, where a single wave-length occupies the full sampling window, (b) maximum readable frequency, with only two samples per period, and (c) aliasing at higher frequencies, where multiple sinusoids can fit the same data [7].

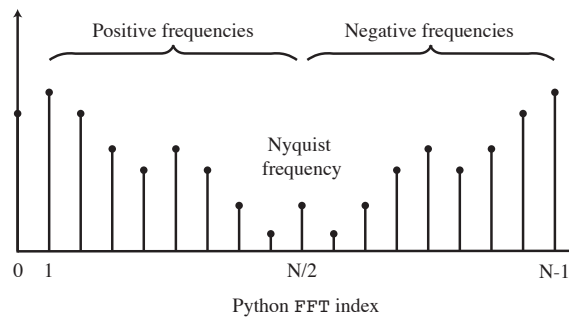


**Figure 8.** Composition of the frequency domain vector produced by `fft` in Python. The highest readable frequency is the Nyquist frequency,  $N/2$ . The second half of the vector represents the complex conjugate of the values in the first half [7].

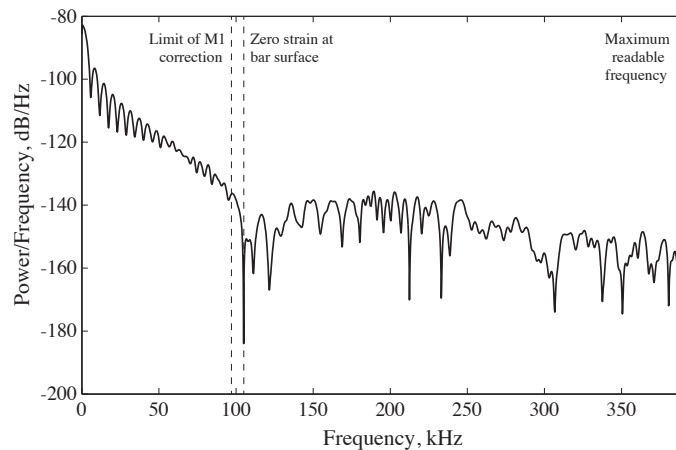


**Figure 9.** Power spectral density for experimental incident wave, from a 25 mm stainless-steel bar with a Poisson's ratio of 0.29, and maximum frequency limits imposed by the strain gauge data and FFT [7].

In Figure 10, the power at these frequencies is orders of magnitude smaller, and so little information is lost during filtering.

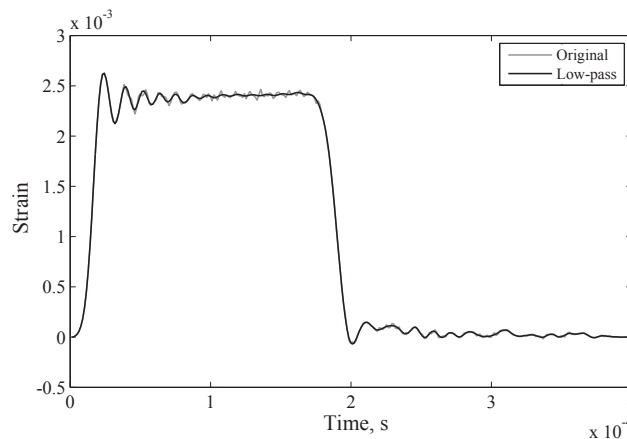


**Figure 10.** This experimental setup’s incident wave and result of low-pass filtering of frequencies above 94 kHz [7].

#### 4.4. Operation of *dispersion.py*

When the option for dispersion correction is selected in *SHPB\_Processing.py*, the open-source Python algorithm *dispersion.py* is called as a subroutine during the processing of the SHPB signals collected from testing.

The function *dispersion.py* was created to automate the application of phase angle and amplitude correction factors generated by *dispersion\_factors.py*, to SHPB pressure bar signals obtained from the experiments, manipulating the frequency components and correcting the effects of dispersion over a specified propagation length.

The programme *dispersion\_factors.py* is a mandatory subroutine of *dispersion.py*. After isolating the incident, reflected, and transmitted waves, *dispersion.py* is used to infer the stress and strain at the bar–specimen interface for each wave using the following command, which includes the input and output variables defined in Table 2. Values for  $\nu$  may be found from mill specification sheets, and  $c_0$  from the strain measurements of a low-frequency content wave oscillating in a bar of a known length. Alternatively, these can be calculated using an iterative method, such as that developed in Shin [1].

The following command line is necessary to run this algorithm:

$$\text{dispersion}(x, fs, a, c_0, E, z)$$

**Table 2.** Input and output variables used in *dispersion.py*.

Inputs	Description
$x$	Zero-padded strain signal in time domain (1xN numeric).
$fs$	Sampling frequency, Hz.
$a$	Bar radius, m.
$c_0$	One-dimensional wave velocity of the bar, m/s.
$E$	Young’s modulus of the bar, GPa.
$z$	Distance to apply correction over, positive in direction of propagation, m.
Outputs	Description
$x\_strain$	Dispersion-corrected strain signal.
$x\_stress$	Dispersion-corrected stress signal, MPa

This subroutine adapts Tyas and Pope’s [10] dispersion correction approach to ensure that the inferred axial stress and strain data accurately depict the specimen behaviour.

The function's operation can be summarised as follows:

1. FFT is used to convert the strain signal to a frequency domain signal.
2. The frequency components above the  $M_1$  correction cut-off are removed using an ideal low-pass filter.
3. Below the Nyquist frequency, for each of the remaining components, the following hold:
  - (a) The `dispersion_factors.py` function is used to calculate the required phase shift as well as the factors  $M_1$  and  $M_2$ . To reduce the computation time, this method employs a pre-calculated, normalised look-up table generated by `phase_velocity.py`.
  - (b) The amplitude correction factor  $M_1$  and the phase angle correction  $\theta'_\omega$  are used to rebuild a dispersion-corrected strain component using the exponential form of the Fourier series shown in Equation (7) as shown below in Equation (8):

$$z_\epsilon = M_1 A e^{i(\theta - \theta'_\omega)} \quad (8)$$

where  $A$  is the original amplitude of the component, and  $\theta$  is the original phase angle.

- (c) A dispersion-corrected stress component is similarly reconstructed using factors  $M_1$  and  $M_2$ , as well as phase angle correction  $\theta'_\omega$  as illustrated in Equation (9) below:

$$z_\sigma = M_1 M_2 A e^{i(\theta - \theta'_\omega)} \quad (9)$$

4. Frequency components above the Nyquist frequency are formed by taking the complex conjugate of these adjusted stress and strain components.
5. The frequency domain stress and strain signals are transformed back to the time domain using inverse FFT `ifft()` from the `numpy` library and returned as output variables `x_strain` and `x_stress`.

These corrected pressure bar stresses and strains are used in `SHPB_Processing.py` to infer the behaviour of the SHPB specimen.

#### 4.5. Operation of `dispersion_factors.py`

The Python algorithm, `dispersion_factors.py`, is a subroutine of the programme `dispersion.py`. The dispersion factors utilised in this script are calculated using the algorithm `phase_velocity.py`, with a Poisson's ratio of 0.29, which is based on the property of the Hopkinson bars used for testing in this case.

Afterwards, `dispersion_factors.py` loads the four dispersion factor files, `m1`, `m2`, `norm_freqs` and `v_ratios`, before calculating the amplitude and phase angle corrections required to account for the dispersion at a specific frequency.

The following command line is necessary to run this algorithm, with details of the input and output variables outlined in Table 3:

```
dispersion_factors (f, a, c0, z)
```

The corrected `angle_mod` and `m1` and `m2` factors are then used in `dispersion.py` to apply the appropriate signal phase shift to obtain the adjusted strain and stress. It was inspired by a MATLAB script created by Barr [19].

**Table 3.** Input and output variables used in `dispersion_factors.py`.

Inputs	Description
f	Frequency, Hz.
a	Bar radius, m.
c0	One-dimensional wave velocity of the bar, m/s.
z	Distance to apply correction over, m.
Outputs	Description
angle_mod	Phase angle correction, rad.
m1	Correction for variation in response across bar cross section.
m2	Correction for variation in ratio of axial stress and axial strain (dynamic Young's modulus).

#### 4.6. Operation of `phase_velocity.py`

`Phase_velocity.py`, is an independent open-source function available on [GitHub](#) and [ORDA](#) [20]. Its objective is to find the first root of Bancroft's equation [6] using the bisection method, for a defined Poisson's ratio, and over a defined range of normalised wavelength ( $d/L$ ). The result is normalised phase velocity  $c_p/c_0$ , which corresponds to the first mode of propagation for longitudinal waves in an elastic cylindrical bar.

Normalised wavelengths are also converted to normalised frequency,  $fa/c_0$ . Normalised phase velocities are then used to calculate Tyas and Wilson's [11] factors  $M_1$  and  $M_2$ , which account for wavelength-dependent radial variations in the strain and Young's modulus, respectively.

The following command line is necessary to run this algorithm, with details of the input and output variables outlined in Table 4:

```
phase_velocity (nu, l_ratios)
```

**Table 4.** Input and output variables used in `phase_velocity.py`.

Inputs	Description
nu	Poisson's ratio of bar material used for SHPB tests.
l_ratios	Normalised wavelength range to calculate the first root of Bancroft's(1941) equation [6].
Outputs	Description
dispersion_factors	Folder which includes 4 .pickle files containing the dispersion factors m1, m2, norm_freqs and v_ratios.

The factors m1, m2, norm\_freqs and v\_ratios are then used in `dispersion_factors.py` and `dispersion.py` by association to carry out the dispersion correction of the acquired SHPB signals as a functionality of the main processing script `SHPB_Processing.py`. It was inspired by a MATLAB script created by Barr [21].

## 5. Practical Applications

### 5.1. SHPB Testing

A split-Hopkinson pressure bar apparatus consisting of two stainless-steel pressure bars, incident and transmitted bars, was utilised for testing (Figure 11). The gauge locations on the incident and transmitter bars required to process the data were placed at a distance of 1000 mm and 500 mm, respectively, from the sample front and back interfaces. On each bar, a pair of Kyowa KSP-2-120-E4 semiconductor strain gauges was used to record the signals.

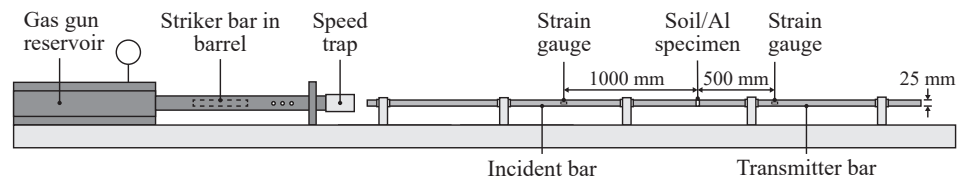


**Figure 11.** Schematic diagram of the SHPB setup for testing.

### 5.2. Kaolin Clay

A 25 mm kaolin clay sample was tested using a SHPB apparatus configuration detailed in Section 5.1 under unconfined conditions. The sample had an initial length of 5.357 mm, a mass of 4.466 g and a dry mass of 3.167 g. The raw signal data for the incident and transmitter bars were recorded on channels 7 and 8. The incident and transmitter bars were amplified by a factor of 10 and 100, respectively. Dispersion correction was applied. The signals were aligned at the start, and the speed of the striker bar was measured. The data were processed using `SHPB_Processing.py` with the following command line:

```
SHPB_Processing (csv file, [5.357, 4.466, 3.167], 'None', [7, 8, 5],
                 [10, 100, 1], True, 'start', True)
```

### 5.3. Sand

A 25 mm medium sand sample was tested using a SHPB apparatus configuration detailed in Section 5.1 under confined conditions. The sample had an initial length of 4.726 mm, a mass of 3.50 g and a dry mass of 3.50 g. The raw signal data for the incident and transmitter bars were recorded on channels 1 and 2. The raw signal for the confining ring was measured on channel 3. The incident and transmitter bars were amplified by a factor of 10. Dispersion correction was applied. The signals were aligned at the start, and the speed of the striker bar fired by the gas gun was measured. The data were processed using `SHPB_Processing.py` with the following command line:

```
SHPB_Processing (csv file, [4.726, 3.50, 3.50], 'Ring', [1, 2, 3],
                 [10, 10, 1], True, 'start', True)
```

### 5.4. Aluminium

A 12 mm aluminium sample was tested using the SHPB apparatus configuration detailed in Section 5.1 under unconfined conditions. The sample had an initial length of 5.000 mm, a mass of 1.530 g and a dry mass of 1.530 g. The raw signal data of the incident bars were recorded on channels 1 and 2. The incident and transmitter bars were amplified by a factor of 1. Dispersion correction was applied. The signals were aligned at the start, and the speed of the striker bar was not measured. The data were processed using `SHPB_Processing.py` with the following command line:

```
SHPB_Processing (csv file, [5.000, 1.530, 1.530], 'None', [1, 2],
                 [1, 1], True, 'start', True)
```

### 5.5. Comparative Analysis of the SHPB Tested Scenarios

With all three SHPB tests processed with the algorithm `SHPB_Processing.py`, its capabilities are evident since different materials with distinctly different behaviours were run successfully. In each case, the dispersion correction adds 1000 mm of wave propagation to the incident wave, and removes 1000 mm of wave propagation from the reflected wave, taking the frequency dependence of phase velocity into account as described above.

As the specimen front stress is calculated by the superposition of the incident and reflected waves, the inferred front stress is greatly improved as a result: Figures 12–14 highlight the benefits of dispersion correction vs. simple time shifting analysis.

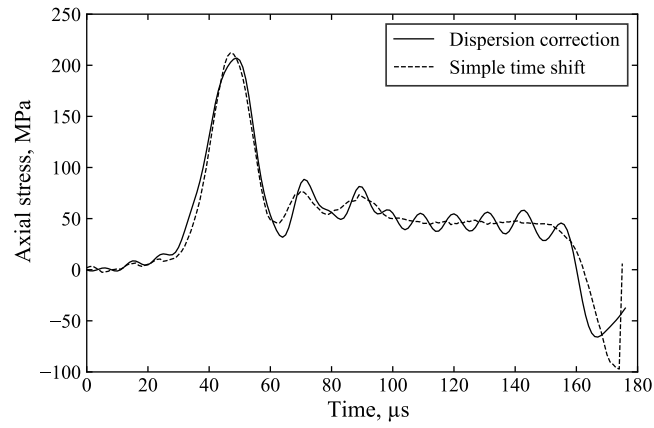
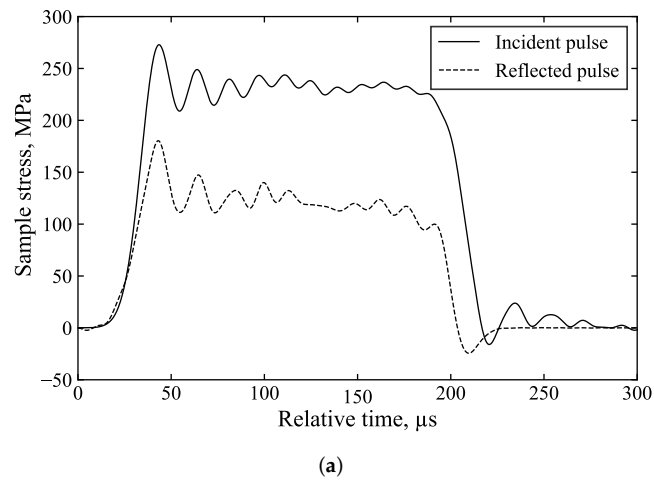
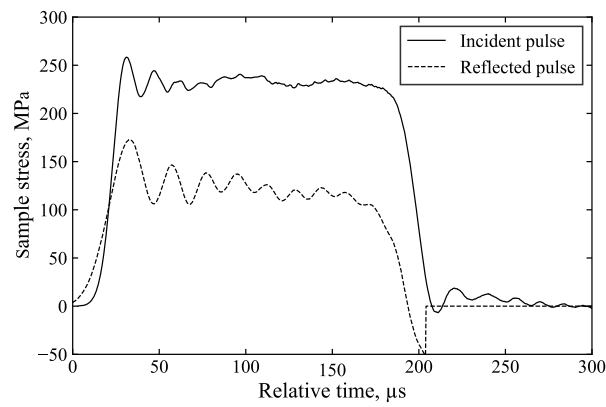


Figure 12. Dispersion vs. time shift analysis of front stress in unconfined SHPB test on kaolin clay.



(a)



(b)

Figure 13. Cont.

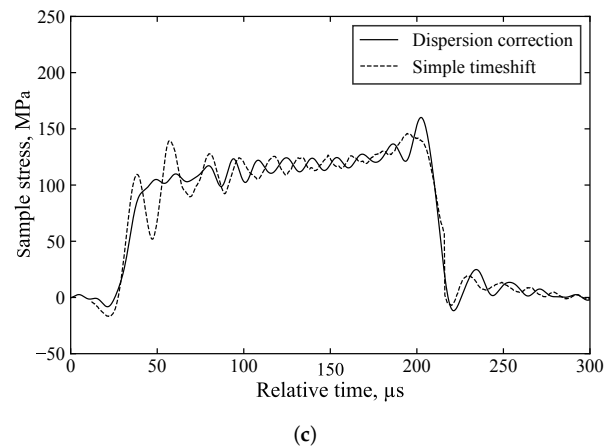


**Figure 13.** Processed results of the unconfined SHPB test on aluminium with (a) dispersion correction of the incident and reflected pulses, (b) simple time shifting of the incident and reflected pulses, and (c) dispersion correction vs. simple time shifting of the front stress.

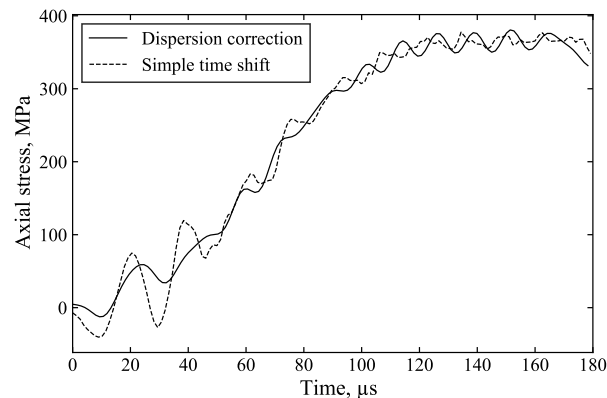
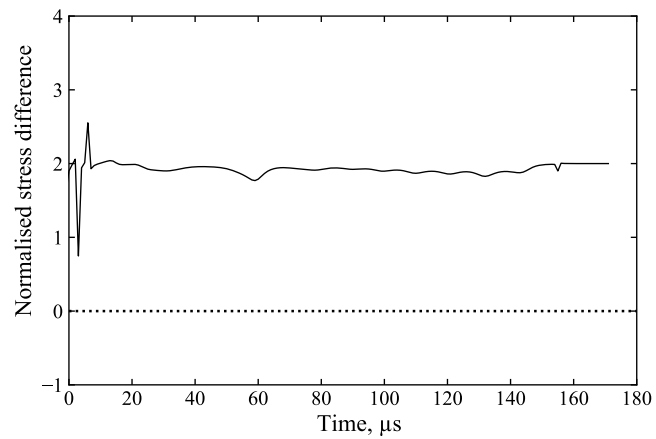


**Figure 14.** Dispersion vs. time shift analysis of front stress in confined SHPB test on sand.

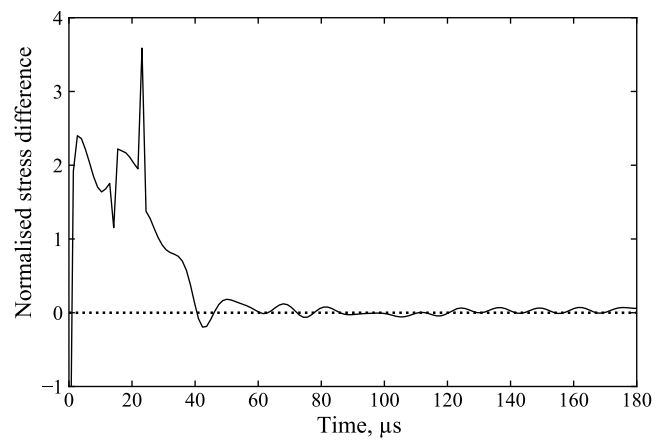
For example, in Figure 13, the measured incident and reflected waves exhibit significant initial oscillations caused by dispersion associated with the rapid stress rise. Dispersion correction (Figure 13a), applied to account for the 1000 mm of travel from the strain gauge to the specimen, ensures that the changing shape of these oscillations is properly accounted for, resulting in their cancellation in the calculation of the specimen front stress (Figure 13c). In contrast, simple time shifting of the signals (Figure 13b) does not account for these changes in shape and position, leading to spurious oscillations in the inferred specimen front stress. This demonstrates that dispersion correction provides more accurate axial stress data and a clearer understanding of specimen behaviour. The additional processing time required for dispersion correction is minimal, approximately 5 s.

### 5.6. Stress Wave Equilibrium

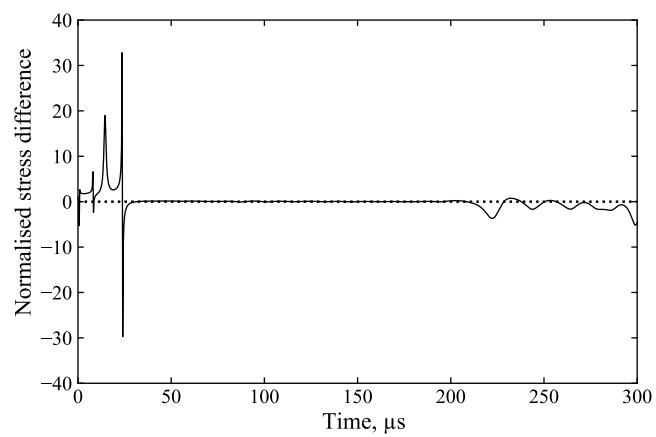
The stress difference between the front and back stress normalised by their mean was plotted for all cases, as shown in Figure 15a–c, to demonstrate that even if stress waves do not achieve equilibrium, SHPB\_Processing.py still runs successfully and produces accurate results.



(a)



(b)



(c)

**Figure 15.** Stress wave difference between front and back stresses, normalised by their mean, for (a) an unconfined SHPB test on kaolin clay, (b) a confined SHPB test on medium sand, and (c) an unconfined SHPB test on aluminium.



In the ideal circumstance, where stress equilibrium is achieved during SHPB testing, the lengths of the pulses detected at the specimen's front and back bar interfaces (i.e., front and back stresses) will be the same. However, there are instances, more commonly in cases where the stress wave does not fully propagate through the specimen, causing a considerable portion to propagate laterally.

Stress equilibrium during a SHPB test can be represented by Equation (10), provided that the deformation of the specimen is uniform and that the axial propagation of the stress wave has been taken into account:

$$\varepsilon_i(t) = \varepsilon_r(t) + \varepsilon_t(t) \quad (10)$$

The ability in `SHPB_Processing.py` to set an alignment to manage the front and back stresses means this function is able to account for cases where stress equilibrium may not be fully obtained but an estimation of the axial stress can still be determined, though with the caveat that it should be coupled with further experimental testing or numerical modelling in order to be utilised for material characterisation.

## 6. Discussion

The algorithm `SHPB_Processing.py` is the main function which performs data processing of the signals obtained from the SHPB tests. It is composed of subroutine `dispersion.py`, which carries out the dispersion correction of the signals acquired from the experiments. Another function titled `dispersion_factors.py` is used in this subroutine.

The programme `dispersion_factors.py` reformats the dispersion correction factors computed by `phase_velocity.py`. These factors are determined using the Poisson's ratio of the cylindrical bar used during SHPB experiments. They can easily be obtained for any material. This function and associated subroutines can be used independently.

As seen in the section of this paper devoted to the script, it has a broad range of capabilities, including confinement, signal amplification, dispersion correction or simple time shifting, signal alignment, striker speed measurement, test log monitoring and data saving. Furthermore, because the input and output signals in the Hopkinson pressure bars are mapped independently, the script runs effectively regardless of whether stress wave equilibrium is attained or not. Since the code focuses on SHPB data processing, as the name suggests, it makes the procedure more efficient.

The script's practical applications were evaluated using SHPB tests with aluminium, kaolin clay and sand samples. An unconfined aluminium sample, an unconfined kaolin clay sample, and a confined medium sand sample were tested with a SHPB apparatus. Most of the script's functionalities were employed to examine these SHPB experiments, most notably, `dispersion.py`, which contrasted dispersion corrected and simple time shift results, demonstrating the importance of this script for reliable data analysis.

As demonstrated in the current work, practical applications of `SHPB_Processing.py` on aluminium, kaolin clay and sand sample data collected from SHPB tests were carried out to illustrate its efficiency, accuracy and broad range of application.

Two of the algorithm's three confinement possibilities were tested, confined and unconfined SHPB experiments, as seen in the practical application section. A SHPB test using a partial lateral confinement apparatus would be extremely valuable for testing data processing quality. This programme has the advantage of working under various testing conditions, regardless of whether stress wave equilibrium is attained during SHPB testing.

The code was run on a SHPB setup with stainless-steel pressure bars (Poisson's ratio of 0.29). Yet, SHPB testing with aluminium or polymer bars, which also require dispersion correction, would be extremely valuable to study the script's performance.

## 7. Conclusions

The essential theory behind dispersion correction and its importance for SHPB experiments were thoroughly investigated. To address this, an invaluable computational tool was created, `SHPB_Processing.py`, with independent subroutines to complement the script's already extensive array of functionalities. Practical applications of this function on SHPB tests conducted on aluminium, kaolin clay, and sand samples demonstrate the improved quality of the results, illustrating the immense potential of this open-source algorithm for future applications.

In conclusion, this study underscores the pivotal role of split-Hopkinson pressure bar (SHPB) testing in advancing geotechnical research. By addressing wave dispersion effects and integrating a robust correction algorithm, the proposed approach significantly enhances the accuracy and reliability of stress analysis in soils and other materials. These findings emphasise the value of SHPB testing in understanding dynamic material behaviour, offering crucial insights for geotechnical applications.

## 8. Code Availability

The algorithms developed in this paper are open-source and accessible on GitHub and ORDA at the following links:

- `gauge_factor.py`: [GitHub](#) and [ORDA](#)
- `phase_velocity.py`: [GitHub](#) and [ORDA](#)
- `SHPB_Processing.py`: [GitHub](#) and [ORDA](#)
- `dispersion.py` & `dispersion_factors.py`: [GitHub](#) and [ORDA](#)

**Author Contributions:** Conceptualisation, A.V.L., K.S.O.L., A.D.B. and S.D.C.; Software development, A.V.L. and K.S.O.L.; Formal analysis, A.V.L. and K.S.O.L.; Validation, A.V.L., K.S.O.L. and A.D.B.; Visualisation, A.V.L., K.S.O.L. and A.D.B.; Writing—original draft preparation, A.V.L.; Writing—review and editing, A.V.L., K.S.O.L., A.D.B. and S.D.C.; Supervision, A.D.B. and S.D.C. All authors have read and agreed to the published version of the manuscript.

**Funding:** This research was funded by the Engineering and Physical Sciences Research Council (EPSRC), and the Defence Science and Technology Laboratory (Dstl).

**Informed Consent Statement:** Not applicable.

**Data Availability Statement:** The data presented in this study are available upon request from the authors.

**Conflicts of Interest:** The authors declare that they have no conflicts of interest.

## References

1. Shin, H. Pochhammer–Chree equation solver for dispersion correction of elastic waves in a (split) Hopkinson bar. *Proc. Inst. Mech. Eng. Part J. Mech. Eng. Sci.* **2022**, *236*, 80–87. [[CrossRef](#)]
2. Kolsky, H. Rader. In *Stress Waves in Solids*; Dover Publications, Inc.: New York, NY, USA, 1963; Volume 21, pp. 140–145.
3. Shin, H. Manual for Calibrating Sound Speed and Poisson's Ratio of (Split) Hopkinson Bar via Dispersion Correction Using Excel<sup>®</sup> and Matlab<sup>®</sup> Templates. *Data* **2022**, *7*, 55. [[CrossRef](#)]
4. Pochhammer, L. Ueber die Fortpflanzungsgeschwindigkeiten kleiner Schwingungen in einem unbegrenzten isotropen Kreiscylinder. *J. Für Die Reine Und Angew. Math.* **1876**, *1876*, 324–336. [[CrossRef](#)]
5. Chree, C. The equations of an isotropic elastic solid in polar and cylindrical co-ordinates their solution and application. *Trans. Camb. Philos. Soc.* **1889**, *14*, 250.
6. Bancroft, D. The velocity of longitudinal waves in cylindrical bars. *Phys. Rev.* **1941**, *59*, 588. [[CrossRef](#)]
7. Barr, A.D. Strain-Rate Effects in Quartz Sand. Ph.D. Thesis, University of Sheffield, Sheffield, UK, 2016.
8. Gray, G.T., III. Classic split-Hopkinson pressure bar testing. In *Mechanical Testing and Evaluation*; ASM International: Almere, The Netherlands, 2000; Volume 8, pp. 462–476.

9. Shin, H. Sound speed and Poisson's ratio calibration of (split) Hopkinson bar via iterative dispersion correction of elastic wave. *J. Appl. Mech.* **2022**, *89*, 061007. [[CrossRef](#)]
10. Tyas, A.; Pope, D.J. Full correction of first-mode Pochhammer–Chree dispersion effects in experimental pressure bar signals. *Meas. Sci. Technol.* **2005**, *16*, 642. [[CrossRef](#)]
11. Tyas, A.; Watson, A.J. An investigation of frequency domain dispersion correction of pressure bar signals. *Int. J. Impact Eng.* **2001**, *25*, 87–101. [[CrossRef](#)]
12. Gorham, D. A numerical method for the correction of dispersion in pressure bar signals. *J. Phys. Sci. Instruments* **1983**, *16*, 477. [[CrossRef](#)]
13. Follansbee, P.; Frantz, C. Wave propagation in the split Hopkinson pressure bar. *J. Eng. Mater. Technol.* **1983**, *105*, 61–66. [[CrossRef](#)]
14. Barr, A.; Rigby, S.; Clayton, M. Correction of higher mode Pochhammer–Chree dispersion in experimental blast loading measurements. *Int. J. Impact Eng.* **2020**, *139*, 103526. [[CrossRef](#)]
15. Davies, R. A critical study of the Hopkinson pressure bar. *Philos. Trans. R. Soc. Lond. Ser. A Math. Phys. Sci.* **1948**, *240*, 375–457. [[CrossRef](#)]
16. Van Lerberghe, A.; Li, K.S.O. *Gauge\_Factor.py—A Python Algorithm for Calculating the Gauge Factor of the Input Bar for Split-Hopkinson Pressure Bar Experiments*; University of Sheffield: Sheffield, UK, 2023. [[CrossRef](#)]
17. Li, K.S.O.; Van Lerberghe, A.; Barr, A. *SHPB\_Processing.py—An Open-Source Python Algorithm for Correcting Stress Wave Dispersion in Split-Hopkinson Pressure Bar Experiments*; University of Sheffield: Sheffield, UK, 2023. [[CrossRef](#)]
18. Van Lerberghe, A.; Barr, A. *Dispersion.py—A Python Algorithm for Phase Angle and Amplitude Correction of Pressure Bar Signals*; University of Sheffield: Sheffield, UK, 2023. [[CrossRef](#)]
19. Barr, A. *Dispersion.m—A MatLab Script for Phase Angle and Amplitude Correction of Pressure Bar Signals*; University of Sheffield: Sheffield, UK, 2016. [[CrossRef](#)]
20. Van Lerberghe, A.; Barr, A. *Phase\_Velocity.py—A Python Algorithm for Calculating Frequency-Dependent Phase Velocity and Radial Variation of Elastic Waves in Cylindrical Bars*; University of Sheffield: Sheffield, UK, 2023. [[CrossRef](#)]
21. Barr, A. *Phasevelocity.m—A Matlab Script to Calculate the Frequency-Dependent Phase Velocity and Radial Variation of Elastic Waves in Cylindrical Bars*; University of Sheffield: Sheffield, UK, 2023. [[CrossRef](#)]

**Disclaimer/Publisher's Note:** The statements, opinions and data contained in all publications are solely those of the individual author(s) and contributor(s) and not of MDPI and/or the editor(s). MDPI and/or the editor(s) disclaim responsibility for any injury to people or property resulting from any ideas, methods, instructions or products referred to in the content.

#### **A.4 Split-Hopkinson pressure bar testing of water with partial lateral confinement**

*Li, K. S. O., Van Lerberghe, A., Barr, A. D., & Clarke, S. D. (2024). Split-Hopkinson pressure bar testing of water with partial lateral confinement. Submitted for publication in Experimental Mechanics*

Work regarding the application of the partial lateral confinement apparatus to conduct SHPB testing on water was submitted for publication to Experimental Mechanics. Journal paper is included as reference.



# Split-Hopkinson Pressure Bar Testing of Water with Partial Lateral Confinement

K.S.O. Li<sup>1</sup> · A. Van Lerberghe<sup>1</sup> · A.D. Barr<sup>1</sup> · A.A. Dennis<sup>1</sup> · S.D. Clarke<sup>1</sup>

Received: 25 March 2024 / Accepted: 7 December 2024  
© The Author(s) 2025

## Abstract

**Background** For the first time, the high-strain-rate behaviour of water is investigated experimentally and validated to LS-DYNA numerical simulations, using Smooth Particle Hydrodynamics (SPH).

**Objective** This paper presents the application of a modified split-Hopkinson pressure bar (SHPB) fitted with a partial lateral confinement apparatus on a water specimen.

**Method** The lateral confinement is provided by a water reservoir surrounding the specimen. A pressure transducer is installed in the reservoir wall to measure lateral stresses, and a dispersion correction algorithm, `SHPB_Processing.py`, is utilised to obtain accurate measurements of axial and radial stresses and strains.

**Results** Experimental results underscore the capability of the modified apparatus to assess triaxial behaviour of water under high-strain rates. Comparisons with numerical modelling reveal that cohesion between water particles is non-existent, highlighting an intrinsic limitation in numerical modelling.

**Conclusion** These results highlight the capability to perform characterisation of fluids under high-strain rates. While limitations in numerical modelling still exist, numerical modelling and experimental testing using the modified apparatus can be applied to characterise fluid behaviour in the future.

**Keywords** High-strain-rate testing · Split-Hopkinson pressure bar · Partial lateral confinement · LS-DYNA · SPH · Water

## Introduction

The split Hopkinson pressure bar (SHPB) is a common tool used for characterising the behaviour of materials under high strain-rate conditions, ranging from  $10^2 \text{ s}^{-1}$  to  $10^4 \text{ s}^{-1}$ . Soils testing employing the SHPB are commonly performed by confining a soil specimen in a rigid tube or ring, limiting lateral displacement. These uniaxial strain experiments are

effective for characterising soil compaction response at different strain rates [1–3], as well as comparing soils with different moisture contents [3, 4], initial densities [5, 6] and particle size distributions [7], but have never been used to characterise the behaviour of liquids.

Several authors have developed methods that allow lateral confinement to alter throughout a SHPB test to generate a triaxial stress state. Pierce and Charlie [8] used a steel tube lined with a membrane to investigate the wave speed of partially saturated sands, at varying confining stresses of 0 kPa and 310 kPa. While the steel tube prevented lateral strains from developing, water pressure applied between the tube and membrane provided additional confining stress, which was also transmitted along the pressure bars via a piston assembly on the transmitter bar. Bailly et al. [9] employed brass confining rings to imitate approximately elastic (near perfectly plastic) behaviour at high strain rates. The material specimen would initially be laterally confined within the rings and deform in uniaxial strain until the radial stress reached the yield point in the ring, at which point the specimen would begin to laterally deform at a quasi-constant confining stress.

✉ K.S.O. Li  
ksoli1@sheffield.ac.uk

A. Van Lerberghe  
avanlerberghe1@sheffield.ac.uk

A.D. Barr  
a.barr@sheffield.ac.uk

A.A. Dennis  
a.a.dennis@sheffield.ac.uk

S.D. Clarke  
sam.clarke@sheffield.ac.uk

<sup>1</sup> Department of Civil & Structural Engineering, University of Sheffield, Mappin Street, Sheffield S1 3JD, UK



Other authors have modified the traditional triaxial cell (CTC) for high-strain-rate testing. Christensen et al. [10] used a large pressure vessel to conduct triaxial tests on sandstone to confining stresses of 207 MPa. The specimen and pressure bars were enclosed in the pressure vessel, which had a hole at one end to facilitate loading of the incident bar, which was secured with a collar. Frew et al. [11] improved the triaxial SHPB further by incorporating pressure vessels around both the specimen and transmitter bar ends, allowing hydrostatic loading to be followed by a high strain rate deviatoric phase. This modified apparatus was utilised by Martin et al. [12] to test the shear response of sand at confining stresses between 25 MPa and 150 MPa, as well as strain rates of 500 s<sup>-1</sup> and 1000 s<sup>-1</sup>.

Barr et al. [13] pioneered a modified SHPB experiment setup involving a partial lateral confinement reservoir that allows a confining stress to build passively during high-strain-rate axial loading. This method combines aspects of unconfined SHPB experiments (usually with a thin membrane) and fully confined SHPB experiments (often with a steel ring) to provide a more comprehensive picture of soil behaviour during high-strain-rate events. This is especially pertinent to blast and impact events, as research into the strain rate dependent behaviour of soils exhibited during high-strain-rates prompts its application in buried explosive scenarios.

The current work seeks to utilise the SHPB set up pioneered by Barr et al. [13] to investigate high-strain-rate effects of liquids, specifically water. This paper will investigate the high-strain-rate effects of water through the employment of the modified SHPB with partial lateral confinement.

## Experimental Setup

The modified SHPB is made up of a standard pressure bar arrangement which consists of a striker, an incident and a transmitter bar, 25 mm in diameter, with a 350 mm, 2500 mm and 1500 mm length, respectively, as shown in Fig. 1. In addition, as illustrated in Fig. 2, a 600 mm long steel water

reservoir is set on linear bearings and centred around the specimen. When the pressure bars are in place, the annular gap present throughout the length of the reservoir is filled with water at atmospheric pressure, as depicted in Fig. 2.

The sample tested is water, therefore the entire reservoir is filled with water, and the radial stress response,  $\sigma_r$ , is measured by a pressure transducer mounted on the reservoir's wall. While a rubber confinement method could also be used to restrict fluid in between the pressure bars, it would prevent radial pressure from being monitored. The axial stress response,  $\sigma_a$ , is measured with Kyowa KSP-2-120-E4 semiconductor strain gauges on the pressure bars, set up in pairs for the Wheatstone bridge arrangement.

The reservoir length was designed so that the time required for a stress wave initiated at the specimen surface to travel to and from the reservoir's end exceeds the loading duration in the specimen, guaranteeing that inward-travelling waves from the boundary do not interfere with pressure measurements [13]. This simplifies the seal between the reservoir and the pressure bars, which are only needed to keep the water at atmospheric pressure.

## Sample Methodology

The application of this testing method was carried out on water to illustrate the capacity of the partially-confined SHPB and to validate that the chosen design results in reliable fluid pressure measurements. The water density tested was 1.0 Mg m<sup>-3</sup>. Preparation of the sample was as follows:

1. Supports were installed on the channel around the incident and transmitter bars of the SHPB setup, prior to installing the steel reservoir providing lateral confinement for the sample.
2. The incident bar was placed into position, approximately 5 mm from the transmitter bar, this was measured as the change in length between the end of the transmitter bar and the final support. It was checked again before all supports were bolted down, and the test launched.

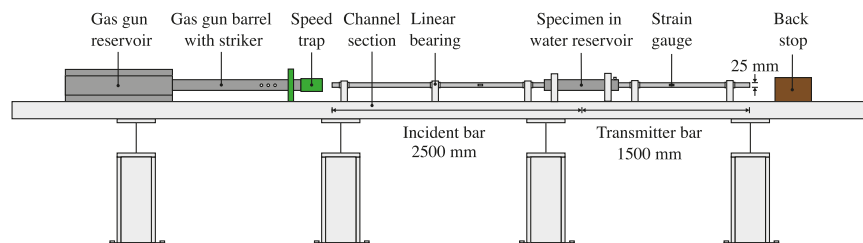


Fig. 1 Schematic of the partially confined SHPB apparatus: Bar and reservoir configuration

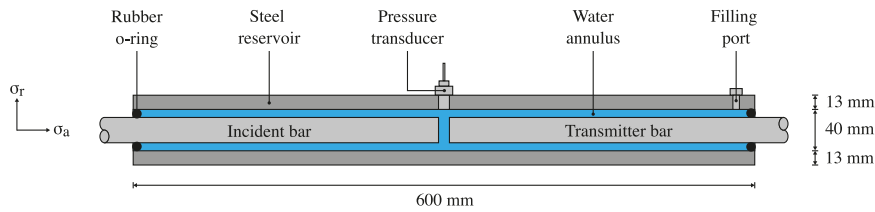


Fig. 2 Schematic of the partially confined SHPB apparatus: water reservoir section with axial/radial axis convention

3. The water reservoir is translated into the centre of the setup, and the pressure port is aligned with the centre of the specimen.
4. The incident bar’s linear bearing, closest to the steel reservoir, is re-adjusted to its initial test position and bolted back down.
5. O-rings were inserted on either side of the water reservoir to seal its ends.
6. The reservoir was filled with water using a filling port and sealed by fitting the pressure transducer and filling port bolt. The transducer used in the experiment was a Kulite HKM-375-2500, calibrated by the manufacturer to perform linearly to a pressure of 25 MPa.
7. Measurement of the length between the two Hopkinson pressure bars was done one last time between the end of the transmitter bar and the final support (Fig. 3).

The method was carried out in the same manner as a standard SHPB experiment. Loading was done by striking the incident bar with a stainless-steel striker bar fired from a gas gun, at varying velocities. Tests were conducted at 16 m/s and 20 m/s, where speeds were recorded using a speed trap placed at the exit of the gas gun barrel.

Signals from the pressure bar strain gauges and pressure transducer were recorded using a TiePie Handyscope four-channel digital oscilloscope using 14-bit A-D resolution and a sample frequency of 1 MHz, with a record length of 131.072 kSa.

From these tests, conducted at two different speeds, a broad range of strain rate was captured, as shown in Fig. 4, where the strain rate increases to  $2095 \text{ s}^{-1}$  and  $4844 \text{ s}^{-1}$ , over approximately  $150 \mu\text{s}$ . Under these high-strain-rate conditions, both the axial and radial stresses of the specimen were measured.

Fig. 3 Schematic of sample measurements process before and after installation inside reservoir

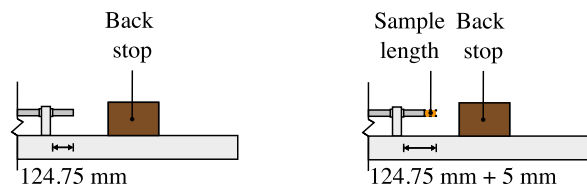
### Signal processing

When processing signals from SHPB experiments, it is frequently believed that longitudinal stress waves in the pressure bars travel one-dimensionally at a common velocity  $c_0$ , and hence measurements recorded at strain gauges are frequently simply translated to the end of the bar using a suitable time delay [14]. In actuality, stress waves travel at a certain phase velocity,  $c_p$ , which is a function of frequency, bar diameter, one-dimensional wave speed and Poisson’s ratio [15], as illustrated in Fig. 5 [3].

As the frequency of a wave grows, the phase velocity drops, resulting in signal dispersion as it propagates down the bar. The dispersion of the stress pulse is accompanied by a frequency-dependent variation in stress and strain across the bar cross-section, so a signal recorded on the surface of the bar at some distance from the specimen will not accurately reflect the stresses the specimen was subjected to, and therefore cannot be used to accurately determine specimen response.

The pressure bar signals were processed using an open-source Python algorithm, `SHPB_Processing.py`, with specific functionalities for partial lateral confinement testing using SHPB setups [16]. It uses an implementation of Tyas and Pope’s dispersion-correction approach via a subroutine titled `dispersion.py`, to verify that the inferred measures of axial stress and strain appropriately depict the specimen behaviour [17]. In this script the method utilised is as follows:

1. Fast Fourier transform (FFT) is used to transfer the time-domain strain signal to the frequency domain.
2. To account for the dispersion over the distance between the strain gauge and the bar end, the phase angle of each



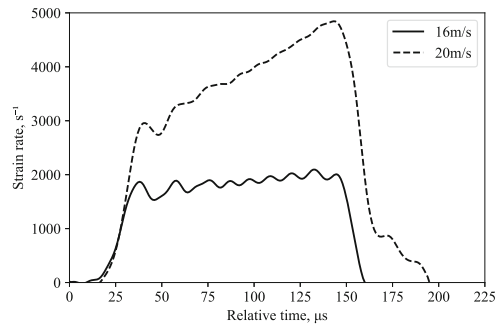


**Fig. 4** Variation of strain rate during partially-confined SHPB experiments on water

frequency component is corrected using the relationship illustrated in Fig. 5.

3. The amplitude of each frequency component is corrected using the factors M1 and M2, which account for the fluctuation of strain and Young's modulus over the bar cross section, respectively. These are derived from Davies' analysis of the radial effects in a cylindrical pressure bar [18].
4. Using the inverse FFT, the signal is then converted back into the time domain.

The dispersion adjustment is especially crucial in determining the stress transmitted into the specimen from the incident bar since it is determined from the sum of the incident and reflected waves, both of which contain considerable high-frequency components.

The incident and reflected stress waves measured at the incident bar strain gauge are assumed to maintain their shape as they are translated along the time axis using simple timeshifting whereas in the corrected method the dispersion associated with 1000 mm travel in the bar is added to the incident wave and removed from the reflected wave.

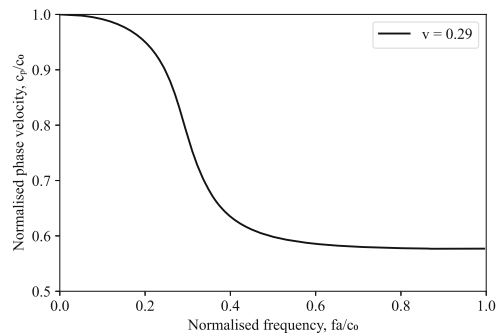


**Fig. 5** Phase velocity frequency relationship for the first mode of propagation of a longitudinal wave [3]

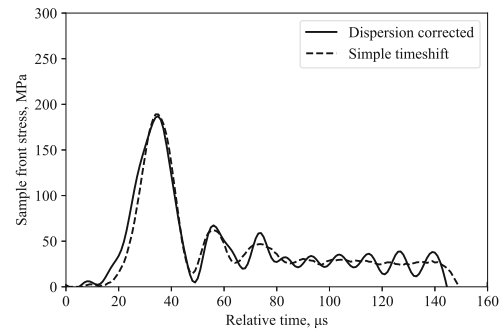


**Fig. 6** Partially confined SHPB test on water: front stress computed using dispersion correction and simple timeshifting

Figure 6 shows how the dispersion-corrected approach minimises the amplitude of the stress wave and eliminates an initial fluctuation in stress, which would have led to incorrect inferences about the specimen's behaviour. In this case, dispersion effects are minimal.

## Numerical Modelling

### Model Setup

The numerical modelisation of the arrangement in Fig. 7 was carried out using the explicit finite element code in LS-DYNA [19], in order to compare numerical and experimental results. A more detailed representation of the water sample and confinement reservoir are shown in Fig. 8. The model was created in 3D, where the striker bar (yellow in Fig. 7), incident bar (blue in Fig. 7) transmitter bar (green in Fig. 7) and steel reservoir (grey in Fig. 7) were modelled as Lagrangian solid mesh. SPH node modelisation was used to model the water sample (red in Fig. 8) [20–23].

For simplicity, the steel reservoir is modelled as a rigid steel boundary material, assuming that the fluid pressures generated will not be large enough to cause significant radial strains in the reservoir. The rubber rings were replaced with a boundary constraint to prevent the water from exiting the reservoir from the ends.

Automatic nodes-to-surface contact were selected for contact representation between the water sample made with SPH nodes and the lagrangian members of the incident and transmitter bars. Automatic nodes-to-surface contact was also utilised between the water sample and the steel reservoir. Manual surface-to-surface contact adjustments were made between lagrangian members in the model, such as between the striker and incident bars, and between the incident and transmitter bars.



Fig. 7 LS-DYNA SHPB partial lateral confinement model set up

### Model material cards

The three steel pressure (striker, incident and transmitter) bars were modelled as linear elastic materials (\*MAT\_ELASTIC) with a density, Young's modulus and Poisson's ratio of  $\rho = 7850 \text{ kg m}^{-3}$ ,  $E = 168 \text{ GPa}$ ,  $\nu = 0.29$  respectively based on existing known properties of steel.

For all analyses, to match the experimental tests conducted, the striker bar was given an initial impact velocity of 16 m/s or 20 m/s similar to match the speeds tested experimentally. The steel reservoir was modelled as rigid (\*MAT\_RIGID), with a density, Young's modulus and Poisson's ratio of  $\rho = 7850 \text{ kg m}^{-3}$ ,  $E = 168 \text{ GPa}$ ,  $\nu = 0.29$  respectively. The SPH water sample that encompassed the water annulus and the gap between the pressure bars was modelled using the linear polynomial equation of state (EOS):

$$P = C_0 + C_1\mu + C_2\mu^2 + C_3\mu^3 + (C_4 + C_5\mu + C_6\mu^2)E \quad (1)$$

where  $C_0, C_1, C_2, C_3, C_4, C_5$  and  $C_6$  are constants,  $\mu = \rho/\rho_0 - 1$ ,  $\rho$  and  $\rho_0$  are the current and initial densities of the fluid, and  $E$  is the specific internal energy of the fluid. Table 1, displays the properties used to apply the null material card (\*MAT\_NULL), which only requires density input, and equation of state parameters utilised in this work for water. The constants for the equation of state were based on previous work by Shin [20], which studied the use of numerical modelling to simulate shock wave effects in water. To assign the initial pressure of the water to be equal to atmospheric pressure (101kPa), the specific internal energy,  $E_0$ , was found by applying eq. (1) with the constants from Table 1 to be 205.36kPa.

### Results

Figure 9 display the typical stress difference between axial and radial stress, illustrating the viability of the current configuration in assisting with the triaxial response of a liquid. The near zero stress difference indicates the translation of

axial stress into radial stress when subject to loading, a property that aligns with the Poisson's ratio of water.

Figures 10 and 11 show that the experimental and numerical incident pulses have the same amplitude at the same gauge locations, but the reflected pulses are very different.

Tests were performed using the modified SHPB fitted with the partial lateral confinement reservoir on water, at 16 m/s and 20 m/s. Figures 12 and 14 show similarities in terms of response behaviour, with a logical increase in amplitude associated with its higher test speed.

Figures 12 and 14 depict the experimentally measured front, back and radial stresses. The radial stress directly adjacent to the water in between the pressure bars was calculated by taking into account the transit time of the radial stress wave through the water annulus ( $5.1 \mu\text{s}$ , assuming a wave speed in water of 1482 m/s). The recorded radial stress shows a radial stress wave with peaks that align relatively well with front and back stresses, indicating that the lateral response recorded with the pressure transducer is a direct result of the axial loading from the SHPB test.

Looking at the Poisson's ratio, experimentally at 16 m/s, the maximum front, back and radial stress recorded are 180, 5 and 46 MPa, respectively, resulting in a Poisson's ratio of 0.5 (Fig. 12), when the axial stress ( $(180 + 5)/2 = 92.5 \text{ MPa}$ ) is divided by the radial stress (46 MPa). Since the theoretical Poisson's ratio for water is 0.5, this indicates that the axial and radial stress data obtained by employing this modified SHPB setup exhibit a degree of accuracy reflected in theory.

At higher striker speeds, the incident bar's inertia and the partial lateral confinement steel reservoir will have an impact on the front, back and radial stresses, as seen in Fig. 14. This will have an effect on the Poisson's ratio of the water specimen, progressively lowering its value.

The back stress values differ by 60-80 %, radial stress values differ by 11-13 %, and the front stress values differ by 76-105 %, when comparing numerical and experimental stresses at 16 m/s and 20 m/s (Figs. 12, 13, 14, and 15).

While there is evidently a distinct disparity between the stress magnitudes from experimental and numerical results, numerical modelling is used in conjunction with experimental results to provide commentary on the viability of the apparatus in investigating stress behaviour of water. As such, qualitative and quantitative comparison between numerical

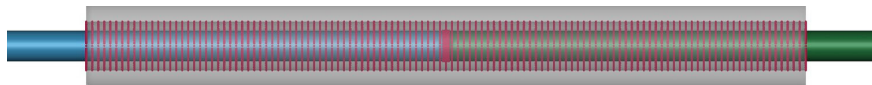
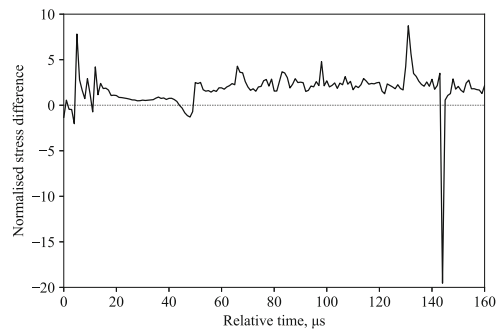


Fig. 8 LS-DYNA cross section zoom-in on the sample inside the partial lateral confinement SHPB set up

**Table 1** Material model and equation of state (EOS) parameters for water (SI units) [20]

MAT_NULL							
1000							
EOS_LINEAR_POLYNOMIAL							
$C_0$	$C_1$	$C_2$	$C_3$	$C_4$	$C_5$	$C_6$	$E_9$
0.0	2.190E9	9.224E9	8.767E9	0.4934	1.3937	0.0	205.36E3



**Fig. 9** Typical response of a partially confined SHPB test on water showing axial and radial stress difference normalised by their mean

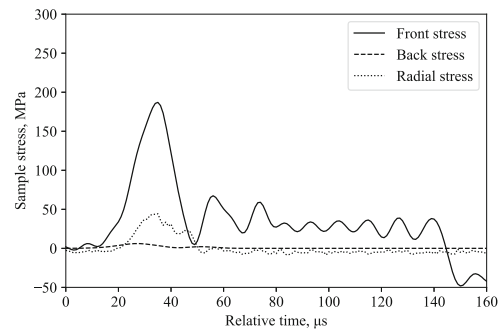


**Fig. 12** Partially confined SHPB test on water at 16 m/s: front, back and radial stresses

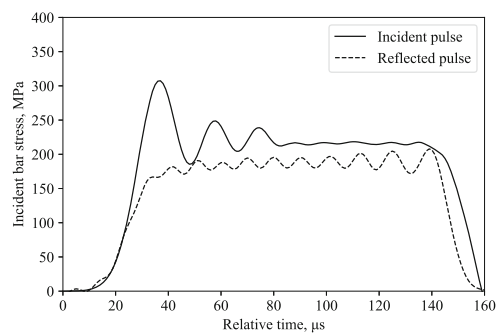


**Fig. 10** Typical behaviour of a partially confined SHPB experimental test on water at 16 m/s: incident and reflected pulses from the incident bar

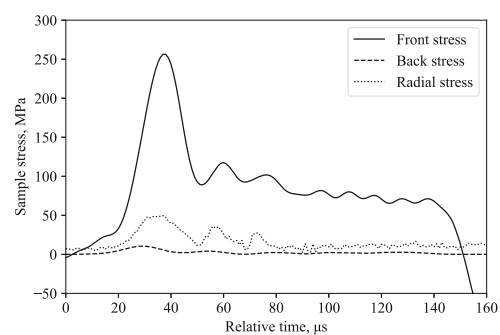


**Fig. 13** Partially confined SHPB LS-DYNA model on water at 16 m/s: front, back and radial stresses

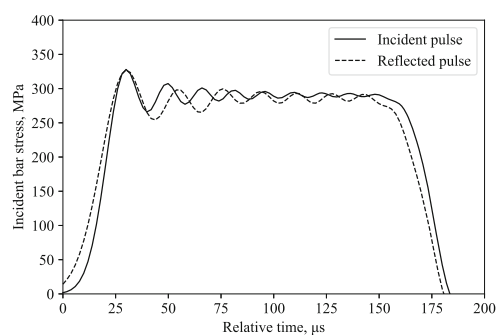


**Fig. 11** Typical behaviour of a partially confined SHPB LS-DYNA model on water at 16 m/s: incident and reflected pulses from the incident bar

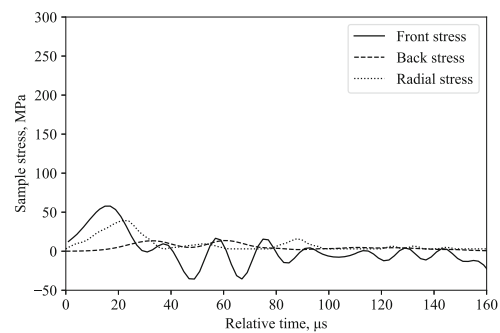


**Fig. 14** Partially confined SHPB test on water at 20 m/s: front, back and radial stresses

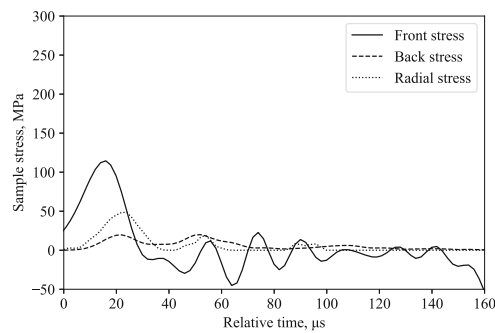


**Fig. 15** Partially confined SHPB LS-DYNA model on water at 20 m/s: front, back and radial stresses

and experimental results still exhibit similarities in terms of stress propagation tendencies through the fluid medium.

## Discussion

The capabilities of the modified SHPB with the implementation of the lateral confinement apparatus allow for high-strain-rate testing on water to explore its axial and lateral responses. The results collected from the experimental tests and numerical model in LS-DYNA, revealed a significant difference in front stress, leading to a considerable lower axial stress. This is due to the numerical model's lack of cohesion between SPH particles when modelling a fluid like water, as evidenced by the two key arguments below:

1. The water sample in the modified SHPB with the lateral confinement apparatus, was modelled in LS-DYNA using SPH. This was done in the same manner as other projects that have modelled water for blast and high impact tests [21]. They used `*MAT_NULL` and the EOS linear polynomial, as shown in Table 1. However, `*MAT_NULL` only uses the initial density of the fluid. It does not include any cohesion parameters, which is a fundamental property of fluids. Water itself is a highly cohesive material. Consequently, omitting this will have a considerable impact on the numerical results.
2. When comparing modelling and experimental test results, the radial stress is within 10-13 % of the experimental values obtained, however, the back and front stresses are more than 60-80 % and 75-105 % away, respectively, from what it should be, experimentally. The radial stress is measured with a pressure transducer, while the front and back stresses are measured at the strain gauge location on the incident and transmitter bars in the model. Hence, the value obtained at these points is from the stress wave as it propagates through the SPH water particles, and hits the transmitter bar interface and pressure

transducer. The significant difference in front and back stresses is due to the instant extrusion of the water sample upon contact from the incident pulse.

There is no cohesion between the SPH particles. The particles are instantaneously displaced in both horizontal and vertical directions, due to the impact of the stress wave considerably changing the size and shape of the specimen. There is no medium for the wave to propagate through. As a result, the water sample is unable to compact sufficiently to let the stress wave propagate through before extruding from in-between the Hopkinson pressure bars.

When comparing experimental and model outputs, it is evident the model is under predicting the stress results. This indicates that adding cohesion properties to this model would intuitively improve the specimen's ability to withstand the stress wave passing through it.

Material cards that consider cohesion in LS-DYNA include `*MAT_PSEUDO_TENSOR`, `*MAT_CONCRETE_DAMAGE`, `*MAT_FHWA_SOIL`, `*MAT_MOHR_COULOMB`, `*MAT_DRUCKER_PRAGER` and `*MAT_JOINTED_ROCK`. However, the material cards `*MAT_PSEUDO_TENSOR`, `*MAT_CONCRETE_DAMAGE`, `*MAT_FHWA_SOIL` and `*MAT_JOINTED_ROCK` can not be used since they are made for steel, concrete, rock and soils, with some requiring an EOS and other parameters which could not be obtained for water. The material cards `*MAT_MOHR_COULOMB` and `*MAT_DRUCKER_PRAGER` had obtainable parameters, but showed the same behaviour as `*MAT_NULL`.

SPH parameters were explored in LS-DYNA, and it was discovered that there was no option to change the cohesion parameter for fluid modelling. Viscosity was evaluated in the numerical model and showed no effect on improving SPH particle cohesiveness, as it simply slowed their lateral and transverse movements.

The ability to evaluate the high-strain-rate behaviour of liquids and record both their lateral and axial stress responses fills a gap in present research that previously restricted SHPB testing to fluid materials.

Also, since high-strain testing on water can be directly used to compare the effect of saturation and actual water, the influence of water content on other materials such as soils can be better understood. The specific effect of soil parameters such as particle size or density can be examined more thoroughly by comparing high-strain and quasi-static triaxial tests on fully saturated soils.

While shear thickening fluids have not been explicitly investigated through this study, the opportunity to perform controlled high-strain-rate tests on specific fluids opens up the future opportunity to examine the ability of shear thickening fluids to dissipate energy. Adjustments to the numerical model including the modification of fluid medium viscos-

ity would be crucial in indicating behaviour under various shear conditions. Shear thickening fluids are widely used in impact protection applications such as in shock absorbers or enhancing Kevlar fabrics, the implications that this apparatus provides would be vital in its further characterisation under high-strain-rate conditions [24, 25].

## Conclusion

An innovative testing methodology for partially-confined SHPB experiments has been used to test water at high-strain-rates, where the specimen is contained in a long sleeve reservoir. A pressure transducer in the wall of the reservoir is used to measure the radial stress of the specimen.

Experimental results showed a clear correlation between the increase of the strain rate and the amplitude of the radial and axial stresses. To compare with the experimental data collected from the tests, LS-DYNA numerical modelling of tests with and SPH water sample was undertaken. Although radial and back stresses were measured and represented in the numerical model with reasonable accuracy, substantial modelling constraints were discovered when looking at the front stress obtained from the model. This was due to a failure to account for the cohesion qualities of the SPH particles in the numerical model, which fluids naturally have.

The material card \*MAT\_NULL, which is commonly used to depict water in LS-DYNA, only requires its initial density; however, this material card does not account for the highly cohesive properties of water particles, an intrinsic property of fluids.

As a result, improvements to the existing model are required, such as creating a new material card in LS-DYNA that incorporates cohesion as a parameter for fluids and upgrading the modelling representation of SPH to account for cohesion between particles.

Experimentally, in addition to its capabilities for testing soils, this apparatus can be used to accurately characterise liquid materials at high strain-rates, which was previously impossible.

Future test series using this new apparatus will aim to define strain rate dependency as well as further investigate the influence of radial inertia observed in current tests. Furthermore, the results of high strain-rate water characterisation can be utilised to characterise very fine, undrained, fully saturated soils under high strain rate conditions.

**Acknowledgements** This research was funded by the Engineering and Physical Sciences Research Council (EPSRC), and the Defence Science and Technology Laboratory (Dstl).

**Data Availability** Data from this paper is available upon request from the corresponding author, Li K. S. O., at [ksoli1@sheffield.ac.uk](mailto:ksoli1@sheffield.ac.uk) or [li.oswald@gmail.com](mailto:li.oswald@gmail.com).

## Declarations

**Conflicts of interest** The authors declare that they have no conflict of interest.

**Open Access** This article is licensed under a Creative Commons Attribution 4.0 International License, which permits use, sharing, adaptation, distribution and reproduction in any medium or format, as long as you give appropriate credit to the original author(s) and the source, provide a link to the Creative Commons licence, and indicate if changes were made. The images or other third party material in this article are included in the article's Creative Commons licence, unless indicated otherwise in a credit line to the material. If material is not included in the article's Creative Commons licence and your intended use is not permitted by statutory regulation or exceeds the permitted use, you will need to obtain permission directly from the copyright holder. To view a copy of this licence, visit <http://creativecommons.org/licenses/by/4.0/>.

## References

1. Bragov AM, Lomunov AK, Sergeichev IV, Tsembelis K, Proud WG (2008) Determination of physicommechanical properties of soft soils from medium to high strain rates. *Int J Impact Eng* 35(9):967–976. <https://doi.org/10.1016/j.ijimpeng.2007.07.004>
2. Song B, Chen W, Luk V (2009) Impact compressive response of dry sand. *Mech Mater* 41(6):777–785. <https://doi.org/10.1016/j.mechmat.2009.01.003>
3. Barr AD, Clarke SD, Petkovski M, Tyas A, Rigby SE, Warren J, Kerr S (2016) Effects of strain rate and moisture content on the behaviour of sand under one-dimensional compression. *Exp Mech* 56(9):1625–1639. <https://doi.org/10.1007/s11340-016-0200-z>
4. Martin BE, Chen W, Song B, Akers SA (2009) Moisture effects on the high strain-rate behavior of sand. *Mech Mater* 41(6):786–798. <https://doi.org/10.1016/j.mechmat.2009.01.014>
5. Lu H, Luo H, Komaduri R (2009) Dynamic compressive response of sand under confinements. Society for experimental mechanics - SEM annual conference and exposition on experimental and applied mechanics 2009. pp 1046–1052
6. Luo H, Lu H, Cooper WL, Komanduri R (2011) Effect of Mass Density on the Compressive Behavior of Dry Sand Under Confinement at High Strain Rates. *Exp Mech* 51(9):1499–1510. <https://doi.org/10.1007/s11340-011-9475-2>
7. Huang J, Xu S, Hu S (2013) Effects of grain size and gradation on the dynamic responses of quartz sands. *Int J Impact Eng* 59:1–10. <https://doi.org/10.1016/j.ijimpeng.2013.03.007>
8. Pierce SJ, Charlie WA (1990) High-intensity Compressive Stress Wave Propagation Through Unsaturated Sands. PhD thesis, Colorado State University
9. Bailly P, Delvare F, Vial J, Hanus JL, Biessy M, Picart D (2011) Dynamic behavior of an aggregate material at simultaneous high pressure and strain rate: SHPB triaxial tests. *Int J Impact Eng* 38(2–3):73–84. <https://doi.org/10.1016/j.ijimpeng.2010.10.005>
10. Christensen RJ, Swanson SR, Brown WS (1972) Split-hopkinson-bar tests on rock under confining pressure. *Exp Mech* 12(11):508–513. <https://doi.org/10.1007/BF02320747>
11. Frew DJ, Akers SA, Chen W, Green ML (2010) Development of a dynamic triaxial Kolsky bar. *Meas Sci Technol* 21(10). <https://doi.org/10.1088/0957-0233/21/10/105704>



12. Martin BE, Kabir ME, Chen W (2013) Undrained high-pressure and high strain-rate response of dry sand under triaxial loading. *Int J Impact Eng* 54:51–63. <https://doi.org/10.1016/j.ijimpeng.2012.10.008>
13. Barr AD, Clarke SD, Rigby SE, Tyas A, Warren JA (2016) Design of a split Hopkinson pressure bar with partial lateral confinement. *Meas Sci Technol* 27(12). <https://doi.org/10.1088/0957-0233/27/12/125903>
14. Gray TG (2000) Classic Split-Hopkinson pressure bar testing. In: *Mechanical testing and evaluation*. ASM International. <https://doi.org/10.31399/asm.hb.v08.a0003296>
15. Bancroft D (1941) The Velocity of Longitudinal Waves in Cylindrical Bars. *Phys Rev* 59(7):588–593. <https://doi.org/10.1103/PhysRev.59.588>
16. Van Lerberghe A, Li K, Barr A, Clarke S (2024) An open-source algorithm for correcting stress wave dispersion in split-Hopkinson pressure bar experiments. Submitted for publication in *Experimental Mechanics*
17. Tyas A, Pope DJ (2005) Full correction of first-mode Pochhammer-Chree dispersion effects in experimental pressure bar signals. *Meas Sci Technol* 16(3):642–652. <https://doi.org/10.1088/0957-0233/16/3/004>
18. Davies RM (1948) A critical study of the Hopkinson pressure bar. *Phil Trans R Soc Lond Ser A Math Phys Sci* 240(821):375–457. <https://doi.org/10.1098/rsta.1948.0001>
19. Livermore Software Technology Corporation (2023) *LS-DYNA Theory Manual*. California, USA
20. Shin YS, Lee M, Lam KY, Yeo KS (1998) Modeling mitigation effects of watershed on shock waves. *Shock Vib* 5(4):225–234. <https://doi.org/10.1155/1998/782032>
21. Varas D, Artero-Guerrero JA, Pernas-Sánchez J, López-Puente J (2017) Numerical modelling of the fluid structure interaction using ALE and SPH: the Hydrodynamic Ram phenomenon. 11th European LS-Dyna Conference
22. Jianming W, Na G, Wenjun G (2010) Abrasive waterjet machining simulation by SPH method. *Int J Adv Manuf Technol* 50(1–4):227–234. <https://doi.org/10.1007/s00170-010-2521-x>
23. Anghileri M, Castelletti LML, Tirelli M (2005) Fluid-structure interaction of water filled tanks during the impact with the ground. *Int J Impact Eng* 31(3):235–254. <https://doi.org/10.1016/j.ijimpeng.2003.12.005>
24. Chatterjee VA, Singh S, Neogi S (2023) In: Gurgun S (ed.) *Energy dissipation in shear thickening fluid integrated structures under ballistic impacts*. Springer, pp 131–162. doi:10.1007/978-3-031-35521-9\_7
25. Xie Z, Chen W, Liu Y, Liu L, Zhao Z, Luo G (2023) Design of the ballistic performance of shear thickening fluid (stf) impregnated kevlar fabric via numerical simulation. *Mater Des* 226:111599. <https://doi.org/10.1016/j.matdes.2023.111599>

**Publisher's Note** Springer Nature remains neutral with regard to jurisdictional claims in published maps and institutional affiliations.

## **A.5 High-strain-rate behaviour of cohesive soils**

*Van Lerberghe, A., Li, K. S. O., Barr, A. D., & Clarke, S. D. (2024). High-strain-rate behaviour of cohesive soils. Submitted for publication in International Journal of Impact Engineering*

Work documenting the high-strain-rate response of cohesive soils and describes the effects of moisture content and strain rate was submitted for publication to International Journal of Impact Engineering. Journal paper is included as reference.

# High strain rate behaviour of cohesive soils

Arthur Van Lerberghe<sup>a,\*</sup>, Kin Shing O. Li<sup>a</sup>, Andrew D. Barr<sup>a</sup>, Sam D. Clarke<sup>a</sup>

<sup>a</sup>*Department of Civil & Structural Engineering, University of Sheffield, Mappin Street, Sheffield, S1 3JD, UK*

---

## Abstract

Soil-filled wire and geotextile gabions are essential components of defensive infrastructure in military bases, leveraging the attenuating properties of soils to safeguard personnel and critical assets against blast and fragmentation effects. However, understanding the behaviour of cohesive soils under extreme loading conditions remains largely unexplored, presenting a crucial knowledge gap for design engineers tasked with developing robust soil constitutive models to address evolving threats. This study investigates the response of cohesive soils, focusing primarily on kaolin clay due to its homogeneity, widespread availability and consistent properties. Through high strain rate experimental testing of kaolin clay specimens, using the split-Hopkinson pressure bar (SHPB) apparatus, both unconfined and confined conditions are explored across varying moisture contents, spanning the spectrum from unsaturated to fully saturated states. The analysis of the experimental results uncovers the strain rate dependence of cohesive soils and identifies distinct phase behaviour for transmitted and radial stresses influenced by factors such as strain rate, moisture content and confinement. Utilising LS-DYNA, and the finite element method (FEM), the SHPB tests are modelled for comparison against experimental findings. While LS-DYNA, supplemented by Smooth Particle Hydrodynamics (SPH) node modelling, provides valuable insights, significant disparities between modelled and practical results underscore the challenges inherent with the accuracy in simulating the behaviour of cohesive soils. Nonetheless, this comprehensive exploration of cohesive soil's high strain rate behaviour yields critical insights for engineers, enabling them to adapt defensive strategies to diverse threats and loading scenarios effectively.

*Keywords:* High strain rate testing, Split-Hopkinson pressure bar, Cohesive soils, Kaolin clay, LS-DYNA modelling, Smooth particle hydrodynamics

---

## 1. Introduction

Fortification engineers face a daunting challenge: ensuring the resilience of defensive structures worldwide. Soil-filled wire and geotextile gabions, exemplified by Hesco Concertainer, stand as stalwart solutions, offering protection against the destructive forces of blast and fragmentation. The versatility and availability of soil make it an attractive defence material, facilitating the rapid and cost-effective construction of robust-barriers. However, despite its ubiquity, the high strain rate behaviour of soil remains enigmatic, especially in the context of emerging threats and evolving landscapes. As conflicts shift from sandy terrains to regions where sand may not be readily available, the need to understand and harness the potential of cohesive soils such as clay and silt becomes imperative. These cohesive materials, found across the globe, constitute the terrestrial and aquatic strata, offering promising alternative for fortifications in diverse settings.

In navigating unfamiliar terrain, fortification engineers require precise data to assess the performance of local soils and adapt their designs accordingly. The development of constitutive models capable of accommodating new soils and emerging threats necessitates comprehensive studies on soil behaviour under extreme loading conditions. In this regard, the focus on kaolin clay, a well-researched and representative soil, provides a foundation for quantitative insights into its mechanical response. By preparing kaolin clay samples at varying moisture contents and testing them under both unconfined and confined conditions using the SHPB apparatus, this study aims to elucidate the effects of strain rate, moisture content and confinement on cohesive soils.

Blast attenuation and cohesive soils are expansive fields. The unique characteristics of cohesive soils, including their undrained behaviour, variable saturation states, and very fine particle size, pose significant challenges in evaluating their response at high strain rates. Unlike cohesionless soils, like sand, which have been extensively studied under high strain rates conditions [1–6], cohesive soils, particularly kaolin clay, remains largely unexplored in this context. This study aims to bridge this gap by delving into new frontiers of understanding, thereby paving the way for more resilient and adaptive fortification designs.

---

\*Corresponding author.

*Email address:* avanlerberghe1@sheffield.ac.uk (Arthur Van Lerberghe)



27 The contemporary SHPB apparatus, named after Bertram Hopkinson, originated from his  
28 method to measure the pressure generated by bullet impacts or explosive detonations [7]. Initially,  
29 the Hopkinson pressure bar consisted of a long steel bar transmitting pressure from the impact,  
30 with a shorter bar serving as a momentum trap, allowing inference of pressure wave magnitude  
31 and duration.

32 Herbert Kolsky expanded upon this design by incorporating two bars in series, separated by a  
33 material specimen. This configuration facilitated recording of stress pulses in each bar, enabling  
34 calculation of the dynamic stress-strain response of the specimen [8]. This system, known as  
35 the split-Hopkinson pressure bar (SHPB) or Kolsky bar, remains fundamentally unchanged. By  
36 employing one-dimensional wave theory, stress pulses measured in the bars provide insights into  
37 the stress and strain histories of the two ends of the specimen [9].

38 Several studies utilising the SHPB apparatus have investigated the high strain rate behaviour of  
39 cohesive soils, with tests conducted up to  $2500 \text{ s}^{-1}$ , under both unconfined and confined conditions,  
40 at different moisture contents. However, these studies lacked detailed material characterisation and  
41 sample preparations of their chosen cohesive soil. This included factors such as moisture content,  
42 particle size distribution and Atterberg limits, which hindered the reproducibility of their findings  
43 and restricted comparative possibilities with other studies [10–13].

44 For instance, SHPB tests conducted on dry clay samples provided some insights into the effects  
45 of moisture content on cohesive soils at high strain rates [10–13]. However, artificially frozen clay  
46 samples compromised the inherent properties of moisture content in cohesive soils, rendering the  
47 results incomparable with other SHPB tests on cohesive soils [11].

48 Confined SHPB tests on dry clay samples were conducted, with steel jackets of different thick-  
49 nesses [10], and utilising gauged steel cylindrical cages [13]. These results provided some infor-  
50 mation on the effect of confinement at high strain rates by measuring the radial stress behaviour of  
51 the sample. Yet, no comparison was made with unconfined SHPB tests on the same soil samples  
52 to determine the effect of confinement.

53 In contrast, high strain rate SHPB testing on cohesionless soils is more comprehensive, with  
54 clearly defined material properties prior to investigating the impact of strain rate, moisture content  
55 and lateral confinement [1–6]. This further underscores the untapped potential of novel research

56 in comprehensively addressing the behaviour of cohesive soils at high strain rates, an area that  
57 remains largely unexplored.

58 Full scale trials of blast and ballistic events entail considerable costs and time investments.  
59 Consequently, numerical techniques serve as invaluable tools for modelling these events. Explo-  
60 sions, blast effects, and impacts are commonly simulated using dynamic software such as LS-  
61 DYNA, which incorporates the Finite Element Method (FEM) [14].

62 The reliability and accuracy of material models are paramount and must be verified against  
63 experimental data [15]. Typically, this involves developing a material model based on experimen-  
64 tal properties and then comparing the results obtained from physical experiments to those of more  
65 complex simulations. Discrepancies between the experimental and modelled data indicate inaccura-  
66 cies in the material model. Adjusting the inputs until the outputs align with experimental data  
67 is not a viable solution, as the model may fail to predict future material responses under different  
68 test configurations.

69 In FEM-based modelling, soil is often treated as a continuum with homogeneous bulk prop-  
70 erties [16]. Since individual particles are not explicitly modelled in continuum approaches, con-  
71 stitutive models are employed to capture crucial bulk properties, which are typically derived from  
72 geotechnical tests.

73 LS-DYNA offers various modelling approaches to create constitutive numerical models for dy-  
74 namic impacts on soils. These include Lagrangian with material erosion and/or mesh adaptivity,  
75 Arbitrary Lagrangian-Eulerian (ALE), and Smooth Particle Hydrodynamics (SPH) [14]. Addi-  
76 tionally, LS-DYNA provides a range of built-in material cards for simulating soil behaviour, from  
77 basic models with compressibility curves and yield surfaces to more complex models incorporat-  
78 ing pore water effects, strain softening & hardening, and strain effects [14].

79 While most finite element (FE) studies using LS-DYNA in the literature focus on buried ex-  
80 plosives, only a small number address SHPB modelling of soils, with an even smaller subset  
81 dedicated to cohesive soils.

82 LS-DYNA has been employed to model high strain rate experiments on cohesive soils, includ-  
83 ing unconfined and confined SHPB tests, utilising material cards such as \*MAT\_SOIL\_AND\_FOAM,  
84 \*MAT\_PSEUDO\_TENSOR, \*MAT\_FHWA\_SOIL, \*MAT\_GEOLOGIC\_CAP\_MODEL as well as \*MAT\_MOHR\_COULOMB.

85 Experimental data is used to build ALE numerical models and comparing their results to collected  
86 test data, yielding limited accuracy [13, 17, 18].

87 These studies highlight critical issues: the lack of clear material characterisation of the inves-  
88 tigated cohesive soil, the absence of soil shear strength data at high pressures during modelling,  
89 and evident limitations in modelling the behaviour of cohesive soils across all saturation levels

90 Furthermore, SPH modelling, an innovative meshless Lagrangian numerical technique for  
91 modelling fluid equations of motion under high strain rate effects, has never been utilised in LS-  
92 DYNA for the modelling of SHPB experiments on cohesive soils. Given the dynamic nature of  
93 SHPB tests and the complex material behaviour of cohesive soils, this presents an ideal opportu-  
94 nity for exploration [19].

## 95 2. Material characterisation

96 The soil selected is defined using EN ISO 14688–1:2002 [20], as white fine CLAY (CL). For  
97 brevity, it is referred to as ‘kaolin clay’. Table 1 provides an overview of the kaolin clay material  
98 properties, which are derived using the methods described in sections 2.1, 2.2, 2.3, 2.4 and 2.5.

Soil properties	Units	Value
Primary mineral	–	Kaolinite
Particle density, $\rho_s$	Mg.m <sup>-3</sup>	2.65
Liquid Limit, LL	%	40
Plastic Limit, PL	%	25
Plastic Index, PI	%	15
$D_{50}$	$\mu\text{m}$	0.74
Particle sphericity	–	Low – Medium
Angularity	–	Subrounded – Subangular
Surface texture	–	Smooth

Table 1: Overview of the kaolin clay material properties.

99 *2.1. Particle mineralogy*

100 X-ray diffraction (XRD) was carried out on the kaolin clay to establish the constituent minerals.  
101 In XRD an incident X-ray beam undergoes diffraction due to the regular atomic structure of a  
102 crystalline specimen. By measuring the intensity of diffraction at different incident angles,  $\theta$ , a  
103 distinct diffraction pattern is obtained. This pattern can be compared to a database of known  
104 patterns to identify the phases present in the specimen. Phase analysis was carried out using a  
PANalytical Aeris diffractometer and the ICDD's Diffraction File (PDF-4+).

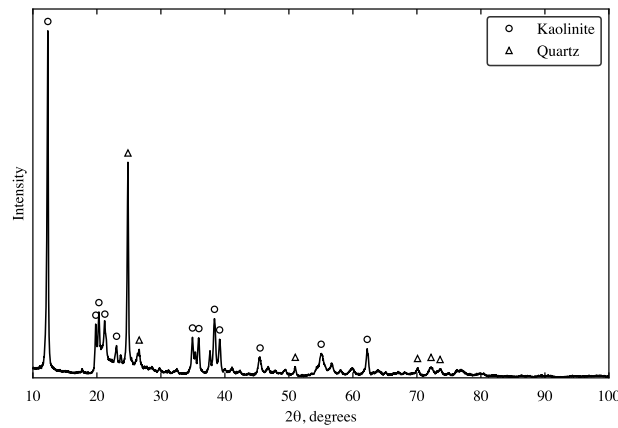


Figure 1: X-ray diffraction data of the kaolin clay soil.

105

106 Figure 1 shows the diffraction pattern of the kaolin clay. As expected, kaolinite is the primary  
107 mineral, followed by quartz. The cohesive soil used in this investigation is composed of 70%  
108 kaolinite and 30% quartz.

109 *2.2. Particle size distribution*

110 The particle size distribution (PSD) of the kaolin clay is assessed using the data sheet provided  
111 by the supplier, IMERYYS. Figure 2 depicts the cumulative PSD of the kaolin clay. The  $D_{50}$  of this  
112 well-graded impermeable soil is  $0.74 \mu\text{m}$ , and the clay and silt contents are calculated to be 80 %  
113 and 20 %, respectively. The soil is therefore characterised as CLAY (CL).

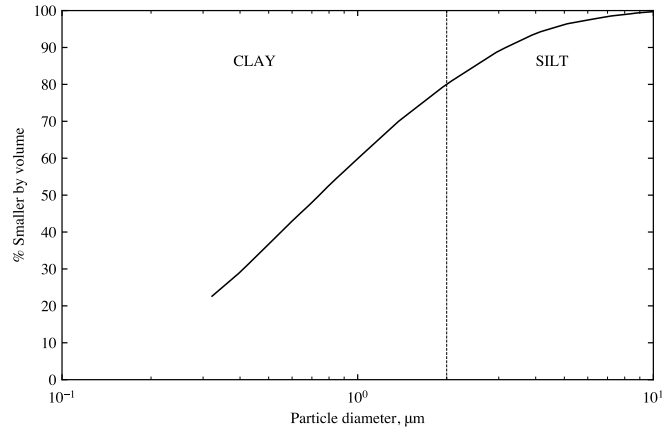


Figure 2: Cumulative particle size distribution of the kaolin clay soil (from IMERYYS data sheet).

### 114 2.3. Particle density

115 The particle density, denoted as  $\rho_s$ , represents the density of the solid mineral particles. It  
 116 is used with the bulk dry density,  $\rho_d$ , to determine the void ratio of a soil using the following  
 117 relationship:

$$e = \frac{\rho_s}{\rho_d} - 1 \quad (1)$$

118 The particle density,  $\rho_s$ , of the kaolin clay was calculated to be  $2.65 \text{ Mg.m}^{-3}$ , using the method  
 119 described in BS 1377-2:1990 §8.2 [21], which is the density of kaolinite.

### 120 2.4. Atterberg limits

121 To ensure sample consistency, Atterberg limits must be consistent across all soil samples. The  
 122 fall cone test was used to obtain consistent Atterberg limit values for the different kaolin clay  
 123 samples [21]. The liquid limit, LL, plastic limit, PL, and plastic index, PI are 40 %, 25 % and 15  
 124 %, respectively [21]. The values of which are above the A-line, confirming the soil selected is a  
 125 CLAY (CL) [22].

126 *2.5. Particle shape*

127 The shape of the kaolinite-sized particles in the soil are assessed qualitatively with a scanning  
128 electron microscope (SEM), using the descriptors provided in EN ISO 14688–1:2002 [20]. The  
129 kaolin clay soil was gold (Au) coated before being inserted into the SEM. Using Figure 3, the  
130 kaolin clay particles vary from low to medium sphericity, are subrounded to subangular, and have  
131 smooth surface texture.

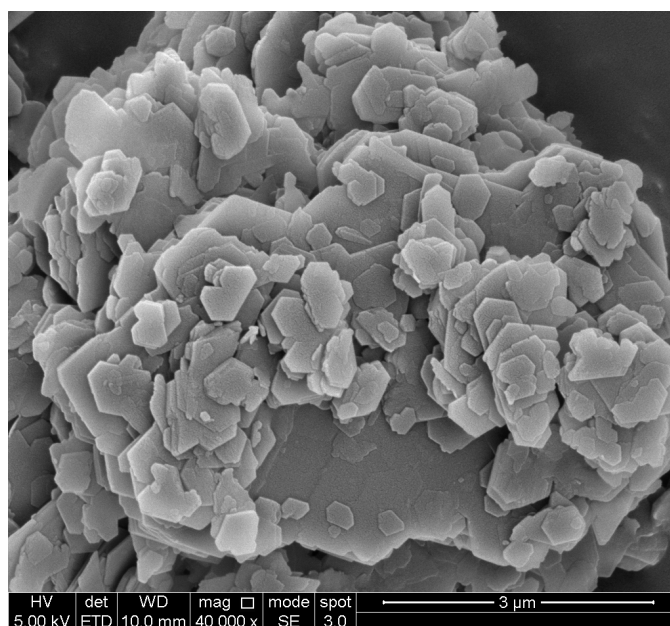


Figure 3: SEM imagery of kaolin clay at 40,000x magnification.

132 **3. Specimen preparation**

133 Kaolin clay samples are made using powdered speswhite kaolin clay. The powder was mixed  
134 with water at a 1:1 ratio to create a kaolin slurry, which was then placed in a pressurised cylindrical  
135 Rowe cell to consolidate the kaolin clay to 600 kPa. This approach was employed to create a  
136 consolidated, fully saturated, kaolin clay wheel, with a corresponding moisture content of 44 %,   
137 as determined after preparation using the material characterisation tests indicated in section 2.

138 A controlled drying procedure was utilised to study the effect of moisture content in kaolin  
139 clay samples at high strain rates. Specimens with moisture content levels of 0, 5, 10, 15, 20, 25,  
140 30, 35, 41, 42 and 44 % were prepared, covering all saturation levels from unsaturated to fully  
141 saturated. To achieve a moisture content of 0%, the samples were oven-dried for 24 hours.

142 The kaolin clay samples used for both unconfined and confined SHPB testing are prepared  
143 using the following procedure:

- 144 1. Cylindrical kaolin clay samples with varying moisture content are made using a 25 mm  
145 stainless-steel cylinder slicer. The specimens have a nominal length of 5 mm and a diameter  
146 of 25 mm. The initial weight of the kaolin clay specimen is recorded immediately after it  
147 has been sliced.
- 148 2. Samples are air dried in a temperature-controlled setting at 20 degrees Celsius, and weighed  
149 at regular intervals to measure their current moisture content based on their initial wet weight  
150 and current weight.
- 151 3. Cut and air-dried samples are wrapped in polyvinylidene chloride to minimise changes in  
152 moisture content between sample preparation and testing. The samples are prepared and  
153 tested in different laboratories, hence they are stored in sealed plastic bags until required for  
154 testing.

#### 155 **4. Experimental setup**

156 The SHPB experimental set up consists of a typical pressure bar arrangement consisting of a  
157 striker, an incident and a transmitter bar each 25 mm in diameter and 350 mm, 2500 mm and 1500  
158 mm long, respectively, as represented in Figure 4. The pressure bars are made of stainless steel,  
159 with the incident bar having a density of 7666 kg/m<sup>3</sup>, a wave speed of 5376 m/s, and strain gauges  
160 with a gauge factor of 123. The transmitter bar has a density of 7677 kg/m<sup>3</sup>, a wave speed of 5305  
161 m/s, and strain gauges with a gauge factor of 127.

162 For confined SHPB testing, the experimental set up includes an additional steel confining ring  
163 shown in Figure 5a, which houses the kaolin clay sample and slots in between the incident and  
164 transmitter bars, as illustrated in Figure 5b.

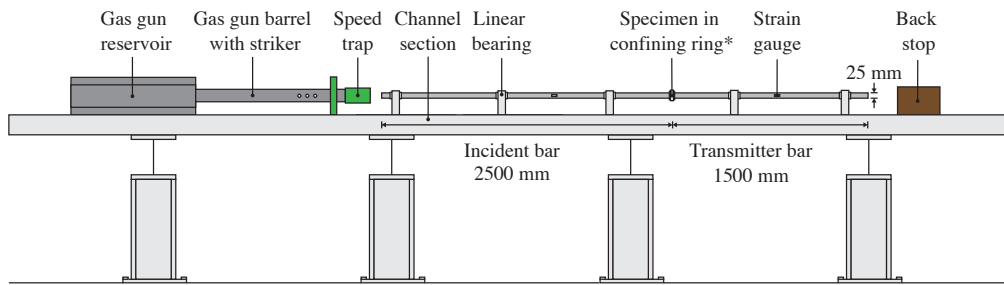


Figure 4: Schematic diagram of the SHPB experimental setup with the confining ring [\* removed for unconfined SHPB tests].

165 Signals from the pressure bar strain gauges are recorded using a TiePie Handyscope four-  
 166 channel digital oscilloscope with a 14-bit A-D resolution, a sample frequency of 1 MHz, and a  
 167 record length of 131.072 kSa. The material's axial stress response is monitored using a pair of Ky-  
 168 owa KSP-2-120-E4 strain gauges mounted on the incident and transmitter bars. The radial stress  
 169 response is measured using a single strain gauge mounted on the outside of the confining ring.  
 170 Strain gauge signals are collected from the incident and transmitter bars using a half Wheatstone  
 171 bridge configuration (Figure 6). Strain gauge signal from the confining ring is acquired using a  
 172 quarter Wheatstone bridge configuration (Figure 7).

## 173 5. Testing procedure

174 This experimental testing procedure was used on kaolin clay samples to demonstrate the  
 175 SHPB's ability to test cohesive soils under unconfined and confined conditions, as well as to  
 176 validate that the chosen design set up produces reliable measurements.

177 Prior to testing, the samples are weighed to three decimal places using an RS Pro weighing  
 178 scale, with a resolution of 0.001 g. The samples' thickness is measured using a digital calliper at  
 179 three different locations and averaged to account for any sample inconsistencies, with a resolution  
 180 of 0.01 mm. These parameters are required to process the experimental data.

181 Unconfined SHPB testing on kaolin clay samples was conducted using the following proce-  
 182 dure:

- 183 1. Supports surrounding the incident and transmitter bars are bolted down to the channel of the



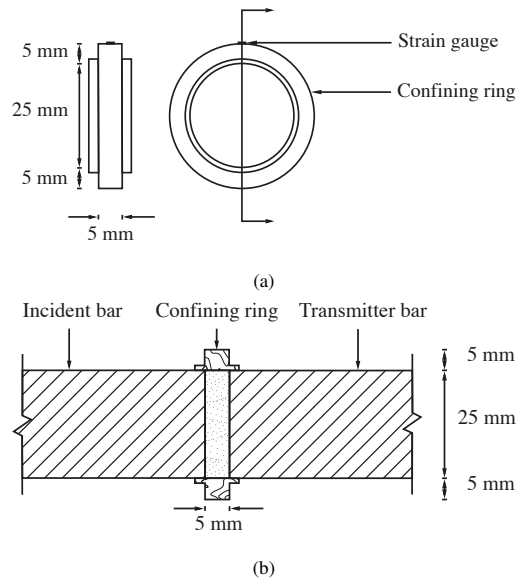


Figure 5: Diagrams showing (a) the confining ring for confined SHPB testing and (b) the confining ring with the sample inside, ready for testing.

184 SHPB setup.

- 185 2. A kaolin clay sample 5 mm in nominal length and 25 mm in diameter was placed in between  
 186 the incident and transmitter bars, inside a Perspex containment box.  
 187 3. The lid of the containment box is closed, ready for testing.

188 For confined SHPB testing, a similar testing procedure was followed, where the confining ring  
 189 was inserted onto the incident bar before the prepared specimen is gently placed in between the  
 190 incident and transmitter bars. After which, the confining ring is slid back over the specimen, ready  
 191 for testing.

192 In both cases, loading was achieved by hitting the incident bar with a steel striker bar fired  
 193 from a gas gun at varied speeds, with speeds measured using a speed trap at the exit of the gas gun  
 194 barrel, to achieve different strain rates.

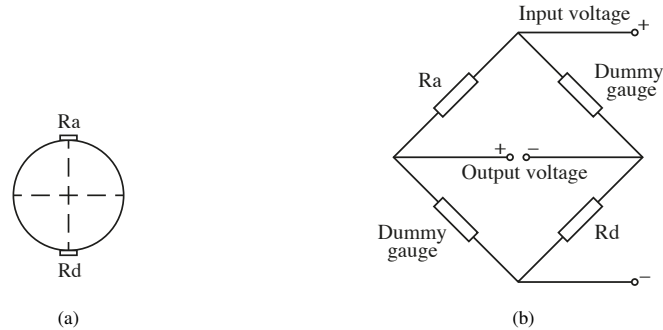


Figure 6: Pressure bars (a) strain gauge arrangement, and (b) half Wheatstone bridge configuration.

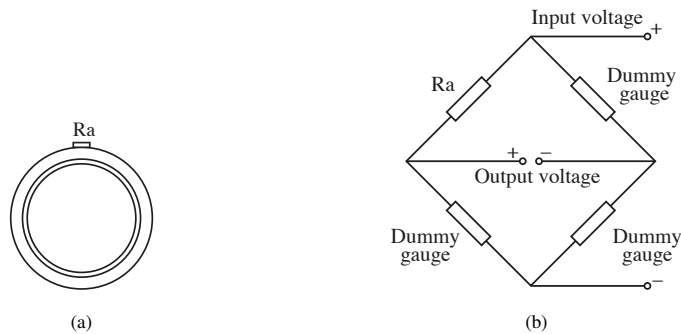


Figure 7: Confining ring (a) strain gauge arrangement, and (b) quarter Wheatstone bridge configuration.

195 **6. Test programme**

196 For unconfined SHPB testing, the test programme began with tests at 8, 12 and 16 m/s on  
 197 kaolin clay samples with varying moisture content ranging from 0 to 44 %. Additional tests were  
 198 carried out at 18, 20 and 22 m/s to evaluate the effects of kaolin clay at higher strain rates. Under  
 199 unconfined conditions, the maximum average strain rate was 1200, 1900 and 2770 s<sup>-1</sup>, for 8, 12  
 200 and 16 m/s, over approximately 150 μs, as shown in Figure 8.

201 For confined SHPB testing, the test programme began with tests at 12 m/s on kaolin clay  
 202 samples with varying moisture content ranging from 0 to 41 % for behavioural comparison with  
 203 the unconfined SHPB tests. Then, tests were carried out at 18, 20 and 22 m/s. Under confined  
 204 conditions, the maximum average strain rate was 2600, 2800 and 3100 s<sup>-1</sup>, for 18, 20 and 22 m/s,  
 205 over approximately 150 μs, as shown in Figure 9.

206 At these high strain rate conditions, the specimen's axial and radial stresses and strains are  
207 measured.

208 The test speed utilised during SHPB testing is setup-specific and depends on the gas gun con-  
209 figuration selected, whereas the strain rate is what the sample experiences during testing.

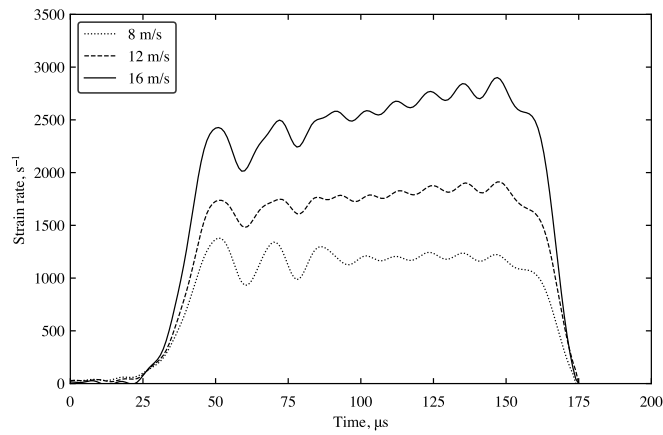


Figure 8: Strain rate variation during unconfined SHPB testing on kaolin clay, from specific tests.

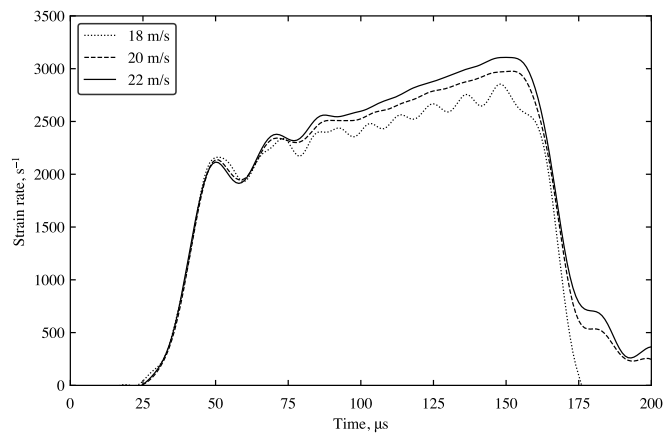


Figure 9: Strain rate variation during confined SHPB testing on kaolin clay, from specific tests.

210 Figures 10 and 11 provide a detailed breakdown of the tested speeds, moisture contents, and  
211 corresponding number of unconfined and confined SHPB tests, respectively.

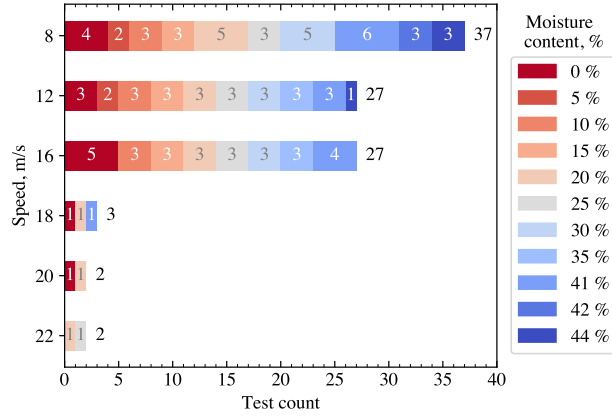


Figure 10: Unconfined SHPB test programme breakdown of the number of tests for each moisture content.

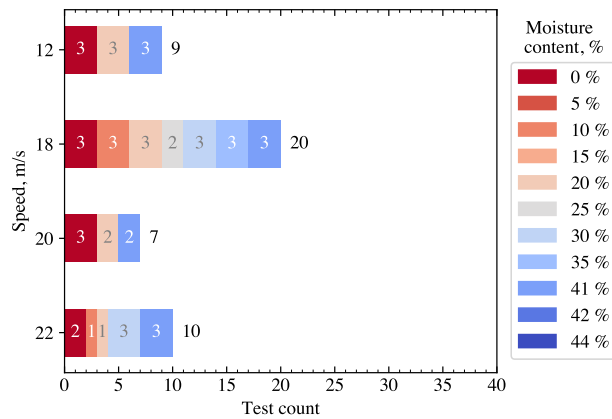


Figure 11: Confined SHPB test programme breakdown of the number of tests for each moisture content.

212 **7. Signal processing**

213 Incident bar, transmitter bar and confining ring signals gathered during SHPB tests on kaolin  
 214 clay samples with varying moisture contents, are processed using the open-source Python algo-  
 215 rithm SHPB\_Processing.py [23], available on ORDA [24]. This code incorporates the subrou-  
 216 tine dispersion.py, which implements Tyas and Pope’s dispersion-correction approach. This  
 217 ensures accurate representation of the sample’s axial and radial stresses and engineering strains  
 218 during testing [25].

219 To run the processing script, the amplification factors for the pressure bars and confining ring  
220 are needed. In the unconfined setup, the factors are 10 for the incident bar and 100 for the trans-  
221 mitter bar. In the confined setup, both bars use a factor of 10, while the confining ring is set to  
222 5.

223 All plots have a fixed y-axis limit for clarity and ease of comparison. Although all plots start  
224 at 0, this may not be immediately visible as the x-axis blends with the first few data points.

225 To aid comparison of the waveforms, stress wave signals were truncated to match the point  
226 where the sample reached its maximum strain, after being aligned at their peak at 50 microseconds.  
227 Outside the plotted range, the stress pulses naturally start and end at 0 as expected.

228 Alignment based on peak stress was performed specifically for this scenario, considering the  
229 tested strains, selected material, and its non-equilibrium stress conditions. Aligning based on peak  
230 stress at smaller strains would obscure the data.

231 Figures 12 and 13 show the front stress for a typical unconfined and confined SHPB test, com-  
232 puted using dispersion correction and simple time shifting. The ‘front’ stress pertains to the inci-  
233 dent bar-clay sample interface, while the ‘back’ stress corresponds to the clay sample-transmitter  
234 bar interface. These figures illustrate how the dispersion-corrected approach reduces stress wave  
235 amplitude, eliminating initial fluctuations and preventing inaccurate inferences about the kaolin  
236 clay specimen’s behaviour during SHPB testing. The amplitude difference between unconfined  
237 and confined SHPB tests is due to radial stresses being redirected axially by the confining ring.

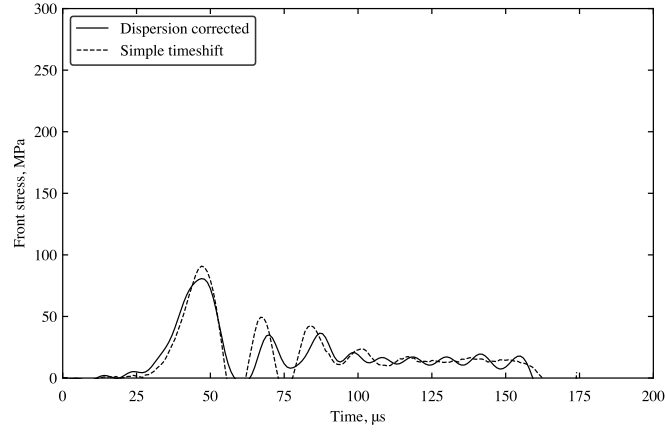


Figure 12: Front stress computed using dispersion correction and simple timeshifting, for a typical unconfined SHPB tests on kaolin clay.

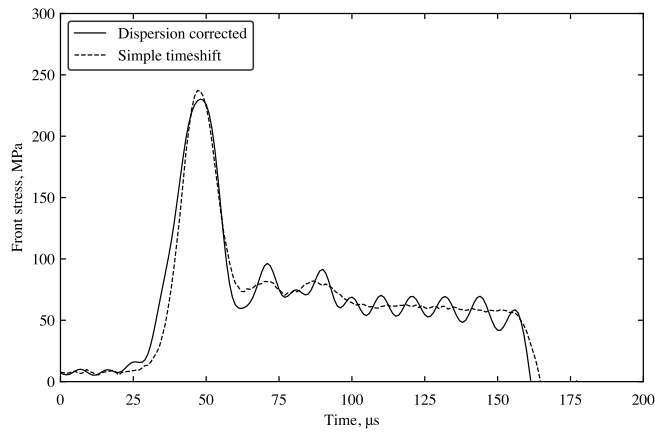


Figure 13: Front stress computed using dispersion correction and simple timeshifting, for a typical confined SHPB test on kaolin clay.

## 238 8. Experimental results

### 239 8.1. Sample material properties

240 After the completion of unconfined and confined SHPB tests, the main sample properties for  
 241 this study being the volume of air in the sample,  $V_{air}$ , volume of water in the sample,  $V_{water}$ , and to-  
 242 tal volume of the sample  $V$  are calculated in order to physically comprehend how the composition

243 of air, water and soil in the sample evolved during testing.

244 The diameter, thickness, wet mass, and dry mass of the sample are measured prior to testing,  
245 and its moisture content is then calculated based on these values. These properties are used to  
246 determine the volume,  $V$ , of the sample. The volume of water is determined by subtracting the dry  
247 mass from the wet mass and dividing the result by  $\rho_w$ , the density of water. The volume of solids  
248 is calculated by dividing the dry mass by the product of the specific gravity and  $\rho_w$ . With these  
249 values, the volume of voids ( $V_{voids} = V - V_{solids}$ ), and the volume of air ( $V_{air} = V_{solids} - V_{water}$ ), can  
250 be calculated.

251 The air volume ratio in the sample is derived by dividing the total volume of air in the sample  
252 ( $V_{air}$ ) by its entire volume ( $V$ ), using Equation 2:

$$\text{Air volume ratio} = \frac{V_{air}}{V} \quad (2)$$

253 the water volume ratio in the sample was computed by dividing the total volume of water in  
254 the sample ( $V_{water}$ ) by the total volume of the sample ( $V$ ), using Equation 3:

$$\text{Water volume ratio} = \frac{V_{water}}{V} \quad (3)$$

255 All these geotechnical properties were determined for each sample prior to testing.

## 256 8.2. Unconfined SHPB test results

257 Unconfined SHPB tests were performed on kaolin clay samples with moisture content levels  
258 ranging from 0 to 44 %, to cover all saturation stages: dry, partially-saturated and fully saturated.  
259 Initially, the samples were tested at 8, 12, 16 m/s, resulting in maximum average strain rates of  
260 1200, 1900 and 2770 s<sup>-1</sup>. The sample's strain, front, back and mid stresses were determined using  
261 the signal processing technique in section 7.

262 Figures 14, 15, 16 and 17 show that in a typical unconfined SHPB test at a moisture content of  
263 0 %, increasing the strain rate correlates with higher material strain, front, back and mid stresses.  
264 Figure 16 portrays kaolin clay's strain rate dependency. A crucial discovery in our understanding  
265 of the high strain rate behaviour of cohesive soils.

266 At the same strain rate, the material's strain and front stress behaviour are consistent across  
 267 all moisture contents. However, the back stress behaviour is dependent on the strain rate and  
 268 moisture content of the tested kaolin clay sample, where it exhibits four distinct phase behaviours,  
 269 as displayed in Figure 18. This means that the material's mid stress for a specific strain rate and  
 270 moisture content, is largely dependent on the measured back stress.

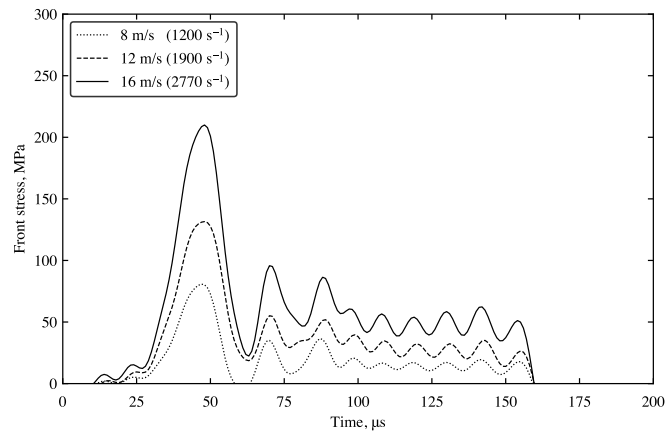


Figure 14: Typical front stress versus time behaviour for an unconfined SHPB tests on kaolin clay, at a moisture content of 0 % and different strain rates.

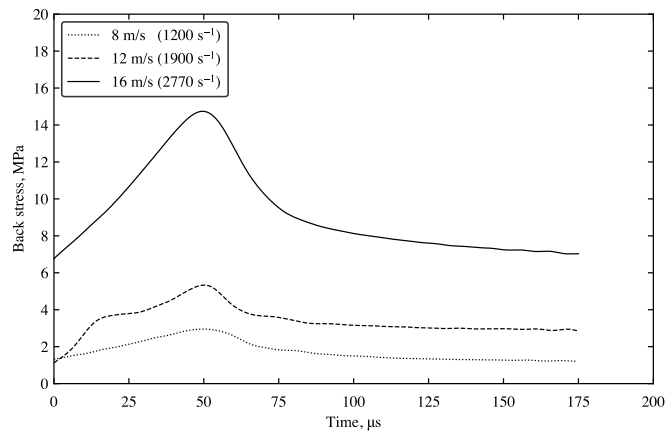


Figure 15: Typical back stress versus time behaviour for an unconfined SHPB tests on kaolin clay, at a moisture content of 0 % and different strain rates.



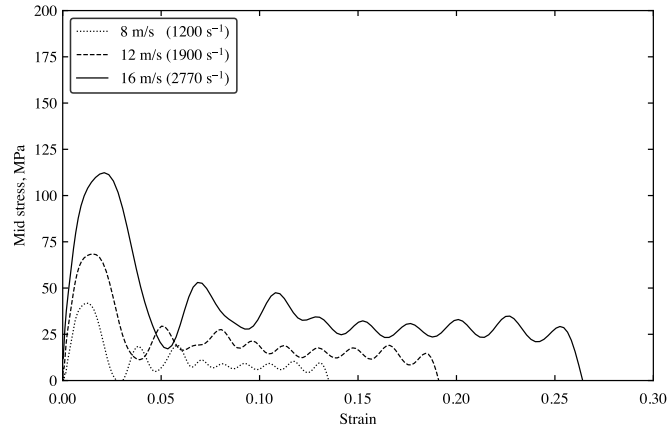


Figure 16: Typical mid stress versus strain behaviour for an unconfined SHPB tests on kaolin clay, at a moisture content of 0 % and different strain rates.

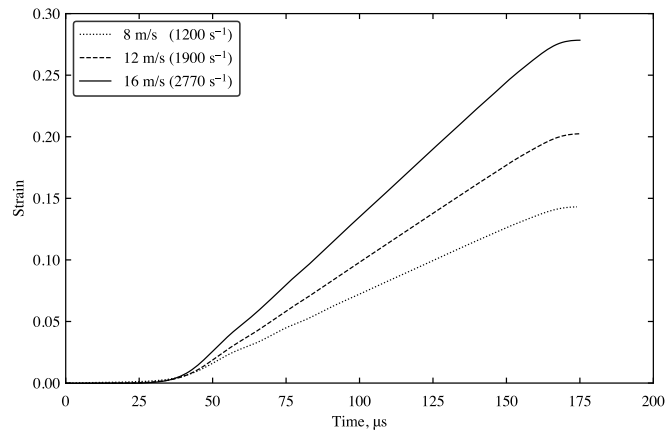


Figure 17: Typical strain versus time behaviour for an unconfined SHPB tests on kaolin clay, at a moisture content of 0 % and different strain rates.

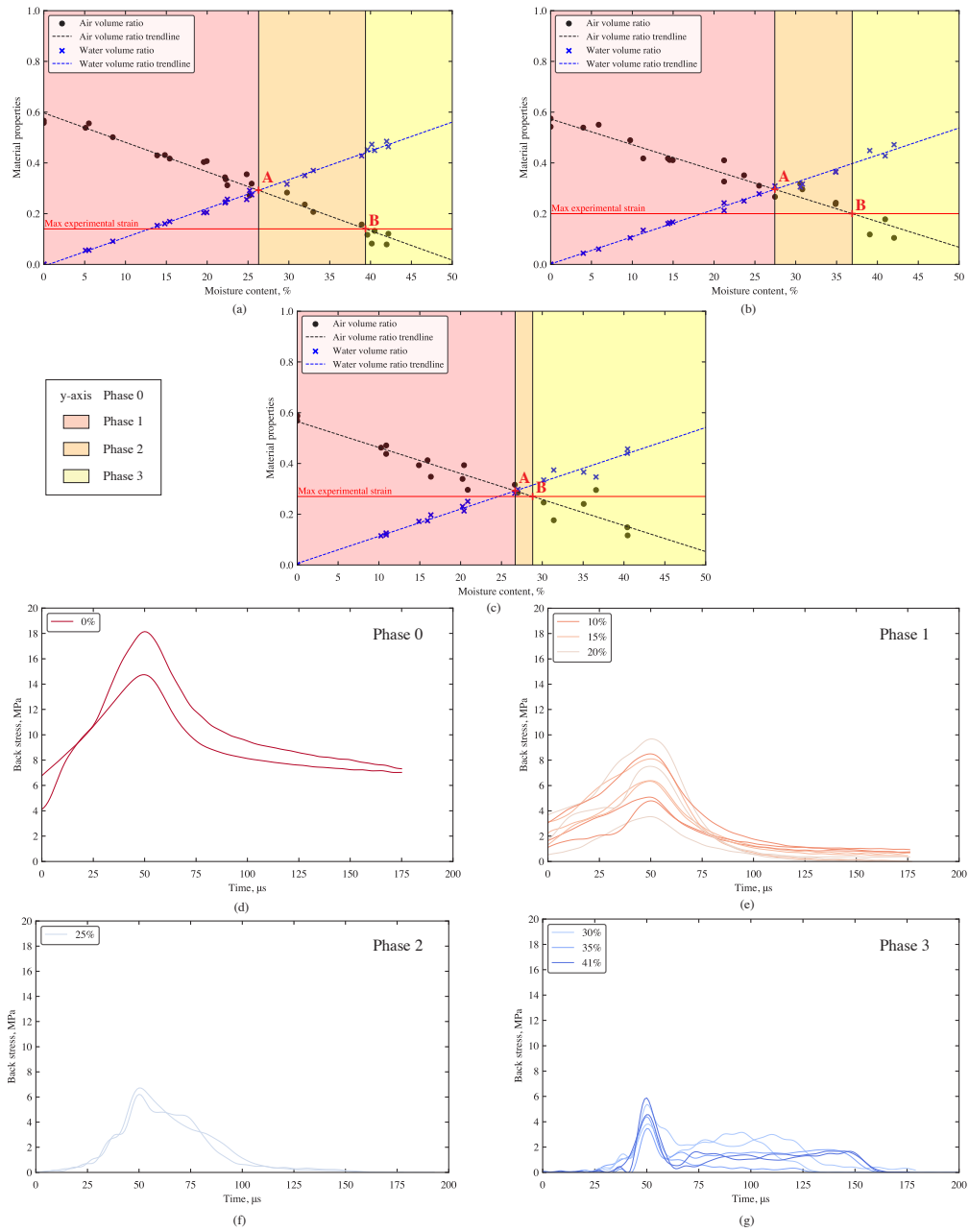


Figure 18: Unconfined SHPB testing of kaolin clay with (a) the phase behaviour at 8 m/s ( $1200 \text{ s}^{-1}$ ), (b) phase behaviour at 12 m/s ( $1900 \text{ s}^{-1}$ ) and (c) phase behaviour at 16 m/s ( $2770 \text{ s}^{-1}$ ), as well as the associated back stress at 16 m/s ( $2770 \text{ s}^{-1}$ ) for (d) Phase 0, (e) Phase 1, (f) Phase 2 and (g) Phase 3.

271 To facilitate the analysis of experimental data collected from SHPB tests, trends in material  
272 response based on the sample's material properties were categorised, each associated with repre-  
273 sentative phase behaviours depicted in Figures 18a, 18b and 18c. The four phases identified can  
274 be defined as follows:

- 275 • **Phase 0:** This phase includes the tests located on the y-axis of Figures 18a, 18b and 18c.  
276 Samples are dry, with a moisture content of 0 %. The sample no longer contains any water;  
277 it is dry, consisting mainly of air and kaolin clay. Since there is no moisture to encourage  
278 lateral extrusion of the sample in this phase, the back stress is the highest, and a larger  
279 proportion of the stress wave travels axially towards the transmitter bar. The back stress does  
280 not return to zero because the sample consolidates, leaving a thin dry kaolin disk between  
281 the bars (Figure 18d).
- 282 • **Phase 1:** This phase is shown in red in Figures 18a, 18b and 18c. Samples in this phase  
283 are partially-saturated throughout the test, and the soil pores are primarily filled with air.  
284 It encompasses tests with a moisture content above 0 % and the intersection of the air and  
285 water volume trendlines (Point A). The back stress during this phase has a distinct shape,  
286 with a magnitude significantly lower than in phase 0, and returns close to zero after reaching  
287 its peak as the sample almost entirely extruded during testing. In phase 1, moisture content  
288 has no effect on the back stress behaviour of the kaolin clay samples (Figure 18e).
- 289 • **Phase 2:** This phase is shown in orange in Figures 18a, 18b and 18c. Samples in this  
290 phase are partially-saturated throughout the test but the soil pores are primarily filled with  
291 water. The range of this phase varies depending on the strain rate of the tests and correlated  
292 between the theoretical and final experimental strains. This phase spans from Point A to the  
293 intersection of the air volume ratio and the maximum experimental strain experienced by  
294 the sample during testing (Point B). In phase 2, moisture content has no effect on the back  
295 stress behaviour of the kaolin clay samples (Figure 18f).
- 296 • **Phase 3:** This phase is shown in yellow in Figures 18a, 18b and 18c. Samples in this phase  
297 become fully saturated during testing. This phase includes tests with a moisture content

298 higher than the intersection of the air volume ratio and the maximum experimental strain  
299 experienced by the sample during testing (Point B). During this phase, the back stress first  
300 consists of an initial peak before levelling off and gradually decreasing back down to zero.  
301 This is due to the fast extrusion of the kaolin clay sample, which is behaving as a fluid.  
302 Within phase 3, moisture content has no effect on the back stress behaviour of the kaolin  
303 clay samples (Figure 18g).

304 To create the phase diagrams in Figures 18a, 18b and 18c, the previously calculated parame-  
305 ters—moisture content, water volume ratio, and air volume ratio—were plotted for each sample  
306 along with their trendlines. The maximum experimental strain for each sample, which indicates  
307 the point at which the sample becomes fully saturated and all air is removed, was recorded. Bound-  
308 ary lines were then added based on the intersections of these trendlines, defining the four distinct  
309 phase behaviours.

310 Figures 18a, 18b and 18c show that as strain rate rises, phase 1 and 3 increase, while phase 2  
311 decreases. This is due to the increase in the maximum experimental strain the sample experiences  
312 during unconfined SHPB testing. Additional tests performed at 18, 20 and 22 m/s have phase 2  
313 disappearing, as the maximum experimental strain achieved a strain of 0.29, at the intersection of  
314 the two trendlines.

### 315 8.3. *Confined SHPB test results*

316 Applying the same processing methodology used for unconfined SHPB tests (section 7), the  
317 sample's stress and strain data from the confined SHPB tests can be obtained. The confining  
318 ring is employed to investigate the effects of strain rate and moisture content and determine if the  
319 previously observed phase behaviour in unconfined testing persists under rigid lateral confinement.

320 Figures 19, 20, 21, 22 and 23 display the strain, radial, front, back and mid stresses for a  
321 typical confined SHPB test on kaolin clay, with 0 % moisture content at different strain rates. These  
322 figures illustrate how the stress and strain responses of the sample increase with higher strain rates,  
323 while the moisture content remains constant. At a given strain rate, strain and front stress remain  
324 consistent regardless of the moisture content of the sample. However, radial and back stresses vary  
325 depending on the sample's moisture content, directly impacting the mid stress response (Figure

326 24). The mid stress versus strain response is displayed in Figure 22. This confirms earlier findings  
327 from unconfined SHPB tests, highlighting the strain rate and moisture content dependence of  
328 cohesive soils (see section 8.2).

329 Similar to the findings in unconfined SHPB tests, moisture content in the sample significantly  
330 influences the high strain rate behaviour of back and radial stresses. Figure 24 illustrates the dis-  
331 tinct differences in stress propagation attributed to the phase behaviour of radial and back stresses.  
332 The rigid lateral confinement provided by the confining ring acts as a barrier, restricting lateral  
333 propagation and redirecting stress axially. This changes the applied loading from one-dimensional  
334 stress to one-dimensional strain. Additionally, the confining ring ensures stress wave equilibrium  
335 during testing and allows precise recording of radial stresses without deformation at high strain  
336 rates.

337 For fully saturated kaolin clay samples, a Poisson's ratio of 0.5 is calculated using confined  
338 SHPB test results, and gradually reduces as the sample's moisture content falls. Nevertheless, as  
339 the phase behaviour evolves from 4 to 3 phases, as seen in Figure 24, the confining ring is unable  
340 to completely seal the sample inside. Therefore, the radial stress obtained is solely a product of  
341 the high incident stresses caused by the speed of the striker bar as it impacts the sample, causing  
342 it to extrude.

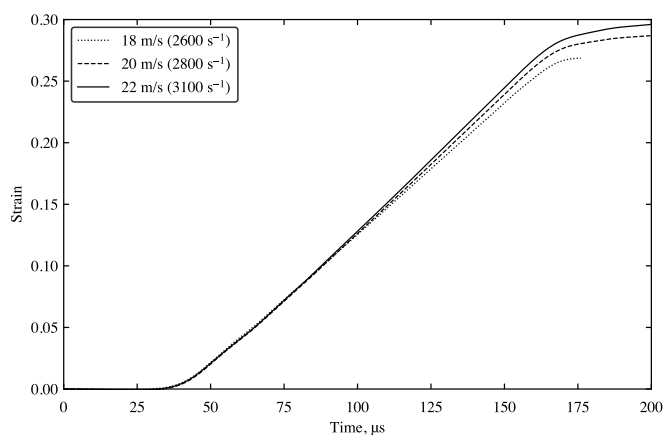


Figure 19: Typical strain versus time behaviour for a confined SHPB tests on kaolin clay, at a moisture content of 0% and different strain rates.

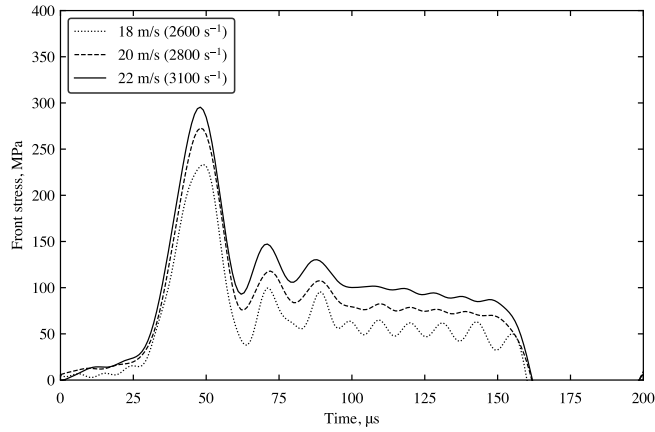


Figure 20: Typical front stress versus time behaviour for a confined SHPB tests on kaolin clay, at a moisture content of 0% and different strain rates.

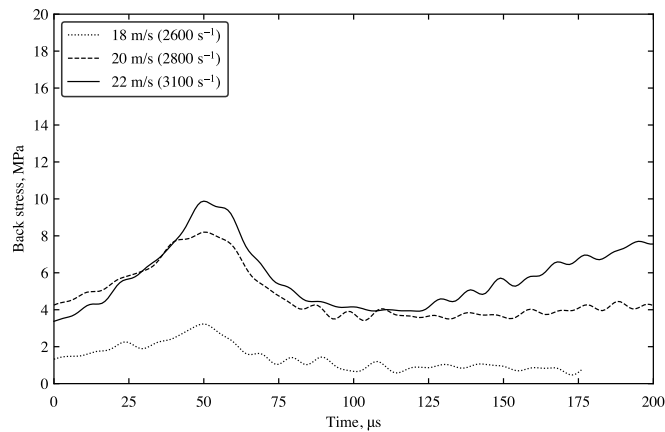


Figure 21: Typical back stress versus time behaviour for a confined SHPB tests on kaolin clay, at a moisture content of 0% and different strain rates.

343 The phase diagrams in Figures 24a, 24b and 24c for the confined SHPB tests were built using  
 344 a similar manner to Figures 18a, 18b and 18c for the unconfined SHPB tests.

345 Confined SHPB tests include four phases at 18 m/s (i.e. 2600 s<sup>-1</sup>) and three phases at 20 and  
 346 22 m/s (i.e. 2800 and 3100 s<sup>-1</sup>, respectively), as seen in Figures 24a, 24b and 24c.

347 In phases 0 and 1, back and radial stresses behave similarly. The back stress starts at zero,  
 348 increases to a maximum, then slowly decreases before levelling off, never returning to zero (Fig-

349 ures 24d and 24e). The radial stress reaches a similar maximum then returns to zero after 50  $\mu\text{s}$   
350 (Figures 24g and 24h).

351 This occurs for phase 0 and 1, since the volume of water in the sample is less than its total  
352 volume of air and soil. During testing, since samples in phase 0 and 1 have a large volume of air  
353 voids, they are compacted upon impact. The sample's compaction throughout testing generates a  
354 shock absorption effect, dampening the stress wave. As a result, just a fraction of the stress wave  
355 propagates through the sample onto the transmitted bar interface. This phenomenon is caused  
356 by the confining ring. This instrument provides a rigid lateral confinement around the sample,  
357 forcing it to consolidate, resulting in a high radial stress and a totally compacted sample at the end  
358 of testing.

359 It is crucial to note that at the same strain rate,  $2700 \text{ s}^{-1}$ , under unconfined conditions, a SHPB  
360 test requires a striker speed of 12 m/s. Hence, speed is relative to our own test setup whereas strain  
361 rate is what the sample exhibits during testing.

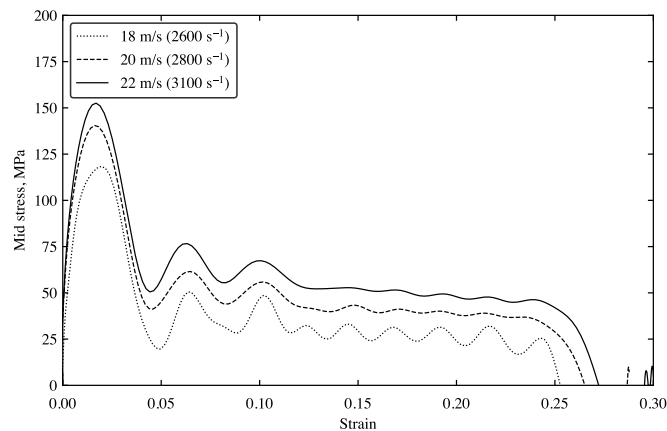


Figure 22: Typical mid stress versus strain behaviour for a confined SHPB tests on kaolin clay, at a moisture content of 0% and different strain rates.

362 Phase 2 manifests only in the confined SHPB tests at 18 m/s (equivalent to  $2600 \text{ s}^{-1}$ ). However,  
363 it completely vanishes when the sample's maximum experimental strain reaches 0.29, occurring at  
364 a strain rate of  $2700 \text{ s}^{-1}$  (Point B equals Point A), a finding empirically validated. Consequently,  
365 Phase 2 is conspicuously absent at higher velocities of 20 and 22 m/s (i.e.  $2800$  and  $3100 \text{ s}^{-1}$ ,

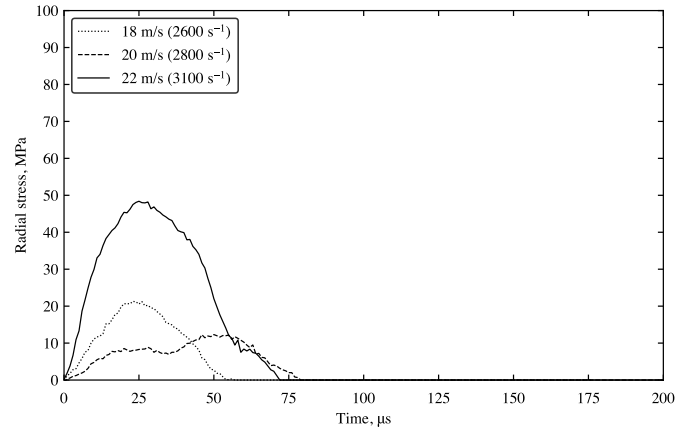


Figure 23: Typical radial stress versus time behaviour for a confined SHPB tests on kaolin clay, at a moisture content of 0% and different strain rates.

366 respectively), as shown in Figures 24a, 24b and 24c.

367 Figures 24f and 24i illustrate the discernible back and radial stress behaviours characteristic of  
 368 phase 3 compared to other phases. Beyond a strain rate of  $2700 \text{ s}^{-1}$ , following the disappearance of  
 369 phase 2, the impact of the incident bar, the effect of inertia, becomes significant enough to prompt  
 370 the sample extrusion, irrespective of confinement.

371 Similar to unconfined experiments, once the moisture content surpasses the threshold for the  
 372 specimen to achieve full saturation, the water content ratio dictates the sample's behaviour, leading  
 373 to complete lateral extrusion.

374 In theory, the confining ring forms a tight seal around the pressure bars, ostensibly preventing  
 375 sample extrusion. However, in practice, kaolin clay particles still undergo extrusion beyond a  
 376 certain strain rate due to the substantial impact caused. The confining ring's influence on stress  
 377 wave propagation in cohesive soils is underscored by several intrinsic factors.

## 378 9. Numerical modelling of SHPB tests

### 379 9.1. Model setup

380 The numerical model of the setup is shown in Figure 25. It was created using the FEM software  
 381 LS-DYNA, in order to compare numerical and experimental SHPB test results on kaolin clay



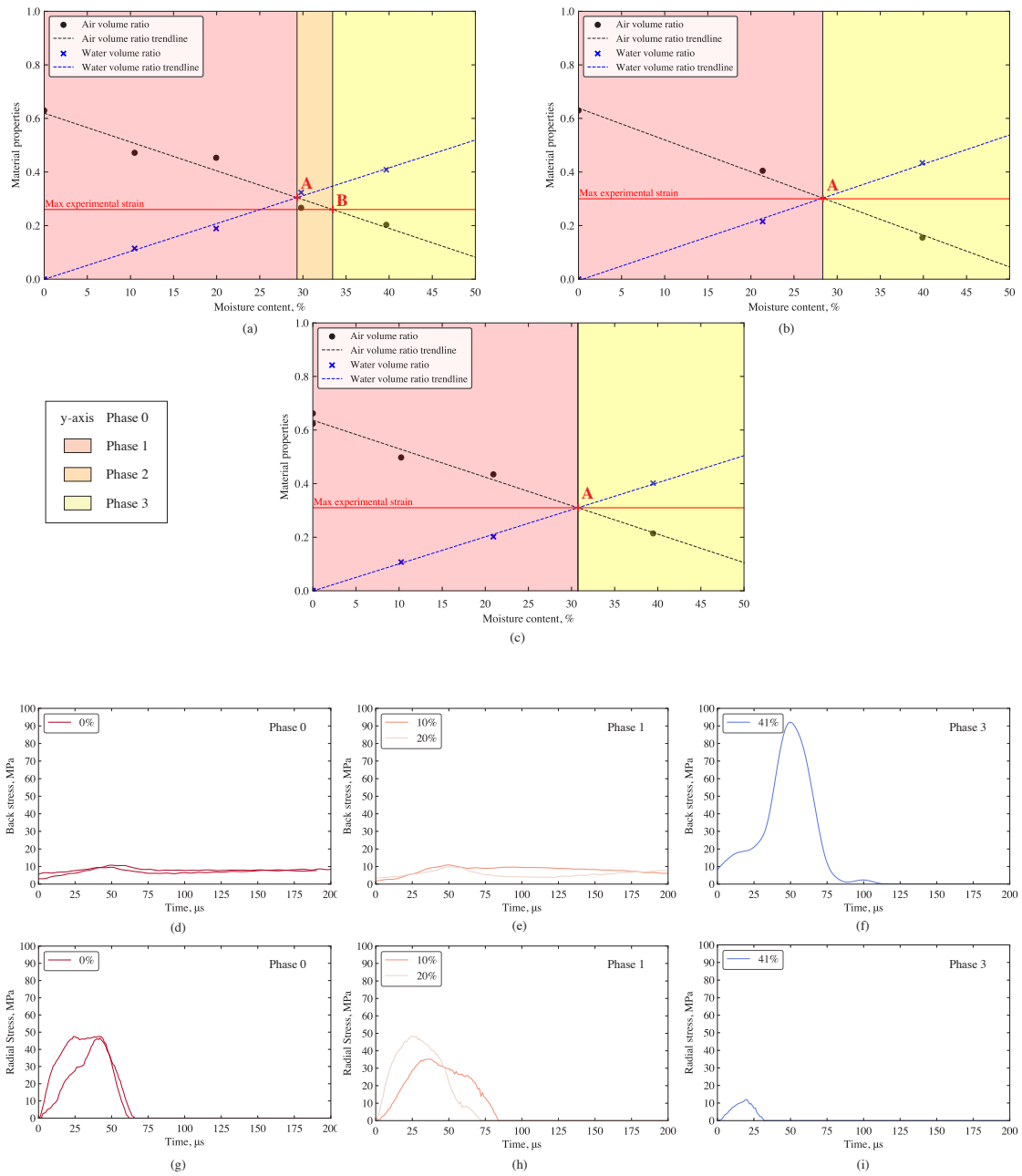


Figure 24: Confined SHPB testing of kaolin clay with (a) phase behaviour at 18 m/s ( $2600 \text{ s}^{-1}$ ), (b) phase behaviour at 20 m/s ( $2800 \text{ s}^{-1}$ ) and (c) phase behaviour at 22 m/s ( $3100 \text{ s}^{-1}$ ), as well as the associated back stress at 20 m/s ( $2800 \text{ s}^{-1}$ ) for (d) Phase 0, (e) Phase 1, and (f) Phase 3, and radial stress at 20 m/s ( $2800 \text{ s}^{-1}$ ) for (g) phase 0, (h) phase 1, and (i) phase 3.

382 samples. The striker (yellow in Figure 25), incident (blue in Figure 25) and transmitter (green in  
383 Figure 25) bars are modelled as 3D solid Lagrangian meshes. The confining ring (orange and pink  
384 in Figure 26b) is also modelled this way. SPH node modelisation was used for the kaolin clay  
385 sample.

386 Figure 26a depicts the 5 mm SPH kaolin clay sample section numerically simulated between  
387 the incident and transmitter bars. A more detailed representation of the confining ring with the  
388 SPH sample slotted inside is illustrated in Figure 26b. A fixed sample length of 5 mm was chosen,  
389 and the model's bulk density was changed to match the precise sample length tested using the  
390 SHPB apparatus.

391 When examined at high strain rates, kaolin clay exhibits high deformation and fluid-like be-  
392 haviour, hence SPH is chosen as the most suitable option over traditional ALE or Lagrangian  
393 meshing procedures. Consequently, there are no problems associated with excessive distortion or  
394 negative volume errors.

395 The contact interface between the SPH-modelled kaolin clay sample and the two Lagrangian  
396 pressure bars (i.e. incident and transmitter bar) was represented in LS-DYNA using the automated  
397 nodes-to-surface contact interaction. The contact interface between the SPH-modelled kaolin clay  
398 sample and the inside of the confining ring was modelled in this similar manner, using automated  
399 nodes-to-surface contact interaction.

400 The interfaces between the striker-incident bar, and incident-transmitter bar are modelled using  
401 manual surface-to-surface contact interactions.



Figure 25: LS-DYNA SHPB model set up with the confining ring [The confining ring is removed for unconfined SHPB modelisation].

## 402 9.2. Model material cards

403 The stainless-steel pressure bars are modelled as linear elastic using the \*MAT\_ELASTIC, with  
404 a density, Young's modulus and Poisson's ratio of  $\rho = 7666 \text{ kg.m}^{-3}$ ,  $E = 222 \text{ GPa}$  and  $\nu = 0.29$ ,  
405 respectively. To mirror the experimental tests, the model's striker bar velocity was set to the

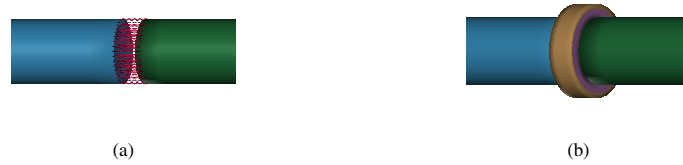


Figure 26: LS-DYNA zoom-in on modelling for (a) the unconfined SHPB setup, and (b) the confined SHPB setup.

406 associated striker speed used in experimental testing: 8, 12, 16 m/s for unconfined SHPB tests and  
 407 18, 20, 22 m/s for confined SHPB tests.

408 The confining ring used for SHPB testing is made of stainless-steel. It was initially modelled as  
 409 linear elastic using `*MAT_ELASTIC`, however, this led to a lot vibration and noise interference with  
 410 the numerical data. A fully rigid confining ring was modelled using the `*MAT_RIGID` to remove  
 411 these interferences associated with the contact between the pressure bars and the confining ring.  
 412 This resulted in no radial stress data being recorded. Therefore, a combination of rigid and elastic  
 413 elements were utilised to model the confining ring to be able to collect radial stress data (orange  
 414 and pink in Figure 26b).

415 The kaolin clay sample made using SPH was modelled with `*MAT_MOHR_COULOMB`, which has a  
 416 bulk density ( $\rho_0$ ), elastic shear modulus ( $G_{mod}$ ), Poisson's ratio ( $\nu$ ), angle of friction ( $\phi$ ) and  
 417 cohesion factor ( $c_{val}$ ). The bulk density ( $\rho_0$ ) and Poisson's ratio ( $\nu$ ) vary depending on the  
 418 moisture content of the kaolin clay sample examined.

419 Unconfined undrained triaxial (UU TXC) tests were conducted on fully saturated kaolin clay  
 420 to populate the LS-DYNA model using known quasi-static parameters. The angle of friction,  
 421  $\phi$ , was estimated by plotting Mohr's circles and adjusting the stress envelope slightly above  
 422 horizontal to avoid a zero value for  $\phi$ , which would cause model failure. This provided  $\phi =$   
 423  $4.62^\circ$  (0.08075 rad). The cohesion factor,  $c_{val}$ , was determined from the same plots, yielding a  
 424 value of 55,759.4 Pa. The elastic shear modulus,  $G_{mod}$ , was calculated as 1.3E7 Pa. The initial  
 425 density ( $\rho_{ttro}$ ) and Poisson's ratio ( $\nu$ ) were adjusted for each sample and are listed as  $x_1$  and  
 426  $x_2$  in Table 2. All these parameters are summarised in Table 2.

*MAT_MOHR_COULOMB								
\$#	mid	ro	gmod	rnu	phi	cval	psi	
	X	x1	1.3E7	x2	0.08075	55759.4	0.0	
\$#		nplanes		lccpdr	lccpt	lccjdr	lccjt	lcsfac
		0		0	0	0	0	0
\$#	gmoddp	gmodgr	lcmep	lcphiep	lcmst	cvalgr	aniso	
	0.0	0.0	0.0	0.0	0.0	0.0	1.0	

[x1 and x2 are adjusted based on the material properties of the sample tested.]

Table 2: Material card for \*MAT\_MOHR\_COULOMB, calibrated for use with kaolin clay [14].

### 427 9.3. Comparison between unconfined SHPB tests and corresponding LS-DYNA numerical models

428 The material card \*MAT\_MOHR\_COULOMB incorporates the bulk density,  $\rho$ , and Poisson's ratio,  $\nu$ ,  
 429 based on the moisture content of the sample being modelled. These parameters are designated as  
 430 x1 and x2 in Table 2.

431 Table 3 provides a comprehensive overview of the inputs utilised in LS-DYNA to model the  
 432 unconfined SHPB tests, along with the corresponding results, specifically the maximum front and  
 433 back stresses within the model. Twelve distinct unconfined SHPB model setups were executed,  
 434 each with varying input parameters, such as striker speed, moisture content, bulk density ( $\rho$ ) and  
 435 Poisson's ratio ( $\nu$ ).

436 Test number 6 highlighted a critical issue: inputting a Poisson's ratio of 0.5 in the \*MAT\_MOHR\_COULOMB  
 437 material card resulted in failure. The Poisson's ratio is a crucial parameter necessary to accurately  
 438 simulate the fluid-like behaviour of kaolin clay under high moisture content and high strain rates  
 439 (Table 3).

440 Test results also indicated that inputting a Poisson's ratio of 0.40, 0.44 or 0.49 yielded identical  
 441 maximum front and back stresses as noticed across tests no. 1, 2 and 3. Similarly, the variation  
 442 in bulk density within the sample, intended to simulate different moisture content levels, had no

443 effect on the output, as demonstrated by the consistent maximum front and back stresses observed  
444 in tests 2, 4 and 5 (Table 3).

445 The incident and reflected pulses as well as the back stress obtained from the LS-DYNA nu-  
446 merical models are compared against the experimental SHPB test data collected, as illustrated in  
447 Figures 27, 28 and 29.

448 Figures 27 and 28 juxtapose the typical experimental and numerical incident and reflected  
449 pulses obtained for a striker speed of 8 m/s ( $1200 \text{ s}^{-1}$ ). The shape of the incident pulse in the  
450 numerical model still mirrors a similar pattern to the experimental results. However, there is  
451 a notable difference in the reflected pulse behaviour. While experimentally, the incident pulse  
452 propagates through the sample, in the LS-DYNA numerical model, the incident pulse is completely  
453 reflected, indicating that the stress wave is unable to propagate through the SPH sample in the  
454 model. As a result, the computed front stress is significantly lower than the experimental results.

455 Figure 29 illustrates a notable disparity between the back stress in LS-DYNA and the exper-  
456 imental back stress. This disparity arises because the incident pulse is entirely reflected upon  
457 contact with the sample. Upon impact from the incident bar, the SPH particles in LS-DYNA eject  
458 both axially and laterally as the stress wave propagates through the kaolin clay sample. Conse-  
459 quently, the particle cohesion properties of the specimen do not contribute to the stress wave's  
460 propagation into the transmitted bar.

461 Despite the limitations in LS-DYNA in modelling cohesive soils at high strain rates, tests  
462 number 2, 4, 5, 7, 8, 9, 10, 11 and 12, conducted at speeds of 8, 12 and 16 m/s, demonstrated that  
463 as the strain rate increases so does the maximum front and back stresses. This indicates that these  
464 LS-DYNA models still adequately capture the effect of strain rate in cohesive soils at high strain  
465 rate.

#### 466 *9.4. Comparison between confined SHPB tests and corresponding LS-DYNA numerical models*

467 The same material card is used to model the confined SHPB tests in LS-DYNA, \*MAT\_MOHR\_  
468 COULOMB. Similarly to the unconfined SHPB models, Table 3 provides an overview of the inputs  
469 utilised in LS-DYNA to model the confined SHPB tests, along with the corresponding outputs,  
470 specifically the maximum front, back and radial stresses from the model.

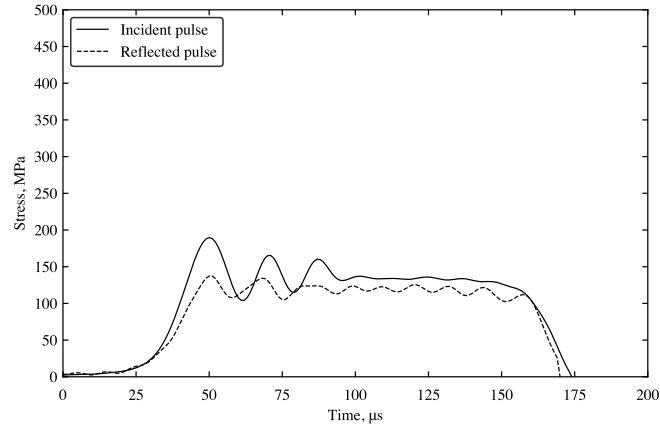


Figure 27: Typical stress behaviour from the incident and reflected pulses of an unconfined SHPB experimental test, at 8 m/s ( $1200 \text{ s}^{-1}$ ).

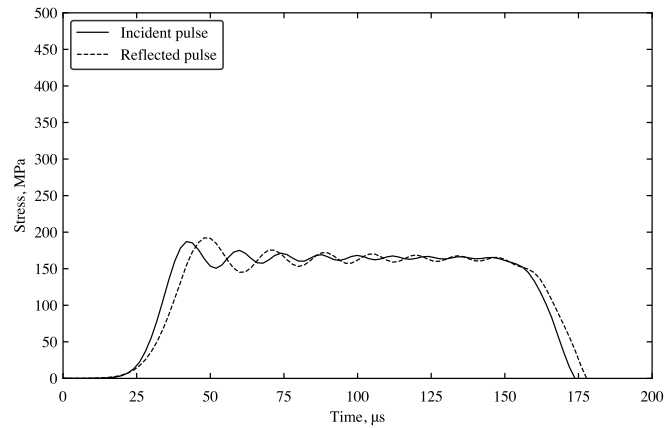


Figure 28: Typical stress behaviour from the incident and reflected pulses of an unconfined SHPB tests in LS-DYNA, at 8 m/s ( $1200 \text{ s}^{-1}$ ).

471 Tests 13 to 24, detailed in Table 3, echo the findings of unconfined SHPB models, confirming  
 472 that Poisson's ratio does not influence the results, with the model failing to run for a Poisson's  
 473 ration of 0.5. Furthermore, adjustments in moisture content through variations in bulk density,  
 474 observed in model tests 13 to 24, do not alter the material's behaviour in the model.

475 Figures 30 and 31 depict the incident and reflected pulses in the experimental tests and numer-  
 476 ical model. The front stress behaviour in the LS-DYNA numerical model resembles that observed

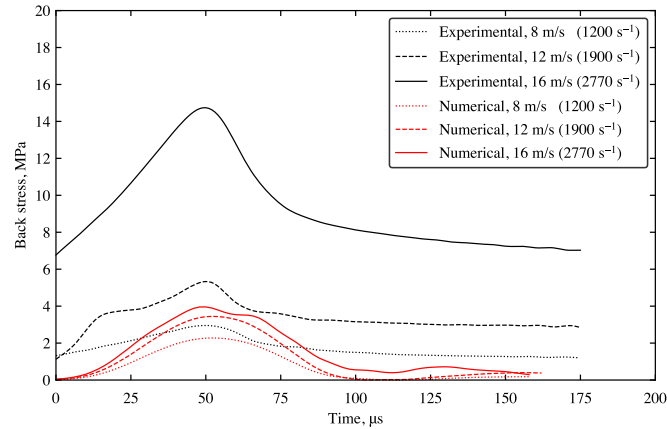


Figure 29: Comparison of back stress from the experimental unconfined SHPB tests and corresponding numerical LS-DYNA models on kaolin clay at a moisture content of 0% and different strain rates.

477 in the SHPB tests, albeit with a higher magnitude due to the sample containment seal in the nu-  
 478 merical model setup of the confining ring (Table 3).

479 Back and radial stresses are shown in Figures 32 and 33. The magnitudes of these stresses  
 480 are considerably higher than those obtained from experimental testing. This is primarily due  
 481 the confining ring's influence in LS-DYNA and its modelling approach, since the confining ring  
 482 effectively seals the SPH specimen inside, preventing extrusion during testing. Nevertheless, the  
 483 model does not accurately reflect the genuine behaviour of cohesive soils, as neither moisture  
 484 content nor Poisson's ratio affects the model outputs.

485 The back stress results from the numerical models show an increasing trend, consistent with  
 486 observations from SHPB testing. Additionally, the radial stress results from the models exhibit  
 487 also an increasing trend as speed increases (Table 3).

488 When the sample is fully saturated, with a Poisson's ratio of 0.5, the model fails to run due  
 489 to limitations of \*MAT\_MOHR\_COULOMB, necessitating the used of \*MAT\_NULL to model the fluid-like  
 490 behaviour of the material. Since there is no sample extrusion in the numerical model, the front,  
 491 back and radial stress results show higher values than in the experimental SHPB tests (Table 3).  
 492 The perfect seal of the ring in the model alters the sample's radial stress behaviour, as there is no  
 493 inertia effect from the incident bar impacting the sample. Hence, the radial stress does not fall due

Test No.	Striker speed m/s	Moisture content %	$\rho$ ( $\tau\text{o}$ ) $\text{kg}\cdot\text{m}^{-3}$	$\nu$ (rnu)	Max front stress MPa	Max back stress MPa	Max radial stress MPa
UNCONFINED SHPB MODELLING							
1	8	0	934	0.40	21.4	2.3	–
2	8	0	934	0.44	21.4	2.3	–
3	8	0	934	0.49	21.4	2.3	–
4	8	20	1087	0.44	21.4	2.3	–
5	8	41	1296	0.44	21.4	2.3	–
6	8	41	1296	0.50	FAIL	FAIL	–
7	12	0	934	0.44	32.8	3.4	–
8	12	20	1087	0.44	32.8	3.4	–
9	12	41	1296	0.44	32.8	3.4	–
10	16	0	934	0.44	44.8	4.0	–
11	16	20	1087	0.44	44.8	4.0	–
12	16	41	1296	0.44	44.8	4.0	–
CONFINED SHPB MODELLING							
13	18	0	934	0.40	324.4	394.3	509.0
14	18	0	934	0.44	324.4	394.3	509.0
15	18	0	934	0.49	324.4	394.3	509.0
16	18	20	1087	0.44	324.4	394.3	509.0
17	18	41	1296	0.44	324.4	394.3	509.0
18	18	41	1296	0.50	FAIL	FAIL	FAIL
19	20	0	934	0.44	365.1	432.6	624.0
20	20	20	1087	0.44	365.1	432.6	624.0
21	20	41	1296	0.44	365.1	432.6	624.0
22	22	0	934	0.44	410.3	481.3	674.0
23	22	20	1087	0.44	410.3	481.3	674.0
24	22	41	1296	0.44	410.3	481.3	674.0

['–': Data not recorded, 'FAIL': LS-DYNA model failed to run]

Table 3: Summary of the LS-DYNA modelling inputs and outputs.

494 to excessive sample extrusion from the ring, before rising again, as seen in testing.



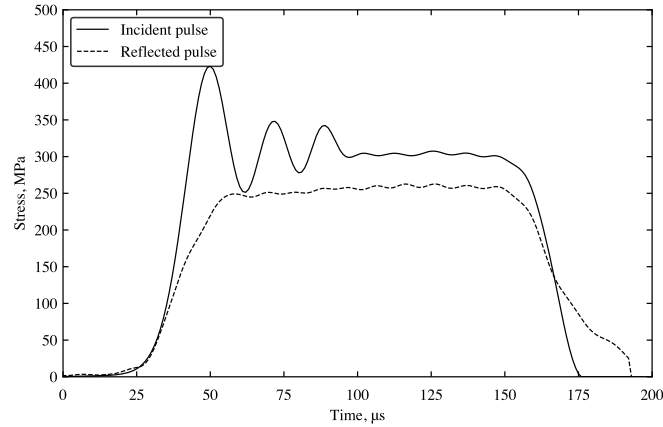


Figure 30: Typical stress behaviour from the incident and reflected pulses of a confined SHPB experimental test, at 18 m/s ( $2600 \text{ s}^{-1}$ ).

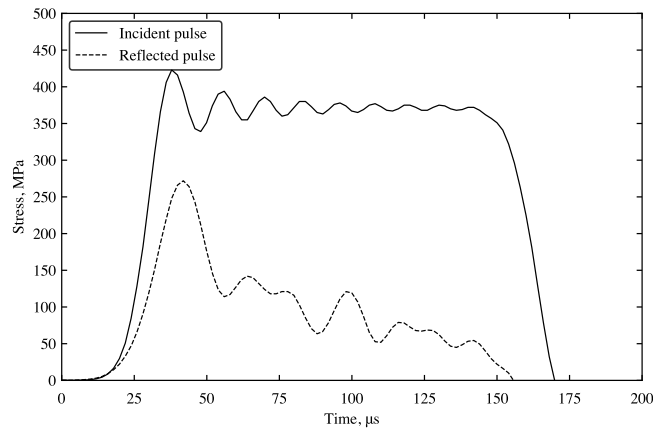


Figure 31: Typical stress behaviour from the incident and reflected pulses of a confined SHPB tests in LS-DYNA, at 18 m/s ( $2600 \text{ s}^{-1}$ ).

495 *9.5. LS-DYNA modelling limitations*

496 Notable LS-DYNA modelling limitations are as follows:

- 497 1. The difficulty in computing a compression curve due to the material's inability to endure  
 498 multi-axial compression without extrusion. Since kaolin clay is strain rate dependent, there  
 499 are no equations of state currently implemented into numerical simulation codes that take

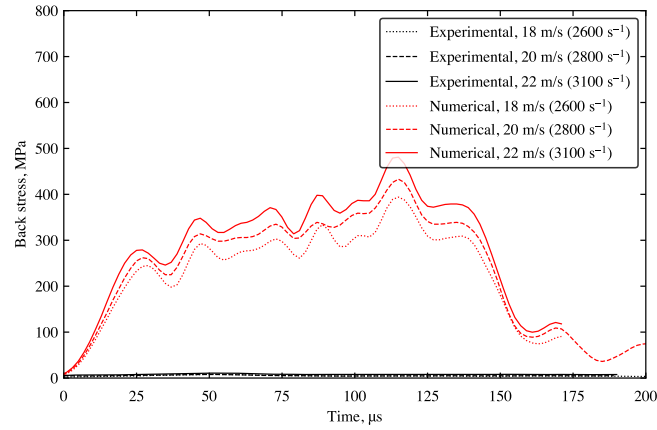


Figure 32: Comparison of back stress from the experimental confined SHPB tests and corresponding numerical LS-DYNA models on kaolin clay at a moisture content of 0% and different strain rates.

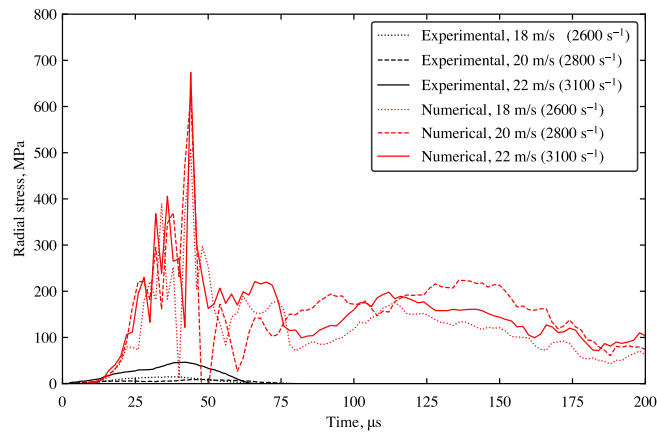


Figure 33: Comparison of radial stress from the experimental confined SHPB tests and corresponding numerical LS-DYNA models on kaolin clay at a moisture content of 0% and different strain rates.

500 account of the complete time- or frequency-dependence of the mechanical response of co-  
 501 hesive soils. Most soil specific and cohesion material models in LS-DYNA require an EOS,  
 502 therefore the list of material models which could be utilised with the parameters we collected  
 503 is very short, leaving \*MAT\_MOHR\_COULOMB as the most suitable option.

504 2. During the comparison of experimental SHPB test data and associated LS-DYNA numerical  
 505 models, the impact of the material's moisture content could not be observed in the numerical

506 model. Therefore, the phase behaviour could not be mapped out in LS-DYNA. This is due  
507 to the model's limitations in modelling cohesive soils at high strain rates.

508 3. The development of the SPH node modelisation technique in LS-DYNA is limited. LS-  
509 DYNA is unable to accurately represent the cohesion properties of cohesive soil particles.  
510 The deficiency, compounded by the lack of cohesion properties in this node modelisation  
511 tool, hinders the ability to accurately model the high strain rate behaviour of cohesive soils  
512 [26].

513 4. The numerical modelling of the confining ring revealed constraints related to sample extru-  
514 sion, seal, vibration and contact, hence it required adjustments. Experimentally, an elastic  
515 stainless-steel ring was used to obtain the radial stress behaviour of the tested specimen, but  
516 its excessive deformation compromised accuracy. Therefore, a rigid-elastic confining ring  
517 was created to fully confine the sample, maintain stress equilibrium, prevent sample extru-  
518 sion with a tight seal, and record radial stresses without complete deformation. The rigid  
519 element is 1/3 the thickness of the ring on the outside, while the elastic element is 2/3 the  
520 thickness on the inside, in contact with the SPH sample. Nevertheless, the perfect seal of  
521 the confining ring affects the stress results produced from the model, making them greater  
522 than they should be.

## 523 **10. Discussion**

524 The effect of moisture content on the behaviour of cohesive soils was thoroughly investigated  
525 through SHPB tests conducted under both confined and unconfined conditions, revealing an in-  
526 herent phase behaviour. This phase behaviour significantly impacts the use of cohesive soils, as  
527 moisture content directly affects the material's ability to propagate stress. Moisture content levels  
528 in phase 1 yielded the most effective results in preventing stress wave propagation in confined test  
529 cases, while in unconfined test cases, phase 4 was the most effective.

530 In unconfined SHPB testing, phase 4 sees the behaviour of the material governed by the water  
531 volume in the specimen. In unconfined testing scenarios, stress propagation through the material  
532 is primarily limited by moisture content, while any remaining stress propagates laterally as the

533 specimen extrudes. However, implementing this in practice poses challenges due to the difficulty  
534 in transporting and moulding the material into specific structures.

535 In confined SHPB testing, phase 1 sees the material's physical behaviour dictated by the soil,  
536 as the volume of soil in the sample exceeds that of water. In contrast to other phases, where  
537 the water volume ratio is either nonexistent (phase 0) or dominant (phases 2 and 3), phase 1  
538 sees the water volume in the sample aiding to the material's strengthening. In cases where a  
539 confining ring restricts lateral propagation, stress is redirected axially, resulting in an increase in  
540 axial stress, as seen in phase 4 for confined SHPB tests. When phase 2 disappears, radial stress  
541 initially drops but then rises again due to inertia effects from the incident bar, resulting in sample  
542 extrusion. This indicates that the confining ring is unable to contain the sample at such high strain  
543 rate levels. Moreover, differing speed and strain rate between unconfined and confined SHPB  
544 tests underscored confinement's impact kaolin clay's high strain rate behaviour. The stress-strain  
545 analysis of the sample revealed a clear strain rate dependence of the material at high strain rates.

546 Given the high strain rate conditions of this research, SPH node modelisation was chosen to  
547 model the kaolin clay sample, due to its suitability for high-impact high-deformation scenarios.  
548 However, the material's strain rate dependency posed challenges in modelling the SHPB tests  
549 using LS-DYNA, as no suitable material cards were available. The absence of dedicated material  
550 cards for cohesive soil modelling in LS-DYNA complicated the depiction of observed behaviour  
551 during testing. Consequently, a general material card \*MAT\_MOHR\_COULOMB, was used to model the  
552 kaolin clay.

553 In the unconfined SHPB models, the incident pulse closely matched that of the SHPB tests,  
554 validating the model setup. However, the reflected pulse exhibited considerable differences, result-  
555 ing in lower front and back stress responses, attributable to the stress wave's inability to propagate  
556 through the sample. The SPH particles dissipated instantly upon contact with the incident pulse.  
557 In the confined SHPB models, the front, back and radial stresses are considerably higher than  
558 those obtained from the SHPB tests, since the confining ring provides a perfect seal in the model  
559 enabling the stress wave to propagate through the sample more easily, resulting in considerably  
560 greater values. The rising trend observed for the front and back stresses in testing was also noticed  
561 in the model. The radial stresses obtained in the model, using a composite half-rigid, half-elastic

562 confining ring with a perfect seal, significantly surpass those observed in testing. This is because  
563 the numerical model is a perfect test representation from which to obtain the radial stress, therefore  
564 it is unable to capture the inertial effect from the incident bar.

565 Comparing the tests to the numerical models for kaolin clay samples with varying moisture  
566 contents, it was observed that the variation in moisture content in model failed to demonstrate the  
567 same phase behaviour. The discrepancy can be attributed to LS-DYNA's limitations in modelling  
568 cohesive soil properties accurately, leading to erroneous modelling findings.

569 Given the proven limitations of LS-DYNA demonstrated in this paper, other FEA packages,  
570 such as ABAQUS using material models such as Cam-Clay [27], may be worth exploring for  
571 modelling the high-strain-rate behaviour of cohesive soils.

572 In conclusion, cohesive soils' ability to limit stress propagation is clearly influenced by mois-  
573 ture content and confinement. The SHPB test derived back stress indicates the stress that can  
574 propagate through the sample, with moisture content acting as a dampener that impedes lateral  
575 stress propagation. Confinement restricts lateral extrusion, redirecting radial stress axially and  
576 consequently affecting stress transmission through the sample.

## 577 **11. Summary**

578 In this study, the high strain rate behaviour of cohesive soils was investigated using the SHPB  
579 apparatus. A comprehensive material characterisation analysis was conducted on the chosen co-  
580 hesive soil, kaolin clay. High strain rate SHPB tests were performed on kaolin clay samples with  
581 different moisture content levels under both unconfined and confined conditions. The experimen-  
582 tal results emphasise the novelty of this research, revealing that strain rate, moisture content and  
583 confinement all influence the behaviour of cohesive soils at high strain rates. The presence of a  
584 soil phase behaviour based on the sample's moisture content was identified, as evidenced by the  
585 back stress for the unconfined SHPB tests and the radial and back stresses for the confined SHPB  
586 tests.

587 The FEM software LS-DYNA was used to simulate the unconfined and confined SHPB tests  
588 performed on kaolin clay samples at varying moisture contents. While modelling the test setup  
589 posed no significant challenges, clear limitations were observed in LS-DYNA when comparing

590 experimental and numerical results: there is no dedicated material card model for cohesive soils,  
591 no cohesive properties in the software and very limited use of SPH for modelling the high strain  
592 rate behaviour of cohesive soils. These findings underscore the existing gap in modelling the high  
593 strain rate behaviour of cohesive soils.

594 Future endeavours in this field will initially focus on developing data-driven parametric models  
595 using all the experimental test data collected. This will enable the prediction of the unconfined and  
596 confined behaviour of cohesive soils, at high strain rates within the explored range, thereby saving  
597 considerable time and costs. Subsequently, in light of the discussed modelling limitations, there  
598 is a clear need for improvements in modelling the high strain rate behaviour of cohesive soils. To  
599 address this, experimental test data will be utilised to develop a hybrid twin model that incorporates  
600 all SHPB test results, enriching the numerical model.

601 Furthermore, the effect of confinement was explored by comparing a free-field unconfined  
602 scenario with a rigid confined SHPB test scenario. However, an intermediate case remains unex-  
603 plored, which would assess the impact of confining pressure on lateral and axial stress propagation.  
604 This avenue presents an opportunity for further investigation.

#### 605 **Author statement**

606 **Arthur Van Lerberghe:** Conceptualisation, Methodology, Investigation, Testing, Analysis  
607 & Writing. **Kin Shing O. Li:** Conceptualisation, Modelling & Analysis. **Andrew D. Barr:**  
608 Conceptualisation, Supervision & Review. **Sam D. Clarke:** Conceptualisation, Supervision &  
609 Review.

#### 610 **Acknowledgements**

611 This research was funded by the Engineering and Physical Sciences Research Council (EP-  
612 SRC), and the Defence Science and Technology Laboratory (Dstl).

#### 613 **Declaration of competing interest**

614 The authors declare that they have no known competing financial interest or personal relation-  
615 ships that could have appeared to influence the work reported in this paper.

616 **References**

- 617 [1] C. A. Ross, P. T. Nash, G. J. Friesenhahn, Pressure waves in soils using a split-hopkinson pressure bar, Tech.  
618 rep., Southwest Research Institute San Antonio TX (1986).
- 619 [2] G. E. Veyera, Uniaxial stress-strain behavior of unsaturated soils at high strain rates, Tech. rep., Wright Lab  
620 Tyndall Afb Fl (1994).
- 621 [3] G. T. Gray III, Classic split hopkinson pressure bar testing, ASM handbook 8 (2000) 462–476.
- 622 [4] A. Bragov, A. Lomunov, I. Sergeichev, K. Tsembelis, W. Proud, Determination of physicomechanical properties  
623 of soft soils from medium to high strain rates, International Journal of Impact Engineering 35 (9) (2008) 967–  
624 976. doi:<https://doi.org/10.1016/j.ijimpeng.2007.07.004>.
- 625 [5] H. Luo, W. L. Cooper, H. Lu, Effects of particle size and moisture on the compressive behavior of dense eglin  
626 sand under confinement at high strain rates, International Journal of Impact Engineering 65 (2014) 40–55. doi:  
627 <https://doi.org/10.1016/j.ijimpeng.2013.11.001>.
- 628 [6] A. D. Barr, Strain-rate effects in quartz sand, Ph.D. thesis, University of Sheffield (2016).
- 629 [7] B. Hopkinson, X. a method of measuring the pressure produced in the detonation of high, explosives or by the  
630 impact of bullets, Philosophical Transactions of the Royal Society of London. Series A, Containing Papers of a  
631 Mathematical or Physical Character 213 (497-508) (1914) 437–456. doi:[https://doi.org/10.1098/rsta.](https://doi.org/10.1098/rsta.1914.0010)  
632 [1914.0010](https://doi.org/10.1098/rsta.1914.0010).
- 633 [8] H. Kolsky, An investigation of the mechanical properties of materials at very high rates of loading, Proceedings  
634 of the physical society. Section B 62 (11) (1949) 676. doi:[https://doi.org/10.1088/0370-1301/62/11/](https://doi.org/10.1088/0370-1301/62/11/302)  
635 [302](https://doi.org/10.1088/0370-1301/62/11/302).
- 636 [9] H. Kolsky, Stress waves in solids. Dover Books on Physics, New York (1963). doi:[https://doi.org/10.](https://doi.org/10.1016/0022-460X(64)90008-2)  
637 [1016/0022-460X\(64\)90008-2](https://doi.org/10.1016/0022-460X(64)90008-2).
- 638 [10] A. Bragov, G. Grushevsky, A. Lomunov, Use of the kolsky method for confined tests of soft soils, Experimental  
639 Mechanics 36 (1996) 237–242. doi:<https://doi.org/10.1007/BF02318013>.
- 640 [11] Q.-Y. Ma, Experimental analysis of dynamic mechanical properties for artificially frozen clay by the split hop-  
641 kinson pressure bar, Journal of Applied Mechanics and Technical Physics 51 (3) (2010) 448–452. doi:[https:](https://doi.org/10.1007/s10808-010-0060-8)  
642 [//doi.org/10.1007/s10808-010-0060-8](https://doi.org/10.1007/s10808-010-0060-8).
- 643 [12] R. Yang, J. Chen, L. Yang, S. Fang, J. Liu, An experimental study of high strain-rate properties of clay under  
644 high consolidation stress, Soil Dynamics and Earthquake Engineering 92 (2017) 46–51. doi:[https://doi.](https://doi.org/10.1016/j.soildyn.2016.09.036)  
645 [org/10.1016/j.soildyn.2016.09.036](https://doi.org/10.1016/j.soildyn.2016.09.036).
- 646 [13] A. Konstantinov, A. Bragov, L. Igumnov, V. Eremeyev, V. V. Balandin, et al., Experimental study and identifi-  
647 cation of a dynamic deformation model of dry clay at strain rates up to 2500 s-1, Journal of Applied and Com-  
648 putational Mechanics 8 (3) (2022) 981–995. doi:<https://doi.org/10.22055/jacm.2022.39321.3387>.
- 649 [14] J. O. Hallquist, et al., Ls-dyna keyword user’s manual, Livermore Software Technology Corporation 970 (2007)

- 650 299–800.
- 651 [15] P. Church, R. Cornish, I. Cullis, P. Gould, I. Lewtas, Using the split hopkinson pressure bar to validate material  
652 models, *Philosophical Transactions of the Royal Society A: Mathematical, Physical and Engineering Sciences*  
653 372 (2023) (2014) 20130294. doi:<https://doi.org/10.1098/rsta.2013.0294>.
- 654 [16] P. A. Cundall, O. D. Strack, A discrete numerical model for granular assemblies, *geotechnique* 29 (1) (1979)  
655 47–65. doi:<https://doi.org/10.1680/geot.1979.29.1.47>.
- 656 [17] C. L. Busch, R. A. Tarefder, Evaluation of appropriate material models in ls-dyna for mm-scale finite element  
657 simulations of small-scale explosive airblast tests on clay soils, *Indian Geotechnical Journal* 47 (2) (2017) 173–  
658 186. doi:<https://doi.org/10.1007/s40098-016-0196-4>.
- 659 [18] V. Eremeyev, V. Balandin, A. Bragov, A. Y. Konstantinov, L. Igumnov, et al., Experimental study and numerical  
660 simulation of the dynamic penetration into dry clay, *Continuum Mechanics and Thermodynamics* 35 (2) (2023)  
661 457–469. doi:<https://doi.org/10.1007/s00161-023-01189-w>.
- 662 [19] J. L. Lacombe, Smooth particle hydrodynamics (sph): a new feature in ls-dyna, in: 6th international LS-DYNA  
663 users conference, 2000, pp. 7–30.
- 664 [20] ISO, 14688-1: 2002: Geotechnical investigation and testing – Identification and classification of soil – Part 1:  
665 Identification and description, British Standards Institution (2002).
- 666 [21] BSI, BS 1377-2: 1990: Methods of test for soils for civil engineering purposes – Part 2: Classification tests  
667 (1990).
- 668 [22] A. Casagrande, Classification and identification of soils, *Transactions of the American Society of Civil Engineers*  
669 113 (1) (1948) 901–930. doi:<https://doi.org/10.1061/TACEAT.0006109>.
- 670 [23] A. Van Lerberghe, K. S. O. Li, A. D. Barr, S. D. Clarke, An open-source algorithm for correcting stress wave  
671 dispersion in split-hopkinson pressure bar experiments - submitted for publication in *Experimental Mechanics*,  
672 currently under review (2024).
- 673 [24] K. S. O. Li, A. Van Lerberghe, A. Barr, SHPB.Processing.py - An open-source Python algorithm for correct-  
674 ing stress wave dispersion in split-Hopkinson pressure bar experiments (2024). doi:[10.15131/shef.data.  
675 24570565.v1](https://doi.org/10.15131/shef.data.24570565.v1).
- 676 [25] A. Tyas, D. J. Pope, Full correction of first-mode pohammer–chree dispersion effects in experimental pres-  
677 sure bar signals, *Measurement science and technology* 16 (3) (2005) 642. doi:[https://doi.org/10.1088/  
678 0957-0233/16/3/004](https://doi.org/10.1088/0957-0233/16/3/004).
- 679 [26] K. S. O. Li, A. Van Lerberghe, A. Barr, S. D. Clarke, A. A. Dennis, Split-hopkinson pressure bar testing of water  
680 with partial lateral confinement - submitted for publication in *Measurement Science and Technology*, currently  
681 under review (2024).
- 682 [27] K. F. Mostafa, R. Y. Liang, Numerical Modeling of Dynamic Compaction in Cohesive Soils, pp. 738–747.  
683 doi:[https://doi.org/10.1061/41165\(397\)76](https://doi.org/10.1061/41165(397)76).



## **A.6 Impact of partial lateral confinement on high-strain-rate behaviour of cohesive soils**

*Li, K. S. O., Van Lerberghe, A., Barr, A. D., & Clarke, S. D. (2024). Impact of partial lateral confinement on high-strain-rate behaviour of cohesive soils. Submitted for publication in Experimental Mechanics*

Work highlighting the capabilities of the partial lateral confined SHPB apparatus in assisting with the characterisation of cohesive soils and the effects of confining pressure was submitted for publication to Experimental Mechanics. Journal paper is included as reference.

# Impact of partial lateral confinement on high-strain-rate behaviour of cohesive soils

Kin Shing Oswald Li<sup>1\*</sup>, Arthur Van Lerberghe<sup>1</sup>, Andrew D. Barr<sup>1</sup>, Sam D. Clarke<sup>1</sup>

<sup>1\*</sup>Department of Civil & Structural Engineering, University of Sheffield, Mappin Street, Sheffield, S1 3JD, UK.

\*Corresponding author(s). E-mail(s): [ksoli1@sheffield.ac.uk](mailto:ksoli1@sheffield.ac.uk);

Contributing authors: [avanlerberghe1@sheffield.ac.uk](mailto:avanlerberghe1@sheffield.ac.uk); [a.barr@sheffield.ac.uk](mailto:a.barr@sheffield.ac.uk);  
[sam.clarke@sheffield.ac.uk](mailto:sam.clarke@sheffield.ac.uk);

## Abstract

**Background:** Traditional free field unconfined and rigid confined split-Hopkinson pressure bar (SHPB) testing lay the groundwork for understanding high-strain-rate behaviour of cohesive soils, however the triaxial response between these two confinement modes remains uncharacterised.

**Objective:** This paper presents the application of a modified SHPB with partial lateral confinement on cohesive soils, focusing on kaolin clay. It validates the method using numerical simulations to explore the effects of confinement and lateral stress development during the deviatoric phase.

**Method:** The kaolin clay sample is encased within a latex membrane and tested using the modified apparatus where radial stresses are measured using a pressure transducer. LS-DYNA numerical modelling is used to validate experimental findings, particularly for cohesive soils exhibiting fluid-like behaviour and extreme deformation under high-strain-rates.

**Results:** Experimental results highlights the modified apparatus' capability to characterise the triaxial behaviour of kaolin clay under high-strain-rates. The similarities in axial stress propagation to free field unconfined tests underscores the effect of confinement and its ability to redirect lateral stresses. While numerical models are crucial for understanding internal behaviour and validating experimental results, limitations arise in modelling cohesive soils.

**Conclusion:** The experimental and numerical results underline the significance of confining pressure in influencing cohesive soil behaviour, highlighting the capability of the modified apparatus for material characterisation.

**Keywords:** high-strain-rate testing, split-Hopkinson pressure bar, partial lateral confinement, cohesive soils, kaolin clay, LS-DYNA, smoothed particle hydrodynamics,

## 1 Introduction

A key property of cohesive soils is its innate ability to retain larger amounts of water compared to other common geomaterials used in fortification engineering. When subject to extremely high and

immediate loading such as that from blast or fragmentation, the material may respond differently due to the lateral inertia applying a confining pressure. Hence, it is important to identify the effect of confinement on the ability of cohesive soils to withstand extreme pressures.

Free field unconfined and rigidly confined split-Hopkinson pressure bar (SHPB) experiments are a common method of characterising the high-strain-rate behaviour of soils within a range from  $10^2 \text{ s}^{-1}$  to  $10^4 \text{ s}^{-1}$  [1–3].

While the presence of a rigid confining ring has been shown to have an effect on the resultant stress transmitted through a kaolin clay specimen [4], it is necessary to investigate whether this effect is consistent when the confining pressure is reduced. It becomes critical for triaxial behaviour under high-strain-rates to be evaluated when confining pressure is not limited. Unconfined SHPB tests allow for free field high-strain-rate tests to be conducted, but does not enable for radial stresses and lateral deformation to be precisely examined.

In contrast to experiments where the hydrostatic pressure is applied before the axial loading [5], this method allows the lateral confinement of the specimen to develop during the deviatoric phase. As the sample is loaded axially, the inertia of the water annulus will resist radial deformation that occurs in response to the behaviour of the sample. The aims for of partial lateral confined experimental testing on kaolin clay are to:

- Demonstrate the capability of the modified SHPB apparatus for high-strain-rate testing on cohesive soils.
- Assess the effects of confinement using radial data obtained from modified SHPB apparatus.

Several authors have devised methods to introduce lateral confinement during SHPB tests, aiming to achieve a triaxial stress state. Pierce et al. [6] utilized a steel tube lined with a membrane to investigate wave speed in partially saturated sands under varying confining stresses. Bailly et al. [7] employed brass confining rings to simulate elastic behaviour at high strain rates. Gong et al. [8] utilized a modified SHPB setup to study compressive strength relationships in sandstone. Additionally, adaptations of the conventional triaxial cell (CTC) were made by Christensen et al. [9] and Frew et al. [10] to investigate sandstone and sand responses under high-strain-rates. This paper employs the modified SHPB with partial lateral confinement, as pioneered by Barr et al. [11], to comprehensively understand soil behaviour during high-strain events.

Unconfined and confined SHPB tests have been fundamental in the understanding of high-strain-rate behaviour of kaolin clay. A key discovery is the identification of distinct phase behaviours corresponding to specific moisture content thresholds. Behaviours within each phase varies based on the volume of water and the peak experimental strain. Notably, the high-strain-rate behaviour of cohesive soils appears to be influenced by internal moisture, leading to a tendency for stress to propagate laterally rather than axially through the sample when subject to high-strain-rate loading [4]. While radial stresses under rigid confinement has been investigated, the partial lateral confined SHPB apparatus allows radial stresses to be measured yet the sample is still allowed to deform laterally during loading. This novel avenue bridges the gap between conventional free field unconfined SHPB testing for solid materials, and rigid confined SHPB testing typically used in soil testing.

Experimental testing with the partial lateral confined apparatus will focus on various saturation levels and striker speeds. Although radial deformation is allowed to develop under this modified setup, the radial inertia caused by the development of hydrostatic pressure means the lateral confining pressure is still greater than in free field unconfined tests, hence a difference in strain rate is expected.

Replicating full-scale physical testing of blast or ballistic conditions is time-consuming and costly. Therefore, the development of comprehensive numerical models to simulate experimental testing serves as invaluable tools for characterizing material behaviour. Numerical modelling has been completed to develop models for unconfined and confined SHPB test conditions with reasonable accuracy with LS-DYNA. Although various geometrical techniques were considered [12], the fluid-like nature of cohesive soils makes SPH node modelling ideal [13]. However, intrinsic numerical limitations associated with depicting cohesion properties prevent the model from fully characterizing physical behaviour. Hence, the `MAT_MOHR_COULOMB` material model has been chosen to represent the sample material due to its lack of requirement for an Equation of State (EOS) and its ability to represent known parameters [4].

## 2 Material characterisation

The material selected is kaolin clay and is defined using EN ISO 14688-1:2002 soil descriptions as 'White fine kaolin clay.' The focus of this work is to investigate the strain rate effects by assessing the sensitivity of strain rate effects to changes in soil properties of kaolin clay. As such it is vital to properly characterise the properties of kaolin clay to guarantee data is accurate and results are repeatable [4]. A summary of the tests conducted and material characterisation properties found for kaolin clay is shown in Table 1.

**Table 1:** Summary of material characterisation tests and findings for kaolin clay.

Properties	Findings	Tests
Primary mineral	Kaolinite	XRD diffraction
$D_{50}$	$0.748 \mu\text{m}$	Data sheet
Particle density	$2.65 \text{ Mgm}^{-3}$	Pycnometer test
Particle sphericity	Low-Medium	SEM
Angularity	SR-SA	SEM
Surface texture	Smooth	SEM
Liquid limit	39.51%	Fall cone test
Plastic limit	25%	Fall cone test
Plastic index	14.89%	Fall cone test

The scanning electron microscope (SEM) was used according to EN ISO 1468801:2002 to determine the particle shape. Kaolin clay was coated with gold and placed into the SEM for imaging and are shown in Figure 1.

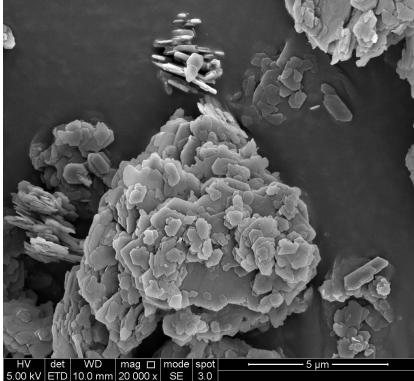


**Fig. 1:** Electron microscope images of kaolin clay under magnification of 20000x

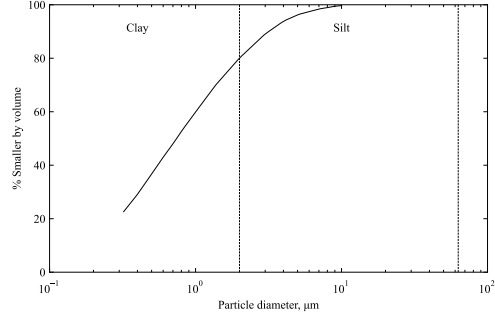


**Fig. 2:** Cumulative particle size distribution histogram of kaolin clay.

The particle size distribution (PSD) of kaolin clay was obtained from the data sheet provided by the supplier (Imerys Performance Minerals). The data sheet for the kaolin clay supplied specified that the particle size of up to 83% of the material was less than  $2 \mu\text{m}$  (particle size range for clay). A cumulative particle size distribution graph is produced as shown in Figure 2.

## 3 Specimen preparation

Kaolin clay specimens are prepared using powdered speciwhite kaolin clay, which are sieved and mixed with water then consolidated at 600kPa to create a solid homogenous kaolin clay sample using a Rowe cell.

To investigate the effects of moisture content and by extension saturation ratio, an air drying procedure was undertaken in order to obtain moisture contents at the levels: 0%, 20%, and 45%, providing a range of saturation levels from dried, partially saturated, and fully saturated specimens. Kaolin clay samples at varying moisture contents are prepared with the intent for use in all SHPB testing using the following procedure:

1. Saturated samples are cut with a stainless-steel, cylindrical cutting tool to diameters of 25 mm and nominal lengths of 5 mm.
2. Specimens are air-dried in a 20 °C temperature controlled room, and weighed at regular intervals until they reach the desirable moisture content.
3. After air-drying, specimens were wrapped in polyvinyl chloride to prevent further changes in moisture content.

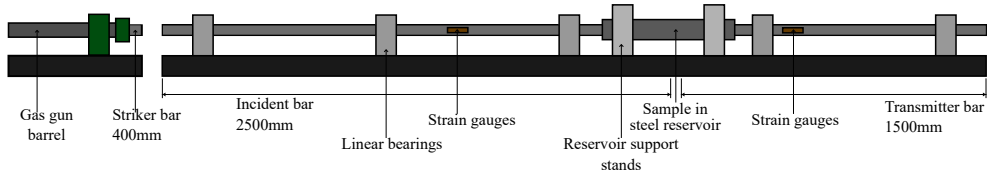


**Fig. 3:** Schematic of the partially lateral confined SHPB apparatus.

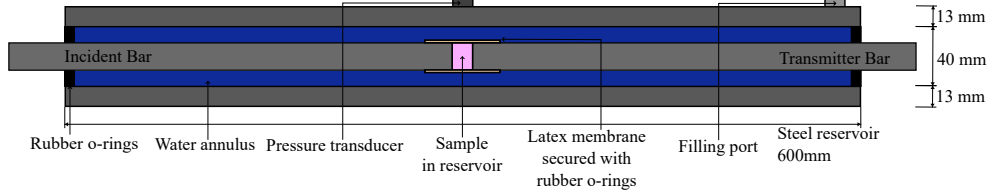


**Fig. 4:** Schematic of the partially lateral confined SHPB apparatus: water reservoir section.

## 4 Experimental setup

The modified SHPB is made up of a standard SHPB arrangement which consists of a striker, an incident and a transmitter bar, 25 mm in diameter, with a 350 mm, 2500 mm and 1500 mm length, respectively, as shown in Figure 3. In addition, as illustrated in Figure 4, a 600 mm long steel water reservoir is set on linear bearings and centred around the specimen. A 0.05mm thick latex membrane is enveloped over the sample and both incident and transmitter bars, and secured by small rubber-orings, this preserves the saturation level of the sample and prevents water from contaminating the sample prior to loading.

The reservoir is filled with water, and radial stress response,  $\sigma_r$ , is measured by a pressure transducer mounted on the walls of the reservoir which detects changes in water pressure during the deviatoric phase. The pressure transducer used is the Kulite HKM-375-2500, which has been calibrated by the manufacturer to perform linearly to a pressure of 25MPa. The axial stress response,  $\sigma_a$ , is measured with Kyowa KSP-2-120-E4 semiconductor strain gauges on the pressure bars, set up in half-Wheatstone bridge arrangements.

The reservoir length was designed so the time required for a stress wave initiated at the specimen surface to travel to and from the reservoir's end exceeds the loading duration in the specimen, guaranteeing that inward-travelling waves from the boundary do not interfere with pressure measurements. This simplifies the seal between the reservoir and the pressure bars, which are only needed to keep the water at atmospheric pressure.

To facilitate the use of the water reservoir for partial lateral confined testing, reservoir support stands were installed for precise manual reservoir alignment and accessible removal of the water reservoir before and after testing. The ball bearings are loosely screwed onto the aluminium frame and capable of being manually adjusted to ensure the reservoir is centred between the pressure bars prior to testing. Figure 5 shows a simplified schematic of the water reservoir stand.

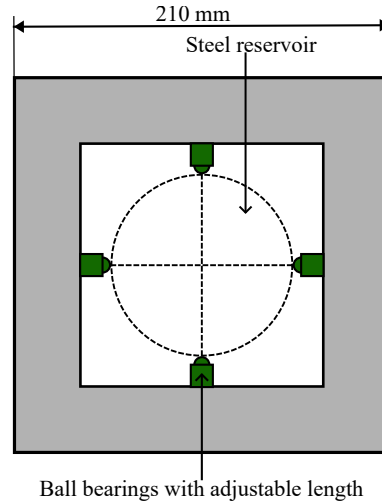


**Fig. 5:** Simplified schematic of the reservoir support stand used for partial lateral confined tests.

## 5 Sample methodology

While the initiation process of partial lateral confined tests follow a similar procedure to traditional SHPB tests, the fitting of the sample in preparation for testing with the water reservoir is crucial to ensure sample measurements are accurately obtained and the sample is properly secured for testing. The procedure to load the sample into the apparatus is as follows:

1. Reservoir support stand is secured onto the channel prior to installation of the water reservoir and fitting of the sample.
2. Linear bearing support closest to specimen interface on incident bar is moved to the left.
3. Water reservoir is slotted in between the reservoir support stands and in between the incident and transmitted pressure bars.
4. Water reservoir is slid to the left in the space of the vacated linear bearing support.
5. Small plastic o-rings are slid onto the incident and transmitted bars.
6. Latex membrane is slid onto the incident bar.
7. Sample is carefully placed in between the incident and transmitted pressure bars.
8. Latex membrane is carefully slid over to fully encompass the specimen and sealed onto the pressure bars with the small o-rings.
9. Water reservoir is slid back and pressure port is aligned directly on top of the specimen.
10. Linear bearing support is slid back towards its original position.
11. Ball bearings on reservoir support stand are manually adjusted to ensure the water reservoir is centred on both the incident and transmitted pressure bars and secured in place.
12. Larger o-rings are used to seal the two open ends of the water reservoir.
13. The reservoir is slowly filled with water through the filling port and the pressure transducer is secured onto the pressure port.
14. Measurement of the sample length is performed based on the distance between the end of the transmitted bar and the final linear bearing support (Figure 6)

The test then proceeded like traditional SHPB tests, loading is provided by firing the striker bar onto the incident bar at a desired striker bar velocity, striker bar speeds are recorded using a speed trap installed on the edge of the gas gun barrel.

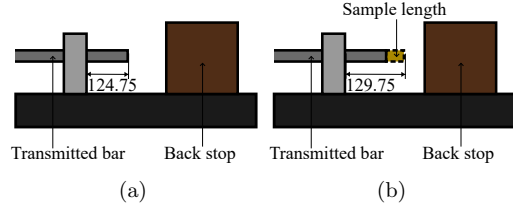


**Fig. 6:** Schematic of sample measurement process a) before and b) after installation within reservoir.

## 6 Test programme

Different moisture contents are tested to investigate the unique phase behaviour under high-strain-rate loading. The majority of the test programme with the partial lateral confined SHPB on kaolin clay is focused around tests at 16 m/s, which corresponds to an average peak strain rate of  $2500 \text{ s}^{-1}$ . Existing SHPB testing on kaolin clay revealed that the boundaries of moisture content phases are reflective of the intrinsic properties of the material and maximum experimental strains.

Hence the moisture contents selected for testing are based on verifying the existence of the same phases and validating prior knowledge about the material properties of kaolin clay. Additional tests on saturated kaolin clays are conducted at striker bar speeds of 12 and 20 m/s, which correspond to average peak strain rates of 1900 and  $3000 \text{ s}^{-1}$  (Figure 7). Ultimately, by comparing the results from unconfined, confined, and partial lateral confined tests, the holistic effect of confinement will be assessed.

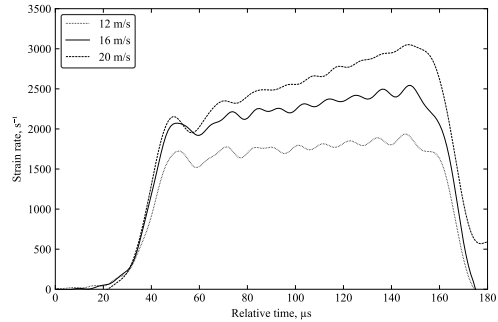


**Fig. 7:** Typical strain rate variation for partial lateral confined SHPB tests on kaolin clay at 12, 16, and 20 m/s, corresponding to an average peak strain of 1800, 2500, and  $3000 \text{ s}^{-1}$ .

## 7 Signal processing

A computational algorithm, `SHPB_processing.py` was used to process a variety of SHPB tests [14].

The key elements of the algorithm can be subdivided into the following functionalities:

- Pulse detection via automatic trigger and optimisation for stress equilibrium
- Adjustment of stresses for confinement modes
- Dispersion correction method [15, 16] (with the inclusion of the subroutine `dispersion.py`)

The transit time through the water annulus has been considered in when raw pressure transducer data is processed taken account by considering the time required to travel through the medium of fluid within the annulus. Thus the time for the stress pulse,  $t_{transit}$ , to travel through the reservoir annulus can be given by:

$$t_{transit} = \frac{l_{reservoir}}{v_{fluid}} \quad (1)$$

where  $l_{reservoir}$  is the thickness of the reservoir annulus, and  $v_{fluid}$  is the wave speed of the fluid in the annulus. The instrument radial stress obtained from processing pressure transducer signal is then timeshifted by the transit time to acquire the radial stress at the surface of the specimen, with the assumption that the fluid wave speed for water is 1482 m/s, as shown in Figure 8.

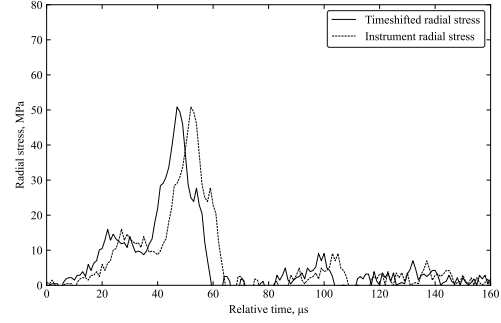


**Fig. 8:** Example of instrument radial stress from pressure transducer and timeshifted radial stress by accounting for transit time through water.

## 8 Experimental results

Cohesive soils exhibit specific phase behaviour based on moisture content limits that depend on material composition and are governed by the volume of water [4], hence the similarities in behaviour between saturated kaolin clay and water [17]. Phase 0 refers to fully dried samples. Phase 1 refers to materials with a lesser composition of moisture than solids and air. Phase 3 refers to materials with a high volume ratio of water. Phase 2, a variable phase, sees increases in maximum experimental strain correlating with reductions in boundary 3 (B3), phase 2 disappears if maximum strain equals boundary 2 (B2). General phase behaviour is visualised in Figure 9.

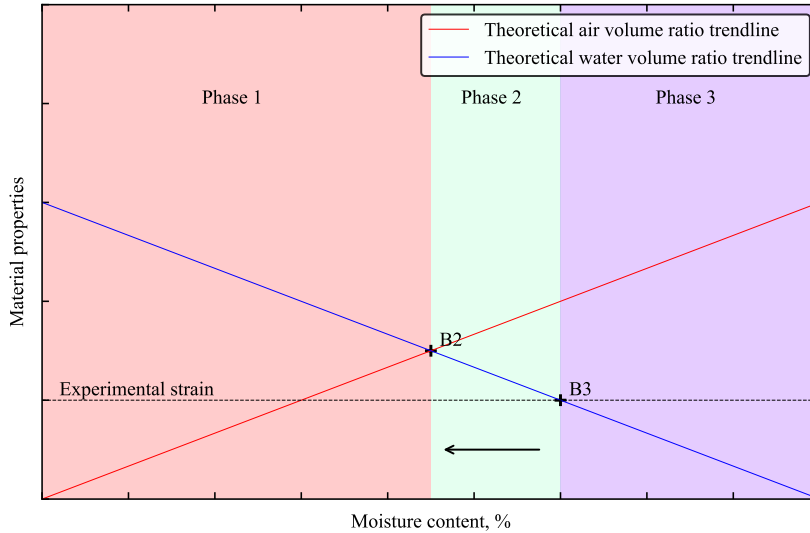


**Fig. 9:** General phase behaviour of kaolin clay under high-strain-rate, governed by material properties.

Sample stress is determined by taking the average of stresses experienced on the front and back interfaces of the specimen, back stress is the main component that undertakes drastic change when moisture content is varied while front stress remains relatively constant. Typical front stresses are shown in Figure 10.

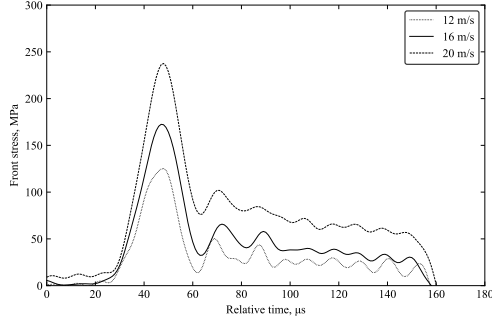


**Fig. 10:** Typical front stress variation for partial lateral confined SHPB tests at 12, 16, and 20 m/s.

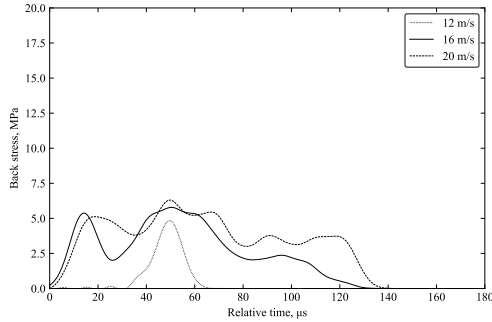


**Fig. 11:** Typical back stress from partially confined SHPB test on saturated kaolin clay at 12, 16, and 20 m/s

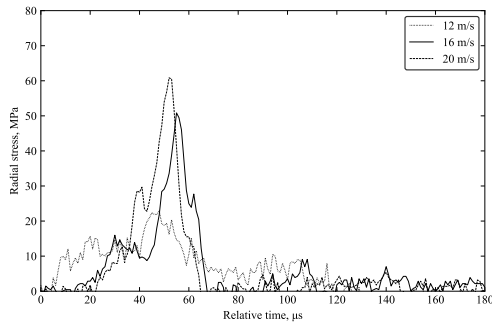


**Fig. 12:** Typical radial stress from partially confined SHPB test on saturated kaolin clay at 12, 16, and 20 m/s

## 8.1 Moisture content and strain rate effects

Cohesive soils such as kaolin clay, under no confining pressure, tend to propagate stress laterally and result in limited transmission of back stress.

Although strain rate affects stress magnitudes within moisture content phases, pulse shapes remain consistent in unconfined and confined SHPB tests. Thus behaviour within each of the phases can be inferred to be similar, albeit with varying magnitudes. Back and radial stresses for saturated kaolin clay samples at various strain rates are seen in Figures 11 and 12 respectively, where increases in strain rate corresponded with increases in both radial and axial stress.

The unique variations of back stress at specific phases observed in unconfined and confined tests are validated on saturated, partially saturated, and dried samples (Figure 13). The advantage of the modified SHPB setup is its ability to characterise lateral behaviour without restricting lateral deformation, prompting the development of lateral stresses to be monitored while the sample deforms under different saturation phases.

An overview of the effects of saturation phases on axial and radial stress behaviour is as follows:

**Phase 0 (0%):** Axial stress during phase 0 retains the same characteristics of unconfined tests where back stress does not return to zero as energy is being used to consolidate the dry sample by filling in existing air gaps. Axial stress propagation is greatest in this phase due to the lack of moisture forcing lateral propagation, naturally inducing a much lower radial pulse due to a lesser degree of lateral propagation. While a radial pulse is still visible, the noise recorded by the pressure transducer reaches up to 3 MPa and overlaps up to 50% of the recorded radial pulse. Hence, other than the interpolation that radial stress is at a minimum, it is not feasible to reach accurate conclusions from tests at low moisture contents at this time.

**Phase 1 (0% to B2):** The presence of moisture means that there is a lesser degree of consolidation due to a portion of the stress being propagated laterally, hence back stress gradually returns to zero. The greater degree of saturation within the sample causes a portion of the stress to propagate laterally. Hence the magnitude of the recorded radial stresses show a considerable increase from phase 0 as seen in Figure 13d.



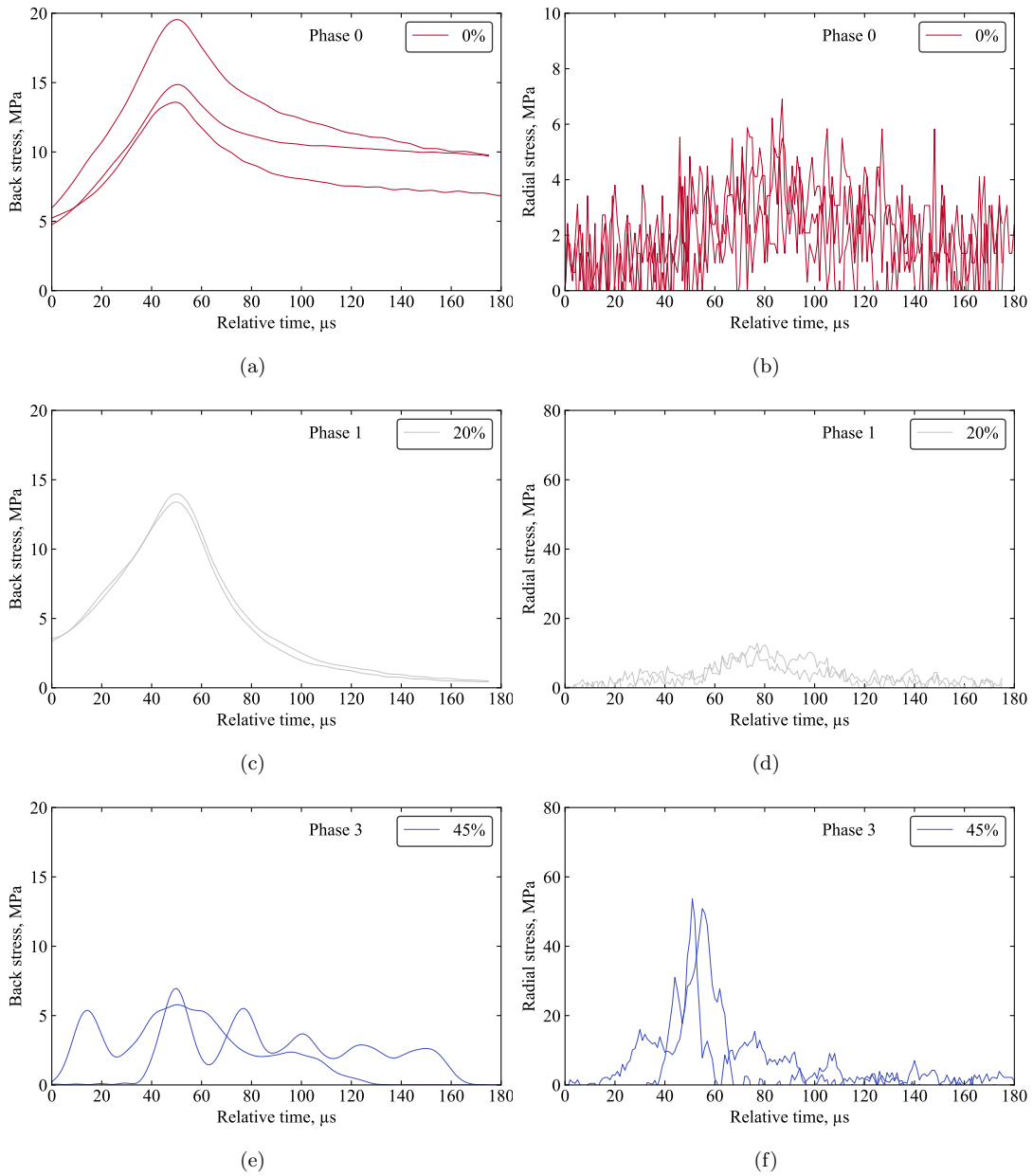


**Fig. 13:** Back and radial stress for partial lateral confined testing on kaolin clay at 16 m/s at phase 0 (a, b), phase 1 (c, d), and phase 3 (e, f).

**Phase 3 (B3 to full saturation):** This phase exhibits the least axial stress propagation, the high volume of water in saturated samples induces maximum lateral stress propagation and the least amount of back stress as moisture dictates the majority of high-strain-rate behaviour within this phase. The capability of the apparatus to measure radial stresses in saturated kaolin clay samples is demonstrated. This phase invokes the greatest magnitude of radial stress, evident from Figure 13f, where a distinct radial stress pulse is observed.

While tests have not been conducted explicitly within phase 2, consistency between characteristics of other phases from existing unconfined and confined tests indicate similar behaviours exist.

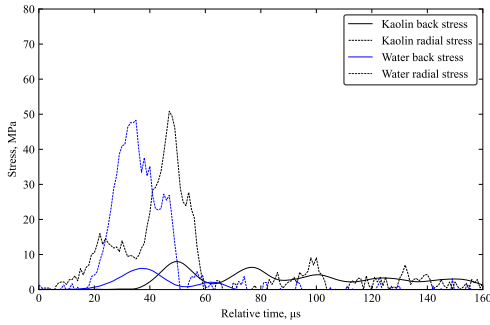


**Fig. 14:** Typical back and radial stresses from partially confined SHPB tests on water and saturated kaolin clay at 16 m/s.

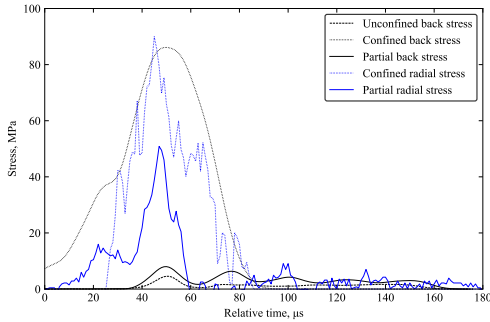


**Fig. 15:** Typical back and radial stress from unconfined, confined, and partial confined SHPB tests.

## 8.2 Similarities to water

The modified apparatus was optimised for tests without soil samples, creating an environment that emulates high-strain-rate impact testing of water. Results are obtained by measuring axial stresses from pressure bar gauge readings and radial stresses from water pressure changes [17].

There is a notable similarity between experimental results of water and saturated kaolin clay (Figure 14). The same effect is observed where axial stress from the incident bar fails to propagate through the sample (or water medium) onto the interface of the transmitted bar. This is coupled with changes in water pressure to indicate lateral transferral of stress during the deviatoric phase.

When a rigidly contained volume of water is axially loaded, pressure is exerted on all other edges of a containment mechanism. This aligns with the behaviour of saturated cohesive soils, where lateral pressure is redirected axially by the confinement mechanism.

## 8.3 Comparison with unconfined and confined SHPB testing

To compare the effect of the partial lateral confined SHPB results with existing results, the pulses from the three confinement modes are visualised in Figure 15 [4]. The magnitude of back stress pulse greatly resemble unconfined tests, albeit to a slightly greater magnitude. This indicates that the same effect is occurring where the stress is being forced laterally rather than being propagated through to the opposing transmitter bar due to minimal initial lateral pressure.

The disparity in radial stress compared to confined tests can be attributed to the concentration of stresses on a rigid ring. The replication of a free field environment within the reservoir prompts lateral stresses to dissipate without being concentrated directly on the surface of the specimen. However, the lack of a rigid restriction means that the stress does not get redirected back towards the transmitter like confined results. This shows that the tendency to propagate stress laterally is an intrinsic property of cohesive soils such as kaolin clay, but the addition of a confining pressure acts to redirect a portion of the lateral stress back towards the axial direction and towards the opposite end of the sample.

## 9 Numerical modelling

### 9.1 Model setup

The numerical modelisation of the arrangement was carried out using the explicit finite element code in LS-DYNA to compare numerical and experimental results as seen in Figure 16. The initial setup of the SHPB apparatus is akin to previous models for unconfined SHPB tests [4], with the addition of a steel reservoir and water annulus (Figure 17). SPH node modelisation has been identified to be optimal for modelling high-strain-rate behaviour of cohesive soils due to its fluid-like nature [18–20].

Two separate SPH node parts have been tested to represent both the SPH sample and water annulus, however the methods to define contact interactions between two different SPH “fluids” with different densities lead to errors in computation due to the inherent method that densities are modelled over quantities of SPH particles ([21]).

All pressure bars are modelled as an elastic material, `MAT_ELASTIC` with steel properties. While the kaolin clay sample was modelled as `MAT_MOHR_COULOMB` with parameters obtained from existing testing. The reservoir was modelled as a rigid material, `MAT_RIGID`, as fluid pressures are assumed to not be significant enough to cause deformation of the steel reservoir. The water annulus was modelled with the null material card, `MAT_NULL`, with the input parameters and equation of state of water [22]. The rubber o-rings are replaced with a boundary constraint to restrict expulsion of the water annulus.

Contact interactions between all Lagrangian model parts are manually designated by specifying interaction surfaces to reduce computation time. But all SPH node to Lagrangian interactions are handled automatically by the `CONTACT_AUTOMATIC_NODE_TO_SURFACE` contact algorithm in order to enhance accuracy regarding sample behaviour [23].

### 9.2 Comparison between LS-DYNA and experimental results

Figure 19 shows the difference in back stress between experimental results and the numerical model. While qualitative behaviour show the same results, the back stress from the numerical model is nearly twice as high as experimental results. While this can be attributed back to the lack of cohesion modelling capabilities, the numerical model is not limited by the rubber o-rings to create a sealed environment within the water annulus. The boundary constraints in the numerical model prevent the leakage of water without interfering with the movement of the pressure bars, creating a perfect condition where both axial and radial stresses can develop within the reservoir. While this was the idealistic environment when the apparatus was conceptualised, in actuality, multiple factors affect the development of lateral confining pressure, notably the movement of the o-rings when stress wave passes through the pressure bars start to create leakage and disrupts the internal water pressure.



**Fig. 16:** LS-DYNA SHPB partial lateral confinement model set up containing the incident bar (blue), transmitted bar (green), striker bar (yellow), and water reservoir (grey). Sample and water annulus are



**Fig. 17:** LS-DYNA cross section zoom-in on the sample inside the partial lateral confinement SHPB set up containing the incident bar (blue), transmitted bar (green), water reservoir (grey), water annulus within reservoir, and the sample (red).

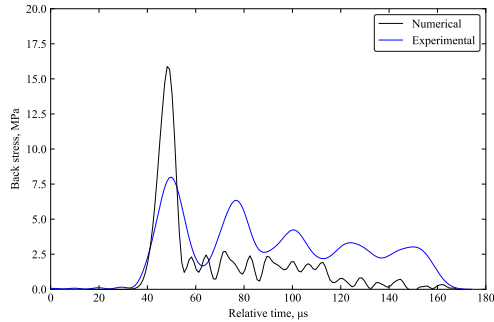


**Fig. 19:** Comparison between back stress from experimental and numerical model for partial lateral confined SHPB test on saturated kaolin clay.

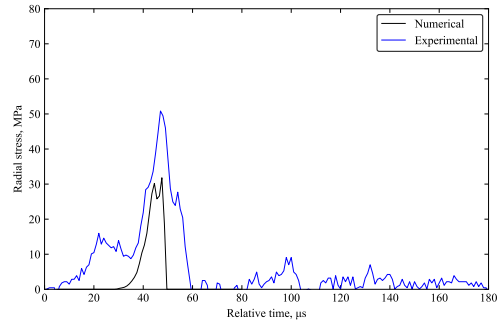


**Fig. 20:** Comparison between radial stress from experimental and numerical model for partial lateral confined SHPB test on saturated kaolin clay.

Figure 20 shows the difference in radial stress between the numerical model and typical experimental results. Evidently, while a similar peak and pulse pattern can be inferred, the numerical model experienced significantly lower lateral stresses. This is primarily a result of the lack of the capability to model cohesion properties, resulting in a much higher reflected pulse in the model. In turn, this culminates in a much lower portion of stress that actually gets transmitted through the sample both radially and axially.

The final state after the model reached completion is shown in Figure 21, the qualitative behaviour exhibited by the SPH nodes are similar to experimental results. The sample extrudes laterally and the large concentration of sample form a loop over the pressure bars, which closely resembles behaviour that occurs during physical testing where the kaolin clay sample forms a loop within the latex membrane.

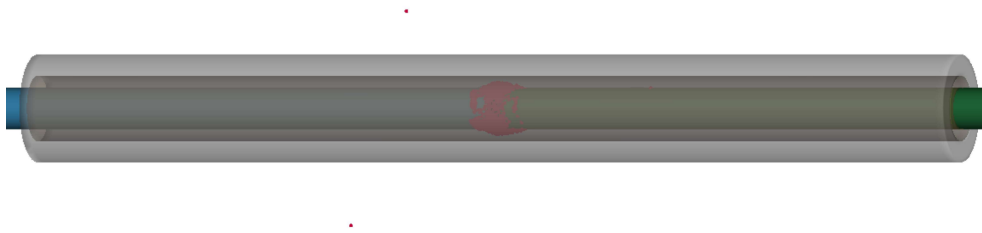


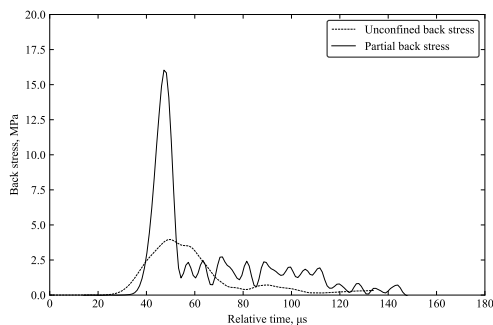
**Fig. 21:** Final time state of partial lateral confined SHPB numerical model on saturated kaolin clay.

### 9.3 Comparison against unconfined and confined numerical models

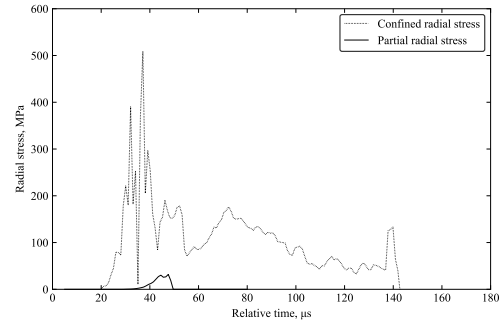
While the same material limitations exist between the unconfined, confined, and partial lateral confined SHPB numerical model, the juxtaposition between the three confinement modes allows for the effects of confinement to be magnified by developing idealistic situations at the three different lateral pressure modes.

Figure 22 shows the difference in back stress experienced by the numerical model under unconfined and partial lateral confined conditions, the back stress for confined cases is significantly larger than both of these magnitudes and so has not been shown. The ability for the partial lateral confined sample to deform laterally is evident due to its similarity to unconfined cases, the lack of rigid confinement to redirect stress back towards the axial direction like results in a significantly lesser back stress unlike confined cases.

The radial effects of confinement can be visualised in Figure 23 depicting the radial stresses obtained from the confining ring and the water pressure directly adjacent to the sample. Evidently, a significant disparity is observed as the model for the confining ring acts as a perfect seal, and forces all lateral stress to be concentrated on the ring. This indicates that the confinement mechanism directly affects the axial transmission as internal radial stresses of the specimen are wrapped and redirected towards the back interface according to the degree of confinement. Thus a system with limited confinement such as the partial lateral confined depicts low measured radial stresses and equally low axial back stresses.



**Fig. 22:** Comparison between back stress from numerical model for unconfined, partial lateral confined SHPB test on saturated kaolin clay.



**Fig. 23:** Comparison between radial stress from numerical model for confined, and partial lateral confined SHPB test on saturated kaolin clay.

While there are obvious physical differences between the three confinement modes, the partial lateral confined approach can be considered a combination of the unconfined and confined cases. Hence the similarities to each of the extreme confinement conditions are a reliable basis of comparison to gauge the effects of confinement.

## 10 Discussion

Due to the ability of cohesive soils such as kaolin clay to retain a larger proportion of moisture, the effect of moisture content is vital in dictating material behaviour. When subject to high-strain-rate axial loading, moisture forces the stress to propagate laterally, this typically creates volume loss as an after effect of the loading. This is supported by partial lateral confined testing, where it is evident that when under no confinement conditions, lateral stress remains at its greatest, and the opposite is true for the recorded back stress.

However, while experimental results have provided an idea of the effect of confinement, apparatus limitations prevent the full characterisation of confinement effects without numerical modelling. From numerical models on confined SHPB tests, a fully rigid ring demonstrates the ability to fully translate lateral stress into axial stress at the back of the specimen interface by creating a condition that prevents volume loss. Comparison to partial lateral confined modelling reveal a similar effect, where a larger portion of radial stress is observed.

Hence it can be said that, while lateral confinement provides eventual redirection of stresses, lateral stress propagation through the sample

remains relatively consistent. This phenomena is consistent even when strain rate is varied, as evident from both numerical and experimental approaches. Where increases in the magnitude of the stress pulses are observed corresponding with increases of strain rate.

Intrinsic limitations associated with modelling cohesive soils under high-strain conditions still persist and hinder comprehensive modelling of physical behaviour. Other than the lack of an accurate material model to depict cohesive soil behaviour, there are also idealistic differences that inherent cause the numerical model to differ from experimental conditions. A prime instance of this is the ability to create perfect boundary conditions. Large rubber o-rings are utilised to seal the water reservoir and ideally create a condition of controlled pressure within the water annulus, yet still allow for the pressure bars to move and propagate stress during loading. The subsequent effect of loading typically involves the water seal being broken immediately, invoked by lateral movement of the rubber o-rings by the sudden pressure change and movement of the pressure bars. While the effect may not be as noticeable given only the initial radial pulse is of primary concern, numerical modelling allows for an idealistic scenario where the pressure in the water annulus can be fully controlled without hindering the stress propagation through the pressure bars.

## 11 Conclusion

Overall, the partial lateral confined apparatus is a suitable method in experimentally determining high-strain-rate effects of cohesive soils. This is especially valuable due to the tendency for cohesive soils to exhibit lateral stress propagation when subject to high-strain-rate loading. However, if radial stresses are limited due to lack of moisture, inaccuracies start to arise due to existence of noise. Further developments of the apparatus would be the addition of an amplification capability and higher accuracy pressure transducers to reduce the noise intake and also increase accuracy of pressure readings if pressure readings are low.

The supplementation of numerical modelling is crucial in enhancing the holistic effect of confinement by creating idealistic conditions that allow the comparison between the various confinement

modes. From which it has been discovered that the holistic effect of confinement is the redirection of stresses (from confined testing), but the tendency for radial stress propagation remains consistent regardless of the confinement mechanism.

Although the effects of strain rate have been monitored and characterised by both experimental and numerical approaches. The effects of moisture content and by extension saturation have not been fully characterised. While interpolation of phase behaviour from existing testing are sufficient in the understanding of high-strain-rate behaviour, future experimental testing should focus on better characterising phase 2 and the radial stress variations that occur within this phase.

Furthermore, the limitations of modern numerical modelling techniques in replicating the behaviour of cohesive soils under high-strain-rates are apparent. The lack of appropriate material model that accounts for the properties of cohesion is a primary factor in the disparities between numerical and experimental results, and avenue that requires explicit development.

**Acknowledgements.** This research was funded by the Engineering and Physical Sciences Research Council (EPSRC), and the Defence Science and Technology Laboratory (Dstl).

## Declarations

**Conflict of interest.** The authors declare that they have no conflict of interest.

## References

- [1] Song, B., Chen, W., Luk, V.: Impact compressive response of dry sand. *Mechanics of Materials - MECH MATER* **41**, 777–785 (2009) <https://doi.org/10.1016/j.mechmat.2009.01.003>
- [2] Barr, A., Clarke, S., Petkovski, M., Tyas, A., Rigby, S., Warren, J., Kerr, S.: Effects of strain rate and moisture content on the behaviour of sand under one-dimensional compression. *Experimental Mechanics* **56** (2016) <https://doi.org/10.1007/s11340-016-0200-z>

- [3] Luo, H., Lu, H., Cooper, W.L., Komanduri, R.: Effect of Mass Density on the Compressive Behavior of Dry Sand Under Confinement at High Strain Rates. *Experimental Mechanics* **51**(9), 1499–1510 (2011) <https://doi.org/10.1007/s11340-011-9475-2>
- [4] Van Lerberghe, A., Li, K., Barr, A., Clarke, S.: High strain rate behaviour of cohesive soils. Submitted for publication in *International Journal of Impact Engineering* (2024)
- [5] Bragov, A.M., Lomunov, A.K., Sergeichev, I.V., Tsembelis, K., Proud, W.G.: Determination of physicochemical properties of soft soils from medium to high strain rates. *International Journal of Impact Engineering* **35**(9), 967–976 (2008) <https://doi.org/10.1016/j.ijimpeng.2007.07.004>
- [6] Pierce, S.J., Charlie, W.A.: High-intensity Compressive Stress Wave Propagation Through Unsaturated Sands. PhD thesis, Colorado State University (1990)
- [7] Bailly, P., Delvare, F., Vial, J., Hanus, J.L., Biessy, M., Picart, D.: Dynamic behavior of an aggregate material at simultaneous high pressure and strain rate: SHPB triaxial tests. *International Journal of Impact Engineering* **38**(2-3), 73–84 (2011) <https://doi.org/10.1016/j.ijimpeng.2010.10.005>
- [8] Gong, F.-Q., Si, X.-F., Li, X.-B., Wang, S.-Y.: Dynamic triaxial compression tests on sandstone at high strain rates and low confining pressures with split hopkinson pressure bar. *International Journal of Rock Mechanics and Mining Sciences* **113**, 211–219 (2019) <https://doi.org/10.1016/j.ijrmms.2018.12.005>
- [9] Christensen, R.J., Swanson, S.R., Brown, W.S.: Split-hopkinson-bar tests on rock under confining pressure. *Experimental Mechanics* **12**(11), 508–513 (1972) <https://doi.org/10.1007/BF02320747>
- [10] Frew, D.J., Akers, S.A., Chen, W., Green, M.L.: Development of a dynamic triaxial Kolsky bar. *Measurement Science and Technology* **21**(10) (2010) <https://doi.org/10.1088/0957-0233/21/10/105704>
- [11] Barr, A.D., Clarke, S.D., Rigby, S.E., Tyas, A., Warren, J.A.: Design of a split Hopkinson pressure bar with partial lateral confinement. *Measurement Science and Technology* **27**(12) (2016) <https://doi.org/10.1088/0957-0233/27/12/125903>
- [12] Livermore Software Technology Corporation: LS-DYNA Theory Manual, California, USA (2023)
- [13] Lacome, J.L.: Smooth particle hydrodynamics (sph): a new feature in ls-dyna. In: 6th International LS-Dyna Users Conference, Detroit, USA (2000)
- [14] Van Lerberghe, A., Li, K., Barr, A., Clarke, S.: An open-source algorithm for correcting stress wave dispersion in split-Hopkinson pressure bar experiments. Submitted for publication in *Experimental Mechanics* (2024)
- [15] Tyas, A., Pope, D.J.: Full correction of first-mode pohammer–chree dispersion effects in experimental pressure bar signals. *Measurement science and technology* **16**(3), 642 (2005)
- [16] Gray, T.G.: Classic Split-Hopkinson Pressure Bar Testing. In: *Mechanical Testing and Evaluation*, pp. 462–476. ASM International, ??? (2000). <https://doi.org/10.31399/asm.hb.v08.a0003296>
- [17] Li, K., Van Lerberghe, A., Barr, A., Dennis, A., Clarke, S.: Split-Hopkinson pressure bar testing of water with partial lateral confinement. Submitted for publication in *Experimental Mechanics* (2024)
- [18] Varas, D., Lopez-Puente, J., Artero-Guerrero, J., Pernas-Sanchez, J.: Numerical modelling of fluid structure interaction using ale and sph: The hydrodynamic ram phenomenon. In: 11th European LS-DYNA Conference (2017)
- [19] Anghileri, M., Castelletti, L.M.L., Tirelli, M.: Fluid-structure interaction of water filled tanks during the impact with the ground. *International Journal of Impact Engineering* **31**(3), 235–254 (2005) <https://doi.org/10.1016/j.ijimpeng.2005.02.005>

- [20] Jianming, W., Na, G., Wenjun, G.: Abrasive waterjet machining simulation by SPH method. *International Journal of Advanced Manufacturing Technology* **50**(1-4), 227–234 (2010) <https://doi.org/10.1007/s00170-010-2521-x>
- [21] Ihmsen, M., Bader, J., Akinici, G., Teschner, M.: Animation of air bubbles with sph. In: *International Conference on Computer Graphics Theory and Applications*, vol. 2, pp. 225–234 (2011). <https://doi.org/10.5220/0003322902250234> . SCITEPRESS
- [22] Shin, Y.S., Lee, M., Lam, K.Y., Yeo, K.S.: Modeling mitigation effects of water-shield on shock waves. *Shock and Vibration* **5**(4), 225–234 (1998) <https://doi.org/10.1155/1998/782032>
- [23] Xu, J., Wang, J.: Interaction methods for the sph parts (multiphase flows, solid bodies) in ls-dyna. In: *Proceedings of the 13th International LS-DYNA Users Conference*, Detroit, MI, USA, pp. 8–10 (2014)





## Chapter B

# Sample measurement data

## B.1 Introduction

This appendix includes all measurement data for SHPB tests on kaolin clay, including trials from unconfined, confined, and partial lateral confined tests. This has been formatted as a condensed version of the test log used to document SHPB trials during experimental testing.

The dry mass of each sample was determined based on the weight of the sample prior to air-drying. Moisture content refers to the desired moisture levels for testing, while actual moisture content refers to the moisture content as calculated based on the dry mass of each sample.

Sample length was obtained by taking the average of three length measurements of the sample at three different points with a digital caliper. While the mass was determined using an electronic scale. Experimental procedure for SHPB tests have been described in Chapter 4.

## B.2 Unconfined tests

This section contains the logs for all unconfined SHPB tests on kaolin clay. Table B.1 shows the pressure-depth combinations used for tests at each striker bar velocity. Additionally, the table references the individual logs for tests at each striker bar velocity.

Table B.1: Unconfined tests on kaolin clay at each striker bar velocity.

<i>Striker bar velocity, m/s</i>	<i>Gas gun pressure, psi</i>	<i>Striker bar depth, mm</i>	<i>Table</i>
8	14	600	B.2
12	28	600	B.3
16	48	600	B.4
18	60	600	B.5
20	72	600	B.6
22	86	600	B.7

Table B.2: Log of unconfined SHPB tests at 8 m/s on kaolin clay sorted by moisture content.

<i>Moisture content, %</i>	<i>Actual moisture content, %</i>	<i>Average length, mm</i>	<i>Wet mass, g</i>	<i>Dry mass, g</i>
0	0.0	5.857	3.345	3.345
0	0.0	5.633	3.175	3.175
0	0.0	6.620	3.809	3.809
0	0.0	5.927	3.107	3.107
5	5.5	5.575	2.965	2.810
5	5.1	5.500	3.057	2.908
10	8.7	5.327	3.261	3.000
10	7.2	5.680	3.036	2.831
10	8.4	5.660	3.253	3.000
15	14.8	5.803	3.541	3.084
15	13.9	5.440	3.360	2.950
15	15.4	5.950	3.697	3.203
20	22.5	5.647	3.880	3.168
20	22.3	5.503	3.659	2.993
20	19.9	5.947	3.598	3.000
20	22.2	5.890	3.871	3.168
20	19.6	5.733	3.503	2.929
25	25.2	5.977	4.248	3.393
25	25.4	5.797	3.851	3.070
25	24.8	5.847	3.692	2.957
30	33.7	5.790	4.256	3.182
30	33.0	5.143	3.765	2.831
30	33.4	5.763	4.048	3.035
30	31.9	5.913	4.199	3.182
30	29.8	5.673	3.838	2.957
41	39.4	5.680	4.556	3.269
41	40.1	5.957	4.829	3.446
41	39.6	5.303	4.150	2.973
41	40.3	6.740	4.498	3.207
41	38.9	5.943	4.455	3.207
41	39.9	6.220	4.625	3.306
42	40.6	5.657	4.227	3.007
42	39.9	5.767	4.765	3.407
42	40.5	5.340	4.086	2.908
44	42.5	5.410	4.163	2.922
44	42.2	5.360	4.115	2.894
44	42.0	5.260	4.237	2.984

Table B.3: Log of unconfined SHPB tests at 12 m/s on kaolin clay sorted by moisture content.

<i>Moisture content, %</i>	<i>Actual moisture content, %</i>	<i>Average length, mm</i>	<i>Wet mass, g</i>	<i>Dry mass, g</i>
0	0.0	5.520	3.051	3.051
0	0.0	5.073	3.019	3.019
5	4.0	5.083	2.866	2.756
5	5.9	5.810	3.112	2.939
10	9.7	5.540	3.210	2.925
10	11.6	4.873	3.360	3.010
15	14.4	5.743	3.603	3.151
15	14.6	5.400	3.416	2.982
15	15.0	6.023	3.800	3.306
20	20.3	5.040	3.586	2.982
20	21.2	6.030	3.589	2.960
25	21.2	5.627	3.609	2.918
25	25.0	5.550	3.947	3.158
25	25.5	5.860	3.937	3.137
30	27.5	5.730	4.034	3.165
30	30.6	6.167	3.948	3.024
30	30.8	6.277	4.140	3.165
35	34.9	5.927	4.089	3.031
35	34.9	5.747	3.993	2.960
35	35.3	5.130	3.921	2.897
40	39.1	5.377	4.215	3.031
41	40.8	6.130	4.326	3.073
41	41.0	6.350	4.590	3.256
44	42.0	5.253	4.111	2.894

Table B.4: Log of unconfined SHPB tests at 16 m/s on kaolin clay sorted by moisture content.

<i>Moisture content, %</i>	<i>Actual moisture content, %</i>	<i>Average length, mm</i>	<i>Wet mass, g</i>	<i>Dry mass, g</i>
0	0.0	5.250	2.805	2.805
0	0.0	5.747	3.183	3.183
0	0.0	6.220	3.148	3.148
5	10.3	5.397	3.272	2.967
10	10.9	5.967	3.533	3.186
10	10.9	5.327	3.353	3.024
15	14.9	5.180	3.369	2.932
15	16.0	5.540	3.449	2.974
20	20.2	5.303	3.568	2.967
20	20.4	5.753	3.548	2.946
25	25.1	4.487	3.561	2.848
25	26.6	5.123	3.383	2.671
25	27.0	5.190	3.572	2.812
30	30.2	5.537	3.927	3.017
30	31.3	5.617	4.192	3.193
30	31.4	5.243	4.029	3.066
35	35.1	5.713	3.951	2.925
35	36.3	5.257	3.833	2.812
35	36.6	6.210	3.947	2.890
40	38.3	6.410	4.846	3.503
40	40.4	5.807	4.524	3.221
40	40.4	5.877	4.414	3.144
41	41.4	6.023	4.506	3.186
41	41.4	5.807	4.524	3.221
41	41.4	5.847	3.149	3.149

Table B.5: Log of unconfined SHPB tests at 18 m/s on kaolin clay sorted by moisture content.

<i>Moisture content, %</i>	<i>Actual moisture content, %</i>	<i>Average length, mm</i>	<i>Wet mass, g</i>	<i>Dry mass, g</i>
0	0.0	6.753	3.309	3.309
20	20.6	6.033	3.435	2.848
41	39.9	6.583	4.388	3.137

Table B.6: Log of unconfined SHPB tests at 20 m/s on kaolin clay sorted by moisture content.

<i>Moisture content, %</i>	<i>Actual moisture content, %</i>	<i>Average length, mm</i>	<i>Wet mass, g</i>	<i>Dry mass, g</i>
0	0.0	6.900	3.413	3.413
20	22.0	6.463	3.914	3.207

Table B.7: Log of unconfined SHPB tests at 22 m/s on kaolin clay sorted by moisture content.

<i>Moisture content, %</i>	<i>Actual moisture content, %</i>	<i>Average length, mm</i>	<i>Wet mass, g</i>	<i>Dry mass, g</i>
20	21.8	6.377	3.836	3.151
25	24.5	5.470	3.694	2.967

### B.3 Confined tests

This section contains the logs for all confined SHPB tests on kaolin clay. Table B.8 shows the pressure-depth combinations used for tests at each striker bar velocity. Additionally, the table references the individual logs for tests at each striker bar velocity.

Table B.8: Unconfined tests on kaolin clay at each striker bar velocity.

<i>Striker bar velocity, m/s</i>	<i>Gas gun pressure, psi</i>	<i>Striker bar depth, mm</i>	<i>Table</i>
12	28	600	B.9
18	60	600	B.10
20	72	600	B.11
22	86	600	B.12



Table B.9: Log of confined SHPB tests at 12 m/s on kaolin clay sorted by moisture content.

<i>Moisture content, %</i>	<i>Actual moisture content, %</i>	<i>Average length, mm</i>	<i>Wet mass, g</i>	<i>Dry mass, g</i>
0	0.0	6.907	3.357	3.357
0	0.0	6.877	3.344	3.344
0	0.0	6.913	3.461	3.461
20	21.5	6.407	3.735	3.073
20	21.9	6.270	3.842	3.151
20	22.2	6.483	3.912	3.200
41	39.0	6.287	4.625	3.326
41	39.6	6.877	4.930	3.531
41	39.8	6.447	4.750	3.397

Table B.10: Log of confined SHPB tests at 18 m/s on kaolin clay sorted by moisture content.

<i>Moisture content, %</i>	<i>Actual moisture content, %</i>	<i>Average length, mm</i>	<i>Wet mass, g</i>	<i>Dry mass, g</i>
0	0.0	6.760	3.257	3.257
0	0.0	6.493	3.121	3.121
0	0.0	6.507	3.273	3.273
10	10.5	5.243	3.115	2.819
10	11.9	5.620	3.314	2.960
10	11.9	5.743	3.193	2.855
20	19.5	5.373	3.402	2.848
20	19.9	6.467	3.610	3.010
20	20.9	5.450	3.501	2.897
25	24.4	6.013	3.798	3.052
25	26.1	6.080	3.769	2.989
30	29.0	5.787	4.000	3.101
30	29.8	6.040	4.181	3.221
30	30.2	5.350	4.211	3.235
35	33.7	6.090	4.136	3.094
35	34.3	5.910	4.099	3.052
35	35.8	6.353	4.365	3.214
41	38.1	6.003	4.244	3.073
41	39.7	5.927	4.184	2.995
41	40.3	6.060	4.224	3.010

Table B.11: Log of confined SHPB tests at 20 m/s on kaolin clay sorted by moisture content.

<i>Moisture content, %</i>	<i>Actual moisture content, %</i>	<i>Average length, mm</i>	<i>Wet mass, g</i>	<i>Dry mass, g</i>
0	0.0	6.470	3.247	3.247
0	0.0	7.123	3.662	3.662
0	0.0	6.940	3.344	3.344
20	21.4	6.300	3.781	3.115
20	21.6	6.393	3.858	3.172
41	39.7	6.347	4.656	3.334
41	39.9	5.843	4.368	3.123

Table B.12: Log of confined SHPB tests at 22 m/s on kaolin clay sorted by moisture content.

<i>Moisture content, %</i>	<i>Actual moisture content, %</i>	<i>Average length, mm</i>	<i>Wet mass, g</i>	<i>Dry mass, g</i>
0	0.0	7.140	3.137	3.137
0	0.0	6.847	3.351	3.351
10	10.2	5.857	3.318	3.010
20	20.9	6.393	3.657	3.023
30	30.2	6.093	3.901	2.996
30	30.5	6.383	4.028	3.087
30	30.7	6.077	3.951	3.024
41	38.1	5.813	4.117	2.982
41	38.6	5.827	4.279	3.087
41	39.5	5.897	4.109	2.946

## B.4 Partial lateral confined tests

This section contains the logs for all partial lateral confined SHPB tests on kaolin clay. Table B.13 shows the pressure-depth combinations used for tests at each striker bar velocity. Additionally, the table references the individual logs for tests at each striker bar velocity.

Table B.13: Partial lateral confined tests on kaolin clay at each striker bar velocity.

<i>Striker bar velocity, m/s</i>	<i>Gas gun pressure, psi</i>	<i>Striker bar depth, mm</i>	<i>Table</i>
12	28	600	B.14
18	60	600	B.15
20	72	600	B.16

Table B.14: Log of partial lateral confined SHPB tests at 12 m/s on kaolin clay sorted by moisture content.

<i>Moisture content, %</i>	<i>Actual moisture content, %</i>	<i>Average length, mm</i>	<i>Wet mass, g</i>	<i>Dry mass, g</i>
35	35.2	6.430	4.125	3.052
45	42.9	5.303	3.982	2.786
45	44.0	6.200	4.507	3.130

Table B.15: Log of partial lateral confined SHPB tests at 16 m/s on kaolin clay sorted by moisture content.

<i>Moisture content, %</i>	<i>Actual moisture content, %</i>	<i>Average length, mm</i>	<i>Wet mass, g</i>	<i>Dry mass, g</i>
0	0.0	5.970	3.331	3.206
0	0.0	5.880	3.024	2.924
0	0.0	5.693	2.888	2.807
20	19.6	5.547	3.430	2.869
20	19.7	5.747	3.781	3.158
20	19.9	5.790	3.581	2.986
45	43.3	5.577	4.328	3.020
45	43.5	5.537	4.263	2.972
45	43.7	5.960	4.468	3.109

Table B.16: Log of partial lateral confined SHPB tests at 20 m/s on kaolin clay sorted by moisture content.

<i>Moisture content, %</i>	<i>Actual moisture content, %</i>	<i>Average length, mm</i>	<i>Wet mass, g</i>	<i>Dry mass, g</i>
45	43.3	6.167	4.456	3.109
45	43.3	6.297	4.653	3.247
45	43.5	5.783	4.560	3.178



## Chapter C

# Striker bar velocity tests

## C.1 Introduction

This appendix contains setup-specific speed trap data used to calibrate the gas gun. Desired striker bar velocities are acquired through multiple combinations of pressure and striker bar depth, relationship between gas gun pressure and striker bar depth are formulated to facilitate knowledge of exact pressure-depth combinations to obtain desired striker bar speeds during SHPB testing.

## C.2 Speed test log

Table C.1 includes a log of pressure and striker bar depth combinations tested with the new gas gun. Pressure refers to the pressure measured on the main pressure gauge when the new gas gun reservoir has been pressurised. Striker bar depth refers to the depth within the new gas gun barrel that the striker bar is inserted within. Striker bar velocities were measured with the speed trap installed on the open end of the barrel.

Based on the data collected, power regression trend lines were calculated for each variation of striker bar depth in order to determine a relationships between gas gun pressure,  $p_g$  and the acquired striker bar velocity,  $v_s$  as visualised in Figure C.1. Table C.2 shows the equations of the four trendlines corresponding to each striker bar depth, the  $r^2$  values are all greater than 0.99, indicating a near perfect match to the data. The designated striker bar velocities for SHPB testing used throughout this thesis relies on deriving the desired combination of pressure and striker bar depth based on these equations.

Table C.1: Pressure and striker bar depth combinations tested with new gas gun, and measured striker bar velocities.

<i>Striker bar depth, mm</i>	<i>Pressure, psi</i>	<i>Striker bar velocity, m/s</i>
200	12	4.04
200	14	4.35
200	16	4.52
200	18	4.93
200	24	5.92
200	30	6.63
200	40	7.85
200	42	7.98
200	50	8.86
200	60	9.57
200	64	9.86
200	66	10.12
400	12	5.92
400	20	8.08
400	30	10.03
400	40	11.65
400	42	12.05
400	50	13.11
400	56	13.99
400	60	14.51
400	64	15.08
600	12	7.37
600	14	8.14
600	16	8.61
600	20	10.07
600	28	12.05
600	36	13.62
600	38	14.12
600	46	15.68
600	48	15.91
600	50	16.56
800	12	8.25
800	16	9.95
800	20	11.56
800	22	12.14
800	28	14.04
800	30	14.39
800	38	16.00

Table C.2: Trend line equations to derive striker bar velocities,  $v_s$ , based on gas gun pressure,  $p_g$ , at various striker bar depths.

Striker bar depth, mm	Pressure-velocity trend line	$r^2$ value
200	$v_s = 1.02p_g^{0.55}$	$r^2 = 0.998$
400	$v_s = 1.53p_g^{0.55}$	$r^2 = 0.999$
600	$v_s = 1.86p_g^{0.56}$	$r^2 = 0.999$
800	$v_s = 1.98p_g^{0.58}$	$r^2 = 0.993$

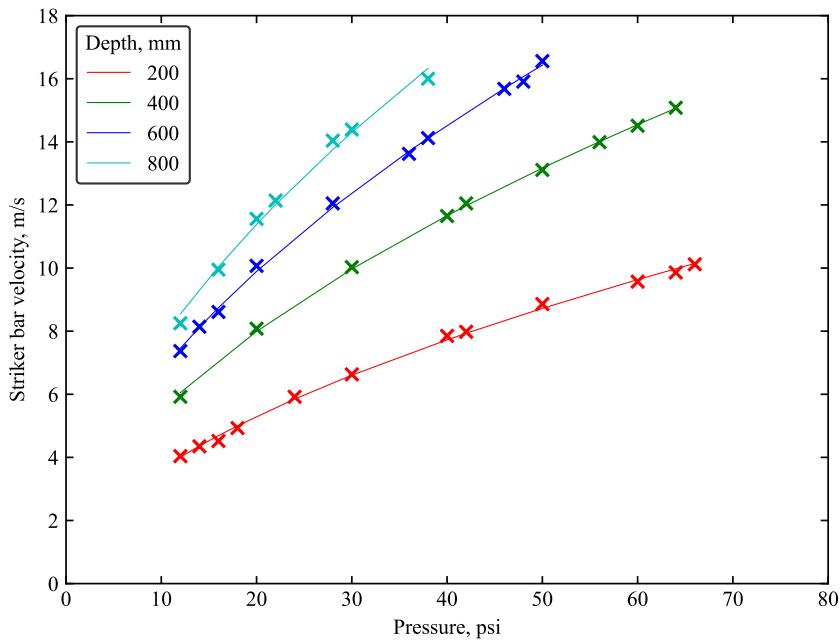


Figure C.1: Relationship between gas gun pressure and striker bar velocity at each striker bar depth, with power regression trend line for each striker bar depth.





## Chapter D

# Signal processing and analysis of SHPB data with computational Python algorithm

## D.1 Introduction

This appendix contains source for computational Python algorithms developed and used for signal processing and data analysis as initially highlighted in Chapter 4. Full source for functions including `SHPB_processing.py` and `dispersion.py` are included for reference.

## D.2 SHPB\_processing.py

SHPB\_processing.py processes raw voltage data from SHPB to obtain values for axial stresses and strains. Radial stresses and strains are included if a confinement mechanism is applied. As discussed in Section sec:code, the primary functions of the algorithm are as follows:

- Pulse detection via automatic trigger and optimisation of pulse boundaries
- Pulse alignment and stress equilibrium
- Adjustment of stresses for various confinement mechanisms
- Dispersion correction (with the inclusion of the subroutine dispersion.py)

The algorithm generates four CSV files containing data on constants, pulse results, sample results, and signal results respectively. Additionally, a text file is generated that contains an operation log, documenting the time and details of each operation.

```
'SHPB_processing.py'  
  
# Signal processing function to correct and evaluate raw voltage  
  signals optimised for high-strain rate SHPB testing.  
  
# CODE DEVELOPED BY: Kin Shing Oswald Li, Arthur Van Lerberghe,  
  Andrew D. Barr.  
# EMAIL: ksoli1@sheffield.ac.uk,  
  
# INPUT ARGUMENTS:  
# csv_path = File path to CSV file containing oscilloscope columns  
  in the form of  
  # Time, CH1, CH2, CH3... (supports combined oscilloscopes)  
  .  
# sample_data = List containing 3 elements that correspond to  
  length (mm), mass (g), and dry mass (g) for the initial sample;  
  # i.e. [initial_length, mass, dry_mass].  
# confinement = Specify confinement of specimen.  
  # 'None', 'Ring', or 'Reservoir' only.  
  # confinement defaults to 'None' if not specified.  
# signal_channels = Specify oscilloscope channels for input,  
  output bars and any confinement mechanism.  
  # i.e. [in_bar_gauge_channel, out_bar_gauge_channel,  
  ring_gauge_channel OR reservoir_gauge_channel].  
  # Input bar channel 7, output bar channel 8, and ring  
  gauge channel 5 would correspond to list of [7, 8, 5].  
  # signal_channels defaults to [7, 8, 5] if not specified.
```

APPENDIX D. SIGNAL PROCESSING AND ANALYSIS OF SHPB DATA WITH  
COMPUTATIONAL PYTHON ALGORITHM

---

```
# signal_amp = Specify oscilloscope signal amplification factors
# for input, output bars and any confinement mechanism.
# i.e. [in_bar_gauge_amp, out_bar_gauge_amp,
#       ring_gauge_amp].
# Input bar amp 10, output bar amp 100, and ring gauge amp
# 10 would correspond to list of [10, 100, 10].
# signal_amp defaults to [10, 100, 10] if not specified.
# disp_correction = Specify if dispersion correction or simple
# timeshift to process pulse.
# True for dispersion correction, False for simple
# timeshift.
# If disp_correction = True, ensure dispersion.py and
# dispersion_factors.py are attached.
# disp_correction defaults to True if not specified.
# alignment = Specify the alignment mode for aligning stress waves
# at front and back of sample interface.
# 'start' aligns the start of incident and transmitted
# pulse.
# 'end' aligns the end of incident and transmitted pulse.
# 'mid' aligns the median time of the pulse of the
# incident and transmitted pulse.
# Integer/float values greater than 1 aligns the peaks of
# the incident and transmitted pulse to specific time (ms
# ).
# Float values greater than 0 and less than 1 aligns the
# incident and transmitted pulse based on a specific
# fraction of the maximum value of each pulse.
# alignment defaults to 'start' if not specified.
# speedtrap = Specify if speed trap is employed and whether
# velocity of striker bar is determined.
# True or False.
# speedtrap is True if not specified (striker velocity is
# calculated).

# Other constants used as inputs for signal processing are defined
# in the 'INPUTS' section within the function, amend values if
# required.

# OUTPUT
# Generates processed data based on test data.
# if savedata=True (within 'INPUTS' section):
#     # Option to save processed data as CSV files within folder
#     .
#     # Log to show history for processing specific data set.

# -----

import os
import pandas as pd
```

## APPENDIX D. SIGNAL PROCESSING AND ANALYSIS OF SHPB DATA WITH COMPUTATIONAL PYTHON ALGORITHM

---

```
import statistics
import math
import numpy as np
import time
import warnings
import shutil

def SHPB_processing(csv_path, sample_data, confinement='None',
signal_channels=[7, 8, 5], signal_amp=[10, 100, 10],
disp_correction=True, alignment='start', speedtrap=True):
    time_start = time.time() # Start timer
    warnings.filterwarnings("ignore") # Ignore error warnings
    # -----
    # INPUTS
    savedata = True # Save data to CSV files after processing. Do
        not save to reduce computation time if not required.

    # Sample inputs:
    sample_diameter = 25 # mm

    # Speed trap inputs:
    if speedtrap is not False:
        speedtrap_distance = 50 # Distance between speed traps, mm
        speedtrap_trigger_voltage = 24 # Voltage when speed traps
            are activated, V
        speedtrap_front_channel = 1 # Speed trap front
            oscilloscope channel (i.e. 1 if CH1 is speed trap front
            ).
        speedtrap_back_channel = 2 # Speed trap back oscilloscope
            channel (i.e. 2 if CH2 is speed trap back).

    # Incident bar inputs - Steel SS-25:
    in_bar_density = 7666 # Bar density, kg/m**3.
    in_bar_diameter = 25 # Bar diameter, mm.
    in_bar_wave_speed = 5376 # Bar wave speed, m/s.
    in_bar_gauge_factor = 123 # Input bar gauge factor.
    in_bar_gauge_voltage = 4 # Input bar signal voltage, V.
    in_bar_gauge_offset = 1000 # Distance from strain gauge to
        sample face, mm.

    # Transmitter bar inputs - Steel SS-25:
    out_bar_density = 7767 # Bar density, kg/m**3.
    out_bar_diameter = 25 # Bar diameter, mm.
    out_bar_wave_speed = 5305 # Bar wave speed, m/s.
    out_bar_gauge_factor = 127 # Output bar gauge factor.
    out_bar_gauge_voltage = 4 # Output bar signal voltage, V.
    out_bar_gauge_offset = 500 # Distance from strain gauge to
        sample face, mm.
```

```

# Confining ring inputs:
confinement_type = str(confinement) # Specimen confinement '
None '/'Ring '/'Reservoir'
if confinement_type == 'Ring':
    ring_outside_diameter = 35 # Outside diameter, mm.
    ring_inside_diameter = 25 # Inside diameter, mm.
    ring_length = 5 # Length, mm.
    ring_gauge_factor = 124 #121 # 120 - Gauge factor.
    ring_gauge_voltage = 8 # 10 or 5 - Signal voltage, V.
    ring_youngs_modulus = 206 # 200 - Young's modulus, GPa.

# Steel reservoir and pressure transducer inputs:
elif confinement_type == 'Reservoir':
    reservoir_fluid_wave_speed = 1482 # Wave speed of water
    1482 m/s.
    reservoir_thickness = 7.5 # Thickness of fluid annulus at
    transducer, mm.
    reservoir_gauge_factor = 2.90 # Reservoir transducer
    calibration, mV/MPa.
    reservoir_gauge_voltage = 10 # Reservoir transducer
    voltage, V.
else:
    confinement_type = 'None'

# -----
# FILE AND LOG
csv_name = os.path.basename(csv_path).split('.')[0] # Name of
raw data CSV file.

with open(os.path.join('.', f'{csv_name}_log.txt'), 'w',
encoding='utf-8') as file:
    file.write("Please refer to SHPB_processing.py for more
info.\n"
              'Code written by: Kin Shing Oswald Li, Arthur
Van Lerberghe, Andrew D. Barr')
def print_save(text): # Function to print text and also write
console log.
    print(text)
    with open(os.path.join('.', f'{csv_name}_log.txt'), 'a',
encoding='utf-8') as file:
        print(text, file=file)

# -----
# READING RAW DATA
# Sample data:
sample_initial_length = sample_data[0] # mm
sample_mass = sample_data[1] # g
sample_dry_mass = sample_data[2] # g
sample_initial_volume = sample_initial_length * math.pi * ((

```

APPENDIX D. SIGNAL PROCESSING AND ANALYSIS OF SHPB DATA WITH  
COMPUTATIONAL PYTHON ALGORITHM

---

```
in_bar_diameter/2)**2) * 10**(-3) # Sample initial volume,
cm^3.

if any(sd < 0 for sd in (sample_initial_length, sample_mass,
sample_dry_mass)):
    raise ValueError('Invalid sample_data - negative value
found.')
```

```
if sample_dry_mass > sample_mass:
    raise ValueError('Invalid sample_data - dry_mass greater
than mass.')
```

```
in_bar_gauge_channel = signal_channels[0] # Input bar
oscilloscope channel.
out_bar_gauge_channel = signal_channels[1] # Output bar
oscilloscope channel (i.e. 8 if CH8 is the input bar).
if confinement_type == 'Ring':
    ring_gauge_channel = signal_channels[2] # Confining ring
oscilloscope channel (i.e. 5 if CH5 is the confining
ring).
elif confinement_type == 'Reservoir':
    reservoir_gauge_channel = signal_channels[2] # Reservoir
pressure transducer oscilloscope channel (i.e. 6 if CH6
is the reservoir pressure transducer).
```

```
if any(ch < 0 for ch in signal_channels):
    raise ValueError('Invalid oscilloscope channel - negative
value found.')
```

```
in_bar_gauge_amp = signal_amp[0] # 1 or 10 - Input bar signal
amplification.
out_bar_gauge_amp = signal_amp[1] # 1 or 10 - Output bar
signal amplification.
if confinement_type == 'Ring':
    ring_gauge_amp = signal_amp[2] # 1 or 10 - Signal
amplification.
```

```
if any(amp < 0 for amp in signal_amp):
    raise ValueError('Invalid oscilloscope amplification -
negative value found.')
```

```
# CSV file format (i.e. Relative time, Channel 1, Channel 2,
Channel 3, Channel 4 ...):
raw_data = pd.read_csv(csv_path, sep=';', skiprows=9, header=
None, nrows=50000) # Read csv file.
time_base = raw_data.iloc[1:3, 0] # First two time values, s.
in_bar_gauge_signal = raw_data[in_bar_gauge_channel].iloc
[1:50000] # V.
out_bar_gauge_signal = raw_data[out_bar_gauge_channel].iloc
[1:50000] # V.
```

```

# -----
# Write intial log file:
print_save('-' * 72 + '\n'
          + f'{time.strftime("%H:%M:%S %d-%m-%Y", time.localtime
            (time_start))}\n'
          + '-' * 72 + '\n'
          + f'PROCESSING DATA FROM:\n {csv_name}\n'
          + '-' * 72 + '\n'
          + 'FILE PATH:\n'
          + f' {csv_path}\n'
          + 'SAMPLE DATA USED:\n'
          + f' Length: {sample_data[0]}mm\n'
          + f' Wet mass: {sample_data[1]}g\n'
          + f' Dry mass: {sample_data[2]}g\n'
          + 'CONFINEMENT TYPE:\n'
          + f" {confinement_type if confinement_type=='Ring' or
            confinement_type=='Reservoir' else 'None'}\n"
          + '-' * 72 + '\n'
          + 'GAUGE INPUT SETTINGS:\n'
          + f' Incident channel: {in_bar_gauge_channel}\n'
          + f' Incident amplification: {in_bar_gauge_amp}\n'
          + f' Transmitted channel: {out_bar_gauge_channel}\n'
          + f' Transmitted amplification: {out_bar_gauge_amp}\n'
          + (f" Ring channel: {ring_gauge_channel}\n Ring
            amplification: {ring_gauge_amp}\n" if
            confinement_type == 'Ring' else '')
          + (f" Reservoir channel: {reservoir_gauge_channel}\n"
            if confinement_type == 'reservoir' else '')
          + '-' * 72)

# -----
# FINDING STRIKER VELOCITY VIA SPEED TRAP
# Finding index that activates speed trap
time_step = time_base[2] - time_base[1] # Oscilloscope time
step, s.
if speedtrap is not False:
    speedtrap_front_trigger = np.argmax(raw_data[
        speedtrap_front_channel].iloc[1:10000] >
        speedtrap_trigger_voltage) # Index that activates front
    speed trap
    speedtrap_back_trigger = np.argmax(raw_data[
        speedtrap_back_channel].iloc[1:10000] >
        speedtrap_trigger_voltage) # Index that activates back
    speed trap

# Determining velocity based on time difference
speedtrap_difference = abs(speedtrap_front_trigger -
    speedtrap_back_trigger) * time_step # Difference in

```



APPENDIX D. SIGNAL PROCESSING AND ANALYSIS OF SHPB DATA WITH  
COMPUTATIONAL PYTHON ALGORITHM

---

```
    time between the two triggers, s.
    speedtrap_velocity = (speedtrap_distance/
        speedtrap_difference) / (10**3) # Velocity of striker
        bar, m/s.

    print_save('STRIKER BAR VELOCITY:\n'
        + ' ' + f'{round(speedtrap_velocity, 1)}m/s\n'
        + '-' * 72)

# -----
# PROCESSING BAR AXIAL SIGNALS
# Bar strain gauge signals:
in_bar_gauge_zero = statistics.mean(in_bar_gauge_signal.iloc
    [1000: 3000]) # Mean input bar "no signal" voltage, V.
out_bar_gauge_zero = statistics.mean(out_bar_gauge_signal.iloc
    [1000: 3000]) # Mean output bar "no signal" voltage, V.

# Strains:
in_bar_strain = ((in_bar_gauge_signal - in_bar_gauge_zero) *
    2) / (in_bar_gauge_factor * in_bar_gauge_voltage *
    in_bar_gauge_amp) # Input bar strain assuming half
    wheatstone bridge.
in_bar_youngs_modulus = (in_bar_wave_speed ** 2) * (
    in_bar_density / (10 ** 9)) # Input bar Young's modulus.
in_bar_stress = in_bar_strain * in_bar_youngs_modulus * 1000 #
    Input bar stress

out_bar_strain = ((out_bar_gauge_signal - out_bar_gauge_zero)
    * 2) / (out_bar_gauge_factor * out_bar_gauge_voltage *
    out_bar_gauge_amp) # Output bar strain assuming half
    wheatstone bridge.
out_bar_youngs_modulus = (out_bar_wave_speed ** 2) * (
    out_bar_density / (10 ** 9)) # Output bar Young's modulus.
out_bar_stress = out_bar_strain * out_bar_youngs_modulus *
    1000 # Output bar stress

# -----
# DETECTING PULSES
# Pulse triggers:
incident_trigger_strain = 10*math.pow(10, math.ceil(math.log10
    (abs(max(in_bar_strain.iloc[1000: 3000]))))) # Find maximum
    absolute strain rounded up to nearest magnitude of 10 to
    use to indicate start of incident pulse.
transmitted_trigger_strain = 10*math.pow(10, math.ceil(math.
    log10(abs(max(out_bar_strain.iloc[1000: 3000]))))) # Find
    maximum absolute strain rounded up to nearest magnitude of
    10 to use to indicate start of transmitted pulse.
if max(in_bar_strain.iloc[:20000]) < 2*incident_trigger_strain
    or max(out_bar_strain.iloc[:20000]) < 2*
```

```

transmitted_trigger_strain: # Raise error if no pulse is
found that is at least 2x larger than the trigger strain.
raise IndexError('Unable to detect pulse - check bar
inputs or raw signal.')

print_save('ABSOLUTE STRAIN TO TRIGGER PULSES:\n'
          f' Incident: {incident_trigger_strain}\n'
          f' Transmitted: {transmitted_trigger_strain}\n'
          + '-' * 72)

# Finding incident pulse:
incident_trigger = np.where(abs(in_bar_strain) >
incident_trigger_strain)[0][0] # Find when incident wave
first has a value larger than incident_trigger_strain.
if in_bar_strain[incident_trigger] < 0:
    in_bar_strain = -in_bar_strain # If incident wave is
negative, invert signal.
incident_start = np.where(np.array(in_bar_strain.iloc[0:
incident_trigger]) * np.array(in_bar_strain.iloc[1:
incident_trigger+1]) < 0)[0][-1] # Find last change of
sign before trigger (start of incident pulse).
incident_end = np.where((np.array(in_bar_strain.iloc[
incident_start:-1]) * np.array(in_bar_strain.iloc[
incident_start + 1:])) < 0)[0][1] + incident_start # Find
the next change of sign after trigger (end of incident
pulse).
incident_end = np.where((np.array(in_bar_strain.iloc[
incident_start:-1]) * np.array(in_bar_strain.iloc[
incident_start + 1:])) < 0)[0][1] + incident_start # Find
the next change of sign after trigger (end of incident
pulse).
incident_length = incident_end - incident_start # Length of
the incident pulse.

# Finding reflected pulse:
reflected_start = incident_start + round(2*in_bar_gauge_offset
/(1000*in_bar_wave_speed*time_step)) # Find start of
reflected wave based on wave speed.
reflected_end = reflected_start + incident_length # Length of
the reflected pulse.

# Finding transmitted pulse:
transmitted_trigger = np.where(abs(out_bar_strain.iloc[
incident_end:]) > transmitted_trigger_strain)[0][0] +
incident_end # Find when transmitted wave first has a
value larger than transmitted_trigger_strain.
if out_bar_strain[transmitted_trigger] < 0:
    out_bar_strain = -out_bar_strain # If transmitted wave is
negative invert signal.

```

## APPENDIX D. SIGNAL PROCESSING AND ANALYSIS OF SHPB DATA WITH COMPUTATIONAL PYTHON ALGORITHM

---

```
transmitted_start = np.where(np.array(out_bar_strain.iloc[0:
    transmitted_trigger]) * np.array(out_bar_strain.iloc[1:
    transmitted_trigger+1]) < 0)[0][-1] # Find last change of
    sign before trigger (start of incident pulse).
transmitted_end = np.where((np.array(out_bar_strain.iloc[
    transmitted_start:-1]) * np.array(out_bar_strain.iloc[
    transmitted_start + 1:])) < 0)[0][1] + transmitted_start #
    Find the next change of sign after trigger (end of
    transmitted pulse).

# -----
# TIME SHIFTING OR DISPERSION CORRECTION:
# Creating signal cut off-length stress waves
signal_cut_off = max(reflected_end, transmitted_end) +
    incident_length

in_bar_incident = np.concatenate((np.zeros(incident_start), np
    .conj(np.array(in_bar_strain.iloc[incident_start:
    reflected_start+1])), np.zeros(signal_cut_off-
    reflected_start-1))) # Concatenation of zero arrays with
    incident pulse.
in_bar_reflected = np.concatenate((np.zeros(reflected_start),
    np.conj(np.array(in_bar_strain.iloc[reflected_start:
    reflected_end+1])), np.zeros(signal_cut_off-reflected_end
    -1))) # Concatenation of zero array with reflected pulse.
out_bar_transmitted = np.concatenate((np.zeros(
    transmitted_start), np.conj(np.array(out_bar_strain.iloc[
    transmitted_start:transmitted_end+1])), np.zeros(
    signal_cut_off-transmitted_end-1))) # Concatenation of zero
    array with transmitted pulse.

# Dispersion correction - see documentation for dispersion.py:
if disp_correction is not False:
    print_save('PROCESSING WITH DISPERSION CORRECTION.' + '\n'
        + '-' * 72)
    fs = 1 / time_step # Sampling frequency, Hz
    from dispersion import dispersion
    [in_bar_incident_strain, in_bar_incident_stress] =
        dispersion(in_bar_incident, fs, in_bar_diameter/2000,
            in_bar_wave_speed, in_bar_youngs_modulus,
            in_bar_gauge_offset/1000)
    [in_bar_reflected_strain, in_bar_reflected_stress] =
        dispersion(in_bar_reflected, fs, in_bar_diameter/2000,
            in_bar_wave_speed, in_bar_youngs_modulus, -
            in_bar_gauge_offset/1000)
    [out_bar_transmitted_strain, out_bar_transmitted_stress] =
        dispersion(out_bar_transmitted, fs, out_bar_diameter
            /2000, out_bar_wave_speed, out_bar_youngs_modulus, -
            out_bar_gauge_offset/1000)
```

```

# Simple timeshift analysis without dispersion correction:
else:
    print_save('PROCESSING WITH SIMPLE TIMESHIFT, NOT
              DISPERSION CORRECTION.' + '\n' + '-' * 72)
    in_bar_shift = round(((in_bar_gauge_offset/1000) /
                          in_bar_wave_speed) / time_step)
    out_bar_shift = round(((out_bar_gauge_offset/1000) /
                           out_bar_wave_speed) / time_step)

    in_bar_incident_strain = np.concatenate((np.array(
        in_bar_incident[-1-in_bar_shift:]), np.array(
        in_bar_incident[:-in_bar_shift])))
    in_bar_reflected_strain = np.concatenate((np.array(
        in_bar_reflected[in_bar_shift:]), np.array(
        in_bar_reflected[:in_bar_shift])))
    out_bar_transmitted_strain = np.concatenate((np.array(
        out_bar_transmitted[out_bar_shift:]), np.array(
        out_bar_transmitted[:out_bar_shift])))

    in_bar_incident_stress = in_bar_incident_strain *
        in_bar_youngs_modulus * 1000
    in_bar_reflected_stress = in_bar_reflected_strain *
        in_bar_youngs_modulus * 1000
    out_bar_transmitted_stress = out_bar_transmitted_strain *
        out_bar_youngs_modulus * 1000

# -----
# PROCESSING AXIAL STRESS AND STRAIN AT SPECIMEN INTERFACE
# Find new start of incident pulse as start of sample stress/
# strain:
incident_trigger_new = np.where(abs(in_bar_incident_strain) >
                                incident_trigger_strain)[0][0] # Find the new position of
                                incident pulse.
incident_start_new = np.where(in_bar_incident_strain[0:
    incident_trigger_new-1] * in_bar_incident_strain[1:
    incident_trigger_new] < 0)[0][-1] # Use new start of
    incident pulse as start of sample interface analysis.

# Bar displacement and sample strain:
in_bar_displacement = np.zeros(signal_cut_off) # Zero array
    placeholder for input bar displacement.
out_bar_displacement = np.zeros(signal_cut_off) # Zero array
    placeholder for ouput bar displacement.
sample_strain = np.zeros(signal_cut_off) # Zero array
    placeholder for sample strain.
in_bar_displacement_alt = np.zeros(signal_cut_off) # Zero
    array placeholder for input bar displacement.

```

APPENDIX D. SIGNAL PROCESSING AND ANALYSIS OF SHPB DATA WITH  
COMPUTATIONAL PYTHON ALGORITHM

---

```
sample_strain_alt = np.zeros(signal_cut_off) # Zero array
placeholder for sample strain.

for i in range(incident_start_new, signal_cut_off):
    in_bar_displacement[i] = in_bar_displacement[i-1] + ((
        in_bar_incident_strain[i] - in_bar_reflected_strain[i])
        * 1000 * time_step * in_bar_wave_speed) # Cumulative
input bar displacement.
    out_bar_displacement[i] = out_bar_displacement[i-1] + (
        out_bar_transmitted_strain[i] * 1000 * time_step *
        out_bar_wave_speed) # Cumulative output bar
displacement.
    sample_strain[i] = (in_bar_displacement[i] -
        out_bar_displacement[i]) / sample_initial_length #
Sample axial strain.
    in_bar_displacement_alt[i] = in_bar_displacement[i-1] + ((
        in_bar_incident_strain[i]) * 1000 * time_step *
        in_bar_wave_speed) # Cumulative input bar displacement
, mm.
    sample_strain_alt[i] = 2 * (in_bar_displacement_alt[i] -
        out_bar_displacement[i]) / sample_initial_length #
Sample axial strain.
    if sample_strain[i] > 0.05 and abs(sample_strain[i] -
        sample_strain[i-1]) < 0.0001 and any(value<=0 for value
        in in_bar_incident_strain[incident_start_new+1:i]): #
Cut off when sample is fully strained i.e. when sample
strain begins to flatten off (set to when strain
difference between timesteps is 0.0001).
        in_bar_displacement = np.trim_zeros(
            in_bar_displacement, 'b')
        out_bar_displacement = np.trim_zeros(
            out_bar_displacement, 'b')
        sample_strain = np.trim_zeros(sample_strain, 'b')
        in_bar_displacement_alt = np.trim_zeros(
            in_bar_displacement_alt, 'b')
        sample_strain_alt = np.trim_zeros(sample_strain_alt, '
        b')
        break

# Final strain as end of sample stress/strain:
sample_end = len(sample_strain) - 1 # Ending index based on
when sample has been fully strained.

# Define new starting index depending on alignment input:
if alignment == 'end': # Alignment mechanism for transmitted
pulse based on detection of the ending of transmitted pulse
.
    transmitted_end_new = np.where((out_bar_transmitted_strain
        [np.argmax(out_bar_transmitted_strain):-1]*
```

```

        out_bar_transmitted_strain[np.argmax(
            out_bar_transmitted_strain)+1:)]<0)[0][0] + np.argmax(
            out_bar_transmitted_strain)
        transmitted_start_new = transmitted_end_new - (sample_end
            - incident_start_new)
elif alignment == 'mid': # Alignment mechanism for transmitted
    pulse on centering transmitted and incident/reflected
    pulses.
    transmitted_trigger_new = np.where(abs(
        out_bar_transmitted_strain[incident_start_new:] >
        transmitted_trigger_strain)[0][0] + incident_start_new
    transmitted_start_new = np.where(
        out_bar_transmitted_strain[incident_start_new:
        transmitted_trigger_new-1] * out_bar_transmitted_strain
        [incident_start_new+1:transmitted_trigger_new] <0)
        [0][-1] + incident_start_new
    transmitted_end_new = np.where((out_bar_transmitted_strain
        [np.argmax(out_bar_transmitted_strain):-1]*
        out_bar_transmitted_strain[np.argmax(
            out_bar_transmitted_strain)+1:)]<0)[0][0] + np.argmax(
            out_bar_transmitted_strain)
    transmitted_start_new = round(transmitted_start_new + ((
        incident_start_new + sample_end)/2) - ((
        transmitted_start_new + transmitted_end_new)/2 ))
    transmitted_end_new = transmitted_start_new + (sample_end
        - incident_start_new)
else:
    print('hi')
    transmitted_trigger_new = np.where(abs(
        out_bar_transmitted_strain[incident_start_new:] >
        transmitted_trigger_strain)[0][0] + incident_start_new
    transmitted_start_new = np.where(
        out_bar_transmitted_strain[:transmitted_trigger_new-1]
        * out_bar_transmitted_strain[1:transmitted_trigger_new]
        <0)[0][-1]
    transmitted_end_new = transmitted_start_new + (sample_end
        - incident_start_new)
    if isinstance(alignment, (int, float)) and 1 <= alignment
        < (sample_end - incident_start_new): # Alignment
        mechanism based for transmitted pulse based on maximums
        of transmitted and incident/reflected pulses set to a
        defined value.
        incident_start_new = incident_start_new + np.argmax(
            in_bar_incident_strain[incident_start_new:
            sample_end+1]) - alignment # Set peak of incident
            pulse to align with stress_peak input.
        transmitted_start_new = transmitted_start_new + np.
            argmax(out_bar_transmitted_strain[
            transmitted_start_new:transmitted_end_new+1]) -

```

```

        alignment # Set peak of transmitted pulse to align
        with stress_peak input.
        transmitted_end_new = transmitted_start_new + (
            sample_end - incident_start_new)
    elif isinstance(alignment, float) and 0 < alignment < 1: #
        Alignment mechanism for transmitted pulse based on a
        proportion of the maximums of transmitted and incident/
        reflected pulses (alignment value should be a decimal
        between 0-1)
        transmitted_trigger_new = np.where(abs(
            out_bar_transmitted_strain[transmitted_start_new:
            transmitted_end_new]) > (alignment * max(abs(
            out_bar_transmitted_strain[transmitted_start_new:
            transmitted_end_new])))))[0][0]
        incident_trigger_new = np.where(abs(
            in_bar_incident_strain[incident_start_new:
            sample_end]) > (alignment * max(abs(
            in_bar_incident_strain[incident_start_new:
            sample_end])))))[0][0]
        transmitted_start_new = transmitted_start_new - (
            incident_trigger_new - transmitted_trigger_new)
        transmitted_end_new = transmitted_start_new + (
            sample_end - incident_start_new)
    else:
        alignment = 'start'

# Sample front stress:
in_bar_incident_strain = in_bar_incident_strain[
    incident_start_new:sample_end+1] # Redefining incident
    strain to be within sample boundaries.
in_bar_reflected_strain = in_bar_reflected_strain[
    incident_start_new:sample_end+1] # Redefining reflected
    strain to be within sample boundaries.
in_bar_incident_stress = in_bar_incident_stress[
    incident_start_new:sample_end+1] # Redefining incident
    stress to be within sample boundaries.
in_bar_reflected_stress = in_bar_reflected_stress[
    incident_start_new:sample_end+1] # Redefining reflected
    stress to be within sample boundaries.

stress_factor = ((in_bar_diameter/2)**2) / ((sample_diameter
    /2)**2) # Stress factor to adjust for difference in
    diameter between sample and pressure bars.
sample_front_stress = stress_factor * (in_bar_incident_stress
    + in_bar_reflected_stress) # Stress at incident bar
    specimen face, MPa.

if len(out_bar_transmitted_stress) - (sample_end -
    incident_start_new) < transmitted_start_new:

```

```

out_bar_transmitted_stress = np.concatenate((np.array(
    out_bar_transmitted_stress), np.zeros(
        transmitted_end_new - (sample_end - incident_start_new)
    )))
out_bar_transmitted_strain = np.concatenate((np.array(
    out_bar_transmitted_strain), np.zeros(
        transmitted_end_new - (sample_end - incident_start_new)
    )))

# Sample back stress:
out_bar_transmitted_strain = out_bar_transmitted_strain[
    transmitted_start_new:transmitted_end_new+1] # Redefining
    transmitted strain to be within sample boundaries.
out_bar_transmitted_stress = out_bar_transmitted_stress[
    transmitted_start_new:transmitted_end_new+1] # Redefining
    transmitted stress to be within sample boundaries.

sample_back_stress = stress_factor *
    out_bar_transmitted_stress # Stress at transmitter bar
    specimen face, MPa.

#Sample stress and strain:
sample_strain = sample_strain[incident_start_new:sample_end+1]
    # New sample strain set within bounds of sample stress/
    strain analysis.
sample_length = (1 - sample_strain) * sample_initial_length #
    Sample length.

sample_mid_stress = (sample_front_stress + sample_back_stress)
    /2 # Mean axial specimen stress, MPa.

# Sample axial strain rate:
rel_time = time_step * np.arange(0, sample_end-
    incident_start_new+1) # Relative time, s.
sample_strain_rate = np.zeros((2, len(sample_strain)))
for i in range(0, len(sample_strain)-1):
    sample_strain_rate[0, i] = (rel_time[i] + rel_time[i+1])/2
    sample_strain_rate[1, i] = ((sample_length[i] -
        sample_length[i+1]) / sample_length[i]) / time_step

sample_strain_rate_1 = sample_strain_rate[0]
sample_strain_rate_2 = sample_strain_rate[1] # Sample strain
    rate

in_bar_displacement = in_bar_displacement[incident_start_new:
    sample_end+1] # Redefining incident bar displacement to be
    within sample boundaries.
in_bar_displacement_alt = in_bar_displacement_alt[
    incident_start_new:sample_end+1] # Redefining incident bar

```



## APPENDIX D. SIGNAL PROCESSING AND ANALYSIS OF SHPB DATA WITH COMPUTATIONAL PYTHON ALGORITHM

---

```
displacement to be within sample boundaries.
out_bar_displacement = out_bar_displacement[incident_start_new
:sample_end+1] # Redefining transmitted bar displacement to
be within sample boundaries.

print_save("SAMPLE AXIAL RESULTS:\n"
          # f" Maximum sample stress: {round(max(
          sample_mid_stress),2)}MPa\n"
          f" Maximum sample strain: {round(max(sample_strain), 3)
          *100}%\n"
          f" Maximum strain rate: {round(max(sample_strain_rate_2)
          ,0)} s1\n"
          + '-' * 72)

strain_difference = in_bar_incident_strain - (
out_bar_transmitted_strain - in_bar_reflected_strain) #
Difference in strain to check condition for stress
equilibrium (strainI = strainT - strainR).

# -----
# PROCESSING RADIAL STRESSES
# Confining ring strain input:
if confinement_type == 'Ring':
    # Processing raw data from confining ring input:
    ring_gauge_signal = raw_data[ring_gauge_channel].iloc
    [1:50000] # Confining ring signal, V.
    ring_gauge_zero = statistics.mean(ring_gauge_signal.iloc
    [:1000]) # Mean confining ring "no signal" voltage, V.
    ring_radial_strain = np.array((ring_gauge_signal -
    ring_gauge_zero) * 4 / (ring_gauge_factor *
    ring_gauge_voltage * ring_gauge_amp)) # Confining ring
    strain assuming quarter wheatstone bridge.

# Finding radial pulse:
ring_trigger_strain = math.pow(10, math.ceil(math.log10(
abs(max(ring_radial_strain[1000: 3000]))))) # Find
maximum absolute strain rounded up to nearest magnitude
of 10 to use to indicate start of radial pulse.
ring_pulse_trigger = np.where(abs(ring_radial_strain[
incident_start_new:]) > ring_trigger_strain)[0][0] +
incident_start_new # Find when transmitted wave first
has a value larger than transmitted_trigger_strain.
if ring_radial_strain[np.argmax(abs(ring_radial_strain[
incident_start_new:transmitted_end_new]))] < 0:
    ring_radial_strain = -ring_radial_strain
if max(ring_radial_strain) < 1.1*ring_trigger_strain: #
Raise error if no pulse is found that is at least 10%
larger than the trigger strain.
    raise IndexError('Unable to detect radial pulse -
```

```

        check ring inputs or raw signal.')
radial_start = np.where((ring_radial_strain[
    incident_start_new:ring_pulse_trigger-1] *
    ring_radial_strain[incident_start_new+1:
    ring_pulse_trigger] < 0)[0][-1] + incident_start_new #
    Find last change of sign before trigger (start of
    radial pulse)).
radial_end = radial_start + (sample_end -
    incident_start_new) # Find end of radial pulse based on
    sample pulse length.

# Sample radial stress and strain:
ring_thick_walled_pipe_factor = (((ring_outside_diameter
    /2)**2) - ((ring_inside_diameter/2)**2)) / (2*(
    ring_inside_diameter/2)**2) # Ratio of internal radial
    stress on the specimen to circumferential stress in
    the ring.
sample_radial_strain = ring_radial_strain[radial_start:
    radial_end+1] # Sample radial strain.
sample_radial_stress = (ring_thick_walled_pipe_factor * (
    ring_youngs_modulus * 1000) * sample_radial_strain) * (
    ring_length / sample_length) # Radial stress from the
    ring, MPa.
sample_volume = sample_initial_volume * (1-sample_strain)
    # Soil sample volume, cm^3.
sample_density = sample_mass / sample_volume # Sample
    density, Mg/m^3.
sample_dry_density = sample_dry_mass / sample_volume #
    Sample dry density, Mg/m^3.
sample_mean_stress = (sample_mid_stress + 2 *
    sample_radial_stress) / 3

print_save('SAMPLE RADIAL RESULTS VIA CONFINING RING
    STRAIN:\n'
    f' Absolute radial strain trigger: {
        ring_trigger_strain}\n'
    f' Maximum radial stress: {round(max(
        sample_radial_stress),2)}MPa\n'
    f' Maximum radial strain: {round(max(
        sample_radial_strain)*100,5)}%\n'
    f' Maximum mean stress: {round(max(
        sample_mean_stress), 2)}MPa\n'
    f' Change in volume: {round(sample_initial_volume -
        sample_volume[-1], 3)}cm^3\n'
    f' Change in density: {round(sample_density[-1] -
        sample_density[0], 3)}Mg/m^3\n'
    f' Change in dry density: {round(sample_dry_density
        [-1] - sample_dry_density[0], 3)}Mg/m^3\n'
    + '-' * 72)

```

```

# Reservoir with pressure transducer input:
elif confinement_type == 'Reservoir':
    #Processing raw data from pressure transducer input:
    reservoir_gauge_signal = raw_data[reservoir_gauge_channel
    ].iloc[1:50000] # Pressure transducer signal, V.
    reservoir_gauge_zero = statistics.mean(
        reservoir_gauge_signal[:1000]) # Mean pressure
        transducer "no signal" voltage, V.
    reservoir_stress = ((reservoir_gauge_signal -
        reservoir_gauge_zero) * 1000) / reservoir_gauge_factor
        # Pressure transducer stress, MPa.

# Timeshifting radial stress based on reservoir travel
time:
reservoir_transit = (reservoir_thickness / 1000) /
    reservoir_fluid_wave_speed # Time for pulse to travel
    through reservoir fluid, s.
reservoir_time_steps = round(reservoir_transit / time_step
    ) # Timeshift in oscilloscope timesteps.
reservoir_radial_stress = np.array(reservoir_stress[
    reservoir_time_steps:-1], reservoir_stress[:
    reservoir_time_steps - 1])
reservoir_radial_stress = np.concatenate((
    reservoir_radial_stress, np.full(reservoir_time_steps
    +1, reservoir_radial_stress[-1])))

# Finding radial pulse:
# reservoir_trigger_stress = math.pow(10, math.ceil(math.
    log10(abs(max(reservoir_radial_stress[:4000])))) #
    Find maximum absolute stress rounded up to nearest
    magnitude of 10 to use to indicate start of radial
    pulse. *(which one?)
reservoir_trigger_stress = abs(max(reservoir_radial_stress
    [incident_start_new-1000: incident_start_new])) # Find
    maximum absolute stress to indicate start of radial
    pulse. *(which one?)
reservoir_pulse_trigger = np.where(abs(
    reservoir_radial_stress[incident_start_new:]) >
    reservoir_trigger_stress)[0][0] + incident_start_new #
    Find when transmitted wave first has a value larger
    than transmitted_trigger_strain.
if max(reservoir_radial_stress) < 0:
    reservoir_radial_stress = -reservoir_radial_stress
if max(reservoir_radial_stress) < 2*
    reservoir_trigger_stress: # Raise error if no pulse is
    found that is at least 2x larger than the trigger
    stress.
    raise IndexError('Unable to detect radial pulse -

```

```

        check_reservoir_inputs_or_raw_signal.')
```

```

radial_start = reservoir_pulse_trigger # Start of radial
pulse.
radial_end = radial_start + (sample_end -
incident_start_new) # Find end of radial pulse based on
sample pulse length.

# Sample radial stress:
sample_radial_stress = reservoir_radial_stress[
radial_start:radial_end+1] # Sample radial stress.

print_save('SAMPLE RADIAL RESULTS VIA WATER RESERVOIR
PRESSURE:\n'
f' Absolute radial stress trigger: {
reservoir_trigger_stress}\n'
f' Maximum radial stress: {round(max(
sample_radial_stress),2)}MPa\n'
+ '-' * 72)

radial_start = radial_start + (np.argmax(
sample_radial_stress) - np.argmax(sample_mid_stress)) #
Aligning maximum of radial pulse with axial mid stress
.
radial_end = radial_start + sample_end -
incident_start_new # New end of radial pulse.
sample_radial_stress = reservoir_radial_stress[
radial_start:radial_end+1] # New sample radial stress
aligned with pulse length of axial mid stress.

else:
print_save('NO RADIAL MEASUREMENT SELECTED:\n'
' No radial stress and strain can be obtained.\n'
' No volume and density data can be obtained.\n'
+ '-' * 72)

# -----
# EXPORTING AND SAVING PROCESSED DATA
if savedata is True:
    if speedtrap == False:
        folder_path = f"./Processed Data/{confinement_type if
confinement_type=='Ring' or confinement_type=='
Reservoir' else 'None'}/{csv_name}" # File path to
find processed data.
    else:
        folder_path = f"./Processed Data/{confinement_type if
confinement_type=='Ring' or confinement_type=='
Reservoir' else 'None'}/{round(speedtrap_velocity)}
ms/{csv_name}"

```

```

os.makedirs(folder_path, exist_ok=True)

# Saving sample results:
sample_results = {
    'Relative time (s)': rel_time,
    'Front stress (MPa)': sample_front_stress,
    'Back Stress (MPa)': sample_back_stress,
    'Mid Stress (MPa)': sample_mid_stress,
    'Strain': sample_strain,
    'Strain rate (s-1)': sample_strain_rate_2,
    'Length (mm)': sample_length,}

# Saving radial sample results if confinement is selected:
if confinement_type == 'Ring':
    sample_results.update({
        'Radial stress (MPa)': sample_radial_stress,
        'Radial strain': sample_radial_strain,
        'Mean stress (MPa)': sample_mean_stress,
        'Volume (cm3)': sample_volume,
        'Density (Mg/m3)': sample_density,
        'Dry density (Mg/m3)': sample_dry_density})
elif confinement_type == 'Reservoir':
    sample_results.update({
        'Radial stress (MPa)': sample_radial_stress})
sample_results = pd.DataFrame(sample_results)
sample_results.to_csv(os.path.join(folder_path, f'{
    csv_name}_sample_results.csv'), index=False)

# Saving constants used as inputs:
constants = {
    'Sample initial length': sample_initial_length,
    'Sample mass': sample_mass,
    'Sample dry mass': sample_dry_mass,
    'Sample diameter': sample_diameter,
    'Sample initial volume': sample_initial_volume,
    'In-bar density': in_bar_density,
    'In-bar diameter': in_bar_diameter,
    'In-bar wavespeed': in_bar_wave_speed,
    'In-bar gauge channel': in_bar_gauge_channel,
    'In-bar gauge factor': in_bar_gauge_factor,
    'In-bar gauge amp': in_bar_gauge_amp,
    'In-bar gauge voltage': in_bar_gauge_voltage,
    'In-bar gauge offset': in_bar_gauge_offset,
    'In-bar Youngs modulus': in_bar_youngs_modulus,
    'Out-bar density': out_bar_density,
    'Out-bar diameter': out_bar_diameter,
    'Out-bar wavespeed': out_bar_wave_speed,
    'Out-bar gauge channel': out_bar_gauge_channel,
    'Out-bar gauge factor': out_bar_gauge_factor,

```

```

        'Out-bar gauge amp': out_bar_gauge_amp,
        'Out-bar gauge voltage': out_bar_gauge_voltage,
        'Out-bar gauge offset': out_bar_gauge_offset,
        'Out-bar Youngs modulus': out_bar_youngs_modulus}

# Saving radial constants if confinement is selected:
if confinement_type == 'Ring':
    constants.update({
        'Ring outside diameter': ring_outside_diameter,
        'Ring inside diameter': ring_inside_diameter,
        'Ring length': ring_length,
        'Ring gauge channel': ring_gauge_channel,
        'Ring gauge factor': ring_gauge_factor,
        'Ring gauge amp': ring_gauge_amp,
        'Ring gauge voltage': ring_gauge_voltage,
        'Ring Youngs modulus': ring_youngs_modulus})
elif confinement_type == 'Reservoir':
    constants.update({
        'Reservoir fluid wave speed':
            reservoir_fluid_wave_speed,
        'Reservoir thickness': reservoir_thickness,
        'Reservoir gauge channel': reservoir_gauge_channel
        ,
        'Reservoir gauge factor': reservoir_gauge_factor,
        'Reservoir gauge voltage': reservoir_gauge_voltage
    })
constants = pd.DataFrame(constants.items(), columns = ['
Constant', 'Value'])
constants.to_csv(os.path.join(folder_path, f'{csv_name}
_constants.csv'), index=False)

# Saving incident and transmitter bar signal data:
signal_results = {
    'Gauge signal (In Bar)': in_bar_gauge_signal,
    'Strain (In Bar)': in_bar_strain,
    'Stress (In Bar)': in_bar_stress,
    'Gauge signal (Out Bar)': out_bar_gauge_signal,
    'Strain (Out Bar)': out_bar_strain,
    'Stress (Out Bar)': out_bar_stress}

# Saving radial signal data if confinement is selected:
if confinement_type == 'Ring' or confinement_type == '
Reservoir':
    if confinement_type == 'Ring':
        signal_results.update({
            'Gauge signal (Ring)': ring_gauge_signal,
            'Strain (Ring)': ring_radial_strain})
    else:
        signal_results.update({

```

```

        'Gauge signal (Reservoir)':
            reservoir_gauge_signal,
        'Stress (Reservoir)': reservoir_stress,
        'Adjusted stress (reservoir) at interface':
            reservoir_radial_stress})
signal_results = pd.DataFrame(signal_results)
signal_results.to_csv(os.path.join(folder_path, f'{{
    csv_name}}_signal_results.csv'), index=False)

# Saving incident, reflected, and transmitted pulse data:
pulse_results = {
    'Incident pulse strain': in_bar_incident_strain,
    'Incident pulse stress': in_bar_incident_stress,
    'Reflected pulse strain': in_bar_reflected_strain,
    'Reflected pulse stress': in_bar_reflected_stress,
    'Displacement (In bar)': in_bar_displacement,
    'Displacement alt (In bar)': in_bar_displacement_alt,
    'Transmitted pulse strain': out_bar_transmitted_strain
    ,
    'Transmitted pulse stress': out_bar_transmitted_stress
    ,
    'Displacement (Out Bar)': out_bar_displacement}
pulse_results = pd.DataFrame(pulse_results)
pulse_results.to_csv(os.path.join(folder_path, f'{{csv_name
    }}_pulse_results.csv'), index=False)

print_save(f'PROCESSED DATA SAVED SUCCESSFULLY\n'
           f" CSV file names: sample_results, constants,
           signal_results, pulse_results\n"
           f' CSV files saved to folder: {os.path.abspath(
           folder_path)}\n'
           f' Console log saved to log.txt\n'
           + '-' * 72)
else:
    print_save('PROCESSED DATA HAS NOT BEEN SAVED\n'
              'savedata=False\n'
              + '-' * 72)

# -----
print_save(f'ALL DATA PROCESSED SUCCESSFULLY\n'
          f' To rerun, enter:\n'
          f" SHPB_processing(r'{{csv_path}}', {{sample_data}}, '{{
          confinement_type}}', signal_channels=[{
          in_bar_gauge_channel}, {out_bar_gauge_channel}{{', '+
          str(ring_gauge_channel) if confinement_type=='Ring'
          else '}}{{', '+ str(reservoir_gauge_channel) if
          confinement_type=='Reservoir' else '}}], signal_amp
          =[{in_bar_gauge_amp}, {out_bar_gauge_amp}{{', '+ str(
          ring_gauge_channel) if confinement_type=='Ring' else
          '}}], disp_correction={False if disp_correction==

```

```

        False else True}, alignment={alignment if isinstance(
        alignment, (int, float)) else repr(alignment)},
        speedtrap={False if speedtrap==False else True})\n"
+ '-' * 72 + '\n'
+ f'TIME REQUIRED: {round(time.time() - time_start, 3)}s
.\n'
+ '-' * 72)

if savedata == True:
    with open(os.path.join(folder_path, f'{csv_name}_log.txt')
, 'a', encoding='utf-8') as file:
        file.write('-' * 8 + "Hope you're doing okay. Stay
        positive and keep vibing!!" + '-' * 9)

    shutil.move(f'./{csv_name}_log.txt', os.path.join(
        folder_path, f'{csv_name}_log.txt'))
else:
    os.remove(f'{csv_name}_log.txt')

# -----
# RETURN STATEMENTS
# Change, add or remove return statements as required:

if confinement_type == 'Ring' or confinement_type == '
Reservoir':
    return [sample_mid_stress, sample_front_stress,
            sample_back_stress, in_bar_stress, out_bar_stress,
            sample_radial_stress, sample_strain,
            sample_strain_rate_2]
else:
    return [sample_mid_stress, sample_front_stress,
            sample_back_stress, in_bar_stress, out_bar_stress,
            sample_strain, sample_strain_rate_2]

```



### D.3 dispersion.py

dispersion.py is a subroutine of SHPB\_processing.py that must be included if dispersion correction method is to be applied. The algorithm applies the process of phase angle and amplitude correction to pulse signals from pressure bar readings.

```
'dispersion.py'

# First-mode dispersion correction of a finite arbitrary signal in
  a cylindrical bar.

# OPERATION:
# - Finds FFT of the signal.
# - Corrects phase velocity and amplitude of each frequency using
  method described by Tyas & Pope (2005).
# - Reconstructs signal using IFFT.
# - Frequencies above  $fa/c0 = 0.2619$  stripped ( $d/L = 0.6$ ), due to
  limitations of  $m1$  correction.

# INPUTS:
# - x: Zero-padded strain signal in time domain (1xN numeric).
# - fs: Sampling frequency, Hz.
# - a: Bar radius, m.
# - c0: One-dimensional wave velocity of the bar, m/s.
# - E: Young's modulus of the bar, GPa.
# - z: Distance to correction over, m (+ve in direction of
  propagation).

# OUTPUTS:
# - xStrain: Dispersion-corrected strain signal.
# - xStress: Dispersion-corrected stress signal, MPa

# REFERENCES:
# - Tyas, A., Pope, D.J., (2005). Full correction of first-mode
  Pochhammer-Chree dispersion effects in experimental
# pressure bar signals. Measurement science and technology, 16(3),
  p.642.

# -----
# Imported modules:
import numpy as np

# Imported function:
from dispersion_factors import dispersion_factors

def dispersion(x, fs, a, c0, E, z):
  # Input signal:
```

```

n = len(x) # Number of elements in signal.
f = np.arange(0, n-1) * (fs/n) # FFT frequencies, Hz.
fmax = 0.2619 * c0/a # Max correctable frequency due to
    factor m1 limitations, Hz.

# FFT the signal:
X = np.fft.fft(x)
XStrain = np.array(X) # Create copy for strain correction.
XStress = np.array(X) # Create copy for stress correction.

# Phase shift, adjust magnitude of frequency components:
number_of_bins = len(X)

if number_of_bins % 2 == 0:
    # n is even:
    positive_bins = np.arange(1, number_of_bins//2) #
        Positive frequency bins.
    negative_bins = np.arange(number_of_bins//2 + 1,
        number_of_bins) # Negative frequency bins.
else:
    # n is odd:
    positive_bins = np.arange(1, (number_of_bins + 1)//2) #
        Positive frequency bins.
    negative_bins = np.arange((number_of_bins + 1)//2,
        number_of_bins) # Negative frequency bins.

for b in positive_bins.astype(int):
    if f[b] <= fmax:
        # Find phase shift and factors m1 and m2 for current
        frequency:
        [angle_mod, m1, m2] = dispersion_factors(f[b], a, c0,
            z)
        # Apply shift and factors m1 to obtain corrected
        strain:
        XStrain[b] = m1 * np.abs(X[b]) * np.exp(1j * (np.angle
            (X[b]) - angle_mod))
        # Apply phase shift and factors m1 & m2 to obtain
        corrected stress [/E]:
        XStress[b] = m1 * m2 * np.abs(X[b]) * np.exp(1j * (np.
            angle(X[b]) - angle_mod))
    else:
        # Above fMax zero X data [Apply perfect low-pass
        filter].
        XStrain[b] = 0
        XStress[b] = 0

# Correct negative bins by taking complex conjugate of
    positive bins:

```

#### APPENDIX D. SIGNAL PROCESSING AND ANALYSIS OF SHPB DATA WITH COMPUTATIONAL PYTHON ALGORITHM

---

```
XStrain[negative_bins.astype(int)] = np.conj(XStrain[
    positive_bins.astype(int)[::-1]])
XStress[negative_bins.astype(int)] = np.conj(XStress[
    positive_bins.astype(int)[::-1]])

# Convert the corrected frequency components back into the
# time domain:
x_strain = np.real(np.fft.ifft(XStrain)) # Corrected strain.
x_stress = np.real(np.fft.ifft(XStress))*E*1000 # Corrected
# stress, MPa.

return [x_strain, x_stress]
```

## Chapter E

# Relevant LS-DYNA keywords

## E.1 Introduction

This appendix contains LS-DYNA material cards and relevant keywords used in the numerical modelling of SHPB experiments in this study. Detailed description of the implementation of these models are presented in Chapter 6.

## E.2 Material cards

Table E.1: Material card for MAT\_ELASTIC, calibrated to represent steel pressure bars.

```
*MAT_ELASTIC_TITLE
Steel
$#      mid      ro      e      pr      da      db  not used
      X      7666.01.68000E11      0.29      0.0      0.0      0.0
```

Table E.2: Material card for MAT\_NULL, calibrated to represent water.

```
*MAT_NULL_TITLE
Water
$#      mid      ro      pc      mu      terod      cerod      ym      pr
X      1000.0      0.0      0.0      0.0      0.0      0.0      0.0
```

Table E.3: Material card for MAT\_MOHR\_COULOMB, calibrated to represent kaolin clay.

```

*MAT_MOHR_COULOMB_TITLE
MC Sample
$# mid ro gmod rnu phi cval psi
X 1296.01.300000E7 0.44 0 0.08075 55760.0 0.0
$# nplanes lccpdr lccpt lccjdr lccjt lcsfac
0 0 0 0 0 0 0
$# gmoddp gmodgr lcgmp lcphep lcpsep lcgms cvalgr aniso
0.0 0.0 0.0 0.0 0.0 0.0 0.0 1.0
    
```

Table E.4: Material card for MAT\_NULL, calibrated to represent air at atmospheric pressure.

```

*MAT_NULL_TITLE
Air
$# mid ro pc mu terod cerod ym pr
3 1.225 0.0 0.0 0.0 0.0 0.0 0.0
    
```

Table E.5: Material card for MAT\_RIGID, calibrated to represent rigid steel reservoir.

```

*MAT_RIGID_TITLE
Rigid steel
$# mid ro e pr n couple m alias
X 7666.01.68000E11 0.28 0.0 0.0 0.0
$# cmo con1 con2
1.0 7 7
$# a1 a2 a3 v1 v2 v3
0.0 0.0 0.0 0.0 0.0 0.0
    
```

### E.3 Contact algorithms

Table E.6: Contact card for CONTACT\_AUTOMATIC\_NODES\_TO\_SURFACE, calibrated to describe SPH node to Lagrangian solid surface interactions.

```

*CONTACT_AUTOMATIC_NODES_TO_SURFACE_ID
$#   cid   title
      X    N-S
$#   ssid  msid  sstyp  mstyp  sboxid  mboxid  spr    mpr
      X    X    4      3      0      0      0      0
$#   fs    fd    dc     vc     vdc    penchk  bt     dt
      0.0  0.0  0.0   0.0   0.0    0      0.01.00000E20
$#   sfs   sfm   sst    mst    sfst   sfmt   fsf    vsf
      5.0  5.0  0.0   0.0   1.0   1.0   1.0    1.0
    
```

Table E.7: Contact card for CONTACT\_AUTOMATIC\_NODES\_TO\_SURFACE, calibrated to describe interactions between Lagrangian solid surfaces.

```

*CONTACT_AUTOMATIC_SURFACE_TO_SURFACE_ID
$#   cid   title
      X    S-S
$#   ssid  msid  sstyp  mstyp  sboxid  mboxid  spr    mpr
      X    X    3      3      0      0      0      0
$#   fs    fd    dc     vc     vdc    penchk  bt     dt
      0.0  0.0  0.0   0.0   0.0    0      0.01.00000E20
$#   sfs   sfm   sst    mst    sfst   sfmt   fsf    vsf
      1.0  1.0  0.0   0.0   1.0   1.0   1.0    1.0
    
```

## E.4 Equations of state (EOS)

Table E.8: EOS card for EOS\_LINEAR\_POLYNOMIAL, calibrated to depict the behaviour of water.

```
*EOS_LINEAR_POLYNOMIAL_TITLE
EOS Water
$#   eosid      c0      c1      c2      c3      c4      c5      c6
      X      0.02.190000E99.223999E98.767000E9  0.4934  1.3937  0.0
$#   e0      v0
      205360.0  1.0
```

Table E.9: EOS card for EOS\_LINEAR\_POLYNOMIAL, calibrated to depict the behaviour of air at atmospheric pressure.

```
*EOS_LINEAR_POLYNOMIAL_TITLE
EOS Air
$#   eosid      c0      c1      c2      c3      c4      c5      c6
      1      0.0      0.0      0.0      0.0      0.4      0.4      0.0
$#   e0      v0
      253400.0  0.0
```

## **Chapter F**

# **Additional SHPB designs**

## **F.1 Introduction**

This appendix contains supplementary designs and schematics relevant to SHPB testing.



## F.2 Reservoir support stand

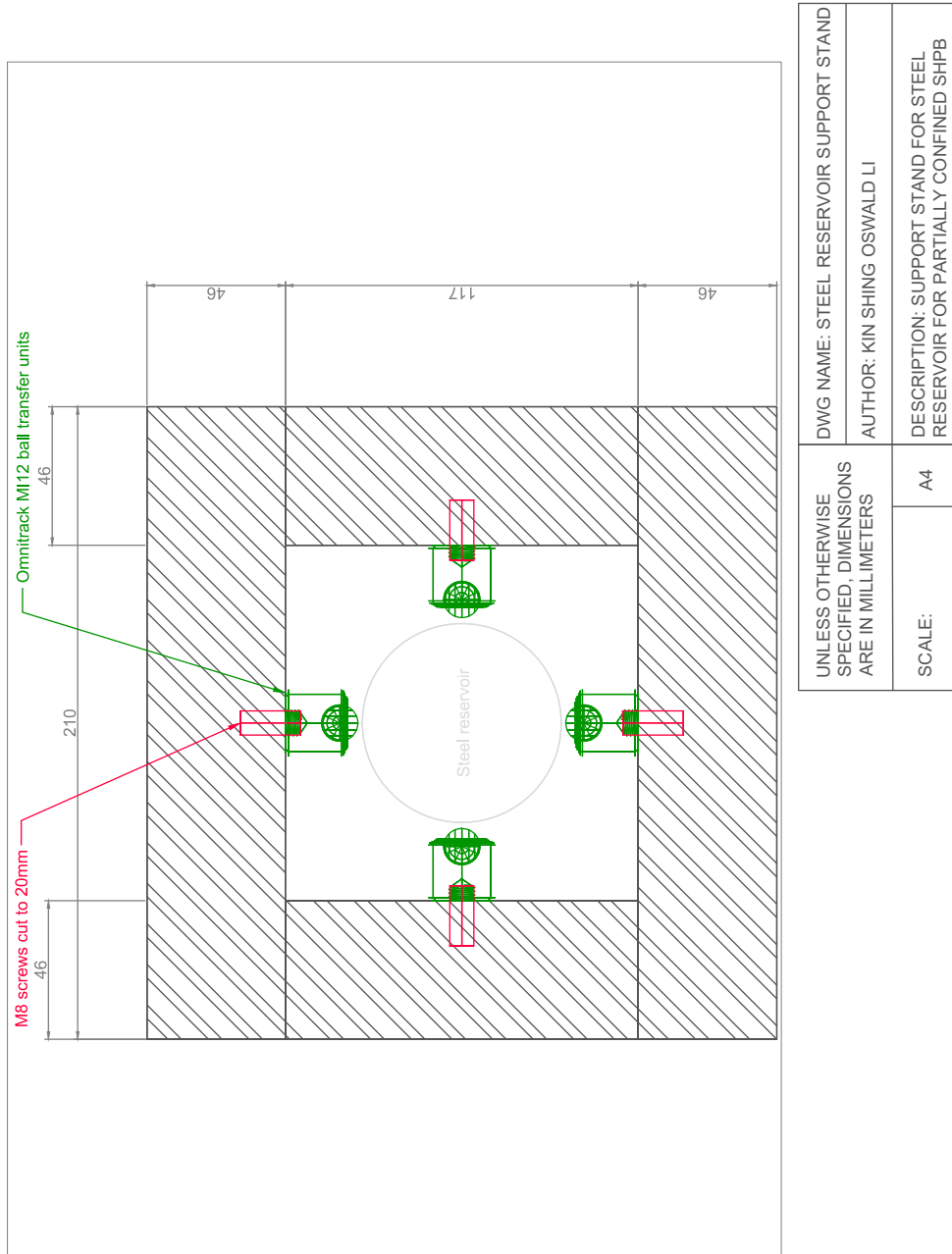


Figure F.1: Design for reservoir support stand for partial lateral confined SHPB apparatus.